

**Supramolecular Polymer  
Additives - Their Molecular  
Structure, Self-Assembly and  
Interaction with the Polymer**

**DISSERTATION**

ZUR ERLANGUNG DES AKADEMISCHEN GRADES  
DOKTOR DER NATURWISSENSCHAFTEN (DR.RER.NAT)  
AN DER FAKULTÄT FÜR BIOLOGIE, CHEMIE UND GEOWISSENSCHAFTEN  
DER UNIVERSITÄT BAYREUTH

Kasper Pieter van der Zwan

geboren in  
Ede (NL)  
Bayreuth, 2022



Die vorliegende Arbeit wurde in der Zeit von November 2017 bis Mai 2022 in Bayreuth am Lehrstuhl für Anorganische Chemie III unter Betreuung von Herrn Professor Dr. Jürgen Senker angefertigt.

Vollständiger Abdruck der von der Fakultät für Biologie, Chemie und Geowissenschaften der Universität Bayreuth genehmigten Dissertation zur Erlangung des akademischen Grades eines Doktors der Naturwissenschaften (Dr. rer. nat.).

Dissertation eingereicht am: 17.05.2022

Zulassung durch die Promotionskommission: 15.06.2022

Wissenschaftliches Kolloquium: 20.04.2023

Amtierender Dekan: Prof. Dr. Benedikt Westermann

Prüfungsausschuss:

Prof. Dr. Jürgen Senker

Gutachter

Prof. Dr. Markus Retsch

Gutachter

Prof. Dr. Peter Strohrriegel

Vorsitz

Prof. Dr.-Ing. Holger Ruckdäschel



FÜR MEINE ELTERN,  
MEINE FRAU  
UND MEINE KINDER



“NMR is wunderbar”

LEO VAN WÜLLEN



# Contents

<b>Danksagung</b>	<b>ix</b>
<b>Abbreviations</b>	<b>xiii</b>
<b>Abstract</b>	<b>xv</b>
<b>Zusammenfassung</b>	<b>xix</b>
<b>1 Introduction</b>	<b>1</b>
1.1 Supramolecular Polymer Nucleating Agents . . . . .	4
1.2 NMR Crystallography . . . . .	6
1.3 DNP Enhanced NMR Spectroscopy . . . . .	8
<b>2 Synopsis</b>	<b>13</b>
2.1 Molecular Structure Solutions . . . . .	14
2.2 Crystal Structure Solutions . . . . .	19
2.3 Investigating Minority Species in Polymers . . . . .	25
<b>References</b>	<b>35</b>
<b>3 Index of Publications</b>	<b>49</b>
3.1 Publications of this work . . . . .	49
3.2 Other Publications . . . . .	51
<b>4 Publications</b>	<b>53</b>

4.1	Synthesis and Characterization of Dual-Functional Carbamates as Blowing and Curing Agents for Epoxy Foam . . . . .	53
4.2	Structural Analysis of CO <sub>2</sub> loaded Diamine Derived from Aqueous Synthesis Route for Epoxy Foaming . . . . .	80
4.3	Crystal Engineering of Supramolecular 1,4-Benzene Bisamides by Side-Chain Modification - Towards Tuneable Anisotropic Morphologies and Surfaces . . . . .	103
4.4	Highly Efficient Supramolecular Nucleating Agents for Poly(3-hexylthiophene) . . . . .	130
4.5	Kinked Bisamides as Efficient Supramolecular Foam Cell Nucleating Agents for Low-Density Polystyrene Foams with Homogeneous Microcellular Morphology . . . . .	158
4.6	<sup>19</sup> F MAS DNP for Probing Molecules in Nanomolar Concentrations: Direct Polarization as Key for Solid-State NMR Spectra without Solvent and Matrix Signals . . . . .	197
4.7	DNP Enhanced <sup>19</sup> F- <sup>19</sup> F DQ Build-Up Curve Confirms Crystal Structure of Supramolecular Additive in PS at Technical Concentration for Batch Foaming . . . . .	223
4.8	DNP Enhanced Solid-State NMR Spectroscopy Meets Microplastic - Sample Preparation for Optimal Sensitivity Enhancement . . . . .	257

## Danksagung

Als Erstes bedanke ich mich bei meinem Doktorvater Prof. Dr. Jürgen Senker für die Möglichkeit meine Promotion am Lehrstuhl ACIII machen zu können. Vielen Dank für die vielen anregenden wissenschaftlichen Diskussionen, die immer respektvoll und wertschätzend ablaufen. Vielen Dank außerdem für die Unterstützung und den Glauben in den Momenten in denen ich starke Zweifel hatte, um mich wieder auf einen grünen Zweig zu bringen.

Direkt anschließen möchte ich alle Mitarbeiter der AC III, die während meiner Zeit am Lehrstuhl dabei waren: Carsten, Tobi, Adrian, Helen, Beate, Marion, Christoph K., Simon, Lisa, Patrick, Sven, Thomas W., Dominik, Marko, Marcel, Anika, Tomas K., Björn, Max und Alex. Mit euch allen hatte ich eine schöne Zeit. Besonders freut mich, dass man mit jedem am Lehrstuhl immer erhellende Diskussionen führen kann und alle sehr hilfsbereit sind.

Vier Personen möchte ich trotzdem noch besonders hervorheben. Paul und Christoph Z., vielen Dank, dass ihr durch die spannenden Praktika das Interesse für die ACIII bei mir geweckt habt.

Ein ganz großes Dankeschön geht an Robert, dafür, dass wir so unzählige Raucher- und Kaffeepausen verbracht haben um uns gegenseitig voranzubringen. Wirklich gerne denke ich daran zurück, dass ich jederzeit mit der Frage "Robert, hast du Lust über etwas nachzudenken?" in dein Büro kommen konnte.

Abschließend geht auch ein riesiges Dankeschön an Renée! Vielen Dank, dass ich in den über fünf Jahren am Lehrstuhl meistens nur meinen Kopf zur Seite legen musste um am Bildschirm vorbei meine Fragen zu stellen. Den Großteil meines NMR Wissens verdanke ich dir!

A big thank you goes to the DNP Lab in Grenoble for giving me a very warm welcome. I learned a lot about DNP in this three months. Thank you, Gaël, Daniel, Sabine, Saumya, Diego and Akshay. A special thanks also goes to Adam for the hikes we did together.

Vielen Dank auch an alle meine Kooperationspartner, die an den Publikationen mitgewirkt haben. Es ist schön, dass ihr alle immer ein offenes Ohr hattet und daran interessiert wart unsere Themen weiterzubringen. Vielen Dank Christoph S., Basti, Felix, Klaus, Nora, Prof. Dr. Strohriegel, Prof. Dr. Schmidt (MCI, UBT); Wiebke, Prof. Dr. Risse (PC, FU Berlin); Fabien, Christian R.(Bruker); Merve, Michaela, Christian B., Prof. Dr. Ruckdäschel, Prof. Dr. Altstädt (Polymer Engineering, UBT); Torsten, Prof. Dr. Buntkowsky (PC, TU Darmstadt).

Vielen Dank an meine Praktikanten und Praktikantinnen. Vielfach habt ihr eine neue Perspektive auf meine Fragestellungen gebracht. Vielfach hat mich die Betreuung des Praktikums auch aus kleinen Motivationslöchern gezogen, weil es einfach schöner ist, gemeinsam an einem Projekt zu arbeiten. Vielen Dank Pascal, Friederike, Celina, Annalena, Dragan, Melanie, Anika (hier nochmal), Ingmar und ein ganz besonderer Dank geht an Tamara, für die schöne Zeit während deiner Praktikums-, Hiwi- und Bachelorarbeitszeit und der vielen produktiven Arbeit, die weit über die Studienanforderungen hinausgingen. Ich freue mich, dass sich daraus auch eine Freundschaft entwickelt hat.

Weiterhin gilt ein ganz großer Dank meiner Familie! Vielen Dank Manu, für die unglaublich schöne Zeit, die wir zusammen erleben und die damit verbundene erholsame Ablenkung von der Arbeit. Vielen Dank, für die unglaublich große Geduld dafür, dass ich während der Promotion häufig lange gearbeitet habe und vielen Dank für die Motivationshilfe und den Glauben, wenn es mal nicht so läuft. Vielen Dank an meine beiden Jungs Samuel und Aaron, dafür, dass ihr zwei es ohne viel zu tun schafft, mir ein Lächeln ins Gesicht zu zaubern und mich wieder aufzubauen!

Ganz herzlich möchte ich mich auch bei meinen Eltern bedanken, für die Unterstützung während des gesamten Studiums und für den ständigen Glauben in mich. Weiterhin gilt mein Dank auch meinen Schwiegereltern.

Vielen Dank auch an meine Freunde, die ich im Studium kennen gelernt habe und die mich mit unzähligen Spieleabenden, Feiern und Reisen durch die Promotion begleitet haben. Vielen Dank an Stefan, Sabrina, Marius, Levke, Leah, Janina, Merten, Tobi, Martin, Ping, Hannah, Robin und Jan.

Ebenfalls vielen Dank an meine Freunde, die mich schon seit der Schulzeit begleiten und mit denen trotz der großen Entfernung alles noch wie früher ist und man sich bei den seltenen Gelegenheiten der Treffen immer noch blendend versteht. Vielen Dank, Darius, Heinrich, Kati, Felix, Niklas, Julia, Jannes, Laura, Peter, Lea, Yannick, Bernhard, Laura, Daniel, Steffen und Sebi.

Abschließend noch ein großes Dankeschön an die deutsche und bayerische Rugbyfamilie, besonders natürlich an meinen Verein, die Bayreuther Turnerschaft, aber auch an alle anderen Menschen, die ich auf und in den unzähligen Rugbyfeldern und Schulungsräumen getroffen habe und die Rugby zu einem so besonderen Sport machen.



## Abbreviations

<b>B-AEP</b>	N-Aminoethylpiperazine Carbamate
<b>B-DMC</b>	4-Methylcyclohexane-1,3-Diamine Carbamate
<b>B-IPDA</b>	Isophorone Diamine Carbamate
<b>BBA</b>	1,4-Benzene Bisamide
<b>BDPA</b>	1,3-Disdiphenylene-2-Phenylallyl
<b>BTA</b>	1,3,5-Benzene Trisamide
<b>CBA</b>	Chemical Blowing Agent
<b>CE</b>	Cross Effect
<b>CSA</b>	Chemical Shift Anisotropy
<b>DFT</b>	Density Functional Theory
<b>DNP</b>	Dynamic Nuclear Polarisation
<b>DQ</b>	Double Quantum
$\epsilon_{on/off}$	DNP enhancement
<b>EPR</b>	Electron Paramagnetic Resonance
<b>F-BTA</b>	1,3,5-Tris(2-Fluoro-2-Methylpropionylamino)Benzene
<b>FC</b>	Film Casting

<b>GF</b>	Glass Forming
<b>HT</b>	High Temperature
<b><i>i</i>-PP</b>	Isotactic Poly(propylene)
<b>IWI</b>	Incipient Wetness Impregnation
<b>LT</b>	Low Temperature
<b>MAS</b>	Magic-Angle-Spinning
<b>MP</b>	Secondary Microplastic
<b>NA</b>	Nucleating Agent
<b>NA1</b>	<i>N,N'</i> -1,4-Phenylenebis[4-Pyridinecarboxamide]
<b>NMR</b>	Nuclear Magnetic Resonance
<b>P3HT</b>	Poly(3-hexylthiophene)
<b>PA</b>	Polarising Agent
<b>PP</b>	Poly(propylene)
<b>PS</b>	Poly(styrene)
<b>S</b>	Absolute Sensitivity
<b>SE</b>	Solid Effect
<b>SEM</b>	Scanning Electron Microscopy
<b>ss-NMR</b>	Solid State Nuclear Magnetic Resonance
<b>TCE</b>	1,1,2,2-tetrachloro-ethane
<b>THF</b>	Tetrahydrofuran
<b>TriCE</b>	Trichloro Ethylene

## Abstract

This work aims to shed light on the complex interplay of polymers and their supramolecular additives with an emphasis, but not exclusively, on polymer foams. To understand the working mechanism, investigations of the molecular and crystal structure are a prerequisite, since these properties define the stability, morphology and surface properties of the additives within the polymer. Therefore, the bulk structures of model substances and technically relevant additives are investigated. However, due to polymorphism the structure in the polymer can be different. To be able to confirm the structure within the polymer, method development for the analysis of minority species within polymers is included and applied. Again, this is done for model and technical systems.

The thesis starts with the molecular structure solution of four dual functional chemical blowing agents (CBA) for epoxy foaming. The CBAs are based on diamines that react with  $\text{CO}_2$  to the metastable CBAs. Solid-state nuclear magnetic resonance (ss-NMR) spectroscopy is used to analyse the structures. If the synthesis of the CBAs is done in ethanol, carbamates are formed. The question we answered was which of the two chemically different amine groups captures the  $\text{CO}_2$  to form the carbamate. For a more sustainable synthesis, the solvent was switched to water. In this case only isophorene diamine (IPDA) reacts with  $\text{CO}_2$ . In depth ss-NMR analysis shows that in this case a urea group including both amine groups forms.

The second part starts with a concept study that analyses how the molecular structure of benzene bisamides (BBA) effects the morphology and surface

polarity of the self-assembled nanoobjects. The key finding is that the bulkiness of the side group directs the formation of a specific crystal structure. Because of the different strengths of the molecular interactions in the crystallographic directions, the crystal faces grow with different speeds. Therefore, BBAs with thin side groups, whose crystal structures only have one direction of preferred growth, macroscopically form ribbons, whereas BBAs with bulky side groups that direct into a crystal growth with two directions of favoured growth form platelets. The terminating surface of the ribbons or platelets consists of the end of the side groups. Thus, bulkiness and polarity of the side groups of BBAs already define the morphology and surface properties of the BBA nanoobjects.

This concept is applied to find very efficient crystal nucleation agents for the semi-conducting polymer poly(3-hexyl-thiophene) (P3HT). Pyridine end groups are slim enough to direct into the crystal structure that macroscopically forms ribbons. The spacing of the pyridine groups at the surface of the nanoobjects provides an excellent epitaxial and electronic match for the thiophene rings of the P3HT backbone.

The concept can even be extended to kinked bisamides, whose central core consists of two phenyl rings that are linked by a methylene bridge, forming the kink in the structure. With slim side chains these sub-class of bisamides macroscopically also self-assembles to ribbons that act as very efficient foam cell nucleating agents for poly(styrene) (PS). An analysis of the crystal structure shows that the synthon of the crystal structure is the same as for the linear BBAs. This underlines the wide applicability of the introduced concept.

To analyse the crystal structures of the additives within polymers at their technical concentrations of a few 100 ppm to a maximum of 2 wt.%, the intrinsically low sensitivity of NMR spectroscopy must be overcome. Therefore, we use hyperpolarisation with dynamic nuclear polarisation (DNP). To distinguish between additive signals, the ones of the polymer and the radical containing solution needed for DNP enhancement, we used the fluorinated benzene trisamide 1,3,5-tris(2-fluoro-2-methylpropionylamino)benzene (F-BTA) and measured the  $^{19}\text{F}$  resonance. Since  $^{19}\text{F}$  is rarely used for DNP enhanced NMR spectroscopy, a study investigating the polarisation mechanism and exploiting the potential of this nucleus is included. This study shows that a direct polarisation of  $^{19}\text{F}$  nuclei up to 25 Å with enhancements up to 260 is achieved. Furthermore, additive

resonances within isotactic poly(propylene) (*i*-PP) at a concentration of 600 ppm are detected.

For analysing PS with DNP adding a solvent is not feasible as it is soluble in many organic solvents. Therefore, in this case, the radical is extruded with the polymer. Since this is an emerging way of sample preparation, the preparation parameters are optimised. A radical concentration of 0.5 wt.% at an extrusion temperature of 180 °C gives the highest sensitivity of both PS and F-BTA resonances. With these conditions, we were able to measure the first  $^{19}\text{F}$ - $^{19}\text{F}$ -DQ build-up curve with DNP enhancement, confirming that the HT polymorph of F-BTA forms within PS.

The knowledge on the sample preparation for DNP enhanced PS samples is then transferred to another minority species, namely defects resulting from accelerated weathering. With DNP enhancement it was possible to reduce the detection limit for these defects by one order of magnitude.



## Zusammenfassung

In dieser Arbeit geht es um die komplexe Interaktion zwischen Polymeren und ihren supramolekularen Additiven mit einem Schwerpunkt auf Polymerschäumen. Um die Funktionsweise zu verstehen, sind Untersuchungen der Molekül- und Kristallstruktur eine Voraussetzung, da diese Eigenschaften die Stabilität, Morphologie und Oberflächenpolarisation der Additive im Polymer bestimmen. Daher werden die Festkörperstrukturen von Modellsubstanzen und technisch relevanten Additiven untersucht. Allerdings kann auf Grund von Polymorphie die Struktur im Polymer eine andere sein. Um die Struktur im Polymer bestätigen zu können, wird die Methodenentwicklung zur Analyse von Minoritätsspezies im Polymer vorangetrieben und angewendet. Diese Studien beinhalten erneut sowohl Modellsubstanzen als auch technisch relevante Polymer/Additiv Systeme.

Die Arbeit beginnt mit der molekularen Strukturaufklärung von vier bifunktionalen chemischen Treibmitteln (CTM) für Epoxidschäume. Die CTMs basieren auf Diaminen, die mit  $\text{CO}_2$  zu den metastabilen CTMs reagieren. Es wird Festkörper NMR (FK-NMR) Spektroskopie zur Strukturaufklärung verwendet. Wird die Synthese der CTMs in Ethanol durchgeführt, entstehen Carbamatverbindungen. Die beantwortete Fragestellung war, welche der beiden chemisch verschiedenen Aminogruppen das  $\text{CO}_2$  bindet und zum Carbamat reagiert. Für eine nachhaltigere Synthese wurde Wasser ebenfalls als Lösungsmittel verwendet. In diesem Fall reagiert ausschließlich Isophorondiamin mit  $\text{CO}_2$ . Eine ausführliche FK-NMR spektroskopische Untersuchung zeigt, dass in diesem Fall eine Harnstoffgruppe gebildet wird, die beide Amine verbrückt.

Der zweite Teil beginnt mit einer konzeptionellen Studie darüber, wie die molekulare Struktur von Benzolbisamiden die Morphologie und die Oberflächenpolarisation der selbst-assemblierten Nanoobjekte bestimmt. Es stellte sich heraus, dass die Sperrigkeit der Seitengruppen die Bildung einer bestimmten Kristallstruktur bedingt. Auf Grund der unterschiedlichen Stärke der molekularen Wechselwirkungen in die unterschiedlichen Raumrichtungen, wachsen die verschiedenen Kristallflächen mit individuellen Geschwindigkeiten. Dies führt dazu, dass Benzolbisamide mit schmalen Seitengruppen, deren Kristallstrukturen nur eine bevorzugte Wachstumsrichtung haben, makroskopisch Bänder bilden. Wohingegen Benzolbisamide mit sperrigen Seitengruppen, die zu einem Kristallwachstum in zwei Richtungen dirigieren, Plättchen ausbilden. Die Oberflächen der Bänder oder Plättchen bestehen aus den Enden der Seitengruppen. Folglich definieren Sperrigkeit und Polarität der Seitengruppen von Benzolbisamiden die Morphologie und Oberflächeneigenschaften der Benzolbisamidnanoobjekte.

Dieses Konzept wird anschließend angewendet um effiziente Kristallnukleierungsmittel für Poly-3-Hexylthiophene (P3HT) zu finden. Pyridinendgruppen sind schmal genug, um die Kristallisation in die Struktur zu dirigieren, die makroskopisch Bänder ausbildet. Der Abstand zwischen Pyridingruppen auf der Oberfläche der Nanoobjekte gewährleistet eine herausragende epitaktische und elektronische Anbindung der Thiophenringe des P3HT.

Das Konzept lässt sich sogar auf gewinkelte Bisamide übertragen, deren Kern aus zwei Benzolringen besteht, die über eine Methylenbrücke verbunden sind, die den Winkel erzeugt. Mit schmalen Seitenketten selbst-assembliert diese Unterklasse der Bisamide ebenfalls zu bandartigen Nanoobjekten, die sehr effizient die Schaumzellbildung von Polystyrol (PS) nukleieren. Die Aufklärung der Kristallstruktur zeigt, dass das Syntheton dasselbe ist wie für die linearen Benzolbisamide. Dies unterstreicht die breite Anwendbarkeit des vorgestellten Konzepts.

Um die Kristallstrukturen der Additive in ihren niedrigen, technischen Konzentrationen im Polymer von wenigen 100 ppm bis 2 wt.% untersuchen zu können, muss die intrinsisch niedrige Sensitivität der NMR Spektroskopie überwunden werden. Dazu nutzen wir Hyperpolarisation mittels dynamischer Kernspinpolarisation (DNP). Um zwischen den Signalen des Additivs, des Polymers und die für die DNP-Verstärkung benötigte, Radikale enthaltenden, Lösung zu

unterscheiden, verwenden wir das fluorierte Benzoltriamid 1,3,5-Tris(2-fluoro-2-methylpropionylamino)benzol (F-BTA) und messen die  $^{19}\text{F}$  Resonanz. Da  $^{19}\text{F}$  für DNP verstärkte NMR Spektroskopie selten verwendet wird, ist eine Studie eingefügt, die den Polarisationsmechanismus und das generelle Potential des Kerns aufklärt. Diese zeigt, dass eine direkte Polarisation über eine Entfernung von bis zu 25 Å mit einer Verstärkung von 260 stattfindet. Ferner wurden die Additivresonanzen in isotaktischem Polypropylen in einer Konzentration von 600 ppm detektiert.

Um PS Proben mit DNP zu messen, ist es nicht praktikabel die Proben mit einem Lösungsmittel zu versetzen, da PS sich in vielen organischen Lösungsmitteln löst. Daher wird in diesem Fall das Radikal mit dem Polymer extrudiert. Da es sich hierbei um eine sich entwickelnde Probenpräparationsmethode handelt, wurden die Prozessparameter optimiert. Bei einer Radikalkonzentration von 0.5 wt.% und einer Extrusionstemperatur von 180 °C werden sowohl für die F-BTA als auch für die PS Resonanzen die höchsten Sensitivitäten erreicht. Mit diesen Bedingungen wurde die erste  $^{19}\text{F}$ - $^{19}\text{F}$ -Doppelquantenaufbaukurve mit DNP Verstärkung gemessen, die bestätigt, dass sich das Hochtemperatur-Polymorph von F-BTA in PS bildet.

Das gesammelte Wissen der Probenpräparation für die DNP Verstärkung von PS Proben wird verwendet, um eine andere Minoritätskomponente, nämlich Defekte, die durch kontrollierte Bewitterung von Mikroplastikpartikeln entstehen, zu untersuchen. Mit DNP Verstärkung war es möglich das Detektionslimit der Signale mit FK-NMR Spektroskopie um eine Größenordnung herabzusetzen.



## Introduction

In the 21<sup>st</sup> century, a world without polymer materials has become unthinkable, which is resembled by a worldwide production of 360 million tons in 2018.<sup>[1]</sup> Polymers feature a lot of advantages like being mostly cheap, lightweight and easy processable. Another big advantage of polymers is their foamability, creating a material that additionally to the pre-mentioned properties also shows excellent heat and sound insulation.<sup>[2]</sup> The most prominent polymer materials are the commodity plastics poly(ethylene), PP and PS.

However, for every polymer application - foam or not - many additives are included in the process.<sup>[3]</sup> For PP foils these are, among others, UV-stabilisers<sup>[4,5]</sup> and clarifiers.<sup>[6-11]</sup> UV-stabilisers are small molecules that react with radicals resulting from UV irradiation that would otherwise lead to a degradation of the material.<sup>[12]</sup> Contra intuitively, clarifiers are mostly additives that provide nucleation sites for the semi-crystalline polymer. If the amount of crystallites within the polymer increases, naturally the size of each individual crystallite decreases. As soon as most of the crystallites are below the size of half of the wave length of optical light, the material appears transparent.<sup>[13]</sup>

Common additives for foam products are nucleation agents<sup>[14]</sup> and blowing agents.<sup>[15]</sup> Blowing agents are the gases that lead to the foaming of the material. They can either be physically dissolved in the pressurised sample<sup>[16]</sup> or chemically bound to another molecule that decomposes when heated.<sup>[17]</sup> Nucleation agents are needed in foams to provide sites where the gas molecules accumulate and form foam bubbles.<sup>[18]</sup> When more nucleation sites are present, the resulting foam cells are smaller, more homogeneous in size and well distributed throughout the material, leading to better insulation because of more phase boundaries and isotropic properties in the material.<sup>[19-21]</sup>

A class of additives that has various applications including the nucleation of semi-crystalline polymers and polymer foams is the class of supramolecular additives.<sup>[22-24]</sup> These organic compounds consist of functional groups that are capable of reversal chemical interactions of which the most prominent is the hydrogen bond.<sup>[25]</sup> The big advantage of this additive class is that the molecular building units are soluble in a polymer melt.<sup>[21]</sup> Therefore, the supramolecular objects form when the melt is cooled down. This provides a very homogeneous distribution of the additive objects, allows for low concentrations and ensures a good processability.<sup>[19]</sup>

Mostly, the development of new additives follows a trial and error scheme. Therefore, analysis on the structure and working mechanism of polymer additives are of fundamental importance. This analysis needs to cover all length scales from molecular investigation over crystal structure analysis to the distribution and structure within the polymer material.

The molecular structure of the additive is important, as it is the basic building block of a material that defines its interactions with itself, leading to crystalline structures, but it also defines the interactions with the polymer and its stability and solubility within. For CBAs, the standard analytical methods are not always feasible.<sup>[26]</sup> ss-NMR spectroscopy as a non destructive method with a low energy impact is a perfect tool for the analysis of such structures. Apart from the well-known analysis of the chemical shift, ss-NMR spectroscopy offers a wide range of measurement techniques that probe connectivities and electron densities of whom some are exclusive to the solid state.<sup>[27-29]</sup>

As already mentioned, a key feature of nucleation agents is that they provide as many nucleation sites as possible. This requires a high surface to volume ratio. Therefore, the shape of the (single) crystals of efficient nucleating agents (NA) is often one or two dimensional.<sup>[30,31]</sup> This makes an analysis with single-crystal X-ray diffraction very challenging as the scattering intensity in at least one direction is very weak. For this reason, supramolecular crystal structures are frequently solved with an NMR crystallographic approach.<sup>[32-35]</sup> This method combines powder X-ray diffraction (PXRD), ss-NMR spectroscopy and computational modelling and is an ideal tool for anisotropically shaped crystals or in general for structures that only yield micro crystalline powders.<sup>[36,37]</sup>

The crystal structure defines the shape and the surface properties of the self-assembled objects.<sup>[38–41]</sup> Since solvent polarity and crystallisation temperature influence the nucleation and crystallisation process<sup>[42]</sup> and polymorphs are common for supramolecular systems,<sup>[43]</sup> the most stable polymorph at ambient conditions is not necessarily the one that crystallises within the polymer.<sup>[44–46]</sup> Therefore, it is important to know the crystal structure of the additive in the polymer.<sup>[9]</sup> For most technical concentrations, the sensitivities of X-ray diffraction and NMR spectroscopy do not suffice. A technique to get insight into the properties of minority species within a polymer nonetheless is hyperpolarisation of the NMR signal by DNP.<sup>[47–50]</sup> For this technique, persistent radicals are introduced to the sample.<sup>[51–54]</sup> With microwave irradiation applied simultaneously to the NMR experiment, the high electron magnetic polarisation is transferred to the nuclear magnetic polarisation, allowing for a theoretical enhancement of  $^1\text{H}$  NMR signals by a factor of 658.<sup>[55]</sup> This significantly reduces the detection limit of NMR spectroscopy and enables the measurement of additives and defects in polymers at concentrations down to a few hundred ppm.<sup>[46]</sup>

In this work, mechanistic investigations on all three length scales are covered. The molecular and crystal structures of supramolecular objects are investigated by established ss-NMR and NMR crystallographic techniques, introducing and applying new concepts of molecular design. This includes the connection between the crystal structure and the morphology of the self-assembled nanoobjects. Furthermore, the effectiveness of the nucleation is explained by the crystal structure and morphology of the additives. However, these crystal structures need to be confirmed within the polymer for very low additive concentrations. Therefore, these minority species must be analysed against a big polymer background. DNP enhanced NMR spectroscopy is a versatile tool for such an analysis and consequently sample preparation for polymer samples is developed and used. Therewith, the polarisation mechanism and general potential of  $^{19}\text{F}$  enhanced DNP spectroscopy is explored. This optimisation enabled the analysis of the crystal structure of F-BTA within *i*-PP and PS. Furthermore, the gained knowledge is used for the first study on polymer defects resulting from accelerated weathering with DNP enhanced NMR spectroscopy.

## 1.1 Supramolecular Polymer Nucleating Agents

Supramolecular structures are similar to polymers.<sup>[22,24]</sup> The difference is that in a polymer the monomeric units are connected by covalent bonds,<sup>[56]</sup> whereas supramolecular structures are connected by intermolecular interactions<sup>[25]</sup> like hydrogen bonds,<sup>[44]</sup> halogen bonds,<sup>[57]</sup>  $\pi$ -stacking,<sup>[58]</sup> or a combination thereof.<sup>[8,43]</sup> This leads to the big advantage of supramolecular structures compared to polymers: the easy reversibility. In solution and molten state, these intermolecular aggregation forces are easily broken and therefore the molecules are isolated and form an isotropic liquid state. When the solution becomes supersaturated or the melt is cooled down, the attractive forces come into play and the molecules self-assemble to supramolecular objects.<sup>[30,59]</sup> These objects can be 1-dimensional fibres,<sup>[41]</sup> 2-dimensional platelets<sup>[30]</sup> or 3-dimensional aggregates.<sup>[60,61]</sup>

The fundamental concept of supramolecular chemistry is the supramolecular synthon.<sup>[25]</sup> It can be compared to reactive groups in organic chemistry. The synthons are the precursors that form the attractive intermolecular forces, mentioned above and determine the direction of the crystal growth. In this work the focus lies on hydrogen bonds and more precisely on the N-H $\cdots$ O hydrogen bonds of amide groups.

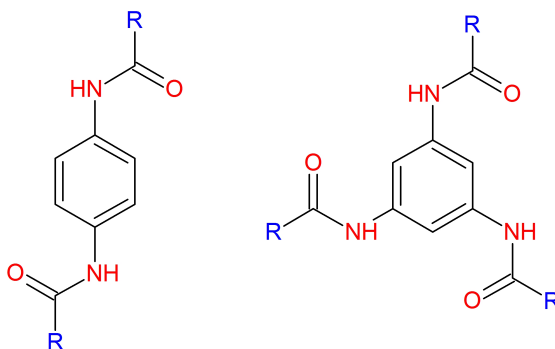


**Figure 1.1: General scheme of BBA (left) and BTA (right). The amide group is labelled red and the peripheral groups are denoted with a blue R.**

The studied materials are BBAs and benzene trisamides (BTA).<sup>[62]</sup> In general these molecules have a benzene core with amid functions at position 1 and 4 (BBA) or 1,3 and 5 (BTA) and some peripheral groups. This general concept is resembled in Figure 1.1. The side groups offer a big variation opportunity to tune the properties<sup>[62]</sup> of the self-assembled aggregates that can even effect the packing behaviour.<sup>[31,44,45]</sup> Long aliphatic side groups will lead to liquid crystalline

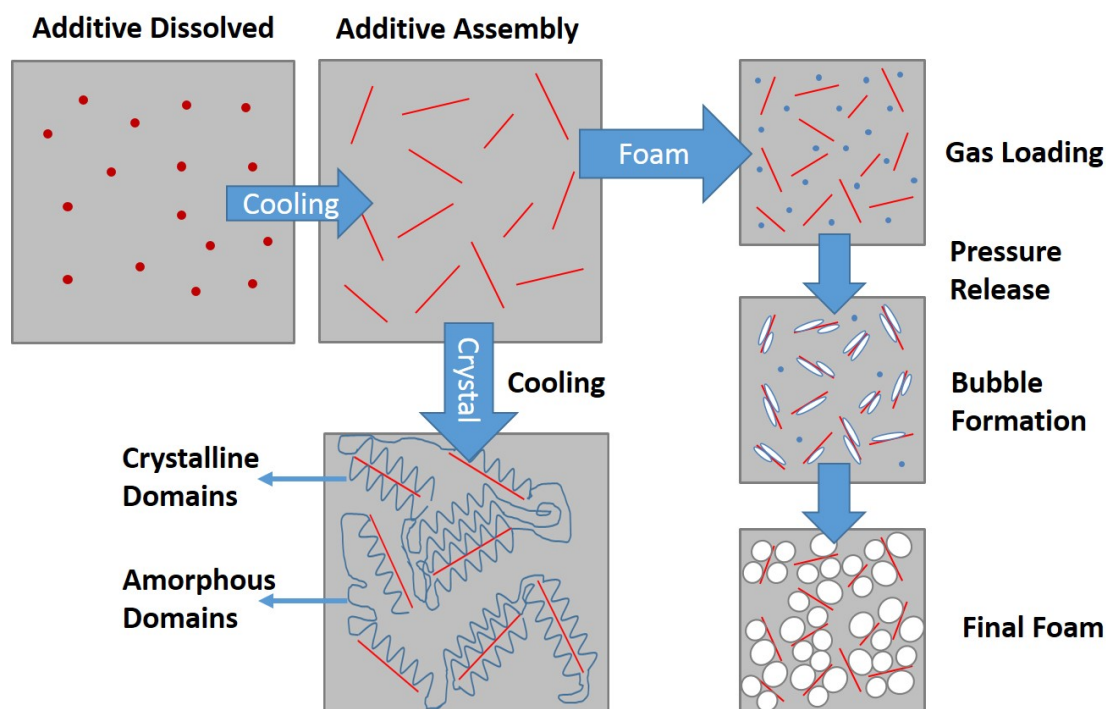


**Figure 1.2:** Sketch of the concept of supramolecular nucleation of foams and semi-crystalline polymers. At the top left, the red dots resemble the molecularly dissolved additive in the polymer melt. When cooling down, the additive crystallises within the polymer melt. When nucleating a semi-crystalline polymer, the melt is cooled down below the melting point of the polymer and it crystallises on top of the supramolecular nanoobjects. Since every polymer is only semi-crystalline, amorphous regions remain. When nucleating a foam, a blowing agent must be applied to the sample as resembled by the blue dots in the top right part of the figure. When the pressure is released, foam bubbles preferentially nucleate at the surface of the supramolecular nanoobjects. These objects are, therefore, mainly found on the surface of the foam cell walls of the final foam.

properties.<sup>[63]</sup> Whereas for short side chains, especially for BTAs, columnar structures with macro dipoles along the columns arise.<sup>[45,64,65]</sup> The side chains can also contain synthons themselves, leading to even more interesting structures.<sup>[66]</sup> If only aliphatic side chains are present, the self-assembly is solely governed by the hydrogen bonds of the amide that can be accomplished by the  $\pi$ -stacking of the benzene cores.<sup>[8]</sup> A newer approach is to substitute the core, for example by a di-phenyl-methylene core, leading to kinked bisamides.<sup>[21]</sup>

BTAs can be used as ferroelectric organics,<sup>[45,63,65]</sup> as flees obtained by electrospinning<sup>[67]</sup>, and as filter materials.<sup>[68]</sup> However, the most prominent application is the use of BBAs and BTAs as crystal nucleation agents for

poly(vinylidene fluoride)<sup>[7]</sup> or isotactic polypropylene (*i*-PP)<sup>[6,10,11,69]</sup> or as foam nucleation agent for *i*-PP<sup>[19,70]</sup> or PS.<sup>[20,21]</sup> The big advantage of this material class is that supramolecular additives can be molecularly dissolved in polymer melts (Figure 1.2 top left).<sup>[19]</sup> This leads to a homogeneous distribution of the additive within the polymer. When the polymer melt is cooled down, the supramolecular (nano-)objects are formed inside the polymer (Figure 1.2 middle).<sup>[9,71]</sup> For foam nucleation, the supramolecular object provides a heterogeneous bubble nucleation site (Figure 1.2 right column). In this case it is important that the nucleating agent (NA) is homogeneously distributed and does not negatively interfere with the processing.<sup>[72]</sup> For crystal structure nucleation (Figure 1.2 bottom), the situation is more complex. To have efficient nucleation properties, there needs to be a lattice match of the NA and the semi-crystalline polymer that enables an epitaxial growth of the polymer on the NA.<sup>[73,74]</sup> This means that one lattice parameter, or another reoccurring distance in the crystal structure of the NA, and the polymer must match.<sup>[11,73]</sup> Therefore, knowing the crystal structures of potential NAs is of fundamental importance.

## 1.2 NMR Crystallography

Supramolecular NAs often crystallise in the form of fibres or platelets, which is a desired feature for their use as NA. Therefore, single-crystals whose size in all three dimensions is suitable, to solve the crystal structure by single-crystal X-ray diffraction are rarely obtained. Therefore, the crystal structure needs to be solved on the powdered material. For best results, a combined approach of PXRD, solid-state-NMR (ss-NMR) spectroscopy and quantum-chemical calculations is taken. This approach is often referred to as NMR crystallography.<sup>[32,33,35]</sup>

In X-ray diffraction, the incoming X-ray beam is scattered at the electron cloud of each atom. Because of the long range order in the crystal and the fact that the wave length of the beam is on the order of inter atomic distances, the beam is diffracted at the crystal lattice, leading to the characteristic interferences of diffraction that are described by Bragg's equation (Figure 1.3).<sup>[75]</sup>

$$n \cdot \lambda = 2d_{hkl} \cdot \sin\Theta \quad (1.1)$$

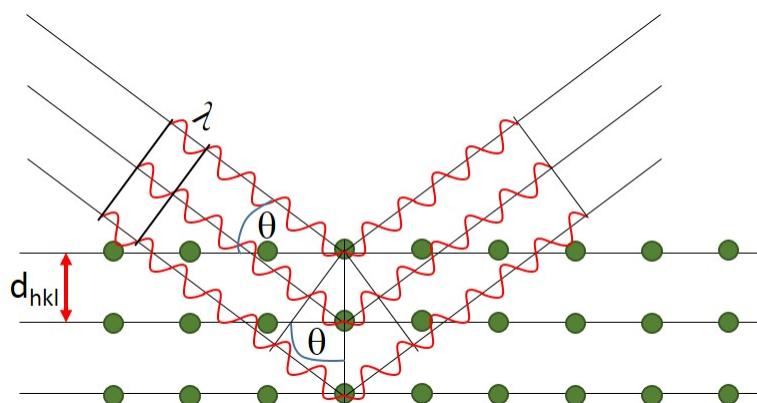


**Figure 1.3:** Graphical representation of Bragg's law. The green dots represent atoms that are arranged on a crystal lattice. The red waves represent the incoming X-ray beam with the wave length  $\lambda$  that is phase coherent. Constructive interference occurs when the distance  $d_{hkl}$  between two lattice planes is such that for a certain angle  $\Theta$  the optical path difference is a multiple of the wave length.

For single crystal X-ray diffraction, the reflections are collected in all three dimensions and for different crystal orientations. However, only the amplitude of the diffracted wave is collected and the information on the phases is not detectable in the experiment.<sup>[76]</sup> By indexing the reflections, the lattice parameters and the space group of the crystal structure can be found.<sup>[75]</sup> The phases contain important information about the atomic or molecular position and arrangement in the unit cell.<sup>[76]</sup> If the phases were known a fourier transformation of the diffraction data would result in a map of the electron density from which the structure could be easily solved. Therefore, crystallographers developed different techniques to retain the loss of information, to be able to solve the complete crystal structures.<sup>[76]</sup> For the crystal structure solution of small molecules, usually direct methods are used to get the phases back.<sup>[77-79]</sup> These methods imply that some phases are guessed and if these provide a chemically sensible structure the other phases can be deduced.<sup>[76]</sup> In PXRD, the three dimensional reciprocal space is projected into one dimension, leading to an overlap of symmetry-equivalent reflections and to an accidental overlap of reflections corresponding to the same or similar lattice spacings.<sup>[80]</sup> This additional loss of information in PXRD is the reason why it was mainly used for a phase control when the technique was established. However, Hugo Rietveld, who investigated magnetic phases with neutron scattering on powders, invented a least squares refinement method to solve crystal structures on powdered samples.<sup>[80]</sup> This method, which still relies on direct methods for the initial structure solution,

was subsequently transferred to X-ray data in the 1970s and 80s<sup>[81,82]</sup> and with increasing computer performances it became a well-established technique to solve crystal structures of powders.<sup>[83,84]</sup>

Nonetheless, it is still challenging to solve a crystal structure solely based on the PXRD data. ss-NMR spectroscopy can help to identify between space groups, as it can identify the content of the asymmetric unit.<sup>[31,44]</sup> Furthermore, it can confirm or exclude models by distance and dynamic measurements.<sup>[8,9,85]</sup> NMR experiments are often accomplished by computational modelling with forcefields<sup>[86]</sup> or density functional theory (DFT)<sup>[87,88]</sup> methods. With these methods, the rigid bodies for the structure solution step are refined<sup>[30,74]</sup> or existing models are optimised.<sup>[45]</sup> Furthermore, DFT can be used to calculate NMR parameters that can be used to simulate NMR spectra that can be compared with the measured ones<sup>[85,89]</sup> and therefore further solidify the obtained models of the structure solution.

### 1.3 DNP Enhanced NMR Spectroscopy

A drawback of NMR spectroscopy is the intrinsically low sensitivity because of the small energy difference between the Zeeman-levels of the nuclear spin. One way to deal with this is increasing the magnetic field that nowadays goes up to proton resonance frequencies of 1.5 GHz.<sup>[90]</sup> These very high field magnets are, however, not readily available and very expensive to operate. Another approach to overcome the low sensitivity is to hyper polarise the sample, meaning to prepare the sample in a way that the population difference of the Zeeman-levels is higher than the thermal population.<sup>[91]</sup> Ways of doing this are for example using para hydrogen<sup>[92]</sup>, spin exchange optical pumping<sup>[93]</sup> or DNP.<sup>[47]</sup>

In the 1950s, Overhauser discovered that upon microwave irradiation the high spin polarisation of an unpaired electron can be transferred to the nucleus.<sup>[47,94]</sup> It still needed another 40 years and the development of stable microwave sources until this technique was established for magic-angle-spinning (MAS) at commercially available NMR magnets.<sup>[48–50]</sup> After this pioneering work of the Griffin group, DNP evolved to a standard technique of hyper polarisation.<sup>[95]</sup> Consequently, a lot of work has been done on a theoretical<sup>[96,97]</sup> and practical<sup>[98]</sup> level to understand and improve DNP enhanced NMR spectroscopy.

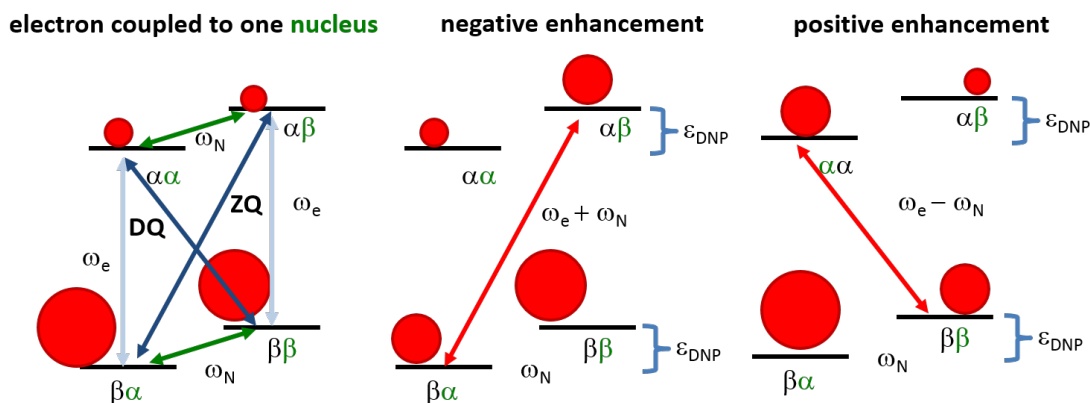


**Figure 1.4: Mechanism of the SE.** The black bars represent energy levels and the red dots represent population densities. The light blue arrows represent the electron transitions, the green arrows represent the nuclear transitions and the dark blue and red arrows show the double and zero quantum transitions. The bracket resembles the gain in nuclear polarisation.

There are two main polarising mechanisms for DNP at high magnetic fields in the solid state, the solid effect (SE)<sup>[96]</sup> and the cross effect (CE).<sup>[99]</sup> For the SE, one electron spin is coupled to one nuclear spin, resulting in four states for the two spins as resembled in Figure 1.4. The single quantum transitions with the energy difference of the electron and nuclear Larmor frequencies are depicted with light blue and green arrows, respectively. When a microwave with a frequency corresponding to the sum or the difference of the two Larmor frequencies hits the sample, the zero or double quantum transitions, respectively, are saturated as indicated by the red arrows in Figure 1.4. Both cases result in a hyper polarisation of the nuclear transition, leading to the observed sensitivity enhancement in the NMR spectrum.<sup>[96]</sup> The solid effect is mainly observed for static samples - no MAS - that use mono radicals like 1,3-bisdiphenylene-2-phenylallyl (BDPA) as polarising agent (PA).<sup>[100]</sup>

For the CE, two coupled electrons are needed.<sup>[99]</sup> This results in a four state system with four different energy levels as depicted in Figure 1.5. The dipolar coupling of these electrons must be on the order of the nuclear Larmor frequency. The microwave irradiation has the frequency of one of the electron single quantum transitions and thus saturates the respective transition. The coupling of this system with a nucleus results in an 8 state system with 3 spin quantum numbers for each state (Figure 1.5 only depicts the 4 relevant

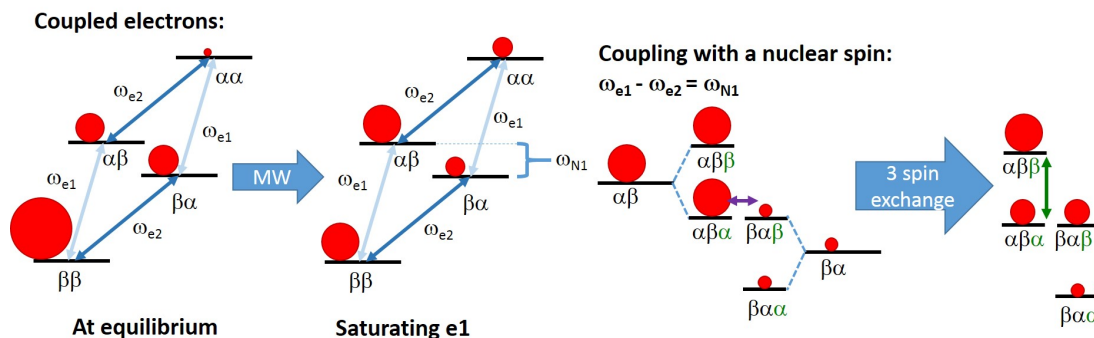


**Figure 1.5: Mechanism of the CE.** The black bars represent energy levels and the red dots represent population densities. The blue arrows represent the single quantum electron transitions. The purple arrow resembles the energy conserving 3-spin flip-flop-flip process and the gain in nuclear polarisation is visualised by the different sizes of the red balls for the nuclear transition (green arrows). In the third scheme, the electron states  $\beta\beta$  and  $\alpha\alpha$  are omitted for clarity and the energy difference is stretched. In the fourth scheme, only the 3 spin states are depicted.

states for the sake of clarity). Since the electron dipolar coupling matches the nuclear Larmor frequency, the  $\alpha\beta\alpha$  and the  $\beta\alpha\beta$  state have the same energy. Due to the saturation of the electron single quantum transition, these states have a significant difference in population, leading to an energy conserving 3-spin flip-flop-flip process that equilibrates the two states. This way, the polarisation difference of the electron spin states is transferred to the nuclear spin states. The CE is the dominant polarisation mechanism when using MAS.<sup>[97,99,101–103]</sup>

However, when MAS is present, the energy of the different states is individually modulated during the rotor period (Figure 1.6).<sup>[102]</sup> This leads to so called rotor events.<sup>[99]</sup> These are very short times during a rotor period at which polarisation transfer takes place. There are three different rotor events: The CE rotor event, the dipolar rotor event and the microwave rotor event. The first two are so called *anti crossings* and happen when the energy levels intersect (Figure 1.6). During this very short time of equivalent energy, the populations can equilibrate. A CE rotor event occurs when all spin numbers are different, meaning when the  $\alpha\beta\alpha$  and the  $\beta\alpha\beta$  state or the  $\beta\alpha\alpha$  and the  $\alpha\beta\beta$  states intersect. This resembles the CE condition in the static case and is the reason for the DNP enhancement.<sup>[103]</sup> An intersection of the states where the nuclear state is the same leads to electron dipolar rotor events ( $\beta\alpha\alpha$  and

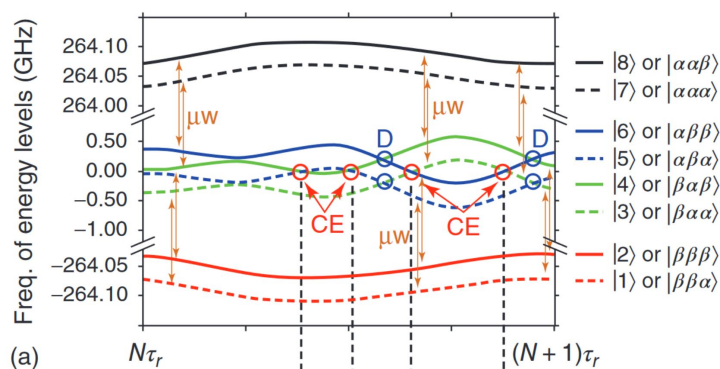


**Figure 1.6: Mechanism of the CE with MAS.** Here, all 8 3-spin energy levels are depicted and their modulation during one rotor period is shown. The rotor events are marked with  $\mu\text{W}$  (microwave), CE (cross effect) and D (electron dipolar). The Figure is reproduced from reference [103], copyright by John Wiley and Sons.

$\alpha\beta\alpha$  or  $\beta\alpha\beta$  and  $\alpha\beta\beta$ ).<sup>[97]</sup> The microwave rotor events are a single quantum electron transition that occur when the energy difference of two states that only differ by one electron spin number (for example  $\beta\beta\alpha$  and  $\beta\alpha\alpha$ ) matches the microwave frequency.<sup>[97]</sup> This modulation of the energy levels leads to a slower polarisation build-up compared to the static case, as the polarisation is only transferred during the rotor events.<sup>[104]</sup> The dipolar rotor events are also the reason for a depolarisation of the sample when no microwave irradiation is present.<sup>[101,103]</sup>

Because two coupled electrons are needed for the CE, PA are usually nitroxyl-biradicals<sup>[51]</sup> like AMUPol (Figure 1.7a),<sup>[52]</sup> AsymPol (Figure 1.7b)<sup>[53]</sup> or TEKPol (Figure 1.7c).<sup>[54]</sup> These radicals must be applied to the sample in order to perform DNP enhanced NMR spectroscopic experiments. Furthermore, to extend the electron relaxation time and thus providing more time for the polarisation transfer and to vitrify the applied solution, experiments are performed at temperatures around 100 K.<sup>[54]</sup>

The first way DNP enhanced NMR experiments were performed, was by dissolving the radical in a glass forming matrix (for example a mixture of glycerol and water) and dispersing the sample of interest in this solution before inserting the sample into the pre-cooled NMR magnet and thus rapidly cooling down the sample and forming a glass.<sup>[49,95]</sup> This technique is mainly used for samples in structural biology and gives the highest enhancements that even reach the theoretical limit of DNP.<sup>[98]</sup> This technique is usually referred to as frozen solution.<sup>[49]</sup> The biggest

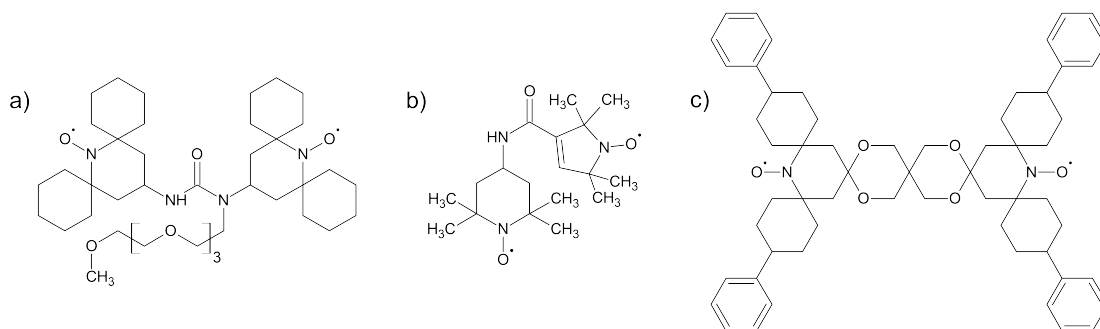


**Figure 1.7: Structures of some biradicals that are used as PA: a) AMUPol b) AsymPol c) TEKPol.**

drawback of this technique is that the sample needs to be soluble or dispersible in the DNP matrix and that therefore only molecular information like protein connectivities are probed.

In materials science, the most common preparation technique is the incipient wetness impregnation (IWI).<sup>[105,106]</sup> For this technique, the radical is again dissolved, but this time the investigated sample is impregnated with the radical containing solution.<sup>[107]</sup> Thereby, the solid state structure of the sample remains intact. A feature of this preparation technique that can be an advantage or a drawback - depending on the perspective - is that the surface of the investigated material is more strongly enhanced than the bulk material.<sup>[108]</sup>

To probe bulk properties of materials - especially for polymers - other preparation techniques are under development. The PA can be extruded with the polymer to homogeneously distribute it in the polymer and enhance the whole polymer bulk.<sup>[109]</sup> Another way to achieve this is to dissolve the polymer in the radical containing solution and to evaporate the solvent afterwards to obtain a radical containing polymer film.<sup>[110,111]</sup>

This work consists of five publications and three manuscripts (see chapters 3 and 4) that cover the scope of structure solution of supramolecular polymer additives from the molecular structure *via* the crystal structure to the structure within the polymer. The three topics are strongly linked and are only in their connection able to add a puzzle piece to the complex interplay of additives and polymers.

The first section (publications 1 & 2) covers the molecular structure solution of four CBAs and shows how ss-NMR spectroscopy can be used for molecular structure solution for molecules that are not stable enough for an analysis by liquid-state NMR spectroscopy. The key is to either use a logical approach (publication 1)<sup>[26]</sup> or to use pulse sequences that rely on nuclear interactions that are averaged out by the fast motion in the liquid state (publication 2).

The molecular structure already defines stability and solubility of the additive within the polymer. However, most supramolecular additives, especially NAs, are used as self-assembled nanoobjects. Therefore, publications 3-5 investigate the crystal structures of supramolecular polymer additives. This section shows which molecular motives of BBAs effect their crystal structure and how these crystal structures direct the morphology and surface polarity of the BBA nanoobjects obtained from self-assembly.<sup>[31]</sup> Publications 4 and 5 show applications of this concept for crystal<sup>[74]</sup> and foam cell<sup>[21]</sup> nucleation of polymers. The BBAs self-assemble in the polymer and the knowledge of the crystal structure helps to explain the efficient nucleation properties.

Since in the second section the nanoobject structure and morphology in the polymer is only deduced from the bulk crystal structure, the last section focusses on method development to analyse minority species within the polymer to confirm the crystal structures of the nanoobjects. The challenge is the very low concentration of down to a few hundred ppm of the additives within the polymer. In this concentration regime, the sensitivity of neither X-ray diffraction, nor conventional ss-NMR spectroscopy suffices. Therefore, DNP enhanced NMR spectroscopy is used in publications 6-8. For a differentiation of the additive resonances from the polymer and the radical containing solution, F-BTA is used, since this introduces a  $^{19}\text{F}$  spin label. Therefore, publication 6 investigates the polarisation mechanism of  $^{19}\text{F}$  with DNP and explores the potential of  $^{19}\text{F}$  DNP enhanced NMR spectroscopy.<sup>[46]</sup> Publication 7 further exploits this potential and features the first DNP enhanced double-quantum (DQ) build-up curve of a  $^{19}\text{F}$ - $^{19}\text{F}$  correlation that confirms which polymorph crystallises in PS. Additionally, the sample preparation to enhance PS samples is improved. This knowledge is then used in the final publication to enhance the signals of another minority species in PS, namely defects resulting from controlled, accelerated weathering. To sum up, this work features mechanistic investigations for supramolecular additives on the nano and the meso scale and method development for the analysis of minority species in polymers.

## 2.1 Molecular Structure Solutions

In the publication “Synthesis and Characterization of Dual-Functional Carbamates as Blowing and Curing Agents for Epoxy Foam”<sup>[26]</sup>, the molecular structure of three carbamates is derived by ss-NMR spectroscopy. All carbamates are synthesised from (liquid) diamines by bubbling  $\text{CO}_2$  through a mixture of the diamine and ethanol, leading to a precipitation of the carbamates as white powders. Elemental analysis confirms that one of the amines reacts with  $\text{CO}_2$ . From a chemical point of view, the logical structure is that a zwitter ionic structure with a carbamate anion and an ammonium cation at the free amine is formed. The interesting question is, which of the two chemically different amines captures the  $\text{CO}_2$  and which amine becomes the ammonium (Figure 2.1a). Because of the low stability of the carbamates in solution, this question can only be answered by ss-NMR spectroscopy.

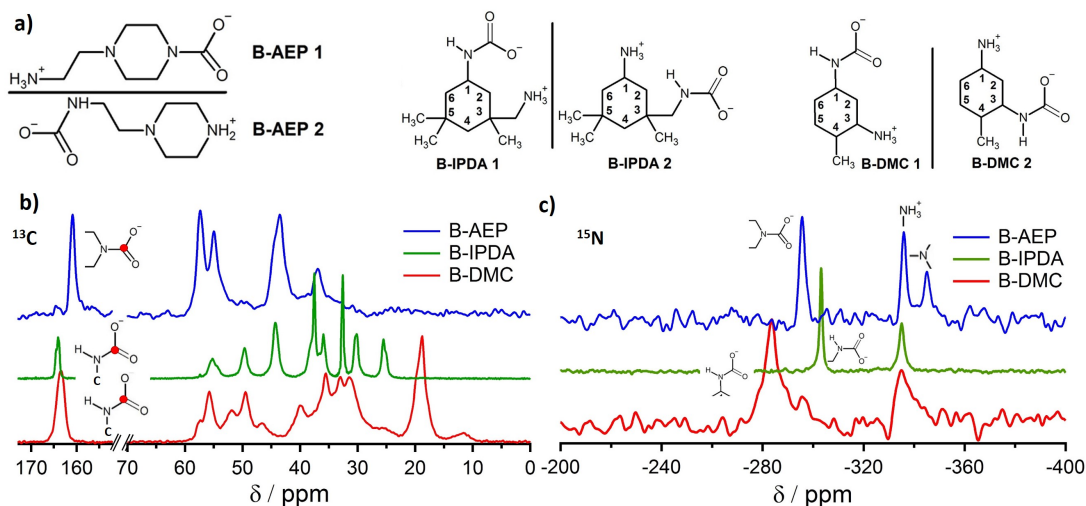


**Figure 2.1:** a) Possible structures of the carbamates B-AEP, B-IPDA and B-DMC. b)  $^{13}\text{C}\{^1\text{H}\}$  and c)  $^{15}\text{N}\{^1\text{H}\}$  CP NMR spectra of the three carbamates B-AEP (blue), B-IPDA (green) and B-DMC (red).

To elucidate the carbamate structures, all NMR spectra need to be compared to each other. From the  $^{13}\text{C}$  NMR spectra (Figure 2.1b) the formation of 4-(2-azaniumylethyl)piperazine-1-carboxylate (B-AEP 1) can be derived, as the carbamate resonance shows a 3 ppm shift compared to the resonances of the isophorone diamine carbamate (B-IPDA) and the 4-methylcyclohexane-1,3-diamine carbamate (B-DMC). Since the latter two, regardless of the formed isomer, will always consist of a secondary nitrogen atom within the carbamate group, the shift of B-AEP indicates a different chemical environment. The shift in the B-AEP spectrum can be attributed to the fact that the carbamate group includes a tertiary nitrogen and thus that the  $\text{CO}_2$  is captured by the secondary amine of the piperazine group. Furthermore, the  $^{15}\text{N}$  NMR spectrum (Figure 2.1c) shows the same ammonium shift as for the other two compounds, indicating the presence of an  $\text{NH}_3^+$  group in this molecule, as an  $\text{NH}_2^+$  group would show a clear shift.

The formation of B-IPDA 2 is mainly derived from the  $^{15}\text{N}$  NMR spectrum, as the carbamate resonance shows a 20 ppm shift compared to B-DMC. Since both isomers of B-DMC have their carbamate nitrogen directly attached to the cyclohexane ring, the drastic shift excludes the formation of B-IPDA 1.

In the  $^{13}\text{C}$  spectrum of B-DMC, at least 14 individual resonances are observed although the molecular structure only suggests a maximum of 8 different carbon

resonances. Furthermore, the resonances of both NMR spectra are very broad. Regardless of the isomer, B-DMC has three stereo centers at the positions 1, 3 and 4 (Figure 2.1a) (note that the numbering in the ring for B-DMC 2 is not according to the IUPAC standard). Additionally, the chemical reactivity of the two amines in the educt is not expected to be very different, as the methyl group next to the amine at position 3 is not a big sterical hindrance. All these facts lead to the assumption that both structural isomers are formed with eight stereo isomers each. This total of 16 chemically different molecules leads to the large number of resonances and their big line widths.

The dual-functional application of the carbamates as blowing and curing agent results from the fact that they can be mixed with the epoxy resin bisphenol A diglycidyl ether. When heating the mixture, the back reaction of the carbamate formation takes place and CO<sub>2</sub> is released to create foam bubbles. The release of the CO<sub>2</sub> yields free amine groups that react with the epoxy groups to solidify the resin and yield a foam. All three carbamates are able to create stable foams with a 70 % volume expansion compared to the bulk resin. However, because of the complex kinetic interplay between decomposition and resin hardening, the foaming temperature for each system is crucial. To achieve full expansion, an adequate foam morphology and a solid material, foaming temperatures were found to be 120, 100 and 80 °C for B-AEP, B-IPDA and B-DMC, respectively.

For a cheaper and more sustainable synthesis, especially for industrial up-scaling, the synthesis of the three carbamates was tried in water as well. Only IPDA reacted with CO<sub>2</sub> in water to a stable product. However, we found that the molecular structure of B-IPDA is different when using water instead of ethanol in the synthesis. These results are summarised in the unpublished manuscript “Structural Analysis of CO<sub>2</sub> Loaded Diamines Derived from Aqueous Synthesis Route for Epoxy Foaming”. Again, the low stability of the product resulted in the need to use ss-NMR to elucidate the structure. Together with DFT calculations, we could even confirm the reaction pathway leading to the new product.

Elemental analysis suggests that compared to the carbamate structure from Figure 2.1, one additional formula unit of water is incorporated in the structure. Since in the solid state water can be incorporated in the crystal structure, the three proposed molecular formulas are a carbonate, a carbamate with one formula unit of structural water and a urea with two formula units of structural water as depicted in Figure 2.2a. The <sup>15</sup>N{<sup>1</sup>H} CP NMR spectrum (Figure 2.2b (red))

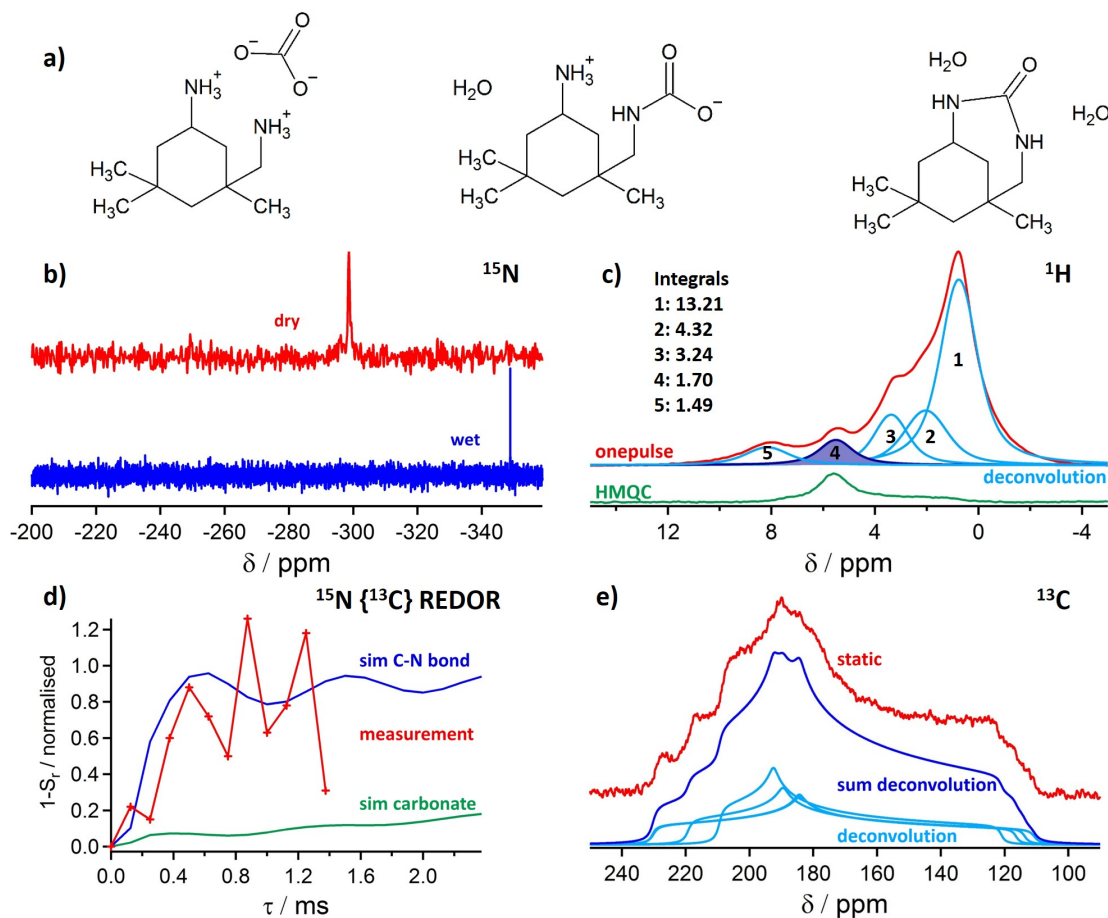


**Figure 2.2:** a) Possible structures of B-IPDA when synthesised in water with their characteristic functional groups from left to right: carbonate, carbamate, urea. b)  $^{15}\text{N}\{^1\text{H}\}$  CP NMR spectra before (blue) and after (red) drying of the reaction product. c) Direct  $^1\text{H}$  ss-NMR excitation (red) with a deconvolution (blue) of the respective resonances and a  $^{14}\text{N}$  filtered HMQC ss-NMR spectrum of B-IPDA. d)  $^{15}\text{N}\{^{13}\text{C}\}$  REDOR build-up curve (red) of B-IPDA together with a simulation of a C-N bond and a carbonate group. e) Static  $^{13}\text{C}\{^1\text{H}\}$  CP NMR spectra of B-IPDA (red) with a deconvolution of the four resonances (blue)

only shows one resonance at -300 ppm, indicating the presence of an electron dragging group in the close proximity, and also shows that both nitrogen atoms have a similar surrounding. Because of the 99.6 % natural abundance of  $^{14}\text{N}$ , performing a  $^{14}\text{N}$  filtered d-HMQC<sup>[28]</sup> proton NMR spectrum (Figure 2.2c (green)) probes which protons are directly bound to a nitrogen atom, as all other proton resonances vanish. A subsequent deconvolution of the regular proton NMR spectrum (Figure 2.2c (red and blue)) shows that only 2 protons are directly bound to a nitrogen. Both experiments only allow for the urea to be formed. Since urea groups are unstable and rarely form, we deemed further analysis to be necessary.

Therefore, we repeated the synthesis of B-IPDA with  $^{13}\text{C}$  enriched  $\text{CO}_2$ . Because the natural abundance of  $^{13}\text{C}$  is roughly 1 %, this procedure increases the sensitivity of the C=O group by two orders of magnitude, allowing for more sophisticated ss-NMR experiments. For example, a  $^{15}\text{N}\{^{13}\text{C}\}$  REDOR<sup>[112,113]</sup> build-up curve was measured and compared with simulations of the proposed structures with the software package SIMPSON.<sup>[114]</sup> The good agreement between the simulated urea build-up curve and the measurement confirms the formation of a C-N bond, further supporting the urea structure. With the  $^{13}\text{C}$  enriched sample, it was also possible to perform a static  $^{13}\text{C}\{^1\text{H}\}$  CP NMR spectrum (Figure 2.2e). In this spectrum, the chemical shift anisotropy (CSA) is - compared to an MAS spectrum - not averaged out. This results in very broad resonances with a distinct shape that holds additional information on the anisotropy of the electron cloud around the nucleus. From the  $^{13}\text{C}$  CP spectrum, at least three different resonances can be resolved. Looking at the urea structure reveals that two stereo centres exist and thus four stereo isomers can form. The deconvoluted resonances are in good agreement with calculated spectra for the 4 urea isomers. So, all NMR experiments confirm the formation of the urea-B-IPDA when synthesised from water.

This raises the question what leads to the formation of the urea functionality. Directly after the synthesis, the reaction product is centrifuged and dried in the oven for 24 h at 40 °C. To investigate the reaction pathway, we performed a  $^{15}\text{N}\{^1\text{H}\}$  CP NMR spectrum (Figure 2.2b (blue)) of the slurry before the drying process. This experiment, again, only shows one resonance. This time, however, at -349 ppm, indicating the formation of  $\text{NH}_3^+$ -groups. The proposed structure that explains this shift is a carbonate formation as shown in Figure 2.2a. To confirm this, we performed a geometry optimisation of the carbonate at DFT level. As a starting model, we placed the carbonate anion very close to the ammonium groups (Figure 2.3a). After the geometry optimisation, the structure obviously has relaxed, leading to a bigger distance of the carbonate C to the cyclohexane ring. However, the close conformation of the carbonate and the ammonium groups in an 11-membered ring remains, although two protons are now closer to the carbonate oxygen atoms than to the nitrogen. We can conclude that this adduct forms within the slurry. The already prepared OH bond facilitates the removal of water during the subsequent drying process and localises the electrons

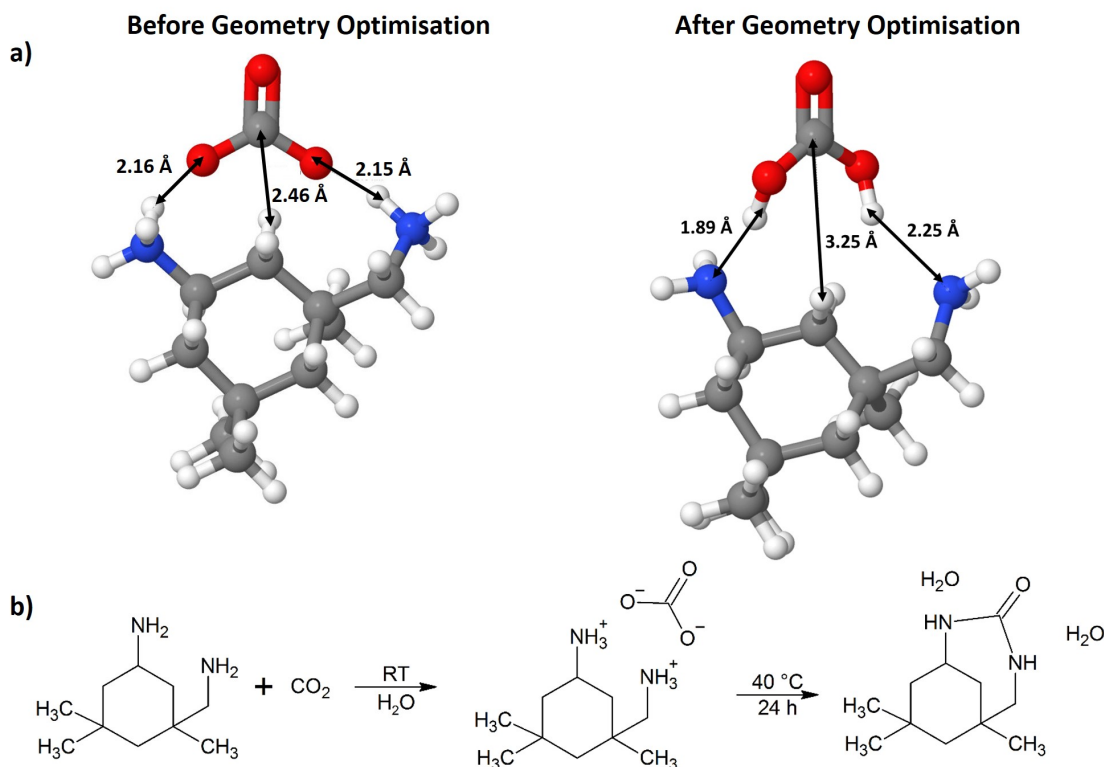


**Figure 2.3:** a) Proposed transition states of the IPDA-CO<sub>2</sub> adduct prior to (left) and after (right) geometry optimisation b) Proposed reaction pathway leading to urea-B-IPDA.

closer to the nitrogen. This, now free, electron pair can then attack the carboxylic carbon. The reduction of water is thus the driving force for the urea formation, although two formula units of water remain in the structure.

Urea-B-IPDA also functions as dual functional blowing agent and hardener for epoxy resins. Because of the different structure, the decomposition and hardening kinetics also change leading to a rise of the ideal foaming temperature to 120 °C.

## 2.2 Crystal Structure Solutions

The molecular structure defines the solubility of the molecules in the polymer melt. However, the crystal structure defines the connection of the polymer with the self-assembled nanoobject, once it emerged from the polymer melt. Therefore, this section presents a general concept for the design of BBAs that predicts the crystal structure and morphology based on the side group substitution. Knowing this is of importance for the rational design of supramolecular additives as both, structure and morphology, have an impact on the additive performance. This concept is then applied to two BBAs that act as crystal or foam cell NAs.

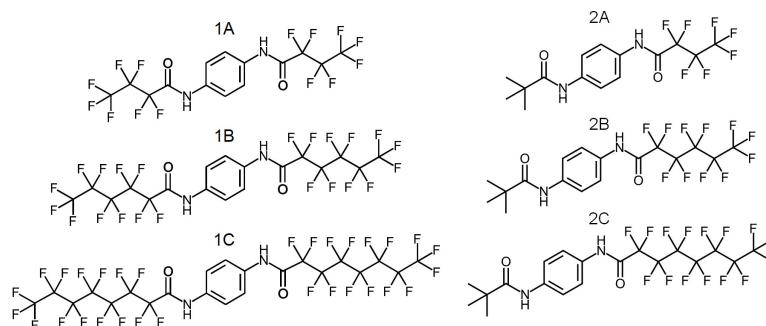


**Figure 2.4:** The two series of investigated BBAs. Series 1 consists of a symmetric substitution pattern of linear, perfluorinated alkyl groups. Whereas for series 2, one side group is replaced by tert-butyl resulting in an asymmetric substitution pattern. Reproduced from reference [31].

In the publication “Crystal Engineering of Supramolecular 1,4-Benzene Bisamides by Side-Chain Modification - Towards Tuneable Anisotropic Morphologies and Surfaces”,<sup>[31]</sup> we obtained an insight into the link between molecular and crystal structure and how this effects the self-assembly of BBAs. Therefore, we synthesised two series of bisamides. The first series consists of a symmetric side group pattern of linear perfluorinated carbon chains of increasing lengths (C3, C5, C7). Within the second series, one side group remains the same as for the first series, the other side group is replaced by a tertiary butyl group, resulting in an asymmetric substitution pattern as depicted in Figure 2.4. Because of their appearance as thin platelets or needles, only three of the compounds yielded single crystals of a sufficient size to solve the crystal structures by single crystal X-ray diffraction (**1A**, **2A**, **2B**). The other structures were solved by an NMR crystallographic approach. Both series show an individual packing pattern governed by their respective hydrogen bond formations.

In series **1**, one molecule forms four hydrogen bonds to two neighbouring molecules (Figure 2.5a), leading to a molecular ribbon along the crystallographic *a*-axis (Figure 2.5b). Along the *b*-axis, these ribbons are loosely connected by the van der Waals forces of the interlocking side chains, and along the *c*-axis only weak interactions are present (Figure 2.5b). In series **2**, one molecule also forms four hydrogen bonds, in this case however, to four neighbouring molecules (Figure 2.5a). This results in a packing pattern where the hydrogen bond strand propagates along the *b*-axis and the molecules zig-zag along the *a*-axis. Only along the *c*-axis, weak van der Waals interactions are present (Figure 2.5c).

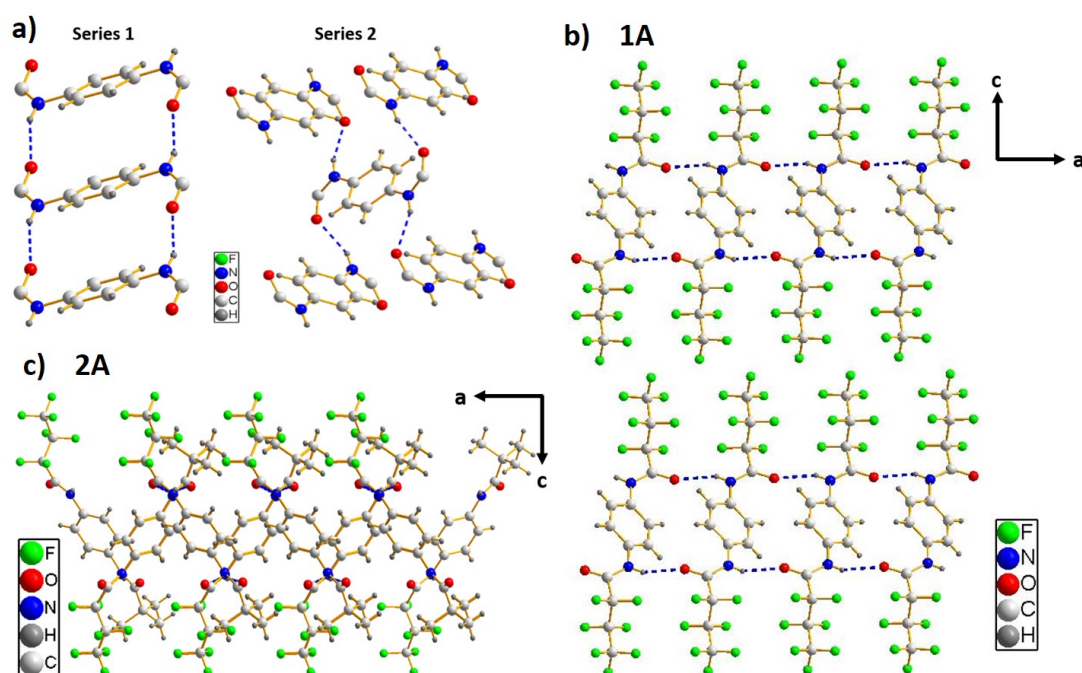


**Figure 2.5:** a) Packing pattern of the two different series. In series 1 one molecule forms hydrogen bonds to two other molecules. In series 2 one molecule forms hydrogen bonds to four other molecules. b) Crystal structure of 1A viewed in the  $ac$ -plane. c) Crystal structure of 2A viewed along the  $ac$ -plane. Figure rearranged from reference [31].

To investigate why these molecularly quite similar compounds form such different crystal structures, models were built and geometry optimised by DFT methods. All molecules of series 1 were forced into the crystal structure of series 2 and vice versa. The outcome of the calculation was that all molecules were able to form a slightly denser structure in the packing of series 1. The molecules of series 1 in the packing of series 2 formed hydrogen bond lengths on the similar order as the molecules of series 2. However, the hydrogen bond lengths of the molecules of series 2 in the packing of series 1 increased significantly (Table 2.1). Since the packing type of series 1 allows for a denser packing, this is the preferred packing pattern, especially as it will be kinetically favoured by the fact that two hydrogen bonds are formed with the same molecule. However, we can conclude that the bulky tert-butyl side groups require too much space to be able to pack in this packing pattern. Therefore, after the first hydrogen bond is formed, the molecules need to rotate and form the remaining three hydrogen bonds with other molecules, resulting in the crossed packing pattern of series 2.

**Table 2.1: Summary of the hydrogen bond lengths and densities of all compounds in both packings. Table rearranged from reference [31].**

	Packing 1			Packing 2		
	CF-H-O /Å	<i>t</i> -Bu-H-O /Å	Density /g·cm <sup>-3</sup>	CF-H-O /Å	<i>t</i> -Bu-H-O /Å	Density /g·cm <sup>-3</sup>
1A	1.96	n.a.	2.00	1.91	n.a.	1.92
1B	2.01	n.a.	2.04	1.91	n.a.	2.02
1C	2.03	n.a.	2.13	2.05	n.a.	2.06
2A	2.39	2.41	1.59	1.82	2.06	1.58
2B	2.47	2.49	1.69	1.80	2.03	1.65
2C	2.31	2.31	1.76	1.80	2.02	1.75

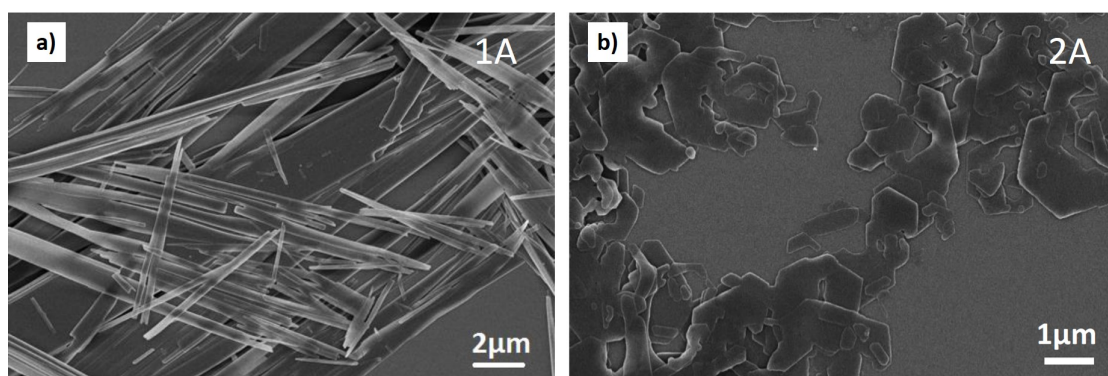


**Figure 2.6: Scanning electron microscope (SEM) images of a) 1A and b) 2A (right). Figure rearranged and altered from reference [31].**

These characteristic packing patterns also effect the self-assembly behaviour of the compounds. The fact that only one direction of favoured growth is present in the crystal structure of series **1** is also resembled in the shape of the self-assembled particles that form needles (Figure 2.6a). The two dimensions of favoured growth in the crystal structures of series **2** results macroscopically in the shape of thin platelets (Figure 2.6b). These preferred growth rates also result in specific surfaces of the self-assembled particles. In both cases the (001) direction shows the slowest growth and thus the (001) face is the terminating surface of the particles. For series **1** this means that the terminating surface is perfluorated and for series **2** this results in alternating rows of CF<sub>3</sub>-groups and tert-butyl groups with different polarities each. This means that with the bulkiness of the side group the crystal structure, the crystal morphology and the surface polarity can be tuned. We can now apply this knowledge for the rational design of new BBAs.

The publication “Highly Efficient Supramolecular Nucleating Agents for Poly(3-hexylthiophene)”<sup>[74]</sup> discusses four new NAs for P3HT and proposes a mechanism for their high efficiency. The nucleating agents are bisamides with

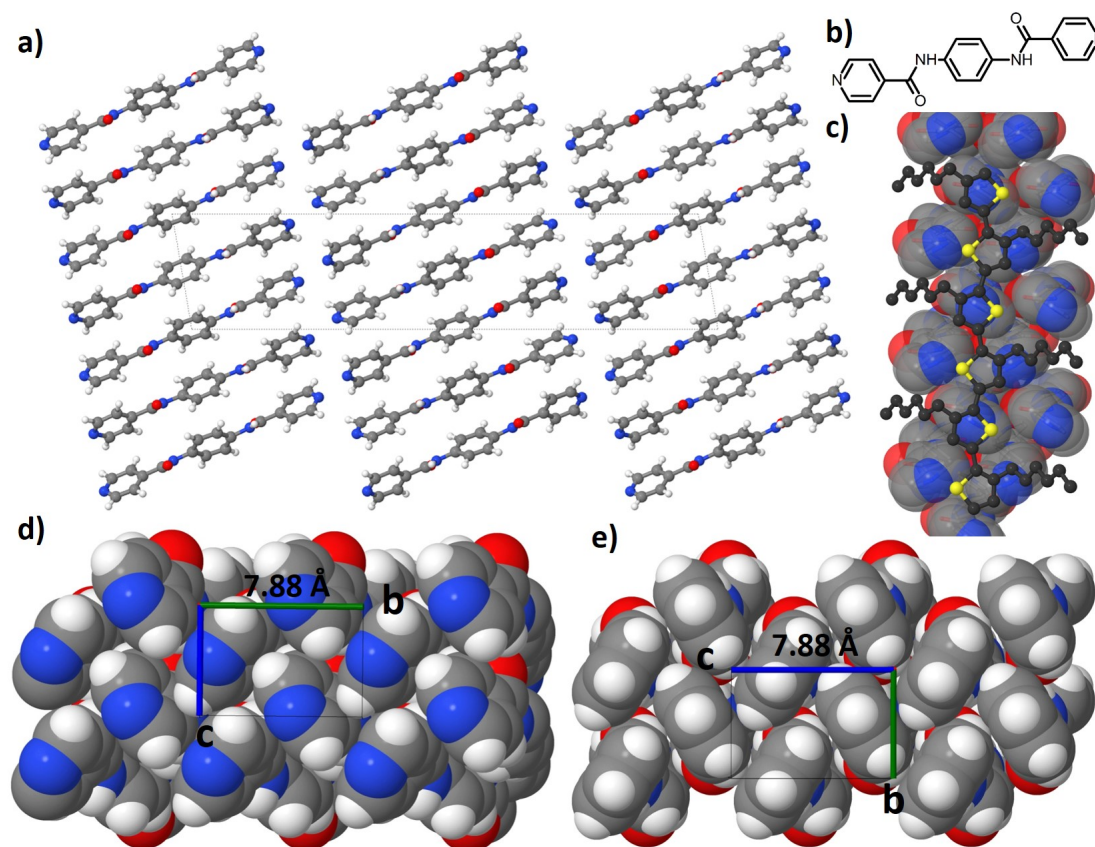


**Figure 2.7:** a) Crystal structure of NA1. The view follows the hydrogen bond pattern. b) Molecular structure of NA1 c) Possible arrangement of P3HT on the surface of NA1 with every nitrogen atom pointing at the middle of a thiophene ring. Protons are omitted for clarity. d) Top view of the layers of NA1 in the *bc*-plane e) same view of *N,N'*-1,4-phenylenebisbenzamide, showing that it has the same crystal structure as NA1. Figure rearranged from reference [74].

either a benzene or cyclohexane core and a pyridine side group. Among these, *N,N'*-1,4-phenylenebis[4-pyridinecarboxamide] (NA1) (Figure 2.7b) showed the best nucleation performance and thus the crystal structure of NA1 was solved by an NMR crystallographic approach to explore the reason for the efficient crystal nucleation.

As for the bisamides of series **1** in the previous paragraphs, one molecule forms four hydrogen bonds to two other molecules, forming a ribbon along the crystallographic *c*-axis (Figure 2.7a and 2.7d). The *b*-axis provides, with a length of 7.88 Å, a very good epitaxial match for the 7.80 Å long *b*- and *c*-axes of P3HT.<sup>[115]</sup> According to the concept developed in the first paragraph of this section, the *b*-axis of NA1 is part of the terminating face of the self-assembled particles within

P3HT. Along this axis, the nitrogen atoms of the pyridine end groups are present in distances of the lattice spacing. This provides, in addition to the epitaxial match, an electronic match because these nitrogen atoms fit perfectly with the distance of every second thiophene ring of P3HT (Figure 2.7c). This hypothesis is supported by the fact that the same bisamide with a benzene instead of pyridine side groups is a worse NA, although it crystallises in exactly the same crystal structure and thus provides the same epitaxial match (Figure 2.7e).<sup>[116]</sup>

The surface structure and therefore the nucleation efficiency is a direct effect of the molecular design of the BBA. This underlines the importance of the concept established in publication number 3.<sup>[31]</sup>

The publication “Kinked Bisamides as Efficient Supramolecular Foam Cell Nucleating Agents for Low-Density Polystyrene Foams with Homogeneous Microcellular Morphology”<sup>[21]</sup> shows a new variation of BBAs that efficiently nucleates the foam cells of PS. As central core not a single benzene ring is used, but two benzene rings connected by a methylene bridge are the core of the structures, introducing a kink in the molecular structures. In total, 12 molecules were synthesised with different substitutions on the benzene rings (H, methyl, ethyl) and the amid groups (cyclohexyl, phenyl, tert-butyl, n-butyl). The morphology of all self-assembled particles is strongly one-dimensional except for the tert-butyl substituted bisamides.

The crystal structure of the bisamide with ethyl and cyclohexyl substitution (Figure 2.8a) was solved by NMR crystallographic methods, as the strong anisotropic shape made the growth of suitable single crystals impossible. The packing pattern is very comparable to the one of series **1** of the “regular” bisamides. One molecule forms four hydrogen bonds to two other molecules, leading to a hydrogen bond ribbon along the *a*-axis (Figure 2.8c). Along the *b*-axis, weak van der Waals interactions of the ribbons form a layer (Figure 2.8b). These layers stack along the *c*-axis. As for the other bisamides, this packing behaviour with only one direction of favoured growth, explains the formation of needles for the self-assembled particles (Figure 2.8d).

The NA is mixable at high temperatures with the polymer melt. If the temperature of the melt falls below the melting point of the additive nanoobjects in the shape of needles form. In accordance to the concept of supramolecular polymer nucleation (Figure 1.2 in Section 1.1), these needles then act as heterogeneous

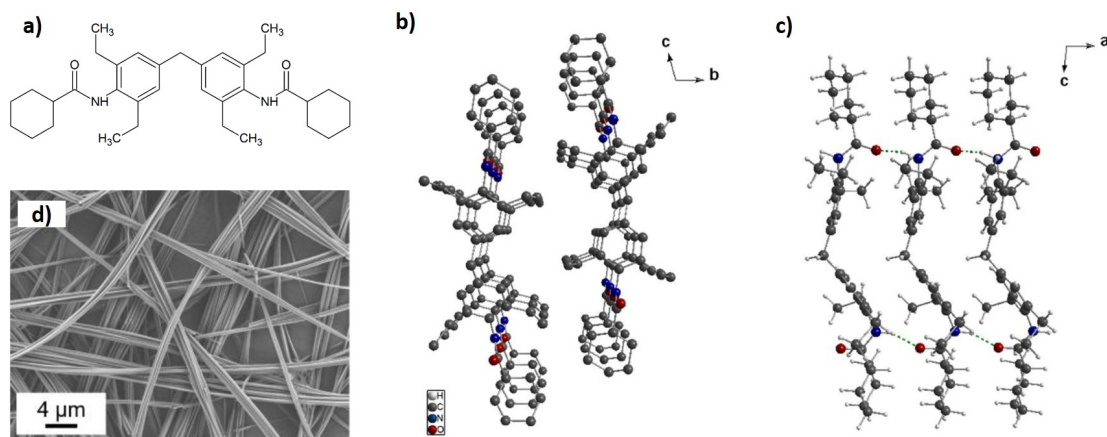


**Figure 2.8:** a) Molecular structure of the investigated kinked bisamide. b) and c) Crystal structure of the kinked bisamide viewed in the *bc*- and *ac*-plane, respectively. d) SEM image of the self-assembled particles of the kinked bisamide. Protons are omitted for clarity. Figure parts b), c) and d) rearranged from reference [21].

nucleation sites for the foam bubbles, thus creating smaller foam cells with a more homogeneous foam cell size distribution. With 0.5 wt.% of the said kinked bisamide, it was possible to reduce the average cell size by two orders of magnitude in an extrusion foaming process compared to a PS foam without an additive.

## 2.3 Investigating Minority Species in Polymers

The crystal structures of the neat additives already help to explain nucleation properties of the NA. However, this assumes that the crystal structure within the polymer is the same as the one of the neat material. Investigating polymer additives in their low technical concentrations within polymers by ss-NMR spectroscopy is often challenging, because of the low sensitivity of this technique. Therefore, the last section focusses on the method development to investigate minority species inside polymers by means of NMR spectroscopy. This is achieved by combining spin labelling the target molecules with  $^{19}\text{F}$  and using DNP to enhance the signal. Since DNP enhanced NMR spectroscopy is still a young field, neither using  $^{19}\text{F}$  as a nucleus nor the sample preparation for polymer samples is fully understood. Therefore, publication 6<sup>[46]</sup> investigates the polarisation mechanism for  $^{19}\text{F}$  enhanced DNP spectroscopy, using standard sample preparation techniques, and publication 7 focusses on the sample preparation technique. In both publications, the crystal structure of F-BTA that is used as an additive is

confirmed by single quantum and double quantum experiments in *i*-PP and PS, respectively. The knowledge about the sample preparation is then used in the final publication of this work to enhance the resonances that are introduced to PS by controlled, accelerated weathering. DNP enhancement is able to reduce the detection limit of these minority species by at least one order of magnitude.

In the publication “ $^{19}\text{F}$  MAS DNP for Probing Molecules in Nanomolar Concentrations: Direct Polarization as Key for Solid-State NMR Spectra without Solvent and Matrix Signals”,<sup>[46]</sup> the polarisation mechanism of  $^{19}\text{F}$  is investigated and the structure of the fluorinated BTA F-BTA within *i*-PP for a concentration of 600 ppm is analysed.

We started the study by investigating the potential and the polarisation pathway of this technique. Therefore, we prepared frozen solutions of 15 mM TEKPol in 1,1,2,2-tetrachloro-ethane (TCE) with three different F-BTA concentrations (187.5, 10 and 2.5 mM)(Figure 2.9a). The solution with the highest concentration showed an DNP enhancement factor ( $\epsilon_{on/off}$ ) of 260. For the other two solutions, the spectra without microwave irradiation did not give a signal, so no  $\epsilon_{on/off}$  could be derived. To still be able to compare the enhancements, the absolute sensitivity (S), the signal-to-noise ratio per square root of time, was derived. It gives  $753 \pm 16$ ,  $1005 \pm 11$  and  $973 \pm 39 \text{ mg}^{-1}\text{h}^{-1/2}$  for the 187.5, 10 and 2.5 mM solutions, respectively. Furthermore, the DNP build-up times were measured for the three solutions and turned out to all have a stretched exponential behaviour that increases upon dilution (3.3, 5.6 and 5.7 s) and a  $^{19}\text{F}$ -DQ experiment confirmed the absence of F-BTA clusters even for the highest concentration (Figure 2.9c).

All three samples exhibit an excellent gain in sensitivity from the DNP treatment. The high sensitivities of the diluted samples show that a major part of the sample is still polarised. Because of the absence of F-BTA clusters, the polarisation is not transferred by spin-diffusion and the increasing DNP build-up times with a stretched exponential confirm a distribution of F-BTA-TEKPol distances rather than a clustering of F-BTA molecules around a TEKPol molecule. From these results we can conclude that the polarisation transfers directly from the electrons to the  $^{19}\text{F}$  nuclei, as proposed by Figure 2.9b). The increase in build-up times has also been observed in other studies that investigated a direct polarisation transfer.<sup>[117,118]</sup> Because of geometric considerations, this leads to a maximum polarisation distance of 25 Å (Figure 2.9d).

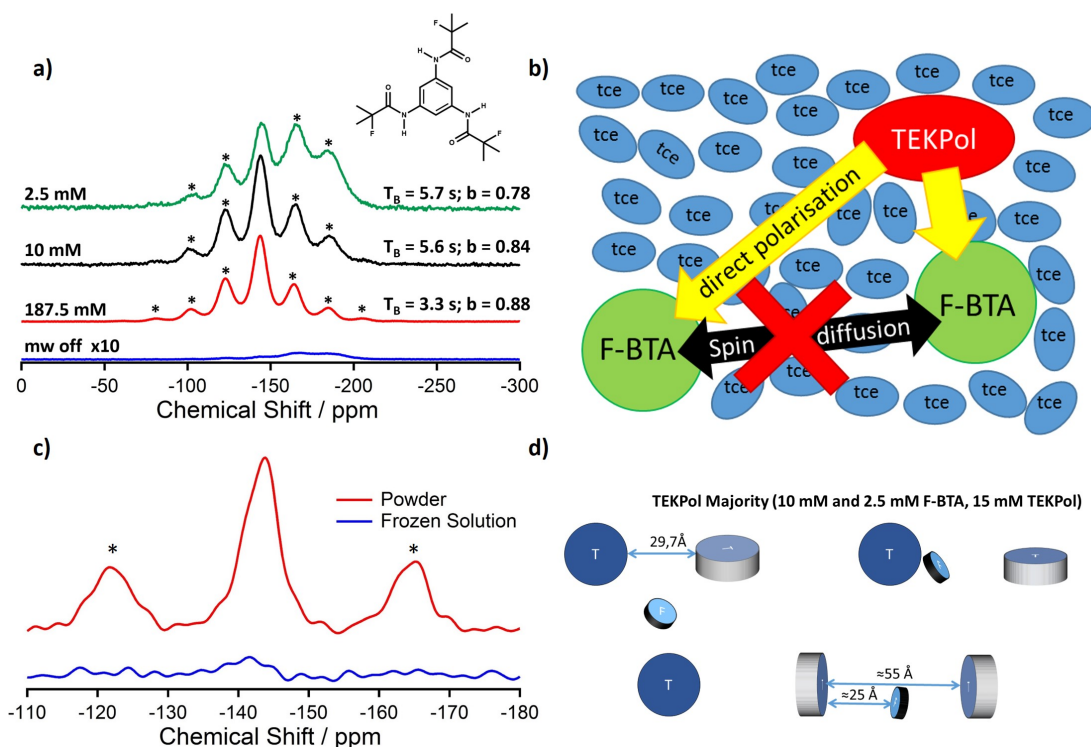


**Figure 2.9:** a) DNP enhanced  $^{19}\text{F}$  NMR spectra of frozen solutions of F-BTA in 15 mM TEKPol in TCE. F-BTA concentrations, DNP build-up times and stretching parameters of the build-up time are placed on the respective graphs and a sketch of F-BTA is depicted in the top right corner. b) Proposed polarisation mechanism c)  $^{19}\text{F}$  DQ NMR spectrum of a neat F-BTA powder (red) and a frozen solution (Intensities are scaled to the same F-BTA amount) d) Geometric model of the frozen solution. The big, dark blue cylinders represent TEKPol and small light blue cylinders represent F-BTA. Spinning side bands in the NMR spectra (a and c) are marked with an asterisk. The Figure is rearranged from reference [46].

The objective was to develop a tool to investigate polymer additives within polymers. Therefore two compounds of F-BTA and *i*-PP with concentrations of 0.06 and 2 wt.% of F-BTA content were prepared. The samples were polarised by the IWI technique with a 15 mM TEKPol solution in TCE. With DNP enhanced NMR spectroscopy, we were able to measure the  $^{19}\text{F}$  F-BTA resonance even in the lower concentrated sample (Figure 2.10a). The resonance shows exactly the same chemical shift as the resonance of the 2 wt.% sample and the neat F-BTA. The linewidth of the neat F-BTA, however, is much smaller. The  $^{13}\text{C}\{^1\text{H}\}$  CP spectrum of the 2 wt.% compound (Figure 2.10b) emphasises the need of a spin label to investigate minority species. The spectrum is very crowded and dominated by the big resonance of TCE. But also the resonances of *i*-PP

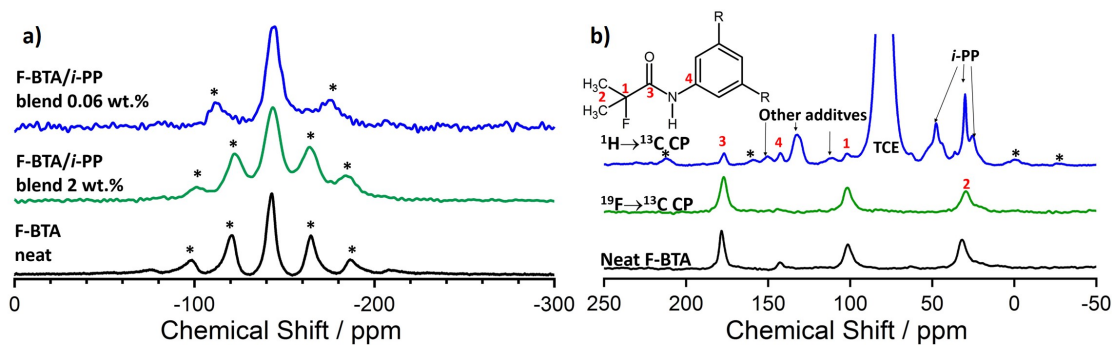


**Figure 2.10:** a) DNP enhanced  $^{19}\text{F}$  NMR spectra of neat F-BTA (black), 2 wt.% F-BTA (green) and 0.06 wt.% (blue) in *i*-PP polarised with IWI. b) DNP enhanced  $^{13}\text{C}\{^1\text{H}\}$  CP (blue) and  $^{13}\text{C}\{^{19}\text{F}\}$  CP (green) NMR spectra of 2 wt.% F-BTA in *i*-PP. For comparison a  $^{13}\text{C}\{^{19}\text{F}\}$  CP spectrum of the neat F-BTA (black) is included. Spinning side bands are marked with an asterisk. The Figure is rearranged from reference [46].

and other additives of the used commercial *i*-PP blend make an assignment of the resonances difficult. The  $^{13}\text{C}\{^{19}\text{F}\}$  CP spectrum is much tidier. Only the resonances of the F-BTA remain. These resonances all fit with the resonances of the neat compound.

From this we can draw two conclusions. First, F-BTA crystallises within *i*-PP in the same structure as in the bulk, as the resonances of both,  $^{19}\text{F}$  and  $^{13}\text{C}$ , fit with the bulk resonances. Since the spectra in *i*-PP exhibit a bigger linewidth for both nuclei, smaller crystallites or a small distortion of the structure within *i*-PP is expected. The second conclusion is the more general one that we showed an efficient way to probe the minority species in a polymer with DNP enhanced ss-NMR spectroscopy by using  $^{19}\text{F}$  as a spin label and exploiting the potential of direct polarisation.

Still, the preparation with the IWI technique also has drawbacks. For example, only the surface up to a few nm of the sample is polarised. Furthermore, it requires the sample to be inert towards the solvent used to apply the PA. For an inert material like *i*-PP, this is not a problem, but PS, for example, is very well soluble in TCE. To address both issues and to further exploit the potential of  $^{19}\text{F}$  DNP, we extruded F-BTA and PS together with the PA AsymPol and summarised the results in the unpublished manuscript “DNP Enhanced  $^{19}\text{F}$ - $^{19}\text{F}$  DQ Build-up Curve Confirms Crystal Structure of Supramolecular Additive in PS at Technical Concentration for Batch Foaming”.

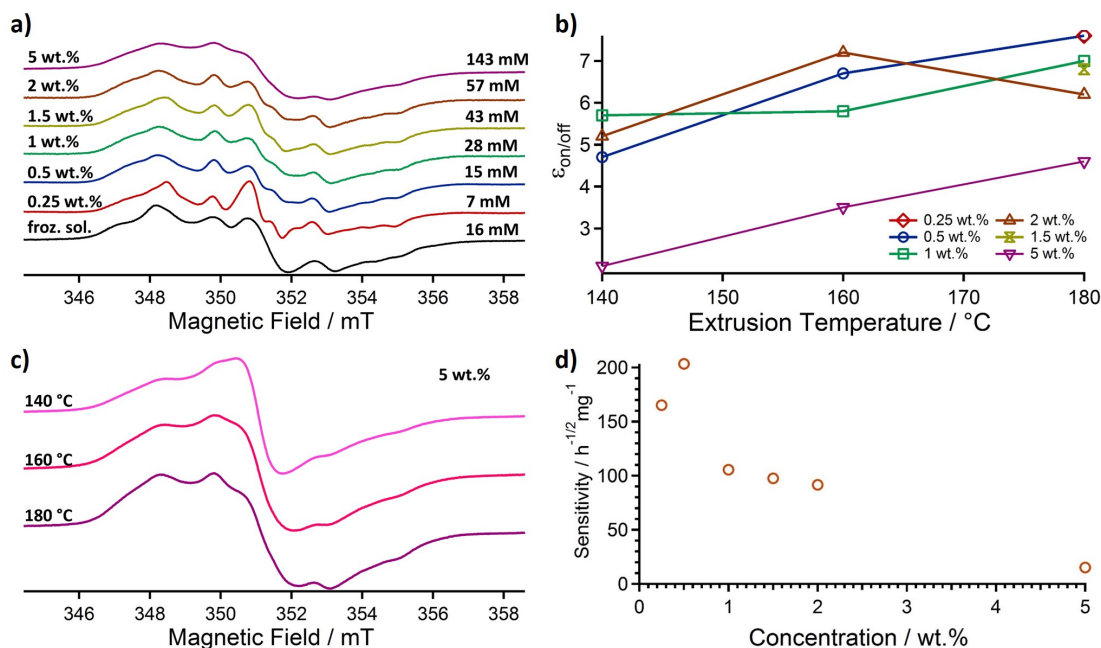


**Figure 2.11:** a) EPR spectra of the AsymPol PS compounds extruded at 180 °C and a 16 mM frozen solution of AsymPol in TCE as indicated on the spectra. For comparison, the molar ratio was calculated and depicted as well. b)  $\epsilon_{on/off}$  values for all 14 samples. c) EPR spectra of the 5 wt.% sample at the three different temperatures. d) Absolute sensitivity versus the AsymPol concentration for the samples extruded at 180 °C.

Extruding a PA was published before.<sup>[109]</sup> However, a detailed understanding of the sample preparation was still missing. Therefore, we prepared 14 PS samples with concentrations between 0.25 and 5 wt. % at extrusion temperatures between 140 and 180 °C. On these samples, we performed electron paramagnetic resonance (EPR) measurements to check the distribution of the radicals within PS. Furthermore, we investigated the enhancement and the sensitivity of the PS signal to evaluate the best AsymPol concentration and extrusion temperature for the additive containing sample.

In EPR spectroscopy, the interactions of unpaired electrons are probed. As AsymPol is a biradical, its EPR spectrum shows a distinct shape resulting from the intramolecular interactions. When two AsymPol molecules are getting close to each other, the inter- and intramolecular interactions superimpose, resulting in a broad featureless line.

In the PS/AsymPol spectra in Figure 2.11a, the line shapes of the samples with an AsymPol content between 0.25 and 2 wt.% do not significantly change. Only the 5 wt.% sample shows signs of radical clustering. The shape of all samples

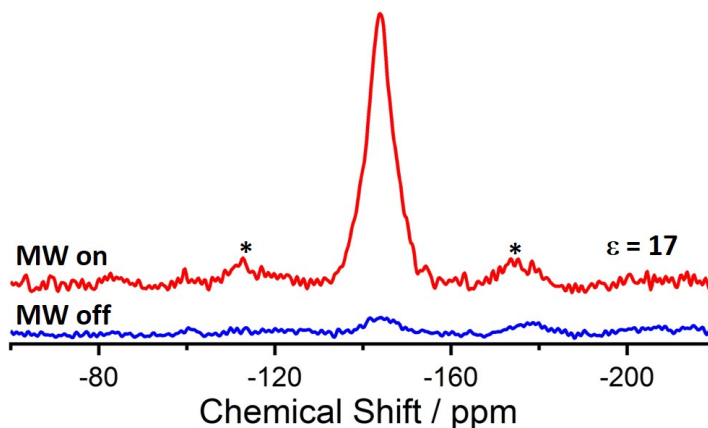


**Figure 2.12:** DNP enhanced  $^{19}\text{F}$  Hahn echo experiments with (red) and without (blue) microwave irradiation of PS with 0.5 wt.% of AsymPol and 0.5 wt.% of F-BTA. Spinning side bands are marked with an asterisk.

is very similar to the one obtained for a 16 mM frozen solution of AsymPol, for which a homogeneous radical distribution can be assumed. This allows to conclude that the radicals are well distributed within PS as well. When evaluating the  $\epsilon_{on/off}$  (Figure 2.11b), we observe a clear trend that with an increased extrusion temperature,  $\epsilon_{on/off}$  increases as well. This is attributed to a more homogeneous radical distribution at higher temperature and can be observed by EPR spectroscopy as well: With increasing temperature, more features appear in the EPR spectra of samples with the same AsymPol concentration, as exemplarily shown for the 5 wt.% series in Figure 2.11c. That the  $\epsilon_{on/off}$  can be misleading was already mentioned before. Therefore, we determined the S and found that it has a maximum at  $203 \text{ mg}^{-1}\text{h}^{-1/2}$  at a radical concentration of 0.5 wt.%, which is almost a factor of 14 higher compared to the 5 wt.% sample (Figure 2.11d). A feature that leads to this high sensitivity is the relatively short DNP build-up time between 36 and 645  $\mu\text{s}$  for all samples that is characteristic for AsymPol.<sup>[53]</sup> To evaluate the potential to enhance additive resonances in the bulk of PS, we extruded it with 0.5 wt.% of F-BTA and with 0.5 and 2 wt.% of AsymPol. Two AsymPol concentrations were chosen to investigate if the same polarisation kinetics apply for the minority component and for the bulk phase. Regardless of the AsymPol concentration, the DNP build-up time is around 8 s. As for the frozen solutions, this indicates a direct polarisation transfer over long distances. The  $\epsilon_{on/off}$  is 17 and 11 with an S of 2646 and 1212  $\text{mg}^{-1}\text{h}^{-1/2}$  for the samples containing 0.5 and 2 wt.% of AsymPol, respectively (Figure 2.12). This shows that the optimal enhancement of the minority species is obtained for the same preparation parameters as for the bulk signals.

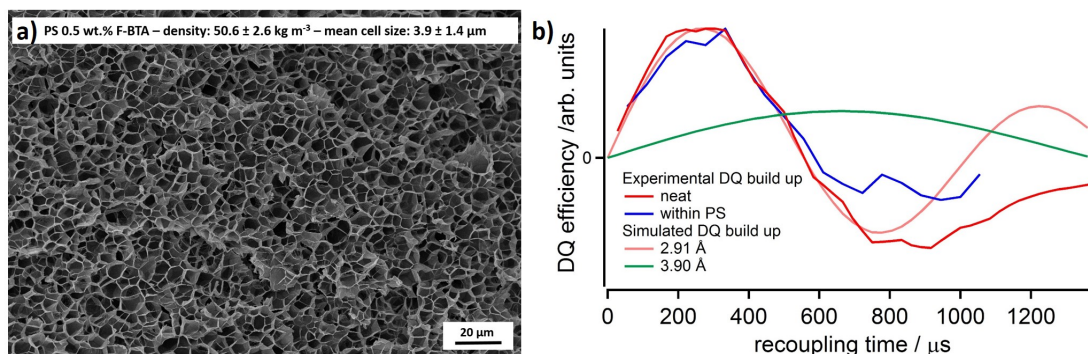


**Figure 2.13:** a) SEM image of the PS foam with 0.5 wt.% of F-BTA with the foam characteristics stated at the top of the image b) Experimental and simulated  $^{19}\text{F}$ - $^{19}\text{F}$ -DQ build-up curves of F-BTA: HT polymorph<sup>[45]</sup> (red), LT polymorph<sup>[44]</sup> (green) and within PS (blue).

The F-BTA concentration of 0.5 wt.% was chosen because at this concentration F-BTA acts as an excellent foam cell nucleation agent for PS, creating a foam density of  $50.6 \text{ kg m}^{-3}$  with a mean cell size of  $3.9 \pm 1.4 \text{ }\mu\text{m}$  (Figure 2.13a). This is an even smaller and more homogeneous cell size as obtained for the kinked bisamide in publication 5.<sup>[21]</sup> To explain the efficient foam cell nucleation, the structure and morphology of F-BTA within PS needs to be found. According to the concept of supramolecular additives (Figure 1.2 in section 1.1), objects form within the polymer at which the foam bubbles nucleate. However, in PS these structures have only been detected indirectly.<sup>[20]</sup> Furthermore F-BTA is known to have two polymorphs.<sup>[44,45]</sup> The high temperature (HT) polymorph<sup>[45]</sup> has a columnar structure and hence a one dimensional nanoobject morphology, whereas the low temperature (LT) polymorph<sup>[44]</sup> has a layered structure and thus a two dimensional nanoobject morphology.

To investigate which polymorph forms, if any objects are formed at all, DNP enhanced  $^{19}\text{F}$ - $^{19}\text{F}$ -DQ build-up curves were measured on the sample. Since the two F-BTA polymorphs have characteristic closest F-F distances of  $2.9 \text{ \AA}$ <sup>[45]</sup> and  $3.9 \text{ \AA}$ <sup>[44]</sup>, the DQ-build-up curve shows which polymorph is formed. The simulated build-up curves of the two polymorphs differ significantly (Figure 2.13b blue and green). The HT polymorph (blue) reaches its maximum DQ efficiency after a recoupling time of roughly  $300 \text{ }\mu\text{s}$ , whereas the LT polymorph has its maximum at  $780 \text{ }\mu\text{s}$ . A measurement of the neat F-BTA without DNP enhancement follows the simulation perfectly. The measured DNP enhanced DQ-build-up curve of F-BTA within PS follows the course of the HT polymorph, it just does not quite reach the

minimum. This confirms that the HT polymorph is formed within PS. The columnar structure of this polymorph results in one-dimensional structures within the polymer, leading to a similar morphology as for the kinked bisamide in the previous section. This explains the excellent foam cell nucleation behaviour and shows the significance of the prediction of nanoobject morphology from the crystal structure.

79 % of all polymeric materials end at landfills or the natural environment,<sup>[119]</sup> where biotic and abiotic fragmentation processes happen that lead to the release of secondary microplastic (MP) into terrestrial and maritime ecosystems.<sup>[120–122]</sup> Once in these ecosystems, further degradation by photo oxidation occurs, leading to the formation of functional groups, like ketones, carboxylic acids, vinylidenes, peroxides and alcohols.<sup>[123]</sup> The quantification and formation time of these defects is still an ongoing question, to be able to evaluate the hazards posed by the MP itself. ss-NMR spectroscopy is a versatile tool for the quantification of these defects, as it is a bulk spectroscopy.<sup>[1]</sup> However, the small concentration of the defects and the intrinsically low sensitivity of NMR spectroscopy results in time consuming measurements. Therefore, we investigated the potential to analyse artificially weathered microplastic particles with different sample preparation techniques of DNP enhanced ss-NMR spectroscopy and summarised the results in the unpublished manuscript “DNP Enhanced Solid-State NMR Spectroscopy Meets Microplastic - Sample Preparation for Optimal Sensitivity Enhancement”. In addition to the already discussed sample preparation techniques of IWI and extrusion, we also prepared samples with the glass forming (GF) and film casting (FC) techniques. GF is very similar to IWI with the difference that the sample is partly or fully soluble in the applied solvent that holds the PA. Upon mixing the solvent and the sample, a gel forms that can be transferred to the MAS rotor. With the insertion to the pre-cooled NMR magnet, the gel vitrifies and forms a glass. For the FC technique, the sample is completely dissolved in the radical containing solvent and cast on a glass plate to let the solvent evaporate. Three different solvents namely TCE, tetrahydrofuran (THF) and Trichloroethylen (TriCE), were tested with AsymPol as a PA.

The best results were obtained with the FC preparation technique. As observed in Figure 2.14a, in all films the ketone, carboxylic acid and peroxide defects that result from the 3200 h weathering are clearly visible and not present in the pristine sample. In the films obtained from TCE and THF, resonances of the

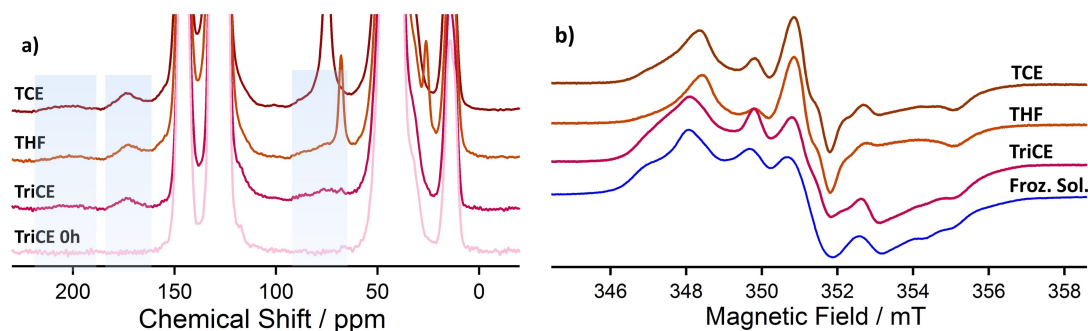


**Figure 2.14:** a) DNP enhanced  $^{13}\text{C}\{^1\text{H}\}$  CP NMR spectra of the 3200h weathered microplastic films obtained from TCE, THF and TriCE. For comparison, the spectrum of a film made of pristine PS is included as well. b) EPR spectra of the same weathered microplastic films. Additionally, the same spectrum of the frozen solution as in Figure 2.11 is shown.

residual solvent are visible in the spectrum at 74 ppm (TCE) and 67 and 25 ppm (THF). This effect of the residual solvent peaks is much more pronounced for the IWI and GF samples, since in the FC technique the solvent is supposed to be completely evaporated. Extrusion disqualified itself as preparation technique, as the microplastic particles were too small to be efficiently forwarded in the extruder. Therefore, they needed to be flushed out with pristine PS. This resulted in uncontrollable long extrusion times that led to the destruction of the defects and a mixing of the weathered and pristine PS. That is why we focus on FC sample in this synopsis. As for the extruded sample in the previous paragraph, it is important to know whether the radical is homogeneously distributed in the film. The EPR measurements (Figure 2.14b) show that the used solvent has a slight influence on the EPR line shape. The spectrum of the film obtained from TriCE follows the spectrum of the frozen solution best, hence we assume the best distribution of the radical in this film. This effect is underlined by the significantly better S of  $572 \text{ mg}^{-1}\text{h}^{-1/2}$  of this film compared to 256 and  $182 \text{ mg}^{-1}\text{h}^{-1/2}$  for TCE and THF, respectively.

The spectra of the films from Figure 2.14a were recorded in less than an hour. In a previous study,<sup>[1]</sup> more than 24 h were needed to acquire a spectrum with a similar sensitivity. Therefore, it was not possible to observe defects in a sample weathered for 400 h in a reasonable measurement time, as it is expected that the concentration of defects is much smaller. With DNP enhancement (Figure 2.15), the same defects as for the 3200 h weathered sample were observed with 12 h of measurement time. However, the intensity and the linewidth are

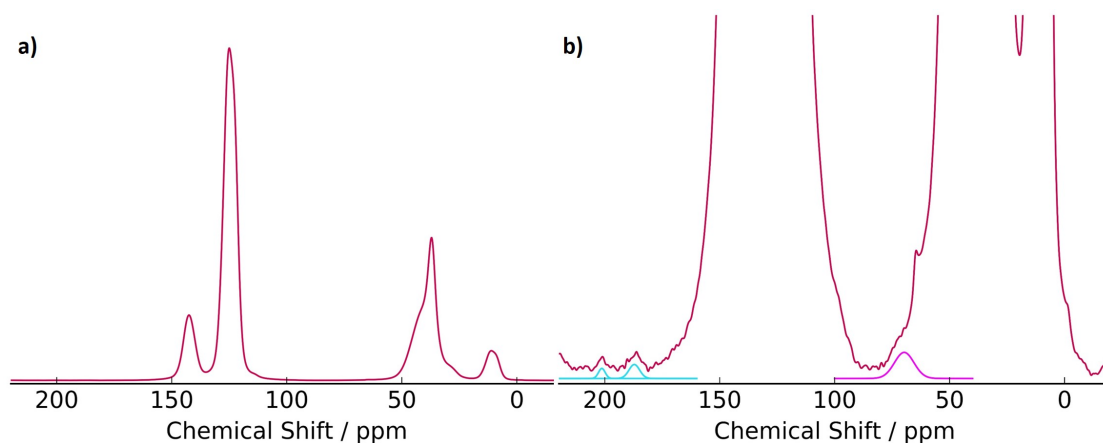


**Figure 2.15:** a) DNP enhanced  $^{13}\text{C}\{^1\text{H}\}$  CP NMR spectra of the 400h weathered microplastic film obtained from TriCE. b) Zoom on the formed defects. Be aware that the very sharp resonance at 65 ppm is a result of an impurity of the batch. The deconvolutions of the ketone defects are plotted in turquoise and the deconvolution of the peroxide defects is plotted in purple. The carboxylic defects (ca. 160 ppm) are hidden in the shoulder of the peak of the ipso carbon and could not be unambiguously deconvoluted.

significantly smaller. Especially the reduced linewidth shows that the respective defects all have a very comparable environment, whereas for the longer weathered samples the degradation of the polymer is so far advanced that a lot of different environments exist. A deconvolution and integration shows that the detection limit of defect concentrations is lowered by one order of magnitude.

This work focussed on method and concept development of polymer additives and their analytics inside and outside the polymer on different length scales. With ss-NMR spectroscopy, the molecular structures of compounds unstable in solution were investigated, showing how a combination of methods can solve the structures. The crystal engineering of BBAs provides a tool to predict the nanoobject morphology and surface polarity based on the molecular structure, which supports a rational design of new polymer additives. Therewith, we found that for efficient foam cell nucleation one-dimensional nanoobject morphologies are preferred. Preparing extruded and film casted samples for DNP enhanced NMR spectroscopy has been optimised and successfully applied to investigate additives and defects within polymers. These methods show great potential to be established as standard techniques to investigate minority species within polymers with solid state NMR spectroscopy, since they reduce the detection limit of NMR spectroscopy by at least one order of magnitude.

## References

- [1] N. Meides, T. Menzel, B. Poetzschner, M. G. J. Löder, U. Mansfeld, P. Strohhriegl, V. Altstaedt, J. Senker, “Reconstructing the Environmental Degradation of Polystyrene by Accelerated Weathering”, *Environ. Sci. Technol.* **2021**, *55*, 7930–7938.
- [2] *Polymeric Foams*, (Ed.: K. C. Khemani), American Chemical Society, Washington, DC, **1997**.
- [3] V. Marturano, P. Cerruti, V. Ambrogi, “Polymer additives”, *Phys. Sci. Rev.* **2017**, *2*, 3197.
- [4] P. Joseph, M. S. Rabello, L. Mattoso, K. Joseph, S. Thomas, “Environmental effects on the degradation behaviour of sisal fibre reinforced polypropylene composites”, *Compos. Sci. Technol.* **2002**, *62*, 1357–1372.
- [5] R. Crous, M. Datt, D. Foster, L. Bennie, C. Steenkamp, J. Huyser, L. Kirsten, G. Steyl, A. Roodt, “Rhodium hydride formation in the presence of a bulky monophosphite ligand: A spectroscopic and solid-state investigation”, *Dalton. Trans.* **2005**, 1108–1116.
- [6] M. Blomenhofer, S. Ganzleben, D. Hanft, H.-W. Schmidt, M. Kristiansen, P. Smith, K. Stoll, D. Mäder, K. Hoffmann, ““Designer” Nucleating Agents for Polypropylene”, *Macromolecules* **2005**, *38*, 3688–3695.
- [7] F. Abraham, H.-W. Schmidt, “1,3,5-Benzenetrisamide based nucleating agents for poly(vinylidene fluoride)”, *Polymer* **2010**, *51*, 913–921.

- [8] M. Schmidt, J. J. Wittmann, R. Kress, D. Schneider, S. Steuernagel, H.-W. Schmidt, J. Senker, “Crystal Structure of a Highly Efficient Clarifying Agent for Isotactic Polypropylene”, *Cryst. Growth Des.* **2012**, *12*, 2543–2551.
- [9] M. Schmidt, J. J. Wittmann, R. Kress, H.-W. Schmidt, J. Senker, “Probing self-assembled 1,3,5-benzenetrisamides in isotactic polypropylene by  $^{13}\text{C}$  DQ solid-state NMR spectroscopy”, *Chem. Commun.* **2013**, *49*, 267–269.
- [10] Y. Shi, Z. Xin, “Study on variable nucleation efficiency of N,N'-Dicyclohexyl-2,6-naphthalenedicarboxamide on isotactic polypropylene”, *J. Thermoplast. Compos. Mater.* **2016**, *29*, 1667–1679.
- [11] Z. Wang, W. Yang, G. Liu, A. J. Müller, Y. Zhao, X. Dong, K. Wang, D. Wang, “Probing into the epitaxial crystallization of  $\beta$  form isotactic polypropylene: From experimental observations to molecular mechanics computation”, *J. Polym. Sci. Part B: Polym. Phys.* **2017**, *55*, 418–424.
- [12] W. Brostow, X. Lu, O. Gencel, A. T. Osmanson, “Effects of UV Stabilizers on Polypropylene Outdoors”, *Materials* **2020**, *13*, 1626.
- [13] Z. Horváth, B. Gyarmati, A. Menyhárd, P. Doshev, M. Gahleitner, J. Varga, B. Pukánszky, “The role of solubility and critical temperatures for the efficiency of sorbitol clarifiers in polypropylene”, *RSC Adv.* **2014**, *4*, 19737–19745.
- [14] J. S. Colton, N. P. Suh, “The nucleation of microcellular thermoplastic foam with additives: Part I: Theoretical considerations”, *Polym. Eng. Sci.* **1987**, *27*, 485–492.
- [15] R. H. Hansen, W. M. Martin, “Novel Methods for the Production of Foamed Polymers. Nucleation of Dissolved Gas by Localized Hot Spots”, *Ind. Eng. Chem. Prod. Res. Dev.* **1964**, *3*, 137–141.
- [16] I. Tsvintzelis, A. G. Angelopoulou, C. Panayiotou, “Foaming of polymers with supercritical  $\text{CO}_2$ : An experimental and theoretical study”, *Polymer* **2007**, *48*, 5928–5939.
- [17] G. Coste, C. Negrell, S. Caillol, “From gas release to foam synthesis, the second breath of blowing agents”, *Eur. Polym. J.* **2020**, *140*, 110029.

- [18] A. E. Kuchma, F. M. Kuni, A. K. Shchekin, “Nucleation stage with non-steady growth of supercritical gas bubbles in a strongly supersaturated liquid solution and the effect of excluded volume”, *Phys. Rev. E* **2009**, *80*, 061125.
- [19] M. Mörl, C. Steinlein, K. Kreger, H.-W. Schmidt, V. Altstädt, “Improved compression properties of polypropylene extrusion foams by supramolecular additives”, *J. Cell. Plast* **2018**, *54*, 483–498.
- [20] M. Aksit, B. Klose, C. Zhao, K. Kreger, H.-W. Schmidt, V. Altstädt, “Morphology control of extruded polystyrene foams with benzene-trisamide-based nucleating agents”, *J. Cell. Plast* **2019**, *55*, 249–261.
- [21] B. Klose, D. Kremer, M. Aksit, K. P. van der Zwan, K. Kreger, J. Senker, V. Altstädt, H.-W. Schmidt, “Kinked Bisamides as Efficient Supramolecular Foam Cell Nucleating Agents for Low-Density Polystyrene Foams with Homogeneous Microcellular Morphology”, *Polymers* **2021**, *13*, 1094.
- [22] J.-M. Lehn, “Perspectives in Supramolecular Chemistry-From Molecular Recognition towards Molecular Information Processing and Self-Organization”, *Angew. Chem. Int. Ed.* **1990**, *29*, 1304–1319.
- [23] K. K. Bejagam, G. Fiorin, M. L. Klein, S. Balasubramanian, “Supramolecular polymerization of benzene-1,3,5-tricarboxamide: a molecular dynamics simulation study”, *J. Phys. Chem. B* **2014**, *118*, 5218–5228.
- [24] H.-W. Schmidt, F. Würthner, “A Periodic System of Supramolecular Elements”, *Angew. Chem. Int. Ed.* **2020**, *59*, 8766–8775.
- [25] G. R. Desiraju, “Supramolecular Synthons in Crystal Engineering-A New Organic Synthesis”, *Angew. Chem. Int. Ed.* **1995**, *34*, 2311–2327.
- [26] C. Bethke, S. T. Kaysser, N. Du Uy Lan, S. M. Goller, K. P. van der Zwan, J. Senker, H. Ruckdäschel, V. Altstädt, “Synthesis and Characterization of Dual-Functional Carbamates as Blowing and Curing Agents for Epoxy Foam”, *Ind. Eng. Chem. Res.* **2021**, *60*, 7065–7080.
- [27] *Solid-state NMR spectroscopy: Principles and applications*, Reprint, (Ed.: M. J. Duer), Blackwell Science, Oxford i.a., **2005**.
- [28] R. Siegel, J. Trébosc, J.-P. Amoureux, Z. Gan, “3D  $^1\text{H}$ - $^{13}\text{C}$ - $^{14}\text{N}$  correlation solid-state NMR spectrum”, *J. Magn. Reson.* **2008**, *193*, 321–325.

- [29] *Handbook of solid state chemistry*, first edition, (Eds.: R. Dronskowski, S. Kikkawa, A. Stein), Wiley-VCH Verlag, Weinheim, **2017**.
- [30] M. Schmidt, C. S. Zehe, R. Siegel, J. U. Heigl, C. Steinlein, H.-W. Schmidt, J. Senker, “NMR-crystallographic study of two-dimensionally self-assembled cyclohexane-based low-molecular-mass organic compounds”, *CrystEngComm* **2013**, *15*, 8784–8796.
- [31] K. P. van der Zwan, C. Steinlein, K. Kreger, H.-W. Schmidt, J. Senker, “Crystal Engineering of Supramolecular 1,4-Benzene Bisamides by Side-Chain Modification - Towards Tuneable Anisotropic Morphologies and Surfaces”, *ChemPhysChem* **2021**, *22*, 2585–2593.
- [32] R. K. Harris, R. E. Wasylshen, M. J. Duer, *NMR Crystallography*, 2. Aufl., Wiley, s.l., **2012**.
- [33] C. Martineau, J. Senker, F. Taulelle, “NMR Crystallography”, *Annu. Rep. NMR Spectrosc.* **2014**, *82*, 1–57.
- [34] A. Hofstetter, L. Emsley, “Positional Variance in NMR Crystallography”, *J. Am. Chem. Soc.* **2017**, *139*, 2573–2576.
- [35] S. E. Ashbrook, P. Hodgkinson, “Perspective: Current advances in solid-state NMR spectroscopy”, *J. Chem. Phys.* **2018**, *149*, 040901.
- [36] P. Hodgkinson, “NMR crystallography of molecular organics”, *Prog. Nucl. Magn. Reson. Spectrosc.* **2020**, *118-119*, 10–53.
- [37] M. Marín-Luna, P. Sánchez-Andrada, I. Alkorta, J. Elguero, M. C. Torralba, P. Delgado-Martínez, D. Santa María, R. M. Claramunt, “A structural analysis of 2,5-diaryl-4*H*-2,4-dihydro-3*H*-1,2,4-triazol-3-ones: NMR in the solid state, X-ray crystallography, and GIPAW calculations”, *Magn. Reson. Chem.* **2021**, *59*, 423–438.
- [38] P. Hartman, W. G. Perdok, “On the relations between structure and morphology of crystals. I”, *Acta. Cryst.* **1955**, *8*, 49–52.
- [39] M. A. Lovette, A. R. Browning, D. W. Griffin, J. P. Sizemore, R. C. Snyder, M. F. Doherty, “Crystal Shape Engineering”, *Ind. Eng. Chem. Res.* **2008**, *47*, 9812–9833.
- [40] A. Mishra, M. K. R. Fischer, P. Bäuerle, “Metal-free organic dyes for dye-sensitized solar cells: From structure: property relationships to design rules”, *Angew. Chem. Int. Ed.* **2009**, *48*, 2474–2499.

- [41] M. A. Lovette, M. F. Doherty, “Needle-Shaped Crystals: Causality and Solvent Selection Guidance Based on Periodic Bond Chains”, *Cryst. Growth Des.* **2013**, *13*, 3341–3352.
- [42] P. Dandekar, Z. B. Kuvadia, M. F. Doherty, “Engineering Crystal Morphology”, *Annu. Rev. Mater. Res.* **2013**, *43*, 359–386.
- [43] C. Butterhof, T. Martin, P. Ectors, D. Zahn, P. Niemietz, J. Senker, C. Näther, J. Brey, “Thermoanalytical Evidence of Metastable Molecular Defects in Form I of Benzamide”, *Cryst. Growth Des.* **2012**, *12*, 5365–5372.
- [44] C. Zehe, M. Schmidt, R. Siegel, K. Kreger, V. Daebel, S. Ganzleben, H.-W. Schmidt, J. Senker, “Influence of fluorine side-group substitution on the crystal structure formation of benzene-1,3,5-trisamides”, *CrystEngComm* **2014**, *16*, 9273–9283.
- [45] C. S. Zehe, J. A. Hill, N. P. Funnell, K. Kreger, K. P. van der Zwan, A. L. Goodwin, H.-W. Schmidt, J. Senker, “Mesoscale Polarization by Geometric Frustration in Columnar Supramolecular Crystals”, *Angew. Chem. Int. Ed.* **2017**, *56*, 4432–4437.
- [46] K. P. van der Zwan, W. Riedel, F. Aussenac, C. Reiter, K. Kreger, H.-W. Schmidt, T. Risse, T. Gutmann, J. Senker, “<sup>19</sup>F MAS DNP for Probing Molecules in Nanomolar Concentrations: Direct Polarization as Key for Solid-State NMR Spectra without Solvent and Matrix Signals”, *J. Phys. Chem. C* **2021**, *125*, 7287–7296.
- [47] A. W. Overhauser, “Polarization of Nuclei in Metals”, *Phys. Rev.* **1953**, *92*, 411–415.
- [48] G. J. Gerfen, L. R. Becerra, D. A. Hall, R. G. Griffin, R. J. Temkin, D. J. Singel, “High frequency (140 GHz) dynamic nuclear polarization: Polarization transfer to a solute in frozen aqueous solution”, *J. Chem. Phys.* **1995**, *102*, 9494–9497.
- [49] D. A. Hall, D. C. Maus, G. J. Gerfen, S. J. Inati, L. R. Becerra, F. W. Dahlquist, R. G. Griffin, “Polarization-Enhanced NMR Spectroscopy of Biomolecules in Frozen Solution”, *Science* **1997**, *276*, 930–932.

- [50] V. S. Bajaj, C. T. Farrar, M. K. Hornstein, I. Mastovsky, J. Vieregg, J. Bryant, B. Eléna, K. E. Kreisler, R. J. Temkin, R. G. Griffin, “Dynamic nuclear polarization at 9 T using a novel 250 GHz gyrotron microwave source”, *J. Magn. Reson.* **2003**, *160*, 85–90.
- [51] A. Zagdoun, G. Casano, O. Ouari, G. Lapadula, A. J. Rossini, M. Lelli, M. Baffert, D. Gajan, L. Veyre, W. E. Maas, M. Rosay, R. T. Weber, C. Thieuleux, C. Coperet, A. Lesage, P. Tordo, L. Emsley, “A Slowly Relaxing Rigid Biradical for Efficient Dynamic Nuclear Polarization Surface-Enhanced NMR Spectroscopy: Expeditious Characterization of Functional Group Manipulation in Hybrid Materials”, *J. Am. Chem. Soc.* **2012**, *134*, 2284–2291.
- [52] C. Sauvée, M. Rosay, G. Casano, F. Aussenac, R. T. Weber, O. Ouari, P. Tordo, “Highly efficient, water-soluble polarizing agents for dynamic nuclear polarization at high frequency”, *Angew. Chem. Int. Ed.* **2013**, *52*, 10858–10861.
- [53] F. Mentink-Vigier, I. Marin-Montesinos, A. P. Jagtap, T. Halbritter, J. van Tol, S. Hediger, D. Lee, S. T. Sigurdsson, G. De Paëpe, “Computationally Assisted Design of Polarizing Agents for Dynamic Nuclear Polarization Enhanced NMR: The AsymPol Family”, *J. Am. Chem. Soc.* **2018**, *140*, 11013–11019.
- [54] A. Zagdoun, G. Casano, O. Ouari, M. Schwarzwälder, A. J. Rossini, F. Aussenac, M. Yulikov, G. Jeschke, C. Copéret, A. Lesage, P. Tordo, L. Emsley, “Large molecular weight nitroxide biradicals providing efficient dynamic nuclear polarization at temperatures up to 200 K”, *J. Am. Chem. Soc.* **2013**, *135*, 12790–12797.
- [55] A. S. L. Thankamony, J. J. Wittmann, M. Kaushik, B. Corzilius, “Dynamic nuclear polarization for sensitivity enhancement in modern solid-state NMR”, *Prog. Nucl. Magn. Reson. Spectrosc.* **2017**, 120–195.
- [56] H. Staudinger, “Über Polymerisation”, *Ber. dtsh. Chem. Ges. A/B* **1920**, *53*, 1073–1085.
- [57] J. A. R. P. Sarma, G. R. Desiraju, “The role of Cl· · · Cl and C-H· · · O interactions in the crystal engineering of 4-Å short-axis structures”, *Acc. Chem. Res.* **1986**, *19*, 222–228.

- [58] M. Zhang, H. N. Tsao, W. Pisula, C. Yang, A. K. Mishra, K. Müllen, “Field-effect transistors based on a benzothiadiazole-cyclopentadithiophene copolymer”, *J. Am. Chem. Soc.* **2007**, *129*, 3472–3473.
- [59] D. Hu, G. Wang, J. Feng, X. Lu, “Exploring supramolecular self-assembly of a bisamide nucleating agent in polypropylene melt: The roles of hydrogen bond and molecular conformation”, *Polymer* **2016**, *93*, 123–131.
- [60] C. Han, D. Zhao, S. Dong, “Three-dimensional supramolecular polymerization based on pillarnarenes ( $n = 5, 6$ ) and halogen bonding interactions”, *Chem. Commun.* **2018**, *54*, 13099–13102.
- [61] O. M. Yaghi, G. Li, H. Li, “Selective binding and removal of guests in a microporous metal–organic framework”, *Nature* **1995**, *378*, 703–706.
- [62] S. Cantekin, T. F. de Greef, A. R. A. Palmans, “Benzene-1,3,5-tricarboxamide: a versatile ordering moiety for supramolecular chemistry”, *Chem. Soc. Rev.* **2012**, *41*, 6125–6137.
- [63] C. F. C. Fitié, W. S. C. Roelofs, M. Kemerink, R. P. Sijbesma, “Remnant polarization in thin films from a columnar liquid crystal”, *J. Am. Chem. Soc.* **2010**, *132*, 6892–6893.
- [64] R. Q. Albuquerque, A. Timme, R. Kress, J. Senker, H.-W. Schmidt, “Theoretical investigation of macrodipoles in supramolecular columnar stackings”, *Chem. Eur. J.* **2013**, *19*, 1647–1657.
- [65] I. Urbanaviciute, X. Meng, T. D. Cornelissen, A. V. Gorbunov, S. Bhat-tacharjee, R. P. Sijbesma, M. Kemerink, “Tuning the Ferroelectric Properties of Trialkylbenzene-1,3,5-tricarboxamide (BTA)”, *Adv. Electron. Mater.* **2017**, *3*, 1600530.
- [66] E. G. Ramírez-Milanés, F. J. Martínez-Martínez, N. E. Magaña-Vergara, S. Rojas-Lima, Y. A. Avendaño-Jiménez, E. V. García-Báez, L. M. Morín-Sánchez, I. I. Padilla-Martínez, “Positional Isomerism and Steric Effects in the Self-Assemblies of Phenylene Bis-Monothiooxalamides”, *Cryst. Growth Des.* **2017**, *17*, 2513–2528.
- [67] J. C. Singer, A. Ringk, R. Giesa, H.-W. Schmidt, “Melt Electrospinning of Small Molecules”, *Macromol. Mater. Eng.* **2015**, *300*, 259–276.

- [68] D. Weiss, D. Skrybeck, H. Misslitz, D. Nardini, A. Kern, K. Kreger, H.-W. Schmidt, “Tailoring Supramolecular Nanofibers for Air Filtration Applications”, *ACS Appl. Mater. Interfaces* **2016**, *8*, 14885–14892.
- [69] N. Mohmeyer, H.-W. Schmidt, P. M. Kristiansen, V. Altstädt, “Influence of Chemical Structure and Solubility of Bisamide Additives on the Nucleation of Isotactic Polypropylene and the Improvement of Its Charge Storage Properties”, *Macromolecules* **2006**, *39*, 5760–5767.
- [70] V. Altstädt, M. Stumpf, H.-W. Schmidt, M. Kersch, DE102011083434 B4, **2016**.
- [71] B. Chang, K. Schneider, R. Vogel, G. Heinrich, “Influence of nucleating agent self-assembly on structural evolution of isotactic polypropylene during uniaxial stretching”, *Polymer* **2018**, *138*, 329–342.
- [72] M. Aksit, C. Zhao, B. Klose, K. Kreger, H.-W. Schmidt, V. Altstädt, “Extruded Polystyrene Foams with Enhanced Insulation and Mechanical Properties by a Benzene-Trisamide-Based Additive”, *Polymers* **2019**, *11*, 268.
- [73] A. Thierry, C. Straupé, J.-C. Wittmann, B. Lotz, “Organogelators and Polymer Crystallisation”, *Macromol. Symp.* **2006**, *241*, 103–110.
- [74] F. A. Wenzel, H. Welz, K. P. van der Zwan, S. Stäter, K. Kreger, R. Hildner, J. Senker, H.-W. Schmidt, “Highly Efficient Supramolecular Nucleating Agents for Poly(3-hexylthiophene)”, *Macromolecules* **2022**, *55*, 2861–2871.
- [75] W. H. Bragg, W. L. Bragg, “The reflection of X-rays by crystals”, *Proc. R. Soc. Lond. A* **1913**, *88*, 428–438.
- [76] G. Taylor, “The phase problem”, *Acta. Crystallogr. D* **2003**, *59*, 1881–1890.
- [77] A. L. Patterson, “A Fourier Series Method for the Determination of the Components of Interatomic Distances in Crystals”, *Phys. Rev.* **1934**, *46*, 372–376.
- [78] A. L. Patterson, “A Direct Method for the Determination of the Components of Interatomic Distances in Crystals”, *Z. Kristallogr. Cryst. Mater* **1935**, *90*, 517–542.
- [79] G. M. Sheldrick, “Phase annealing in SHELX-90: Direct methods for larger structures”, *Acta. Crystallogr. A* **1990**, *46*, 467–473.

- [80] H. M. Rietveld, “A profile refinement method for nuclear and magnetic structures”, *J. Appl. Crystallogr.* **1969**, *2*, 65–71.
- [81] J.-E. Berg, P.-E. Werner, “On the use of Guinier-Hägg film data for structure analysis The crystal structure of tetraammonium  $\alpha'$ - $\mu$ -oxobis- [gied'- $\mu_3$ (S)-malato-O(1),O(2),O(4),O(4')]-di- $\mu$ -oxobis[dioxo-molybdate(VI)] monohydrate”, *Z. Kristallogr. Cryst. Mater* **1977**, *145*, 310–320.
- [82] D. Louër, M. Louër, “Crystal structure of  $\text{Nd}(\text{OH})_2\text{NO}_3 \cdot \text{H}_2\text{O}$  completely solved and refined from X-ray powder diffraction”, *J. Solid State Chem.* **1987**, *68*, 292–299.
- [83] K. D. M. Harris, M. Tremayne, “Crystal Structure Determination from Powder Diffraction Data”, *Chem. Mater.* **1996**, *8*, 2554–2570.
- [84] A. A. Coelho, “TOPAS and TOPAS-Academic: An optimization program integrating computer algebra and crystallographic objects written in C++”, *J. Appl. Crystallogr.* **2018**, *51*, 210–218.
- [85] N. Eichstaedt, K. P. van der Zwan, L. Mayr, R. Siegel, J. Senker, J. Brey, “Crystal structure of phenanthrenide salts stabilized by 15-crown-5 and 18-crown-6”, *Z. Naturforsch. B* **2021**, *77*, 197–201.
- [86] S. L. Mayo, B. D. Olafson, W. A. Goddard, “DREIDING: A generic force field for molecular simulations”, *J. Phys. Chem.* **1990**, *94*, 8897–8909.
- [87] W. Kohn, L. J. Sham, “Self-Consistent Equations Including Exchange and Correlation Effects”, *Phys. Rev.* **1965**, *140*, A1133–A1138.
- [88] P. Hohenberg, W. Kohn, “Inhomogeneous Electron Gas”, *Phys. Rev.* **1964**, *136*, B864–B871.
- [89] S. J. Clark, M. D. Segall, C. J. Pickard, P. J. Hasnip, M. I. J. Probert, K. Refson, M. C. Payne, “First principles methods using CASTEP”, *Z. Kristallogr. Cryst. Mater* **2005**, *220*, 567–570.
- [90] M. D. Bird, I. R. Dixon, J. Toth, “Large, High-Field Magnet Projects at the NHMFL”, *IEEE Trans. Appl. Supercond.* **2015**, *25*, 1–6.
- [91] *Hyperpolarization Methods in NMR Spectroscopy*, (Ed.: L. T. Kuhn), **2013**.

- [92] T. C. Eisenschmid, R. U. Kirss, P. P. Deutsch, S. I. Hommeltoft, R. Eisenberg, J. Bargon, R. G. Lawler, A. L. Balch, "Para hydrogen induced polarization in hydrogenation reactions", *J. Am. Chem. Soc.* **1987**, *109*, 8089–8091.
- [93] T. G. Walker, W. Happer, "Spin-exchange optical pumping of noble-gas nuclei", *Rev. Mod. Phys.* **1997**, *69*, 629–642.
- [94] A. Abragam, W. G. Proctor, "Dynamic polarization of atomic nuclei in solids", *C. R. Hebd. Seances Acad. Sci* **1958**, *246*, 2253–2256.
- [95] T. Maly, G. T. Debelouchina, V. S. Bajaj, K.-N. Hu, C.-G. Joo, M. L. Mak-Jurkauskas, J. R. Sirigiri, P. C. A. van der Wel, J. Herzfeld, R. J. Temkin, R. G. Griffin, "Dynamic nuclear polarization at high magnetic fields", *J. Chem. Phys.* **2008**, *128*, 052211.
- [96] B. Corzilius, "Theory of solid effect and cross effect dynamic nuclear polarization with half-integer high-spin metal polarizing agents in rotating solids", *Phys. Chem. Chem. Phys.* **2016**, *18*, 27190–27204.
- [97] K. Kundu, F. Mentink-Vigier, A. Feintuch, S. Vega, "DNP Mechanisms", *e.Mag.Res.* **2019**, *8*, 295–337.
- [98] E. Bouleau, P. Saint-Bonnet, F. Mentink-Vigier, H. Takahashi, J.-F. Jacquot, M. Bardet, F. Aussenac, A. Pureau, F. Engelke, S. Hediger, D. Lee, G. De Paëpe, "Pushing NMR sensitivity limits using dynamic nuclear polarization with closed-loop cryogenic helium sample spinning", *Chem. Sci.* **2015**, *6*, 6806–6812.
- [99] K. R. Thurber, R. Tycko, "Theory for cross effect dynamic nuclear polarization under magic-angle spinning in solid state nuclear magnetic resonance: The importance of level crossings", *J. Chem. Phys.* **2012**, *137*, 084508.
- [100] M. Afeworki, R. A. McKay, J. Schaefer, "Selective observation of the interface of heterogeneous polycarbonate/polystyrene blends by dynamic nuclear polarization carbon-13 NMR spectroscopy", *Macromolecules* **1992**, *25*, 4084–4091.
- [101] F. Mentink-Vigier, S. Paul, D. Lee, A. Feintuch, S. Hediger, S. Vega, G. De Paëpe, "Nuclear depolarization and absolute sensitivity in magic-angle spinning cross effect dynamic nuclear polarization", *Phys. Chem. Chem. Phys.* **2015**, *17*, 21824–21836.

- [102] F. Mentink-Vigier, Ü. Akbey, H. Oschkinat, S. Vega, A. Feintuch, “Theoretical aspects of Magic Angle Spinning - Dynamic Nuclear Polarization”, *J. Magn. Reson.* **2015**, *258*, 102–120.
- [103] S. Hediger, D. Lee, F. Mentink-Vigier, G. De Paëpe, “MAS-DNP Enhancements: Hyperpolarization, Depolarization, and Absolute Sensitivity”, *e.Mag.Res.* **2018**, *7*, 105–117.
- [104] F. Mentink-Vigier, A.-L. Barra, J. van Tol, S. Hediger, D. Lee, G. De Paëpe, “De novo prediction of cross-effect efficiency for magic angle spinning dynamic nuclear polarization”, *Phys. Chem. Chem. Phys.* **2019**, *21*, 2166–2176.
- [105] A. Lesage, M. Lelli, D. Gajan, M. A. Caporini, V. Vitzthum, P. Mieville, J. Alauzun, A. Roussey, C. Thieuleux, A. Mehdi, G. Bodenhausen, C. Copéret, L. Emsley, “Surface Enhanced NMR Spectroscopy by Dynamic Nuclear Polarization”, *J. Am. Chem. Soc.* **2010**, *132*, 15459–15461.
- [106] M. Lelli, D. Gajan, A. Lesage, M. A. Caporini, V. Vitzthum, P. Miéville, F. Héroguel, F. Rascón, A. Roussey, C. Thieuleux, M. Boualleg, L. Veyre, G. Bodenhausen, C. Copéret, L. Emsley, “Fast characterization of functionalized silica materials by silicon-29 surface-enhanced NMR spectroscopy using dynamic nuclear polarization”, *J. Am. Chem. Soc.* **2011**, *133*, 2104–2107.
- [107] A. J. Rossini, A. Zagdoun, F. Hegner, M. Schwarzwälder, D. Gajan, C. Copéret, A. Lesage, L. Emsley, “Dynamic nuclear polarization NMR spectroscopy of microcrystalline solids”, *J. Am. Chem. Soc.* **2012**, *134*, 16899–16908.
- [108] A. J. Rossini, A. Zagdoun, M. Lelli, A. Lesage, C. Coperet, L. Emsley, “Dynamic Nuclear Polarization Surface Enhanced NMR Spectroscopy”, *Acc. Chem. Res.* **2013**, *46*, 1942–1951.
- [109] Q. Z. Ni, F. Yang, T. V. Can, I. V. Sergeyev, S. M. D’Addio, S. K. Jawla, Y. Li, M. P. Lipert, W. Xu, R. T. Williamson, A. Leone, R. G. Griffin, Y. Su, “In Situ Characterization of Pharmaceutical Formulations by Dynamic Nuclear Polarization Enhanced MAS NMR”, *J. Phys. Chem. B* **2017**, *121*, 8132–8141.

- [110] D. Le, G. Casano, T. N. T. Phan, F. Ziarelli, O. Ouari, F. Aussenac, P. Thureau, G. Mollica, D. Gigmes, P. Tordo, S. Viel, “Optimizing Sample Preparation Methods for Dynamic Nuclear Polarization Solid-state NMR of Synthetic Polymers”, *Macromolecules* **2014**, *47*, 3909–3916.
- [111] D. Le, F. Ziarelli, T. N. T. Phan, G. Mollica, P. Thureau, F. Aussenac, O. Ouari, D. Gigmes, P. Tordo, S. Viel, “Up to 100% Improvement in Dynamic Nuclear Polarization Solid-State NMR Sensitivity Enhancement of Polymers by Removing Oxygen”, *Macromol. Rapid Commun.* **2015**, *36*, 1416–1421.
- [112] T. Gullion, J. Schaefer, “Rotational-echo double-resonance NMR”, *J. Magn. Reson.* **1989**, *81*, 196–200.
- [113] S. Matsuoka, M. Inoue, “Application of REDOR NMR in natural product chemistry”, *Chem. Commun.* **2009**, 5664–5675.
- [114] M. Bak, J. T. Rasmussen, N. C. Nielsen, “SIMPSON: A general simulation program for solid-state NMR spectroscopy”, *J. Magn. Reson.* **2000**, *147*, 296–330.
- [115] M. Brinkmann, P. Rannou, “Effect of Molecular Weight on the Structure and Morphology of Oriented Thin Films of Regioregular Poly(3-hexylthiophene) Grown by Directional Epitaxial Solidification”, *Adv. Funct. Mater.* **2007**, *17*, 101–108.
- [116] N. Cheng, Q. Yan, S. Liu, D. Zhao, “Probing the intermolecular interactions of aromatic amides containing N-heterocycles and triptycene”, *CrystEngComm* **2014**, *16*, 4265–4273.
- [117] Ü. Akbey, B. Altin, A. Linden, S. Özçelik, M. Gradzielski, H. Oschkinat, “Dynamic nuclear polarization of spherical nanoparticles”, *Phys. Chem. Chem. Phys.* **2013**, *15*, 20706–20716.
- [118] O. Lafon, M. Rosay, F. Aussenac, X. Lu, J. Trébosc, O. Cristini, C. Kinnowski, N. Touati, H. Vezin, J.-P. Amoureux, “Beyond the silica surface by direct silicon-29 dynamic nuclear polarization”, *Angew. Chem. Int. Ed.* **2011**, *50*, 8367–8370.
- [119] R. Geyer, J. R. Jambeck, K. L. Law, “Production, use, and fate of all plastics ever made”, *Sci. Adv.* **2017**, *3*, e1700782.

- [120] L. Lebreton, A. Andrady, “Future scenarios of global plastic waste generation and disposal”, *Palgrave Commun.* **2019**, *5*, 2922.
- [121] A. L. Andrady, “Microplastics in the marine environment”, *Mar. Pollut. Bull.* **2011**, *62*, 1596–1605.
- [122] G. Erni-Cassola, V. Zadjelovic, M. I. Gibson, J. A. Christie-Oleza, “Distribution of plastic polymer types in the marine environment; A meta-analysis”, *J. Hazard. Mater.* **2019**, *369*, 691–698.
- [123] B. Gewert, M. M. Plassmann, M. MacLeod, “Pathways for degradation of plastic polymers floating in the marine environment”, *Environ. Sci. Process. Impacts.* **2015**, *17*, 1513–1521.



### 3.1 Publications of this work

1. C. Bethke, S.T. Kaysser, N.D.U. Lan, S.M. Goller, K.P. van der Zwan, J.S Senker, H. Ruckdäschel, V. Altstädt “Synthesis and Characterization of Dual-Functional Carbamates as Blowing and Curing Agents for Epoxy Foam”, *Industrial & Engineering Chemistry Research* **2021**, *60*, 7065-7080.
2. K.P. van der Zwan, C. Bethke, A. Pongratz, D. Schweser, R. Siegel, H. Ruckdäschel, V. Altstädt, J. Senker “Structural Analysis of CO<sub>2</sub> Loaded Diamine Derived from Aqueous Synthesis Route for Epoxy Foaming”, *to be submitted*.
3. K.P. van der Zwan, C. Steinlein, K. Kreger, H.-W. Schmidt, J. Senker “Crystal Engineering of Supramolecular 1,4-Benzene Bisamides by Side-Chain Modification - Towards Tuneable Anisotropic Morphologies and Surfaces”, *ChemPhysChem* **2021**, *22*, 2585-2593
4. F.A. Wenzel, H. Welz, K.P. van der Zwan, S. Stäter, K. Kreger, R. Hildner, J. Senker, H.-W. Schmidt “Highly Efficient Supramolecular Nucleating Agents for Poly(3-hexylthiophene)” *Macromolecules* **2022**, *55*, 2861–2871.

5. B. Klose, D. Kremer, M. Aksit, K.P. van der Zwan, K. Kreger, J. Senker, V. Altstädt, H.-W. Schmidt “Kinked Bisamides as Efficient Supramolecular Foam Cell Nucleating Agents for Low-Density Polystyrene Foams with Homogeneous Microcellular Morphology”, *Polymers* **2021**, *13*, 1094.
  
6. K.P. van der Zwan, W. Riedel, F. Aussenac, C. Reiter, K. Kreger, H.-W. Schmidt, T. Risse, T. Gutmann, J. Senker “<sup>19</sup>F MAS DNP for Probing Molecules in Nanomolar Concentrations: Direct Polarization as Key for Solid-State NMR Spectra without Solvent and Matrix Signals”, *Journal of Physical Chemistry C* **2021**, *125*, 7287-7296.
  
7. K.P. van der Zwan, W. Riedel, B. Klose, T. Fischer, R. Siegel, F. Aussenac, C. Reiter, A. Mauel, K. Kreger, G. de Paëppe, H.-W. Schmidt, T. Risse, J. Senker “DNP Enhanced <sup>19</sup>F-<sup>19</sup>FDQ Build up Curve Confirms Crystal Structure of Supramolecular Additive in PS at Technical Concentration for Batch Foaming”, *to be submitted*.
  
8. K.P. van der Zwan, A. Mauel, W. Riedel, N. Meides, T. Fischer, M. Meinhart, P. Strohriegel, T. Risse, J. Senker “DNP Enhanced Solid-State NMR Spectroscopy Meets Microplastic - Sample Preparation for Optimal Sensitivity Enhancement”, *to be submitted*.

## 3.2 Other Publications

1. N. Eichstaedt, K.P. van der Zwan, L. Mayr, R. Siegel, J. Senker, J. Breu “Crystal structure of phenanthrenide salts stabilized by 15-crown-5 and 18-crown-6”, *Zeitschrift für Naturforschung B* **2021**, 4-5, 197-201.
2. C. L. Teske, A.-L. Hansen, R. Wehrich, L. Kienle, M.Kemp, K.P. van der Zwan, J. Senker, C. Dosche, G. Wittstock, W. Bensch “Synthesis, Crystal Structure, and Selected Properties of  $[\text{Au}(\text{S}_2\text{CNH}_2)_2]\text{SCN}$  - A Precursor for Gold Macro-Needles Consisting of Gold Nanoparticles Glued by Graphitic Carbon Nitride”, *Chemistry European Journal* **2019**, 25, 6763-6772.



## 4.1 Synthesis and Characterization of Dual-Functional Carbamates as Blowing and Curing Agents for Epoxy Foam

This work is a cooperation between the Inorganic Chemistry III and the Polymer Engineering of the University of Bayreuth and will be reprinted with permission from C. Bethke, S.T. Kaysser, D.N.U. Lan, S.M. Goller, K.P. van der Zwan, J.S. Senker, H. Ruckdäschel, V. Altstädt, *Industrial & Engineering Chemistry Research* **2021**, *60*, 7065-7080. Copyright 2021 American Chemical Society.

My contributions are:

- conception and authorship of the article with a focus on the paragraphs related to the structure solution
- performing all NMR experiments

The contributions of the other authors are:

- conception and main authorship of the article
- synthesis of the materials
- recording the FTIR measurements
- performing the TGA and DSC measurements
- performing the batch foaming experiments
- evaluating the foam properties

## Synthesis and Characterization of Dual-Functional Carbamates as Blowing and Curing Agents for Epoxy Foam

Christian Bethke, Simon T. Kaysser, Du Ngoc Uy Lan, Sebastian M. Goller, Kasper P. van der Zwan, Jürgen Senker, Holger Ruckdäschel, and Volker Altstadt\*

Cite This: *Ind. Eng. Chem. Res.* 2021, 60, 7065–7080

Read Online

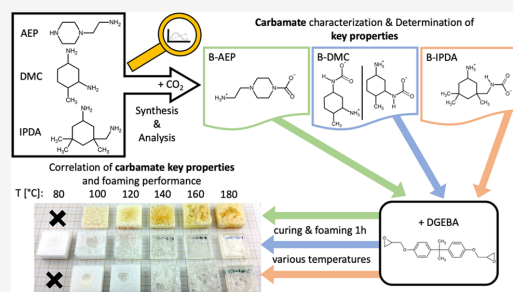
ACCESS |

Metrics & More

Article Recommendations

Supporting Information

**ABSTRACT:** With regard to upcoming regulations of common chemical blowing agents for epoxy foams, carbamates provide suitable alternatives. They act as blowing agents releasing CO<sub>2</sub> and cure epoxy resins after decomposition and amine release. Thus, no undesired byproducts occur. In this study, a detailed analysis of the chemical structures, the decomposition, and the curing behavior of the carbamates received from *N*-aminoethylpiperazine (B-AEP), 4-methylcyclohexane-1,3-diamine (B-DMC), and isophorone diamine (B-IPDA) was attempted. The carbamates were finally used for foaming of diglycidylether of bisphenol-A (DGEBA)-based epoxy resins at different temperatures. By this, the performance of the carbamates in a foaming experiment could be qualitatively compared. The results show that all carbamates are suitable for foaming at specifically adapted temperatures. While B-DMC is able to foam properly only at 80 °C, B-IPDA requires 100–120 °C, and B-AEP is best used for foaming in the range between 120 and 140 °C.



### 1. INTRODUCTION

The development of thermoset epoxy foams started around 1950, and today they are mainly established for applications, where the performance of thermoplastic foams is not sufficient.<sup>1,2</sup> The high degree of cross-linking leads to outstanding characteristics in thermal stability, chemical resistance, and electrical properties. Furthermore, epoxy foams possess adhesive strength toward many materials, excellent rigidity, moisture resistance, and low shrinkage. Due to these specific characteristics, they are mainly applied in electronics, marine, aeronautics, and space applications.<sup>1–4</sup>

Recent evaluations, for example, the “Significantly New Alternatives Policy” (SNAP) or “Registration, Evaluation, Authorization and Restriction of Chemicals” (REACH), lead to ongoing abolition of many blowing agents (BAs) used for epoxy foam systems, as many of the established organic foaming agents and/or their obtained byproducts are toxic, harmful for health and the environment, or explosive. Since CO<sub>2</sub> is a common blowing agent with no strict regulations and low costs, its use in the polymer industry is highly attractive and applied for thermoplastics in a broad range.<sup>5</sup> However, the exothermal step-polymerization of epoxy resins from a liquid monomer to a solid three-dimensional network is leading to a dynamic viscosity profile, causing issues with physical blowing agents such as gaseous or supercritical CO<sub>2</sub>. The solubility and the solution stability are incompatible with most of the currently established ways of thermoset foam

processing, such as cast molding and reactive injection molding, due to the reaction kinetics and the low-pressure conditions thereof.<sup>5,6</sup>

A recent study by Lyu et al. revealed an influence of gaseous CO<sub>2</sub> on the reaction kinetics with regard to a faster cross-linking reaction with increasing CO<sub>2</sub> pressure.<sup>6</sup> The use of precured or even solid-state systems is suggested in the literature for an improved physical foaming performance in batch processing.<sup>7,8</sup> Precuring of the epoxy resin systems for viscosity adjustment was also found to be beneficial for the foam morphology in the literature,<sup>9–11</sup> similar to a high reaction rate during the foaming step.<sup>12</sup> There is only a small number of chemical BAs releasing CO<sub>2</sub> without harmful byproducts.<sup>5</sup> One example is carbonates such as sodium bicarbonate (NaHCO<sub>3</sub>), which is commonly used.<sup>5,13</sup> A remaining aspect is the byproducts, which remain in the foam after decomposition of the chemical blowing agent (CBAs). The mechanical properties can be negatively affected by these residues, which is, next to higher costs compared to physical blowing agents, one of the main concerns about CBAs.<sup>5</sup>

Received: October 27, 2020

Revised: April 16, 2021

Accepted: April 21, 2021

Published: May 7, 2021



The use of carbamates for foaming of epoxy resins was first described in the 1960s.<sup>14</sup> As carbamates exhibit a complex dual function as a blowing and a curing agent, they were rarely applied in the past due to the high availability and diversity of other BAs with less complex kinetics. Currently, due to SNAP and REACH, carbamates have gained more interest due to their environmental-friendly approach of decomposing without releasing harmful byproducts. One state-of-the-art application for such epoxy foam systems can be found in lightweight adhesives for special applications.<sup>15,16</sup> Amine-based carbonates and carbamate salts can be derived from amine hardeners reacting with CO<sub>2</sub> in a prior synthesis step, resulting in a dual-functional molecule with CO<sub>2</sub> as a foaming agent and amine as a curing agent upon decomposition. The CO<sub>2</sub> uptake happens at low temperatures in an exothermal reaction. For this reaction, two amine groups (either primary or secondary) are required to capture one CO<sub>2</sub> molecule. The resulting product is a salt of the carbamic acid, so-called carbamate. When water is involved, the formation of carbonates from tertiary amines is possible.<sup>17–19</sup> The reaction is illustrated in Figure 1. Tertiary

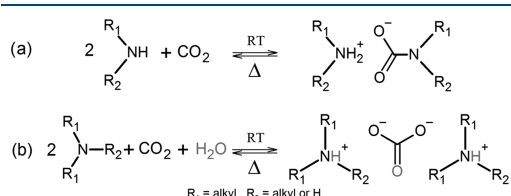


**Figure 1.** Reaction of amines with (a) CO<sub>2</sub> for carbamate formation and (b) with CO<sub>2</sub> and H<sub>2</sub>O for carbonate formation.

amines are able to form carbonates only. The carbamate and carbonate formation is reversible at elevated temperatures, releasing the amine, CO<sub>2</sub>, and water, if involved. Here, the molecular structure is expected to influence the behavior.

Ren et al. focused mainly on *N*-aminoethylpiperazine (AEP)<sup>20</sup> but also others such as *m*-xylenediamine (*m*XDA) and 4,4'-diaminodicyclohexylmethane (DDCM) for the formation of carbamate salts. 3-(Diethylamino)propylamine (DEAPA) was found to be less suitable due to its aliphatic backbone, leading to a gel-like product. The fact that 4,4'-diaminodiphenylmethane (DDM), with a p*K*<sub>a</sub> value of 4.8, was not able to form a carbamate in their study indicates that a medium basicity (p*K*<sub>a</sub> value higher than 9) is required to achieve a proper CO<sub>2</sub> blocking reaction at ambient conditions.<sup>21</sup> Thus, aliphatic primary amines are the most suitable. The foaming performance with adjusted porosities of different carbamates and diglycidylether of bisphenol-A (DGEBA) was investigated using fumed silica as the nucleating agent and poly(ethylene glycol)-*block*-poly(propylene glycol)-*block*-poly(ethylene glycol) (PEG-*b*-PPG-*b*-PEG) foam stabilizer. Densities in the range of 110–330 kg m<sup>-3</sup> were achieved. The morphology of only two out of five samples allowed proper cell size evaluation, resulting in a cell diameter between 145 ± 86 μm for B-AEP at 270 kg m<sup>-3</sup> and 300 ± 221 μm for B-DDCM at 330 kg m<sup>-3</sup>.<sup>21</sup>

In a previous work, the influence of the type of epoxy resin on the applicability of the B-AEP was investigated. It was found that the foam morphology was improved if a high-viscosity epoxy Novolac (EN) resin with a functionality of

3.8 is used compared to a low-viscosity diglycidylether of bisphenol-A (DGEBA) resin with a functionality of 2. In addition, a mixture of blocked and unblocked hardeners was found to further improve the morphology and to obtain a structural foam.<sup>22</sup> Another previous study focused on the process optimization of flame-retardant DGEBA and EN-based epoxy foams with blocked isophorone diamine (B-IPDA) as the primary blowing and curing agent with tailorable thermomechanical properties and density. Herein, densities of 300 and 500 kg m<sup>-3</sup> were adjusted. The compressive behavior was shown to be influenced by density, morphology adjustment by precuring, and the flame-retardant fillers. A combination of 9,10-dihydro-9-oxa-10-phosphaphenanthrene-10-oxide (DOPO) and aluminum trihydroxide (ATH) resulted in the best compromise between the burning behavior and low density.<sup>23</sup>

Thus, carbamates were proven to be applicable for foaming, resulting in high-performance materials. It was noted that B-AEP and B-IPDA act differently during processing with regard to synthesis and also during foaming and curing, resulting in specific adjustments. To the authors' best knowledge, no detailed study on the synthesis behavior, the carbamate structure, or the relation between the amine structure and the resulting carbamate has been published yet. This is assumed to be of importance to improve the applicability of carbamates for future applications.

This study will present a detailed investigation with the focus on the dependency of the amine structure on the carbamate synthesis and its decomposition behavior. Additionally, the link between the decomposition behavior of the carbamate and the curing behavior of the released amines is investigated. This is important to understand the foamability at different process conditions, which will be simulated in a final qualitative foaming experiment using DGEBA and a target density of around 350 kg m<sup>-3</sup>. Furthermore, the chemical structure of the received carbamates will be studied in detail.

For this study, the synthesis of carbamates of three common amine hardeners for epoxy resins with different molecular structures will be analyzed. AEP contains three types of amines, one primary, one secondary, and one tertiary amine, whereof the secondary and tertiary ones are located in the piperazine ring. In addition, two amines where the carbamate formation is not yet fully described in the literature, namely, 4-methylcyclohexane-1,3-diamine (DMC) and IPDA, will be investigated. Both exhibit suitable chemical structures with certain similarities. DMC has two primary amines linked directly to the cyclohexane, while IPDA has one primary amine directly linked to the cyclohexane, while the second one is a methyl amine group. These differences in the structures are expected to lead to different carbamate structures, synthesis behaviors as well as different curing kinetics with the epoxy resin. This can be already seen by the *T*<sub>g</sub> of 110 °C for DGEBA + AEP, 160 °C in the case of DGEBA + DMC, and 155 °C in the case of DGEBA + IPDA.<sup>26</sup> The epoxy-carbamate foams will have potential use as a sandwich core material for high-performance applications,<sup>23</sup> as the adhesion between the epoxy foam core and the epoxy composite face-sheet would be enhanced because they are both originated from the epoxy source.

## 2. MATERIALS AND PROCEDURE

**2.1. Materials.** **2.1.1. Amines and CO<sub>2</sub> for Carbamate Synthesis.** Three types of amines were used for carbamate synthesis. *N*-Aminoethylpiperazine (AEP) with a purity of 99%, a  $M_w$  of 129 g mol<sup>-1</sup>, and an amino hydrogen equivalent weight (AHEW) of 43.1 g mol<sup>-1</sup> (Sigma-Aldrich, St. Louis, Missouri) was used as received. 4-Methylcyclohexane-1,3-diamine (DMC) with a purity of >95%, a  $M_w$  of 128.22 g mol<sup>-1</sup>, and an AHEW of 32.1 g mol<sup>-1</sup> (Aradur XB50021B, Huntsman, Texas) was used as received. Isophorone diamine (IPDA) with a purity of >95%, a  $M_w$  of 170.3 g mol<sup>-1</sup>, and an AHEW of 42.6 g mol<sup>-1</sup> (Aradur 22962, Huntsman, Texas) was used as received.

Gaseous bottled CO<sub>2</sub> with a quality grade of 4.5 (from Rießner Gase, Lichtenfels, Germany) was used for the reaction. As a solvent, technical-grade ethanol with a purity of 98.9% denatured with 1.1% butanone (from CSC Jäckle Chemie GmbH & Co. KG, Nuernberg, Germany) was used as received.

**2.1.2. Epoxy for Foaming.** Diglycidylether of bisphenol-A (DGEBA, DER331, Olin, Missouri) with a  $M_w$  of 340.4 g mol<sup>-1</sup>, an epoxy equivalent weight (EEW) of 187 g mol<sup>-1</sup>, and a predetermined viscosity of 13 Pa s (25 °C) was used.

**2.2. Experimental Procedure.** **2.2.1. Synthesis of CO<sub>2</sub> Blocked Amines.** The reaction of amine and CO<sub>2</sub> was carried out in ethanol for a better heat diffusion and a controllable reaction. Two syntheses were conducted in parallel for comparison. The experimental setup is shown in Figure 2.

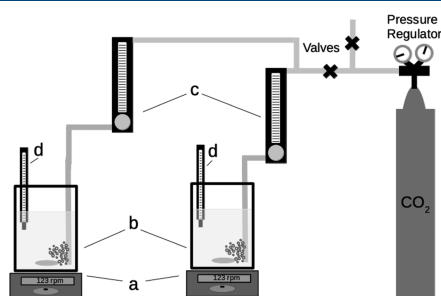


**Figure 2.** Experimental setup for the CO<sub>2</sub> blocking reaction of amine curing agents. A magnetic stirrer (a) stirs the EtOH/amine solution in the reaction flask (b), while the CO<sub>2</sub> flow is regulated by flow regulation valves (c) and the temperature is monitored by thermal sensors (d).

The mixture was prepared by adding and mixing 14 g of amine in 70 g of ethanol (1:5 weight ratio) for each reaction flask (125 mL) using a magnetic stirrer (a). The reaction flasks (b) were attached to the CO<sub>2</sub> cylinder through airflow regulation valves (c). The CO<sub>2</sub> flow was introduced at 100 mL min<sup>-1</sup> and at ambient pressure from the bottom of the flasks through a 2.2 mm-diameter flexible tube for 300 min. The thermal sensors (d) monitored the temperature during the whole synthesis period. The first 120 min of reactions were recorded by video for detailed analyses. Afterward, photos were taken every 30 min.

The reactions were conducted in a fume hood with a surrounding temperature of 21 °C. The initial temperature of the reaction was recorded, and the changes in temperature throughout 300 min were reported. After the reaction time,

the products were filtered and washed with 300 mL of EtOH. The received white powders were dried at room temperature for 16 h in a fume hood and subsequently dried under a vacuum at 30 °C for 16 h. Finally, the powders were milled for 2 h at 170 rpm using a planetary ball mill PM100 (Retsch, Haan, Germany) equipped with a zirconium oxide cup and five balls. The samples were stored at ambient conditions in the lab.

**2.2.2. Characterization of Carbamates.** **2.2.2.1. Structure Analysis by Fourier Transform Infrared (FTIR) and NMR Spectroscopies.** The purity and structural characteristics of the unblocked and blocked amine curing agents were investigated via FTIR-spectroscopic measurements with a Nicolet Nexus 470 FTIR coupled with a KBr beam separator (Thermo Scientific, Waltham, Massachusetts). The samples were measured with 32 scans at room temperature using a wavelength from 600 to 3500 cm<sup>-1</sup>. In addition, thermogravimetric analysis (TGA)-FTIR coupled measurements were carried out to investigate the decomposition products of the blocked amines over time.

Detailed analysis of the chemical structures was performed with solid-state NMR spectroscopy. <sup>13</sup>C{<sup>1</sup>H} cross-polarization magic-angle spinning (CP MAS) NMR spectra were acquired on an Avance III spectrometer (Bruker BioSpin, Rheinstetten, Germany) operating at a proton resonance frequency of 400 MHz. The three samples were packed in 3.2 mm zirconia rotors and transferred to a 3.2 mm triple-resonance probe. The spectra were acquired with ramped cross-polarization and a MAS spinning speed of 12.5 kHz. During the contact time of 3 ms, the nutation frequency on the <sup>1</sup>H channel was varied linearly from 50 to 100%.<sup>24</sup> The maximum nutation frequency during the contact time was set to 61.4 kHz for the <sup>1</sup>H channel, and the <sup>13</sup>C channel was adjusted to maximize the intensity. During acquisition on the <sup>13</sup>C channel, <sup>1</sup>H was decoupled using the Spinal-64 sequence<sup>25</sup> with a nutation frequency of 70.2 kHz. Chemical shifts are referenced to tetramethylsilane (TMS) using adamantane as a secondary reference.

<sup>15</sup>N{<sup>1</sup>H} CP MAS NMR spectra were acquired on an Avance II spectrometer (Bruker BioSpin, Rheinstetten, Germany) operating at a proton resonance frequency of 300 MHz. The three samples were packed in 7 mm zirconia rotors and transferred to a 7 mm triple-resonance probe. The spectra were acquired with square cross-polarization and a MAS spinning speed of 5 kHz. During the contact time of 5 ms, the nutation frequency on the <sup>1</sup>H channel was set to 37.9 kHz for the <sup>1</sup>H channel and the <sup>15</sup>N channel was adjusted to maximize the intensity. During acquisition on the <sup>15</sup>N channel, <sup>1</sup>H was decoupled using the Spinal-64 sequence<sup>25</sup> with a nutation frequency of 55.5 kHz. Chemical shifts are referenced to CH<sub>3</sub>NO<sub>2</sub> using glycine as a secondary reference.

<sup>1</sup>H liquid-state NMR was carried out on a 500 MHz spectrometer (Bruker BioSpin, Rheinstetten, Germany) using EtOH-*d*<sub>6</sub> as a solvent.

**2.2.2.2. Molecular Analysis by Elemental Analysis (EA).** Elemental analysis (EA) was conducted with a UNICUBE (Elementar, Langenselbold, Germany) for detailed analysis of the synthesis products with regard to carbon (C), hydrogen (H), and nitrogen (N) atom contents. The combustion temperature was set to 1150 °C, while the reduction was performed at 950 °C, and the flush time was set to 25 s. All samples were measured in triplicate. For the calculations of

the number of atoms ( $n$ ), the molecular mass ( $M_A$ ) values of C, 12.011 g mol<sup>-1</sup>; H, 1.008 g mol<sup>-1</sup>; N, 14.007 kg mol<sup>-1</sup>; and O, 15.999 g mol<sup>-1</sup> were used.

The wt % of each atom (wt %<sub>A</sub>) related to the total mass of the molecule ( $M_M$ ) was calculated by eq 1

$$\text{wt \%}_A = \frac{n \times M_A \left[ \frac{\text{g}}{\text{mol}} \right]}{M_M \left[ \frac{\text{g}}{\text{mol}} \right]} \times 100\% \quad (1)$$

This is used to determine the remaining mass, which is expected as O-atoms according to the expected molecular formula.

**2.2.2.3. Thermal Characterization.** Differential scanning calorimetry (DSC) was conducted with a DSC1 Star<sup>®</sup> System (Mettler Toledo, Columbus, Ohio) to determine the reaction enthalpy and kinetics. All measurements were carried out in the range of -30 to 300 °C at 10 °C min<sup>-1</sup> with 50 mL min<sup>-1</sup> N<sub>2</sub>. The sample weight was set around 6 mg. For the model free kinetics (MFK) study, additional heating ramps of 5 and 20 °C min<sup>-1</sup> were performed and the MFK was simulated with Mettler Toledo STARe Software v 13.00a (Build 6917).

Thermogravimetric analysis (TGA) was conducted with a TGA/SDTA851e system (Mettler Toledo, Columbus, Ohio) to investigate the decomposition behavior and evaporation temperature of the amines in the range of 30–300 °C at 10 °C min<sup>-1</sup> with 50 mL min<sup>-1</sup> N<sub>2</sub>. Additional isothermal TGA measurements at defined temperatures were carried out to get an impression of the decomposition rate of the carbamates. The sample weight was set around 15 mg for standard measurements and around 35 mg for FTIR coupled measurements.

The CO<sub>2</sub> content was calculated theoretically by the amount of available amino groups per molecule combined with the results gained from TGA and EA.

**2.2.3. Foaming Experiments.** To examine the characteristics of the carbamates' dual function as a blowing and curing agent, they were mixed with DGEBA resin based on the stoichiometric ratio by EEW and AHEW of the carbamates, which means a weight ratio of 1:3.2 for B-AEP, 1:4.2 for B-DMC, and 1:3.4 for B-IPDA. Therefore, the resin was preheated to 30 °C. The mixing was carried out by adding the corresponding amounts of resin and carbamate to a 10 mL cup, and after a short manual mixing, it was set at room temperature for 1 min at 3500 rpm in a DAC 150 (Speed-Mixer, Hamm, Germany) mixing system. For foaming, an aluminum mold, made by the mechanical workshop of the University Bayreuth, with a cavity of 30 mm × 30 mm × 10 mm ( $l \times w \times h$ ) and a bulk volume of 9 cm<sup>3</sup> was used, treated with Loctite Frekote 770-NC (from Henkel, Duesseldorf, Germany) release agent. For each experiment, the specific amount of 30% mold volume of resin-carbamate mixture was filled into the mold, corresponding to a theoretical expansion factor of 3.3. Afterward, the filled mold was set into a hot-press PW 20 (P/O/Weber, Remshalden, Germany) for 1 h at various temperatures to undergo the foaming and curing reaction. After the mold was cooled to room temperature (RT), the epoxy foams were demolded and qualitatively investigated.

**2.2.4. Foam Characterization.** The density measurements were performed in distilled water with an AG245 analytical

balance (Mettler Toledo, Columbus, Ohio) with the use of a density kit for AG balances.

To obtain the foam morphology, the samples were cut with a DiaDisc 2000 saw (Mutronic, Rieden am Forggensee, Germany) and sputtered with gold in a SPUTTER Coater 108auto (Cressington Coating Systems, Dortmund, Germany). The scanning electron microscopy (SEM) pictures were recorded with a Leo 1530 (Zeiss, Oberkochen, Germany). The cell size was evaluated with ImageJ version 1.51m9.

### 3. RESULTS AND DISCUSSION

#### 3.1. Carbamate Synthesis and Characterization.

**3.1.1. Analysis of Carbamate Synthesis.** The difference in temperature between the current reaction temperature and the initial temperature of the CO<sub>2</sub> blocking reaction mixture over time for all three investigated amines was recorded. Thereby, the exothermal synthesis behavior was confirmed. The results are shown in Table 1 and Figure 3.

**Table 1. Timeline and Observations with Regard to the Color, the Average Precipitation Time ( $t_p$ ), Maximum Temperature Change ( $\Delta T_{\text{max}}$ ), and Its Time ( $t_{T_{\text{max}}}$ )**

system	observations and time (min)	$t_p$ (min)	$\Delta T_{\text{max}}$ (°C)	$t_{T_{\text{max}}}$ (min)
AEP	clear mixture turned yellowish at 19 ± 2 min and kept the same color	32 ± 1	15 ± 1	15 ± 1
DMC	light-brown color became lighter after precipitation $t_p$	12 ± 1	18 ± 1	20 ± 2
IPDA	clear mixture with no changes	13 ± 1	16 ± 1	16 ± 1

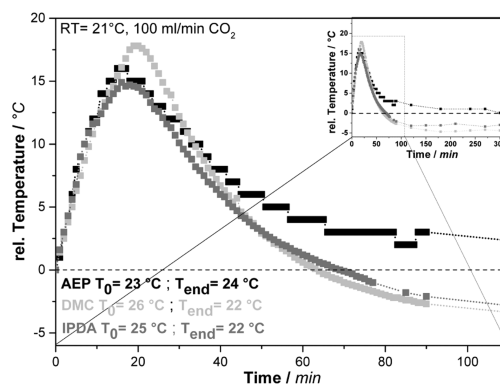


**Figure 3.** Time–relative temperature profile closed up in the range of 0–110 min of AEP, DMC, and IPDA blocking reactions in ethanol, using a CO<sub>2</sub> flow rate of 100 mL min<sup>-1</sup> with indicated temperatures at start ( $T_0$ ) and end ( $T_{\text{end}}$ ) of the experiment.

It is noted that the initial temperatures for each EtOH–amine solution were different and in the range of 23–26 °C due to the mixing enthalpy. The initial color of three reaction mixtures was based on the original amine colors. The change in color of the AEP solution might be the result of an intermediate product or side reaction. As the yellow color remained in the EtOH phase and was washed out, no investigations were further carried out there. Finally, all

**Table 2. Results of the Elementary Analysis of wt % H, C, and N Atoms, the Resulting Calculated wt % Remaining Mass (Seen as Oxygen), and Suggested Elemental Formula<sup>a</sup>**

molecule	H (wt %)	C (wt %)	N (wt %)	remaining mass (wt %)	suggested elemental formula	$M_M$ (g mol <sup>-1</sup> )	D (%)	AHEW (g equiv <sup>-1</sup> )
AEP	11.43	52.54	31.42	4.61	C <sub>6</sub> H <sub>13</sub> N <sub>3</sub>	129.21	9.23	43.07
B-AEP	8.58	48.30	24.05	19.08	C <sub>7</sub> H <sub>13</sub> N <sub>3</sub> O <sub>2</sub>	173.22	1.21	57.74
DMC	12.20	60.74	21.77	5.29	C <sub>7</sub> H <sub>16</sub> N <sub>2</sub>	128.22	10.57	32.05
B-DMC	9.68	54.20	14.39	21.72	C <sub>8</sub> H <sub>16</sub> N <sub>2</sub> O <sub>2</sub>	172.23	2.37	43.06
IPDA	12.84	68.05	16.13	2.99	C <sub>10</sub> H <sub>22</sub> N <sub>2</sub>	170.30	3.47	42.58
B-IPDA	10.39	60.54	12.77	16.30	C <sub>11</sub> H <sub>22</sub> N <sub>2</sub> O <sub>2</sub>	214.31	2.73	53.58

<sup>a</sup>In addition, the resulting molar mass ( $M_M$ ), the total deviation between calculated theoretical and measured values ( $D$ ), and amino hydrogen equivalent weight (AHEW) of the proposed carbamate molecules are presented.

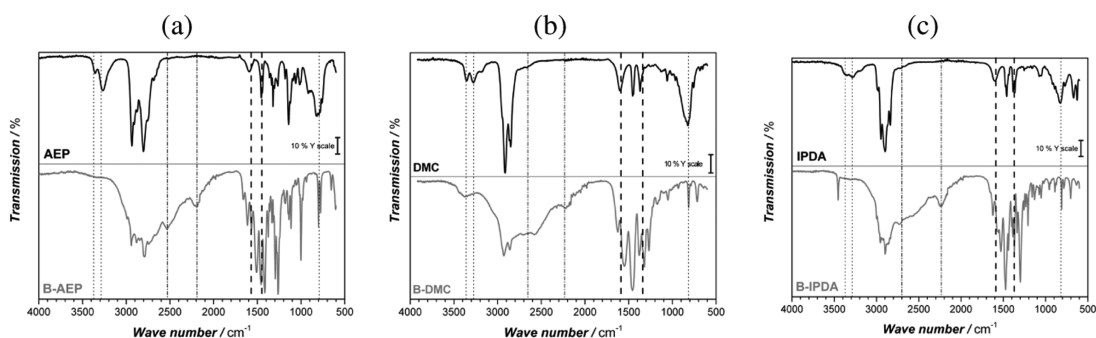


**Figure 4.** (a) Comparison of FTIR spectra of AEP and B-AEP, (b) comparison of DMC and B-DMC, and (c) comparison of IPDA and B-IPDA. Characteristic changes for blocked hardener formation are indicated by lines. The neat amine spectra are measured as a liquid film, while the blocked hardeners were measured as powder.

carbamate powders exhibited a white color after purification and drying.

The maximum difference between the reaction temperature and the initial temperature ( $\Delta T_{max}$ ) was between 15 and 18 °C, which could be attributed to the energy released during the formation of an ionic compound during CO<sub>2</sub> blocking. DMC exhibited not only the highest  $\Delta T_{max}$  but also the longest  $t_{T_{max}}$ . Due to their similar chemical structures, DMC and IPDA (see Figure 6) possessed close  $t_p$  values, which both indicate a precipitation before  $t_{T_{max}}$  is reached. Two primary amines of DMC and IPDA reacted easily with CO<sub>2</sub> to form a carbamate, so their reactions went below  $T_0$  at the time of 65–75 min, as shown in Figure 3. In contrast, AEP contains three types of amines, one primary, one secondary, and one tertiary amine, whereof the secondary and tertiary ones are located in the piperazine ring. Therefore, the reaction of AEP and CO<sub>2</sub> was more complex, which was proved by the color change. The higher  $t_p$  and  $T_{end}$  of the AEP reaction could not go below  $T_0$  but came close to it after 300 min. Theoretically, CO<sub>2</sub> could react with both the aliphatic primary amine and the secondary amine of piperazine to form the carbamate salt.

**3.1.2. Characterization of the Molecular Structure of the Synthesized Carbamate Products.** To evaluate the CO<sub>2</sub> uptake and the purity of the products, an elementary analysis (EA) was conducted for neat and blocked amines. During EA measurement, the wt % contents of carbon (C), hydrogen (H), and nitrogen (N) atoms were analyzed. The wt % oxygen (wt %<sub>O</sub>) content was calculated from the difference to 100% mass.

The expected elemental formula for B-AEP is taken from the suggestion of Ren et al.<sup>20</sup> and our previous work<sup>22</sup> with C<sub>15</sub>H<sub>32</sub>N<sub>6</sub>O<sub>7</sub>, corresponding to a carbonate at the tertiary amine involving two AEP molecules with a total  $M_M$  of 408.45 g mol<sup>-1</sup>. This would lead to a wt %<sub>O</sub> of 27.42 according to the calculation with eq 1. The experiment revealed for B-AEP a value of 19.08% (see Table 3). Thus, a deviation of 8.34 occurs between theoretical and experimental wt %<sub>O</sub>. The theoretical calculations of C, H, and N also lead to high deviations compared to the measured values, leading to a total deviation ( $D$ ) of 16.68% between measured and calculated values, corresponding to 64.12 g mol<sup>-1</sup>.

With respect to the findings that only carbamate, without the carbonated tertiary amine site, is formed and the fact that CO<sub>2</sub> corresponds to a molecular mass of around 44 g mol<sup>-1</sup> and H<sub>2</sub>O to around 18 g mol<sup>-1</sup>, an elemental formula of C<sub>7</sub>H<sub>13</sub>N<sub>3</sub>O<sub>2</sub> with a  $M_M$  of 173.22 g mol<sup>-1</sup> was taken for the calculations. The wt %<sub>O</sub> in this case was calculated to 18.47 according to eq 1.

The results for O, but also H, C, and N, match significantly better with the measured values, with a total deviation ( $D$ ) of 1.21%, corresponding to 2.1 g mol<sup>-1</sup>. Within the range of measurement error, this result clearly leads to the conclusion that the tertiary amine does not have any carbonate attached, as also observed in NMR spectroscopy. Thus, a carbamate-only structure can be confirmed for the synthesized product. This procedure was conducted for all neat amine hardeners and their carbamates. The results are summarized in Table 2.

The resulting number of atoms confirms the molecular structures of the unblocked hardeners. The remaining mass found here can be attributed to certain impurities due to

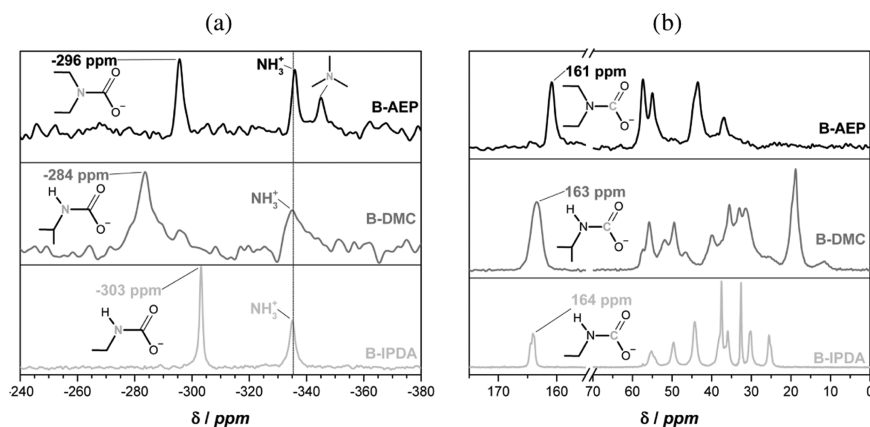


**Figure 5.** Chemical shifts for B-AEP, B-DMC, and B-IPDA in (a)  $^{15}\text{N}\{^1\text{H}\}$  CP MAS NMR spectra and (b)  $^{13}\text{C}\{^1\text{H}\}$  CP MAS NMR spectra. The related molecular environment of the related highlighted atoms, N or C, is shown.

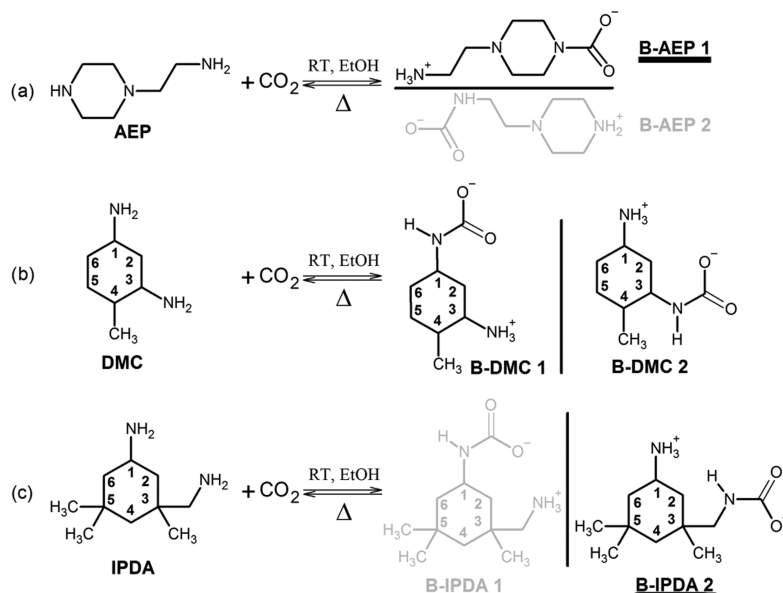


**Figure 6.** Molecular structures of neat amine hardeners (a) AEP, (b) DMC, and (c) IPDA and the suggested molecular structures of the received carbamates thereof. Both possibilities for  $\text{CO}_2$  addition to the carbamates are indicated; the most likely structure in the cases of B-AEP (a) and B-IPDA (c) is highlighted, while B-DMC (b) is assumed to result in a mixture of both structures.

adsorption effects from the environmental air as well as the purity grades of the neat amine references AEP (99%), DMC (>95%), and IPDA (>95%) as received. This is also confirmed by a lower  $D$  value of the carbamates, as they are purified due to the synthesis and subsequent washing. The low  $D$  values also support the suggested structures of carbamates without water involved, as shown for the example of B-AEP.

For detailed information on the molecular structure of the synthesized products, FTIR and NMR spectra were recorded. The particular position and degree of carbamate formation were investigated by  $^{13}\text{C}$  and  $^{15}\text{N}$  CP MAS NMR spectra.

Figure 4a shows the FTIR spectra of AEP and B-AEP, Figure 4b presents DMC and B-DMC, and Figure 4c shows IPDA and B-IPDA.

The characteristic changes indicated in Figure 4 of the FTIR spectra of the neat amine and its related synthesis product indicate the success of  $\text{CO}_2$  loading. According to the reaction as proposed in Figure 1, two primary amines react with  $\text{CO}_2$  by forming an ionic amide ( $\text{R-NH-CO}_2^-$ ) and an  $\text{R-NH}_3^+$  group. Primary amines provide two stretching peaks around  $3300\text{ cm}^{-1}$ , while an ionic amide has one peak around  $3300\text{--}3500\text{ cm}^{-1}$  in FTIR. New peaks and the general broad peak in the range of  $2600\text{--}2200\text{ cm}^{-1}$

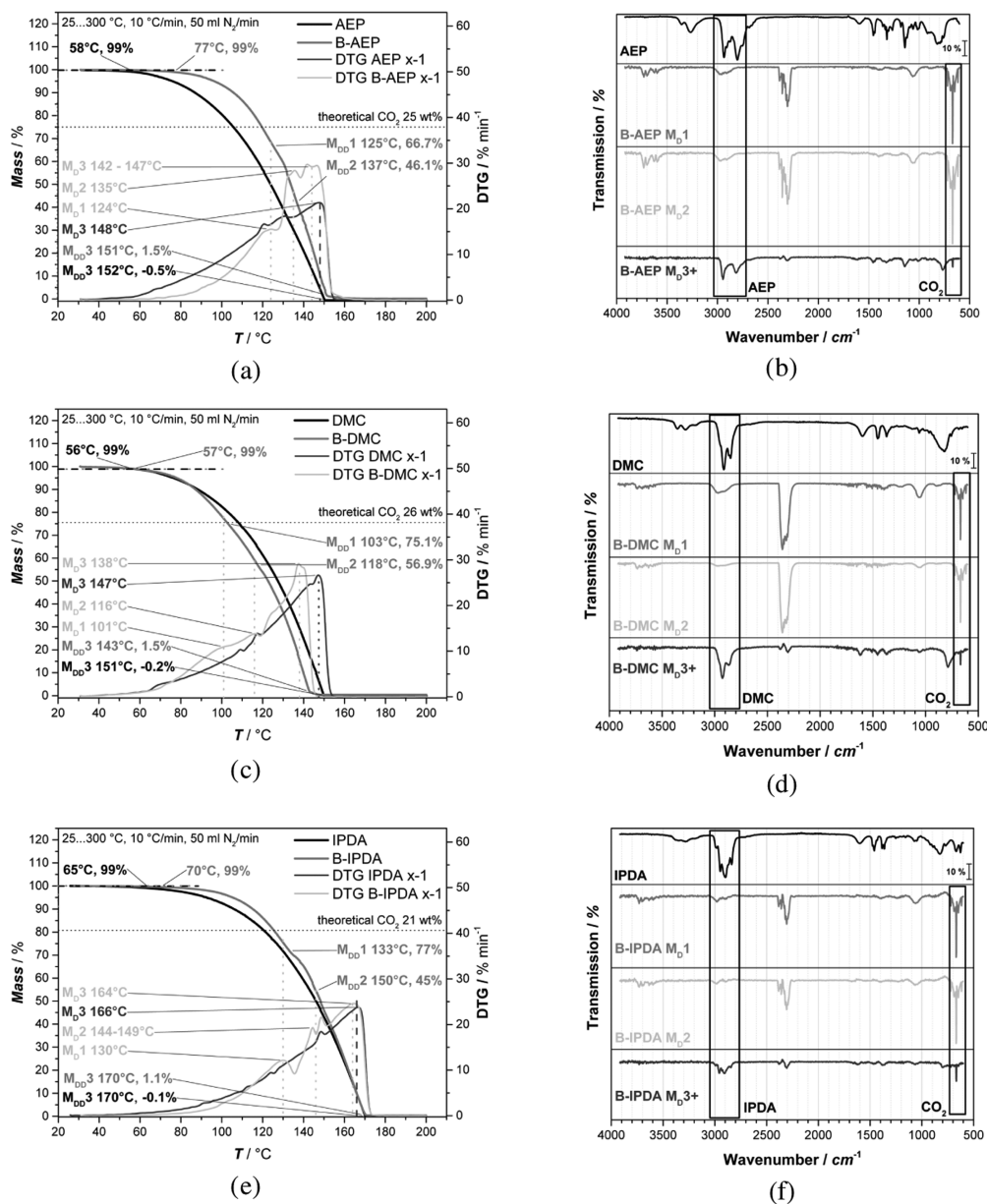


**Figure 7.** TGA results of (a) AEP versus B-AEP, (b) DMC versus B-DMC, and (c) IPDA versus B-IPDA presenting temperatures at 1% weight loss, maxima of the first derivation ( $M_D$ ) and the second derivation ( $M_{DD}$ ), and an indicator for the theoretical CO<sub>2</sub> content. In addition, the corresponding FTIR curves at  $M_D$  of (d) B-AEP, (e) B-DMC, and (f) B-IPDA are presented together with an identification of the decomposition products in the gas stream.

are related to NH<sub>3</sub><sup>+</sup> signals. Peaks in the range of 1700–1500 cm<sup>-1</sup> and further changes in the fingerprint region, such as the broad –NH– out-of-plane and deformation vibrations around 800 cm<sup>-1</sup> changing to a sharp signal due to NH<sub>3</sub><sup>+</sup> rocking vibrations, indicate an NH<sub>3</sub><sup>+</sup>-carbamate formation. New peaks around 1400 and 1300 cm<sup>-1</sup> are attributed to the

CO<sub>2</sub> capture and the formation of an ionic structure thereof.<sup>20,22,27,28</sup>

To further confirm which of the amine groups within AEP, DMC, and IPDA are turned into carbamates upon CO<sub>2</sub> exposure, <sup>13</sup>C{<sup>1</sup>H} CP and <sup>15</sup>N{<sup>1</sup>H} CP MAS NMR spectra were recorded and are presented in Figure 5.

The  $^{15}\text{N}$  CP MAS NMR spectra (Figure 5a) feature typical resonances for carbamate structures in the range of  $-280$  to  $-310$  ppm as well as for  $\text{NH}_3^+$  units in the range of  $-335$  ppm with similar intensities for B-AEP, B-DMC, and B-IPDA, confirming that only one amine of each molecule takes up  $\text{CO}_2$ , while the other one buffers the proton. The  $^{13}\text{C}\{^1\text{H}\}$  CP MAS NMR spectra (Figure 5b) feature typical resonances for the carbonate structure in the range of  $160$ – $165$  ppm. Figure 6 provides the molecular structures of the neat amines, as well as suggested molecular structures for the carbamates.

The FTIR and NMR spectroscopic results allow one to further distinguish between the proposed structures and highlight a preferred product for B-AEP and B-IPDA.

For B-AEP, the two peaks around  $3300\text{ cm}^{-1}$  almost disappear and become a small shoulder in the FTIR spectrum. In addition, there was no new peak at  $3500\text{ cm}^{-1}$ . In the  $^{15}\text{N}$  CP MAS NMR spectrum, the  $\text{NH}_3^+$  and the  $\text{R}_2\text{-N-CO}_2^-$  carbamate resonances were observed. An  $\text{NH}_2^+$  group can be excluded as an individual resonance shifted downfield compared to the  $\text{NH}_3^+$  should be observed. The  $\text{R}_2\text{-N-CO}_2^-$  can be distinguished from the  $\text{R-NH-CO}_2^-$  carbamate in B-IPDA by a downfield shift of  $8$  ppm. From the  $^{13}\text{C}\{^1\text{H}\}$  CP MAS NMR spectra, an upfield shift around  $3$  ppm compared to B-DMC and B-IPDA, both having secondary carbamate-N regardless of the tautomeric forms, was observed. This upfield shift strongly suggests a  $\text{CO}_2$  coupling to the secondary amine located in the piperazine ring. The combined results of FTIR and NMR spectroscopies led to the conclusion that the structure of B-AEP 1, with the carbamate being attached at the piperazine nitrogen, is formed. This is in agreement with the results of Ren et al. and our previous study.<sup>20,22</sup>

In the case of B-DMC, the amine peaks of  $3300\text{ cm}^{-1}$  are slightly shifted to higher wavenumbers and form a broad ionic amide peak at  $3500\text{ cm}^{-1}$ . Just as for FTIR, the resonances for both nuclei for B-DMC in NMR are broad, indicating an amorphous structure of the salt. At least  $14$   $^{13}\text{C}$  resonances with varying intensities were identified. As one B-DMC conformer accounts for eight resonances only (Figure 6), it suggests that both amines of DMC take part in the  $\text{CO}_2$  capture. Additionally, due to the stereocenters, up to eight diastereomers for both B-DMC 1 and B-DMC 2 are possible with slightly different chemical shifts and FTIR resonances, explaining the broad signals in both spectra. Thus, no defined carbamate structure can be identified and both tautomers are received.

In the case of B-IPDA, the two amine peaks disappeared and a new sharp ionic amide peak around  $3450\text{ cm}^{-1}$  was formed in FTIR, indicating a preferred amine site for  $\text{CO}_2$  capture. The  $^{13}\text{C}$  MAS NMR spectra of B-DMC and B-IPDA exhibit a slight chemical shift for the carbamate-C of  $1$  ppm only, which does not allow one to distinguish between the two sites. The carbamate  $^{15}\text{N}$  shift, however, varies between B-DMC at  $-284$  and B-IPDA at  $-303$  ppm, indicating individual chemical environments. Since the carbamate group of B-DMC is always directly attached to the cyclohexane ring, the same chemical shift for B-IPDA is expected in the case of a carbamate formation at position 1. Thus, the upfield shift of about  $20$  ppm proves that the tautomer B-IPDA 2 is formed.

The results of FTIR and NMR spectroscopies and EA lead to the overall conclusion that the experiments lead to the uptake of one molecule  $\text{CO}_2$  per molecule B-AEP, B-DMC, and B-IPDA. A proton shift leading to the formation of the

acid structures can be excluded by liquid-state proton NMR spectroscopy. The spectra can be found in the Figure S1, Supporting Information.

In conclusion, a highly selective carbamate formation of B-AEP 1 and B-IPDA 2 can be confirmed, while for B-DMC both tautomers are possible. The  $\text{CO}_2$  content of  $25$  wt % for B-AEP,  $26$  wt % for B-DMC, and  $21$  wt % for B-IPDA can be evaluated. This allows one to calculate and adjust the  $\text{CO}_2$  load for later foaming mixtures.

**3.1.3. Carbamate Decomposition Behavior.** To understand the decomposition behavior, thermogravimetric analysis (TGA) coupled to an FTIR was performed for all samples. The resulting TGA curves of AEP versus B-AEP, DMC versus B-DMC, and IPDA versus B-IPDA are summarized in Figure 7a,c,e, showing the mass loss and the first derivation (derivative thermogravimetry (DTG)), as well as the maxima of the second derivation ( $M_{\text{D}2}$ ), and an indicator for the theoretical  $\text{CO}_2$  weight loss. In addition, the corresponding FTIR spectra of the blocked hardeners at the point of maximum decomposition rates ( $M_{\text{D}}$ ) with identified molecules in the gas stream are presented in Figure 7b,d,f.

It is noted that for the three liquid neat amines AEP, DMC, and IPDA, only evaporation is observed and the  $1\%$  weight loss is considered as the evaporation onset. In the case of the solid carbamates B-AEP, B-DMC, and B-IPDA, the temperature at  $1\%$  weight loss was assigned as the carbamate decomposing temperature and thus corresponds to the  $\text{CO}_2$  release. Afterward, besides  $\text{CO}_2$  release, the evaporation of the released amines contributes in addition to the weight loss as shown by the FTIR spectra (Figure 7b,d,f). Depending on the different chemical structures of the amines, the evaporation temperature of the neat amines was found to be higher than or similar compared to the decomposition temperature of the related carbamates.

As the gas stream of the TGA reaches the coupled FTIR device with a certain delay, the FTIR spectra of  $M_{\text{D}3}$  were chosen with a short time delay for proper resolution, corresponding to  $M_{\text{D}3+}$ . The released amines are identified by the  $\text{CH}_2$  vibrations around  $2800\text{ cm}^{-1}$  as they provide the strongest signal of all groups. As the amines are in the gas phase, the detected signals are slightly shifted compared to the liquid phase.<sup>27</sup> For  $\text{CO}_2$ , three characteristic regions around  $650$ – $500$ ,  $2400$ – $2300$ , and  $3750$ – $3600\text{ cm}^{-1}$  can be identified according to the literature.<sup>18,28</sup> The region around  $650$ – $500\text{ cm}^{-1}$  presents the strongest signal and thus was chosen as the indicator.

It is observed among all samples (Figure 7b,d,f) that each mass loss step includes the  $\text{CO}_2$  release and evaporation of released amines. However, the ratio changes from  $M_{\text{D}1}$  to  $M_{\text{D}3+}$ . This can be explained by the decomposition mechanism, where  $\text{CO}_2$  has to be released before the amines are able to evaporate. In the first stage, high amounts of  $\text{CO}_2$  were detected, which are directly released in the gas phase, while only small amounts of the released amines evaporate. The high amounts of  $\text{CO}_2$  released in a short time lead to a fast detection. At  $M_{\text{D}3+}$ , where the main evaporation of the amine already took place, only weak signals can be detected. This can be explained by a slow movement in the gas stream through the pipe and the resulting time shift related to the detector. First, proper amine signals were detected in the FTIR spectra around  $30$  s after the TGA peak  $M_{\text{D}3}$  was reached. Here, the ratio of amines and  $\text{CO}_2$  changed as only small amounts of  $\text{CO}_2$  remain in the overall system. The

numerical results of the TGA measurement are summarized in Table 3.

**Table 3. Results of the TGA Measurement and the Maxima of the first Derivative ( $M_{D1}$ ) of the Different Neat Amines and Carbamates<sup>a</sup>**

system	1 wt % loss (°C)	$M_{D1}$ (°C)	$M_{D2}$ (°C)	$M_{D3}$ (°C)	residual mass (%)
AEP	58			148	-0.4
B-AEP	77	124	135	147	0.2
DMC	56			147	-0.3
B-DMC	57	101	116	138	0.2
IPDA	65			167	-0.4
B-IPDA	70	130	149	165	0.4

<sup>a</sup>1 wt % loss temperature and residual mass (at 300 °C) are indicated in the figure.

It is seen from Table 3 that the decomposition temperature of B-AEP at 77 °C is higher compared to the evaporation temperature of the neat amine AEP at 58 °C. The low flexibility of the piperazine ring combined with the out-sourced  $\text{NH}_2$  site by the ethyl group, providing a lower molecular tension due to high flexibility as shown in Figure 6, could be considered as the reason. Both observations result in an increased decomposition stability of the carbamate. However, once B-AEP decomposed to release gaseous  $\text{CO}_2$ , the AEP is able to evaporate into the gas phase quickly. This is confirmed by FTIR measurements in Figure 7b, where at  $M_{D1}$  already both AEP and  $\text{CO}_2$  can be detected. The higher energy state of the released AEP leads to a faster evaporation, resulting in a higher slope of the curve in the second decomposition step of B-AEP as observed in Figure 7a. This leads to the fact that both AEP and B-AEP reach 100% weight loss at a similar temperature.

IPDA and B-IPDA exhibit similar behavior, where the evaporation temperature of the neat amine IPDA is 65 °C, while the B-IPDA carbamate's decomposition temperature is 70 °C. The temperature gap is lower compared to AEP as in

the case of IPDA the cyclohexane ring provides higher molecular flexibility, which is affected by the  $\text{CH}_3$  side groups. As one carbamate site is out-sourced from the cyclohexane ring by a  $\text{CH}_2$  bridge (Figure 6), the intermolecular tension is lowered. Both factors result in an increased decomposition stability of the carbamate. Each mass loss step contains next to  $\text{CO}_2$  also evaporating amine (Figure 7d). Finally, the 100% weight loss is comparable between IPDA and B-IPDA at a similar temperature (Figure 7c).

In contrast, DMC and B-DMC present a different response. The neat amine DMC evaporated at 56 °C and B-DMC starts to decompose at 57 °C. This can be explained by the molecular structure. Both functional groups, the  $-\text{NH}_3^+$  and  $-\text{NHCO}_2^-$ , are attached directly to the cyclohexane ring of DMC, leading to an increased tension. The high molecular mobility of the cyclohexane ring and the resulting less stiffness of the molecule, combined with the molecular tension of the ionic carbamate structure, can be assumed to cause the easy decomposition. The FTIR of B-DMC  $M_{D1}$  (Figure 7d) shows both DMC and  $\text{CO}_2$  spectra. It is observed that B-DMC ends up with 100% weight loss at 143 °C, which is a lower temperature than the 151 °C of DMC. Thus, fast  $\text{CO}_2$  release can be observed, which leads to a higher mass loss compared to the evaporation of DMC only during the initial state. It is observed from Figure 7c that after  $M_{D2}$ , when the main  $\text{CO}_2$  is released, the overall mass loss rate is comparable to DMC. However, due the fact that B-DMC contains the highest wt %  $\text{CO}_2$ , a lower amount of DMC is left, which can evaporate more easily.

The negative residual mass of the neat amines indicates adsorbed molecules from the environment, which are observed by small peaks in DTG. The coupled FTIR revealed small amounts of  $\text{CO}_2$  in IPDA and DMC but not AEP. The adsorbed  $\text{N}_2$  would not be detected as it was used as a carrier gas.

Furthermore, the second derivative was evaluated to get the end temperature of the corresponding decomposition to calculate the weight loss during the related decomposition

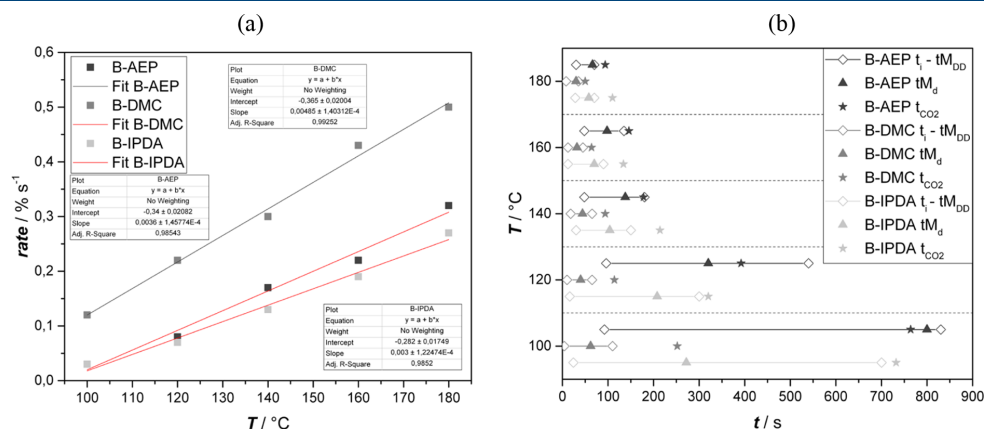


**Figure 8.** (a) Decomposition rates of B-AEP, B-DMC, and B-IPDA at different temperatures and (b) results of isothermal TGA measurements with regard to time until the initial 100 wt % ( $t_i$ ) (left diamond marker), time until the end of the first mass loss step (max. second derivative) ( $t_{MDD}$ ) (right diamond marker), time to the maximum of the first derivative ( $t_{MD1}$ ) (triangle marker), and time until the theoretical total  $\text{CO}_2$  release ( $t_{\text{CO}_2}$ ) (star marker) at defined temperatures.

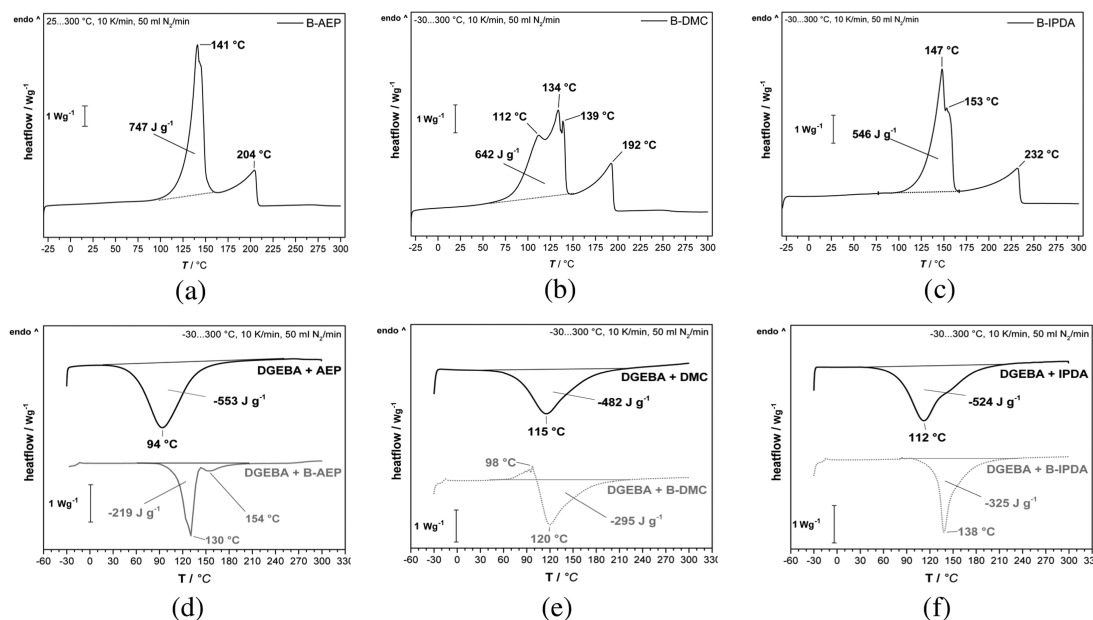


**Figure 9.** DSC results of (a) B-AEP, (b) B-DMC, and (c) B-IPDA with presented peak temperatures and integration range of the decomposition peak, as well as the DSC first heating ramp for the curing reaction with total reaction enthalpy, onset, and peak temperature of (d) AEP and B-AEP, (e) DMC and B-DMC, and (f) IPDA and B-IPDA.

step. Especially  $M_{DD}1$  and 2 are of interest as they contribute to the main  $\text{CO}_2$  release, whereby the ratio  $\text{CO}_2/\text{amine}$  is expected to be higher from the start up to  $M_{DD}1$  than in the range  $M_{DD}1$  up to  $M_{DD}2$ .

To get an impression of the decomposition rate, isothermal TGA measurements at 100, 120, 140, 160, and 180 °C were performed. A slight weight increase of up to 1.6 wt % was observed in most of the samples at the beginning, attributed to condensation effects when the cold sample enters the hot measurement cell. Thus, the onset time of fitting was chosen when the value hits the initial 100 wt % again ( $t_i$ ). As the mass loss takes place in multiple steps, the time to the first extrema, maximum or minimum, of the second derivative ( $t_{M_{DD}}$ ) was chosen to separate the initial mass loss step from the next one, as here the main  $\text{CO}_2$  release is expected, which is of importance for later foaming and curing. Thus, the curve fitting for the decomposition rate takes place in the time range between  $t_i$  and  $t_{M_{DD}}$ . As shown in the TGA-FTIR, the second mass loss step is more influenced by evaporating amines than released  $\text{CO}_2$ . To estimate the influence of possible amine evaporation on the fit, the time until the theoretical  $\text{CO}_2$  wt % content ( $t_{\text{CO}_2}$ ) of the carbamates is released is also indicated. The time when the first maximum of decomposition ( $t_{M_D}$ ) occurs was found within the fit range at all samples; however, it can be found at different times. Figure 8a shows the decomposition rate at indicated temperatures, and Figure 8b illustrates the time dependence of  $t_i$ ,  $t_{M_{DD}}$ ,  $t_{\text{CO}_2}$ , and  $t_{M_D}$  at different temperatures. The numerical results are summarized in the Table S1, Supporting Information.

Figure 8a reveals that there is a nearly linear correlation between the decomposition rate for the first decomposition step and the temperature within the investigated temperature range. However, B-DMC reveals the highest decomposition rates and increase with temperature, compared to B-AEP and B-IPDA, which behave similarly at 100 °C and exhibit slightly increasing differences until 180 °C. Thus, the lower decomposition onset and the already discussed influence of the chemical structure at B-DMC compared to B-AEP and B-IPDA can be seen (see Table 3).

Figure 8b allows one to draw a conclusion on the decomposition timeline of the first decomposition step, starting at  $t_i$  and ending at  $t_{M_{DD}}$ . The best case for determination of the  $\text{CO}_2$  release rate is given, when  $t_{M_D}$  is in between the range of  $t_i$  and  $t_{M_{DD}}$ , while  $t_{\text{CO}_2}$  is higher than  $t_{M_{DD}}$ . This ensures that  $\text{CO}_2$  release is the main action and only low amounts of released amine evaporate.

It is found that B-DMC exhibits a significantly shorter time period of  $t_{\text{ini}} - t_{M_{DD}}$  from 100 up to 160 °C compared to those of B-AEP and B-IPDA. B-DMC also reveals a  $t_{M_{DD}}$  much lower than  $t_{\text{CO}_2}$  along the whole temperature range. This result is in good agreement with the results of Figure 7c, showing a fast mass loss of B-DMC in the initial state due to  $\text{CO}_2$  release. Only small amounts of evaporating DMC can be expected. The same trends are observed for B-IPDA. However, the time period of  $t_{\text{ini}} - t_{M_{DD}}$  is elongated, which is confirmed by the lower decomposition rate (Figure 8a). In the case of B-AEP,  $t_{\text{CO}_2}$  is within or close to the range of  $t_{\text{ini}} - t_{M_{DD}}$ . In this case, higher amounts of evaporating AEP can be assumed to influence the determined decomposition rate.

In conclusion, B-AEP and B-IPDA show comparable decomposition rates, whereas the decomposition characteristics are significantly different. B-DMC was found to show the highest decomposition rate among the samples and a fast CO<sub>2</sub> release within the investigated temperature range. Taking into account the fact that the released amines do not evaporate but build up the epoxy network during the later foaming process, the indicated decomposition characteristics are expected to lead to different foaming behaviors.

### 3.2. Foaming of DGEBA with Different Carbamates.

**3.2.1. Curing and Foaming Behavior by DSC.** In a first step, DSC measurements of the neat carbamates were performed to examine the endothermic decomposition behavior, where CO<sub>2</sub> release and amine reactivation take place. Then, the curing behavior of the neat amine hardeners with DGEBA versus their carbamates with DGEBA was compared using DSC. The results are summarized in Figure 9.

The resulting DSC curves in Figure 9a–c confirm the expectations with regard to endothermic decomposition. The second endothermic peak is related to amine evaporation and is not considered to affect the later foaming behavior.

It is noted that the maximum degradation temperatures of B-AEP, B-DMC, and B-IPDA observed by DSC are obtained from the energy difference between the sample in a crucible with a small breathing hole and the reference crucible, while the ones from TGA were obtained from the weight loss of the sample in an open crucible in an oven. This affects the observed temperature values. As observed from the experiments, for the consideration of the onset of carbamate decomposition, the TGA results are more applicable because they reflect the actual CO<sub>2</sub> release.

In Figure 9d–f, higher reaction onset and peak temperatures can be observed when carbamates are involved. In addition, a lower total energy release can be confirmed. The numerical results are summarized in Table 4.

**Table 4. Results of the DSC Measurement of the Neat Carbamates as Well as Different Hardener and Carbamate Systems with DGEBA Resin<sup>a</sup>**

system DGEBA resin +	decomposition of carbamate		curing reaction with DGEBA		
	$T_{D, on}$ (°C)	$\Delta E_{dec}$ (J g <sup>-1</sup> )	$T_{C, on}$ (°C)	$T_{C, p}$ (°C)	$\Delta E_r$ (J g <sup>-1</sup> )
AEP			15	94	-554
B-AEP	85	747	70	130	-219
DMC			22	115	-482
B-DMC	55	642	57	120	-295
IPDA			29	112	-524
B-IPDA	71	546	83	138	-325

<sup>a</sup>The values of the observed carbamate decomposition onset ( $T_{D, on}$ ) and decomposition enthalpy ( $\Delta E_{dec}$ ), as well as observed reaction onset temperature ( $T_{C, on}$ ), reaction peak temperature ( $T_{C, p}$ ), and total reaction enthalpy ( $\Delta E_r$ ) are presented.

The onset for the decomposition and reaction was chosen by including the observed edges of the fit, rather than using the standard calculated onset resulting from the tangents of the peak crossing the baseline. This method was found to be more accurate with regard to the experimental results. The details about this method and the values of the standard calculated onset for comparison can be found in Figure S2 and Table S2, Supporting Information.

For all of the neat amine + DGEBA systems, the curing started at low curing  $T_{C, on}$  around room temperature and resulted in a broad peak. When carbamates are used, the curing  $T_{C, on}$  is shifted for all systems to higher temperatures around the decomposition  $T_{D, on}$  of the carbamates, as shown in Table 4. This proves the blocking of amine sites in the carbamates at a high percentage, as no free amine groups trigger a reaction before  $T_{D, on}$ . The highest deviation between  $T_{C, on}$  and  $T_{D, on}$  was observed for the B-IPDA system at 13 °C, while for the B-AEP system, it was 8 °C and in the case of B-DMC, it was 2 °C. This can be explained by the complex interaction between decomposition of the carbamate and the reaction kinetics of the released amines and the measurement principle in DSC. The decomposition of B-IPDA starts at temperatures way lower than the observed reaction onset in DSC ( $T_{D, on}$  71 °C vs  $T_{C, on}$  83 °C). As the endothermic decomposition is overlapped with the exothermic curing reaction of the released amine, the net heat flow measured by the DSC remains nearly constant. At higher temperatures, the decomposition and curing accelerate until the point where the exothermic curing reaction overcomes the endothermic decomposition and a significant, nearly straight drop in DSC can be observed for the initial curing reaction. In the case of B-AEP, where the released AEP is able to react fast and is highly exothermic, this balance becomes closer ( $T_{D, on}$  91 °C vs  $T_{C, on}$  99 °C). In addition, AEP shows a second smaller exothermic peak around 173 °C, which is notably separated from the main peak. This effect is expected to result from the molecular structure of B-AEP, where the released secondary nitrogen atom in the piperazine is highly activated and reacts, together with the primary amine, quickly to form a linear polymer chain. This results in the first sharp and highly exothermic peak. The remaining secondary amine is sterically hindered and reacts later, resulting in the small shoulder at the first peak and finally the second peak, as a higher activation energy is required for the reaction.

For the B-DMC system, the gap nearly disappears ( $T_{D, on}$  55 °C vs  $T_{C, on}$  57 °C) and a notable endothermic peak at 98 °C overlaps the reaction onset region. This can be explained by the lowest thermal stability and highest decomposition rate of B-DMC observed among the investigated carbamates (Figures 8 and 10) even at low temperatures. This is combined with the slow and less exothermic reaction of DMC compared to the other systems (Figure 9). Thus, the decomposition reaction consumes more energy in the initial state than the curing reaction can release. Around the temperature of 103 °C, high amounts of B-DMC are already decomposed and the exothermic reaction is accelerated. The measured curve crosses the original zero-level and thus turns from endothermic to exothermic. Afterward, the slope of the exothermic peak is not as high compared with IPDA or even AEP, which confirms the comparably slow reaction speed.

To get an impression about the reaction rate of the amines and blocked amine systems at relevant temperatures, a model free kinetics (MFK) analysis was performed. Figure 10 compares the MFK-determined reaction rate of the systems containing DGEBA + neat amines and DGEBA + carbamates up to 99% conversion ( $R_{99}$ ) with the decomposition rate of the blocked amines ( $r_d$ ) received from the TGA at defined temperatures (Figure 8a).

The determined reaction rates by MFK confirm the overall expectations from the DSC results. As the more complex

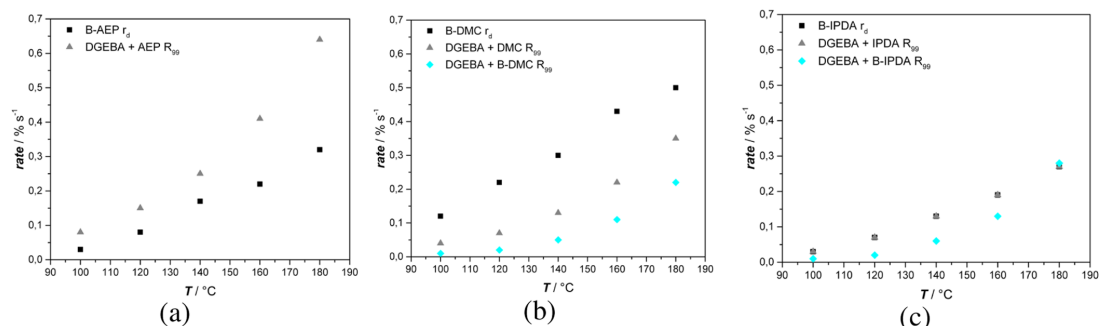


**Figure 10.** Comparison of the decomposition rate of carbamate ( $r_d$ ) received from TGA and the reaction rate up to 99% conversion of the corresponding DGEBA + neat amine and DGEBA + carbamate systems ( $R_{99}$ ) based on (a) AEP, (b) DMC, and (c) IPDA. It is noted that for B-AEP (a), no proper evaluation of  $R_{99}$  was applicable at MFK.

	80 °C	100 °C	120 °C	140 °C	160 °C	180 °C
DbA						
	No sample	1126 kg/m <sup>3</sup>	499 kg/m <sup>3</sup>	503 kg/m <sup>3</sup>	379 kg/m <sup>3</sup>	454 kg/m <sup>3</sup>
DbD						
	334 kg/m <sup>3</sup>	692 kg/m <sup>3</sup>	651 kg/m <sup>3</sup>	988 kg/m <sup>3</sup>	1072 kg/m <sup>3</sup>	1128 kg/m <sup>3</sup>
DbI						
	No sample	349 kg/m <sup>3</sup>	365 kg/m <sup>3</sup>	508 kg/m <sup>3</sup>	745 kg/m <sup>3</sup>	1077 kg/m <sup>3</sup>

**Figure 11.** Overview of samples achieved with DGEBA and different carbamates at selected temperatures in top and side views with indicated densities.

reactivity of B-AEP (as described for Figure 9) leads to invalid values for the MFK, no proper determination of the  $R_{99}$  value was possible. However, for AEP, a higher reaction rate  $R_{99}$  compared to the decomposition rate  $r_d$  of B-AEP can be found, which further increases with temperature in a nonlinear manner. This effect is confirmed by the sharp reaction peak in the DSC curve, indicating a fast reaction of

the released AEP. For B-AEP, a slightly lower  $R_{99}$  value can be expected with regard to the overall trends seen by B-DMC and B-IPDA.

In the case of B-DMC, the  $r_d$  is higher than  $R_{99}$  of the amines in general. The values of  $r_d$  and  $R_{99}$  are even divergent in the range from 100 to 160 °C. When B-DMC is used,  $R_{99}$  is lowered further due to the energy uptake of the

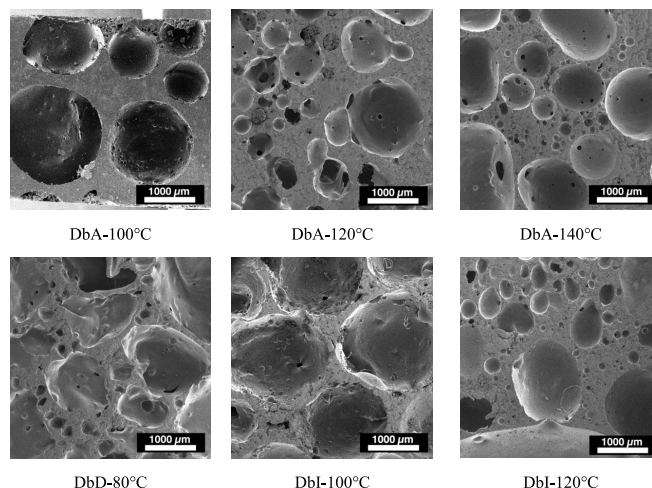


**Figure 12.** SEM images of selected DbA, DbD, and DbI foams. The number behind the sample name indicates the foaming temperature.

endothermal decomposition, which has to occur first, before the released amine is available for reaction. This is in accordance with the endothermal characteristic at the beginning of the reaction as observed by the DSC measurements (Figure 9e), which turns exothermal only when the ratio of the released DMC is higher than the leftover B-DMC.

The  $r_d$  of B-IPDA is almost similar to the  $R_{99}$  of IPDA. A lowered reaction rate results when B-IPDA is used as the endothermal decomposition is able to consume energy of the system during decomposition. However, the reaction rates approximate and finally match at 180 °C. This agrees with the delayed reaction onset as observed in the DSC experiments, where no significant heat flow is detected until a certain ratio of released IPDA and remaining B-IPDA in the system results finally in an exothermal peak.

These results lead to the conclusion that foaming with B-AEP will be most dependent on the  $r_d$ , as the released AEP will react fast and limit the expansion. Thus, higher temperatures are expected to be favorable to boost  $r_d$ . In contrast, B-DMC is expected to lose high amounts of CO<sub>2</sub> due to the lower  $R_{99}$  values. In this case, lower temperatures are expected to be beneficial for a slower CO<sub>2</sub> release and to provide more time for network formation. B-IPDA is expected to show the same tendency as B-DMC but with a lower temperature impact as the  $R_{99}$  is closer to the  $r_d$ .

**3.2.2. Foaming with Carbamates.** To examine the applicability of the carbamates for curing and foaming epoxy resins, they were mixed with DGEBA and foamed in a mold at different temperatures. The samples are named according to the following scheme: DGEBA + B-AEP (DbA), DGEBA + B-DMC (DbD), and DGEBA + B-IPDA (DbI). A 30 vol % mold filling degree was chosen to allow a maximum expansion of around 70%. By this, the expected foam density at full expansion is around 350 kg m<sup>-3</sup>. The experiments were carried out in a temperature range between 80 and 180 °C.

During foaming, the diffusion and interaction of the released CO<sub>2</sub> with the curing matrix are of importance to achieve foams with the desired homogeneous morphology. As

already shown, both CO<sub>2</sub> release and matrix curing are directly linked. Thus, an optimal balance between the decomposition rate ( $r_d$ ) and the curing reaction ( $R_{99}$ ) is required to match suitable conditions for foaming and expansion. The achieved cuboid-shaped foam samples are shown in Figure 11.

It is observed from Figure 11 that foams can be achieved with all three carbamates. However, the foaming/curing temperature reveals a significant influence on foam development for each carbamate. This contributed to the different decomposition behaviors of the carbamates and the reaction speeds of the corresponding released amines at each temperature, as discussed above, which is in accordance with the literature.<sup>12</sup> Figure 12 shows SEM images of the most promising samples with adequate foaming behaviors. The corresponding numerical values are presented in Table 5.

**Table 5. Numerical Values of Cell Size ( $c_s$ ) and Cell Distribution ( $c_d$ ) of Selected Foam Samples<sup>a</sup>**

system	$c_d$ (cells cm <sup>-3</sup> )	$c_s$ ( $\mu$ m)	$c_{max}$ ( $\mu$ m)	$c_{min}$ ( $\mu$ m)
DbA-100 °C	830	583 ± 650	2097	37
DbA-120 °C	691	547 ± 322	1575	55
DbA-140 °C	1152	463 ± 457	2412	83
DbD-80 °C	965	512 ± 462	1905	93
DbI-100 °C	193	1473 ± 363	1964	813
DbI-120 °C	1999	368 ± 530	4523	53

<sup>a</sup>In addition, the maximum ( $c_{max}$ ) and minimum ( $c_{min}$ ) cell size observed are provided.

In the case of B-AEP, a temperature of 80 °C leads to a compact, unfoamed, highly viscous gel-like sample after 1 h without notable expansion. It was not possible to reveal an undamaged sample after demolding. This agrees with the finding that the decomposition onset of the samples is around 77 °C (TGA). Thus, at 80 °C, a slow decomposition, if any, can be expected, leading to low amounts of AEP to react with DGEBA and the system remains mainly in the viscous stage. At 100 °C and above, the expected relationship between  $r_d$  and  $R_{99}$  comes into effect. The low  $r_d$  of B-AEP

results in a low CO<sub>2</sub> pressure, which hardly expands the matrix at 100 °C. In combination with the fast R<sub>99</sub> of the released AEP, as seen by DSC and MFK, this leads to a solidification before a proper expansion can take place. Thus, numerous small cells can be observed in the cell walls of some bigger cells (Figure 12), with high cell size deviation and comparably high cell distribution number in an overall compact matrix. Some remaining B-AEP is trapped, as indicated by a yellowish-white shiny color. This leads to a sample with sufficient stability for proper demolding with the drawback of low expansion and a density of around 1126 kg m<sup>-3</sup>, close to the unfoamed system with around 1160 kg m<sup>-3</sup>.<sup>22</sup> With increasing foaming temperature, the r<sub>d</sub> and thus the CO<sub>2</sub> pressure increase, finally resulting in a foamlike structure. A density of around 500 kg m<sup>-3</sup> was achieved at mold temperatures of 120 and 140 °C without full expansion in the mold. At 140 °C foaming temperature, a larger c<sub>max</sub> and increased deviation in c<sub>c</sub> could be observed compared to a foaming temperature of 120 °C. This is due to the increased r<sub>d</sub> of B-AEP. At 160 and 180 °C, the foams were able to rise to the top side of the closed mold and densities of 379 and 454 kg m<sup>-3</sup>, respectively, can be achieved. However, in the upper half of the sample, the prior expanded foam structure collapsed into the center direction and some foam cells are located only at the four sidewalls. The foaming at the mold sidewall could be stabilized by some membrane effect and the direct temperature influences of the sidewalls of the mold. In contrast, insulation effects shield the center region of the samples and combined with the high CO<sub>2</sub> pressure in the center region, coalescence and collapse of the foam structure can occur. Large pores at the centers of the samples are the consequence. In both cases, the R<sub>99</sub> is close to the r<sub>d</sub> but does not lead to homogeneously distributed cell sizes.

In comparison to B-AEP, B-DMC and B-IPDA show a completely different response to the applied foaming temperatures. The morphology and the rising height are different, as the DSC and MFK results already indicated. The higher the foaming temperature, the lower are the rising heights of DbD and DbI foams. At 80 °C, B-DMC was able to foam with adequate stability of the foam. The r<sub>d</sub> and R<sub>99</sub> match sufficiently to achieve a full expansion and stabilization, resulting in a foam with a density of 334 kg m<sup>-3</sup>. However, the cell shape is irregular (Figure 12) with high deviation in c<sub>c</sub>, indicating an irregular cell expansion mechanism resulting from the low R<sub>99</sub>. At 100 °C and above, the morphology of the DbD systems becomes worse and the density approaches the bulk value of around 1130 kg m<sup>-3</sup>. This is due to the faster increase of r<sub>d</sub> compared to R<sub>99</sub> along the temperature (Figure 10b), leading to coalescence, collapse, and escape of CO<sub>2</sub>.

For DbI, the achieved foam structure at 80 °C collapsed during demolding, as solidification was not fully achieved within 1 h of the curing time. This indicates a sufficient r<sub>d</sub>, as the decomposition onset of around 70 °C is sufficiently low, but the R<sub>99</sub> is insufficient to achieve a stabilization. On increasing the temperature to 100 °C, the r<sub>d</sub> and R<sub>99</sub> match sufficiently to achieve full stabilization. The morphology exhibits a spherical cell shape and a low deviation in c<sub>c</sub>. At 120 °C, the foam expands to the top. However, the morphology becomes less desirable since a high c<sub>c</sub> deviation is observed. In addition, elongated cells indicate a movement

of the gas upward as a result of the less suitable ratio of r<sub>d</sub> and R<sub>99</sub>. This is also notable in a very high deviation in c<sub>c</sub>.

At 140 °C and higher, no proper expansion can be observed and the cell coalescence and collapse become more significant until 180 °C, where the density gets close to the bulk value of around 1105 kg m<sup>-3</sup>.

In general, it has to be noted that curing and foaming below the final T<sub>g</sub> of the systems require postcuring beyond this temperature to achieve the maximum temperature stability and mechanical strength of the systems. This means around 120 °C for AEP and 160 °C for B-DMC and B-IPDA. In the case of the samples made of B-AEP and B-IPDA, foamed at 80 °C, stable foams could be achieved by a postcuring process in the mold. However, the system properties with regard to the curing degree, viscosity, and residual carbamate changed during the 1 h exposure to 80 °C and further curing at increased temperatures. Thus, these samples were not considered valid for this study.

#### 4. CONCLUSIONS

The synthesis of carbamates from three amines, namely, AEP, DMC, and IPDA, was successfully performed. The elemental analysis confirmed the atomic composition of the obtained carbamate products. The FTIR and <sup>13</sup>C and <sup>15</sup>N CP MAS NMR spectra confirmed the formation of a carbamate salt for B-AEP, B-DMC, and B-IPDA. For B-AEP and B-IPDA, the salts consist exclusively of the tautomers B-AEP 1 and B-IPDA 2 (Figure 6). For B-DMC, the two amines exhibit a high structural similarity, resulting in broad signals in the respective spectra. This does not allow an identification of a preferred amine for CO<sub>2</sub> capture.

The investigation of the decomposition behavior revealed that the lowest decomposition onset temperatures found by TGA are 77 °C for B-AEP, 57 °C for B-DMC, and 70 °C for B-IPDA. Due to the fact that the related amines are released after carbamate decomposition, they can also be evaporated. A gradual change in the ratio of CO<sub>2</sub> and amine concentration in the gas stream of TGA-FTIR was detected with increasing temperature. Thus, the decomposition rates were determined in the first decomposition step, where the influence of amine evaporation is the lowest. The highest decomposition rate was determined for B-DMC, followed by B-AEP and B-IPDA, which are more comparable to each other. The influence of these carbamate characteristics on the curing and foaming kinetics was investigated and compared to the neat amines. Here, the change in curing characteristics was observed by a shift of the reaction onset from room temperature up to the decomposition temperature of the carbamates with a subsequent high initial curing rate. The interactions between decomposition and the reaction rate were finally visualized by a foaming experiment, where the dual function of the carbamates as a CO<sub>2</sub> blowing agent and an amine curing agent was verified. DGEBA epoxy foams were obtained at various densities and morphologies, depending on the foaming temperature and the carbamate system. It was shown that for B-AEP, high temperatures above 120 °C are suitable to balance the reaction and decomposition rate properly. In the case of B-DMC, low foaming temperatures at around 80 °C were beneficial to achieve full expansion with an adequate morphology and low density. The same trend can be observed for B-IPDA, where a reaction temperature of 100 °C resulted in a full expansion and stabilization, as well as the most homogeneous

morphology combined with the lowest density. Further research will focus on the influence of the rheology on foam development to achieve improved cell morphologies and foam properties.

## ■ ASSOCIATED CONTENT

### SI Supporting Information

The Supporting Information is available free of charge at <https://pubs.acs.org/doi/10.1021/acs.iecr.0c05262>.

Liquid-state proton NMR spectra (Figure S1); numerical values related to Figure 10b (Table S1); DSC evaluation method of “including edges” (Figure S2); and different fit results of “standard” fit and “including edges” (Table S2) (PDF)

## ■ AUTHOR INFORMATION

### Corresponding Author

Volker Altstädt – Department of Polymer Engineering, University of Bayreuth, 95447 Bayreuth, Germany; [orcid.org/0000-0003-0312-6226](https://orcid.org/0000-0003-0312-6226); Email: [altstaedt@uni-bayreuth.de](mailto:altstaedt@uni-bayreuth.de)

### Authors

Christian Bethke – Department of Polymer Engineering, University of Bayreuth, 95447 Bayreuth, Germany  
 Simon T. Kaysser – Department of Polymer Engineering, University of Bayreuth, 95447 Bayreuth, Germany  
 Du Ngoc Uy Lan – Department of Polymer Engineering, University of Bayreuth, 95447 Bayreuth, Germany  
 Sebastian M. Goller – Department of Polymer Engineering, University of Bayreuth, 95447 Bayreuth, Germany  
 Kasper P. van der Zwan – Department of Inorganic Chemistry III and North Bavarian NMR Center, University of Bayreuth, 95447 Bayreuth, Germany; [orcid.org/0000-0003-3568-5129](https://orcid.org/0000-0003-3568-5129)  
 Jürgen Senker – Department of Inorganic Chemistry III and North Bavarian NMR Center, University of Bayreuth, 95447 Bayreuth, Germany; [orcid.org/0000-0002-7278-7952](https://orcid.org/0000-0002-7278-7952)  
 Holger Ruckdäschel – Department of Polymer Engineering, University of Bayreuth, 95447 Bayreuth, Germany

Complete contact information is available at: <https://pubs.acs.org/doi/10.1021/acs.iecr.0c05262>

### Author Contributions

C.B.: conceptualization, experimental route and proceedings, discussions, and main writing; S.T.K. and D.N.U.L.: conceptualization, discussions, and writing; S.M.G.: experimental support and discussions; K.P.v.d.Z.: experimental analysis, support, and discussions; J.S.: experimental analysis, labs, and discussion; H.R.: discussions and labs; V.A.: labs and supervision.

### Notes

The authors declare no competing financial interest.

## ■ ACKNOWLEDGMENTS

This project has received funding from the Eurostars-2 joint program with cofunding from the European Union Horizon 2020 research and innovation program with the grant number 01QE1816B. The authors further kindly thank Huntsman and Olin Blue Cube Assets Germany GmbH for material samples used in this research. Furthermore, we would like to thank

Prof. Birgit Weber and A. Dietel of the Department of Inorganic Chemistry VI at the University of Bayreuth for the ability to perform the elemental analysis. Furthermore, we appreciate the support of the Deutsche Forschungsgemeinschaft (DFG) within the SFB840 project B4. We thank the Elite Network of Bavaria for support by the study program “Macromolecular Science”, as well as the Bavarian Polymer Institute (BPI) for the ability to work in their labs and equipment.

## ■ REFERENCES

- (1) Frisch, K. C. History of Science and Technology of Polymeric Foams. *J. Macromol. Sci., Chem.* **1981**, *15*, 1089–1112.
- (2) Kurek, K.; Bledzki, A. Fatigue Behavior of Composites with Foamed Matrix. *J. Reinf. Plast. Compos.* **1994**, *13*, 1116–1134.
- (3) Lee, H.; Neville, K. *Handbook of Epoxy Resins*; McGraw-Hill Inc.: New York, 1967.
- (4) Pascalut, J.-P.; Williams, R. J. J. *Epoxy Polymers, New Materials and Innovations*; Wiley-VCH Verlag GmbH & Co. KGaA: Weinheim, Germany, 2010.
- (5) Guilhem, C.; Negrell, C.; Caillol, S. From gas release to foam synthesis, the second breath of blowing agents. *Eur. Polym. J.* **2020**, *140*, No. 110029.
- (6) Lyu, J.; Hu, D.; Liu, T.; Zhao, L. Non-isothermal Kinetics of Epoxy Resin Curing Reaction Under Compressed CO<sub>2</sub>. *J. Therm. Anal. Calorim.* **2018**, *131*, 1499–1507.
- (7) Ito, A.; Semba, T.; Taki, K.; Oshima, M. Effect of the Molecular Weight Between Crosslinks of Thermally Cured Epoxy Resins on the CO<sub>2</sub>-Bubble Nucleation in a Batch Physical Foaming Process. *J. Appl. Polym. Sci.* **2014**, *131*, No. 40407.
- (8) Lyu, J.; Liu, T.; Xi, Z.; Zhao, L. Effect of Pre-Curing Process on Epoxy Resin Foaming Using Carbon Dioxide as Blowing Agent. *J. Cell. Plast.* **2017**, *53*, 181–197.
- (9) Takiguchi, O.; Ishikawa, D.; Sugimoto, M.; et al. Effect of Rheological Behavior of Epoxy during Pre-curing on Foaming. *J. Appl. Polym. Sci.* **2008**, *110*, 657–662.
- (10) Wang, L.; Yang, X.; Jiang, T.; Zhang, C.; He, L. Cell Morphology, Bubbles Migration, and Flexural Properties of Non-Uniform Epoxy Foams Using Chemical Foaming Agent. *J. Appl. Polym. Sci.* **2014**, *131*, No. 41175.
- (11) Wang, L.; Zhang, C.; Gong, W.; Ji, Y.; Qin, S.; He, L. Preparation of Microcellular Epoxy Foams through a Limited-Foaming Process: A Contradiction with the Time–Temperature–Transformation Cure Diagram. *Adv. Mater.* **2018**, *30*, No. 1703992.
- (12) Wang, L.; Ji, Y.; Peng, X. A new two-step process to prepare microcellular epoxy foams based on kinetic analysis. *J. Mater. Sci.* **2018**, *53*, 1540–1555.
- (13) Hajimichael, M.; Lewis, A.; Scholey, D.; Simmonds, C. Investigation and Development of Epoxy Foams. *Br. Polym. J.* **1986**, *18*, 307–311.
- (14) Kühkamp, A.; Mauz, O.; Göwecke, S. Process for Making Epoxy Resin Foam Plastics. US3,406,131, 1968.
- (15) Weller, E. E.; Plagains, J. Adhesive Composition Comprising an Epoxy Resin, an Amine Carbamate and Water. US3,275,587, July 27, 1966.
- (16) Barrisu, E.; Bankmann, D.; Lammerschop, O.; Renkel, M.; Wucherpfennig, S.; Braun, K. Use of Low-Temperature Foamable Epoxide Resins in Hollow Chamber Structures. EP2473559A1, July 11, 2012.
- (17) Caplow, M. Kinetics of Carbamate Formation and Breakdown. *J. Am. Chem. Soc.* **1968**, *90*, 6795–6803.
- (18) Richner, G.; Puxty, G. Assessing the Chemical Speciation during CO<sub>2</sub> Absorption by Aqueous Amines Using In Situ FTIR. *Ind. Eng. Chem. Res.* **2012**, *51*, 14317–14324.
- (19) Li, K.; Kress, J. D.; Mebane, S. S. The Mechanism of CO<sub>2</sub> Adsorption under Dry and Humid Conditions in Mesoporous Silica-Supported Amine Sorbents. *J. Phys. Chem. C* **2016**, *120*, 23683–23691.

(20) Ren, Q.; Zhu, S. One-Pack Epoxy Foaming with CO<sub>2</sub> as Latent Blowing Agent. *ACS Macro Lett.* **2015**, *4*, 693–697.

(21) Ren, Q.; Xu, H.; Yu, Q.; Zhu, S. Development of Epoxy Foaming with CO<sub>2</sub> as Latent Blowing Agent and Principle in Selection of Amine Curing Agent. *Ind. Eng. Chem. Res.* **2015**, *54*, 11056–11064.

(22) Bethke, C.; Sanchez-Vanquez, S. A.; Raps, D.; et al. Effect of Resin and Blocked/Unblocked Hardener Mixture on the Production of Epoxy Foams with CO<sub>2</sub> Blocked Hardener in Batch Foaming Process. *Polymers* **2019**, *11*, No. 793.

(23) Kaysser, S. T.; Keun, C. A.; Bethke, C.; Altstädt, V. In *Tailoring Epoxy Foam Properties with an Innovative Process Approach Using CO<sub>2</sub> as Blowing Agent*, SAMPE 2020 Virtual Conference Proceedings in Manufacturing Technology, 2020; pp 1–15.

(24) Sakellariou, D.; Lesage, A.; Hodgkinson, P.; Emsley, L. Homonuclear dipolar decoupling in solid-state NMR using continuous phase modulation. *Chem. Phys. Lett.* **2000**, *319*, 253–260.

(25) Fung, B. M.; Khitrin, A. K.; Ermolaev, K. An Improved Broadband Decoupling Sequence for Liquid Crystals and Solids. *J. Magn. Reson.* **2000**, *142*, 97–101.

(26) Gracia, F. G.; Soares, B. G.; Pita, V. J. R. R.; Sánchez, R.; Rieumont, J. Mechanical Properties of Epoxy Networks Based on DGEBA and Aliphatic Amines. *J. Appl. Polym. Sci.* **2007**, *106*, 2047–2055.

(27) Coates, J. Interpretation of Infrared Spectra, A Practical Approach. In *Encyclopedia of Analytical Chemistry*; Meyers, R. A., Ed.; John Wiley & Sons Ltd.: Chichester, 2000; pp 10815–10837.

(28) Danon, A.; Stair, P. C.; Weitz, E. FTIR Study of CO<sub>2</sub> Adsorption on Amine-Grafted SBA-15: Elucidation of Adsorbed Species. *J. Phys. Chem. C* **2011**, *115*, 11540–11549.

Supporting Information for

# Synthesis and characterization of dual functional carbamates as blowing and curing agents for epoxy foam

*Christian Bethke<sup>1</sup>, Simon T. Kaysser<sup>1</sup>, Du Ngoc Uy Lan<sup>1</sup>, Sebastian  
M. Goller<sup>1</sup>, Kasper P. van der Zwan<sup>2</sup>, Jürgen Senker<sup>2</sup>, Holger  
Ruckdäschel<sup>1</sup>, Volker Altstädt<sup>1\*</sup>*

\*Corresponding Author: altstaedt@uni-bayreuth.de

<sup>1</sup>Department of Polymer Engineering, University of Bayreuth,  
Universitätsstraße 30, 95447 Bayreuth, Germany

<sup>2</sup>Department of Inorganic Chemistry III and North Bavarian NMR  
Center, University of Bayreuth, Universitätsstraße 30, 95447  
Bayreuth, Germany

**Additional supporting information****For chapter 3.1.2. Characterization of chemical structure of synthesized carbamate products**

Due to the possible proton shift in the carbamate structure to form the acid group, a liquid state NMR proton shift spectra for B-AEP, B-DMC and B-IPDA in Ethanol-D<sub>6</sub> was recorded and is presented in **Figure S1**.

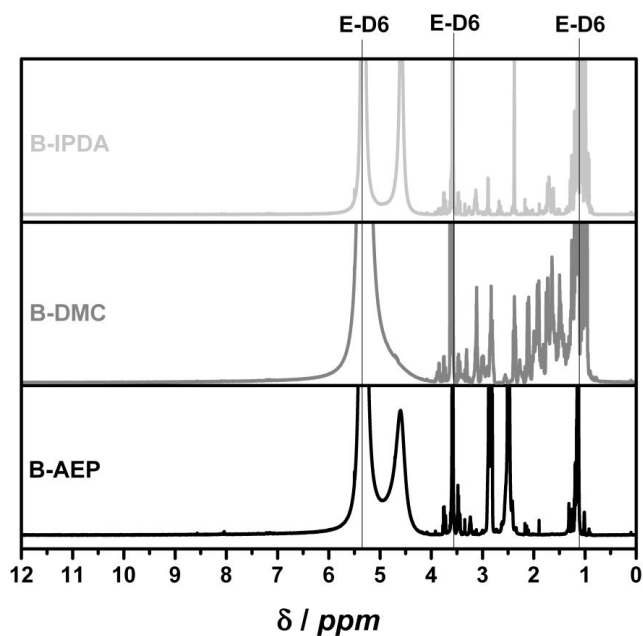


**Figure S1.** Liquid-state <sup>1</sup>H NMR spectra of the three carbamates. The shifts for the solvent Ethanol-D<sub>6</sub> (ED<sub>6</sub>) are indicated.

As the carbamates are already sufficiently characterized by FTIR, EA, <sup>13</sup>C and <sup>15</sup>N CP MAS NMR, a detailed investigation on the large amount of multiplets between 1 and 5 ppm was not proceeded.

However, the absence of resonances in the shift region of 9-11 ppm, which are typical for carboxylic acids, leads to the conclusion that a formation of acid groups can be excluded for the products.

**For chapter 3.1.3. The carbamate decomposition behavior**

The numerical values of **Figure 7b**, namely the onset time of fitting when the TGA value hits the 100 wt.% again ( $t_i$ ), the time to the first extrema, maximum or minimum, of the 2<sup>nd</sup> derivative ( $t_{M_{DD}}$ ), the time until the theoretical CO<sub>2</sub> wt.% content ( $t_{CO_2}$ ) of the blocked amines is released and the time where the first maximum of decomposition ( $t_{M_D}$ ) occurs, as well as the determined reaction rate up to 99 % conversion ( $R_{99}$ ) received from MFK in DSC of DGBA + unblocked amine are summarized in **Table S1**.

**Table S1.** Results of the isothermal TGA measurements for determination of decomposition rates ( $r_D$ ), time until 100 wt.% ( $t_i$ ), time until maxima of 2<sup>nd</sup> derivative ( $tM_{DD}$ ), time until theoretical total CO<sub>2</sub> release ( $t_{CO_2}$ ) and time to maximum of 1<sup>st</sup> derivative  $tM_d$  at defined temperatures. Additionally, the determined reaction rate up to 99 % conversion ( $R_{99}$ ) received from MFK in DSC of DGBA + unblocked amine is presented.

System	100 °C		120 °C		140 °C		160 °C		180 °C	
AEP	$R_{99}$ %s <sup>-1</sup>	0.08	$R_{99}$ %s <sup>-1</sup>	0.15	$R_{99}$ %s <sup>-1</sup>	0.25	$R_{99}$ %s <sup>-1</sup>	0.41	$R_{99}$ %s <sup>-1</sup>	0.64
B-AEP	$r_D$ %s <sup>-1</sup>	0.03	$r_D$ %s <sup>-1</sup>	0.08	$r_D$ %s <sup>-1</sup>	0.17	$r_D$ %s <sup>-1</sup>	0.22	$r_D$ %s <sup>-1</sup>	0.32
	$tM_d$	800 s	$tM_d$	320 s	$tM_d$	138 s	$tM_d$	98 s	$tM_d$	66 s
	$t_i$	92 s	$t_i$	96 s	$t_i$	48 s	$t_i$	8 s	$t_i$	30 s
	$tM_{DD}$	830	$tM_{DD}$	540	$tM_{DD}$	180	$tM_{DD}$	135	$tM_{DD}$	70 s
	s	$t_{CO_2}$								
	746 s		392 s		178 s		146 s		94 s	
DMC	$R_{99}$ %s <sup>-1</sup>	0.04	$R_{99}$ %s <sup>-1</sup>	0.07	$R_{99}$ %s <sup>-1</sup>	0.13	$R_{99}$ %s <sup>-1</sup>	0.22	$R_{99}$ %s <sup>-1</sup>	0.35
B-DMC	$r_D$ %s <sup>-1</sup>	0.12	$r_D$ %s <sup>-1</sup>	0.22	$r_D$ %s <sup>-1</sup>	0.30	$r_D$ %s <sup>-1</sup>	0.43	$r_D$ %s <sup>-1</sup>	0.50
	$tM_d$	62 s	$tM_d$	40 s	$tM_d$	44 s	$tM_d$	32 s	$tM_d$	30 s
	$t_i$	4 s	$t_i$	10 s	$t_i$	18 s	$t_i$	12 s	$t_i$	8 s
	$tM_{DD}$	110	$tM_{DD}$	65	$tM_{DD}$	65 s	$tM_{DD}$	45 s	$tM_{DD}$	35 s
	s	$t_{CO_2}$								
	252 s		114 s		94 s		64 s		50 s	
IPDA	$R_{99}$ %s <sup>-1</sup>	0.03	$R_{99}$ %s <sup>-1</sup>	0.05	$R_{99}$ %s <sup>-1</sup>	0.10	$R_{99}$ %s <sup>-1</sup>	0.17	$R_{99}$ %s <sup>-1</sup>	0.27
B-IPDA	$r_D$ %s <sup>-1</sup>	0.03	$r_D$ %s <sup>-1</sup>	0.07	$r_D$ %s <sup>-1</sup>	0.13	$r_D$ %s <sup>-1</sup>	0.19	$r_D$ %s <sup>-1</sup>	0.27
	$tM_d$	272 s	$tM_d$	208 s	$tM_d$	104 s	$tM_d$	70 s	$tM_d$	58 s
	$t_i$	24 s	$t_i$	16 s	$t_i$	30 s	$t_i$	12 s	$t_i$	28 s
	$tM_{DD}$	700	$tM_{DD}$	300	$tM_{DD}$	150	$tM_{DD}$	90 s	$tM_{DD}$	70 s

s	$t_{CO_2}$	s	$t_{CO_2}$	s	$t_{CO_2}$	$t_{CO_2}$	$t_{CO_2}$
732 s		320 s		214 s		134 s	110 s

**For chapter 3.2.1. Curing and foaming behavior by DSC**

A schematic of the applied method for DSC evaluation "including onset" (O) compared to "standard" (S) is schematically shown in **Figure S2** for the sample DGEBA + AEP.

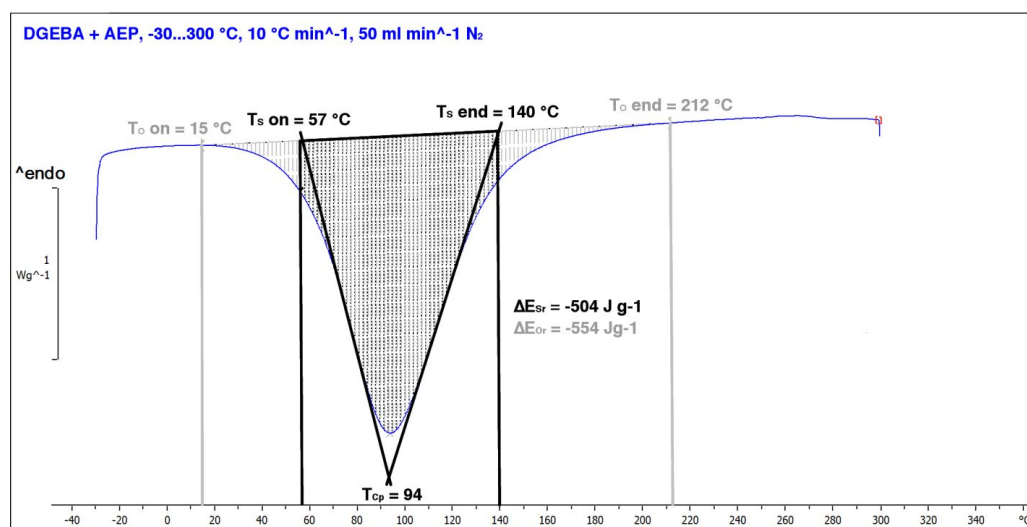


**Figure S2.** Scheme for different evaluation methods with different temperatures for the onset (T<sub>on</sub>) and endset (T<sub>end</sub>) temperature, depending on "standard" (S) (black lines and values) and "including edge" (O) (grey lines and values) for DSC evaluation, shown by example DGEBA + AEP. The reaction Enthalpy peak (T<sub>D</sub> and T<sub>cp</sub>) is not affected by the method compared to the calculated enthalpy (ΔE). Lines are drawn for better illustration.

A certain error of the method can be discussed with regards to the way of finding the exact T<sub>on</sub>. The procedure was done by the best of our knowledge, and the more comparable results to the experimental findings compared to the standard method prove the

consistence. The range between indicated onset ( $T_{O_{on}}$  &  $T_{S_{on}}$ ) and endset temperatures ( $T_{O_{end}}$  &  $T_{S_{end}}$ ) result in the peak range and effective area of integration, which affects the value of energy release ( $\Delta E_{Or}$  &  $\Delta E_{Sr}$ ). The total influence of the chosen  $T_{end}$  was found to be low. However, especially for the carbamates and its decomposition onset, the deviation is notably. The decomposition and reaction peak temperature ( $T_{C_p}$ ) is not affected by the method. Additional values of DSC measurements for comparison of the "standard" and the values from "including edge" are provided in **Table S2**.

**Table S2.** Results of the DSC measurement of the neat carbamates as well as different hardener and carbamate systems with DGEBA resin. The values of observed "including edge" and "standard" calculated carbamate decomposition onset ( $T_{DO_{on}}$  &  $T_{DS_{on}}$ ) and decomposition enthalpy ( $\Delta E_{Odec}$  &  $\Delta E_{Sdec}$ ), as well as both reaction onset temperatures ( $T_{CO_{on}}$  &  $T_{CS_{on}}$ ), reaction peak temperature ( $T_{C_p}$ ), and total reaction enthalpy ( $\Delta E_{Or}$  &  $\Delta E_{Sr}$ ) are presented.

System DGEBA resin +	Decomposition of carbamate				Curing reaction with DGEBA				
	$T_{DO_{on}}$ [°C] ]	$T_{DS_{on}}$ [°C] ]	$\Delta E_{Odec}$ [J g <sup>-1</sup> ]	$\Delta E_{Sdec}$ [J g <sup>-1</sup> ]	$T_{CO_{on}}$ [°C] ]	$T_{CS_{on}}$ [°C] ]	$T_{C_p}$ [°C] ]	$\Delta E_{Or}$ [J g <sup>-1</sup> ]	$\Delta E_{Sr}$ [J g <sup>-1</sup> ]
AEP	-	-	-	-	15	57	94	-554	-504
B-AEP	85	129	747	610	70	115	130	-219	-181

DMC	-	-	-	-	22	76	115	-482	-418
B-DMC	55	114	642	375	57	101	120	-295	-280
IPDA	-	-	-	-	29	77	112	-524	-417
B- IPDA	71	131	546	407	83	130	138	-325	-180

## 4.2 Structural Analysis of CO<sub>2</sub> loaded Diamine Derived from Aqueous Synthesis Route for Epoxy Foaming

This work is a cooperation between the Inorganic Chemistry III and the Polymer Engineering of the University of Bayreuth with the following authors: K.P. van der Zwan, C. Bethke, A. Pongratz, D. Schweser, R. Siegel, H. Ruckdäschel, V. Altstädt, J. Senker.

My contributions are:

- conception and shared main authorship
- performing all NMR experiments
- synthesis of the <sup>13</sup>C enriched material
- quantum chemical calculations

The contributions of the other authors are:

- conception and authorship of the article
- assistance with the NMR experiments
- synthesis of the materials
- recording the FTIR measurements
- performing the TGA and DSC measurements
- performing the batch foaming experiments
- evaluating the foam properties

## Structural Analysis of CO<sub>2</sub> Loaded Diamine Derived from Aqueous Synthesis Route and its Basic Epoxy Foaming Performance

Kasper P. van der Zwan,<sup>a‡</sup> Christian Bethke,<sup>b‡</sup> Annalena Pongratz,<sup>a</sup> Denise Schweser<sup>b</sup>, Lukas Endner<sup>b</sup>, Renée Siegel,<sup>a</sup> Volker Altstädt<sup>b</sup>, Holger Ruckdäschel,<sup>b</sup> and Jürgen Senker<sup>a\*</sup>

<sup>a</sup> Inorganic Chemistry III and Northern Bavarian NMR Center, University of Bayreuth, Universitätsstraße 30, D-95447 Bayreuth, Germany

<sup>b</sup> Polymer Engineering, University of Bayreuth, Universitätsstraße 30, D-95447 Bayreuth, Germany

\* juergen.senker@uni-bayreuth.de; ruckdaeschel@uni-bayreuth.de

‡ These authors contributed equally to this work.

### Abstract

A new dual functional chemical blowing agent for epoxy resins is presented. Compared to previous publications the solvent of the synthesis of the CO<sub>2</sub>-blocked diamine is changed from ethanol to water, leading to an even more eco-friendly synthesis. Following the change of the solvent, the received product B-IPDA<sub>aq</sub> contains an urea group and additionally two formula units of structural water. The structure is confirmed by solid-state NMR spectroscopic experiments including D-HMQC and REDOR. The reaction pathway and stability of the structure is investigated by computational modelling and shows that a carbonate intermediate is formed. This new blowing agent is also capable to foam and harden the epoxy resin DGEBA. The degradation kinetics at different temperatures were investigated by TGA. The crystalline water is released in an independent step along the CO<sub>2</sub> release. The results of the isothermal foaming experiments revealed a proper correlation of the degradation and reaction kinetics in the foaming system. The best foaming temperature range was found between 120 and 140 °C at given conditions.

### Introduction

Epoxy foams are one of the most used thermoset polymer foams,<sup>1,2</sup> because of their thermal stability, chemical resistance and electrical properties.<sup>3,4</sup> Other advantageous properties are their low shrinkage, moisture resistance and good adhesive towards other materials.<sup>3,4</sup> A main challenge in the production of epoxy foams is the timing of blowing and curing of the material.<sup>5</sup> Typically, chemical blowing agents (CBA) are used in the epoxy foam industry, as they can be chosen by its temperature of activity and get matched with the hardening resin system.<sup>6</sup>

Another way is the use of dual functional CBAs that act as latent curing and blowing agent.<sup>7-9</sup> This inherent dual functionality makes the hardener directly available after the decomposition and gas release, and will not cure the resin prior to the foaming process. This offers the benefit to adjust the timing of curing and hardening and thus to tune the foam morphology by pre-curing to a precise level, as shown in our previous study.<sup>10</sup>

The main disadvantage of many established CBAs are toxic by-products and residuals in the resulting foamed polymer.<sup>6</sup> The growing amount of environmental regulations (SNAP, REACH) results in a ban of many established systems. The use of dual functional hardeners such as carbamates bypasses this aspect, as no by-products remain in the foam.

In a previous work,<sup>11</sup> we presented three zwitterionic carbamates of N-Aminoethylpiperazine (AEP), 4-Methylcyclohexane-1,3-diamine (DMC) and Isophorone diamine (IPDA) that were proven to be useable as such a dual functional, CBA and hardener, molecule. They can be synthesised by bubbling CO<sub>2</sub> through a mixture of the diamine and Ethanol. To further reduce the environmental impact during the synthesis of these CO<sub>2</sub> loaded amines, we changed the solvent for the synthesis from ethanol to water in this work. However, only the synthesis with IPDA yielded a stable product with water as solvent.

Realising that this synthesis route results in the formation of other products than expected, we used solid state NMR spectroscopy to identify the molecular structure of CO<sub>2</sub> loaded IPDA received in water (B-IPDA<sub>AQ</sub>). Its decomposition characteristics and kinetics were determined and the capability to act as a dual functional CBA and hardener was investigated in a final step.

## Experimental Section

Amine and CO<sub>2</sub> for synthesis: Isophorone diamine (IPDA) with a purity of > 95 %, a M<sub>w</sub> of 170.3 g/mol and an AHEW 42.6 g/mol, (Aradur 22962, Huntsman, Texas, United States) was used as received. For the lab-scale synthesis, gaseous bottled CO<sub>2</sub> with a quality grade of 4.5 (from Rießner Gase, Lichtenfels, Germany) was used for reaction. As solvent, deionised H<sub>2</sub>O was used as received from the in house line.

For the <sup>13</sup>C enriched B-IPDA<sub>AQ</sub> synthesis, a <sup>13</sup>C enriched CO<sub>2</sub> (99% <sup>13</sup>C enriched, Cortecnet, France) was used.

Epoxy for foaming: Diglycidylether of Bisphenole-A (DGEBA, DER331, Olin, Missouri, United States) with a M<sub>w</sub> of 340.4 g/mol, an epoxy equivalent weight (EEW) of 187 g/mol and a pre-determined viscosity of 13 Pa\*s (25 °C) was used.

### *Lab-scale Synthesis of B-IPDA<sub>AQ</sub>*

The reaction of IPDA and CO<sub>2</sub> was carried out in H<sub>2</sub>O. The mixture was prepared by adding and mixing 14 g IPDA in 70 g of H<sub>2</sub>O (1:5 weight ratio) in a reaction flask (125 ml) by using a magnetic stirrer (a). The reaction flask (b) was attached to the CO<sub>2</sub> cylinder through the air flow

regulation valve (c). The CO<sub>2</sub> flow was introduced at 100 ml min<sup>-1</sup> and at ambient pressure from the bottom of the flask through a 2.2 mm diameter flexible tube for 300 min. A scheme of the synthesis setup is shown in Figure 1.

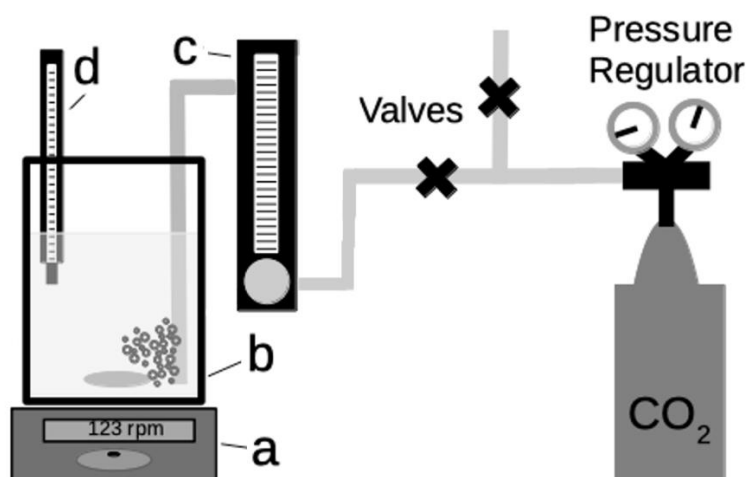


**Figure 1.** Experimental setup for CO<sub>2</sub> blocking reaction of amine curing agents. A magnetic stirrer (a) stirs the EtOH:Amine solution in the reaction flask (b), while the CO<sub>2</sub> flow is regulated by flow regulation valves (c) and the temperature is monitored with thermal sensors (d).

The reaction was conducted in a fume hood with a surrounding temperature of 21 °C. After the reaction, the products were filtered and washed with 300 ml of H<sub>2</sub>O. The received white powder was dried for 16 h in a ventilated hot air oven at 40 °C.

#### *Synthesis of <sup>13</sup>C-B-IPDA<sub>AQ</sub>*

For the synthesis of the <sup>13</sup>C enriched B-IPDA<sub>AQ</sub>, 300 mg IPDA were mixed with 1.5 g of water. <sup>13</sup>C enriched CO<sub>2</sub> was bubbled through the mixture with 2 bar. After roughly 3 minutes, when the solution became turbid and highly viscous, the synthesis was stopped. The mixture was washed with a little bit of water and afterwards centrifuged at 8000 rpm for 10 minutes. The white slurry was then transferred into a petri dish and dried in the oven at 40 °C for 12 h.

#### *Elemental Analysis*

Elemental analysis (EA) was conducted with an UNICUBE (Elementar, Langenselbold, Germany). The combustion temperature was set to 1150 °C while the reduction was proceeded at 950 °C, and the flush time was set to 25 s. All samples were measured in triplicate. For the calculations of the number of atoms (n), the molecular mass (M<sub>A</sub>) of C, 12.011 g mol<sup>-1</sup>, H, 1.008 g mol<sup>-1</sup>, N, 14.007 kg mol<sup>-1</sup>, and O, 15.999 g mol<sup>-1</sup>, were used.

The wt.% of each atom (wt.%<sub>A</sub>) related to the total mass of the molecule (M<sub>M</sub>) was calculated by Equation 1:

$$wt. \%_A = \frac{n * M_A \left[ \frac{g}{mol} \right]}{M_M \left[ \frac{g}{mol} \right]} * 100\% \quad (1)$$

This is used to determine the remaining mass, which is expected as O-Atoms according to expected molecular formula.

#### *Solid-state NMR experiments*

$^1\text{H}$  and  $^{13}\text{C}$  solid-state NMR experiments were performed on a Bruker Avance III 600 NMR spectrometer operating at Larmor frequencies of 600.15 MHz ( $^1\text{H}$ ), 150.93 MHz ( $^{13}\text{C}$ ) and 43.35 MHz ( $^{14}\text{N}$ ). The  $^1\text{H}$  onepulse and the  $^1\text{H}\{^{14}\text{N}\}$  D-HMQC experiments were conducted in a 1.3 mm rotor with MAS spinning speeds of 62.5 and 50 kHz, respectively. For the onepulse experiment the rf field was set to 83.3 kHz. For the D-HMQC experiment the  $^1\text{H}$   $90^\circ$  and  $180^\circ$  pulses were set to 208.3 kHz, the rf field in the recoupling sequence was set to 2 times the MAS frequency and thus 100 kHz. The  $^{14}\text{N}$  pulse was 55 kHz with a 28  $\mu\text{s}$  pulse. The  $^{13}\text{C}\{^1\text{H}\}$  CP experiment was conducted in 1.9 mm rotor with a ramped CP sequence<sup>12</sup> with an linear increase of the  $^1\text{H}$  nutation frequency from 50 to 100 % with a maximum of 81.7 kHz. During acquisition the protons were decoupled at 108.1 kHz using the spinal64<sup>13</sup> sequence.

The  $^{15}\text{N}\{^1\text{H}\}$ CP/ $^{13}\text{C}$  REDOR experiment was performed on a Bruker Avance III 400 NMR spectrometer operating at Larmor frequencies of 400.14 MHz ( $^1\text{H}$ ), 100.63 MHz ( $^{13}\text{C}$ ) and 40.55 MHz ( $^{15}\text{N}$ ). A ramped CP with a linear increase of the  $^1\text{H}$  nutation frequency from 90 to 100 % with a maximum frequency of 49.1 kHz was used to obtain polarisation on the  $^{15}\text{N}$  nuclei. The rf frequencies for the  $180^\circ$  pulses were 58.8 kHz and 42.0 kHz for  $^{15}\text{N}$  and  $^{13}\text{C}$ , respectively. During the REDOR block and the acquisition protons were decoupled at 67.3 kHz using the spinal64 sequence.

The  $^{15}\text{N}\{^1\text{H}\}$  CP and  $^{15}\text{N}$  onepulse experiments were performed on a Bruker Avance III 400 NMR spectrometer operating at Larmor frequencies of 400.50 MHz ( $^1\text{H}$ ) and 40.58 MHz ( $^{15}\text{N}$ ). For the CP experiment a nutation frequency of 29.2 kHz (no ramp) was used and protons were decoupled at 73.1 kHz using the spinal64 sequence. For the  $^{15}\text{N}$  onepulse  $30^\circ$  pulses with a nutation frequency of 34.7 kHz were used.

#### *Computational methods*

The models for the quantum chemical calculations were built with jmol.<sup>14</sup> The geometry optimisation on DFT<sup>15,16</sup> level were done with the CASTEP<sup>17</sup> code and standard parameters.<sup>18–22</sup> NMR parameters, namely the chemical shift anisotropy and the asymmetry were also calculated with CASTEP<sup>23,24</sup>

The NMR simulations of the REDOR build up curves were done with the SIMPSON software.<sup>25</sup>

#### *Thermogravimetry*

Thermogravimetric analysis (TGA) was conducted with a TGA 209 F1 Libra (Netzsch, Selb, Germany) in order to investigate the decomposition behavior and evaporation temperature of the amines in the range of 30 – 300 °C at 10 °C min<sup>-1</sup> with 50 ml min<sup>-1</sup> N<sub>2</sub>. Additional isothermal TGA measurements at defined temperatures were proceeded to get an impression of the decomposition rate of the carbamates. The sample weight was set around 10.7 mg

#### *Differential Scanning Calometry*

Differential scanning calorimetry (DSC) was conducted with a DSC1 STARe System (Mettler Toledo, Columbus, Ohio, USA) to determine the reaction enthalpy and kinetics. All measurements were carried out in the range of -30 to 300 °C at 10 °C min<sup>-1</sup> with 50 ml min<sup>-1</sup> N<sub>2</sub>. The sample weight was set around 6 mg. For the model free kinetics (MFK) study, additional heating ramps of 5 and 20 °C min<sup>-1</sup> were proceeded and the MFK was simulated with the Mettler Toledo STARe Software V 13.00a (Build 6917).

#### *Foaming Experiments*

To examine the characteristics of the new B-IPDA<sub>AQ</sub> with its dual function as a blowing and curing agent, it was mixed with DGEBA resin based on the stoichiometric ratio by EEW and AHEW, resulting in a weight ratio of 1:3.13 B-IPDA<sub>AQ</sub>. Therefore, the resin was pre-heated to 30 °C. The mixing was carried out by adding the corresponding amount of resin and B-IPDA<sub>AQ</sub> to a 10-ml cup and after short manual premixing it was processed at room temperature for 1 min at 3500 rpm in a DAC 150 (Speed-Mixer, Hamm, Germany) mixing system. For foaming, an aluminum mold, made by the mechanical workshop of the University Bayreuth, with a cavity of 30 mm x 30 mm x 10 mm (l x w x h) and a bulk volume of 9 cm<sup>3</sup> was used, treated with Loctite Frekote 770-NC (from Henkel, Duesseldorf, Germany) release agent. For each experiment, the specific amount of 30 % mold volume was filled with the mixture, corresponding to a theoretical expansion factor of 3.3 resulting in a target density of 350 g m<sup>-3</sup>. Afterwards, the filled mold was set into a hot-press PW 20 (P/O/Weber, Remshalden, Germany) for 1 h at various temperatures to undergo the foaming and curing reaction. After the mold was cooled to RT, the epoxy foams were demolded and qualitatively investigated.

#### *Density measurement*

The density measurements were performed in distilled water with an AG245 analytical balance (Mettler Toledo, Columbus, Ohio, USA) with the use of a density kit for AG balances.

#### *SEM Sample preparation*

To obtain the foam morphology, the samples were cut with a DiaDisc 2000 saw (Mutronic, Rieden am Forggensee, Germany) and sputtered with gold in a SPUTTER Coater 108auto (Cressington Coating systems, Dortmund, Germany). The SEM pictures were recorded with a Leo 1530 (Zeiss, Oberkochen, Germany).

## Results and Discussion

### Structure elucidation of B-IPDA<sub>AQ</sub>

The first step of the structure elucidation of B-IPDA<sub>AQ</sub> is the elemental analysis shown in Table 1. The proposed formula is C<sub>11</sub>H<sub>24</sub>N<sub>2</sub>O<sub>3</sub>, which includes 2 hydrogen and 1 oxygen more than expected for the carbamate that forms in ethanol. This could be explained by the incorporation of structural water in the carbamate, the formation of a carbonate salt or a urea structure with two formula units of structural water as depicted in Figure 2.

**Table 1.** Results from the Elemental analysis.

Element	Mass /wt.%	Stoichiometry
N	12.11	2
C	56.96	11
H	10.35	24
O	20.58	3
Sum	100	C <sub>11</sub> H <sub>24</sub> N <sub>2</sub> O <sub>3</sub>

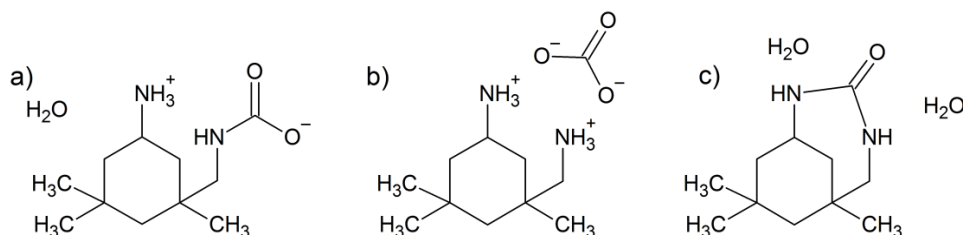


**Figure 2.** Proposed molecular structures of B-IPDA<sub>AQ</sub> a) carbamate with one formula unit of structural water b) carbonate c) urea with two formula units of structural water.

Information on the nitrogen surrounding can be obtained from an  $^{15}\text{N}\{^1\text{H}\}$  CP MAS NMR spectrum (Figure 3a). In this spectrum only one peak at -300 ppm was observed. This resonance can be assigned to a C-N bond, thus the presence of  $\text{NH}_3^+$  groups and with this the carbonate and carbamate structures were excluded. In solid state NMR spectroscopy a  $^1\text{H}$  spectrum only grants limited insight into the structure because of the strong homonuclear couplings. However, when coupled with an indirect detection of  $^{14}\text{N}$  by a D-HMQC experiment<sup>26</sup> the amount of protons binding on the nitrogen atoms can be derived. This experiment showed that only two protons are directly bound to nitrogen atoms (Figure 3b).

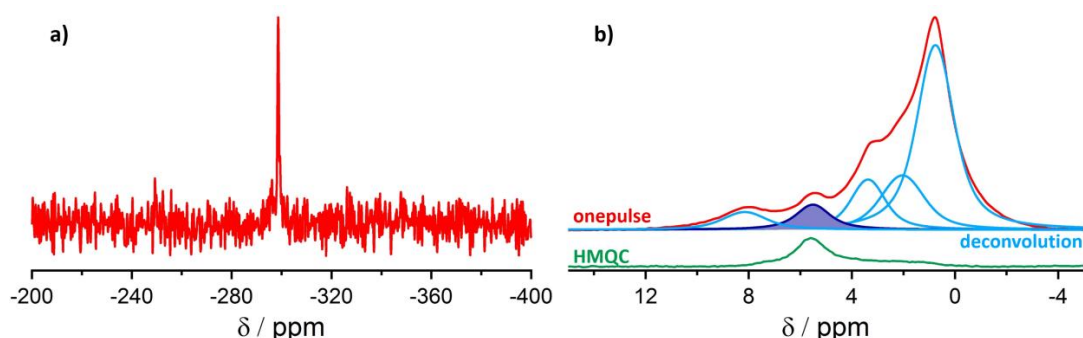


**Figure 3.** a)  $^{15}\text{N}\{^1\text{H}\}$  CP MAS NMR spectrum of B-IPDA<sub>AQ</sub> (For a comparison to the  $^{15}\text{N}$  spectrum obtained from a synthesis in Ethanol see SI Figure S1. b)  $^1\text{H}$  onepulse MAS NMR spectrum (red) with a deconvolution of the respective resonances (blue) and a  $^1\text{H}\{^{14}\text{N}\}$  HMQC MAS NMR spectrum (green) showing only proton resonances in close proximity of  $^{14}\text{N}$  nuclei. In purple, the integral of these H-N protons is depicted. The integral of this signal is 1.7 when the sum of the integrals of all deconvoluted resonances is set to 24, which is the amount of protons obtained from elemental analysis.

A structure model that fits this requirement implies the formation of a urea group that connects the two amine groups (Figure 2c). To proof this hypothesis we synthesised B-IPDA<sub>AQ</sub> with  $^{13}\text{C}$  enriched  $\text{CO}_2$  to increase the C=O sensitivity in the upcoming experiments. To confirm the existence of the C-N bond, a REDOR<sup>27</sup> experiment that estimates the  $^{13}\text{C}$ - $^{15}\text{N}$  distance was performed. With the software package simpson<sup>25</sup> theoretical REDOR build-up curves for the urea and carbonate model were calculated. A comparison of these theoretical and the measured build-up curves (Figure 4 a) confirms the formation of a C-N bond and thus highly supports the formation of the urea structure. To finally secure the formation of the urea structure a static  $^{13}\text{C}$  solid-state NMR spectrum was performed. From this spectrum, the chemical shift anisotropy (CSA) of the urea carbon can be extracted. In this spectrum, as well as in the MAS spectrum (SI Figure S2) it was observed that at least three carbonyl resonances exist in the sample (Figure 4 b). This can be explained with the stereo centres that can be identified at position 1 and 3 of the cyclohexane ring (Figure 2c). This leads to the formation of four different stereo isomers. These isomers have different cyclic stresses of the 7-membered urea rings and therefore different bond and torsion angles leading to different chemical shift anisotropies of the carbonyl resonance. Therefore, the molecular structures of the four isomers were geometry optimised on DFT level with the CASTEP code. Afterwards the CSA parameters and the anisotropies  $\eta$  were calculated with the MAGRES<sup>28</sup> package within CASTEP. With the resulting parameters the static spectrum is resembled decently (SI Figure S3). Fitting the spectrum using the calculated values as starting parameters shows that the DFT calculation overestimates the CSA by roughly 5-15 % (Table 2 and Figure 4b). Nonetheless, this result confirms the formation of the urea functional group within B-IPDA when

synthesised in water. To account for the elemental analysis two formula units of water are present in the structure. The mild drying conditions (40 °C) that are needed to prevent the back reaction are causing this.

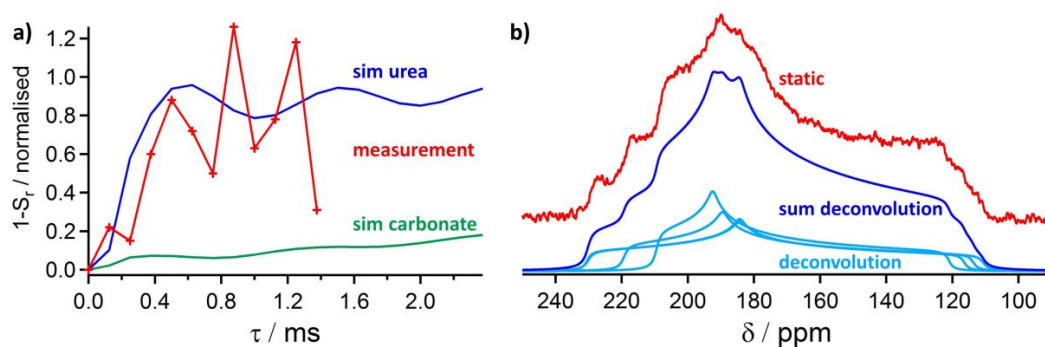


**Figure 4.** a) Measured (red) and simulated (blue, urea; green carbonate) REDOR build up curves of B-IPDA<sub>AQ</sub>. B) <sup>13</sup>C static CP{<sup>1</sup>H} NMR spectrum (red) with a deconvolution of the respective resonances (light blue) and the sum of the four deconvoluted resonances (dark blue).

**Table 2.** Display of the calculated and fitted chemical shift anisotropies and asymmetry values.

Peak #	$\delta_{\text{CSA}}$ calc	$\delta_{\text{CSA}}$ fit	$\eta$ calc	$\eta$ fit
1	67.0	60.7	0.53	0.76
2	65.4	64.4	0.81	0.72
3	67.6	60.5	0.68	0.49
4	62.6	53.3	0.62	0.32

#### Reaction pathway and stability

Since Wang et al.<sup>29</sup> claim that the formation of a urea group can only form with a catalyst it is worth investigating the reaction pathway leading to the urea formation as well as the stability of the transition state. Therefore, a <sup>15</sup>N NMR spectrum of the wet slurry obtained after centrifuging was recorded. Interestingly, in this case only one resonance assignable to NH<sub>2</sub>/NH<sub>3</sub><sup>+</sup> (-348.7 ppm) was detected (Figure 5). This means that during the bubbling of the CO<sub>2</sub> the carbonate species is formed and reacted to the urea upon drying. This raises the question what is special about IPDA that enables the formation of a urea derivate. Therefore, a model of the proposed carbonate transition state was built and geometry optimised with the CASTEP code.

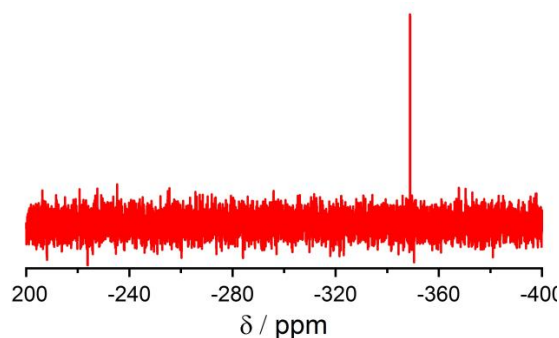


**Figure 5.**  $^{15}\text{N}$  one-pulse NMR spectrum of B-IPDA<sub>AQ</sub> prior to drying.

In the starting model, the carbonate is positioned in a way that the single bonded oxygen atoms have a distance of 2.15 Å to one proton of the  $\text{NH}_3^+$  group. This results in a distance of 2.46 Å of one  $\text{CH}_2$  carbon on position 2 of the cyclohexane ring (Figure 6).

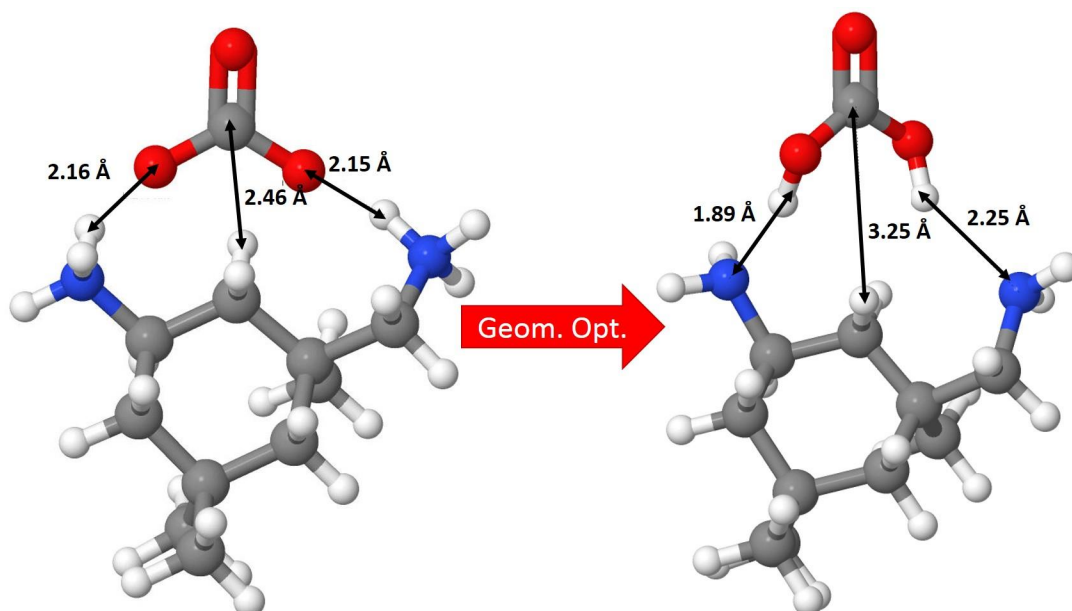


**Figure 6.** Model of an IPDA carbonate aggregate prior and after the geometry optimisation

After the geometry optimisation, the hydrogen atoms were connected to the single bonded oxygen atoms. These hydrogens form hydrogen bonds to their “original” nitrogen atoms of 1.8 and 2.3 Å. The cyclohexane ring relaxes in a way that the distance of the  $\text{CH}_2$  proton increases to 3.3 Å (Figure 6). It is reasonable to assume that the hydrogen bond lengths in the real system are closer to the same value and change dynamically as the system at this state is still fluent and DFT calculation suppose a temperature of 0 K. This is also resembled by the fact that the  $^{15}\text{N}$  NMR spectrum only features one resonance. If there would be a static divergence of two hydrogen bond lengths a second resonance would appear. This calculation underlines the phenomenon seen by NMR spectroscopy that IPDA can form a stable carbonate adduct.

We performed this calculation also for another diamine and there no stable carbonate forms (for details see SI section 2), underlining the unique conformation of the IPDA/B-IPDA<sub>AQ</sub> system. Therefore, we can even confirm the reaction pathway as depicted in Figure 7 that the first step is the formation of a carbonate aggregate. Upon drying at 40 °C the urea group forms and 2 formula units of structural water remain in the structure.

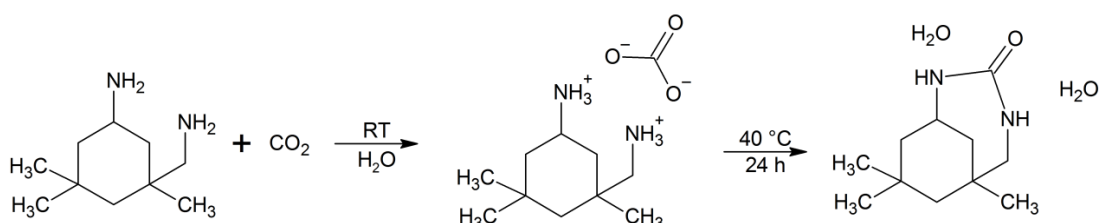


**Figure 7.** Reaction pathway for the formation of B-IPDA<sub>AQ</sub>.

#### *Decomposition behaviour of B-IPDA<sub>AQ</sub>*

The dynamic DSC measurement revealed an endothermal decomposition with 815 J g<sup>-1</sup> and an onset temperature ( $T_D$ ) around 64 °C. The observed decomposition peak shown in Figure 8a does not allow any precise conclusion on the decomposition steps, as the measurement noise due to the bubbling in the crucible shows at least three smaller peaks in the main peak in the range between 129 to 143 °C. The dynamic TGA revealed a  $T_D$  of 1% weight loss around 74 °C which is 10 °C higher compared to the DSC. The difference can be explained by the different crucibles and masses required for each technique. The dynamic TGA and its first derivative is shown in Figure 8b.

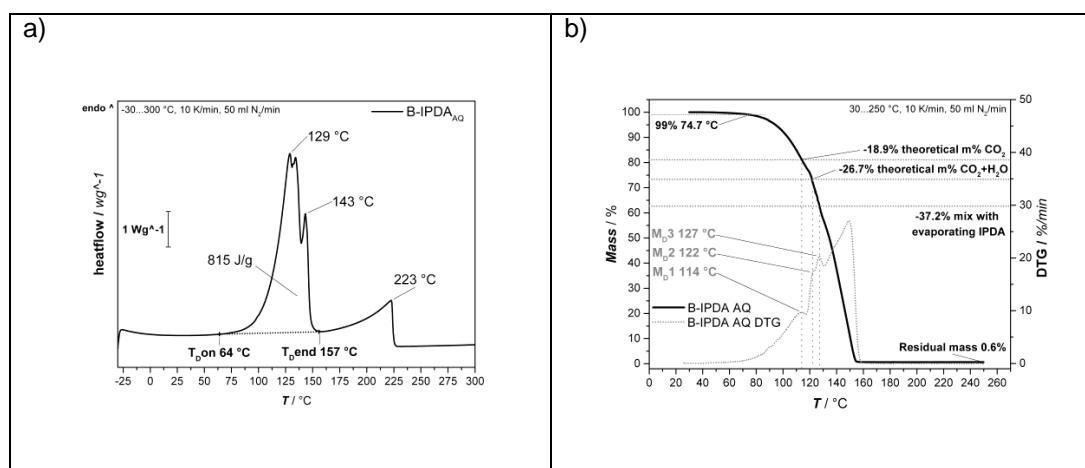


**Figure 8.** a) Dynamic DSC measurement and b) dynamic TGA measurement of IPDA<sub>AQ</sub> and its first derivative with indicated maxima and degradation steps.

The  $T_D$  determined by TGA of 74 °C for the B-IPDA<sub>AQ</sub> is slightly higher compared to the B-IPDA<sub>ET</sub>, synthesized in Ethanol, with 70 °C as shown in a previous study.<sup>11</sup> This indicates an increased stability of the B-IPDA<sub>AQ</sub>. In addition, a two-step decomposition can be observed,

which is also different compared to B-IPDA<sub>ET</sub>, where only a one step decomposition caused by the CO<sub>2</sub> release is observed.<sup>11</sup> As a reason, the crystalline water entrapped in the B-IPDA<sub>AQ</sub> structure (see Figure 7) can be seen. While for the CO<sub>2</sub> release of B-IPDA<sub>AQ</sub> the Urea-structure has to react back with one water molecule to the IPDA + CO<sub>2</sub>, one water molecule is remaining as crystalline water which can be released separately. Taking a closer look at the decomposition, even a third step can be expected. However, this contributed to evaporating IPDA during the measurement. This gets clearer when looking at the isothermal experiments. In order to get an impression of the decomposition rate, isothermal TGA measurements at 80, 100, 120, 140, 160 and 180 °C were proceeded. A slight weight increase of up to 0.9 wt.% was observed for two samples at the beginning, contributed to condensation effects. These effects were found to be lower compared to B-IPDA<sub>ET</sub> in the previous study.<sup>11</sup> As a reason, the already saturated system with crystalline water can be seen. Thus, the onset time for fitting the decomposition rate ( $r_D$ ) was chosen when the value hits the initial 100 wt.% again ( $t_i$ ). In order to determine the decomposition rate of the first decomposition step, the time to the first extrema, maximum or minimum, of the 2nd derivative ( $t_{M_{DD}1}$ ) was chosen. The second decomposition step was chosen from  $t_{M_{DD}1}$  to the next maximum  $t_{M_{DD}2}$ . The overall rate was determined from  $t_i$  until  $t_{M_{DD}2}$ .

The maxima of the first derivative ( $t_{M_D1}$  and  $t_{M_D2}$ ) were taken to indicate the decomposition products in the corresponding step. Here, at  $t_{M_D1}$  the weight loss of 7.75 wt.% fits well to H<sub>2</sub>O and at  $t_{M_D2}$  the weight loss of 26.7 wt.% fits well to the release of H<sub>2</sub>O and CO<sub>2</sub>. Thus, it can be concluded, that during the first step mainly the crystalline water is released and the second step is contributed to the CO<sub>2</sub> release. Small deviations in the first step indicate a simultaneous CO<sub>2</sub> release, while in the second step the evaporation of IPDA influence the accuracy. It has to be noted that the CO<sub>2</sub> release can take place only when the urea derivate is reacting back with one water molecule to form the IPDA + CO<sub>2</sub>. To estimate the influence of possible amine evaporation on the fit, the time until the theoretical H<sub>2</sub>O ( $t_{H_2O}$ ) and H<sub>2</sub>O+CO<sub>2</sub> wt.% content ( $t_{H_2O+CO_2}$ ) of the B-IPDA<sub>AQ</sub> is released, is also indicated.

Figure 9a illustrates the time dependence of  $t_i$ ,  $t_{M_{DD}}$ ,  $t_{H_2O}$ ,  $t_{H_2O+CO_2}$ ,  $t_{M_D1}$  and  $t_{M_D2}$  at different temperatures and Figure 9b shows the determined decomposition rates of Step1, Step2 and total decomposition (Step1+2) at indicated temperatures. It is noted that for 80 °C the detailed analysis was not possible due to a total overlap of both reactions in one step. Thus, only the  $r_D$  in Figure 9b is presented.

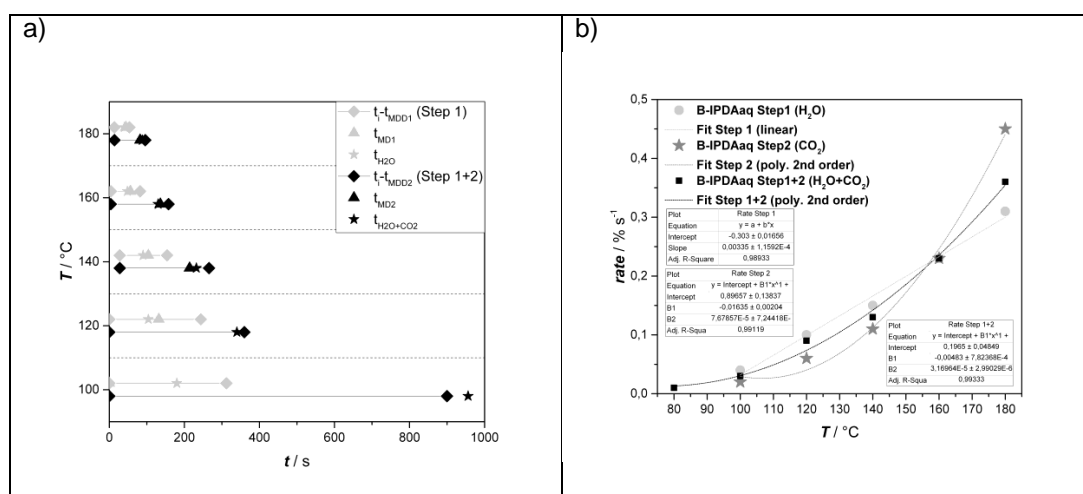


**Figure 9.** a) Results of isothermal TGA measurements with regards to time until initial 100 wt.% ( $t_i$ ) (left diamond marker), time until end of corresponding mass loss step  $t_{MDD1}$  for Step 1 (grey) or  $t_{MDD2}$  for step 2 (black) (right diamond marker), time to first maximum of 1<sup>st</sup> derivative ( $t_{MD1}$ ) (grey triangle marker) or 2<sup>nd</sup> maximum of first derivative ( $t_{MD2}$ ) (black triangle marker) and time until theoretical total H<sub>2</sub>O ( $t_{H2O}$ ) (grey star marker) or H<sub>2</sub>O+CO<sub>2</sub> release ( $t_{H2O+CO2}$ ) (black star marker) at defined temperatures and b) decomposition rates of B-IPDA<sub>AQ</sub> Step1 (grey), Step 2 (dark grey) and overall Step1+2 (black).

Figure 9a allows to draw a conclusion on the decomposition behavior and time-line. The separation of the decomposition into two steps reveals a more detailed analysis. As shown in the previous study<sup>11</sup> the best case for the determination of the release rate is given, when  $t_{MD}$  is in between the range of  $t_i$  and  $t_{MDD}$  while  $t_{H2O}$  or  $t_{H2O+CO2}$  is higher than its corresponding  $t_{MD}$ . This ensures that the release is the main action and only low amounts of byproducts, such as released CO<sub>2</sub> in Step 1 or evaporating IPDA in Step 2 affect the value. At 100 °C, the  $t_{MD1}$  and  $t_{MD2}$  and at 120 °C the  $t_{MD2}$  could not be determined properly as the shape of the derivative curve was more like a shoulder. The fact that  $t_{H2O}$  is always lower than  $t_{MD1}$  indicates that the theoretical amount of water is evaporated before the maximum is reached. Thus, it can be concluded that there is a certain mix-up with Step 2. However, the second decomposition step was determined from  $t_{MDD1}$  to  $t_{MDD2}$  and is contributed to the CO<sub>2</sub> release. In this step, the  $t_{H2O+CO2}$  is higher than  $t_{MD2}$  and both merge at temperatures of 160 °C and higher. This indicates that the mass loss is mainly caused by the CO<sub>2</sub> release and only low amounts of IPDA evaporate.<sup>11</sup> This is in accordance with the rates shown in Figure 9b. At 80 °C, the H<sub>2</sub>O release and CO<sub>2</sub> release go along simultaneously and at  $t_{MDD1}$  the mass loss for H<sub>2</sub>O and CO<sub>2</sub> can be observed. Thus, a rate for the total decomposition can be determined. It increases non linear with the temperature up to 180 °C. For Step 1, a linear fit can be put on the determined values. This is in accordance with the release of the crystalline H<sub>2</sub>O, which follows a simple

temperature dependence. In contrast, for Step 2, a polynomial fit is required to match with the data points. This can be explained by the fact that the  $\text{CO}_2$  release is coupled with the chemical reaction of the B-IPDA<sub>AQ</sub> urea derivate back to IPDA +  $\text{CO}_2$ . Thus, the temperature dependence of the reaction kinetics affects the rate. Around 160 °C, both rates cross each other. This means that the actual decomposition of the B-IPDA<sub>AQ</sub> is accelerating and getting faster than the release of crystalline  $\text{H}_2\text{O}$ .

In conclusion, the decomposition of B-IPDA<sub>AQ</sub> can be separated in two steps. Step 1 is assigned to a linear temperature dependent release of crystalline  $\text{H}_2\text{O}$  and Step 2 to the actual decomposition of the urea B-IPDA<sub>AQ</sub> back to IPDA and  $\text{CO}_2$  with a nonlinear temperature dependence. Considering the fact that the released IPDA does not evaporate but build up the epoxy network during the later foaming process, the indicated decomposition characteristics are expected to affect the foaming behavior at indicated temperatures. To draw a conclusion on that, Figure 10 compares the  $r_D$  of B-IPDA<sub>AQ</sub> with the reaction rate up to 99% conversion of DGEBA+IPDA and DGEBA+B-IPDA<sub>AQ</sub> gained from MFK calculations.

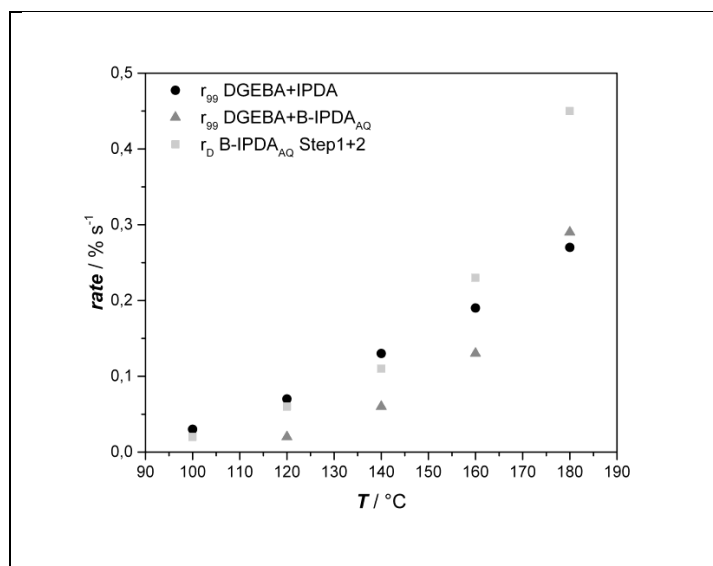


**Figure 10.** Comparison of the decomposition rate of B-IPDA<sub>AQ</sub> ( $r_D$ ) and the reaction rate of DGEBA+IPDA and DGEBA+B-IPDA<sub>AQ</sub> up to 99% conversion gained from MFK calculations ( $r_{99}$ ).

It can be observed from Figure 10 that the overall reaction rate is lower for DGEBA+B-IPDA<sub>AQ</sub> compared with DGEBA+IPDA. This is expected due to the initial decomposition required to activate the IPDA for reaction with DGEBA. At 100 °C and below, the  $r_{99}$  of DGEBA+B-IPDA<sub>AQ</sub> could not be determined by the MFK in the range of 2h. Thus, no proper foaming can be expected. Furthermore, it can be observed, that the reaction of DGEBA+IPDA is higher than the  $r_D$  of B-IPDA<sub>AQ</sub> up to 140 °C. At 160 °C, the decomposition is faster than the reaction of the

released IPDA. These findings can be transferred to the isothermal foaming experiment. The samples are shown in Figure 11.

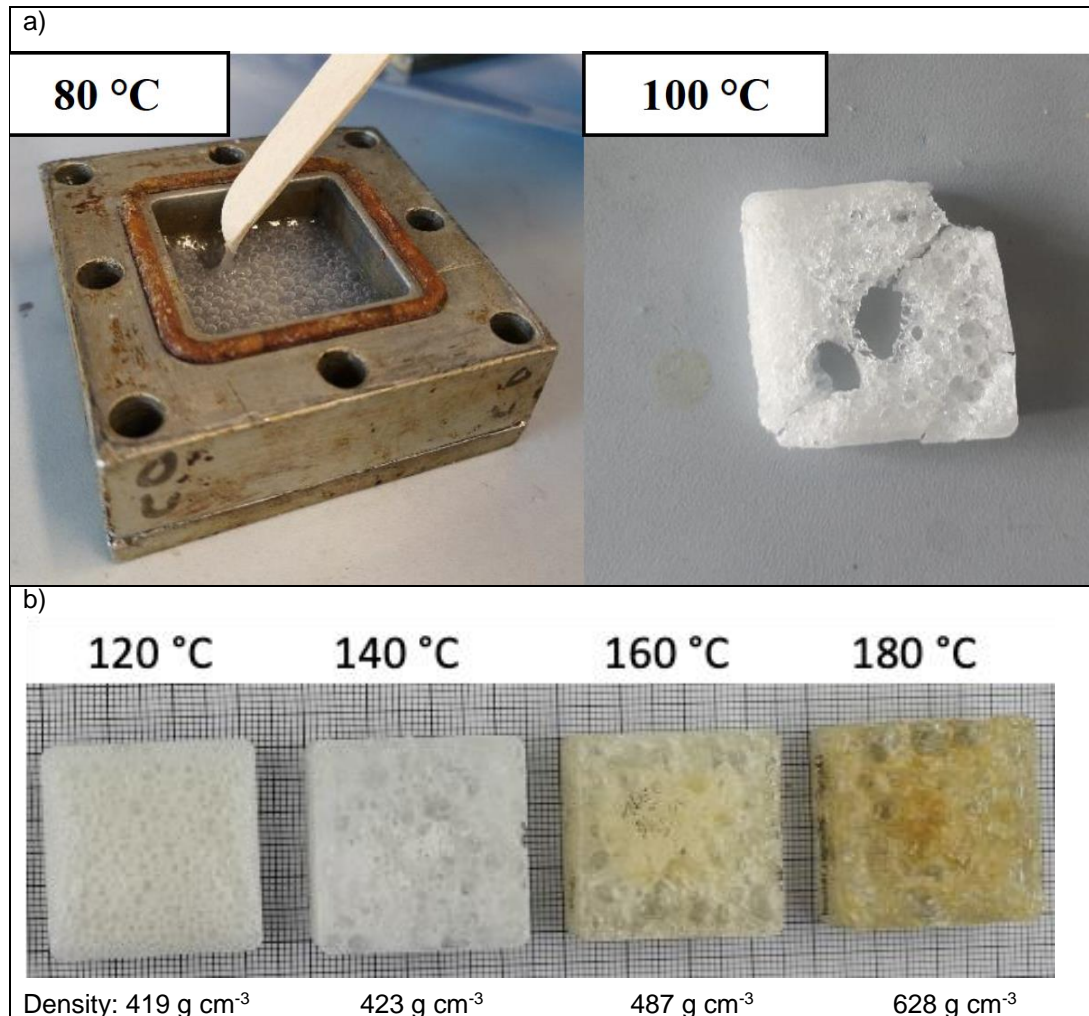


**Figure 11.** a) Received samples at 80 and 100 °C and b) Received foam samples at 120, 140, 160 and 180 °C cured for 1h with a target density of 350 g cm<sup>-3</sup>.

As shown in Figure 11a, at 80 °C a viscous rather expanded transparent sample with bubbles inside is achieved after 1h. This is in accordance with the slow decomposition and reaction of the system at the given temperature. At 100 °C, a properly foamed structure can be achieved. However, the sample was still flexible and got damaged during demolding. In this case, the system did not have enough time to fully cure. This was confirmed by multiple samples which were cured for longer time at given temperature. These samples were not taken into account for this study. In Figure 11b, the foams cured at 120 and 140 °C exhibit a white color while the foams received at 160 and 180 °C exhibit a yellow color. This is explained by the higher  $r_D$  of B-IPDA<sub>AQ</sub> than the  $r_{99}$  of DGEBA+IPDA (Figure 10). Thus, the IPDA is released faster than it can react with DGEBA and allows side reactions resulting in the yellow color. The target density

was not reached for all samples. This is due to insufficient expansion of the sample at 120 °C and an increasing foam collapse of the foam structure from 140 up to 180 °C.

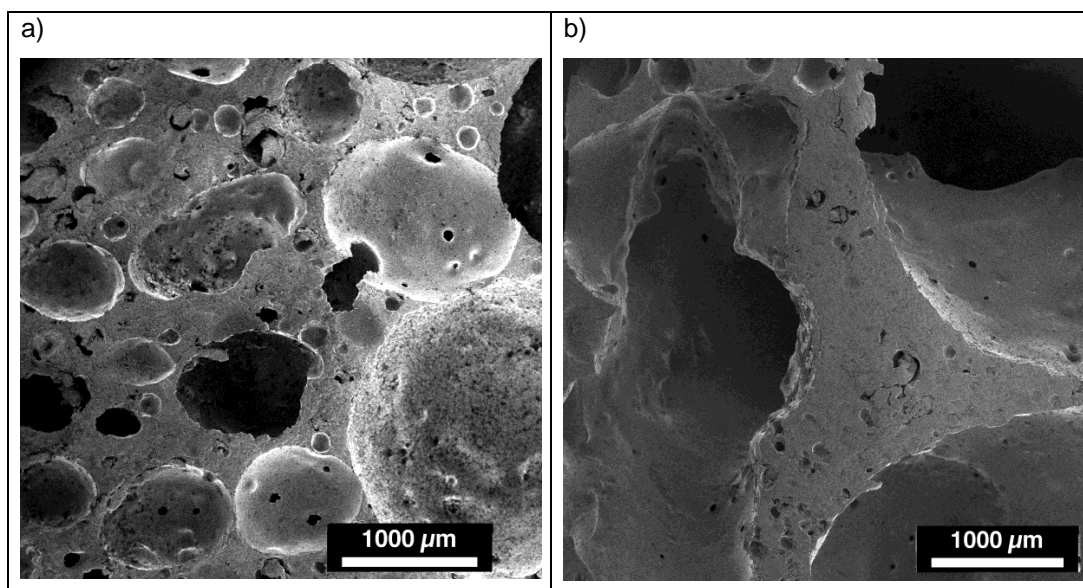


**Figure 12.** SEM images of foamed samples a) at 120 and b) at 140 °C.

The irregular foam structures observed in the SEM images (Figure 12a and b) lead to no detailed cell size evaluation. However, the temperature range between 120 and 140 °C was found to be the most promising in this study.

### Conclusion

The formally known B-IPDA has been synthesized with water as solvent. Compared to the known synthesis in ethanol that results in the formation of a carbamate, a urea derivate is formed in water. The formation of this thermodynamically rare product is confirmed by various solid state NMR experiments. As confirmed by quantum chemical calculations and further NMR measurements, a stable eleven-membered ring in the carbonate transition state precipitates during the reaction. A subsequent reduction of water is the driving force for the formation of the urea group.

The detailed analysis of the decomposition of B-IPDA<sub>aq</sub> reveals a two step mechanism. In a first step, the release of crystalline water takes place with a linear dependency on the temperature. In a second step, the reaction back from the urea derivate to IPDA and CO<sub>2</sub> takes place with a non linear temperature dependency. With regard to the foaming performance of the B-IPDA<sub>aq</sub>, the initial experiment show promising results. A clear dependency between the decomposition behaviour and the isothermal foaming performance at different temperatures was found. The balance between decomposition rate of the B-IPDA<sub>aq</sub> and the reactivity of the released IPDA showed a strong influence. Based on the results of this study, further

optimizations can be proceeded to optimize the foaming performance and the final foam properties, especially with regard to the morphology.

### **Acknowledgment**

We gratefully acknowledge financial support that was granted by the Deutsche Forschungsgemeinschaft DFG within the SFB 840, B4 as well as the Eurostars-2 joint program with co-funding from the European Union Horizon 2020 research and innovation program with the grant number 01QE1816B. We thank the Elite Network of Bavaria for support by the study program “Macromolecular Science”.

## References

- (1) Frisch, K. C. History of Science and Technology of Polymeric Foams. *Journal of Macromolecular Science: Part A - Chemistry* **1981**, *15*, 1089–1112.
- (2) Kurek, K.; Bledzki, A. K. Fatigue Behavior of Composites with Foamed Matrix. *Journal of Reinforced Plastics and Composites* **1994**, *13*, 1116–1134.
- (3) Lee, H.; Neville, K. *Handbook of Epoxy Resins*; McGraw-Hill: New York, 1967.
- (4) Pascault, J.-P.; Williams, R. J. J. *Epoxy Polymers: New Materials and Innovations*; John Wiley & Sons, 2009.
- (5) Lyu, J.; Hu, D.; Liu, T.; Zhao, L. Non-isothermal kinetics of epoxy resin curing reaction under compressed CO<sub>2</sub>. *J Therm Anal Calorim* **2018**, *131*, 1499–1507.
- (6) Coste, G.; Negrell, C.; Caillol, S. From gas release to foam synthesis, the second breath of blowing agents. *European Polymer Journal* **2020**, *140*, 110029.
- (7) Ren, Q.; Zhu, S. One-Pack Epoxy Foaming with CO<sub>2</sub> as Latent Blowing Agent. *ACS Macro Lett.* **2015**, *4*, 693–697.
- (8) Bethke, C.; Sanchez-Vazquez, S. A.; Raps, D.; Bakis, G.; Bard, S.; Du Ngoc, U. L.; Volker, A. Effect of Resin and Blocked/Unblocked Hardener Mixture on the Production of Epoxy Foams with CO<sub>2</sub> Blocked Hardener in Batch Foaming Process. *Polymers* **2019**, *11*, 793.
- (9) Ren, Q.; Xu, H.; Yu, Q.; Zhu, S. Development of Epoxy Foaming with CO<sub>2</sub> as Latent Blowing Agent and Principle in Selection of Amine Curing Agent. *Ind. Eng. Chem. Res.* **2015**, *54*, 11056–11064.
- (10) Bethke, C.; Goller, S. M.; Du Ngoc, U. L.; Kaysser, S. T.; Altstädt, V.; Ruckdäschel, H. Tailoring Epoxy Resin Foams by Pre-Curing with Neat Amine Hardeners and Its Derived Carbamates. *Polymers* **2021**, *13*, DOI: 10.3390/polym13081348.
- (11) Bethke, C.; Kaysser, S. T.; Du Uy Lan, N.; Goller, S. M.; van der Zwan, K. P.; Senker, J.; Ruckdäschel, H.; Altstädt, V. Synthesis and Characterization of Dual-Functional Carbamates as Blowing and Curing Agents for Epoxy Foam. *Ind. Eng. Chem. Res.* **2021**, *60*, 7065–7080.
- (12) Metz, G.; Wu, X. L.; Smith, S. O. Ramped-Amplitude Cross Polarization in Magic-Angle-Spinning NMR. *J. Magn. Reson.* **1994**, *110*, 219–227.
- (13) Fung, B. M.; Khitrin, A. K.; Ermolaev, K. An improved broadband decoupling sequence for liquid crystals and solids. *J. Magn. Reson.* **2000**, *142*, 97–101.
- (14) *Jmol: an open-source Java viewer for chemical structures in 3D.* <http://www.jmol.org/>.
- (15) Hohenberg, P.; Kohn, W. Inhomogeneous Electron Gas. *Phys. Rev.* **1964**, *136*, B864–B871.
- (16) Kohn, W.; Sham, L. J. Self-Consistent Equations Including Exchange and Correlation Effects. *Phys. Rev.* **1965**, *140*, A1133–A1138.
- (17) Clark, S. J.; Segall, M. D.; Pickard, C. J.; Hasnip, P. J.; Probert, M. I. J.; Refson, K.; Payne, M. C. First principles methods using CASTEP. *Z. Kristallogr. Cryst. Mater* **2005**, *220*, 567–570.
- (18) McNellis, E. R.; Meyer, J.; Reuter, K. Azobenzene at coinage metal surfaces: Role of dispersive van der Waals interactions. *Phys. Rev. B* **2009**, *80*, 1.
- (19) Tkatchenko, A.; Scheffler, M. Accurate molecular van der Waals interactions from ground-state electron density and free-atom reference data. *Phys. Rev. Lett* **2009**, *102*, 73005.
- (20) Pfrommer, B. G.; Côté, M.; Louie, S. G.; Cohen, M. L. Relaxation of Crystals with the Quasi-Newton Method. *J. Comput. Phys.* **1997**, *131*, 233–240.
- (21) Payne, M. C.; Teter, M. P.; Allan, D. C.; Arias, T. A.; Joannopoulos, J. D. Iterative minimization techniques for ab initio total-energy calculations: Molecular dynamics and conjugate gradients. *Rev. Mod. Phys.* **1992**, *64*, 1045–1097.
- (22) Monkhorst, H. J.; Pack, J. D. Special points for Brillouin-zone integrations. *Phys. Rev. B* **1976**, *13*, 5188–5192.
- (23) Profeta, M.; Mauri, F.; Pickard, C. J. Accurate first principles prediction of <sup>17</sup>O NMR parameters in SiO<sub>2</sub>: Assignment of the zeolite ferrierite spectrum. *J. Am. Chem. Soc.* **2003**, *125*, 541–548.
- (24) Bonhomme, C.; Gervais, C.; Babonneau, F.; Coelho, C.; Pourpoint, F.; Azaïs, T.; Ashbrook, S. E.; Griffin, J. M.; Yates, J. R.; Mauri, F. *et al.* First-principles calculation of NMR parameters using the gauge including projector augmented wave method: A chemist's point of view. *Chem. Rev.* **2012**, *112*, 5733–5779.
- (25) Bak, M.; Rasmussen, J. T.; Nielsen, N. C. SIMPSON: A general simulation program for solid-state NMR spectroscopy. *J. Magn. Reson.* **2000**, *147*, 296–330.
- (26) Siegel, R.; Trébosc, J.; Amoureux, J.-P.; Gan, Z. 3D 1H-13C-14N correlation solid-state NMR spectrum. *J. Magn. Reson.* **2008**, *193*, 321–325.
- (27) Matsuoka, S.; Inoue, M. Application of REDOR NMR in natural product chemistry. *Chem. Commun.* **2009**, 5664–5675.
- (28) Pickard, C. J.; Mauri, F. All-electron magnetic response with pseudopotentials: NMR chemical shifts. *Phys. Rev. B* **2001**, *63*, 245101.
- (29) Wang, H.; Xin, Z.; Li, Y. Synthesis of Ureas from CO<sub>2</sub>. *Topics in current chemistry (Cham)* **2017**, *375*, 49.

**Supporting Information for****Structural Analysis of CO<sub>2</sub> Loaded Diamine Derived from Aqueous Synthesis Route  
and its Basic Epoxy Foaming Performance**

Kasper P. van der Zwan,<sup>a‡</sup> Christian Bethke,<sup>b‡</sup> Annalena Pongratz,<sup>a</sup> Denise Schweser<sup>b</sup>,  
Lukas Endner<sup>b</sup>, Renée Siegel,<sup>a</sup> Volker Altstädt<sup>b</sup>, Holger Ruckdäschel,<sup>b</sup> and Jürgen Senker<sup>a\*</sup>

<sup>a</sup> Inorganic Chemistry III and Northern Bavarian NMR Center, University of Bayreuth,  
Universitätsstraße 30, D-95447 Bayreuth, Germany

<sup>b</sup> Polymer Engineering, University of Bayreuth,  
Universitätsstraße 30, D-95447 Bayreuth, Germany

\* [juergen.senker@uni-bayreuth.de](mailto:juergen.senker@uni-bayreuth.de); [ruckdaeschel@uni-bayreuth.de](mailto:ruckdaeschel@uni-bayreuth.de)

‡ These authors contributed equally to this work.

**Contents**

1. Additional NMR spectra .....	3
2. Synthesis and Calculation of B-DMC aq .....	5

## 1. Additional NMR spectra

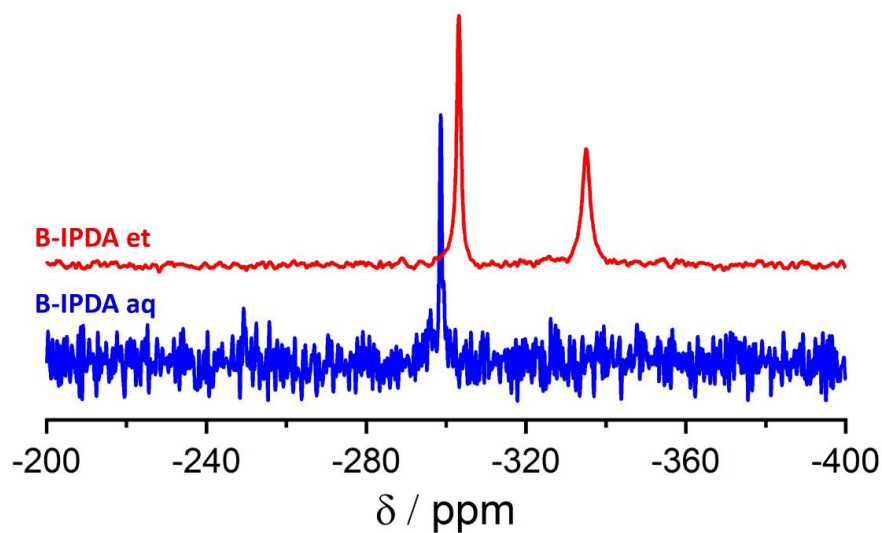


**Figure S1.**  $^{15}\text{N}\{^1\text{H}\}$  CP MAS NMR spectrum of B-IPDA synthesised in ethanol (red) and water (blue) (The latter is identical to Figure 2a from the main text).

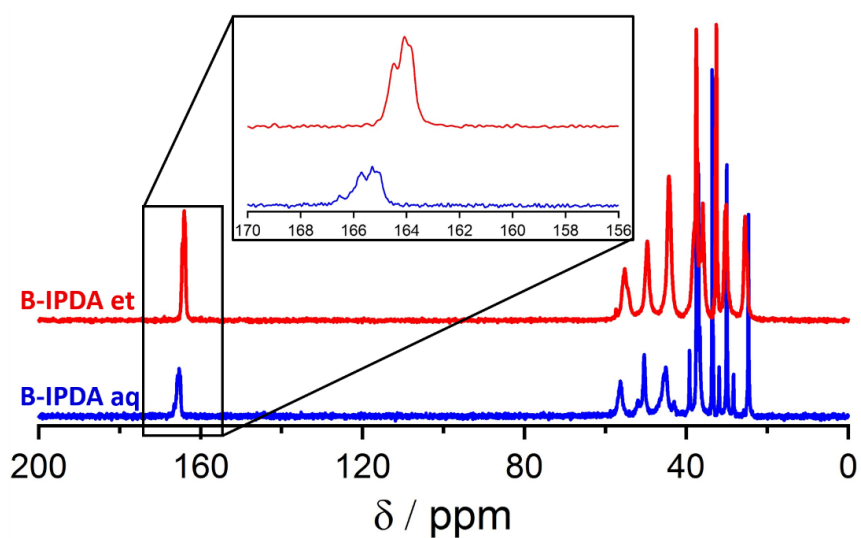


**Figure S2.**  $^{13}\text{C}\{^1\text{H}\}$  CP MAS NMR spectrum of B-IPDA synthesised in ethanol (red) and water (blue). The inset zooms on the C=O region. The red spectrum is reproduced from reference 11 main text.

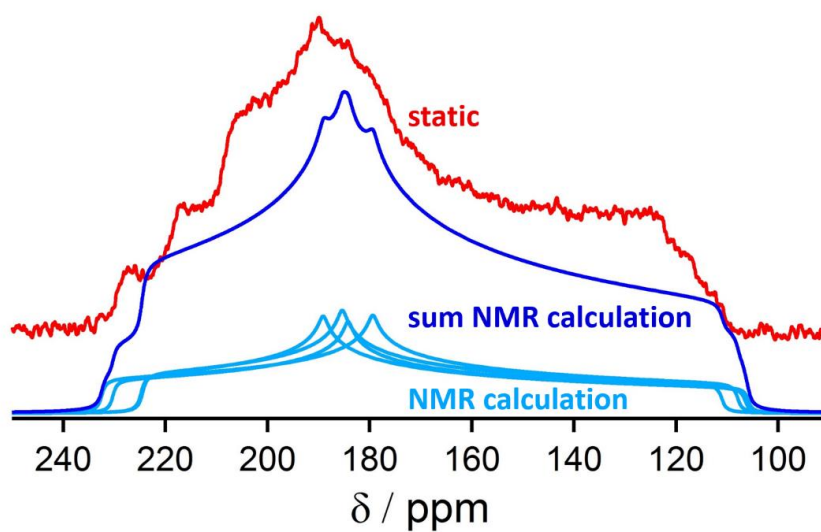


**Figure S3.**  $^{13}\text{C}$  static CP{ $^1\text{H}$ } NMR spectrum (red) with the calculated resonances from the 4 stereo isomers without further fitting (light blue). The dark blue spectrum gives the sum over all 4 resonances. The intensities of the individual resonances was set to the same value and the sum was chosen to fit best with the intensity of the measurement.

## 2. Synthesis and Calculation of B-DMC aq

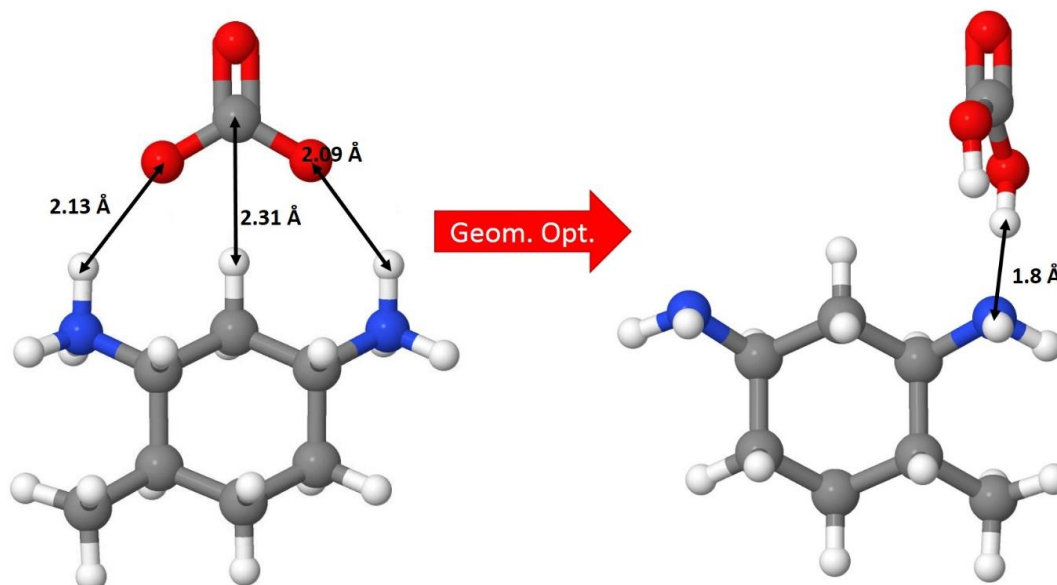


**Figure S4.** Model of a DMC carbonate aggregate prior and after geometry optimisation.

In reference 11 main text, we synthesized three blocked diamines in ethanol. Therefore, we also tried the same synthesis in water for all three of them. However, DMC and AEP would not react in water. To explain this we built the same carbonate-amine aggregate for DMC (Figure S4) as for IPDA that would be the transition state of the urea formation. However, aggregate is not stable during the geometry optimization. Instead, the carbonate takes a proton of one ammonium group and turns to get out of the way of the cyclohexane ring. The resulting carbonic acid that is only hydrogen bond bound to one amine is not stable in an aqueous solution and thus the carbonate aggregate cannot precipitate and the urea cannot form in the second step.

This shows that for IPDA the additional  $\text{CH}_2$  group gives enough flexibility to bind the carbonate to both amines to form a stable aggregate.

### 4.3 Crystal Engineering of Supramolecular 1,4-Benzene Bisamides by Side-Chain Modification - Towards Tuneable Anisotropic Morphologies and Surfaces

This work is a cooperation between the Inorganic Chemistry III and the Macromolecular Chemistry I at the University of Bayreuth and will be reprinted from K.P. van der Zwan, C. Steinlein, K. Kreger, H.-W. Schmidt, J. Senker *ChemPhysChem* **2021**, *22*, 2585-2593 under the creative common license.

My contributions are:

- conception and main authorship of the article
- measuring all X-ray diffractograms and solving the crystal structures
- performing all NMR experiments
- conducting all quantum chemical simulations

The contributions of the other authors are:

- conception and co-authorship of the article
- synthesis of the materials
- recording the SEM images
- performing the contact angle measurements

# Crystal Engineering of Supramolecular 1,4-Benzene Bisamides by Side-Chain Modification – Towards Tuneable Anisotropic Morphologies and Surfaces

Kasper P. van der Zwan,<sup>[a]</sup> Christoph Steinlein,<sup>[b]</sup> Klaus Kreger,<sup>[b]</sup> Hans-Werner Schmidt,<sup>\*[b]</sup> and Jürgen Senker<sup>\*[a]</sup>

Benzene bisamides are promising building blocks for supramolecular nano-objects. Their functionality depends on morphology and surface properties. However, a direct link between surface properties and molecular structure itself is missing for this material class. Here, we investigate this interplay for two series of 1,4-benzene bisamides with symmetric and asymmetric peripheral substitution. We elucidated the crystal structures, determined the nano-object morphologies and derived the wetting behaviour of the preferentially exposed surfaces. The crystal structures were solved by combining single-crystal and powder X-ray diffraction, solid-state NMR spectroscopy and computational modelling. Bulky side groups, here t-butyl groups, serve as a structure-directing motif into a packing pattern, which favours the formation of thin platelets.

The use of slim peripheral groups on both sides, in our case linear perfluorinated, alkyl chains, self-assemble the benzene bisamides into a second packing pattern which leads to ribbon-like nano-objects. For both packing types, the preferentially exposed surfaces consist of the ends of the peripheral groups. Asymmetric substitution with bulky and slim groups leads to an ordered alternating arrangement of the groups exposed to the surface. This allows the hydrophobicity of the surfaces to be gradually altered. We thus identified two leitmotifs for molecular packings of benzene bisamides providing the missing link between the molecular structure, the anisotropic morphologies and adjustable surface properties of the supramolecular nano-objects.

## 1. Introduction

Two-dimensional nanostructures emerge as an advanced materials class that can be applied in various fields such as sensing, separation and electronics.<sup>[1]</sup> Among the variety of building blocks for these architectures, hydrogen-bonded supramolecular systems like bis-acylurea,<sup>[2]</sup> cyclic dipeptide<sup>[3]</sup> and peptoid<sup>[4]</sup> derivatives resemble an interesting class of molecules since their high melting points allow for their use as supramolecular polymer additives. These additives rely on *in situ* formed solid-state nanoobjects in the polymer melt.<sup>[5–9]</sup> Prominent examples are hydrogen-bonded structures based on

sorbitols,<sup>[10,11]</sup> diacids,<sup>[12]</sup> benzene trisamides<sup>[5–7,13,14]</sup> and various bisamides derivatives.<sup>[8,15]</sup> These nanoobjects are formed *in situ* due to the reversible nature of their secondary interactions<sup>[16]</sup> during processing at elevated temperatures. This results in a high degree of dispersion of the objects within the polymer matrix. When these additives are used as nucleating agents for semi-crystalline polymers such as *i*-PP,<sup>[5,8,13,17]</sup> PVDF,<sup>[18]</sup> and PLA,<sup>[19]</sup> function and efficiency arises also from the epitaxial match of the nanoobjects' surface with the polymer crystal.<sup>[10,20]</sup> This in turn allows to control the polymer solid-state morphology in terms of crystal size and shape as well as crystal modification.

For the design of supramolecular additives, however, a fundamental understanding is required, how the supramolecular structure translates into specific packing patterns and anisotropic crystal morphologies. In particular, two concepts were derived to reach this goal. Crystal engineering<sup>[21]</sup> provides motifs to predict the formation of specific packing patterns. They should favour the anisotropic growth of the obtained nanoobjects, which in turn can be enhanced by morphology engineering.<sup>[22]</sup> In this context, crystal engineering relies on anisotropic supramolecular synthons<sup>[23]</sup> based on a combination of  $\pi$ -stacking,<sup>[24]</sup> hydrogen<sup>[25,26]</sup> or halogen<sup>[27]</sup> bonds that are usually programmed into the supramolecular structure. Examples on how this effects the macroscopic structure are summarized in a recent perspective<sup>[28]</sup> and a recent review article.<sup>[29]</sup>

Applied to 1,4-benzene bisamides the two amide groups are the foundation of the supramolecular synthon with the

[a] K. P. van der Zwan, Prof. Dr. J. Senker  
Inorganic Chemistry III  
and North Bavarian NMR Center  
University of Bayreuth  
Universitätsstraße 30  
95447 Bayreuth, Germany  
E-mail: juergen.senker@uni-bayreuth.de

[b] C. Steinlein, Dr. K. Kreger, Prof. Dr. H.-W. Schmidt  
Macromolecular Chemistry  
and Bavarian Polymer Institute  
University of Bayreuth  
Universitätsstraße 30  
95447 Bayreuth, Germany  
E-mail: hans-werner.schmidt@uni-bayreuth.de

Supporting information for this article is available on the WWW under <https://doi.org/10.1002/cphc.202100597>

© 2021 The Authors. ChemPhysChem published by Wiley-VCH GmbH. This is an open access article under the terms of the Creative Commons Attribution License, which permits use, distribution and reproduction in any medium, provided the original work is properly cited.

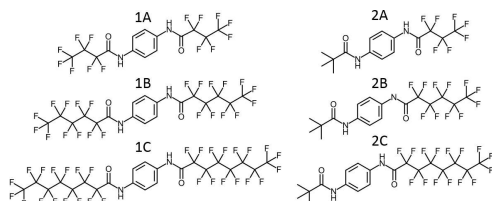


**Figure 1.** Molecular structures of the target compounds: **1A–1C** symmetrically substituted 1,4-benzene bisamides and **2A–2C** asymmetrically substituted 1,4-benzene bisamides.

possibility to form two acceptor and two donor hydrogen bonds each. Up to now, two supramolecular synthons have been observed. Either one molecule forms hydrogen bonds to two<sup>[30–33]</sup> or to four<sup>[34–37]</sup> other molecules. In the first case a linear arrangement of the molecules arises that features a packing with strong interactions in one dimension.<sup>[30–33]</sup> This implies the growth of an object with one preferred growth rate and an anisotropic morphology. In the second case, the twisted arrangement of the five molecules involved in the supramolecular synthon induces packings with strong interactions in two dimensions.<sup>[34–37]</sup>

However, a detailed understanding how the side groups have to be designed to guide into a specific packing pattern and in turn programme a one or two directions of preferred growth is missing. Therefore, we investigate two series of 1,4-benzene bisamides (Figure 1) featuring a symmetric peripheral substitution with linear perfluorinated alkyl chains (series 1) and an asymmetric peripheral substitution pattern with a *tert*-butyl (*t*-Bu) group and a linear perfluorinated alkyl chain (series 2). The side chains vary in size and shape but do not introduce additional hydrogen bond acceptors or donors. This allows to probe, whether their steric demand<sup>[38]</sup> is able to switch between characteristic supramolecular synthons for 1,4-benzene bisamides. To avoid a potential odd-even effect, we incremented the chain length each time by 2 CF<sub>2</sub> groups.<sup>[39]</sup>

Therefore, we elucidated the crystal structures for all 6 target molecules by a combination of single crystal and NMR crystallography.<sup>[40]</sup> NMR crystallography features the combination of solid-state NMR spectroscopy together with simulations on the density functional theory (DFT)<sup>[41]</sup> level to assist Rietveld refinements<sup>[42]</sup> of powder X-ray diffractograms. This approach showed to be the method of choice to solve the crystal structure of trisamides,<sup>[43]</sup> cyclohexane bisamides<sup>[44]</sup> and many other supramolecular<sup>[45]</sup> and inorganic<sup>[46]</sup> systems. All these systems exhibit inherently high defect concentrations and disorder<sup>[47]</sup> making this combined approach necessary. The crystal structures were correlated to the morphology of the supramolecular nanoobjects and the polarities of the dominantly exposed surfaces were investigated.

## 2. Results and Discussion

Two series of 1,4-benzene bisamides (Figure 1) were synthesised based on 1,4-diaminobenzene as core and different perfluorinated carboxylic acids or pivalic acid as side groups. Details on the synthesis and characterization are given in the supporting information (Section 1). The first series (**1A–1C**) comprises a symmetric side group pattern containing linear perfluorinated alkyl chains with increasing length. In contrast, the second series (**2A–2C**) consists of an asymmetric side group pattern with one bulky *t*-Bu group and one linear perfluorinated alkyl chain with increasing length.

### 2.1. Crystal Structure Solution

By recrystallization from methanol single crystals could be obtained for **1A**, **2A** and **2B** (Figure 1). *Ab initio* structure solution based on direct methods resulted in triclinic (**1A**) and monoclinic (**2A**, **2B**) metrics with R<sub>int</sub> values of 8.3% (**1A**), 20.1% (**2A**) and 7.6% (**2B**). The centrosymmetric compound **1A** crystallises with one half of a molecule in the asymmetric unit in space group *P* $\bar{1}$ . Both **2A** and **2B** crystallise with one molecule in the asymmetric unit. As the space group of **2A** (*P*<sub>2<sub>1</sub>/n) is centrosymmetric, four molecules are positioned in the unit cell. **2B** crystallises in a smaller unit cell with two molecules accounting for the asymmetric space group *P*<sub>2<sub>1</sub>. Further crystallographic data of the corresponding structure solutions are listed in Table S2 and in the CIF files deposited in the CSD (compare SI). The phase purity of **1A**, **2A** and **2B** were confirmed by Rietveld refinements of the powder X-ray diffractograms (PXRD) (Table S2, Figures S2–S4). In particular, for **2A**, where the single crystals were extremely anisotropic (thin platelets), the good agreement between the observed and calculated PXRD underlines the structure solution.</sub></sub>

As crystallisation experiments for compounds **1B**, **1C** and **2C**, yielded only microcrystalline powders, a combined crystallographic approach with multinuclear (<sup>1</sup>H, <sup>13</sup>C, <sup>15</sup>N and <sup>19</sup>F) solid-state NMR spectroscopic experiments and computational modelling was applied to compensate for the intrinsic loss of information when solving the crystal structure based on powder samples.

The <sup>1</sup>H, <sup>13</sup>C{<sup>1</sup>H} CP and <sup>15</sup>N{<sup>1</sup>H} CP magic-angle-spinning (MAS) NMR spectra (Figures 2, S5–S8) of compound **1B** are very similar in both number and position of the observed resonances compared to the spectra acquired for **1A**. This is also true for the powder diffractogram of **1B** (Figures 3 and S2). In accordance with the structure solution of **1A**, the NMR spectra confirm one half of a molecule in the asymmetric unit for **1B** as well. For example, only one <sup>13</sup>C NMR resonance was observed for the amide unit (Figure 2). Indexing of the PXRD (Figure S4) yields a very similar metric except for a 5 Å longer *c*-axis, which can be attributed to the larger space requirement due to the increasing length of the perfluorinated side chains. These results suggest an isomorphic structure differing only by the additional two CF<sub>2</sub>-units in the side chains. Therefore, we extended the structure model of **1A** by adding two CF<sub>2</sub> groups

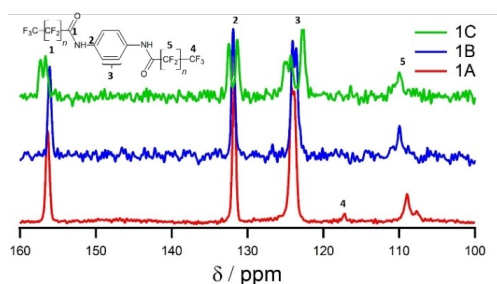


**Figure 2.**  $^{13}\text{C}\{^1\text{H}\}$  CP MAS NMR spectra of **1A**, **1B** and **1C**. The carbon atoms of the fluorinated side chains are not well visible as in the CP sequence the polarisation is transferred from the protons to the carbon atoms.

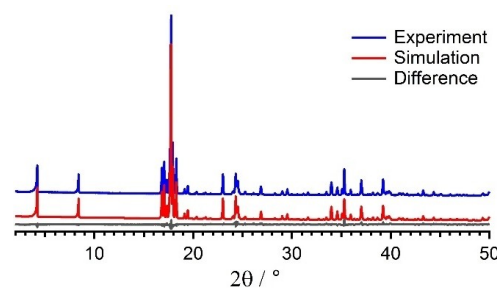


**Figure 3.** Rietveld profile plot for **1B**. The  $R_{\text{wp}}$  value is 6.0% and relevant refinement parameters are given in Table S2. The Rietveld plots of the other compounds are displayed in Figures S2–S4.

for the structure refinement of **1B**. Before the Rietveld refinement, the structure model was geometry optimized with DFT methods. The calculated PXRD of the obtained model is in good agreement with the measured one. (Figure 2 and Table S3). This confirms that **1A** and **1B** are isomorphic.

The powder pattern of **1C** looks very similar to the ones observed for **1A** and **1B** (Figure S3). The obtained metrics are again very similar and the *c*-axis is elongated by another 6 Å to fit the space requirements of the additional  $\text{CF}_2$  groups. For the *a*- and *b*-axes similar lengths as for **1A** and **1B** or integer multiples thereof were observed. Although this prevented an unambiguous structure solution for an *ab initio* structure solution, the results imply that **1C**, again, is isomorphic to **1A** and **1B**. Since the  $^{13}\text{C}$  CP MAS NMR spectrum of **1C** exhibits a splitting of all resonances, the space symmetry is reduced to *P1*, probably due to arbitrary torsions of the side chains.

For series 2, all NMR spectra (Figures 4 and S5–S8) have a high level of resemblance, indicating that also **2C** crystallises in a unit cell with one molecule in the asymmetric unit. Furthermore, this high degree of consistency between the spectra strongly suggests a very similar local environment. Especially, the identical proton shifts (Figure S5) indicate a uniform hydrogen bond pattern. Indexing the powder diffractogram of **2C** leads to a very similar metric compared to **2B** with

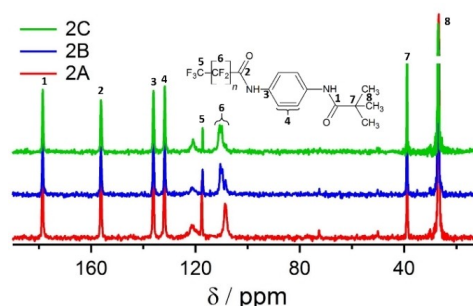


**Figure 4.**  $^{13}\text{C}\{^1\text{H}\}$  CP MAS NMR spectra of **2A**, **2B** and **2C**. The carbon atoms of the fluorinated side chains are not well visible as in the CP sequence the polarisation is transferred from the protons to the carbon atoms.

only the *c*-axis being elongated to account for the increased space requirement of the longer  $\text{CF}_2$ -chain. Therefore, the structure model of **2B** was used as a starting point for the structure model of **2C**. The lattice parameters were adapted to the ones obtained from the PXRD and two  $\text{CF}_2$ -groups were added to the structure model. The obtained model was geometry optimized with DFT calculations and afterwards refined with Rietveld methods. Again, a very good agreement of the calculated and measured diffractograms was achieved (Figure S4 and Table S2).

To sum up, using single crystal refinements and NMR crystallography in a conjunctive way the crystal structures of **1A**, **1B** and **2A–2C** were obtained. The crystallographic data of all compounds is deposited in the CSD (compare SI). For **1C**, a unit cell is obtained and the NMR spectra together with the unit cell parameters suggest an isomorphic structure, albeit with lower symmetry as for **1A** and **1B**.

## 2.2. Self-Assembly and Packing Patterns

Each series of bisamides shows a characteristic hydrogen bond arrangement, which is depicted in Figure 5. For series 1, one molecule binds to two neighbouring molecules with two hydrogen bonds each, one as a donor and one as an acceptor. This corresponds to the supramolecular synthon observed in references.<sup>[30–33]</sup> Thereby the molecules form a ribbon along the crystallographic *a*-axis. Along the *b*-axis, the molecules assemble *via* van der Waals interactions by the interlocking side chains. Along the *c*-axis only weak van der Waals interactions are detected. Within series 2 one molecule builds four hydrogen bonds to four other molecules as reported within references.<sup>[34–37]</sup> This leads to a fence-like crossing pattern with the hydrogen bonds propagating along the *b*-axis. Along the *a*-axis the molecules stack in a zig-zig fashion and along the *c*-axis, as for series 1, only van der Waals interactions are present. A simplified representation of the hydrogen bond patterns is depicted in Figure S9 in the Etter notation.<sup>[25]</sup>

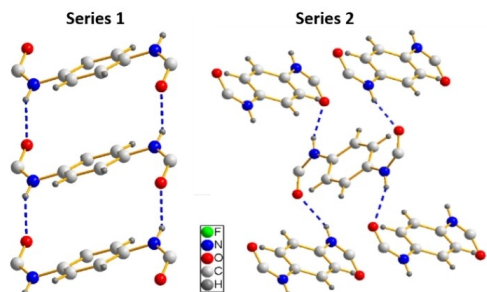


Figure 5. Hydrogen bond arrangement of series 1 (left) and series 2 (right).

The local packing of both series lead to layered crystal structures in all cases. The hydrogen bonded ribbons along the *a*-axis are the basis of the layers of series 1. The ribbons stack to each other by van der Waals interactions along the *b*-axis (Figure 6). For series 2, the layers consist of molecules in a zig-

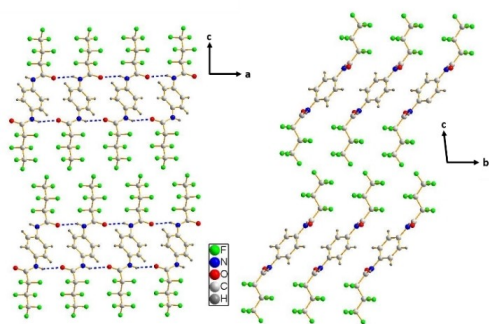


Figure 6. Crystal structure of 1A. On the left the *a/c* plane is visualised. The hydrogen bond along the *a*-axis is visible. On the right the *b/c*-plane is depicted. The interlocking CF-chains along the *b*-axis are visible.

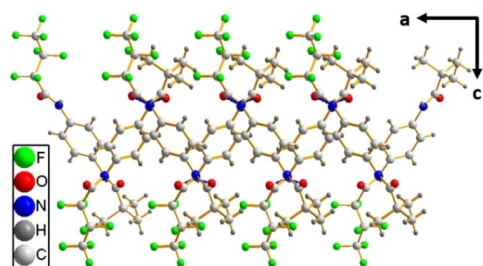


Figure 7. Crystal structure of 2A. The *a/c* plane is depicted. The propagation of the zig-zag pattern along the *a*-axis is visible.

zag arrangement along the *a*-axis and hydrogen bonds along the *b*-axis (Figure 7). The different orientations of these layers to each other result in different space groups within series 2. When viewing along the *c*-axis, all molecules of 2B and 2C are oriented in the same direction, whereas for 2A adjacent molecules in *c*-direction alter their orientation. This introduces an inversion centre, that leads to the doubling of the *c*-axis and therefore to 4 molecules in the unit cell. For a graphical explanation, see Figure S10.

These results raise the question why the two series exhibit different packing patterns although their chemical structure is not that different. To investigate this, all crystal structures were geometry optimized on DFT level. For 1C, a model created from 1B was used, as no final crystal structure could be obtained. Furthermore, models were built for each compound in the respective packing pattern of the compound of the other series. For example, a model of 1A was built in the crossed packing pattern of series 2 and so on. For placing the asymmetric molecules of series 2 in the structure type of series 1 several options arise (for more details please refer to SI section 7). For the following discussion, we chose the model with the smallest number of parameters (model 1 in Figure S11) in order to remain comparable to the other set of calculations. These models were geometry optimized on DFT level. The unit cell parameters were allowed to relax, to account for the different space requirements of the molecules.

For all models the dispersion corrected final energy, the lengths of all hydrogen bonds and the densities were extracted (Tables 1 and 2.). The experimentally observed crystal structure is favoured for all compounds by roughly 20 kJ mol<sup>-1</sup> per molecule.

Table 1. Summary of the hydrogen bond lengths and densities obtained from the geometry optimisation on DFT level for all compounds in the packing type of series 1.

	Packing 1		
	CF–H–O [Å]	tBu–H–O [Å]	Density [g cm <sup>-3</sup> ]
1A	1.96	n.a.	2.002
1B	2.01	n.a.	2.040
1C	2.03	n.a.	2.131
2A	2.39	2.41	1.587
2B	2.47	2.49	1.694
2C	2.31	2.31	1.755

Table 2. Summary of the hydrogen bond lengths and densities obtained from the geometry optimisation on DFT level for all compounds in the packing type of series 2.

	Packing 2		
	CF–H–O [Å]	tBu–H–O [Å]	Density [g cm <sup>-3</sup> ]
1A	1.91 <sup>[a]</sup>	n.a.	1.916
1B	1.91	n.a.	2.023
1C	2.05 <sup>[a]</sup>	n.a.	2.061
2A	1.82	2.06	1.577
2B	1.80	2.03	1.648
2C	1.80	2.02	1.752

[a] averaged.

For the packing type of series 1, the hydrogen bond lengths for the three molecules crystallising in this packing type (1A–1C) increases moderately from 1.96 Å (1A) to 2.03 Å (1C). In the same packing type, the hydrogen bond lengths of 2A–2C vary between 2.31 and 2.48 Å (Table 1). This demonstrates the sensitivity of this packing pattern towards the steric demand of the side groups.

In contrast, the hydrogen bond lengths for the packing type of series 2 shows significantly less deviation, regardless if it's the native packing pattern of this compound or not. For 1A and 1B the average hydrogen bond lengths vary only between 1.91–1.94 Å; 1C exhibits a slightly longer hydrogen bond of 2.05 Å. For 2A–2C the hydrogen bond next to the CF-chains range between 1.80 and 1.82 Å, whereas the hydrogen bonds on the other side of the molecule vary between 2.02 and 2.06 Å (Table 2). The hydrogen bond lengths of the symmetric molecules 1A–1C is the average value of the hydrogen bond lengths of the asymmetric molecules 2A–2C in the packing type of series 2. This demonstrates the robustness of this packing type towards the steric demand of the side group.

These observations are in line with the trend of the <sup>1</sup>H chemical shifts (Figure S5). For series 1 the increase of the hydrogen bond lengths from 1A to 1C translates into a decreasing chemical shift of the N–H protons from 9.5 to 9.1 ppm. The equivalent N–H protons of series 2 (next to the CF-chain) resonate at 10.7 ppm, independent of the chemical composition of the individual compound. The higher shift for series 2 indicates a shorter and thus stronger hydrogen bond for this series.

These findings demonstrate that 1A–1C crystallise in their native packing pattern, although slightly shorter hydrogen bonds could be achieved when crystallizing in packing type of series 2. Apparently, within this series, the loss in hydrogen bond strengths is over compensated by a gain in van der Waals interactions due to a denser packing of the molecules in packing type of series 1 (Tables 1 and 2). Also, for 2A–2C the calculated densities (Tables 1 and 2) is higher when crystallising in packing type of series 1, promising a gain in van der Waals interactions. However, due to the steric demand of the side groups, only weak hydrogen bonds, that are 0.6 Å longer compared to the native structure, could be realised. This loss in hydrogen bond strength cannot be compensated by the gain in van der Waals interactions when crystallising in the packing type of series 1.

From this, we identified two coupled driving forces (density, hydrogen bond strength) that determine the crystal structure of benzene bisamides. On the one hand, a dense packing is favoured on the other hand, this should not increase the hydrogen bond length markedly. For 1A–1C, the slim CF chains allow for a dense packing with one molecule forming four hydrogen bonds to two neighbouring molecules with short hydrogen bonds. For 2A–2C, the bulky *t*-Bu groups prevent short hydrogen bonds in the same arrangement. Therefore, the molecules rotate and the central molecule forms four hydrogen bonds to four other molecules.

A comparison with published structures from the literature are in agreement with these findings. For example, Dharmo-

drahn et al. published a structure with a bulky 1-brom-1-methyl-ethyl side group, which crystallises in the crossed packing of series 2.<sup>[35]</sup> The same is true for the structure where both side groups contain *t*-butyl.<sup>[36]</sup> Whereas, Mangalgui et al. published the crystal structure of a bisamide with a slim 3-chloro-propyl side chain, which assembles in the parallel packing of series 1.<sup>[32]</sup> A bisamide with cyclohexane side groups is also slim enough to crystallise in the packing type of series 1.<sup>[17]</sup> For very bulky side groups, like leucine derivatives, the structure opens up further and builds a so called nano-staircase.<sup>[34]</sup> These results show how the crystal structure of a 1,4-benzene bisamide derivatives can be tailored by a thoughtful choice of the peripheral substitution pattern. We thus identified the bulkiness of the side group as the molecular motif that directs the crystal structure.

### 2.3. Morphology of the Self-Assembled Nano-objects

To probe the influence of the anisotropic interactions between the molecules within the crystal structure, we investigated the self-assembly behaviour to nanoobjects of compounds 1A–1C and 2A–2C in solution. Since self-assembly to a well-defined morphology typically depends not only on the molecular structure but also on the applied temperature protocol, solvent, and concentration of the compounds, we have evaluated these process parameters. We found that by selecting *o*-dichlorobenzene as solvent, all 1,4-benzene bisamides can be molecularly dissolved at a temperature of 120 °C at a concentration of 500 ppm. Upon rapid cooling, the initially clear solution turned turbid indicating the formation of solid objects. These dispersions were drop casted onto silicon wafers and investigated by means of scanning electron microscopy (SEM).

Figure 8 shows exemplarily SEM micrographs of the anisotropic morphology obtained from 1A and 2A. The SEM micrographs of 1B–1C and 2B–2C are given in Figures S11 and S12. All molecules form apparently thin 2D structures, however, with distinct differences in their morphology. For instance, all structures formed by the symmetrically substituted 1,4-benzene bisamides (1A–1C) feature a defined ribbon-like shape. In contrast, all structures formed by the asymmetrically substituted 1,4-benzene bisamides (2A–2C) feature platelet-like shapes with an irregular body. Moreover, in series 1 the width of the ribbons increases with increasing size of the perfluorinated side groups. In contrast, the diameter of the platelets of series 2 decreases with increasing size of the perfluorinated side groups.

These findings fit very well to the crystallographic data, where each series self-assembles into one distinct packing pattern. For instance, in series 1 the hydrogen bond pattern propagates along the crystallographic *a*-axis, whereas along the other two axes only weak van der Waals interactions are effective. During the self-assembly, this results into the anisotropic nanostructures featuring a preferred growth rate in one direction. Along the crystallographic *b*-axis, the close packing of the CF-chains leads to a stronger van der Waals interaction compared to the one present along the *c*-axis. With

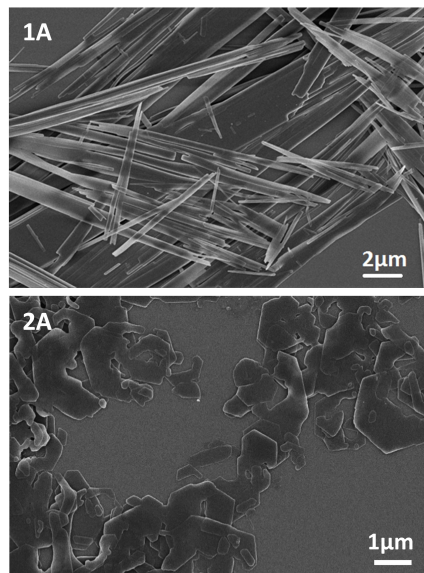


Figure 8. SEM images of platelets of 1A (top) and of 2A (bottom).

increasing number of  $\text{CF}_2$  groups, the former becomes stronger while the latter remains unchanged. This explains the ribbon-like structure with increasing widths of the ribbons when the length of the perfluorinated side chain increases.

In contrast, for series 2 we derived two directions of favoured growth from the crystal structure. Because of the zig-zag-pattern of the hydrogen bond motif along the  $a$ - and  $b$ -axes, the platelet like morphology observed for all self-assembled nanoobjects of series 2 is explained. The platelets, prepared under identical conditions, become smaller with increasing lengths of the perfluorinated chains. We attribute this to the geometrical mismatch of the perfluorinated and the alkyl side chains that alternate along the  $a$ -axis. This results in the formation of smaller platelets when the perfluorinated side chain increases.

Atomic force microscopic (AFM) images (Figure S13) of the self-assembled nanoobjects show distinct terraces for all compounds. The height of these terraces is in all cases in the order of the lengths of the corresponding crystallographic  $c$ -axis of the respective bisamides ( $1/2 c$  for 2A) implying that the terminating face of the macroscopic structures is in all cases the (001) face. This interpretation is in line with the discussion of the growth rates. For series 1 the crystal growth mainly propagates along the  $a$ -axis and secondary along the  $b$ -axis. This leaves the perfluorinated (001) face (Figure 9 left) as the terminating surface of the ribbons, since this face has the lowest tendency to grow further. For series 2 crystal growth propagates along the  $a$ - and  $b$ -axes leading to a surface that has alternating rows of  $\text{CF}_3$  and  $t\text{-Bu}$  end groups (Figure 9 right).

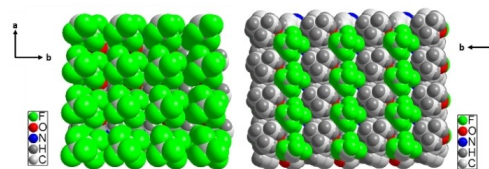


Figure 9. Surfaces of series 1 (left) and series 2 (right).

Due to the different composition of the surfaces, different polarities are expected. Since the nanoobjects are too small to be directly measured by contact angle measurements, we deposited 1A and 2A on silanised glass wafers by physical vapour deposition. X-ray diffraction measurements on the resulting thin films show that in both cases only reflexes of the (00 $l$ ) series (Figure 10) remain proving the successful deposition of an oriented thin film with the crystal structure of the corresponding bulk phases and a terminating (001) face. For 2A, where two layers of molecules are present in the  $c$ -direction of the crystal structure the symmetry is broken when depositing the material on the glass wafer. Therefore, only even numbers of  $l$  are present in the diffractogram since these reflexions correspond to the layer spacing.

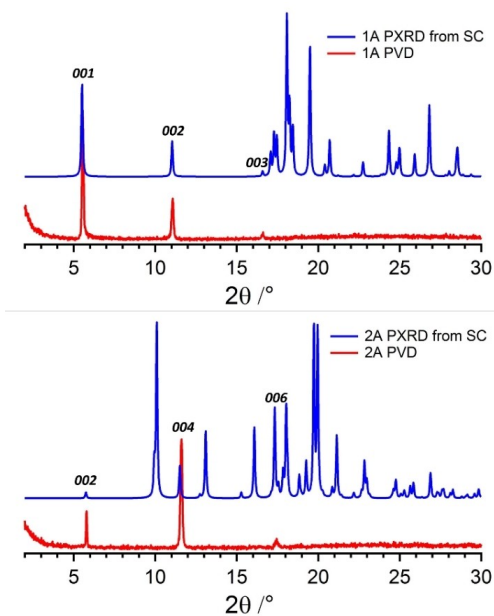


Figure 10. Simulated X-ray diffractograms from the single crystal structure (blue) and measured X-ray diffractograms of the deposited samples (red) of 1A (top) and 2A (bottom).

On these glass wafers, water/air contact angle measurements were performed (Figure S14). The measurements on the film of **1A** yielded an average contact angle of  $115^\circ$ , that is in the range of neat Teflon films,<sup>[46]</sup> showing that this film is highly hydrophobic. For the film of **2A**, a less hydrophobic average contact angle of  $105^\circ$  was obtained, which is in line with the lower amount of fluorine on the surface due to alternating arrangement of *t*-Bu and  $\text{CF}_3$  groups. Still this contact angle is higher compared to purely aliphatic surfaces.<sup>[49]</sup>

We are thus able to predict and tune the resulting morphology and surface polarities of the self-assembled nanoobjects based on the crystal structure, which itself can be predicted by the molecular structure.

### 3. Conclusion

The crystal structures of two series of 1,4-benzene bisamides with symmetric and asymmetric peripheral substitution were solved using a combination of single crystal diffraction and NMR crystallography. The symmetric series **1** consists of two linear, perfluorinated alkyl chains of increasing length (2/4/6  $\text{CF}_2$  units). The three compounds of series **1** crystallise in the same packing type, where one bisamide molecule forms four hydrogen bonds to two neighbouring molecules (Figure 5). These molecules are arranged parallel and thus create ribbons. These ribbons are densely packed along the other two crystallographic directions (Figure 6). For the asymmetric series **2** one side chain is substituted by a *t*-butyl group. The compounds of this series prefer a second packing type, where one bisamide molecule expresses four hydrogen bonds to four other molecules (Figure 5). These molecules are arranged in a zig-zag fashion creating a 2D layer (Figure 7). These layers are stacked in the third crystallographic direction.

SEM micrographs of the self-assembled nanoobjects showed that series **1** crystallises in thin ribbons, whereas series **2** self-assembles into thin platelets. Thus, for both series the molecular self-assembly translates into a distinct anisotropic morphology of the resulting objects. Contact angle measurements on thin films, vapour deposited on silanised glass wafers, demonstrate that the exposed surfaces are markedly hydrophobic, with series **1** exceeding the hydrophobicity of series **2**. The X-ray diffraction measurements of these films (Figure 10) showed that in both cases the (001) face is exposed, which coincides with the dominantly exposed surface of the self-assembled nanoobjects. The (001) surface consists of  $\text{CF}_3$  groups for series **1** and of alternating rows of *t*-butyl and  $\text{CF}_3$  groups for series **2**, explaining the different wetting behaviour for both series.

Based on DFT calculations, we identified two interacting driving forces – the hydrogen bond strength within the amide core and the crystal density – that, when tailored, allow to switch between the two packing patterns. Slim side chains like perfluorinated alkyl groups, favour dense packings without reducing the hydrogen bond strength in either of the packing types and packing pattern of series **1** with its 1D preferentially crystal growth is energetically favoured. Bulky side groups like

*t*-butyl groups, weaken the hydrogen bonds at the bisamide core if ribbons would form. Therefore, they prefer packing type of series **2**, in spite of its lower density.

Essentially, we show that the steric demand of the peripheral substitution of 1,4-substituted benzene bisamides can be used as a leitmotif to programme the crystal structure which in turn guides the crystal growth due to the spatial anisotropy within the interaction strength. This allows for tailoring the crystal morphology and the surface properties like polarity of bisamide nanoobjects and will be beneficial for identifying promising candidates for applications such as polymer additives in the future.

### Experimental Section

Details on the synthesis, characterisation and temperature of 5% weight loss (Table S1) of the symmetric and asymmetric 1,4-bisamides are given in the supporting information (Section 1).

Self-assembly experiments were performed by dissolving 500 ppm of the respective 1,4-benzene bisamide in 2.5 mL of *o*-dichlorobenzene in a 4 mL glass vial with screw cap and subsequent rapid cooling of the solution in an ice bath for 15 min.

Single crystal X-ray diffraction experiments were carried out on a STOE IPDS II instrument (Mo- $K_\alpha$  radiation) equipped with a Ge(111) monochromator at 173 K. The crystals were mounted on a glass tip with glue. Data collection, indexing, space group determination, data reduction and reconstruction of reciprocal space layers were performed with the software package X-Area (Stoe). Structure solution was carried out with the software package Shelx.<sup>[50]</sup>

Powder X-ray diffraction measurements were carried out on a STOE STADI P diffractometer equipped with a Ge(111) monochromator using  $\text{Cu-}K_{\alpha 1}$  radiation. The powders were filled in 0.5 mm or 0.3 mm capillary tubes and were measured in Debye-Scherrer geometry under ambient conditions or at 173 K. Indexing, simulated annealing and Rietveld refinement were done with the software package TOPAS.<sup>[51]</sup> Models were built with Materials Studio.

X-ray diffraction patterns of thin films were obtained using nickel filtered  $\text{Cu-}K_\alpha$  radiation on a Bragg-Brentano-type diffractometer (XPRT-PRO, PANalytical B.V) equipped with an X'Celerator Scientific RTMS detector.

NMR spectroscopic experiments were performed on a Bruker Avance III 600 NMR Spectrometer (600.15 MHz).  $^1\text{H}$  and  $^{19}\text{F}$  experiments were performed in a 1.3 mm  $\text{ZrO}_2$  rotor at 62.5 kHz MAS frequency.  $^{13}\text{C}$   $\{^1\text{H}\}$  CP and  $^{13}\text{C}$   $\{^{19}\text{F}\}$  CP experiments were carried out with a 3.2 mm rotor at 16 kHz. The CP experiments were done with a ramped CP sequence<sup>[52]</sup> where the nutation frequency on the  $^1\text{H}$  or  $^{19}\text{F}$  channel was varied linearly from 50–100%. The maximum nutation frequencies during the contact time were set to 87 kHz ( $^1\text{H}$ ) and 95 kHz ( $^{19}\text{F}$ ), respectively. During acquisition on the  $^{13}\text{C}$  channel,  $^1\text{H}$  and  $^{19}\text{F}$  were decoupled using the Spinal64<sup>[53]</sup> decoupling sequence with nutation frequencies of 92 and 89 kHz, respectively.  $^{15}\text{N}$   $\{^1\text{H}\}$  CP NMR spectroscopic experiments were performed on a Bruker Avance III 400 NMR Spectrometer (400.13 MHz). Samples were packed in 3.2 mm Zirconia rotors and measured at 10 kHz MAS frequency. The same ramped CP sequence as above was applied with a maximum proton nutation of 70 kHz but only protons were decoupled with Spinal64 at 75 kHz.

Scanning electron microscopy: Prior to the investigation, the dispersion of the samples were drop casted on a silicon wafer and

dried. Subsequently, the samples were sputtered with a platinum layer with a thickness of 1.3 nm using a Cressington 208HR sputter coater. SEM was performed with a field emission scanning electron microscope (Zeiss LEO 1530) using an acceleration voltage of 3 kV.

Physical vapor deposition (PVD) was performed using a custom-made vacuum chamber (Balzers PLS 500) equipped with three effusion cells. The evaporation setup is described in detail in the literature.<sup>[54]</sup> Prior to the evaporation, glass substrates were silanized with HDMS applying a standard procedure. The vacuum chamber was evacuated to  $4 \times 10^{-6}$  mbar and the effusion cells were heated to 130 °C for **1A** and 105 °C for **2A** during the evaporation. A constant evaporation rate of about  $0.3 \text{ \AA s}^{-1}$  was used. The evaporation time was typically 60 min resulting in film thickness of about 100 nm.

Atomic force microscopy (AFM) measurements were performed using a Veeco dimension 3100 atomic force microscope equipped with a NanoScope IV controller. Bruker OTESPA-R3 silicon cantilevers were used in tapping mode. Images were evaluated using Bruker NanoScope Analysis software (version 1.40).

Contact angle measurements were performed on vapour deposited thin films with the sessile drop method using a Krüss DSA25S drop shape analyser. For each thin film, the average contact angle of at least five measurements was determined.

For the quantum mechanical calculations the structures obtained from single crystal and powder X-ray refinement were geometry optimised<sup>[55]</sup> on DFT level with the software package CASTEP<sup>[56]</sup> using the PBE functional and the Tkatchenko-Scheffler<sup>[57]</sup> dispersion correction scheme. An electronic cut off energy of 900 eV and a Monkhorst k point grid spacing of  $0.07 \text{ \AA}^{-1}$  was used.<sup>[58]</sup> Force field calculations were done with the DREIDING<sup>[59]</sup> force field and charges were applied using Gasteiger.<sup>[60]</sup>

This work was financially supported by the German Research Foundation (DFG), project number 79971943 (Collaborative Research Center SFB 840, project B4). KvdZ thanks the Elite Study Program Macromolecular Science within the Elite Network of Bavaria (ENB) for support. The authors would like to thank Dr. Tiziana Boffa-Ballaran (Bavarian Geoinstitute), Dr. Wolfgang Milius and Dr. Thomas Martin (Inorganic Chemistry I, UBT) for fruitful discussions on crystallography. Markus Stihl (Macromolecular Chemistry I, UBT) is gratefully acknowledged for preparing thin films by physical vapor deposition. Sandra Ganzleben (Macromolecular Chemistry I, UBT) is thanked for the synthesis of the molecules.

### Conflict of Interest

The authors declare no conflict of interest.

**Keywords:** ab initio structure solution · DFT calculations · NMR crystallography · self-assembly · supramolecular polymer additives

[1] a) T. Govindaraju, M. B. Avinash, *Nanoscale* **2012**, *4*, 6102–6117; b) M. Osada, T. Sasaki, *Adv. Mater.* **2012**, *24*, 210–228; c) R. Mas-Ballesté, C. Gómez-Navarro, J. Gómez-Herrero, F. Zamora, *Nanoscale* **2011**, *3*, 20–30; d) Y. Wei, J. Tian, Z. Zhang, C. Zhu, J. Sun, Z. Li, *Macromolecules* **2019**, *52*, 1546–1556.

- [2] a) R. Davis, R. Berger, R. Zentel, *Adv. Mater.* **2007**, *19*, 3878–3881; b) R. Meziene, M. Brehmer, U. Maschke, R. Zentel, *Soft Matter* **2008**, *4*, 1237–1241.
- [3] T. Govindaraju, M. Pandeewar, K. Jayaramulu, G. Jaipuria, H. S. Atreya, *Supramol. Chem.* **2011**, *23*, 487–492.
- [4] K. T. Nam, S. A. Shelby, P. H. Choi, A. B. Marciel, R. Chen, L. Tan, T. K. Chu, R. A. Mesch, B.-C. Lee, M. D. Connolly et al., *Nat. Mater.* **2010**, *9*, 454–460.
- [5] M. Blomenhofer, S. Ganzleben, D. Hanft, H.-W. Schmidt, M. Kristiansen, P. Smith, K. Stoll, D. Mäder, K. Hoffmann, *Macromolecules* **2005**, *38*, 3688–3695.
- [6] M. Mörl, C. Steinlein, K. Kreger, H.-W. Schmidt, V. Altstadt, *J. Cell. Plast.* **2018**, *54*, 483–498.
- [7] M. Aksit, B. Klose, C. Zhao, K. Kreger, H.-W. Schmidt, V. Altstadt, *J. Cell. Plast.* **2019**, *55*, 249–261.
- [8] D. Hu, G. Wang, J. Feng, X. Lu, *Polymer* **2016**, *93*, 123–131.
- [9] M. Schmidt, J. J. Wittmann, R. Kress, H.-W. Schmidt, J. Senker, *Chem. Commun.* **2013**, *49*, 267–269.
- [10] M. Gahleitner, C. Grein, S. Kheirandish, J. Wolfschwenger, *Int. Polym. Process.* **2011**, *26*, 2–20.
- [11] a) D. Libster, A. Aserin, N. Garti, *Polym. Adv. Technol.* **2007**, *18*, 685–695; b) M. Kristiansen, M. Werner, T. Tervoort, P. Smith, M. Blomenhofer, H.-W. Schmidt, *Macromolecules* **2003**, *36*, 5150–5156.
- [12] B. Isare, L. Petit, E. Bugnet, R. Vincent, L. Lapalu, P. Sautet, L. Bouteiller, *Langmuir* **2009**, *25*, 8400–8403.
- [13] S. Cantekin, T. F. A. de Greef, A. R. A. Palmans, *Chem. Soc. Rev.* **2012**, *41*, 6125–6137.
- [14] a) M. Stumpf, A. Spörrer, H.-W. Schmidt, V. Altstadt, *J. Cell. Plast.* **2011**, *47*, 519–534; b) M. Aksit, C. Zhao, B. Klose, K. Kreger, H.-W. Schmidt, V. Altstadt, *Polymer* **2019**, *11*, 268.
- [15] a) Y. Shi, Z. Xin, *J. Thermoplast. Compos. Mater.* **2016**, *29*, 1667–1679; b) B. Klose, D. Kremer, M. Aksit, K. P. van der Zwan, K. Kreger, J. Senker, V. Altstadt, H.-W. Schmidt, *Polymer* **2021**, *13*, 1094.
- [16] J.-M. Lehn, *Angew. Chem. Int. Ed.* **1990**, *29*, 1304–1319; *Angew. Chem.* **1990**, *102*, 1347–1362.
- [17] Z. Wang, W. Yang, G. Liu, A. J. Müller, Y. Zhao, X. Dong, K. Wang, D. Wang, *J. Polym. Sci. Part B* **2017**, *55*, 418–424.
- [18] F. Abraham, H.-W. Schmidt, *Polymer* **2010**, *51*, 913–921.
- [19] T. Wang, Y. Yang, C. Zhang, Z. Tang, H. Na, J. Zhu, *J. Appl. Polym. Sci.* **2013**, *130*, 1328–1336.
- [20] A. Thierry, C. Straupé, J.-C. Wittmann, B. Lotz, *Macromol. Symp.* **2006**, *241*, 103–110.
- [21] G. R. Desiraju, *J. Am. Chem. Soc.* **2013**, *135*, 9952–9967.
- [22] P. Dandekar, Z. B. Kuvadia, M. F. Doherty, *Annu. Rev. Mater. Res.* **2013**, *43*, 359–386.
- [23] G. R. Desiraju, *Angew. Chem. Int. Ed.* **1995**, *34*, 2311–2327; *Angew. Chem.* **1995**, *107*, 2541–2558.
- [24] M. Zhang, H. N. Tsao, W. Pisula, C. Yang, A. K. Mishra, K. Müllen, *J. Am. Chem. Soc.* **2007**, *129*, 3472–3473.
- [25] M. C. Etter, *Acc. Chem. Res.* **1990**, *23*, 120–126.
- [26] B. Hachula, A. Polasz, M. Książek, J. Kusz, V. Kozik, M. Matussek, W. Pisarski, *Tetrahedron* **2017**, *73*, 2901–2912.
- [27] a) J. A. R. P. Sarma, G. R. Desiraju, *Acc. Chem. Res.* **1986**, *19*, 222–228; b) A. Mukherjee, G. R. Desiraju, *Cryst. Growth Des.* **2011**, *11*, 3735–3739.
- [28] A. K. Nangia, G. R. Desiraju, *Angew. Chem. Int. Ed.* **2019**, *58*, 4100–4107; *Angew. Chem.* **2019**, *131*, 4142–4150.
- [29] H.-W. Schmidt, F. Würthner, *Angew. Chem. Int. Ed.* **2020**, *59*, 8766–8775; *Angew. Chem.* **2020**, *132*, 8846–8856.
- [30] J. P. Weyrauch, A. S. K. Hashmi, A. Schuster, T. Hengst, S. Schetter, A. Littmann, M. Rudolph, M. Hamzic, J. Visus, F. Rominger et al., *Chem. Eur. J.* **2010**, *16*, 956–963.
- [31] L. Huang, H. Li, *Acta Crystallogr. Sect. E* **2007**, *63*, o4657.
- [32] O. Cuzan, S. Shova, C. Turta, I. I. Mangalagiu, *Acta Crystallogr. Sect. E* **2012**, *68*, o463.
- [33] V. Y. Shuvalov, I. V. Eltsov, N. A. Tumanov, E. V. Boldyreva, A. A. Nefedov, G. P. Sagitullina, *Eur. J. Org. Chem.* **2017**, *2017*, 5410–5416.
- [34] S. Ray, R. P. Hegde, A. K. Das, N. Shamala, A. Banerjee, *Tetrahedron* **2006**, *62*, 9603–9609.
- [35] N. Haridharan, V. Ramkumar, R. Dhamodharan, *Acta Crystallogr. Sect. E* **2012**, *68*, o811.
- [36] H.-Z. Guo, G.-D. Yin, N.-F. She, A.-X. Wu, *Acta Crystallogr. Sect. E* **2005**, *61*, o4062–o4063.
- [37] V. Martí-Centelles, D. K. Kumar, A. J. P. White, S. V. Luis, R. Vilar, *CrystEngComm* **2011**, *13*, 6997–7008.
- [38] P. Bombicz, T. Gruber, C. Fischer, E. Weber, A. Kálmán, *CrystEngComm* **2014**, *16*, 3646–3654.

- [39] a) P. J. M. Stals, M. M. J. Smulders, R. Martín-Rapún, A. R. A. Palmans, E. W. Meijer, *Chem. Eur. J.* **2009**, *15*, 2071–2080; b) E. K. Burnett, Q. Ai, B. P. Chermiawski, S. R. Parkin, C. Risko, A. L. Briseno, *Chem. Mater.* **2019**, *31*, 6900–6907.
- [40] a) R. K. Harris, R. E. Wasylshen, M. J. Duer, *NMR Crystallography*, 2. Aufl., Wiley, s.l., **2012**; b) C. Martineau, J. Senker, F. Taulelle, *Annu. Rep. NMR Spectrosc.* **2014**, *82*, 1–57; c) S. E. Ashbrook, P. Hodgkinson, *J. Chem. Phys.* **2018**, *149*, 40901; d) A. Hofstetter, L. Emsley, *J. Am. Chem. Soc.* **2017**, *139*, 2573–2576.
- [41] a) W. Kohn, L. J. Sham, *Phys. Rev.* **1965**, *140*, A1133–A1138; b) P. Hohenberg, W. Kohn, *Phys. Rev.* **1964**, *136*, B864–B871.
- [42] H. M. Rietveld, *J. Appl. Crystallogr.* **1969**, *2*, 65–71.
- [43] M. Schmidt, J. J. Wittmann, R. Kress, D. Schneider, S. Steuernagel, H.-W. Schmidt, J. Senker, *Cryst. Growth Des.* **2012**, *12*, 2543–2551.
- [44] M. Schmidt, C. S. Zehe, R. Siegel, J. U. Heigl, C. Steinlein, H.-W. Schmidt, J. Senker, *CrystEngComm* **2013**, *15*, 8784–8796.
- [45] a) M. A. Hope, T. Nakamura, P. Ahlawat, A. Mishra, M. Cordova, F. Jahanbakhshi, M. Mladenović, R. Runjhun, L. Merten, A. Hinderhofer et al., *J. Am. Chem. Soc.* **2021**, *143*, 1529–1538; b) M. Marin-Luna, P. Sánchez-Andrada, I. Alkorta, J. Elguero, M. C. Torralba, P. Delgado-Martínez, D. Santa María, R. M. Claramunt, *Magn. Reson. Chem.* **2021**, *59*, 423–438; c) P. Hodgkinson, *Prog. Nucl. Magn. Reson. Spectrosc.* **2020**, *118–119*, 10–53; d) A. C. Pöppler, E. K. Corlett, H. Pearce, M. P. Seymour, M. Reid, M. G. Montgomery, S. P. Brown, *Acta Crystallogr. Sect. C* **2017**, *73*, 149–156.
- [46] a) D. M. Dawson, L. E. Macfarlane, M. Amri, R. I. Walton, S. E. Ashbrook, *J. Phys. Chem. C* **2021**, *125*, 2537–2545; b) R. Giovine, C. Volkringer, J. Trébosc, J. P. Amoureux, T. Loiseau, O. Lafon, F. Pourpoint, *Acta Crystallogr. Sect. C* **2017**, *73*, 176–183; c) K. Datta, A. Richter, M. Göbbels, D. A. Keen, R. B. Neder, *Phys. Rev. B* **2016**, *93*; d) C. Bornes, M. Sardo, Z. Lin, J. Amelse, A. Fernandes, M. F. Ribeiro, C. Geraldes, J. Rocha, L. Mafra, *Chem. Commun.* **2019**, *55*, 12635–12638.
- [47] a) C. S. Zehe, J. A. Hill, N. P. Funnell, K. Kreger, K. P. van der Zwan, A. L. Goodwin, H.-W. Schmidt, J. Senker, *Angew. Chem. Int. Ed.* **2017**, *56*, 4432–4437; *Angew. Chem.* **2017**, *129*, 4502–4508; b) D. A. Keen, A. L. Goodwin, *Nature* **2015**, *521*, 303–309.
- [48] J. Zhang, J. Li, Y. Han, *Macromol. Rapid Commun.* **2004**, *25*, 1105–1108.
- [49] A. Augsburg, K. Grundke, K. Pöschel, H.-J. Jacobasch, A. W. Neumann, *Acta Polym.* **1998**, *49*, 417–426.
- [50] G. M. Sheldrick, *Acta Crystallogr. Sect. C* **2015**, *71*, 3–8.
- [51] A. A. Coelho, *J. Appl. Crystallogr.* **2018**, *51*, 210–218.
- [52] G. Metz, X. L. Wu, S. O. Smith, *J. Magn. Reson.* **1994**, *110*, 219–227.
- [53] B. M. Fung, A. K. Khitrin, K. Ermolaev, *J. Magn. Reson.* **2000**, *142*, 97–101.
- [54] a) M. Thelakkat, C. Schmitz, C. Neuber, H.-W. Schmidt, *Macromol. Rapid Commun.* **2004**, *25*, 204–223; b) C. Neuber, M. Bäte, M. Thelakkat, H.-W. Schmidt, H. Hänsel, H. Zettl, G. Krausch, *Rev. Sci. Instrum.* **2007**, *78*, 72216.
- [55] a) B. G. Pfrommer, M. Côté, S. G. Louie, M. L. Cohen, *J. Comput. Phys.* **1997**, *131*, 233–240; b) E. R. McNellis, J. Meyer, K. Reuter, *Phys. Rev. B* **2009**, *80*, 1.
- [56] S. J. Clark, M. D. Segall, C. J. Pickard, P. J. Hasnip, M. I. J. Probert, K. Refson, M. C. Payne, *Z. Kristallogr. Cryst. Mater.* **2005**, *220*, 567–570.
- [57] A. Tkatchenko, M. Scheffler, *Phys. Rev. Lett.* **2009**, *102*, 73005.
- [58] H. J. Monkhorst, J. D. Pack, *Phys. Rev. B* **1976**, *13*, 5188–5192.
- [59] S. L. Mayo, B. D. Olafson, W. A. Goddard, *J. Phys. Chem.* **1990**, *94*, 8897–8909.
- [60] J. Gasteiger, H. Saller, *Angew. Chem. Int. Ed.* **1985**, *24*, 687–689; *Angew. Chem.* **1985**, *97*, 699–701.

---

 Manuscript received: August 11, 2021

Revised manuscript received: October 11, 2021

Accepted manuscript online: October 13, 2021

Version of record online: November 8, 2021

# ChemPhysChem

Supporting Information

## **Crystal Engineering of Supramolecular 1,4-Benzene Bisamides by Side-Chain Modification – Towards Tuneable Anisotropic Morphologies and Surfaces**

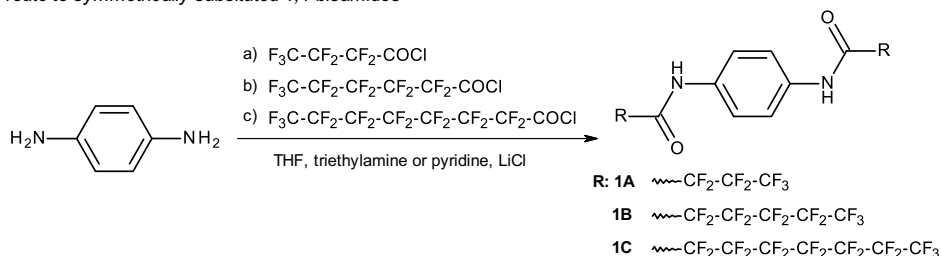
Kasper P. van der Zwan, Christoph Steinlein, Klaus Kreger, Hans-Werner Schmidt,\* and Jürgen Senker\*

**Table of content**

<b>1:</b> Synthesis and characterization of symmetric 1,4-benzene bisamides <b>1A-C</b> and asymmetric 1,4-benzene bisamides <b>2A-C</b> .....	2
<b>2:</b> Crystallographic information of the single crystal structure solutions .....	6
<b>3:</b> Powder X-ray diffractograms with Rietveld refinements.....	8
<b>4:</b> Additional MAS NMR spectra of symmetric 1,4-benzene bisamides <b>1A-C</b> and asymmetric 1,4-benzene bisamides <b>2A-C</b> .....	9
<b>5:</b> Different coordination of the two series .....	10
<b>6:</b> Different global packing of <b>2A</b> compared to <b>2B</b> and <b>2C</b> . .....	10
<b>7:</b> Structure models of <b>2A</b> in the structure type of series <b>1</b> .....	11
<b>8:</b> Scanning electron microscopy of self-assembled platelets of symmetric 1,4-benzene bisamides <b>1B-C</b> and asymmetric 1,4-benzene bisamides <b>2B-C</b> .....	13
<b>9:</b> AFM of self-assembled platelets of both series.....	14
<b>10:</b> Thin film preparation and wetting behavior with water on vapor deposited thin films of symmetric 1,4-benzene bisamides <b>1A</b> and asymmetric 1,4-benzene bisamides <b>2A</b> .....	16

### 1: Synthesis and characterization of symmetric 1,4-benzene bisamides **1A-C** and asymmetric 1,4-benzene bisamides **2A-C**

Synthetic route to symmetrically substituted 1,4-bisamides



Synthetic route to asymmetrically substituted 1,4-bisamides

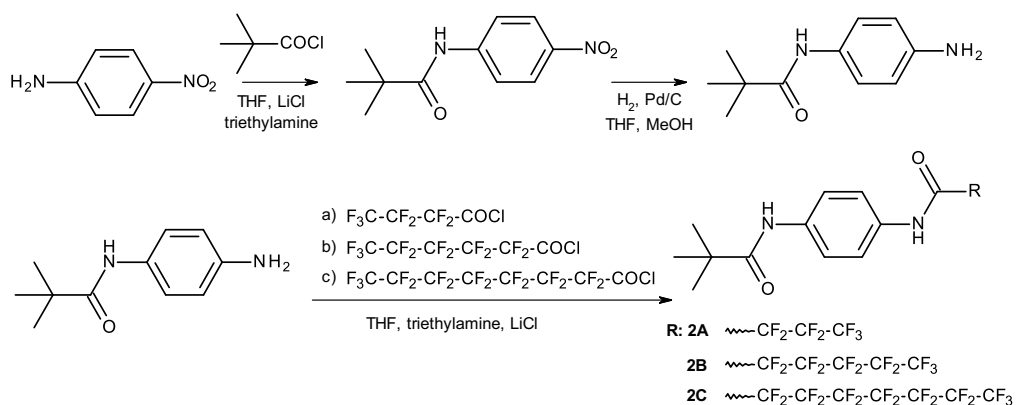


**Figure S1.** Top: One step synthesis to symmetric 1,4-bisamides **1A-C** by conversion of 1,4-diaminobenzene with the respective perfluorinated acid chlorides. Bottom: Three step synthesis to asymmetric 1,4-bisamides **2A-C**: Conversion of 4-nitroaniline with pivaloyl chloride, hydrogenation of 2,2-dimethyl-N-(4-nitrophenyl)propanamide and subsequent conversion of 2,2-dimethyl-N-(4-aminophenyl)propanamide with the respective perfluorinated acid chlorides.

#### Synthesis of *N,N'*-1,4-phenylenebis(2,2,3,3,4,4,4-heptafluorobutanamide) **1A**

4.7 g of perfluorobutanoyl chloride was added to a mixture of 1.0 g of 1,4-phenylenediamine, 3 mL of pyridine, a small amount of LiCl and 100 mL of anhydrous THF at 0 °C under argon atmosphere. The reaction mixture was heated to 40 °C for 12 h. After evaporation of the solvent, the solid residue was dispersed in water and filtered off. Crystallization from methanol yielded 4.4 g (94%) of the product as white crystals.

$^1\text{H NMR}$  (300 MHz,  $\text{DMSO-d}_6$ )  $\delta$  (ppm): 11.40 (2 H, s), 7.71 (4 H, s).

MS-EI (m/z, %): 500 ( $[\text{M}]^+$ , 100), 481 (31), 331 (15), 303 (98), 108 (65), 81 (15), 69 (23).

*Synthesis of N,N'-1,4-phenylenebis(2,2,3,3,4,4,5,5,6,6,6-undecafluorohexanamide) 1B*

5.3 g of perfluorohexanoyl chloride were slowly added to a mixture of 0.66 g of 1,4-phenylenediamine, 3 mL of pyridine, a small amount of LiCl and 100 mL of anhydrous THF at 0 °C under argon atmosphere. The reaction mixture was refluxed for 12 h. After solvent removal, the solid residue was dispersed in water and filtered off. Crystallization from methanol yielded 1.8 g (43%) of the product as white solid.

<sup>1</sup>H NMR (300 MHz, DMSO-d<sub>6</sub>) δ (ppm): 11.39 (2 H, s), 7.69 (4 H, s).

MS-EI (m/z): 700 ([M]<sup>+</sup>, 100), 681 (10), 431 (13), 303 (95), 133 (12), 108 (38), 69 (11).

*Synthesis of N,N'-1,4-phenylenebis(2,2,3,3,4,4,5,5,6,6,7,7,8,8,8-pentadecafluorooctanamide) 1C*

6.6 g of perfluorooctanoyl chloride were slowly added to a mixture of 0.75 g of 1,4-phenylenediamine, 5 mL of triethylamine, a small amount of LiCl and 200 mL of anhydrous THF at 0 °C under argon atmosphere. Subsequently, the reaction mixture was refluxed for 12 h. After solvent evaporation, the solid residue was dispersed in water and filtered off. Crystallization from N,N-dimethylformamide yielded 5.1 g (81%) of the product as white solid.

<sup>1</sup>H NMR (300 MHz, DMF-d<sub>6</sub>) δ (ppm): 11.68 (2 H, s), 8.20 (4 H, s).

MS-EI (m/z): 900 ([M]<sup>+</sup>, 100), 881 (47), 531 (6), 503 (55), 133 (6), 108 (28), 69 (11).

*Synthesis of 2,2-dimethyl-N-(4-nitrophenyl)propanamide*

2.9 g of pivaloyl chloride was added to a mixture of 3.0 g of 4-nitroaniline, 20 mL of trimethylamine and 150 mL of anhydrous THF at 0 °C under argon atmosphere. The reaction mixture was refluxed for 12 h. After removal of the solvents, the solid residue was washed with water and recrystallized from hexane, yielding 4.3 g (89%) of the product.

<sup>1</sup>H NMR (300 MHz, DMSO-d<sub>6</sub>) δ (ppm): 9.79 (1 H, s), 8.21 (2 H, m), 7.95 (2 H, m), 1.25 (9 H, s).

*Synthesis of 2,2-dimethyl-N-(4-aminophenyl)propanamide*

4.3 g of 2,2-dimethyl-N-(4-nitrophenyl)propanamide were added to 250 mL of THF and 50 mL of MeOH together with 0.4 g palladium on activated charcoal (10% Pd). Hydrogenation was performed with H<sub>2</sub> at a pressure of 3 bar and 35 °C for 12 h. The catalyst was removed by filtration of the reaction mixture over Alox N. After evaporation of the solvent, the product was obtained as white powder in quantitative yield (3.7 g).

<sup>1</sup>H NMR (300 MHz, DMSO-d<sub>6</sub>) δ (ppm): 8.80 (1 H, s), 7.18 (2 H, m), 6.48 (2 H, m), 4.84 (2 H, s), 1.18 (9 H, s).

*Synthesis of N-[4-[(2,2-dimethyl-1-oxopropyl)amino]phenyl]-2,2,3,3,4,4,4-heptafluorobutanamide 2A*

3.1 g of perfluorobutanoyl chloride were slowly added to a mixture of 2.0 g of 2,2-dimethyl-N-(4-aminophenyl)propanamide, 10 mL of triethylamine, a small amount of LiCl and 100 mL of anhydrous THF at 0 °C under argon atmosphere. Subsequently, the reaction mixture was refluxed for 12 h. After evaporation of solvents, the solid residue was dispersed in water and filtered off. Crystallization from methanol yielded 2.6 g (64%) of the product as white crystals.  $^1\text{H}$  NMR (300 MHz, DMSO- $d_6$ )  $\delta$  (ppm): 11.23 (1 H, s), 9.30 (1 H, s), 7.62 (4 H, m), 1.22 (9 H, s) MS-EI (m/z, %): 388 ([M]<sup>+</sup>, 72), 304 (29), 107 (17), 85 (15), 57 (100), 41 (12).

*Synthesis of N-[4-[(2,2-dimethyl-1-oxopropyl)amino]phenyl]-2,2,3,3,4,4,5,5,6,6,6-undecafluorohexanamide **2B***

4.5 g of perfluorohexanoyl chloride were slowly added to a mixture of 2.0 g of 2,2-dimethyl-N-(4-aminophenyl)propanamide, 10 mL of triethylamine, a small amount of LiCl and 100 mL of anhydrous THF at 0 °C under argon atmosphere. Subsequently, the reaction mixture was refluxed for 12 h. After evaporation of solvents, the solid residue was dispersed in water and filtered off. Crystallization from methanol yielded 1.0 g (20%) of the product as white crystals.  $^1\text{H}$  NMR (300 MHz, DMSO- $d_6$ )  $\delta$  (ppm): 11.23 (1 H, s), 9.30 (1 H, s), 7.62 (4 H, m), 1.22 (9 H, s). MS-EI (m/z, %): 488 ([M]<sup>+</sup>, 77.0), 469 (14), 404 (31), 107 (14), 85 (15), 57 (100), 41 (11).

*Synthesis of N-[4-[(2,2-dimethyl-1-oxopropyl)amino]phenyl]-2,2,3,3,4,4,5,5,6,6,7,7,8,8,8-pentadecafluorooctanamide **2C***

4.4 g of perfluorooctanoyl chloride were slowly added to a mixture of 1.5 g of 2,2-dimethyl-N-(4-aminophenyl)propanamide, 10 mL of triethylamine, a small amount of LiCl and 100 mL of dry THF at 0 °C in inert atmosphere. The mixture was refluxed for 12 h. After solvent removal, the solid was dispersed in water and filtered off. Crystallization from ethyl acetate yielded 3.85 g (84%) as white crystals.  $^1\text{H}$  NMR (300 MHz, DMSO- $d_6$ )  $\delta$  (ppm): 11.21 (1 H, s), 9.30 (1 H, s), 7.61 (4 H, m), 1.22 (9 H, s). MS-EI (m/z, %): 588 ([M]<sup>+</sup>, 27), 569 (8), 504 (14), 107 (11), 85 (15), 57 (100).

For all substances, melting and sublimation points, as determined by DSC and TGA measurements, are too close to each other to be distinguished properly. Therefore, we provide the temperature of 5 % mass loss in Table S1.

**Table S1.** Temperature of 5 % weight loss.

Compound	Temperature /°C
1A	221
1B	221
1C	221
2A	212
2B	216
2C	235

*Analytical characterization methods*

Nuclear magnetic resonance spectroscopy:  $^1\text{H}$  NMR (300 MHz) experiments were carried out on a Bruker Avance AC 300 spectrometer at room temperature. For all compounds solid state  $^{13}\text{C}$  NMR spectra are given in Figures 2,4 and S8.

Mass spectroscopy: Mass spectra were recorded on a Finnigan MAT 8500 spectrometer (Thermo Fisher Scientific) (EI, 70 eV) using direct injection mode.

**2:** Crystallographic information of the single crystal structure solutions

**Table S2.** Crystallographic information for single crystal structure solutions. The CIF files are deposited in the Cambridge Structural Database with the deposition numbers 2101449, 2101447 and 210144 for **1A**, **2A** and **2B**, respectively.

Compound	1A	2A	2B
Molecular formula	C <sub>14</sub> H <sub>6</sub> F <sub>14</sub> N <sub>2</sub> O <sub>2</sub>	C <sub>15</sub> H <sub>15</sub> F <sub>7</sub> N <sub>2</sub> O <sub>2</sub>	C <sub>17</sub> H <sub>15</sub> F <sub>11</sub> N <sub>2</sub> O <sub>2</sub>
M/g mol <sup>-1</sup>	500.19	388.29	488.3
Radiation	Mo-K $\alpha$	Mo-K $\alpha$	Mo-K $\alpha$
No. of reflections	2269	4120	5351
No. of reflections(I/ $\sigma$ >2)	1557	2192	4938
Theta range	2.54-29.24	2.29-28.28	2.19-29.15
Completeness	99.7	99.5	99.5
h,k,l range	$\pm 6, \pm 7, \pm 21$	$\pm 12, \pm 7, \pm 40$	$\pm 12, \pm 7, \pm 25$
Crystal system	triclinic	monoclinic	monoclinic
Space group	P $\bar{1}$	P2 <sub>1</sub> /n	P2 <sub>1</sub>
a/Å	5.1278(10)	9.2124(18)	9.2340(18)
b/Å	5.2125(10)	5.8994(12)	5.8718(12)
c/Å	16.090(3)	30.732(6)	18.787(4)
$\alpha$ /°	95.27(3)	90	90
$\beta$ /°	90.74(3)	91.57(3)	98.87(3)
$\gamma$ /°	91.74(3)	90	90
V/Å <sup>3</sup>	428.00(15)	1669.6(6)	1006.5(3)
Z'/Z	0.5/1	1/4	1/2
r/g cm <sup>-3</sup>	1.940	1.547	1.61
T/K	173	173	173
Goodness of fit	1.069	1.485	1.124
R <sub>all</sub>	0.0828	0.2008	0.0764
R (I/ $\sigma$ >2.0)	0.0533	0.1404	0.067
wR <sub>all</sub>	0.1469	0.35	0.1804
wR (I/ $\sigma$ >2.0)	0.1241	0.3098	0.1708
Residual electron density	0.374 e/Å <sup>3</sup>	0.621 e/Å <sup>3</sup>	1.04 e/Å <sup>3</sup>

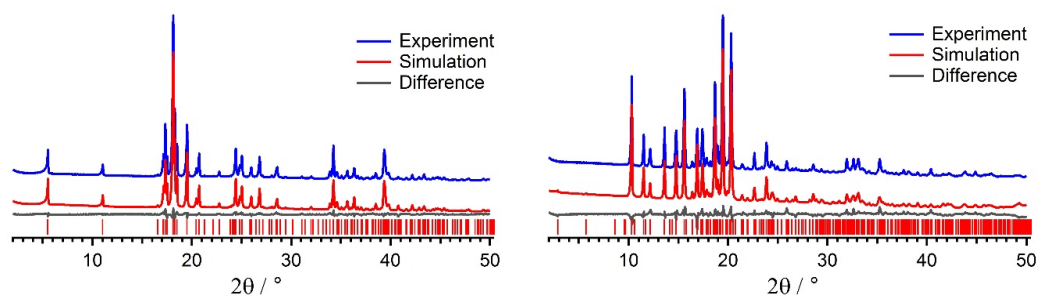
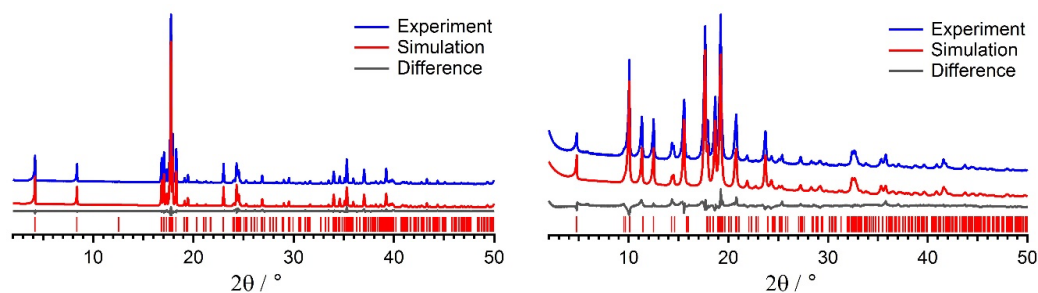
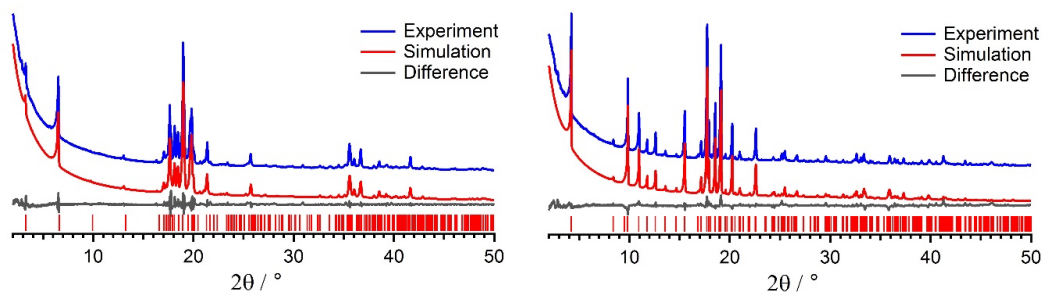
**Table S3.** Crystallographic information for powder X-ray crystal structure solutions. The CIF files are deposited in the Cambridge Structural Database with the deposition numbers 2101446, 2101445, 2101450, 2101448 and 210143 for **1A**, **1B**, **2A**, **2B** and **2C**, respectively.

Compound	1A	1B	1C	2A	2B	2C
Refinement	Rietveld	Rietveld	Pawley	Rietveld	Rietveld	Rietveld
Molecular formula	C <sub>14</sub> H <sub>6</sub> F <sub>14</sub> N <sub>2</sub> O <sub>2</sub>	C <sub>18</sub> H <sub>6</sub> F <sub>22</sub> N <sub>2</sub> O <sub>2</sub>	C <sub>22</sub> H <sub>6</sub> F <sub>30</sub> N <sub>2</sub> O <sub>2</sub>	C <sub>15</sub> H <sub>15</sub> F <sub>7</sub> N <sub>2</sub> O <sub>3</sub>	C <sub>17</sub> H <sub>15</sub> F <sub>11</sub> N <sub>2</sub> O <sub>2</sub>	C <sub>19</sub> H <sub>15</sub> F <sub>15</sub> N <sub>2</sub> O <sub>2</sub>
M/g mol <sup>-1</sup>	500.19	700.22	900.25	389.29	488.3	588.31
Crystal system	triclinic	triclinic	triclinic	monoclinic	monoclinic	monoclinic
Space group	<i>P</i> $\bar{1}$	<i>P</i> $\bar{1}$	n.A.	<i>P</i> 2 <sub>1</sub> / <i>n</i>	<i>P</i> 2 <sub>1</sub>	<i>P</i> 2 <sub>1</sub>
<i>a</i> /Å	5.11628(6)	5.11602(4)	5.5187(5)	9.2727(5)	9.3315(7)	9.3809(2)
<i>b</i> /Å	5.19633(10)	5.28202(5)	5.7129(5)	6.1044(4)	5.9830(3)	5.9346(1)
<i>c</i> /Å	16.1019(4)	21.1591(3)	27.0745(43)	30.9098(27)	18.7312(18)	22.0028(11)
$\alpha$ /°	95.382(2)	93.976(1)	90.662(9)	90	90	90
$\beta$ /°	90.723(2)	88.824(2)	92.243(10)	96.440(6)	98.496(4)	106.682(4)
$\gamma$ /°	91.641(2)	89.255(2)	114.576(5)	90	90	90
<i>V</i> /Å <sup>3</sup>	425.97(1)	570.22(1)	775.31(17)	1738.61(1)	1034.31(1)	1173.40(8)
<i>Z</i> '/ <i>Z</i>	0.5/1	0.5/1	n.A.	1/4	1/2	1/2
$\rho$ /g cm <sup>-3</sup>	1.950	2.039	1.928	1.292	1.568	1.66
T/K	173	293	293	293	293	293
R <sub>p</sub>	0.034	0.041	0.029	0.044	0.043	0.035
R <sub>wp</sub>	0.046	0.060	0.046	0.060	0.060	0.056

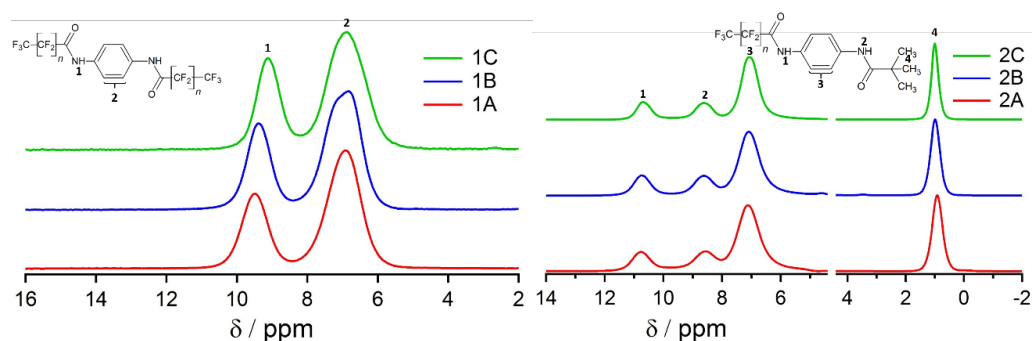
A preferred orientation of the 4<sup>th</sup> order using spherical harmonics <sup>[1]</sup> has been applied to all models except the Pawley fit.

The single crystal solution of **2A** yielded a cell in the space group *P*2<sub>1</sub>/*n*, however, the R-values are relatively poor. This is explained by the habitus of the crystal. The compound crystallizes in very thin platelets leading to a limited number of strong reflexions. Indexing the PXRD led to a similar but slightly different cell in the space group *P*2<sub>1</sub>. The absence of the glide plane leads to a doubling of the asymmetric unit. The single crystal data was refined in this space group as well and the obtained model placed in the cell obtained from PXRD. This model was geometry optimised by force field and DFT methods to correct for the now incorrect bond lengths and angles. The geometry optimized model could be refined with a good agreement with Rietveld methods. Then, the glide plane was found again and the Rietveld refinement could be redone with the space group *P*2<sub>1</sub>/*n* yielding even better R-values (Figure S3). This shows that although the R-values result in an A-Alert in the CheckCIF report, the structure solution arising from the single crystal is correct and the data quality arises from the desired and consequently engineered morphology as a thin platelet.

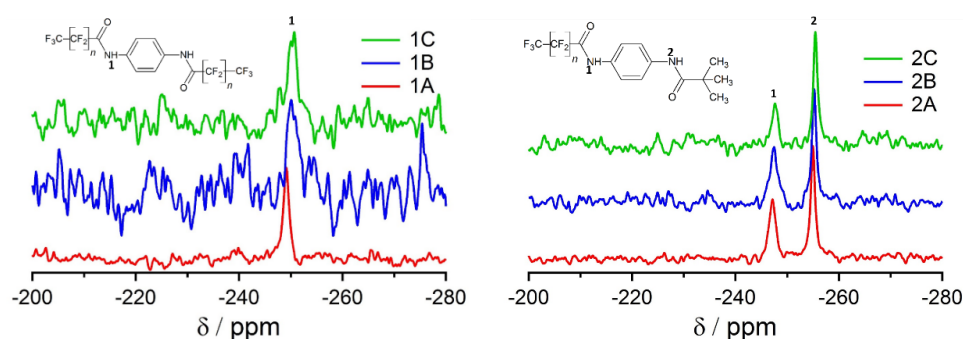
<sup>[1]</sup> M. Järvinen, J Appl Crystallogr 1993, 26, 525.

**3: Powder X-ray diffractograms with Rietveld refinements****Figure S2.** Powder X-ray diffractogram with Rietveld refinement of **1A** (left) and **2A** (right).**Figure S3.** Powder X-ray diffractogram with Rietveld refinement of **1B** (left) and **2B** (right).**Figure S4.** Powder X-ray diffractogram with Pawley refinement of **1C** (left) and with Rietveld refinement of **2C** (right).

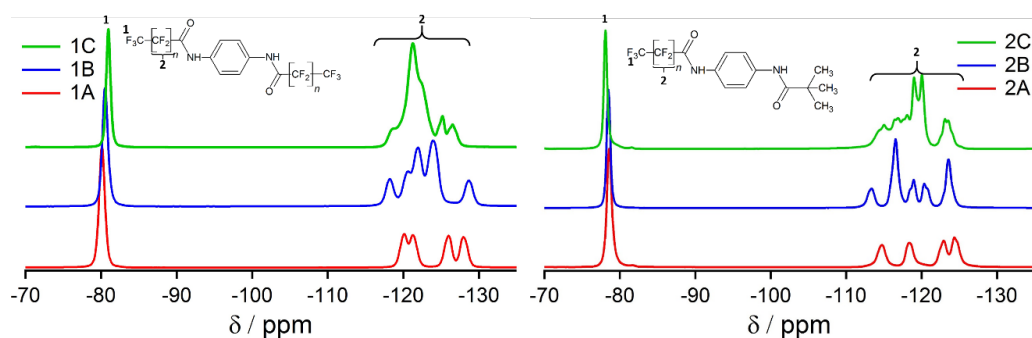
**4:** Additional MAS NMR spectra of symmetric 1,4-benzene bisamides **1A-C** and asymmetric 1,4-benzene bisamides **2A-C**



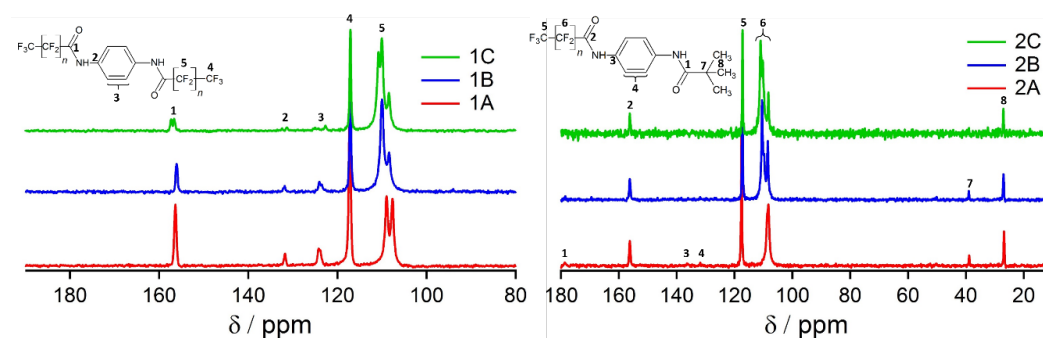
**Figure S5.**  $^1\text{H}$  MAS-NMR spectra of series **1** (left) and series **2** (right).



**Figure S6.**  $^{15}\text{N}\{^1\text{H}\}$  CP MAS-NMR spectra of series **1** (left) and series **2** (right).

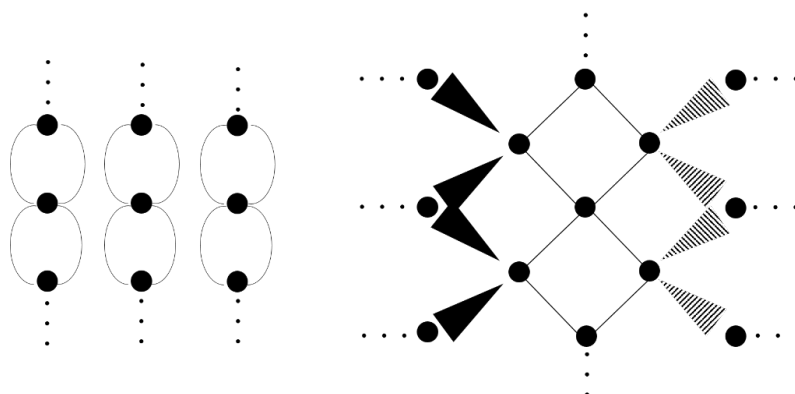


**Figure S7.**  $^{19}\text{F}$  MAS-NMR spectra of series **1** (left) and series **2** (right).

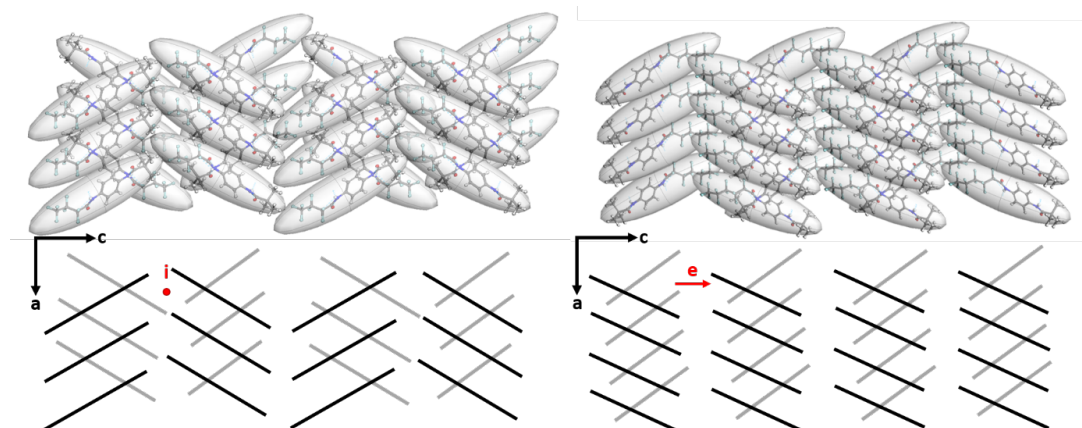


**Figure S8.**  $^{13}\text{C}\{^{19}\text{F}\}$  CP MAS-NMR spectra of series **1** (left) and series **2** (right).

## 5: Different coordination of the two series

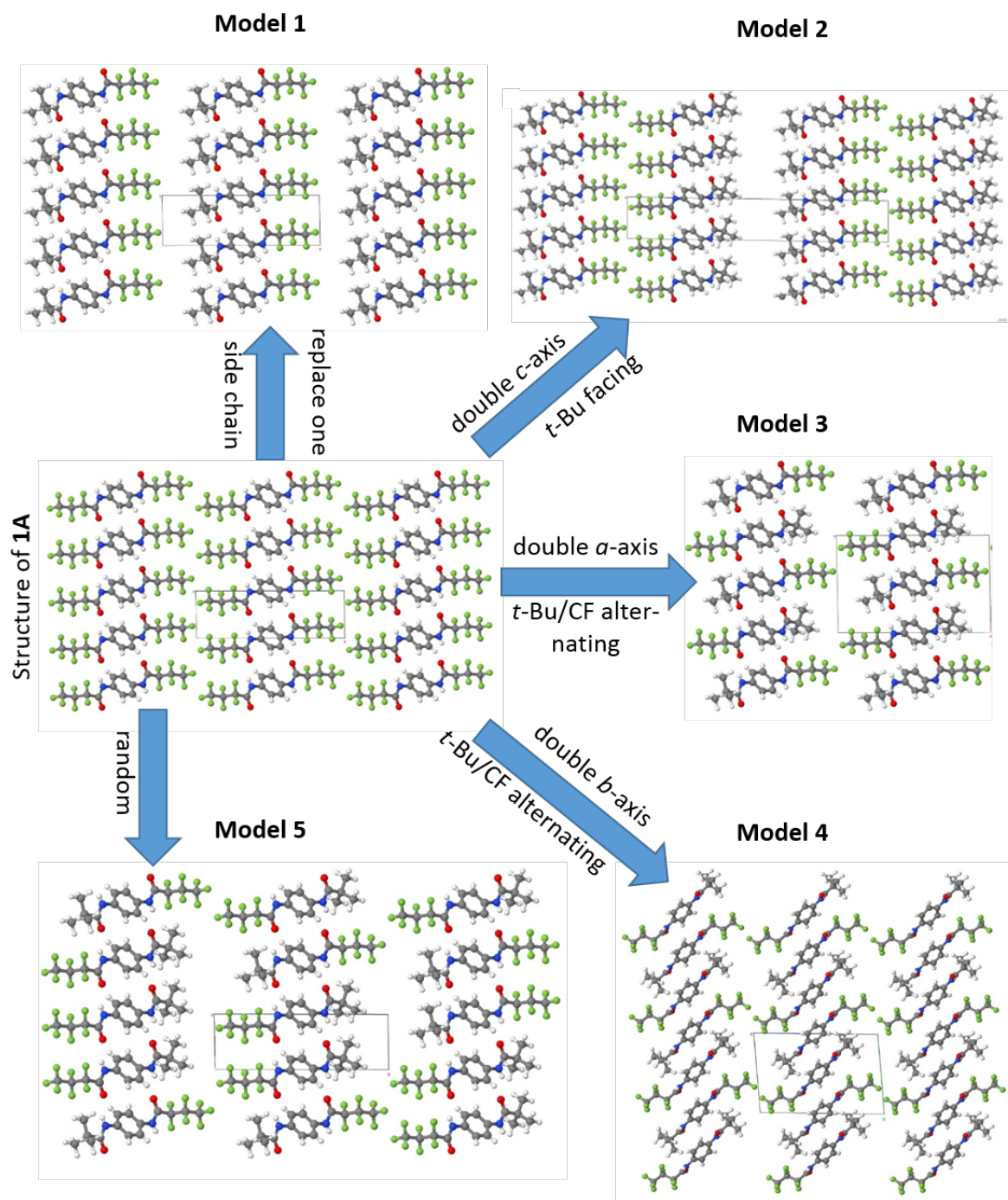


**Figure S9.** Hydrogen bond pattern of series **1** (left) and series **2** (right) in the so-called Etter notation <sup>[2]</sup>. The big black dots resemble molecules and the lines resemble hydrogen bonds. The three small dots represent propagation of the pattern in this direction.

6: Different global packing of **2A** compared to **2B** and **2C**.

**Figure S10.** Difference in the global packing of **2A** (left) and series **2B** and **2C** (right). In the sketch on the bottom the black lines resemble the orientation of the top layer and the grey lines resemble the 2<sup>nd</sup> layer. In red, the symmetry element that determines the space group is depicted.

<sup>[2]</sup> M. C. Etter, *Acc. Chem. Res.* 1990, 23, 120

7: Structure models of **2A** in the structure type of series **1**Figure S11. Possibilities of packing **2A** in the structure of **1A**.

To investigate the driving force that leads to the different structure types models of all molecules were built in the structure of the respective molecule of the other series. Since the molecules of series **1** are symmetric, there is only one way to place them into the unit cells of series **2**. For the asymmetric molecules of series **2**, different options arise as depicted for **2A** in Figure S11. These options are:

Model 1: The space symmetry is reduced from  $P\bar{1}$  to  $P1$  while maintaining the original metric.

One side chain of **1A** is then replaced by a *t*-Bu group. The resulting unit cell consists of one molecule leading to a model where *t*-Bu and the CF groups are facing each other at the interlayer gap.

Model 2: The *c*-axis is doubled creating two molecules within the unit cell. The molecules are placed in a way that similar side chains, the *t*-Bu groups and the fluorinated alkyl chains from neighbouring molecules face each other.

Model 3: The *a*-axis is doubled and the CF chains are replaced by *t*-Bu in a way that they are alternating along the *a*-axis. The unit cell consists of two molecules.

Model 4: The *b*-axis is doubled and the CF chain is replaced by *t*-Bu in a way that they are alternating along the *b*-axis. The unit cell consists of two molecules.

Model 5: Finally, a random combination of all models is possible. Here, however, the unit cell increases dramatically.

For models 1, 2 and 4 the local binding situations around the NH...O hydrogen bonds is similar. In all cases, both the NH and the carbonyl function are terminated by the same side chain. Thus, for the comparison between packing pattern **1** and **2**, both models will lead to the similar results. Model 3 shows a different local environment. Here, the NH and the carbonyl function are terminated by different side chains. Therefore, DFT calculations were restricted to models 1 and 3. They lead to very similar energies per molecules. Doubling one unit cell axis results in an alternating pattern of longer (2.4 Å) and shorter (2.1 Å) hydrogen bond lengths due to the additional degrees of freedom as the molecules are now able to rotate against each other. Model 5 is a superposition of the other models and will show similar results. Thus, for the discussion within the manuscript the smallest model with only one molecule in the asymmetric unit was chosen for the comparison with molecules of series **1** calculated in packing pattern **2**, in order to keep the number of variable parameters similar.

**8: Scanning electron microscopy of self-assembled platelets of symmetric 1,4-benzene bisamides **1B-C** and asymmetric 1,4-benzene bisamides **2B-C****

For the preparation of SEM samples from dispersions, a drop was cast on a clean silicon wafer. The supernatant solvent was removed with a filter paper and the sample was dried at ambient conditions. Subsequently, the sample was sputtered with a platinum layer with a layer thickness of 1.3 nm using a Cressington 208HR sputter coater. SEM measurements were performed with a field emission scanning electron microscope (Zeiss LEO 1530) using an accelerating voltage of 3 kV.

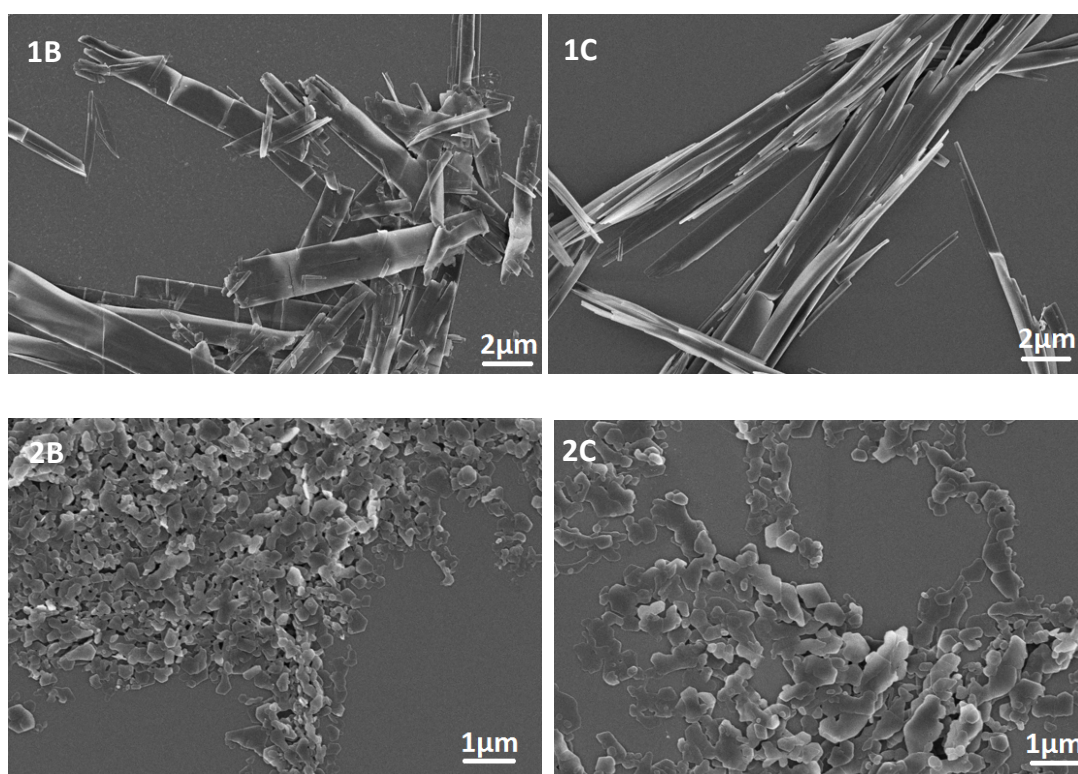


**Figure S12.** Additional SEM image of platelets of symmetric 1,4-benzene bisamides **1B**, **1C** and asymmetric 1,4-benzene bisamides **2B** and **2C**.

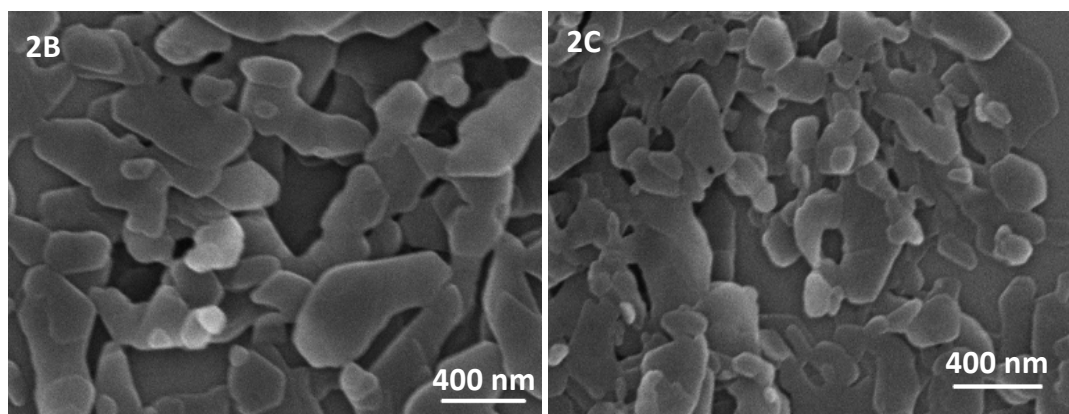


**Figure S13.** Additional SEM of asymmetric 1,4-benzene bisamides **2B** and **2C** with higher magnification.

#### 9: AFM of self-assembled platelets of both series

AFM measurements were performed using a Veeco dimension 3100 atomic force microscope equipped with a NanoScope IV controller. Bruker OTESPA-R3 silicon cantilevers were used in tapping mode. Square images were captured with 512 lines and 512 points per line and evaluated using Bruker NanoScope Analysis software (version 1.40). Prior to analysis, the images were flattened (1<sup>st</sup> order). To analyze the layer terraces, small sections from crystals' top surfaces were used. A step analysis, which considers many parallel lines to reduce noise in z direction, gave a profile of the terraces along the x axis. From this profile, tilts were removed using the evaluation software. Parallel lines were fitted to the different terrace levels and the lines' distance was measured to obtain the terrace heights.

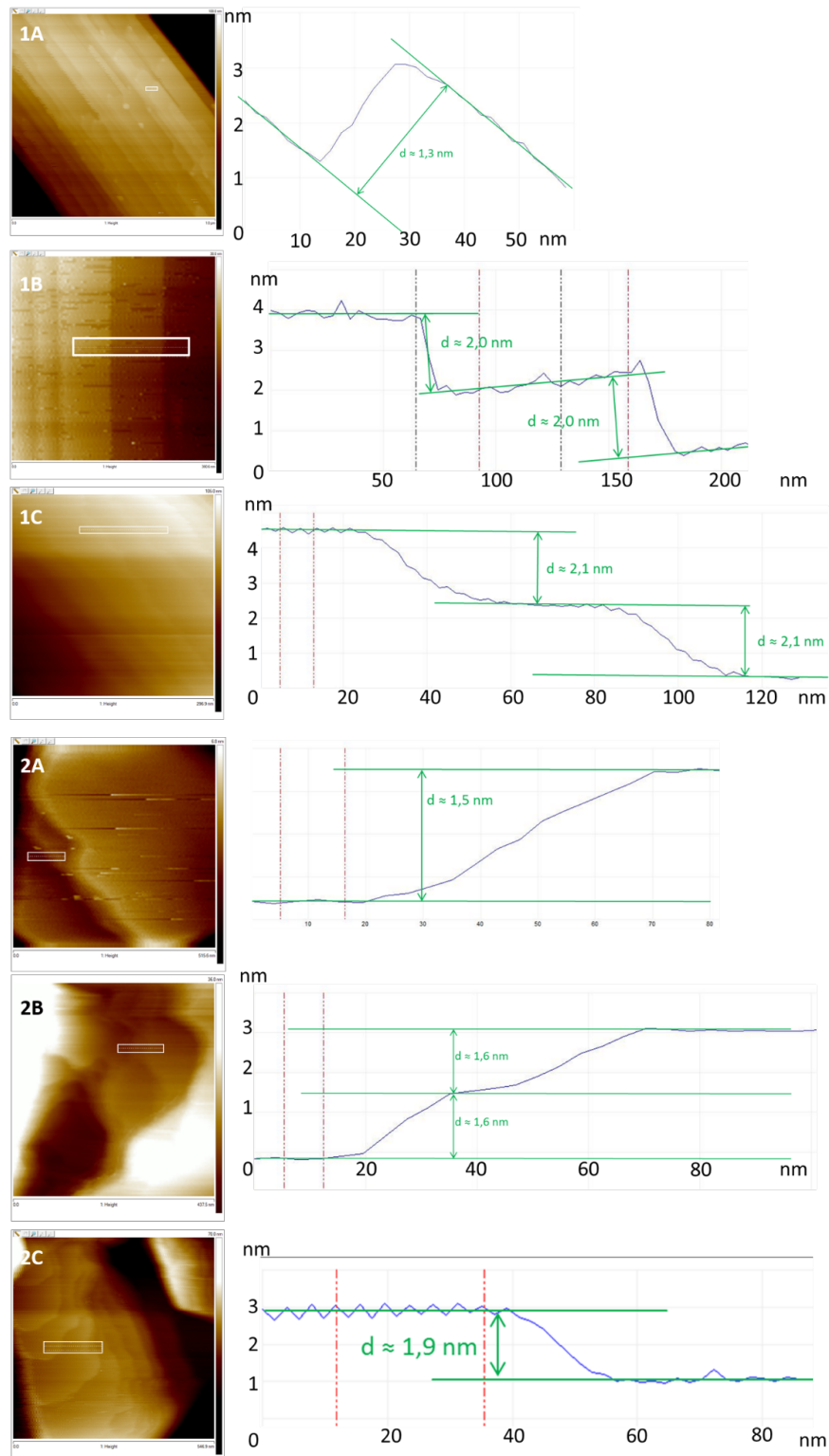


**Figure S14.** Topographical AFM image (left) of a platelet surface based on **1A**, **1B**, **1C**, **2A**, **2B** and **2C** with corresponding height profile (right) of the white rectangle as indicated in the AFM image.

**10: Wetting behavior with water on vapor deposited thin films of symmetric 1,4-benzene bisamides **1A** and asymmetric 1,4-benzene bisamides **2A****

As representative model compounds for their wetting behaviour with water by means of contact angle measurements, the symmetric 1,4-benzene bisamides **1A** and asymmetric 1,4-benzene bisamides **2A** were chosen. Both films were prepared by physical vapour deposition.

Subsequently, contact angles on the flat surfaces of the thin films were determined with the sessile drop method using a Krüss DSA25S drop shape analyzer. For each thin film, the average contact angle of at least five measurement was determined (**Figure S14**). The average contact angle for **1A** was found to be  $114.9^\circ$  and for **2A**  $104.6^\circ$ , respectively.

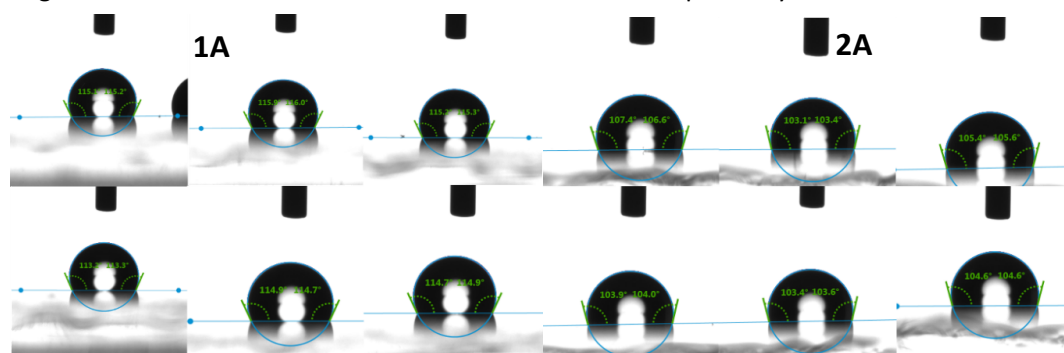


**Figure S15.** Photographs of contact angle measurements on thin films of **1A** (left) and **2A** (right).

## 4.4 Highly Efficient Supramolecular Nucleating Agents for Poly(3-hexylthiophene)

This work is a cooperation between the Inorganic Chemistry III and the Macromolecular Chemistry I at the University of Bayreuth and the Zernike Institute of Advanced Materials of the University of Groningen and will be reprinted with permission from F.A. Wenzel, H. Welz, K.P. van der Zwan, S. Stäter, K. Kreger, R. Hildner, J. Senker, H.-W. Schmidt *Macromolecules* **2022**, *55*, 2861-2871  
Copyright 2022 American Chemical Society

My contributions are:

- conception and authorship of the article with a focus on the paragraphs related to the structure solution
- measuring the X-ray diffractogram and solving the crystal structure
- assisting with the epitaxial concept and arranging the respective Figures

The contributions of the other authors are:

- conception and main authorship of the article
- synthesis of the materials
- recording the polarisation microscope images
- performing the DSC measurements
- performing the photoluminescence measurements

# Macromolecules

pubs.acs.org/Macromolecules

Article

## Highly Efficient Supramolecular Nucleating Agents for Poly(3-hexylthiophene)

Felix A. Wenzel, Hannes Welz, Kasper P. van der Zwan, Sebastian Stäter, Klaus Kreger, Richard Hildner, Jürgen Senker, and Hans-Werner Schmidt\*



Cite This: *Macromolecules* 2022, 55, 2861–2871



Read Online

ACCESS |



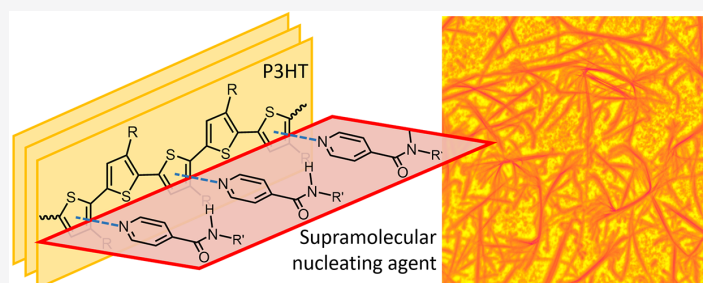
Metrics &amp; More



Article Recommendations



Supporting Information



**ABSTRACT:** Controlling the solid-state morphology of semiconducting polymers is crucial for the function and performance of optoelectronic and photonic devices. Nucleation is a commonly used and straightforward approach to tailor the solid-state morphology of semi-crystalline polymers. However, efficient nucleating agents for semiconducting polymers are still rare. Here, we present a conceptual approach to tailor supramolecular nucleating agents for the semiconducting polymer, poly(3-hexylthiophene) (P3HT). Using this approach, we developed a class of supramolecular nucleating agents, which can achieve outstanding nucleation efficiencies of more than 95% at concentrations as low as 0.1 wt %. Such efficiencies can be achieved by combining an exceptionally high epitaxial match with highly regularly arranged donor–acceptor interactions between the nucleating agent and the polymer. Notably, the supramolecular agents do not induce trap states in thin films of P3HT and are beneficial for the film stability by controlling the solid-state morphology. We anticipate that this approach can be transferred to other semi-crystalline conjugated polymers, resulting in defined solid-state morphologies.

### INTRODUCTION

Semiconducting semi-crystalline polymers are an established class of materials combining polymer science and technology with optoelectronics and photophysics.<sup>1,2</sup> These materials are of particular interest in thin-film architectures processed from solution.<sup>3,4</sup> Controlling the morphology, i.e., the relationship between the highly ordered crystalline domains and the entangled disordered amorphous phase, plays a decisive role in the optical and electronic characteristics and, ultimately, the device performance.<sup>1,4–10</sup> In general, the solid-state morphology can be controlled mainly by changes to the nucleation and crystal growth process. A multitude of approaches have evolved in this context, including thermal<sup>11</sup> and solvent vapor annealing,<sup>12</sup> solvent evaporation control<sup>13</sup> and antisolvent usage,<sup>14</sup> as well as processing additives<sup>15,16</sup> and nucleating agents.<sup>17</sup>

Poly(3-hexylthiophene) (P3HT), is one of the most investigated materials in the field of semiconducting polymers, rendering it an ideal model compound for fundamental studies.<sup>3</sup> In this context, different strategies to achieve morphology control during and after processing were widely

investigated.<sup>4,18</sup> For example, multiple studies employed preformed P3HT nanofiber dispersions to improve device performances,<sup>19,20</sup> especially when the fibers are oriented under flow.<sup>21</sup> Different techniques have been used that include rubbing methods to orient the P3HT films<sup>22,23</sup> or nanostructured surfaces,<sup>24,25</sup> to name just a few. A common approach uses different small molecules as processing aids, such as 1,8-diiodooctane,<sup>26</sup> 4-bromoanisole,<sup>27</sup> or 2-hydroxypyridine.<sup>15</sup> Furthermore, nucleating agents, for example, based on carbon nanotubes,<sup>28</sup> graphene,<sup>29,30</sup> thiophene-containing copolymers,<sup>31,32</sup> as well as sorbitol and benzene-trisamide derivatives,<sup>5,17,33</sup> have been used to modify the crystallization process.

**Received:** November 5, 2021

**Revised:** February 18, 2022

**Published:** March 17, 2022



Heterogeneous nucleation, in general, is highly desirable because it controls the nucleation density during polymer processing.<sup>34,35</sup> As a result, nucleation reduces the average crystal size and size distribution and, in exceptional cases, allows to induce a specific crystal modification. Hence, heterogeneous nucleation can significantly alter the final property profile, including mechanical, electronic, and optical properties.<sup>17,36–39</sup>

Apart from often employed insoluble inorganic compounds such as talc, silica, and mica, supramolecular nucleating agents represent a recently established class of additives relying on the intrinsic reversibility of the structure formation.<sup>36,40</sup> These compounds dissolve at elevated temperatures, ensuring a homogeneous distribution in the polymer melt. Upon cooling, the building blocks self-assemble to highly regular solid nanostructures, which are finely dispersed in the polymer melt and induce polymer crystallization. Thus, these nucleating agents do not require elaborative dispersion additives and procedures.<sup>17,36</sup> For commodity polymers and engineering plastics, the use of inorganic and supramolecular nucleating agents are well investigated and widely established.<sup>41,42</sup> However, tailored and efficient supramolecular nucleating agents for semi-crystalline conjugated polymers are still rare.

Here, we report on a conceptual approach to design supramolecular nucleating agents for the semiconducting polymer, P3HT. We devised a class of molecular building blocks capable of forming supramolecular objects that act as efficient heterogeneous nucleation sites for the crystallization of P3HT. The synthesized series of bisamide building blocks, *N,N'*-1,4-phenylenebis[4-pyridinecarboxamide] (NA 1) to *N*<sup>1</sup>,*N*<sup>4</sup>-di-4-pyridinyl-*trans*-1,4-cyclohexanedicarboxamide (NA 4) is based on symmetrically substituted central units linked via amides to peripheral 4-pyridine units. We systematically varied both the central unit, either 1,4-substituted benzene or *trans*-1,4-cyclohexane, and the arrangement of the amide linkage (see Figure 1A). This design approach combines an attractive interaction between the donor thiophene groups of the polymer and the acceptor moieties of the nucleating agent, with a high epitaxial match encoded in the crystal structure of the nucleating agent (see Figure 1B). We demonstrate that this molecular design achieves excellent nucleation efficiencies for the semi-crystalline polymer P3HT, making it a promising candidate to control the P3HT solid-state morphology.

## EXPERIMENTAL SECTION

**Materials.** All solvents were purified according to standard procedures unless otherwise noted. The synthesis of pyridine-functionalized supramolecular nucleating agents NA 1–NA 4 was conducted by amidation reactions as schematically depicted in the Supporting Information, Section S1. Details on the syntheses, purification, and characterization are given in the Supporting Information, Section S2. Regioregular poly(3-hexylthiophene) (grade: RMI-001-EE) was purchased from Rieke Metals and used as received. It features a weight average molecular weight  $M_w$  of 57 kg mol<sup>-1</sup> and a dispersity  $\bar{D}$  of 2.4 as determined by size exclusion chromatography. Size exclusion chromatography was performed with a Waters HPLC pump 515 and a WATERS 2998 as a UV detector. For separation, a guard column (PL, ResiPore, length: 5 cm, diameter: 0.8 cm) and two analytical columns (PL, ResiPore, length: 30 cm, diameter: 0.8 cm) were used. Tetrahydrofuran (THF) was used as eluent at a flow rate of 0.5 mL min<sup>-1</sup>, and the molecular weight was reported with respect to narrowly distributed polystyrene standards.

Regioregular poly(3-butylthiophene) (grade: 4001-E) and regioregular poly(3-octylthiophene) (grade: 4003-E) were also purchased from Rieke Metals and used as received.

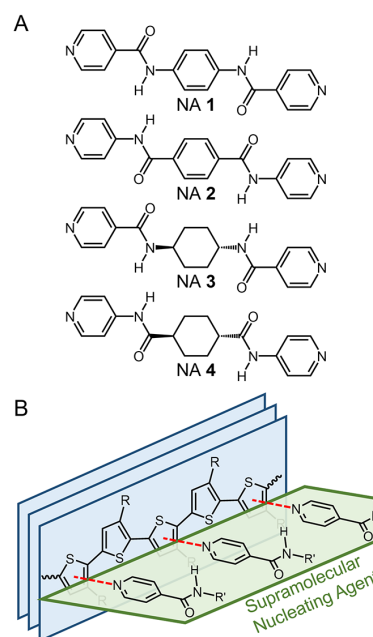


**Figure 1.** (A) Chemical structures of the four supramolecular building blocks: *N,N'*-1,4-phenylenebis[4-pyridinecarboxamide] (NA 1), *N*<sup>1</sup>,*N*<sup>4</sup>-di-4-pyridinyl-1,4-benzenedicarboxamide (NA 2), *N,N'*-*trans*-1,4-cyclohexanediylbis[4-pyridinecarboxamide] (NA 3), and *N*<sup>1</sup>,*N*<sup>4</sup>-di-4-pyridinyl-*trans*-1,4-cyclohexanedicarboxamide (NA 4). The molecules are based on substituted benzene or cyclohexane central unit and peripheral 4-pyridine moieties linked via different arrangements of the amide group. (B) Conceptual approach for supramolecular hydrogen-bonded nanostructures (green) providing efficient heterogeneous nucleation sites for the nucleation of P3HT (blue). We designed the supramolecular nucleating agent featuring an epitaxial match and attractive interactions between the pyridine acceptor moieties of the supramolecular nucleating agent and the thiophene donor moieties of the P3HT (indicated by dashed red lines).

**Differential Scanning Calorimetry.** Differential scanning calorimetry (DSC) was conducted using Mettler Toledo DSC 3<sup>+</sup>. For the preparation of bulk samples, a stock solution with 1 wt % of P3HT was prepared in chlorobenzene by dissolving the polymer at an elevated temperature until a clear solution was obtained. For samples with the different compounds NA 1–NA 4, amounts of 0.01 to 1 wt % with respect to the P3HT weight were dissolved in the stock solution. Prior to the DSC measurements, the solvent was completely removed under vacuum at 100 °C overnight. About 3–10 mg of the dried samples were weighed into the DSC pans and closed with a cover lid. A neat P3HT reference sample was prepared in the same manner by drying the pure stock solution.

**Dynamic Differential Scanning Calorimetry Measurements.** Prior to the dynamic experiments, all samples were heated from 100 to 300 °C under nitrogen and held for 5 min to erase the thermal history. Afterward, a first cooling, second heating, and second cooling run were performed. The cooling and heating rates were always 10 K min<sup>-1</sup>. The values of the second cooling curves are reported. The reported thermal transition temperatures refer to peak temperatures in the DSC thermograms.

**Isothermal Differential Scanning Calorimetry Measurements.** Pretreatment of the sample was performed in a similar manner as described above to erase the thermal history. The sample was heated to 300 °C and held for 5 min at this temperature. It was subsequently cooled with a scan rate of 10 K min<sup>-1</sup> to the isothermal temperature,

i.e., 212, 214, 216, 218, 220, and 222 °C, respectively, and held at this temperature for 60 to 180 min.

**Polarized Light Microscopy.** Polarized light microscopy was performed on a Nikon Invers Diaphot TMD 300 optical microscope. Thin films of neat P3HT and P3HT with 1 wt % of NA 1 were prepared via drop-casting a solution containing 1 wt % of P3HT in chlorobenzene on a glass slide. Contact samples were prepared by depositing a large amount of crystals of NA 1 on top of a thin film of neat P3HT. Temperature-dependent investigations on thin films and contact samples were performed using an HS82 hot-stage system from Mettler Toledo in the temperature range between room temperature and 300 °C under nitrogen flow. Optical micrographs were recorded using a Nikon DS-Ri2 digital camera and Nikon ACT-1 software.

**Structure Elucidation.** Single crystals of NA 1 were prepared by dissolving NA 1 in *N,N*-dimethylformamide (DMF) and exposing the solution to a heptane atmosphere. The heptane slowly diffuses into the DMF solution, and the crystals of NA 1 are formed. The solvents were slowly evaporated, and the larger crystals were collected. Single crystals were investigated using an STOE STADIVARI single-crystal diffractometer with Mo  $K_{\alpha}$  radiation equipped with an Oxford Cryostream low-temperature unit. Data collection, indexing, and space group determination were done with the software package X-area (Stoe). Structure solution and refinement were done with ShelXL,<sup>43</sup> ShelXT,<sup>44</sup> and Olex.<sup>45</sup>

Powder X-ray diffraction data were collected on an STOE STADI P diffractometer equipped with a Ge(111) monochromator using Cu  $K_{\alpha 1}$  radiation. The powder was filled in a 0.5 mm capillary tube and was measured in Debye–Scherrer geometry under ambient conditions. Indexing, simulated annealing, and Rietveld refinement were done with the software package TOPAS.<sup>46</sup>

Geometry optimization was done using the software package CASTEP<sup>47</sup> using the Perdew–Burke–Ernzerhof (PBE) functional and the Tkatchenko–Scheffler<sup>48</sup> dispersion correction scheme. Electronic cut-off energy of 900 eV and a Monkhorst k point grid spacing of 0.07 Å<sup>-1</sup> were used.<sup>49</sup>

Geometric models for the combination of the crystal structures of NA 1 and P3HT were built with Jmol.<sup>50</sup>

**Hyperspectral Imaging.** For hyperspectral imaging, thin films were prepared using solutions with 1 wt % of P3HT in chlorobenzene containing no or 0.1 wt % of NA 1 with respect to the polymer. Thin films were obtained by spin-coating with a Coros OP15 (Siemens) with a CONVAC 1001 onto glass slides at 1000 rpm for 60 s. The samples were heated under an inert atmosphere to 300 °C, held for 15 min at this temperature, and subsequently cooled to room temperature.

Hyperspectral photoluminescence imaging was performed with a home-built microscopy setup. To excite the sample, a pulsed white light laser system with a tunable wavelength filter (NKT SuperK EXTREME EXU-6 PP, SuperK SELECT), tuned to 560 nm, was used. In an inverted epi-illumination microscope layout, the excitation beam passes a 575 nm dielectric short-pass filter (Edmund, 84-709) and reflects off a 580 nm dichroic mirror (Semrock, FF580-FDi01-25 × 36) toward an oil-immersion objective (Olympus, PLAPON60-XOPH UIS2). To achieve widefield illumination, an additional lens in front of the dichroic mirror was inserted. The fluorescence signal is collected by the same objective, which then passes the dichroic mirror and a 568 nm long-pass filter (Semrock, BLP01-568R-25) to suppress residual laser light. The signal is then focused onto the slit of an imaging spectrograph (Princeton Instruments, IsoPlane 160, 150 g mm<sup>-1</sup>) equipped with a cooled electron-multiplying charge-coupled device (emCCD) camera (Andor iXon Ultra 897). In an individual emCCD image, the photoluminescence signal is spectrally dispersed along rows (along the *x*-axis) of the chip, while spatial information is retained along columns, i.e., along the slit (*y*)-axis. The imaging quality of the spectrograph allows to retrieve and analyze 83 spectra along the *y*-axis, which corresponds to a distance of ~40 μm using the magnification of the microscope of 67. After taking an image, the sample was moved by 500 nm in the *x*-direction with a piezo translation stage (piezosystems jena, TRITOR 102 CAP). These steps were repeated until an area of 40 × 40 μm<sup>2</sup> was scanned,

corresponding to a total of 83 × 80 = 6640 individual photoluminescence spectra from each area.

## RESULTS AND DISCUSSION

Apart from the numerous structural motifs which were used to achieve supramolecular (nano)objects and act as nucleating agents, we selected C<sub>2</sub>-symmetrical linear structures such as 1,4-benzenebisamides and 1,4-cyclohexanebisamide derivatives. These compounds are known to form a one-dimensional strand of hydrogen bonds, resulting in platelet or ribbon-like structures on the nano and mesoscale.<sup>51,52</sup> In particular, at least two opposite surfaces in these structures form a very regular and linear sequence of their used side groups, which may serve as nucleation sites for the extended P3HT backbone. For this, we explored a set of supramolecular nucleating agents for the semiconducting polymer, P3HT, consisting of four structurally similar bisamides NA 1–NA 4, each featuring two peripheral 4-pyridine moieties. The chemical structures of the four bisamides are shown in Figure 1A. The central unit of the bisamides is either based on 1,4-substituted benzene or *trans*-1,4-substituted cyclohexane moieties. The central units are connected with the pyridine moieties via different arrangements of amide linkages. These variations not only typically result in slightly different crystallographic parameters but also alter the strength of the directed hydrogen bond pattern. As a result, the thermal properties, as well as the solubility and self-assembly behavior of the molecules in the polymer melt, can be tuned. The syntheses of the four compounds, *N,N'*-1,4-phenylenebis[4-pyridinecarboxamide] (NA 1), *N*<sup>1</sup>,*N*<sup>4</sup>-di-4-pyridinyl-1,4-benzenedicarboxamide (NA 2), *N,N'*-*trans*-1,4-cyclohexanediybis[4-pyridinecarboxamide] (NA 3), and *N*<sup>1</sup>,*N*<sup>4</sup>-di-4-pyridinyl-*trans*-1,4-cyclohexanedicarboxamide (NA 4), were performed via standard amidation reactions. Details on the synthetic route, the synthetic procedure, and the molecular characterization are given in the Supporting Information, Sections S1 and S2. All compounds feature melting points above 300 °C. These high phase transitions are required because dissolution and self-assembly of the compounds in the polymer melt strongly depend on, for instance, molecular structure, medium, concentration, and processing temperature. At elevated temperatures, the mandatory dissolution of the compounds to a molecular level in the P3HT melt results in a single homogeneous phase. Under appropriate conditions, this also allows for the self-assembly of well-dispersed solid nanoobjects before the polymer crystallization occurs.

The most common method to evaluate the performance of supramolecular nucleating agents is based on bulk studies of a polymer crystallization process. Here, the nucleating agents are evaluated using the difference ( $\Delta T_c$ ) between the maximum achievable crystallization temperature  $T_{c,max}$  and the standard crystallization temperature  $T_{c0}$  of the neat polymer.<sup>53</sup> Standard crystallization temperatures  $T_{c0}$  are commonly obtained by dynamic differential scanning calorimetry (DSC) experiments. The maximal achievable crystallization temperature  $T_{c,max}$  can be determined by self-nucleation experiments, as described in the literature.<sup>54</sup> In such self-nucleation experiments, a dynamic temperature protocol is used to melt the polymer partially. Tiny polymer crystals remain in the melt. These crystals eventually act as excellent nucleation sites for polymer crystallization because they have the same chemical composition and a perfectly epitaxial matching surface. For our studies, we selected the commercial P3HT grade RMI-001-EE

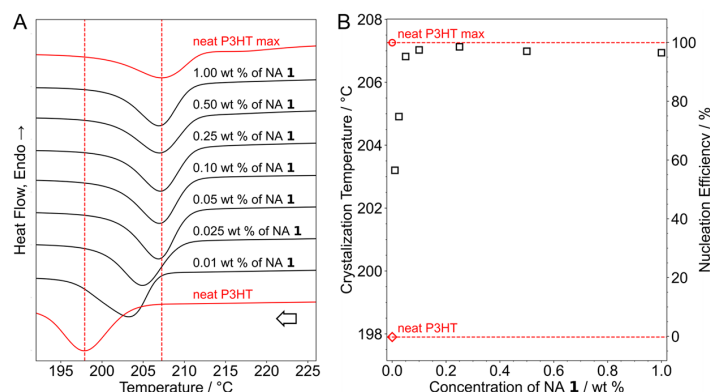


**Figure 2.** (A) Second DSC cooling curves of the standard and self-nucleated crystallization of neat P3HT (in red) and P3HT with NA 1 in the concentration range from 0.01 to 1 wt % (in black). The addition of NA 1 to P3HT shifts the polymer crystallization peak increasingly closer toward  $T_{c,max}$  demonstrating the outstanding performance of this nucleation agent for P3HT. (B) Peak minima of the P3HT polymer crystallization and nucleation efficiency as a function of the concentration of NA 1. The standard and self-nucleated crystallization temperatures for neat P3HT are shown as the lower and upper limits (in red).

(see Materials section). This polymer has a  $T_{c,max}$  of 207.3 °C and a  $T_{c,0}$  of 197.9 °C, resulting in a  $\Delta T_c$  of 9.4 °C (Supporting Information, Section S3). This  $\Delta T_c$  value provides a sufficiently large window to determine the nucleation efficiency of our supramolecular nucleating agents.

We have performed a series of dynamic DSC experiments using P3HT and the supramolecular building blocks NA 1–NA 4 at different additive concentrations ranging from 0.01 to 1 wt %. In Figure 2A, the corresponding second DSC cooling scans comprising the polymer crystallization of P3HT with NA 1 at different concentrations as well as the neat and self-nucleated P3HT are shown. Details on the experimental procedure and DSC thermograms of NA 2–NA 4 are presented in the Supporting Information, Section S4. The crystallization peak of P3HT notably shifts to higher temperatures at very low concentrations of NA 1 of only 0.01 wt %. With an increasing amount of NA 1, the shift rapidly approaches a constant value close to the maximal achievable crystallization temperature  $T_{c,max}$  of P3HT. A more straightforward presentation is provided by plotting the corresponding peak crystallization temperatures, as depicted in Figure 2B. For example, the addition of only 0.01 wt % of NA 1 already increases the crystallization temperature by 6.2 to 204.1 °C. The addition of 0.1 wt % of NA 1 increases the crystallization temperature of P3HT already by 9.2 to 207.1 °C, which is only slightly lower than the maximal achievable crystallization temperature  $T_{c,max}$  of 207.3 °C.

Based on these values, the nucleation efficiency (NE) according to Lotz and Wittman was determined.<sup>53</sup> The nucleation efficiency is defined as the ratio of two temperature differences, namely, the crystallization temperature of the nucleated sample ( $T_c$ ) to the standard crystallization of the neat polymer ( $T_{c,0}$ ) and the self-nucleated sample ( $T_{c,max}$ ) to the standard crystallization temperature (eq 1).

$$NE = \frac{T_c - T_{c,0}}{T_{c,max} - T_{c,0}} \quad (1)$$

In this situation,  $T_{c,0}$  represents the lower limit, and  $T_{c,max}$  correlates to the upper limit of the crystallization temperature. Thus, it provides a measure to quantify and compare different nucleating agents with respect to their nucleation performance.

Figure 3 displays the nucleation efficiencies of all four nucleating agents as a function of concentration. Already at

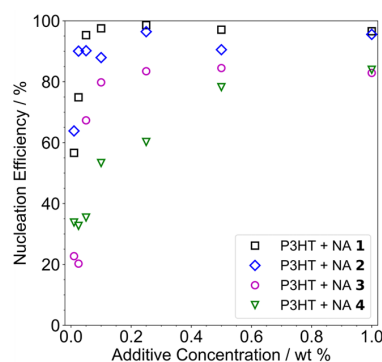


**Figure 3.** Nucleation efficiencies as a function of additive concentration: NA 1 (black squares), NA 2 (blue diamonds), NA 3 (magenta circles), and NA 4 (green triangles). Already at low concentrations, all four nucleating agents increase the polymer crystallization temperature significantly. NA 1 features an outstanding P3HT nucleation efficiency of 98% at already a concentration of 0.1 wt %.

concentrations of 0.1 wt %, all nucleating agents feature a significant nucleation efficiency of more than 50%. At a concentration of 0.5 wt %, the nucleating agents feature efficiencies of more than 75%. In general, with increasing concentration, the nucleation efficiency saturates and reaches a plateau. This plateau is very close to 100% for NA 1 and NA 2, and in the case of NA 3 and NA 4, still above 80%. In particular, the bisamides based on benzene as the central unit, NA 1 and NA 2, exhibit outstanding performance at concentrations of 0.1 wt %. To the best of our knowledge, the determined nucleation efficiency of 98% for NA 1 at a concentration of 0.1 wt % is the highest reported value for the nucleation of P3HT. Therefore, we have focused in the following on this supramolecular nucleating agent, NA 1.

With isothermal DSC measurements, it is possible to investigate the influence of nucleating agents on the

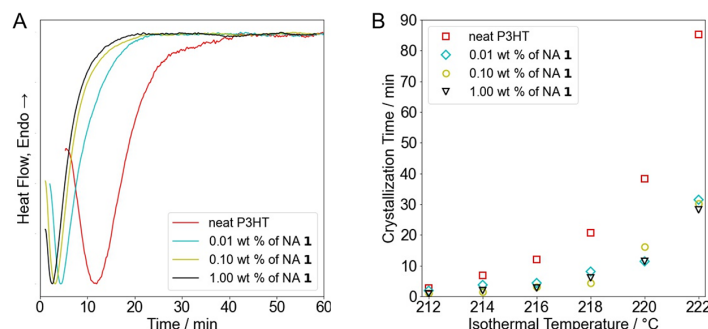


**Figure 4.** (A) Isothermal crystallization curves at 216 °C for 1 h for neat P3HT and P3HT with different concentrations of NA 1. The heat flow is normalized to the minima of each sample and the baseline value at 60 min. (B) Time to reach the enthalpic minimum of the respective crystallization peaks at different isothermal temperatures. With increasing isothermal temperature, the time to reach the minimum is prolonged. In all cases, the addition of NA 1 results in a significant reduction of the crystallization time.

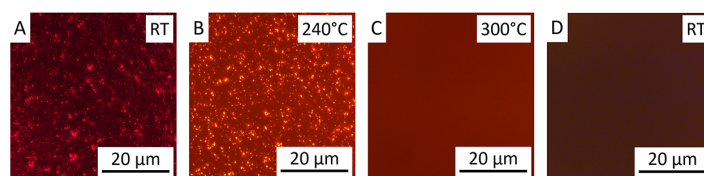


**Figure 5.** Optical light micrographs between crossed polarizers of P3HT films with 1 wt % of NA 1 before the first melting at RT (A) and after P3HT melts at 240 °C (B). The birefringence in panels A and B is caused by the crystals of NA 1. Upon further heating to 300 °C (C), NA 1 dissolves in the P3HT melt, visible by the disappearance of the birefringence. Cooling back to room temperature (D) results only in a uniform color change.

crystallization kinetics of the polymer by providing a tunable number of nucleation sites at a constant polymer crystallization growth rate. We performed isothermal DSC studies for different neat P3HT and P3HT with 0.01, 0.1, and 1.0 wt % of NA 1. Exemplarily, DSC curves for such experiments at 216 °C, a temperature well above the standard crystallization temperature  $T_{c,0}$ , are depicted in Figure 4A. At these conditions, the enthalpic minimum for the neat P3HT is close to 12 min. Already with 0.01 wt % of NA 1, the P3HT crystallization significantly accelerates, resulting in an enthalpic minimum at 4.3 min. Higher concentrations of NA 1 further reduce this time to 3.2 min with 0.1 wt % and to 2.6 min for the sample with 1.0 wt % of NA 1. This data shows that even at low concentrations, NA 1 acts as an efficient nucleating agent, which is in line with the previous results for nucleation efficiencies. The isothermal DSC curves do not cover the entire crystallization process for the samples. Analyzing these data by the Avrami crystallization kinetic model is not applicable.<sup>55</sup>

As a qualitative guide for the kinetics of the crystallization process, we plotted the times to reach the minima of the crystallization enthalpy as a function of the isothermal temperature (Figure 4B). Expectedly, with increasing isothermal temperature, the crystallization time increases.<sup>33</sup> Notably, the crystallization times for the different concentrations of NA 1 at each temperature are essentially the same, demonstrating the effectiveness of the nucleating agent even at low concentrations. Moreover, the absolute difference between the P3HT samples with NA 1 and the neat P3HT becomes more significantly pronounced with an increasing isothermal temperature. For instance, at a high temperature of 222 °C, the enthalpic minima of the P3HT crystallization with NA 1 are reached within approximately 30 min, whereas for the neat

P3HT, 85 min are required. In all cases shown in Figure 4B, the addition of NA 1 reduces the time to reach the enthalpic minimum by a factor of about three compared to the neat P3HT.

In a typical approach, the nucleation and crystallization process of semi-crystalline polymers with supramolecular nucleating agents is visualized by temperature-dependent polarized light microscopy. Here, we used polarized light microscopy to particularly demonstrate the homogeneous distribution of nanoscale supramolecular objects in a thin film of P3HT. For this, we prepared a drop-casted film comprising P3HT and 1 wt % of NA 1 crystals (see Figure 5). At room temperature (Figure 5A), the film shows birefringent features of finely dispersed NA 1 crystals. During heating to 240 °C, the P3HT starts to melt, as shown by the color change of the film, whereas the birefringent features are still present at this temperature (Figure 5B). Upon further heating to 300 °C, these structures vanish (Figure 5C), demonstrating the dissolution of NA 1 and its homogeneous distribution in the polymer melt. Upon cooling to room temperature, only a uniform color change of the thin film is observed, which is attributed to the crystallization of P3HT (Figure 5D). The absence of the birefringent structures indicates that supramolecular aggregates of NA 1 are finely dispersed with a size significantly below the diffraction limit of the optical light microscope.

In fact, the formation of supramolecular objects of NA 1 upon cooling can be seen with dynamic DSC experiments. Figure 6 shows dynamic DSC cooling curves using P3HT with different concentrations of NA 1 in the temperature range from 290 to 190 °C. The mixture comprising P3HT and 1 wt % of NA 1 shows a small but distinct exothermic peak at 274 °C, which is attributed to the crystallization of NA 1 in the

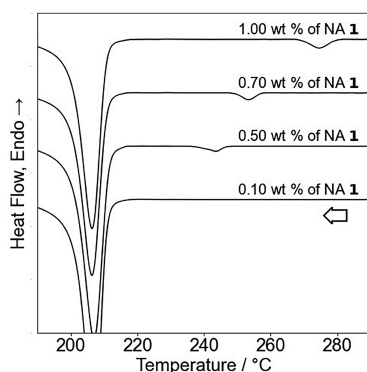


**Figure 6.** DSC cooling curves from 290 to 190 °C of P3HT with different concentrations of NA 1 (1.0, 0.7, 0.5, and 0.1 wt %). The samples with high concentrations of NA 1 feature an exothermic peak at elevated temperatures, which is attributed to the crystallization of NA 1. The position of this peak shifts to lower temperatures, and the integral of this peak decrease with decreasing NA 1 concentration. All four DSC curves show a strong exothermic peak at about 207 °C, which is attributed to the crystallization of P3HT.

P3HT melt. This exothermic peak shifts for the sample with a lower concentration of 0.7 wt % of NA 1 to 253 °C. A further shift to lower temperatures of 244 °C is observed for the sample with only 0.5 wt % of NA 1. Furthermore, the integral of these exothermic peaks also decreases as expected with decreasing additive concentration. The formation of supramolecular objects takes place in the melt clearly before P3HT starts to crystallize. Upon cooling, these three samples show a strong exothermic peak at about 207 °C, which is attributed to the crystallization of P3HT. For the concentration of 0.1 wt % of NA 1, no exothermic peak for NA 1 was detected due to the low concentration and the sensitivity of the instrument. However, supramolecular objects, which act as heterogeneous nucleation sites, are present because the crystallization of P3HT also takes place at about 207 °C, well above the standard crystallization temperature  $T_{c,0}$ .

All data clearly suggests that self-assembly to solid objects of NA 1 must be present, giving rise to a nucleation effect. We note that as shown in Figure 5 above, the dimensions of the *in situ* formed supramolecular objects are well below the optical diffraction limit, and thus, the objects must be on the nanoscale. Since it is difficult to visualize the shape and size of these objects within the bulk film of P3HT by, e.g., electron microscopy, we visualize the trans-crystallization process of P3HT onto the nucleating agent by investigating contact samples. Contact samples were prepared by placing a large amount of  $\mu\text{m}$ -sized crystals of NA 1 on top of a P3HT film. The temperature-dependent crystallization behavior was studied by polarized light microscopy. These samples were heated to 240 °C. At this temperature, the P3HT is completely molten without dissolving the crystals of NA 1, as already shown in Figure 5B. Upon cooling to 230 °C, only birefringent structures of NA 1 are present on top of the melt of P3HT, as shown in Figure 7A. Upon further cooling to 200 °C, additional birefringent features are formed, which occur close to the solid fiber-like structures of NA 1 (Figure 7B). This finding can be clearly assigned to the trans-crystallization process of P3HT on the nucleating agents. An additional series of micrographs under crossed polarizers showing a more

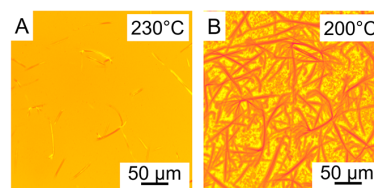


**Figure 7.** Optical light micrographs between crossed polarizers with a lambda-quarter plate of contact samples comprising fiber-like  $\mu\text{m}$ -sized objects of NA 1 on a thin film of P3HT. (A) At 230 °C, the P3HT film is molten, and birefringent structures of NA 1 are visible. (B) Upon cooling to 200 °C, trans-crystallization of P3HT from the structures of NA 1 takes place.

detailed picture of the process is depicted in the Supporting Information, Section S5. Further evidence is provided by performing similar contact sample experiments using *N,N'*-1,4-phenylenebisbenzamide as a reference. This compound is very similar to that of NA 1, but performing experiments revealed no additional birefringence, i.e., no trans-crystallization (see Supporting Information, Section S6).

To understand how the surface of NA 1 can nucleate P3HT on a molecular level, X-ray diffraction experiments were performed to elucidate the crystal structure of NA 1, and the results were correlated with the crystal structure of P3HT. Single-crystal X-ray diffraction of NA 1 yielded a first structure model with the space group *PI*. However, the unit cell parameters show a pseudo-monoclinic setting, and the structure model featured structural imperfections. Therefore, additional powder X-ray diffraction (PXRD) measurements were performed. Indexing of the powder X-ray diffractogram yielded a monoclinic unit cell in the space group *P*<sub>2</sub>1/*c*. The model obtained from the single-crystal X-ray analysis was geometry-optimized by density functional theory (DFT) and placed in the unit cell obtained from PXRD. This model was refined using the Rietveld method, yielding a good agreement between the measured and simulated diffractogram as demonstrated by a small weighted discrepancy factor ( $R_{wp}$ ) of 6.51%. The powder X-ray diffractogram is given in the Supporting Information, Section S7. Analyzing the results, we found that NA 1 crystallizes with one molecule in the asymmetric unit, leading to four molecules in the unit cell. The relevant crystallographic data are shown in the Supporting Information, Section S8.

The packing of the molecules along the *c*-axis and in the *ab*-plane (001) is shown in the Supporting Information, Section S9. Characteristic of the packing pattern is a hydrogen bond motif, where one molecule is connected to two other molecules by four hydrogen bonds. Consequently, the hydrogen bonds form a ribbon along the crystallographic *c*-axis. In each molecule, the pyridine rings are tilted by 70° toward the central benzene ring. The benzene rings of the molecules in neighboring ribbons along the *b*-axis are tilted by 60°, and only weak interactions between the molecules are present along the *a*-axis. Furthermore, Figure 8 provides a closer look at the packing by focusing on the *bc*-surface (100) of NA 1. This surface features highly regular pyridine moieties along the *b*-axis, with the nitrogen atom facing outward.

Important for heterogeneous nucleation is an epitaxial match between the nucleating agent and the semi-crystalline polymer. For comparison, Table 1 provides the unit cell parameters of the crystal structures of NA 1 and P3HT.<sup>56</sup> In P3HT, the *c*-

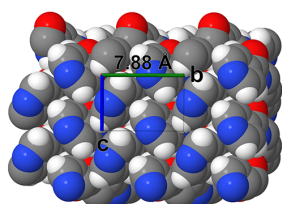


**Figure 8.** View on top of the  $bc$ -plane (100) of NA 1. The spacing along the  $b$ -axis (green) of 7.88 Å is shown. The surface features a highly regular arrangement of the pyridine moieties, with the nitrogen atoms facing outward.

direction represents the direction of the polymer backbone, which has a characteristic periodic distance of 7.8 Å. In NA 1, a periodic distance of 7.88 Å was found in the  $b$ -direction corresponding to the distance between neighboring nitrogen atoms of pyridine units of two molecules. This distance fits about 99% to the  $c$ -directions of the P3HT unit cell, demonstrating an excellent epitaxial match between the nucleating agent NA 1 and P3HT.

We also conducted nucleation experiments with P3HT using structurally very similar bisamides, where the pyridine moieties are replaced by benzene or cyclohexane groups. These reference compounds are  $N,N'$ -1,4-phenylenebisbenzamide,  $N^1,N^4$ -diphenyl-1,4-benzenedicarboxamide, and  $N^1,N^4$ -dicyclohexyl-1,4-benzenedicarboxamide (see Supporting Information, Section S10). Due to their structural similarities, they are expected to be highly efficient supramolecular nucleating agents for P3HT as well. In particular, the crystal structure of  $N,N'$ -1,4-phenylenebisbenzamide<sup>57</sup> shows the same packing pattern as NA 1 and also features a repeating distance of 7.88 Å, which matches the  $c$ -direction of P3HT (see Supporting Information, Section S10). However, the DSC experiments of the reference compounds at an additive concentration of 1 wt % reveal no or only a poor performance concerning the nucleation of P3HT. The fact that NA 1 is more efficient at a concentration two orders of magnitude lower than these reference compounds makes its performance even more impressive. Furthermore, these results strongly suggest that an epitaxial match alone is insufficient to achieve high nucleation performances in P3HT.

To explain why NA 1 exhibits such an outstanding nucleation performance, we combined the crystal structures of the nucleating agent NA 1 and P3HT. For this, we cleaved the crystallographic surface of NA 1 along the  $bc$ -plane (100) and positioned an extended P3HT chain from the crystal structure,<sup>56</sup> as depicted in Figure 9. The representation reveals that the nitrogen atoms of the pyridine units of the crystal structure of NA 1 can be arranged precisely with the centers of every second thiophene moiety along the P3HT backbone. This periodic sequence provides an attractive donor–acceptor interaction between the pyridine and the thiophene units. Thus, we conclude that the combination of the perfect donor–

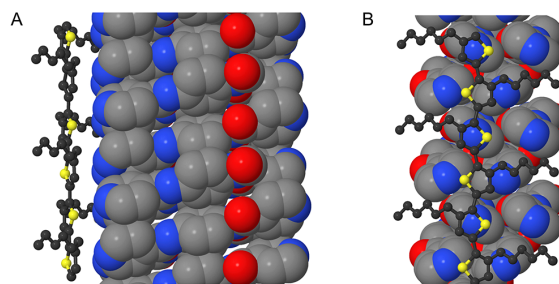


**Figure 9.** Geometric model combining the crystal structures of P3HT,<sup>56</sup> as depicted in a ball-and-stick model, and NA 1, as depicted in a space-filling model. In both cases, the hydrogens are omitted for clarity. (A) View is on top of the  $ab$ -plane (001) of NA 1. (B) View is rotated by 90° and is now on top of the  $bc$ -plane (100) of NA 1. As depicted, the center of every second thiophene group almost perfectly matches the distance of the nitrogen atoms of the pyridine groups of NA 1.

acceptor interactions with the high epitaxial match between the nucleating agent and the polymer backbone is responsible for the outstanding nucleation efficiency of NA 1 with respect to P3HT.<sup>9</sup>

These data suggest that the P3HT crystallization proceeds perpendicularly to the  $bc$  surface of the nucleating agents. Consequently, the formation of P3HT lamella can be expected, resulting in a similar superstructure, as shown by multiple research groups.<sup>56,58–60</sup> The isolation and use of such so-called shish-kebab superstructures might be beneficial for directed energy or charge transport along the crystalline lamella of the P3HT.<sup>61</sup>

We also experimentally demonstrated the applicability of this nucleation concept to other poly(3-alkylthiophenes) such as poly(3-butylthiophene), P3BT, and poly(3-octylthiophene), P3OT. These polymers are chemically similar to P3HT but differ in their solubility and thermal behavior due to the different lengths of their aliphatic side groups. As shown in Supporting Information, Section S11, NA 1 is also a highly effective nucleating agent for P3BT and P3OT. We found that with 1 wt % of NA 1, an outstanding nucleation efficiency of 98% for P3BT was obtained. For P3OT, a nucleation efficiency of 94% was obtained already at a concentration of only 0.1 wt %. These results also indicate that varying the length of the aliphatic side chain plays only a minor role in nucleation.

Photoluminescence imaging is a tool to assess the homogeneity of a film and its optical properties on microscopic scales. Therefore, we prepared a P3HT film with NA 1 and a neat P3HT film via spin-coating and employed a comparable temperature protocol as used in the previous DSC experiments. We collected spatially resolved photoluminescence (PL) spectra from a  $40 \times 40 \mu\text{m}^2$  area of both films, each data set comprising 6640 individual spectra. Figure 10A shows the averaged and normalized PL spectra. Both averaged spectra

**Table 1.** Unit Cell Parameters for the Crystal Structure of P3HT from Literature and NA 1, as Obtained by PXRD in This Work

	space group	$a$ [Å]	$b$ [Å]	$c$ [Å]	$\alpha$ [°]	$\beta$ [°]	$\gamma$ [°]
P3HT <sup>a</sup>	$P2_1/c$	16	7.8	7.8	90	90	86.5
NA 1 <sup>b</sup>	$P2_1/c$	35.4581(27)	7.8848(3)	5.2719(3)	90	90	99.792(6)

<sup>a</sup>Values taken from reference.<sup>56</sup> <sup>b</sup>As obtained by PXRD in this work.

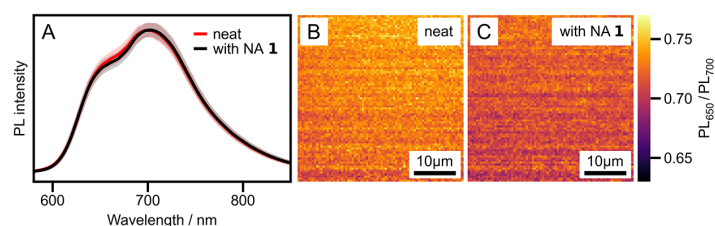


**Figure 10.** Hyperspectral imaging of thin films of neat P3HT and P3HT with NA 1. (A) PL spectra of a neat P3HT film (red) and a P3HT film with 0.1 wt % NA 1 (black). Both PL spectra are averaged over an area of  $40 \times 40 \mu\text{m}^2$  comprising 6640 individual spectra. The shaded area shows the degree of variation within the films. (B, C) Maps of the PL-ratio  $PL_{650}/PL_{700}$  for the neat P3HT film (B) and for the P3HT film with 0.1 wt % NA 1 (C).

feature the characteristic shape of P3HT film spectra with a weaker electronic 0–0 PL transition around 650 nm compared to the 0–1 transition at around 700 nm. Yet, the film with NA 1 shows a slightly more suppressed 0–0 PL transition, indicating a slight reduction of the intra-aggregate disorder of P3HT<sup>62</sup> when crystallized in the presence of a nucleating agent. From the individual spectra, we then extracted the ratio between the PL intensities at 650 and 700 nm (indicated by the arrows),  $PL_{650}/PL_{700}$ , and visualized it as maps in Figure 10B,C. On the length scale of the optical resolution limit ( $<300$  nm), we detect no considerable variation of the ratio of  $PL_{650}/PL_{700}$  within both P3HT films, indicating that NA 1 is uniformly distributed, and the nucleation has occurred homogeneously within the film. Moreover, the PL spectra of P3HT films with NA 1 are slightly red-shifted with respect to neat P3HT films (Supporting Information, Section S12), indicating a slightly higher order of aggregates<sup>62</sup> and thus a slightly more controlled P3HT crystallization in the presence of the nucleating agent. Notably, the integrated PL signal from P3HT films with NA 1 increased by ca. 8% compared to that from neat P3HT films. This observation indicates that the nucleating agent does not introduce trap states quenching the PL. The optical homogeneity of the film is further confirmed by hyperspectral absorption imaging (Supporting Information, Section S13), which is in agreement with the previously discussed results of our polarized light microscopy data, where we observe no birefringent structures of NA 1 (see also Figure 5D). These data also suggest that these supramolecular nucleating agents can be used to prepare P3HT-based thin-film architectures without introducing microscale inhomogeneities by applying proper processing protocols.

Our observations during spatially resolved hyperspectral photoluminescence measurements suggest that in thin films of P3HT with NA 1, the supramolecular nucleating agent does not induce trap states in P3HT that quench PL. To further elucidate the role of the nucleating agents in thin-film architectures, we have prepared thin films of neat P3HT and P3HT with 0.1 and 1 wt % of NA 1 on organic field effect transistors (OFET) silicon substrates and studied their film stability and their charge carrier mobility.

To investigate the film stability, all films were treated in the same manner, including a heating step to 300 °C after spin-coating and subsequent cooling to room temperature under an inert atmosphere. Under these conditions, we found that thin films of neat P3HT feature a significant surface roughness, which also comprises microcracks (Supporting Information, Section S14). This is in strong contrast to thin films of P3HT with 0.1 or 1 wt % of NA 1. With increasing concentration of NA 1, the homogeneity of the surface is maintained, and

microcracks are not observed. Such findings may be attributed to the presence of networks of solid supramolecular objects of NA 1. These networks are most likely formed upon rapid self-assembly when initiating the cooling step and may be beneficial in preserving the initial thin-film architecture.

Moreover, we measured the charge carrier mobilities<sup>63</sup> in the OFET geometry at room temperature using thin films of P3HT with and without NA 1, which we determined from the transfer characteristics (Supporting Information, Section S15). After spin-coating, drying, heating to 300 °C, and cooling to room temperature, we found no significant difference in mobility between these films, indicating that the supramolecular nucleating agents do not act as traps for the charge carriers in P3HT-based OFETs. Interestingly, after a 4-week storage of the devices at room temperature, we found a further drop in the charge carrier mobility of the OFET for thin films with the neat P3HT, whereas the charge carrier mobilities for the devices with 0.1 and 1 wt % of NA 1 remain constant. This demonstrates the beneficial role of the nucleating agents during aging of the device, which may be attributed to a stabilized solid-state morphology.

## CONCLUSIONS

We presented a successful approach for tailored supramolecular nucleating agents to induce the polymer crystallization of the family of semiconducting poly(3-alkylthiophenes). This approach combines a high epitaxial match with highly regular attractive interactions between the donor thiophene moieties of the polymer and the pyridine acceptor moieties of the nucleating agent.

We demonstrated that symmetrically substituted bisamides with peripheral 4-pyridine moieties are highly efficient supramolecular nucleating agents for poly(3-alkylthiophenes). By structure elucidation, we revealed supramolecular nucleating agents feature a directed hydrogen ribbon pattern and surfaces with highly regular arrangements of the pyridine moieties. These regular arrangements are responsible for the donor–acceptor interactions, as demonstrated for P3HT. With the best nucleating agent, we achieved outstanding nucleation efficiencies of 98% at a low concentration of 0.1 wt %. We also showed the applicability of this supramolecular nucleating agent to other poly(3-alkylthiophenes) such as P3BT and P3OT, leading to nucleation efficiencies of more than 90% for both polymers.

Moreover, spatially resolved hyperspectral photoluminescence measurements suggest that in thin films of P3HT with NA 1, the supramolecular nucleating agent does not induce trap states that quench photoluminescence. Similar results were found in OFETs, where the charge carrier mobility

remains constant upon increasing the concentration of NA 1 and upon aging of films. Our data therefore suggest that the use of these supramolecular nucleating agents is beneficial to control the solid-state morphology of P3HT films.

We anticipate that this approach can be transferred to design highly efficient supramolecular nucleating agents for other semi-crystalline semiconducting polymers. Such nucleating agents may ultimately allow controlling the processing and the morphology of thin-film architectures, thus optimizing the optical and electronic properties of conjugated polymers and leading to more reproducible device fabrications.

## ■ ASSOCIATED CONTENT

### SI Supporting Information

The Supporting Information is available free of charge at <https://pubs.acs.org/doi/10.1021/acs.macromol.1c02283>.

Synthesis and characterization of the nucleating agents, the self-nucleation experiment, further dynamic DSC studies, temperature-dependent polarized light microscopy studies, the elucidation and visualization of the crystal structure of NA 1, DSC studies with reference compounds, DSC studies with different poly(3-alkylthiophenes), and further information about the hyper-spectral imaging. The crystal structure data of NA 1 is deposited at the Cambridge Crystallographic Data Centre with the deposition number 2103040 (PDF)

## ■ AUTHOR INFORMATION

### Corresponding Author

Hans-Werner Schmidt – *Macromolecular Chemistry I and Bavarian Polymer Institute, University of Bayreuth, 95447 Bayreuth, Germany*; [orcid.org/0000-0002-1761-1153](https://orcid.org/0000-0002-1761-1153); Email: [hans-werner.schmidt@uni-bayreuth.de](mailto:hans-werner.schmidt@uni-bayreuth.de)

### Authors

Felix A. Wenzel – *Macromolecular Chemistry I and Bavarian Polymer Institute, University of Bayreuth, 95447 Bayreuth, Germany*

Hannes Welz – *Macromolecular Chemistry I and Bavarian Polymer Institute, University of Bayreuth, 95447 Bayreuth, Germany*

Kasper P. van der Zwan – *Inorganic Chemistry III, University of Bayreuth, 95447 Bayreuth, Germany*; [orcid.org/0000-0003-3568-5129](https://orcid.org/0000-0003-3568-5129)

Sebastian Stäter – *Zernike Institute for Advanced Materials, University of Groningen, 9747 AG Groningen, The Netherlands*

Klaus Kreger – *Macromolecular Chemistry I and Bavarian Polymer Institute, University of Bayreuth, 95447 Bayreuth, Germany*; [orcid.org/0000-0003-3021-1311](https://orcid.org/0000-0003-3021-1311)

Richard Hildner – *Zernike Institute for Advanced Materials, University of Groningen, 9747 AG Groningen, The Netherlands*; [orcid.org/0000-0002-7282-3730](https://orcid.org/0000-0002-7282-3730)

Jürgen Senker – *Inorganic Chemistry III, University of Bayreuth, 95447 Bayreuth, Germany*; [orcid.org/0000-0002-7278-7952](https://orcid.org/0000-0002-7278-7952)

Complete contact information is available at: <https://pubs.acs.org/doi/10.1021/acs.macromol.1c02283>

## Author Contributions

The manuscript was written through contributions of all authors. All authors have given approval to the final version of the manuscript.

## Notes

The authors declare no competing financial interest.

## ■ ACKNOWLEDGMENTS

The authors acknowledge financial support from the Bavarian State Ministry of Science and the Arts through the Collaborative Research Network “Solar Technologies go Hybrid” and by the German Research Foundation (DFG), Project Number 79971943: Collaborative Research Center SFB 840, Project B4. The authors also acknowledge support by the Elite Network of Bavaria (ENB) through the study program “Macromolecular Science” (F.A.W., K.P.v.d.Z.). The authors are grateful to Sandra Ganzleben (Macromolecular Chemistry, University of Bayreuth) for her help with the synthesis of the additives. The authors thank Florian Meissner (Macromolecular Chemistry, University of Bayreuth) for help with the SEC measurement and Robin Freitag (Inorganic Chemistry II, University of Bayreuth) for the assistance in setting up the single-crystal X-ray measurement. The authors thank Adrian Hochgesang and Prof. Mukundan Thelakkat for their support with OFET device fabrication and valuable discussions. The authors acknowledge the KeyLab Device Engineering of the Bavarian Polymer Institute, the University of Bayreuth, for support.

## ■ REFERENCES

- (1) Noriega, R.; Rivnay, J.; Vandewal, K.; Koch, F. P. V.; Stingelin, N.; Smith, P.; Toney, M. F.; Salleo, A. A general relationship between disorder, aggregation and charge transport in conjugated polymers. *Nat. Mater.* **2013**, *12*, 1038–1044.
- (2) Botiz, I.; Durbin, M. M.; Stingelin, N. Providing a Window into the Phase Behavior of Semiconducting Polymers. *Macromolecules* **2021**, *54*, 5304–5320.
- (3) Ludwigs, S. *P3HT Revisited – From Molecular Scale to Solar Cell Devices*; Springer Berlin Heidelberg: 2014; Vol. 265.
- (4) Brinkmann, M. Structure and morphology control in thin films of regioregular poly(3-hexylthiophene). *J. Polym. Sci., Part B: Polym. Phys.* **2011**, *49*, 1218–1233.
- (5) Diao, Y.; Shaw, L.; Bao, Z.; Mannsfeld, S. C. B. Morphology control strategies for solution-processed organic semiconductor thin films. *Energy Environ. Sci.* **2014**, *7*, 2145–2159.
- (6) Hildner, R.; Köhler, A.; Müller-Buschbaum, P.; Panzer, F.; Thelakkat, M.  $\pi$ -Conjugated Donor Polymers: Structure Formation and Morphology in Solution, Bulk and Photovoltaic Blends. *Adv. Energy Mater.* **2017**, *7*, No. 1700314.
- (7) Zhao, F.; Wang, C.; Zhan, X. Morphology Control in Organic Solar Cells. *Adv. Energy Mater.* **2018**, *8*, No. 1703147.
- (8) Choi, D.; Chang, M.; Reichmanis, E. Controlled Assembly of Poly(3-hexylthiophene): Managing the Disorder to Order Transition on the Nano- through Meso-Scales. *Adv. Funct. Mater.* **2015**, *25*, 920–927.
- (9) Lee, H.; Park, C.; Sin, D. H.; Park, J. H.; Cho, K. Recent Advances in Morphology Optimization for Organic Photovoltaics. *Adv. Mater.* **2018**, *30*, No. 1800453.
- (10) Dolynchuk, O.; Schmode, P.; Fischer, M.; Thelakkat, M.; Thurn-Albrecht, T. Elucidating the Effect of Interfacial Interactions on Crystal Orientations in Thin Films of Polythiophenes. *Macromolecules* **2021**, *54*, 5429–5439.
- (11) Verploegen, E.; Mondal, R.; Bettinger, C. J.; Sok, S.; Toney, M. F.; Bao, Z. Effects of Thermal Annealing Upon the Morphology of Polymer-Fullerene Blends. *Adv. Funct. Mater.* **2010**, *20*, 3519–3529.

- (12) Verploegen, E.; Miller, C. E.; Schmidt, K.; Bao, Z.; Toney, M. F. Manipulating the Morphology of P3HT–PCBM Bulk Heterojunction Blends with Solvent Vapor Annealing. *Chem. Mater.* **2012**, *24*, 3923–3931.
- (13) Goto, O.; Tomiya, S.; Murakami, Y.; Shinozaki, A.; Toda, A.; Kasahara, J.; Hobara, D. Organic single-crystal arrays from solution-phase growth using micropattern with nucleation control region. *Adv. Mater.* **2012**, *24*, 1117–1122.
- (14) Minemawari, H.; Yamada, T.; Matsui, H.; Tsutsumi, J.; Haas, S.; Chiba, R.; Kumai, R.; Hasegawa, T. Inkjet printing of single-crystal films. *Nature* **2011**, *475*, 364–367.
- (15) Xu, B.; Sai-Anand, G.; Unni, G. E.; Jeong, H.-M.; Kim, J.-S.; Kim, S.-W.; Kwon, J.-B.; Bae, J.-H.; Kang, S.-W. Pyridine-based additive optimized P3HT:PC61BM nanomorphology for improved performance and stability in polymer solar cells. *Appl. Surf. Sci.* **2019**, *484*, 825–834.
- (16) Stingelin-Stutzmann, N.; Smits, E.; Wondergem, H.; Tanase, C.; Blom, P.; Smith, P.; Leeuw, D. de. Organic thin-film electronics from vitreous solution-processed rubrene hypereutectics. *Nat. Mater.* **2005**, *4*, 601–606.
- (17) Treat, N. D.; Nekuda Malik, J. A.; Reid, O.; Yu, L.; Shuttle, C. G.; Rumbles, G.; Hawker, C. J.; Chabiny, M. L.; Smith, P.; Stingelin, N. Microstructure formation in molecular and polymer semiconductors assisted by nucleation agents. *Nat. Mater.* **2013**, *12*, 628–633.
- (18) Persson, N. E.; Chu, P.-H.; McBride, M.; Grover, M.; Reichmanis, E. Nucleation, Growth, and Alignment of Poly(3-hexylthiophene) Nanofibers for High-Performance OFETs. *Acc. Chem. Res.* **2017**, *50*, 932–942.
- (19) McBride, M.; Bacardi, G.; Morales, C.; Risteen, B.; Keane, D.; Reichmanis, E.; Grover, M. A. Control of Nucleation Density in Conjugated Polymers via Seed Nucleation. *ACS Appl. Mater. Interfaces* **2019**, *11*, 37955–37965.
- (20) Oh, J. Y.; Shin, M.; Lee, T. I.; Jang, W. S.; Min, Y.; Myoung, J.-M.; Baik, H. K.; Jeong, U. Self-Seeded Growth of Poly(3-hexylthiophene) (P3HT) Nanofibrils by a Cycle of Cooling and Heating in Solutions. *Macromolecules* **2012**, *45*, 7504–7513.
- (21) Chu, P.-H.; Kleinhenz, N.; Persson, N.; McBride, M.; Hernandez, J. L.; Fu, B.; Zhang, G.; Reichmanis, E. Toward Precision Control of Nanofiber Orientation in Conjugated Polymer Thin Films: Impact on Charge Transport. *Chem. Mater.* **2016**, *28*, 9099–9109.
- (22) Hamidi-Sakr, A.; Biniek, L.; Fall, S.; Brinkmann, M. Precise Control of Lamellar Thickness in Highly Oriented Regioregular Poly(3-Hexylthiophene) Thin Films Prepared by High-Temperature Rubbing: Correlations with Optical Properties and Charge Transport. *Adv. Funct. Mater.* **2016**, *26*, 408–420.
- (23) Untilova, V.; Biskup, T.; Biniek, L.; Vijayakumar, V.; Brinkmann, M. Control of Chain Alignment and Crystallization Helps Enhance Charge Conductivities and Thermoelectric Power Factors in Sequentially Doped P3HT:F4TCNQ Films. *Macromolecules* **2020**, *53*, 2441–2453.
- (24) Brinkmann, M.; Contal, C.; Kayunkid, N.; Djuric, T.; Resel, R. Highly Oriented and Nanotextured Films of Regioregular Poly(3-hexylthiophene) Grown by Epitaxy on the Nanostructured Surface of an Aromatic Substrate. *Macromolecules* **2010**, *43*, 7604–7610.
- (25) Johnston, D. E.; Yager, K. G.; Hlaing, H.; Lu, X.; Ocko, B. M.; Black, C. T. Nanostructured surfaces frustrate polymer semiconductor molecular orientation. *ACS Nano* **2014**, *8*, 243–249.
- (26) Reichenberger, M.; Baderschneider, S.; Kroh, D.; Grauf, S.; Köhler, J.; Hildner, R.; Köhler, A. Watching Paint Dry: The Impact of Diiodooctane on the Kinetics of Aggregate Formation in Thin Films of Poly(3-hexylthiophene). *Macromolecules* **2016**, *49*, 6420–6430.
- (27) Liu, X.; Huettner, S.; Rong, Z.; Sommer, M.; Friend, R. H. Solvent additive control of morphology and crystallization in semiconducting polymer blends. *Adv. Mater.* **2012**, *24*, 669–674.
- (28) Dias, Y.; Yerushalmi-Rozen, R. Entropic effects in carbon nanotubes-templated crystallization of Poly(3-alkyl thiophenes, P3HT, P3OT). *Polymer* **2013**, *54*, 6399–6405.
- (29) Acevedo-Cartagena, D. E.; Zhu, J.; Trabanino, E.; Pentzer, E.; Emrick, T.; Nonnenmann, S. S.; Briseno, A. L.; Hayward, R. C. Selective Nucleation of Poly(3-hexyl thiophene) Nanofibers on Multilayer Graphene Substrates. *ACS Macro Lett.* **2015**, *4*, 483–487.
- (30) Yang, Z.; Lu, H. Nonisothermal crystallization behaviors of poly(3-hexylthiophene)/reduced graphene oxide nanocomposites. *J. Appl. Polym. Sci.* **2013**, *128*, 802–810.
- (31) Bechara, R.; Leclerc, N.; Lévêque, P.; Richard, F.; Heiser, T.; Hadziioannou, G. Efficiency enhancement of polymer photovoltaic devices using thieno-thiophene based copolymers as nucleating agents for polythiophene crystallization. *Appl. Phys. Lett.* **2008**, *93*, No. 013306.
- (32) Deribew, D.; Pavlopoulou, E.; Fleury, G.; Nicolet, C.; Renaud, C.; Mougner, S.-J.; Vignau, L.; Cloutet, E.; Brochon, C.; Cousin, F.; Portale, G.; Geoghegan, M.; Hadziioannou, G. Crystallization-Driven Enhancement in Photovoltaic Performance through Block Copolymer Incorporation into P3HT:PCBM Blends. *Macromolecules* **2013**, *46*, 3015–3024.
- (33) Yuan, N.; Huo, H. 1,2,3,4-Bis(p-methylbenzylidene sorbitol) accelerates crystallization and improves hole mobility of poly(3-hexylthiophene). *Nanotechnology* **2016**, *27*, No. 06LT01.
- (34) Wang, B.; Utzeri, R.; Castellano, M.; Stagnaro, P.; Müller, A. J.; Cavallo, D. Heterogeneous Nucleation and Self-Nucleation of Isotactic Polypropylene Microdroplets in Immiscible Blends: From Nucleation to Growth-Dominated Crystallization. *Macromolecules* **2020**, *53*, 5980–5991.
- (35) Gahleitner, M.; Grein, C.; Kheirandish, S.; Wolfschwenger, J. Nucleation of Polypropylene Homo- and Copolymers. *Int. Polym. Process.* **2011**, *26*, 2–20.
- (36) Blumenhofer, M.; Ganzleben, S.; Hanft, D.; Schmidt, H.-W.; Kristiansen, M.; Smith, P.; Stoll, K.; Mäder, D.; Hoffmann, K. “Designer” Nucleating Agents for Polypropylene. *Macromolecules* **2005**, *38*, 3688–3695.
- (37) Liu, L.; Zhao, Y.; Zhang, C.; Dong, Z.; Wang, K.; Wang, D. Morphological Characteristics of  $\beta$ -Nucleating Agents Governing the Formation of the Crystalline Structure of Isotactic Polypropylene. *Macromolecules* **2021**, *54*, 6824–6834.
- (38) Kersch, M.; Schmidt, H.-W.; Altstadt, V. Influence of different beta-nucleating agents on the morphology of isotactic polypropylene and their toughening effectiveness. *Polymer* **2016**, *98*, 320–326.
- (39) Yue, Y.; Yi, J.; Wang, L.; Feng, J. Toward a More Comprehensive Understanding on the Structure Evolution and Assembly Formation of a Bisamide Nucleating Agent in Polypropylene Melt. *Macromolecules* **2020**, *53*, 4381–4394.
- (40) Kristiansen, M.; Werner, M.; Tervoort, T.; Smith, P.; Blumenhofer, M.; Schmidt, H.-W. The Binary System Isotactic Polypropylene/Bis(3,4-dimethylbenzylidene)sorbitol: Phase Behavior, Nucleation, and Optical Properties. *Macromolecules* **2003**, *36*, 5150–5156.
- (41) Karger-Kocsis, J.; Bárány, T. *Polypropylene Handbook [electronic resource]: Morphology, Blends and Composites*; Karger-Kocsis, J.; Bárány, T., Eds.; Springer, 2019.
- (42) Zweifel, H.; Maier, R. D.; Schiller, M. *Plastics Additives Handbook*, 6th ed.; Hanser Publications, 2009.
- (43) Sheldrick, G. M. Crystal structure refinement with SHELXL. *Acta Crystallogr., Sect. C: Struct. Chem.* **2015**, *71*, 3–8.
- (44) Sheldrick, G. M. SHELXT - integrated space-group and crystal-structure determination. *Acta Crystallogr., Sect. A: Found. Crystallogr.* **2015**, *71*, 3–8.
- (45) Dolomanov, O. V.; Bourhis, L. J.; Gildea, R. J.; Howard, J. A. K.; Puschmann, H. OLEX2: a complete structure solution, refinement and analysis program. *J. Appl. Crystallogr.* **2009**, *42*, 339–341.
- (46) Coelho, A. A. TOPAS and TOPAS-Academic: an optimization program integrating computer algebra and crystallographic objects written in C++. *J. Appl. Crystallogr.* **2018**, *51*, 210–218.
- (47) Clark, S. J.; Segall, M. D.; Pickard, C. J.; Hasnip, P. J.; Probert, M. I. J.; Refson, K.; Payne, M. C. First principles methods using CASTEP. *Z. Kristallogr. - Cryst. Mater.* **2005**, *220*, 567–570.

- (48) Tkatchenko, A.; Scheffler, M. Accurate molecular van der Waals interactions from ground-state electron density and free-atom reference data. *Phys. Rev. Lett.* **2009**, *102*, No. 073005.
- (49) Monkhorst, H. J.; Pack, J. D. Special points for Brillouin-zone integrations. *Phys. Rev. B* **1976**, *13*, 5188–5192.
- (50) Jmol: an open-source Java viewer for chemical structures in 3D. <http://www.jmol.org/> (accessed 2022-3-14).
- (51) Schmidt, M.; Zehe, C. S.; Siegel, R.; Heigl, J. U.; Steinlein, C.; Schmidt, H.-W.; Senker, J. NMR-crystallographic study of two-dimensionally self-assembled cyclohexane-based low-molecular-mass organic compounds. *CrystEngComm* **2013**, *15*, 8784.
- (52) Zwan, K. P.; Steinlein, C.; Kreger, K.; Schmidt, H.-W.; Senker, J. Crystal Engineering of Supramolecular 1,4-Benzene Bisamides by Side-Chain Modification - Towards Tuneable Anisotropic Morphologies and Surfaces. *ChemPhysChem* **2021**, *22*, 2585–2593.
- (53) Fillon, B.; Thierry, A.; Lotz, B.; Wittmann, J. C. Efficiency scale for polymer nucleating agents. *J. Therm. Anal.* **1994**, *42*, 721–731.
- (54) Fillon, B.; Wittmann, J. C.; Lotz, B.; Thierry, A. Self-nucleation and recrystallization of isotactic polypropylene ( $\alpha$  phase) investigated by differential scanning calorimetry. *J. Polym. Sci., Part B: Polym. Phys.* **1993**, *31*, 1383–1393.
- (55) Lorenzo, A. T.; Arnal, M. L.; Albuerno, J.; Müller, A. J. DSC isothermal polymer crystallization kinetics measurements and the use of the Avrami equation to fit the data: Guidelines to avoid common problems. *Polym. Test.* **2007**, *26*, 222–231.
- (56) Brinkmann, M.; Rannou, P. Effect of Molecular Weight on the Structure and Morphology of Oriented Thin Films of Regioregular Poly(3-hexylthiophene) Grown by Directional Epitaxial Solidification. *Adv. Funct. Mater.* **2007**, *17*, 101–108.
- (57) Cheng, N.; Yan, Q.; Liu, S.; Zhao, D. Probing the intermolecular interactions of aromatic amides containing N-heterocycles and triptycene. *CrystEngComm* **2014**, *16*, 4265–4273.
- (58) Brinkmann, M.; Chandezon, F.; Pansu, R. B.; Julien-Rabant, C. Epitaxial Growth of Highly Oriented Fibers of Semiconducting Polymers with a Shish-Kebab-Like Superstructure. *Adv. Funct. Mater.* **2009**, *19*, 2759–2766.
- (59) Zhang, X.; Yuan, N.; Ding, S.; Wang, D.; Li, L.; Hu, W.; Bo, Z.; Zhou, J.; Huo, H. Growth and carrier-transport performance of a poly(3-hexylthiophene)/1,2,3,4-bis(p-methylbenzylidene) sorbitol hybrid shish-kebab nanostructure. *J. Mater. Chem. C* **2017**, *5*, 3983–3992.
- (60) Liu, J.; Zou, J.; Zhai, L. Bottom-up Assembly of Poly(3-hexylthiophene) on Carbon Nanotubes: 2D Building Blocks for Nanoscale Circuits. *Macromol. Rapid Commun.* **2009**, *30*, 1387–1391.
- (61) Kreger, K.; Schmidt, H.-W.; Hildner, R. Tailoring the excited-state energy landscape in supramolecular nanostructures. *Electron. Struct.* **2021**, *3*, No. 023001.
- (62) Spano, F. C.; Clark, J.; Silva, C.; Friend, R. H. Determining exciton coherence from the photoluminescence spectral line shape in poly(3-hexylthiophene) thin films. *J. Chem. Phys.* **2009**, *130*, No. 074904.
- (63) Krauss, G.; Meichsner, F.; Hochgesang, A.; Mohanraj, J.; Salehi, S.; Schmode, P.; Thelakkat, M. Polydiketopyrrolopyrroles Carrying Ethylene Glycol Substituents as Efficient Mixed Ion-Electron Conductors for Biocompatible Polydiketopyrrolopyrroles Carrying Ethylene Glycol Substituents as Efficient Mixed Ion-Electron Conductors for Biocompatible Organic Electrochemical Transistors. *Adv. Funct. Mater.* **2021**, *31*, No. 2010048.

Supporting Information to

# Highly Efficient Supramolecular Nucleating Agents for Poly(3-hexylthiophene)

*Felix A. Wenzel<sup>1</sup>, Hannes Welz<sup>1</sup>, Kasper P. van der Zwan<sup>2</sup>, Sebastian Stäter<sup>3</sup>, Klaus Kreger<sup>1</sup>,*

*Richard Hildner<sup>3</sup>, Jürgen Senker<sup>2</sup>, Hans-Werner Schmidt<sup>\*1</sup>*

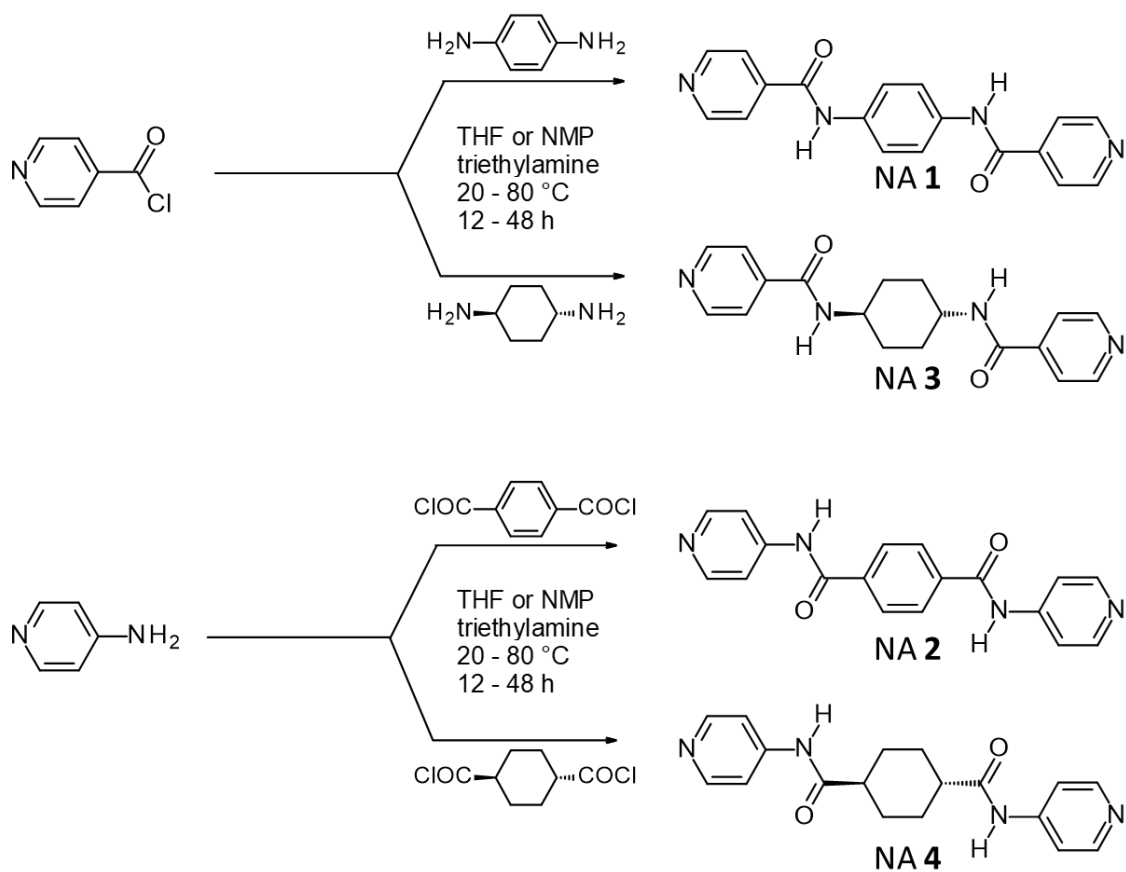
<sup>1</sup>Macromolecular Chemistry I and Bavarian Polymer Institute, University of Bayreuth,  
Universitätsstraße 30, 95447 Bayreuth, Germany.

<sup>2</sup>Inorganic Chemistry III, University of Bayreuth, Universitätsstraße 30, 95447 Bayreuth,  
Germany.

<sup>3</sup>Zernike Institute for Advanced Materials, University of Groningen, Nijenborgh 4, 9747 AG  
Groningen, The Netherlands.

**Table of contents**

- S1. Synthetic routes to pyridine-functionalized *trans*-1,4-cyclohexane- and 1,4-benzene-bisamides NA **1** – NA **4**
- S2. Synthetic procedures and characterization of pyridine-functionalized *trans*-1,4-cyclohexane- and 1,4-benzene-bisamides NA **1** – NA **4**
- S3. Self-nucleation studies of P3HT
- S4. Dynamic crystallization studies of P3HT with supramolecular nucleating agents NA **2** – NA **4**
- S5. Temperature-dependent polarized light microscopy
- S6. Powder X-ray diffractogram of NA **1**
- S7. Unit cell and relevant crystallographic information of NA **1**
- S8. Visualization of the crystal packing of NA **1**
- S9. Dynamic crystallization studies of P3HT with reference compounds
- S10. Applicability of this class of nucleation agents to other poly(3-alkylthiophenes)
- S11. Hyperspectral imaging of neat P3HT and P3HT with NA **1**

**S1. Synthetic routes to pyridine-functionalized *trans*-1,4-cyclohexane- and 1,4-benzene-bisamides NA 1 – NA 4**

**Figure S1.** Schematic representation of the synthetic routes to pyridine-functionalized *trans*-1,4-cyclohexane- and 1,4-benzene-bisamides NA 1 – NA 4.

## S2. Synthetic procedures and characterization of pyridine-functionalized *trans*-1,4-cyclohexane- and 1,4-benzene-bisamides NA 1 – NA 4

### *Molecular characterization*

<sup>1</sup>H-NMR spectra in solution were recorded on a Bruker Avance Ultrashield 300 (300 MHz) at room temperature. For the preparation of the NMR samples, approx. 5 mg of the compounds were dissolved in 1.2 mL of DMSO-d<sub>6</sub>.

Mass spectra (MS) were carried out on a FINNIGAN MAT 8500 spectrometer from Thermo-Fisher Scientific using electron spray ionization.

Infrared (IR) spectra were recorded on a PerkinElmer Spectrum 100 FT-IR spectrometer in ATR mode in the range from 4000 cm<sup>-1</sup> to 650 cm<sup>-1</sup>.

Melting points (Mp) of the as-synthesized compounds were determined with a melting point system MP 90 from Mettler Toledo. Approx. 10 mg of the compounds were filled in a measuring tube. Data were recorded with a heating rate of 10 K·min<sup>-1</sup> in a temperature range from 30 °C to 400 °C. Melting points were determined at the transmission of 5 %. Three measurements were performed simultaneously, and the mean value of the measurements was reported.

### *Synthesis of N,N'-1,4-phenylene bis[4-pyridinecarboxamide] NA 1 (CAS: 55119-42-1)*

5.0 g of 1,4-phenylenediamine and 50 ml of triethylamine were placed in a Schlenk flask together with 300 mL of dried tetrahydrofuran under nitrogen. 18.87 g of isonicotinoyl chloride hydrochloride was then added under ice-cooling. The reaction was stirred and refluxed for 48 hours. The solvents were removed, and the crude product was recrystallized in DMSO. The resulting powder was filtered off and washed with acetone. Finally, the product was dissolved in DMSO and precipitated in water. The product was washed with acetone and dried under vacuum, yielding 48% of a whitish powder.

<sup>1</sup>H-NMR (DMSO-d<sub>6</sub>, δ in ppm): 10.55 (2H, s); 8.74-8.84 (4H, m); 7.83-7.93 (4H, m); 7.78 (4H, s).

MS (m/z in %): 318 (100, [M]<sup>+</sup>); 240 (12); 212 (12); 106 (99); 78 (84); 51 (20).

IR (ν̄ in cm<sup>-1</sup>): 3330; 1645; 1545; 1520; 1410.

Mp: >300°C.

### *Synthesis of N<sup>1</sup>,N<sup>4</sup>-di-4-pyridinyl-1,4-benzenedicarboxamide NA 2 (CAS: 216079-39-9)*

2.53 g of 4-aminopyridine, 10 mL of triethylamine, and approx. 10 mg of LiCl were placed in a Schlenk flask together with 50 mL of N-methylpyrrolidone under nitrogen. 2.53 g of terephthaloyl dichloride was then added under ice-cooling. The reaction mixture was stirred at 80 °C for 48 hours. After cooling to room

temperature, the mixture was precipitated in ice water. The solid was filtered off and then dissolved in a small amount of dimethylsulfoxide and precipitated again in 500 mL of water. The final product was dried at 60 °C under a high vacuum yielding 54% of a greyish powder.

<sup>1</sup>H-NMR (DMSO-d<sub>6</sub>, δ in ppm): 10.77 (2H, s); 8.51 (4H, dd); 8.13 (4H, s); 7.81 (4H, dd).

MS (m/z in %): 318 (72, [M]<sup>+</sup>); 225 (100); 198 (25); 104 (45); 76 (23).

IR (ν̄ in cm<sup>-1</sup>): 1689; 1593; 1513; 1418; 1328.

Mp: >300°C.

*Synthesis of N,N'-trans-1,4-cyclohexanediyl bis[4-pyridinecarboxamide] NA 3 (CAS: 306766-51-8)*

1.0 g of trans-cyclohexane-1,4-diamine, 10 mL of triethylamine, and approximately 10 mg of LiCl were placed in a Schlenk flask together with 100 mL of dried THF under nitrogen. 3.42 g of isonicotinoyl chloride hydrochloride was then added under ice-cooling. The reaction mixture was stirred at room temperature for 48 hours. The mixture was precipitated in ice water; the solid was filtered off and dried. The crude product was then recrystallized in 30 mL of DMSO, filtered, and dried under a high vacuum to obtain a white powder in 27% yield.

<sup>1</sup>H-NMR (DMSO-d<sub>6</sub>, δ in ppm): 8,72 (4H, dd); 8,59 (2H, d); 7,74 (4H, dd); 3,65-2,90 (2H, m); 1,80- 2,05 (4H, m); 1,35-1,60 (4H, m).

MS (m/z in %): 324 (6, [M]<sup>+</sup>); 218 (15); 202 (100); 123 (99); 106 (95); 78 (75); 51 (20).

IR (ν̄ in cm<sup>-1</sup>): 3312; 2947; 1640; 1529; 1490; 1412.

Mp: >300°C.

*Synthesis of N<sup>l</sup>,N<sup>t</sup>-di-4-pyridinyl-trans-1,4-cyclohexanedicarboxamide NA 4 (CAS: 1367879-00-2)*

2.31 g of 4-aminopyridine, 10 mL of triethylamine, and LiCl were placed in a Schlenk flask to a mixture of 50 mL of N-methylpyrrolidone and 100 mL of tetrahydrofuran under nitrogen. 2.34 g of trans-cyclohexane-1,4-dicarbonyl dichloride was then added under ice-cooling. The reaction mixture was stirred at room temperature for 12 hours and subsequently precipitated in ice water. The solid was filtered off and dried in a vacuum. The crude product was recrystallized DMSO, filtered off, and dried under vacuum to get a white powder in 64% yield.

<sup>1</sup>H-NMR (DMSO-d<sub>6</sub>, δ in ppm): 10.29 (2H, s); 8.40 (4H, dd); 8.57 (4H, dd); 2.25-2.45 (2H, m); 1.80- 2.10 (4H, m); 1.35-1.60 (4H, m).

MS (m/z in %): 324 (51, [M]<sup>+</sup>); 231 (16); 203 (100); 121 (52); 95 (77); 81 (43).

IR (ν̄ in cm<sup>-1</sup>): 1695; 1594; 1512; 1418; 1376.

Mp: >300°C.

### S3. Self-nucleation studies of P3HT

The maximal achievable crystallization temperature utilizing the own P3HT crystal as an ideal nucleation site can be revealed by self-nucleation studies utilizing dynamic DSC experiments. In a typical procedure, the sample is heated with  $10 \text{ K min}^{-1}$  to a maximal temperature, which is at the upper end of the melting range to maintain tiny P3HT crystals and is subsequently isothermally held for 5 min. Afterward, the sample was cooled down to  $150^\circ\text{C}$  with  $10 \text{ K min}^{-1}$ . Here,  $248^\circ\text{C}$  was selected as the maximal heating temperature. The maximal temperature was decreased by one Kelvin steps for each following scan. The last measurement was conducted with  $239^\circ\text{C}$  as maximal temperature. The resulting cooling curves for the self-nucleation measurements and standard cooling curves are shown in Figure S2.

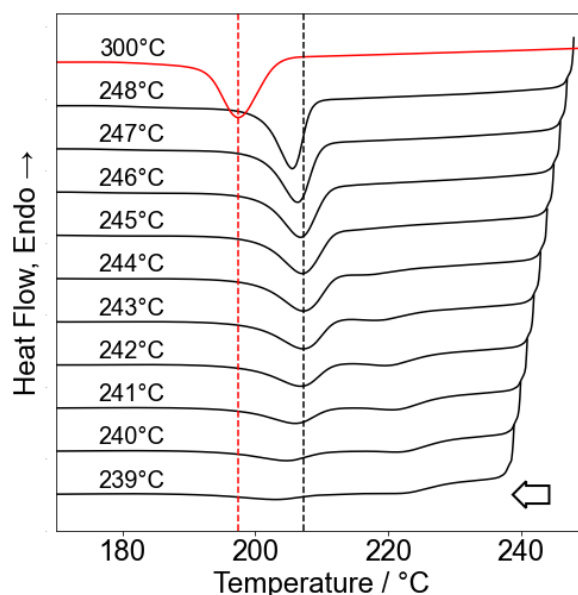
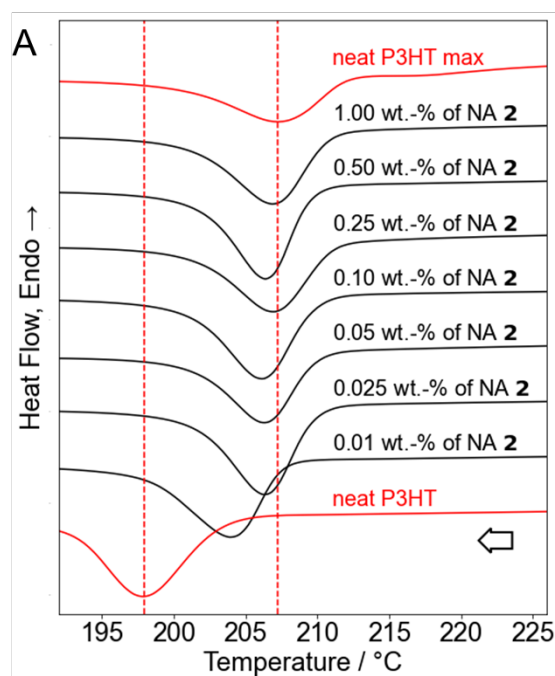


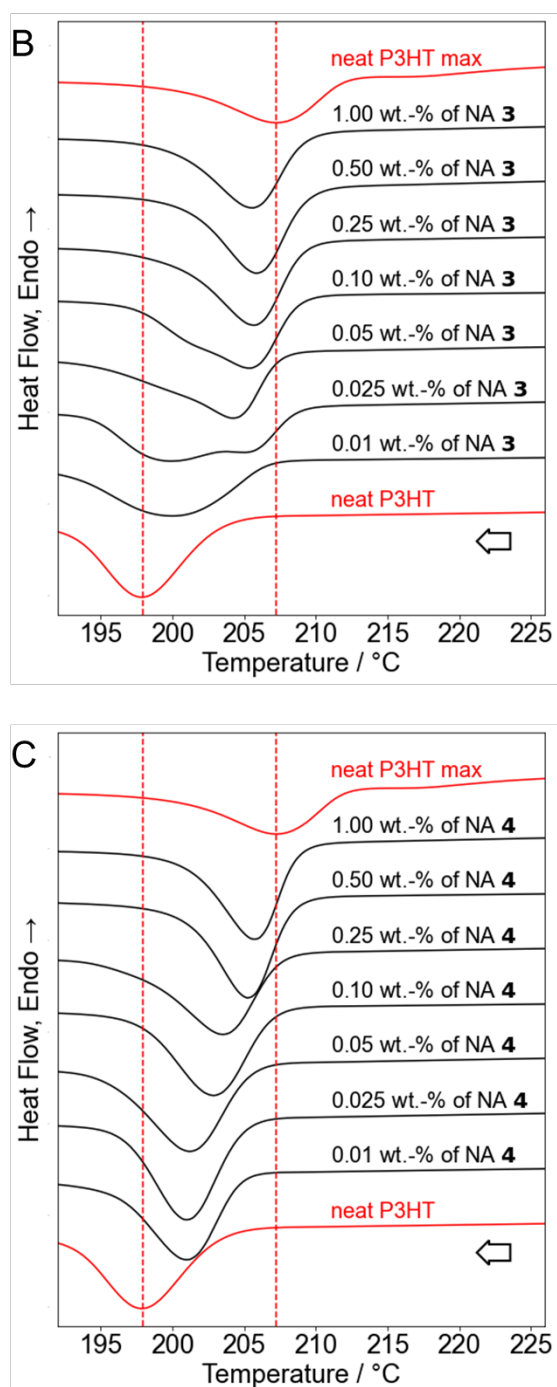
**Figure S2.** DSC curves of neat P3HT at various starting temperatures for the cooling process with a rate of  $10 \text{ K min}^{-1}$  under an inert atmosphere. The red curve represents a typical scan at standard conditions where the thermal history of the sample was eliminated. The black curves represent conditions to reveal maximal achievable crystallization temperature. Due to an incomplete melting of the P3HT upon the applied heating step, the remaining P3HT crystallites act as ideal nucleation sites upon cooling, causing an increase in the crystallization temperatures. The maximum achievable crystallization temperature is found to be at about  $207^\circ\text{C}$  if the initial heating process is stopped at  $244^\circ\text{C}$ .

#### S4. Dynamic crystallization studies of P3HT with supramolecular nucleating agents

##### *Temperature protocol for nucleation experiments by dynamic DSC*

Prior to all nucleation experiments by dynamic DSC, the thermal history was erased by heating the sample from 100°C to 300°C with a heating rate of 10 K min<sup>-1</sup> and keeping the sample isothermally for 5 min at 300°C. Afterward, the sample was cooled again to 100°C. All DSC scans of such thermally pretreated samples were performed with a heating and cooling rate of 10 K min<sup>-1</sup> in the temperature range from 150°C to 300°C. The corresponding cooling thermograms for the samples containing different amounts of nucleation agent NA 2 – NA 4 are depicted in Figure S3.

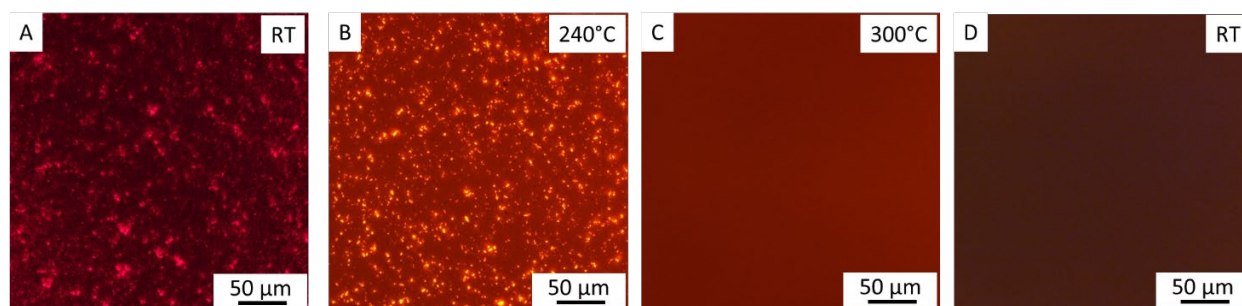




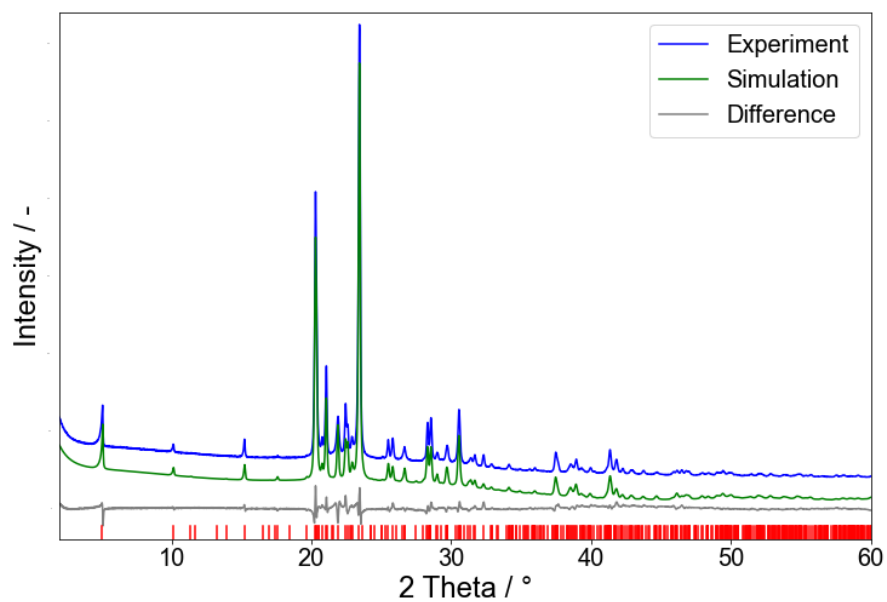
**Figure S3.** Second cooling curves of P3HT with different concentrations of NA 2 (A), NA 3 (B), or NA 4 (C). The neat and self-nucleated P3HT cooling scans are shown in red as references. The addition of the nucleating agents significantly shifts the polymer crystallization to higher temperatures.

### S5. Temperature-dependent polarized light microscopy

Supramolecular nucleating agents should dissolve at high temperatures in the polymer melt. This ensures a homogenous distribution of the molecules in the melt. The process of dissolution can be investigated by polarized light microscopy. For the sample preparation, a solution of 1 wt.-% of P3HT in chlorobenzene in which 100 ppm of NA **1** (1 wt.-% in relation to P3HT) are dispersed was drop-casted onto a glass slide. The dried resulting film consists of P3HT and crystals of NA **1** (see Figure S4 A), which are birefringent. Heating to 240°C results in a P3HT melt, and the crystals of NA **1** are still visible (Figure S4 B). Upon further heating of the sample to 300°C, the dissolution of NA **1** in the melt is visible (Figure S4 C). Upon cooling back to room temperature, the crystallization of NA **1** and P3HT is not visible with distinct features. Only a uniform color change attributed to the crystallization of P3HT is observed (Figure S4 D).

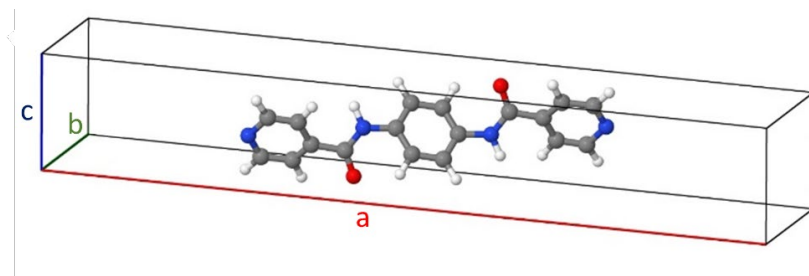


**Figure S4.** Polarized light microscopy images of P3HT films with 1 wt.-% of NA **1** before the first melting at RT (A) and after the P3HT melts at 240°C (B). The birefringence in A and B is caused by the crystals of NA **1**. Upon further heating to 300°C (C), NA **1** dissolves in the P3HT melt, visible by the disappearance of the birefringence. Cooling back to room temperature (D) results only in a uniform color change.

**S6. Powder X-ray diffractogram of NA 1**

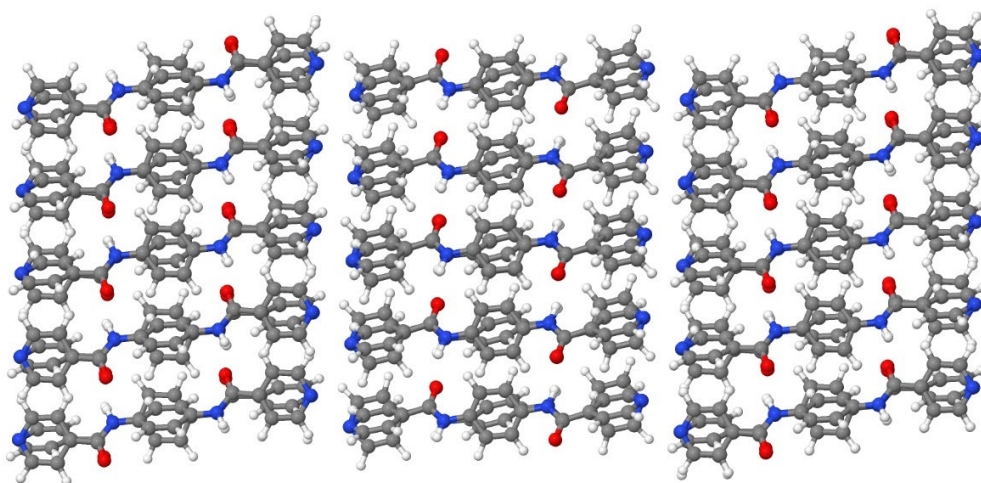
**Figure S5.** Measured (blue) and simulated (green) PXRD of NA 1 as well as the difference plot (grey). The red bars indicate all possible reflections for the space group  $P2_1/c$ .

### S7. Unit cell and relevant crystallographic information of NA 1



Compound	NA 1
Molecular formula	C <sub>18</sub> H <sub>14</sub> N <sub>4</sub> O <sub>2</sub>
M/g mol <sup>-1</sup>	318.33
Crystal system	monoclinic
Space group	<i>P</i> 2 <sub>1</sub> / <i>c</i>
<i>a</i> /Å	35.45805(274)
<i>b</i> /Å	7.88484(32)
<i>c</i> /Å	5.27197(27)
$\alpha^\circ$	90.0000
$\beta^\circ$	90.0000
$\gamma^\circ$	99.791(6)
<i>V</i> /Å <sup>3</sup>	1452.5(5)
<i>Z</i> '/ <i>Z</i>	1/4
$\rho$ /g cm <sup>-3</sup>	0.877
T/ K	293(2)
R <sub>p</sub>	0.046
R <sub>wp</sub>	0.065

**Figure S6.** Visualization of the asymmetric unit placed in the unit cell (top). The other three molecules of the unit cell are created by the symmetry operations of the space group *P*2<sub>1</sub>/*c* and are omitted in the figure for clarity. Relevant crystallographic data of NA 1 are shown at the bottom.

**S8. Visualization of the crystal packing of NA 1**

**Figure S7.** Packing of NA 1. The hydrogen bond pattern propagates from top to bottom along the crystallographic *c*-axis.

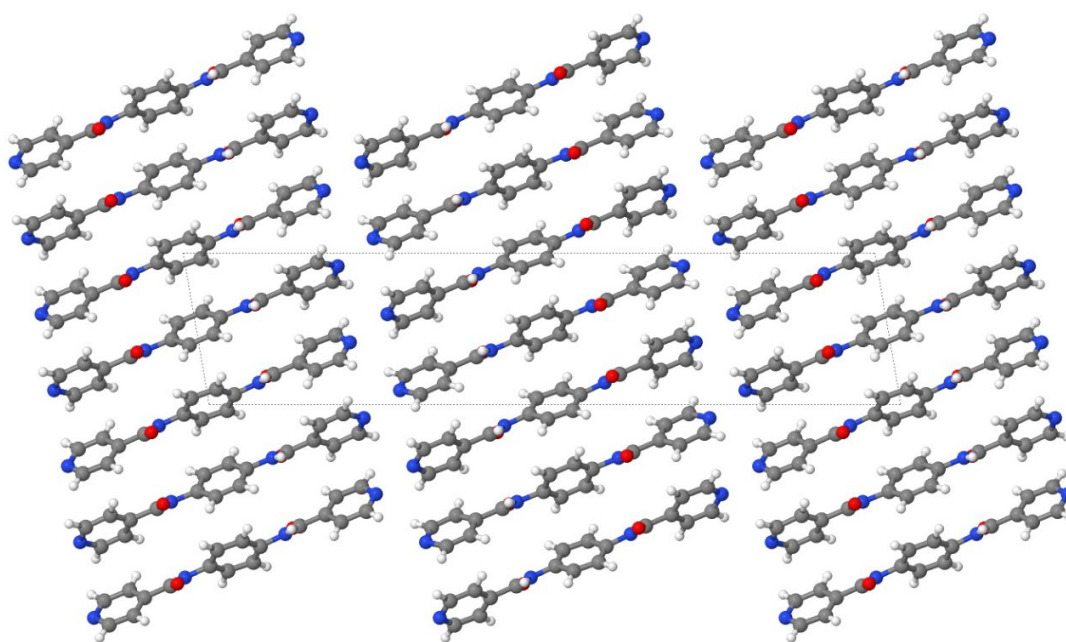


**Figure S8.** Packing of NA 1 in the *ab*-plane (100). The pyridine units point in a regular fashion to the *bc*-plane (100).

## S9. Dynamic crystallization studies of P3HT with reference compounds

### Reference compounds 1-3

For a comparative study, we have selected three reference compounds (Ref 1 - 3), which are structurally very similar to the highly efficient supramolecular nucleating agents NA 1 and NA 2. As reference compound Ref 1, we have selected *N,N'*-1,4-phenylenebisbenzamide (CAS: 5467-04-9) which is very similar to NA 1. As reference compound Ref 2, we selected *N*<sup>1</sup>,*N*<sup>4</sup>-diphenyl-1,4-benzenedicarboxamide (CAS: 7154-31-6) which is very similar to NA 2. Both structures differ compared to NA 1 and NA 2 by the use of benzene units instead of pyridine as peripheral units. In addition, the reference compound Ref 3, *N*<sup>1</sup>,*N*<sup>4</sup>-dicyclohexyl-1,4-benzenedicarboxamide (CAS: 15088-29-6) with non-aromatic side groups with similar bulkiness in the periphery was investigated.

### Nucleation experiments by dynamic DSC

Comparative nucleation experiments by DSC were carried out with P3HT and an additive concentration of 1 wt.-%, as described in the experimental section. The resulting cooling curves, including the one of neat P3HT and self-nucleated P3HT, are compared in Figure S9.

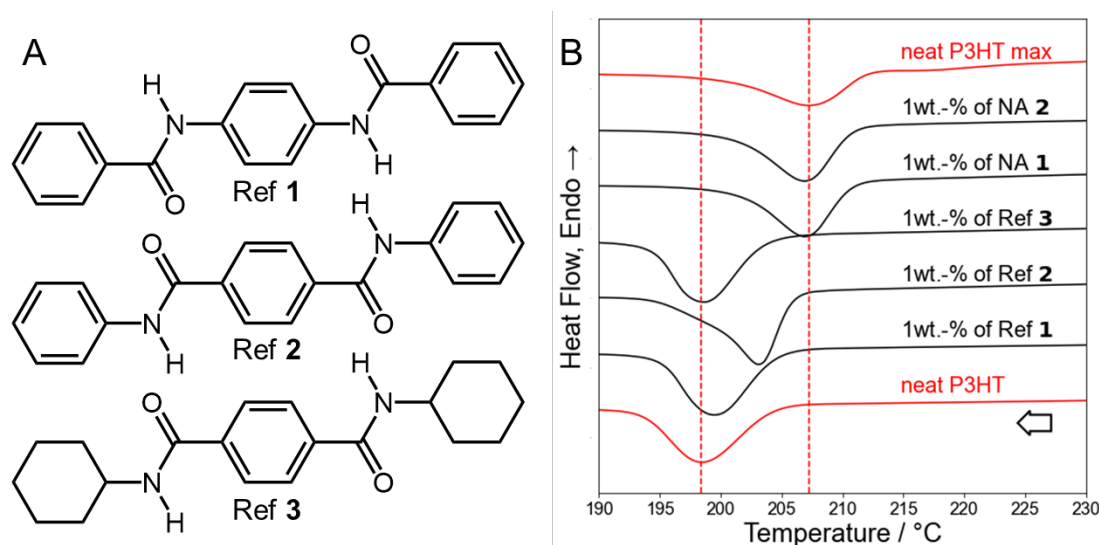


**Figure S9.** A) Molecular structures of the reference compounds Ref 1 – Ref 3. B) Second cooling curves of neat and self-nucleated P3HT (red curves) and P3HT with 1 wt.-% of NA 1 (97%), NA 2 (96%), Ref 1 (12%), Ref 2 (53%) and Ref 3 (2%). The determined nucleation efficiencies of the additives are given in brackets.

*Crystal structure visualization of reference compound Ref 1 compared to NA 1*

Based on the structure solution of reference compound Ref **1**, which is known from literature<sup>1</sup>, a view of the bc-plane (100) was constructed (Figure S10A). For comparison, the same view is shown for the crystal structure of NA **1** (Figure S10B). Both compounds feature identical packing patterns. The distance between the phenyl groups of Ref **1** features a distance of 7.88 Å. This distance also matches the c-axis of P3HT almost perfectly.

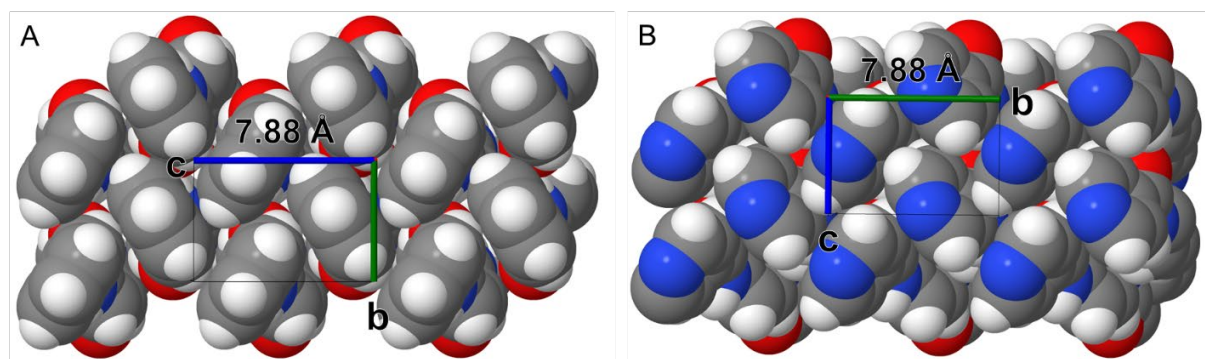


**Figure S10:** A) View on top of the bc-plane (100) of Ref **1**, *N,N'*-1,4-phenylenebisbenzamide as taken from reference<sup>1</sup>. B) For comparison, the crystal structure of NA **1** is shown in the same view.

<sup>1</sup> Cheng, N.; Yan, Q.; Liu, S.; Zhao, D. Probing the intermolecular interactions of aromatic amides containing N-heterocycles and triptycene. *CrystEngComm* **2014**, *16* (20), 4265–4273.

### S10. Applicability of this class of nucleation agents to other poly(3-alkylthiophenes)

Nucleation experiments with poly(3-butylthiophenes) (P3BT) and poly(3-octylthiophenes) (P3OT) with selected concentrations of NA **1** were performed via dynamic DSC in a similar manner as described before (see Section 3 and Section 4). The investigated temperature range was adjusted to the respective poly(3-alkylthiophenes) due to the different melting properties. For P3BT, the measurements were performed between 100 and 300 °C, and for P3OT, between 75 and 225 °C. Also, self-nucleation experiments and the determination of  $T_{c,max}$  were carried out for both polymers.

Figure S11 depicts the second cooling curves of P3BT and P3OT samples with different concentrations of NA **1** (black curves) as well as a neat and self-nucleated sample as references (red curves). The addition of NA **1** significantly shifts the polymer crystallization peak in both cases to higher temperatures. We found that with 1 wt.-% of NA **1**, an outstanding nucleation efficiency of 98% for P3BT was obtained. For P3OT, a nucleation efficiency of 94% was obtained already at a concentration of only 0.1 wt.-%.

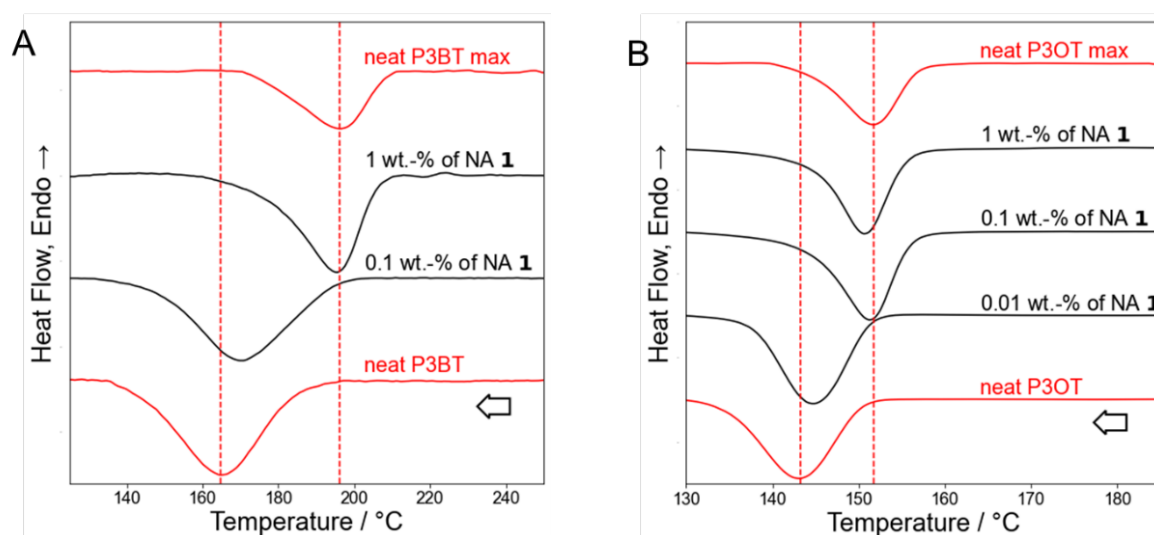


**Figure S11.** A) Second cooling curves of neat and self-nucleated poly(3-butylthiophenes) (P3BT) (red curves) and P3BT with 0.1 and 1 wt.-% of NA **1**. B) Second cooling curves of neat and self-nucleated poly(3-octylthiophenes) (P3OT) (red curves) and P3OT with 0.01, 0.1, and 1 wt.-% of NA **1**. The addition of NA **1** shifts the polymer crystallization peak to higher temperatures close to the respective  $T_{c,max}$ .

### S11. Hyperspectral imaging of neat P3HT and P3HT with NA 1

In P3HT films with the nucleating agent NA 1, we observed a slight decrease of the 0-0 PL peak at around 650 nm, compared to neat P3HT films (as explained in the main text). Furthermore, analyzing the same data, we observe a slight red-shift of the low-energy (high wavelength) flank of the PL spectrum. This shift is visible in the averaged spectrum (black line) in Figure S12 A, at around 750nm (indicated by the arrow). We visualize this shift by evaluating the PL intensity at 60 % of the maximum intensity (around 750 nm) for each individual spectrum of the  $40 \times 40 \mu\text{m}^2$  area and plot a map of the wavelengths at which this intensity is obtained. Figure S12 B and C show those maps of the extracted flank positions for a neat P3HT film and for a P3HT film with 0.1 wt.-% NA 1, respectively. As with the maps in Figure 9, we also observe no inhomogeneities.

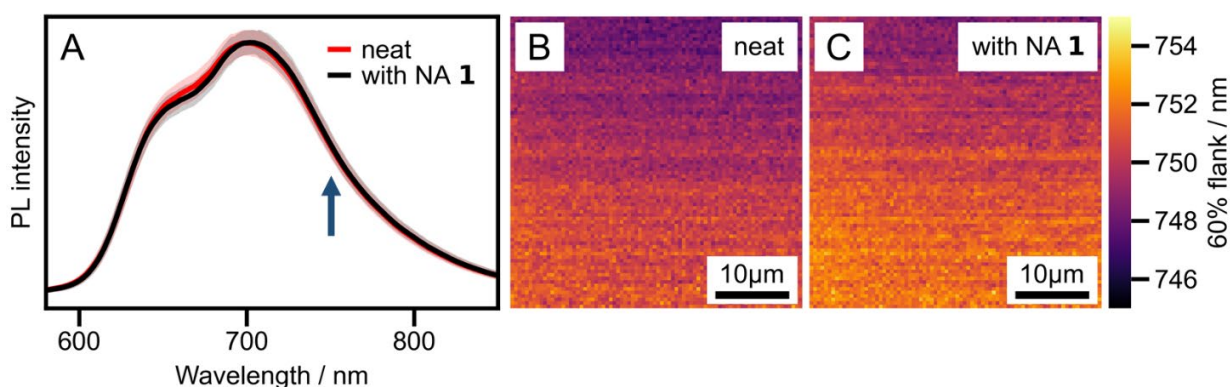


**Figure S12.** Hyperspectral imaging of thin films of neat P3HT and P3HT with NA 1. A) PL spectra of a neat P3HT film (red) and a P3HT film with 0.1 wt.-% NA 1 (black). Both PL spectra are averaged over an area of  $40 \times 40 \mu\text{m}^2$  comprising 6640 individual spectra. The shaded area shows the degree of variation within the films. B) and C) Maps of the spectral position of the low-energy (high-wavelength) flank, retrieved at 60 % of the maximum intensity for the neat P3HT film (B) and the P3HT film with 0.1 wt.-% NA 1 (C).

## 4.5 Kinked Bisamides as Efficient Supramolecular Foam Cell Nucleating Agents for Low-Density Polystyrene Foams with Homogeneous Microcellular Morphology

This work is a cooperation between the Inorganic Chemistry III, Polymer Engineering and the Macromolecular Chemistry I at the University of Bayreuth and will be reprinted from B. Klose, D. Kremer, M. Aksit, K.P. van der Zwan, K. Kreger, J. Senker, V. Altstädt, H.-W. Schmid, *Polymers* **2021**, *13*, 1094 under the creative common license.

My contributions are:

- conception and authorship of the article with a focus on the paragraphs related to the structure solution
- measuring the X-ray diffractogram and solving the crystal structure
- performing all NMR experiments

The contributions of the other authors are:

- conception and main authorship of the article
- synthesis of the materials
- recording the SEM images
- performing the batch and extrusion foaming experiments
- evaluating the foam properties

Article

# Kinked Bisamides as Efficient Supramolecular Foam Cell Nucleating Agents for Low-Density Polystyrene Foams with Homogeneous Microcellular Morphology

Bastian Klose <sup>1</sup>, Daniel Kremer <sup>1</sup>, Merve Aksit <sup>2</sup> , Kasper P. van der Zwan <sup>3</sup> , Klaus Kreger <sup>1</sup> ,  
Jürgen Senker <sup>3,4,\*</sup> , Volker Altstädt <sup>2,4,\*</sup>  and Hans-Werner Schmidt <sup>1,4,\*</sup> 

- <sup>1</sup> Macromolecular Chemistry I, University of Bayreuth, Universitaetsstrasse 30, 95447 Bayreuth, Germany; bastian.klose@uni-bayreuth.de (B.K.); daniel.kremer@uni-bayreuth.de (D.K.); klaus.kreger@uni-bayreuth.de (K.K.)
- <sup>2</sup> Department of Polymer Engineering, University of Bayreuth, Universitaetsstrasse 30, 95447 Bayreuth, Germany; merve.aksit@uni-bayreuth.de
- <sup>3</sup> Inorganic Chemistry III, University of Bayreuth, Universitaetsstrasse 30, 95447 Bayreuth, Germany; kasper.van-der-Zwan@uni-bayreuth.de
- <sup>4</sup> Bavarian Polymer Institute and Bayreuth Institute of Macromolecular Research, University of Bayreuth, Universitaetsstrasse 30, 95447 Bayreuth, Germany
- \* Correspondence: juergen.senker@uni-bayreuth.de (J.S.); altstaedt@uni-bayreuth.de (V.A.); hans-werner.schmidt@uni-bayreuth.de (H.-W.S.); Tel.: +49-921552532 (J.S.); +49-921557471 (V.A.); +49-921553200 (H.-W.S.)



**Citation:** Klose, B.; Kremer, D.; Aksit, M.; Zwan, K.P.v.d.; Kreger, K.; Senker, J.; Altstädt, V.; Schmidt, H.-W. Kinked Bisamides as Efficient Supramolecular Foam Cell Nucleating Agents for Low-Density Polystyrene Foams with Homogeneous Microcellular Morphology. *Polymers* **2021**, *13*, 1094. <https://doi.org/10.3390/polym13071094>

Academic Editor: José Ignacio Velasco

Received: 5 March 2021

Accepted: 25 March 2021

Published: 30 March 2021

**Publisher's Note:** MDPI stays neutral with regard to jurisdictional claims in published maps and institutional affiliations.



**Copyright:** © 2021 by the authors. Licensee MDPI, Basel, Switzerland. This article is an open access article distributed under the terms and conditions of the Creative Commons Attribution (CC BY) license (<https://creativecommons.org/licenses/by/4.0/>).

**Abstract:** Polystyrene foams have become more and more important owing to their lightweight potential and their insulation properties. Progress in this field is expected to be realized by foams featuring a microcellular morphology. However, large-scale processing of low-density foams with a closed-cell structure and volume expansion ratio of larger than 10, exhibiting a homogeneous morphology with a mean cell size of approximately 10  $\mu\text{m}$ , remains challenging. Here, we report on a series of 4,4'-diphenylmethane substituted bisamides, which we refer to as kinked bisamides, acting as efficient supramolecular foam cell nucleating agents for polystyrene. Self-assembly experiments from solution showed that these bisamides form supramolecular fibrillary or ribbon-like nanoobjects. These kinked bisamides can be dissolved at elevated temperatures in a large concentration range, forming dispersed nano-objects upon cooling. Batch foaming experiments using 1.0 wt.% of a selected kinked bisamide revealed that the mean cell size can be as low as 3.5  $\mu\text{m}$ . To demonstrate the applicability of kinked bisamides in a high-throughput continuous foam process, we performed foam extrusion. Using 0.5 wt.% of a kinked bisamide yielded polymer foams with a foam density of 71  $\text{kg}/\text{m}^3$  and a homogeneous microcellular morphology with cell sizes of  $\approx 10 \mu\text{m}$ , which is two orders of magnitude lower compared to the neat polystyrene reference foam with a comparable foam density.

**Keywords:** supramolecular additives; foam nucleating agents; batch foaming; foam extrusion; cell nucleation; low-density polymer foams; microcellular foams; foam morphology

## 1. Introduction

Polystyrene (PS) foams are widely used in a variety of applications, e.g., packaging, building and construction or in the automotive sector [1–3]. This is attributed to the low cost and established manufacturability of the polymer and foamed products, with the latter in particular excelling in their superior mechanical as well as thermal and acoustic insulation properties. These macroscopic properties are directly related to the foam morphology and foam density, with the key aspects being cell size and cell size distribution, cell density, and the open or closed cellular structure [1,4,5]. In this context, homogeneous microcellular and closed-cell foams with cell sizes of 10  $\mu\text{m}$  or below as well as low foam densities

with volume expansion ratios (VER) of larger than 10 are expected to show improved mechanical and thermal properties compared to macroscopic foams featuring cell sizes above 300  $\mu\text{m}$  [1,2,4].

Numerous studies have been dedicated to investigating the structure–property relations of polymer materials and processing parameters in view of the foam cell morphology. This includes the influence of the physical blowing agent or mixture of those in view of the gas solubility and diffusivity and the rheological behavior of the (gas-loaded) polymer melt [3]. One important aspect is the use of additives and fillers, particularly to influence the melt strength or to act as heterogeneous nucleating agents for the foam cells to achieve polymer foams with a fine cellular or microcellular morphology [1,3]. For example, inorganic additives such as talc [6], silica [7,8] including mesoporous silica particle grafted with polystyrene brushes, (nano)clay [9,10], reduced and functional graphite oxide [11,12], expanded graphite [13], multi-walled carbon nanotubes [4,14,15], or carbon nanofibers [13,16] were investigated as additives. In general, inorganic additives tend to agglomerate within the polymer melt, reducing the effective surface-to-volume ratio, which together with a nonuniform distribution and dispersion of the additive leads to an inhomogeneous foam morphology [1,17].

An interesting aspect in this context is the use of shape-anisotropic inorganic additives, such as glass fibers with a high aspect ratio, which were beneficially employed to achieve foamed isotactic polypropylene (iPP) samples with water as a blowing agent. These injection-molded foamed specimens featured improved mechanical properties compared to the conventional injection molded ones [18]. Another interesting approach is based on the use of polymer fibers as additives to achieve fine cellular or microcellular foams, which was comprehensively investigated by the research group of Park [3]. In particular, they found that these fibrillated polymers improve the melt strength and foaming ability of thermoplastic polymers, such as polyethylene (PE) [19], iPP [20], or poly(lactic acid) (PLA) [21]. For instance, the addition of 5 wt.% of iPP nanofibers with diameters in the range of 100 nm to 300 nm to a PE melt resulted in a reduction of the average cell size from 900  $\mu\text{m}$  to 28  $\mu\text{m}$ . As a result, the cell density was significantly increased by four orders of magnitude. They also showed that adding 0.3–3.0 wt.% of polytetrafluoroethylene fibers (PTFE) with an average diameter of less than 500 nm and lengths above 100  $\mu\text{m}$  to the thermoplastic polymer iPP improves the strain-hardening behavior of the melt, which leads to low-density foams with an increased cell density [20].

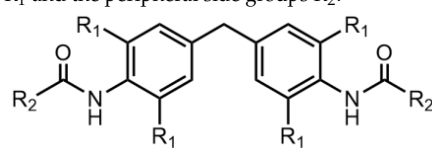
Apart from these insoluble additives based on inorganic materials or on polymer fibers used to improve the morphology of polymer foams, a rather novel class of additives is based on supramolecular materials. In contrast, the manner of functioning of supramolecular materials relies on the dissolution at elevated temperatures of the building blocks on a molecularly level in the polymer melt and the in situ formation of nano-objects via secondary interactions upon cooling the melt. Most typically, the formation and morphology of supramolecular objects depend on the molecular design of the building blocks, the polymer type, additive concentration, and other processing conditions such as temperature. Common examples, which are suitable to be used as additives in the polymer melt are based on naphthalene-bisamides [22], sorbitol-based derivatives [23] or benzenetrisamides (BTAs) [24]. In particular, BTAs have been successfully used as polymer crystal nucleating agents in various semi-crystalline polymers such as iPP [24,25], polybutylene terephthalate (PBT) [26], PLA [27], and polyvinylidene fluoride (PVDF) [28]. In a similar manner, such supramolecular nano-objects can be used as foam cell nucleating agents. Specifically, after the preparation of a polymer/additive mixture at ambient conditions, this approach involves dissolution of the supramolecular additive at elevated temperatures, resulting in homogeneously distributed building blocks in the polymer melt via molecular diffusion. Upon cooling, supramolecular nanoobjects are formed via secondary interactions by consumption of the dissolved building blocks, which effectively serves as heterogeneous nucleation sites for the added physical blowing agent. Since the homogeneously dispersed nano-objects provide a large number of predetermined nucleation sites for the physical

blowing agent, this allows for control over the foam morphology with a homogeneous fine cellular structure (see the Supplementary Materials, Section S1). The potential as efficient foam nucleating agents has been successfully demonstrated by our research groups using selected BTAs for injection-molded iPP foams and extrusion foamed iPP, PS, and PBT [29–33]. However, using BTAs at large concentrations in nonpolar polymers remains challenging due to restrictions in the solubility and the concentration-dependent formation of larger sized objects. This probably limits the number of finely dispersed nano-objects in the polymer melt under conventionally employed conditions and ultimately restricts a very large number of nucleation sites necessary for a fine-celled polymer foam.

Recently, a novel class of supramolecular polymer additives, which were based on a 4,4'-diaminodiphenylmethane central unit with two side groups linked via two amide units, has been shown to efficiently act as crystal nucleating agents for iPP [34]. However, very little is known about this class of additives, which we refer to as kinked bisamides.

Here, we report on a comprehensive investigation of kinked bisamides with respect to structure–property relations regarding their bulk properties, self-assembly in solution, and their nano-object morphology as well as their capability to act as foam cell nucleating agents for polystyrene. The molecular design of these kinked bisamides was systematically varied at two selected positions (see Table 1) to tune the thermal properties and the self-assembly behavior of the supramolecular building blocks. Substitution at the ortho-positions of the amide groups with an increasing sterically demand of  $R_1$  from hydrogen to methyl or ethyl-groups enforces a torsion of the amide groups and consequently results in increased phase transitions of the kinked bisamides. Thus, we selected 4,4'-diaminodiphenylmethane, 4,4'-methylenebis-(2,6-dimethylaniline), and 4,4'-methylenebis(2,6-diethylaniline) to vary the structural features of the central unit. Similarly, systematic structural variations with respect to the peripheral side groups  $R_2$  were conducted using cyclohexane, phenyl, t-butyl, and n-butyl as peripheral side groups to investigate their thermal properties and the self-assembly behavior in the nonpolar solvent xylene. These two structural variations result in a total number of twelve kinked bisamides, which were utilized as foam cell nucleating agents in a thermally induced batch foam process of PS. A continuous foam extrusion process on technical scale was implemented to study the influence of a foam cell nucleating agent with respect to the foamability, foam morphology, and density of PS under harsh processing conditions including large shear forces, and high barrel temperatures and pressures. For both types of foaming processes, neat PS was prepared in the same manner to obtain a reference foam.

**Table 1.** Structural variation of the kinked bisamides **1a–3d** at the ortho-positions to the amide groups  $R_1$  and the peripheral side groups  $R_2$ .



$R_1$	$R_2$	Cyclohexyl	Phenyl	Tert-Butyl	N-Butyl
H		1a	1b	1c	1d
methyl		2a	2b	2b	2d
ethyl		3a	3b	3b	3d

## 2. Materials and Methods

### 2.1. Materials

All solvents were purified and distilled according to standard procedures. The amines and acid chlorides employed were obtained from Sigma Aldrich (Darmstadt, Germany) and used as received.

The synthesis of all kinked bisamides based on selected 4,4'-diaminodiphenylmethane central units and aliphatic or aromatic side groups (Table 1) were performed via conversion of the respective amines with acid chlorides according to standard procedures. Details on the syntheses, purification and characterization are given in the Supplementary Materials, Section S2. Details on the thermal characterization and properties of all kinked bisamides are reported in the Supplementary Materials, Section S3.

PS 168N (INEOS Styrolution, Frankfurt am Main, Germany) was used as PS grade for batch and extrusion foaming experiments featuring a melt volume rate (MVR) (200 °C, 5 kg) of  $1.5 \text{ cm}^3 (10 \text{ min})^{-1}$  and a bulk density  $\rho$  of  $1040 \text{ kg}\cdot\text{m}^{-3}$  [35].

## 2.2. Self-Assembly of Kinked Bisamides and Nano-Object Characterization

For the self-assembly experiments to achieve and investigate supramolecular nano-objects in a nonpolar solvent at elevated temperatures, 500 ppm of the corresponding kinked bisamide was molecularly dissolved in 2 mL of xylene at 130 °C for 30 min in a closed vial. Subsequent cooling to room temperature yielded a turbid dispersion containing the self-assembled nanostructures. Prior to the morphology investigation via scanning electron microscopy (SEM), a drop of the suspension was deposited on a silicon wafer and the solvent was evaporated at ambient conditions. The samples were sputtered with a 2.0 nm thick platinum layer under argon atmosphere using a Sputter Coater 208HR (Cressington, Dortmund, Germany). SEM characterization of the samples were performed with a LEO Gemini 1530 FESEM (Zeiss, Jena, Germany) using an acceleration voltage of 2 to 3 kV. The dimensions of the supramolecular objects were measured with the program AxioVision (Zeiss, Jena, Germany). The reported data on the nano-objects' dimensions refer to mean values of at least 70 determined objects for each sample.

## 2.3. Structural Studies of Kinked Bisamide 3a

To gain insight into the driving force for supramolecular nano-object formation and the corresponding morphology, structural methods were applied to reveal the crystal structure of kinked bisamide 3a. Powder X-ray diffraction (PXRD) was performed on a crystalline powder of 3a obtained from different solvents such as acetone and xylene. Prior to Rietveld refinement, density-functional theory (DFT) simulations were performed to optimize the molecular structure. Details on the structural elucidation are given in the Supplementary Materials, Section S4. Moreover, to provide additional evidence on the structural data, solid-state NMR (see the Supplementary Materials, Section S5) as well as Fourier-transform infrared spectroscopy (FTIR) on powder samples were performed (see the Supplementary Materials, Section S6).

## 2.4. Polymer Processing and Foaming

### 2.4.1. Masterbatch Preparation

The polystyrene PS168N pellets were grinded in a ZM200 freezer mill (Retsch, Haan, Germany) using a mesh size of 1000  $\mu\text{m}$  at a rotation speed of 18.000 rpm. The powdered PS was mixed with 1.0 wt.% (batch foaming) or 5.0 wt.% (extrusion foaming) of the finely powdered corresponding kinked bisamide. A Reax 2 overhead shaker (Heidolph, Schwabach, Germany) was used for 24 h at 50 rpm to achieve a homogeneous powder-powder mixture of the PS and kinked bisamides.

### 2.4.2. Compounding and Preparation of Injection-Molded Specimen for Batch Foaming

Compounding was performed using a twin-screw micro-compounder, Xplore 15 mL (DSM, Heerlen, The Netherlands) under nitrogen atmosphere. As compounding conditions, a temperature of 260 °C, a residence time of 5 min, and a rotational speed of 50 rpm were selected. Different concentrations of 1.0, 0.75, 0.5, 0.25, 0.1, 0.05, 0.025, and 0.01 wt.% of the kinked bisamides in PS were achieved by preparing a dilution series. For this, 13.5 g of the masterbatch with a concentration of 1.0 wt.% of the kinked bisamide was compounded first. About 5.4 g of the molten polymer-additive mixture remained in the compounder

after depletion, which was subsequently diluted to the selected concentration by adding a respective amount of neat PS granulates.

Injection molding was performed using a micro-injection-molding machine, Xplore 12 mL (DSM, Heerlen, The Netherlands). The barrel temperature of the injection molding unit was set to 250 °C, and an injection pressure of 6 bar was used. The molten compounded mixtures were transferred from the compounder to the micro-injection-molding machine and subsequently injected into a polished mold for the duration of 20s, yielding round platelets with a diameter of 27 mm and a thickness of 1.1 mm. To eliminate the internal stress of the specimens resulting from the injection molding process, the samples were annealed in a closed iron mold at 135 °C for 4 h.

#### 2.4.3. Batch Foaming

To saturate the injection-molded specimens with a physical blowing agent, a HR 500 high-pressure autoclave (Berghof, Eningen, Germany) was used. Saturation was performed at room temperature using CO<sub>2</sub> at a pressure of 50 bar for 24 h. A CO<sub>2</sub> uptake of approximately 6.5 wt.% was determined by weighing the specimens prior foaming. Batch foaming experiments were performed by immersing the CO<sub>2</sub>-loaded injection-molded specimens in a silicon oil bath at 130 °C for 15 s. The foamed samples were allowed to cool in an oil bath at ambient conditions for 20 s and then in water bath for a further 20 s. Oil residues were removed by washing the foams with soap water, and the foamed specimens were dried at ambient conditions for 24 h prior analysis.

#### 2.4.4. Extrusion Foaming

Foam extrusion experiments were carried out using a tandem extrusion line (Dr. Collin GmbH, Maitenbeth, Germany) comprising a twin-screw extruder with a 25 mm screw and a L/D ratio of 42 (A-Extruder), and a single-screw extruder with a 45 mm screw and L/D ratio of 30 (B-Extruder) equipped with a slit die with a gap of 0.6 mm and a width of 30 mm. Extruded PS (XPS) foams with the kinked bisamide **3a** at three selected concentrations, i.e., 0.1, 0.2, and 0.5 wt.%, were produced. For this, a masterbatch powder–powder mixture with 5.0 wt.% of **3a** was prepared in the same manner as described above. XPS foams with varying concentrations of **3a** were obtained by diluting the masterbatch with neat PS granulates by controlling the flow rates. A combination of 4 wt.% CO<sub>2</sub> and 3 wt.% EtOH was used as a physical blowing agent. This ratio was found to be highly beneficial, since this composition can act as an efficient plasticizer for the polymer melt resulting in a homogeneous foam morphology [11,30]. As processing parameters, a screw speed of 8 rpm at the B-Extruder with an overall throughput of 4.5 kg h<sup>-1</sup> was selected. The melt temperature in the A-Extruder was adjusted to 220 °C to ensure complete dissolution of the kinked bisamide **3a** in the PS melt. The melt temperature near the outlet of the B-extruder and the die temperature were selected between 110–120 °C and 126 °C, respectively. PS reference foams were prepared using neat PS granulates in the same manner.

### 2.5. Foam Characterization

#### 2.5.1. Foam Morphology

Batch or extrusion foam morphologies, which were evaluated with respect to the cell sizes and their distribution, were investigated via SEM imaging. Prior to the SEM investigation, the foamed specimens were cryo-fractured under liquid nitrogen yielding uniform breaking edges. The cryo-fractured specimens were clued on a silicon wafer and additionally wrapped with a copper foil to ensure better conductivity. The samples were sputtered with a 2-nm thick platinum layer under argon atmosphere using a Sputter Coater 208HR (Cressington). The field emission-scanning electron microscope, LEO Gemini 1530 FESEM (Zeiss), with an acceleration voltage of 3 kV was used to investigate the foam morphologies. The areas of the foam cells  $A_{\text{cell}}$  were determined using the software ImageJ.

Assuming that the cells are circular, the cell diameters  $D_{cell}$  were calculated according to following equation:

$$D_{cell} = 2\sqrt{\frac{A_{cell}}{\pi}} \quad (1)$$

The areas and corresponding cell diameters of at least 70 cells of each foam sample were taken into account, and the average values were given.

### 2.5.2. Foam Density

Foam densities were calculated using the water-displacement method in agreement with ISO 1183 based on Archimedes' principle using a XP 205 balance with density kit (Mettler Toledo). Samples were prepared by cutting a small rectangle of the foamed specimen, which was subsequently weighed in air ( $m_{air}$ ). The cut specimen was submerged in water, and its apparent mass ( $m_{water}$ ), which was reduced by the buoyant force, was measured. The foam density ( $\rho_{foam}$ ) was given according to the following equation [4].

$$\rho_{foam} = \frac{m_{air}}{m_{air} - m_{water}} \cdot \rho_{water} \text{ with } \rho_{water} (296.3 \text{ K}) = 0.997541 \text{ g/cm}^3 \quad (2)$$

Foam densities were measured on at least three cut samples from different locations of the foam, and the mean values were given.

### 2.5.3. Cell Density

Cell densities  $\rho_{cell}$  with respect to the unfoamed solid polymer were calculated according to Equation (3), with  $N_c$  being the number of cells in the selected area and  $A_s$  being the area of the selected section [4,36,37].

$$\rho_{cell} = \left(\frac{N_c}{A_s}\right)^{\frac{3}{2}} \cdot VER \quad (3)$$

with the volume expansion ratio (VER) calculated by dividing the average foam density by the polystyrene density, according to Equation (4).

$$VER = \frac{\rho_{PS,bulk}}{\rho_{foam}} \text{ with } \rho_{PS,bulk} = 1040 \text{ kg/m}^3 \quad (4)$$

## 3. Results and Discussion

### 3.1. Synthesis, Characterization, and Thermal Properties of Kinked Bisamides

The class of supramolecular building blocks based on a 4,4'-diaminodiphenylmethane central unit with two peripheral side groups linked via two amide units, which we refer to here as kinked bisamides (see Table 1), is rather unnoticed and less investigated, in particular, in view of their thermal properties, self-assembly capabilities, and their use as foam cell nucleating agents. To reveal the structure–property relationships of this class, we systematically designed and synthesized a total of twelve kinked bisamides. In general, we anticipated that the central methylene group results in a kinked structure, which improves the solubility in nonpolar media. Structural variations of the molecular design were performed with respect to the substitution pattern of the ortho-position to the amide units ( $R_1$ ) as well as to the peripheral side groups ( $R_2$ ). Variation in the substituents  $R_1$  enforces a torsion of the amide groups due to an increasing steric demand from hydrogen to the methyl or ethyl groups, influencing the melting behavior of the kinked bisamides. Thus, we selected 4,4'-diaminodiphenylmethane, 4,4'-methylenebis(2,6-dimethylaniline), and 4,4'-methylenebis(2,6-diethylaniline) as central unit molecules. Systematical structural variations in the peripheral side groups to further tune the thermal properties were conducted with respect to bulkiness and stiffness of the side groups  $R_2$  using the bulkier cyclohexane and phenyl side groups as well as the smaller but stiff t-butyl and the more flexible n-butyl side groups.

Syntheses of the kinked bisamides were performed according to standard procedures in a straightforward manner, converting the amine moieties of the central units with the corresponding acid chlorides of the peripheral side groups. To ensure sufficient solubility of the products, tetrahydrofuran (THF) or N-methyl-2-pyrrolidone (NMP) was used as a solvent and a tertiary amine such as triethylamine or pyridine was used as a hydrogen chloride scavenger. All kinked bisamides were obtained in high yield, ranging from 56 to 95%, and were identified and characterized by common analytical methods of the organic chemistry. The purity of the compounds was determined by means of HPLC and found for most of the compounds to be more than 95%. Details on the syntheses, purification, and characterization are given in the Supplementary Materials, Section S2. The thermal stabilities and the phase transition temperatures of all compounds were determined by thermogravimetric analysis (TGA) and differential scanning calorimetry (DSC) experiments (see the Supplementary Materials, Section S3). The  $T_{-5wt.}$  values were close to 300 °C or higher, demonstrating a high thermal stability of the compounds. With the exception of **3d**, the melting temperatures were in the range of 190 °C to 320 °C and the crystallization temperatures were in the range of 170 °C to 310 °C. These findings suggest that these kinked bisamides can be processed at high temperatures and can self-assemble at elevated temperatures in the polymer melt. Both are a prerequisite for the additives to be used as supramolecular foam cell nucleating agents.

### 3.2. Self-Assembly of Kinked Bisamides from Xylene

An important aspect is the morphology of the supramolecular objects, which may act as nucleating sites for the cell formation. To gain insight on how the morphology and shape of the supramolecular objects may develop in a nonpolar polymer melt, self-assembly experiments were performed at elevated temperatures using a nonpolar solvent because solvents allow for straightforward isolation of the objects and their subsequent investigation by microscopic techniques. Xylene was chosen as a nonpolar model solvent, since it features structural similarities to the PS repeating unit and a reasonable high boiling point. For these screening experiments, 500 ppm was selected as the concentration to ensure complete solubility at elevated temperatures. The applied self-assembly protocol included dissolving the respective kinked bisamides at elevated temperatures until an optically clear solution was obtained. Subsequent cooling to room temperature resulted in a turbid dispersion indicating supramolecular object formation. Evaporation of the solvent allows for isolation of the supramolecular structures and subsequent characterization by SEM.

An overview of the self-assembled structures of the twelve kinked bisamides is shown in Figure 1. In general, most of the structures are strongly elongated with a fibrillar- or ribbon-like morphology. This indicates that there is at least one preferred direction with a fast growth rate, which is typically driven by the formation of a hydrogen bond pattern. In the case of the kinked bisamides **1a–3a** with cyclohexyl substituents in the periphery, a dense network of fibrillar-like structures can be observed. While the fibrillar structures of **1a** exhibit a width in the range of 0.2–1.3  $\mu\text{m}$ , they are in the range of 0.5–4.5  $\mu\text{m}$  for **2a**. The widths of the fibrillar structures of **3a** are between 0.1 and 0.6  $\mu\text{m}$ . The kinked bisamides **1b–3b** with phenyl groups as peripheral substituents feature a distinctly different morphology, resembling ribbon- or plate-like structures. The widths of the ribbon-like structures of **1b** and **3b** are in the range of 0.8–3.8  $\mu\text{m}$  and 0.3–2.4  $\mu\text{m}$ , respectively.

In contrast, **2b** forms micrometer-sized less-defined plate-like structures. Kinked bisamides **1c–3c** with tert-butyl groups in the periphery show again supramolecular objects of different morphology. While **1c** and **3c** self-assemble into plate-like structures with large widths between 1.0  $\mu\text{m}$  and 20.0  $\mu\text{m}$ , a dense fibrillary-like network with widths between 0.2  $\mu\text{m}$  and 1.0  $\mu\text{m}$  is obtained for **2c**. All three kinked bisamides **1d–3d** with n-butyl substituents in the periphery build up dense networks of fibrillar structures. The widths of the fibrillar structures are in the ranges of 0.2–1.5  $\mu\text{m}$  for **1d**, 0.3–1.6  $\mu\text{m}$  for **2d**, and 0.1–1.0  $\mu\text{m}$  for **3d**. To conclude, the results of the self-assembly experiments indicate that all kinked bisamides can form small supramolecular nano-objects. In particular, the

kinked bisamides **1a–3a** and **1d–3d** show the most promising self-assembled structures in terms of finely dispersed fibrillary objects.

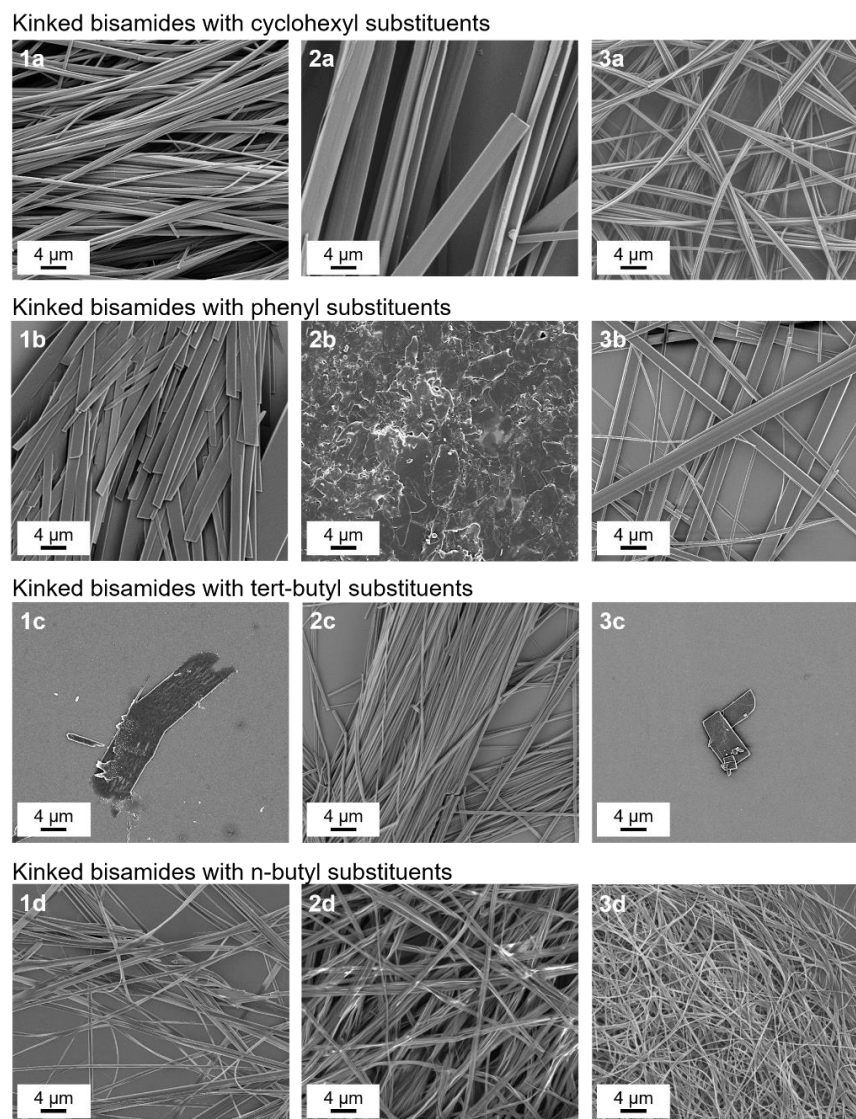


**Figure 1.** SEM micrographs (2000×) of isolated supramolecular nano-objects of kinked bisamides self-assembled from xylene at an additive concentration of 500 ppm.

### 3.3. Crystal Structure Solution of **3a**

The findings of the self-assembly experiments in a nonpolar solvent demonstrated that most of the kinked bisamides feature very long and fine fibrillar- or ribbon-like structures, which is indicative of a highly preferred directed growth of the structures. In general, the mesoscopic growth and shape of nanostructures is reflected by the molecular structure and the specific pattern of the hydrogen bonds in the crystallographic unit cell. For none of the twelve kinked bisamides, single crystals suitable for single crystal x-ray diffraction could be achieved, which often is the case for compounds yielding supramolecular nanostructures.

Thus, we selected a well-ordered crystalline powder of kinked bisamide **3a** recrystallized from the polar solvent acetone suitable to reveal the crystal structure by powder x-ray diffraction (PXRD). The structure was solved using real space methods. Details on the PXRD investigation, simulation, refinement, and solid-state NMR spectroscopy are given in the Supplementary Materials, Section S4 (structure solution) and S5 (solid state NMR). Structure elucidation of the crystalline powder of the kinked bisamide **3a** from acetone features a reasonably low value of  $R_{wp}$  of 3.56 after Rietveld refinement, demonstrating a high agreement of the PXRD experiment with the simulation, validating the structure model. It was found that **3a** crystallizes in the triclinic space group  $P\bar{1}$ , with the parameters  $a = 4.6882(8) \text{ \AA}$ ,  $b = 15.4521(19) \text{ \AA}$ ,  $c = 22.5115(66) \text{ \AA}$ ,  $\alpha = 105.23(2)^\circ$ ,  $\beta = 93.88(4)^\circ$ , and  $\gamma = 93.07(3)^\circ$ . The triclinic unit cell contains two molecules linked by an inversion center and has a volume of  $1565.57(1) \text{ \AA}^3$  as well as a crystallographic density of  $1.12591 \text{ g/cm}^3$ . The corresponding crystal packaging plots of kinked bisamide **3a** are depicted in Figure 2. When viewed along the a-axis (Figure 2a), the molecules are arranged in columnar stacks. These columnar stacks comprise two parallel arranged strands of hydrogen bonds along the a-axis, which is most likely the driving force for the elongated or fibrillar-like morphology. A crystal packaging plot of **3a** with a viewing direction along the b-axis is depicted in Figure 2b, showing that the molecules are arranged in an elongated manner along the c-axis. This arrangement resembles a 2D layer with a thickness of a single molecule. Within both directions, along the b-axis as well as the c-axis, the molecules are held together by weaker van der Waals forces, which can be assumed to represent the two other dimensions of the nanostructures yielding under proper conditions a ribbon or plate-like morphology depending on the individual growth rate. Figure 2b also provides a clearer picture of the intermolecular hydrogen bonds pattern of the two strands between the molecules in the crystalline state (green dotted lines). Each amide group forms a ditopic hydrogen bond pattern with the same amide group of the next two neighboring molecules, resulting in total four intermolecular hydrogen bonds per molecule. The average  $\text{NH}\cdots\text{O}$  distances were found to be  $\approx 1.7 \text{ \AA}$ , which corresponds to a medium strong hydrogen bond [38]. This hydrogen bond length fits the observed proton shift of 8.5 ppm (Figure S4) [39]. Interestingly, the oxygen atoms within a strand of hydrogen bonds in a column point in the opposite direction. Thus, the hydrogen bond pattern formed within a stack is arranged in an antiparallel manner. PXRD on samples of kinked bisamide **3a** self-assembled from xylene results in broad diffraction peaks and could therefore not be used for a structure solution. This clearly indicates that the self-assembled structures of **3a** feature a much higher degree of disorder.

To verify that the fundamental supramolecular motif, that is the arrangement into columnar stacks with two parallel arranged strands of hydrogen bonds, is comparable, we performed solid-state NMR spectroscopy (see the Supplementary Materials, Section S5). It was found that the number of carbon resonances from the  $^{13}\text{C}\{^1\text{H}\}$  CP NMR spectrum matches the obtained crystal structure, as there is one molecule in the asymmetric unit resulting in an individual carbon shift for all carbon atoms. Comparing both spectra, the  $^1\text{H}$  and  $^{13}\text{C}\{^1\text{H}\}$  CP NMR spectra of **3a** recrystallized from acetone and from xylene show that all chemical shifts and intensities of all resonances are similar; however, the resonances for the sample prepared from xylene are broader. Therefore, we assume the same topology with a similar molecular coordination and self-assembly behavior from xylene. Moreover, we performed FTIR measurements on both samples (see the Supplementary Materials, Section S6). Specific vibrations are very sensitive to strongly bonded hydrogen bonds of amide groups as well as their arrangement in a crystalline packing. This in particular includes amide A (N–H stretch vibrations) and amide II (C–N deformation vibration). The comparison of both spectra shows that they are almost identical particularly in view of the amide-related vibrations. Similarly, as shown before, it was found that the amide A vibration of the xylene sample is slightly broadened. This finding is in agreement with the PXRD and the solid-state NMR spectroscopic results indicating that structural arrangement in the xylene sample is most likely the same, however, with a lower degree of order.

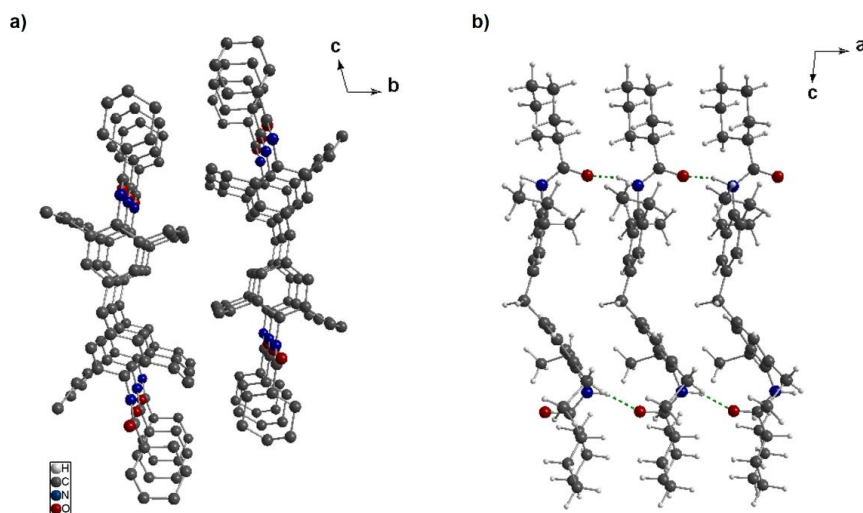


**Figure 2.** Crystal packaging plots of **3a** recrystallized from acetone. (a) A section of the crystal structure of **3a** with a viewing direction along the a-axis (hydrogens were omitted for clarity). The molecules are arranged in a stacking-type manner, whereas each stack comprises two strands of hydrogen bonds along the a-axis. (b) A section of the crystal structure of **3a** with a viewing direction along the b-axis. Every molecule forms two ditopic hydrogen bonds (green dotted lines) to two neighboring molecules. Notably, the hydrogen bonds pattern of the two strands point in the opposite direction.

#### 3.4. Batch Foaming of Polystyrene Using Kinked Bisamides

To evaluate how supramolecular objects of the kinked bisamide can act as foam cell nucleating agents for PS foams, a thermally induced batch foaming process was used as a screening method. The additive concentration was varied in the range from 0.01 to 1.0 wt.% to investigate the concentration-dependent influence of the kinked bisamides on the PS foam properties. All foams were characterized with respect to their cell morphology, the mean cell size, cell density and homogeneity, as well as the foam density. Exemplarily, the SEM micrographs and histograms of the foam cells for PS foams with the kinked bisamide **1a** at concentrations of 0.1, 0.5, and 1.0 wt.% as well as a neat PS reference foam are shown in Figure 3.

Using these conditions, the neat PS reference foam exhibits cell sizes in the range from 5  $\mu\text{m}$  and 55  $\mu\text{m}$ , yielding a mean cell size of  $20.3 \pm 8.3 \mu\text{m}$  with a significantly large cell size distribution. The cell density and the foam density of the reference sample was found to be  $2.1 \times 10^9 \text{ cm}^{-3}$  and  $67.1 \pm 16.3 \text{ kg/m}^3$ , respectively. PS foams containing only 0.01 wt.% of the kinked bisamide **1a** already exhibits a reduction in the mean cell size to  $11.9 \pm 3.8 \mu\text{m}$  including a significant narrower cell size distribution. Whereas the cell density was larger by a factor of 2, the foam density with  $70.4 \pm 2.9 \text{ kg/m}^3$  was found to be comparable, demonstrating that the foam density is not influenced significantly by addition of the additive. Upon further increasing the concentration to 0.5 wt.%, the mean cell size is further reduced to  $8.8 \pm 2.8 \mu\text{m}$ . The overall morphology of the PS foam is highly homogeneous and does not possess cells with sizes above 20  $\mu\text{m}$ , with the foam density being  $50.0 \pm 2.8 \text{ kg/m}^3$ . For PS foams with a highest concentration of 1.0 wt.%, a foam density of  $69.8 \pm 3.3 \text{ kg/m}^3$  with 20-fold increase in cell density and a mean cell size of  $6.4 \pm 3.5 \mu\text{m}$  was achieved, with the latter being noticeably smaller than the values found for the other foams with the kinked bisamide **1a**. However, these foams feature a cell morphology with a distinct inhomogeneity, as is indicated by the slightly increased standard deviation compared to the PS foams with a concentration of 0.5 wt.% of **1a**. As shown in Figure 3, the SEM micrographs as well as the corresponding histogram exhibit a large number of cells with sizes below 10  $\mu\text{m}$  and some cells with sizes in the range of

20  $\mu\text{m}$ . Notably, the large fraction of the smaller sized cells is significantly smaller compared to the PS foams with lower additive concentration. This indicates that a larger number of nucleating sites is still present and lets us assume that there is no severe dissolution and self-assembly issue at a high concentration of **1a**. Although bimodal foam morphologies were reported in the literature [2,40], we cannot clearly assign at the current stage this inhomogeneity to a specific effect caused by the additive.

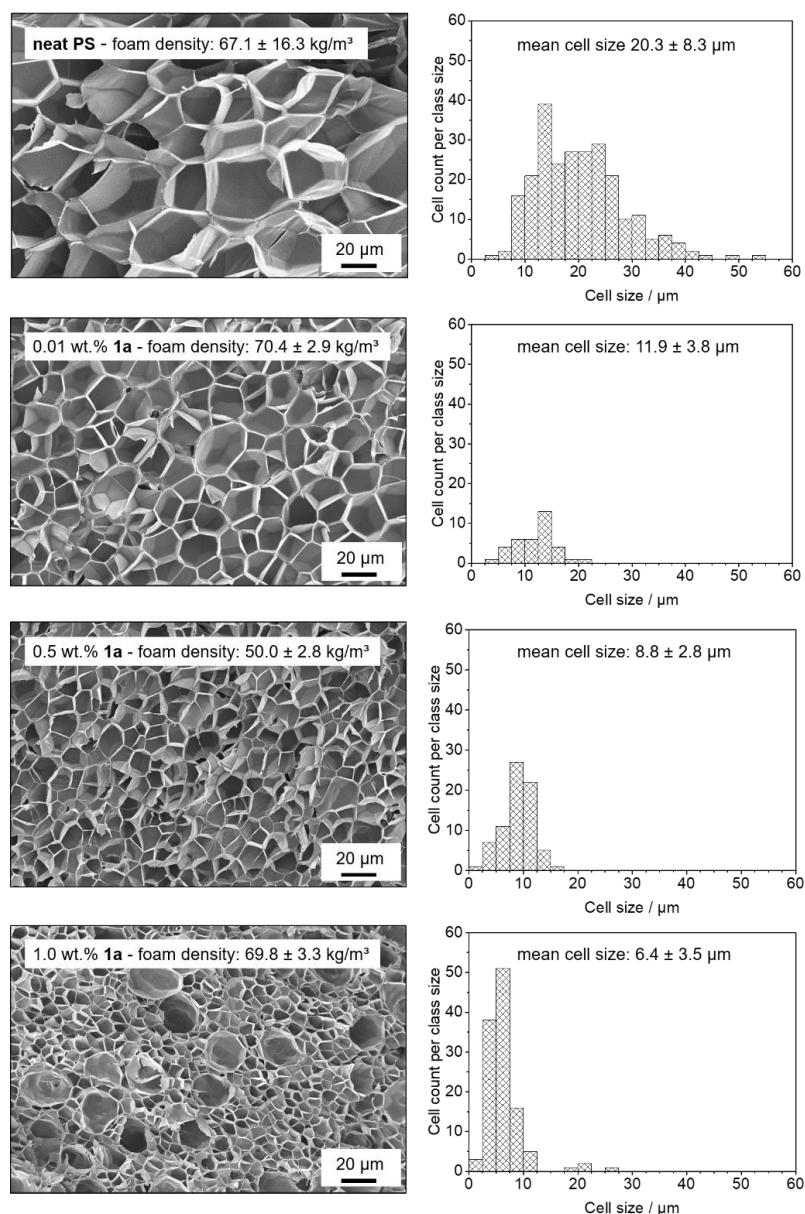


**Figure 3.** (Left): SEM micrographs ( $500\times$ ) depicting the cell morphologies of batch foamed neat PS specimens and batch foamed PS specimens with 0.01, 0.5, and 1.0 wt.% of kinked bisamide **1a**. The mean foam density is given for each concentration. (Right): corresponding histograms of the cell sizes including the mean cell sizes.

To gain further insight into structure–property relations with respect to the molecular design and the cell nucleation capabilities, we compare the concentration-dependent evolution of the foam morphology of **1a** with those foams obtained with **2a** and **3a**. Within this series, the substitution pattern  $R_1$  is varied from H to methyl to ethyl moieties at the ortho-positions close to the amide units. All of these compounds feature a fibrillary-like morphology when self-assembled from nonpolar solvents yet higher transition temperatures for **2a** and **3a**. After batch foaming of PS with the various concentrations and investigating the foam densities, all foams featured mean foam densities in the range from 46.8 to 72.8 kg/m<sup>3</sup>, corresponding to volume expansion ratios between 13 and 20. Figure 4 shows the concentration-dependent evolution of the mean cell size of PS batch foams with kinked bisamides of **1a**, **2a**, and **3a**. Similarly, as shown above, all kinked bisamides are capable of reducing the mean cell size in the investigated additive concentration range from 0.01 wt.% to 1.0 wt.% significantly. In general, compared to neat PS foams, a reduction in the mean cell size by more than 40% was found at concentrations larger than 0.25 wt.% for all additives. In addition, a significant reduction in the standard deviations of the mean cell sizes was achieved at these concentrations. Interestingly, when comparing the concentration-dependent series of **1a** with **2a** and **3a**, it was found that foams with the latter two additives showed a much more homogenous microcellular morphology and a significant smaller distribution of foam cell sizes. Thus, we conclude that these additives provide more nucleation sites. This is clearly demonstrated in Figure 4 in the SEM micrographs for the concentration of 0.5 wt.% for each kinked bisamide. Moreover, as already indicated by the smaller standard deviation of foams with **2a** and **3a**, no SEM micrograph shows an inhomogeneous cell morphology (see the Supplementary Materials, Section S7). Together with the smaller cells at high concentrations, this finding strongly indicates that there are no dissolution and dispersion issues present using this kind of additive. The PS foams with the finest morphologies were found by using a concentration of 1.0 wt.% of **2a** and **3a** featuring a microcellular morphology with mean cell sizes of  $3.5 \pm 1.1 \mu\text{m}$  and  $3.9 \pm 1.3 \mu\text{m}$  and cell densities of  $5.7 \times 10^{11}$  and  $3.5 \times 10^{11} \text{ cm}^{-3}$ , respectively. Thus, compared to the reference foam, the mean cell sizes can be improved by a factor of 5 and the cell densities by two orders of magnitude.

These concentration-dependent batch foam experiments were also performed with the kinked bisamides of **1b**, **2b**, and **3b** comprising peripheral phenyl side groups; the kinked bisamides of **1c**, **2c**, and **3c** with peripheral tert-butyl side groups; and **1d**, **2d**, and **3d** with peripheral n-butyl side groups. For the sake of completeness, all details on the foaming process, concentration-dependent evolution of the mean cell size and representative micrographs are given in the Supplementary Materials, Section S7. A summary of all relevant PS batch foam properties with kinked bisamides are given in the Supplementary Materials, Section S8. In general, all investigated kinked bisamides feature a highly efficient foam cell nucleation capability, resulting in a comparable mean cell size reduction of 30–40%. Moreover, the foam densities of all PS foams remain similar, demonstrated by the volume expansion ratio in the range of 10–20.

Although the different kinked bisamides feature a slightly different morphology of the nanostructures, this has no clear influence on the foam morphology. However, the trend observed for the series **1a**, **2a**, and **3a** can also be found for the other series demonstrating that the substitution pattern  $R_1$  has a beneficial effect on foam cell nucleation and thus on the microcellular morphology.

### 3.5. Extrusion Foaming of Polystyrene Using Kinked Bisamides

Foam extrusion was selected to demonstrate the applicability of the concept using kinked bisamides as foam cell nucleating agents on a technically relevant continuous process. We selected the kinked bisamide **3a** for these experiments. To perform a concentration-dependent series of experiments with a kinked bisamide and to evaluate suitable parameters on our setup, a total amount of the additive on a 100 g scale is required. Foam extrusion, including material feeding and temperature protocols, was performed in a similar manner

as described before (see also the Materials and Methods section) and in References [29,30]. To study the influence of the concentration of **3a** with respect to the foam morphology and density, we prepared PS foams with 0.1, 0.2, and 0.5 wt.% of **3a**. This also provides information on the dissolution and self-assembly behavior of **3a** in the gas-loaded polymer melt under harsher processing conditions such as large shear forces, and high barrel temperature and pressure.

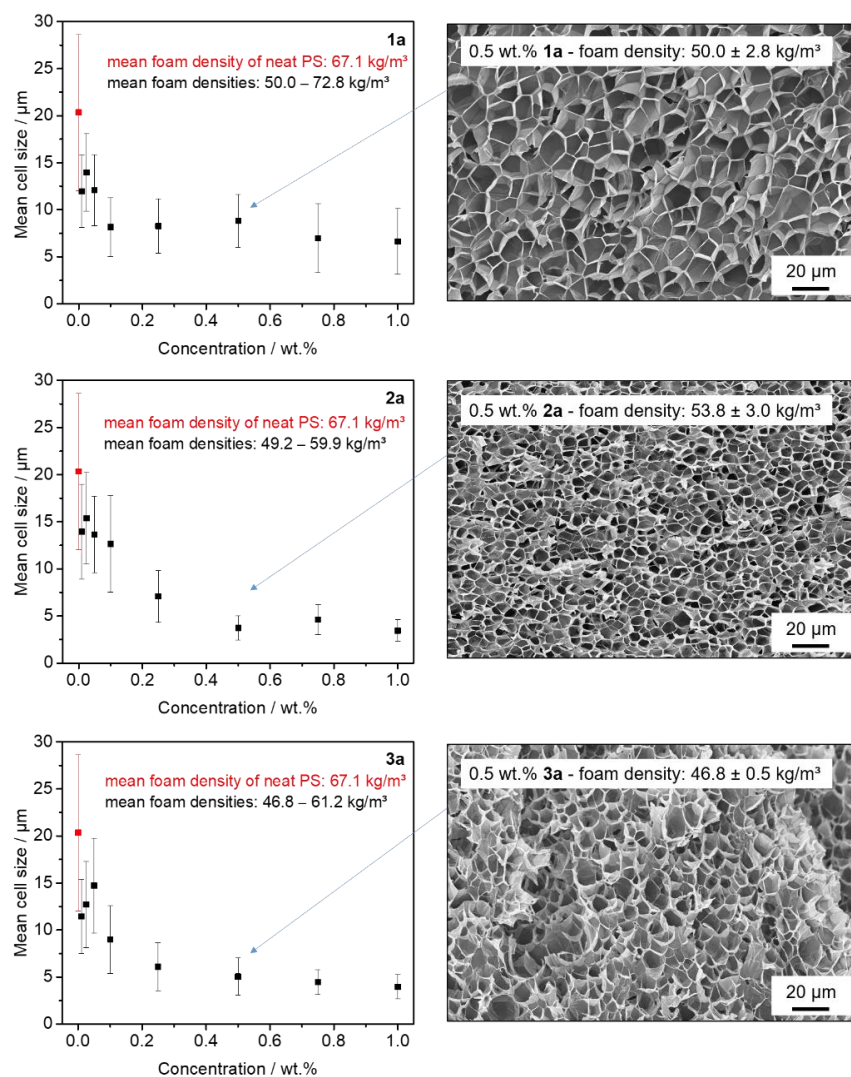


**Figure 4.** (Left): evolution of the mean cell size with increasing concentrations of the kinked bisamides **1a**, **2a**, and **3a** of batch foamed polystyrene specimens. Data for the neat PS reference foam are shown in red. (Right): SEM micrographs (500×) depicting the homogeneous microcellular morphology of batch foamed polystyrenes at a concentration of 0.5 wt.% for **1a**, **2a** and **3a**, including the mean foam densities.

Similar to the batch foamed samples, we obtained macroscopically comparable extruded polystyrene foams with the kinked bisamide **3a** and the neat PS reference foam (for a photographic image, see the Supplementary Materials, Section S9) featuring low foam den-

sities with volume expansion ratios in the range of 15. In detail, while the foam density of the neat XPS foam was found to be  $61.6 \pm 4.1 \text{ kg/m}^3$ , the foam densities with **3a** were found to be  $76.5 \pm 1.5 \text{ kg/m}^3$  at 0.1 wt.%,  $73.7 \pm 2.0 \text{ kg/m}^3$  at 0.2 wt.%, and  $71.2 \pm 1.9 \text{ kg/m}^3$  at 0.5 wt.%, respectively (see Figure 5). The neat PS reference foam clearly possesses a coarse macro-cellular foam morphology with large cell sizes and cell size distribution (see Supplementary Materials, Section S10) and determined to be  $1094 \pm 377 \mu\text{m}$ . Correspondingly, a cell density of  $1.5 \times 10^4 \text{ cm}^{-3}$  was calculated. In contrast, XPS foams with the kinked bisamide **3a** applying the same or very similar conditions exhibit significant smaller cell sizes. XPS foams with 0.1 wt.% of **3a** already leads to a 70 times cell size reduction with a mean cell size of  $14.4 \pm 4.7 \mu\text{m}$ . Upon further increasing the concentration of **3a** to 0.2 wt.% and 0.5 wt.%, the mean cell sizes were found to be  $19.0 \pm 6.7 \mu\text{m}$  and  $10.7 \pm 4.3 \mu\text{m}$ , respectively. Thus, using a concentration of 0.5 wt.% of **3a** results in a reduction in the cell size by two orders of magnitude. Expectedly, for the foams with to 0.1 wt.%, 0.2 wt.% and 0.5 wt.% of **3a**, the cell densities were significantly increased by 6 orders of magnitude with respect to the reference foam featuring values of  $5.9 \times 10^9 \text{ cm}^{-3}$ ,  $2.8 \times 10^9 \text{ cm}^{-3}$ , and  $1.8 \times 10^{10} \text{ cm}^{-3}$ , respectively.

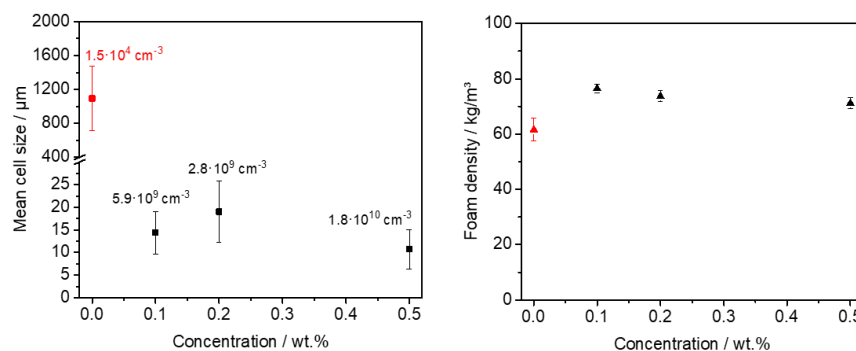


**Figure 5.** Left: mean cell sizes versus additive concentration of XPS foam specimens nucleated with **3a**. The respective cell densities are added for each concentration. Right: foam densities versus additive concentration of extrusion foamed polystyrene specimens nucleated with **3a**. Data for the XPS reference foam are shown in red.

In Figure 6, SEM micrographs of the cell morphologies of XPS foam specimens with different concentrations of **3a** and the corresponding cell size histograms are shown. The micrographs reveal that no significant portion of an open-cell content can be seen. Moreover, for all concentrations, a homogeneous morphology was found. This is in agreement with the results from the batch-foamed samples demonstrating the suitability of **3a** as a foam cell nucleating agent over a large concentration range. These data strongly suggest that there is no dissolution, self-assembly, or dispersion issue with this class of molecules at the selected conditions. To sum up, the results show that the kinked bisamide **3a** is a very effective foam cell nucleating agent for the foam extrusion even at a concentration of 0.1 wt.%. Interestingly, this class of compounds can be used over a large concentration range without an indication of a dissolution, self-assembly, or dispersion issue. At larger concentrations of 0.5 wt.%, closed small cells in the range of  $10 \mu\text{m}$  can be found without sacrificing the foam density, rendering this material class as highly promising in preparing low-density polystyrene foams with homogeneous microcellular morphology.

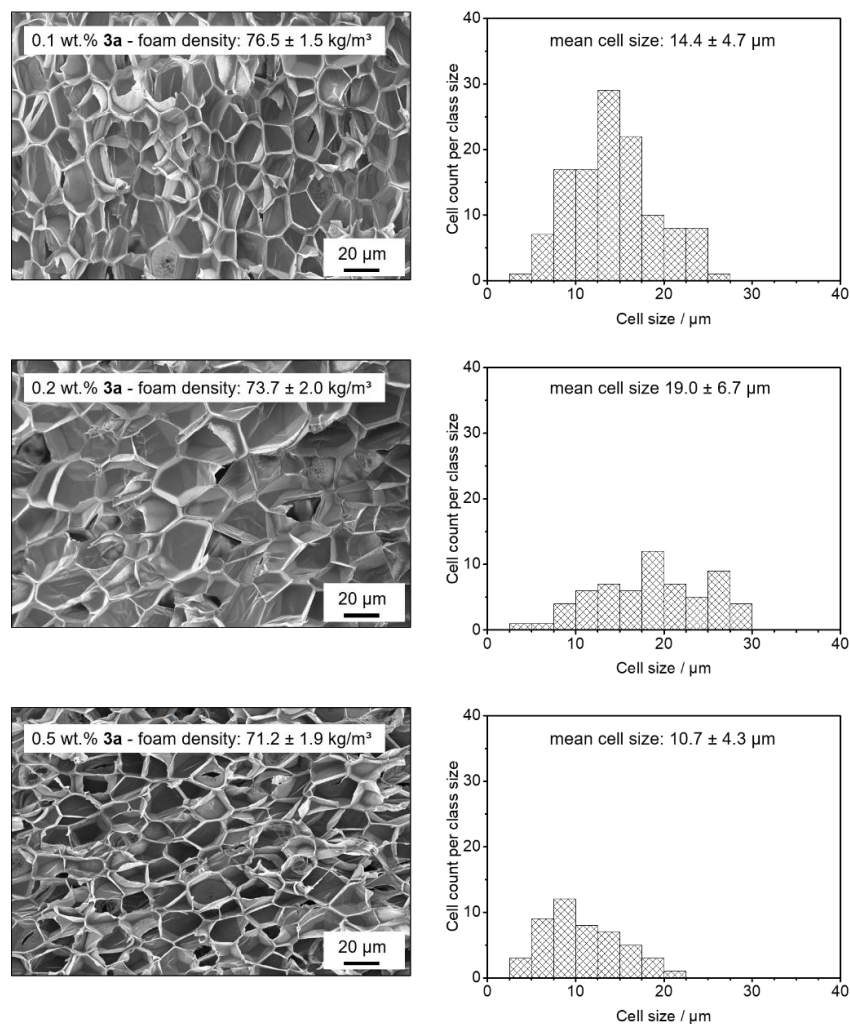


**Figure 6.** (Left): SEM micrographs (500×) of the cell morphologies and mean foam densities of extrusion foamed polystyrene specimens with 0.1 wt.% (top), 0.2 wt.% (middle), and 0.5 wt.% (bottom) of kinked bisamide **3a**, demonstrating the homogeneity of the morphology for all foams. (Right): corresponding histograms of the cell sizes including the mean cell sizes.

#### 4. Conclusions

We demonstrated that the class of kinked bisamides, based on various 4,4'-diphenylmethane central units and via amide-linked peripheral side groups, is highly suitable to act as efficient supramolecular foam cell nucleating agents for PS. Systematic variation of the molecular design allows us to tune the thermal properties as well as the mesoscopic morphology of the nano-objects from fibrillary to ribbon to a plate-like shape. Structural elucidation on a selected kinked bisamide reveals that such an elongated fibrillary or ribbon-like shape is attributed to the formation of two strands of hydrogen bonds, which can be regarded as the main driving force for a preferred one-dimensional crystal growth. It was found that all kinked bisamides can be conveniently dissolved at elevated temperatures in a large range of concentrations, which subsequently forms homogeneously dispersed nano-objects upon cooling, providing a large number of nucleation sites for the foam cell nucleating. In a series of batch foaming experiments, we have shown that using

1.0 wt.% of the kinked bisamide with cyclohexane side groups and a methyl substituent in ortho position to the amide groups feature a highly homogeneous cell morphology of the resulting PS foam with a mean cell size as low as 3.5  $\mu\text{m}$  and a foam density of 52  $\text{kg}/\text{m}^3$ . Kinked bisamide **3a** with cyclohexane side groups and ethyl substituents at the ortho-positions of the amide groups was selected to study the concentration-dependent behavior of the additive in a continuous foam extrusion process. All XPS foams feature comparable foam densities in the range of 67 to 80  $\text{kg m}^{-3}$ . Using 0.5 wt.% of **3a**, we were able to achieve polymer foams with a homogeneous morphology and cell sizes in the range of 10  $\mu\text{m}$ , which is lower by a factor 100 and a cell density of  $\approx 10^{10} \text{ cm}^{-3}$ , which is higher by 6 orders of magnitude compared to the neat PS reference foam. These findings demonstrate that the class of kinked bisamides is a promising candidate to achieve microcellular PS foams with a defined microcellular morphology, a regime in which the Knudsen effect becomes relevant.

**Supplementary Materials:** The following are available online at <https://www.mdpi.com/article/10.3390/polym13071094/s1>, Section S1: Schematic representation of foam cell nucleation with supramolecular nanoobjects, Section S2: Synthesis and characterization of kinked bisamides, Section S3: Thermal properties of kinked bisamides, Section S4: PXRD investigation of kinked bisamide **3a**, Section S5: Solid-state NMR spectroscopy of kinked bisamide **3a**, Section S6: FT-IR spectroscopy of kinked bisamide **3a**, Section S7: Cell morphologies of polystyrene foams by batch foaming with kinked bisamides, Section S8: Summary of polystyrene batch foam properties with kinked bisamides, Section S9: Photograph of an extruded neat polystyrene foam and a polystyrene foam with 0.5 wt.% **3a**, Section S10: Photograph and light microscopy image of neat polystyrene foams by extrusion foaming. A crystallographic information file (CIF) is provided as additional supporting information.

**Author Contributions:** Conceptualization, B.K., K.K., J.S., V.A., and H.-W.S.; methodology, B.K., K.K., M.A., K.P.v.d.Z., J.S., V.A., and H.-W.S.; investigation, formal analysis, validation, and visualization, B.K. and D.K.; data curation, B.K., D.K., and K.P.v.d.Z.; writing—original draft preparation, B.K., D.K., and K.K.; writing—review and editing, B.K., D.K., M.A., K.P.v.d.Z., K.K., J.S., V.A., and H.-W.S.; supervision and project administration, J.S., V.A., and H.-W.S. All authors have read and agreed to the published version of the manuscript.

**Funding:** This research was funded by the German Research Foundation (DFG) within the Collaborative Research Center 840 (SFB 840, Project B4). This publication was funded by the German Research Foundation (DFG) and the University of Bayreuth in the funding program Open Access Publishing.

**Institutional Review Board Statement:** Not applicable.

**Informed Consent Statement:** Not applicable.

**Data Availability Statement:** The presented data are available by the authors upon request.

**Acknowledgments:** Doris Hanft, Jutta Failner, and Sandra Ganzleben (Macromolecular Chemistry I, University of Bayreuth) are gratefully acknowledged for their help during synthesis of the kinked bisamides. We appreciate the support of Sebastian Gröschel (Department of Polymer Engineering, University of Bayreuth) during the foam extrusion process. The authors thank the support from the KeyLabs of the Bavarian Polymer Institute. K.P.V.D.Z. gratefully acknowledges support by the Elite Network of Bavaria within the study program “Macromolecular Science”.

**Conflicts of Interest:** The authors declare no conflict of interest.

## References

1. Kumar, A.; Patham, B.; Mohanty, S.; Nayak, S.K. Polyolefinic nanocomposite foams: Review of microstructure-property relationships, applications, and processing considerations. *J. Cell. Plast.* **2020**. [CrossRef]
2. Dugad, R.; Radhakrishna, G.; Gandhi, A. Recent advancements in manufacturing technologies of microcellular polymers: A review. *J. Polym. Res.* **2020**, *27*. [CrossRef]
3. Zhao, C.; Mark, L.H.; Kim, S.; Chang, E.; Park, C.B.; Lee, P.C. Recent progress in micro-/nano-fibrillar reinforced polymeric composite foams. *Polym. Eng. Sci.* **2021**. [CrossRef]
4. Okolieocha, C.; Raps, D.; Subramaniam, K.; Altstädt, V. Microcellular to nanocellular polymer foams: Progress (2004–2015) and future directions—A review. *Eur. Polym. J.* **2015**, *73*, 500–519. [CrossRef]

5. Guo, A.; Li, H.; Xu, J.; Li, J.; Li, F. Effect of microstructure on the properties of polystyrene microporous foaming material. *e-Polymers* **2020**, *20*, 103–110. [[CrossRef](#)]
6. Wong, A.; Park, C.B. The effects of extensional stresses on the foamability of polystyrene-talc composites blown with carbon dioxide. *Chem. Eng. Sci.* **2012**, *75*, 49–62. [[CrossRef](#)]
7. Zhai, W.; Park, C.B.; Kontopoulou, M. Nanosilica Addition Dramatically Improves the Cell Morphology and Expansion Ratio of Polypropylene Heterophasic Copolymer Foams Blown in Continuous Extrusion. *Ind. Eng. Chem. Res.* **2011**, *50*, 7282–7289. [[CrossRef](#)]
8. Yang, J.; Huang, L.; Zhang, Y.; Chen, F.; Zhong, M. Mesoporous silica particles grafted with polystyrene brushes as a nucleation agent for polystyrene supercritical carbon dioxide foaming. *J. Appl. Polym. Sci.* **2013**, *130*, 4308–4317. [[CrossRef](#)]
9. Zhai, W.; Park, C.B.; Wang, L.; Park, C.B.; Lee, E.K.; Naguib, H.E. Cell Structure Evolution and the Crystallization Behavior of Polypropylene/Clay Nanocomposites Foams Blown in Continuous Extrusion. *Ind. Eng. Chem. Res.* **2010**, *49*, 9834–9845. [[CrossRef](#)]
10. Wang, M.Y.; Zhu, R.M.; Zhou, N.Q.; Park, C.B. Effects of Nanoclay and CO<sub>2</sub> Content on Foaming Behaviors of PP/PS Alloys. *Adv. Mat. Res.* **2014**, *898*, 107–110.
11. Okolieocha, C.; Köppl, T.; Kerling, S.; Tölle, F.J.; Fathi, A.; Mühlaupt, R.; Altstädt, V. Influence of graphene on the cell morphology and mechanical properties of extruded polystyrene foam. *J. Cell. Plast.* **2015**, *51*, 413–426. [[CrossRef](#)]
12. Kausar, A. Synthesis and properties of novel polystyrene/polyurea and functional graphene-based nanocomposite foams. *J. Cell. Plast.* **2017**, *53*, 305–318. [[CrossRef](#)]
13. Zhang, C.; Zhu, B.; Lee, L.J. Extrusion foaming of polystyrene/carbon particles using carbon dioxide and water as co-blowing agents. *Polymer* **2011**, *52*, 1847–1855. [[CrossRef](#)]
14. Gong, P.; Buahom, P.; Tran, M.-P.; Saniei, M.; Park, C.B.; Pötschke, P. Heat transfer in microcellular polystyrene/multi-walled carbon nanotube nanocomposite foams. *Carbon* **2015**, *93*, 819–829. [[CrossRef](#)]
15. Fu, D.; Kuang, T.; Yen, Y.-C.; Li, D.; Benatar, A.; Peng, X.F.; Lee, L.J. Polystyrene/multi-wall carbon nanotube composite and its foam assisted by ultrasound vibration. *J. Cell. Plast.* **2017**, *53*, 273–285. [[CrossRef](#)]
16. Antunes, M.; Gedler, G.; Velasco, J.I. Multifunctional nanocomposite foams based on polypropylene with carbon nanofillers. *J. Cell. Plast.* **2013**, *49*, 259–279. [[CrossRef](#)]
17. Gutiérrez, C.; Garcia, M.T.; Mencia, R.; Garrido, I.; Rodríguez, J.F. Clean preparation of tailored microcellular foams of polystyrene using nucleating agents and supercritical CO<sub>2</sub>. *J. Mater. Sci.* **2016**, *51*, 4825–4838. [[CrossRef](#)]
18. Zhou, Y.-G.; Su, B.; Turng, L.-S. Mechanical properties, fiber orientation, and length distribution of glass fiber-reinforced polypropylene parts: Influence of water-foaming technology. *Polym. Compos.* **2018**, *39*, 4386–4399. [[CrossRef](#)]
19. Rizvi, A.; Park, C.B. Dispersed polypropylene fibrils improve the foaming ability of a polyethylene matrix. *Polymer* **2014**, *55*, 4199–4205. [[CrossRef](#)]
20. Rizvi, A.; Tabatabaei, A.; Barzegari, M.R.; Mahmood, S.H.; Park, C.B. In situ fibrillation of CO<sub>2</sub>-philic polymers: Sustainable route to polymer foams in a continuous process. *Polymer* **2013**, *54*, 4645–4652. [[CrossRef](#)]
21. Kakroodi, A.R.; Kazemi, Y.; Ding, W.; Ameli, A.; Park, C.B. Poly(lactic acid)-Based in Situ Microfibrillar Composites with Enhanced Crystallization Kinetics, Mechanical Properties, Rheological Behavior, and Foaming Ability. *Biomacromolecules* **2015**, *16*, 3925–3935. [[CrossRef](#)]
22. Libster, D.; Aserin, A.; Garti, N. Advanced nucleating agents for polypropylene. *Polym. Adv. Technol.* **2007**, *18*, 685–695. [[CrossRef](#)]
23. Gahleitner, M.; Grein, C.; Kheirandish, S.; Wolfschwenger, J. Nucleation of Polypropylene Homo- and Copolymers. *Int. Polym. Process.* **2011**, *26*, 2–20. [[CrossRef](#)]
24. Blomenhofer, M.; Ganzleben, S.; Hanft, D.; Schmidt, H.-W.; Kristiansen, M.; Smith, P.; Stoll, K.; Mäder, D.; Hoffmann, K. “Designer” Nucleating Agents for Polypropylene. *Macromolecules* **2005**, *38*, 3688–3695. [[CrossRef](#)]
25. Abraham, F.; Ganzleben, S.; Hanft, D.; Smith, P.; Schmidt, H.-W. Synthesis and Structure-Efficiency Relations of 1,3,5-Benzenetrisamides as Nucleating Agents and Clarifiers for Isotactic Poly(propylene). *Macromol. Chem. Phys.* **2010**, *211*, 171–181. [[CrossRef](#)]
26. Richter, F.; Schmidt, H.-W. Supramolecular Nucleating Agents for Poly(butylene terephthalate) Based on 1,3,5-Benzenetrisamides. *Macromol. Mater. Eng.* **2013**, *298*, 190–200. [[CrossRef](#)]
27. Wang, T.; Yang, Y.; Zhang, C.; Tang, Z.; Na, H.; Zhu, J. Effect of 1,3,5-trialkyl-benzenetricarboxylamide on the crystallization of poly(lactic acid). *J. Appl. Polym. Sci.* **2013**, *130*, 1328–1336. [[CrossRef](#)]
28. Abraham, F.; Schmidt, H.-W. 1,3,5-Benzenetrisamide based nucleating agents for poly(vinylidene fluoride). *Polymer* **2010**, *51*, 913–921. [[CrossRef](#)]
29. Aksit, M.; Zhao, C.; Klose, B.; Kreger, K.; Schmidt, H.-W.; Altstädt, V. Extruded Polystyrene Foams with Enhanced Insulation and Mechanical Properties by a Benzene-Trisamide-Based Additive. *Polymers* **2019**, *11*, 268. [[CrossRef](#)]
30. Aksit, M.; Klose, B.; Zhao, C.; Kreger, K.; Schmidt, H.-W.; Altstädt, V. Morphology control of extruded polystyrene foams with benzene-trisamide-based nucleating agents. *J. Cell. Plast.* **2019**, *55*, 249–261. [[CrossRef](#)]
31. Aksit, M.; Gröschel, S.; Kuhn, U.; Aksit, A.; Kreger, K.; Schmidt, H.-W.; Altstädt, V. Low-Density Polybutylene Terephthalate Foams with Enhanced Compressive Strength via a Reactive-Extrusion Process. *Polymers* **2020**, *12*, 2021. [[CrossRef](#)]
32. Mörl, M.; Steinlein, C.; Kreger, K.; Schmidt, H.-W.; Altstädt, V. Improved compression properties of polypropylene extrusion foams by supramolecular additives. *J. Cell. Plast.* **2018**, *54*, 483–498. [[CrossRef](#)]

33. Stumpf, M.; Spörrer, A.; Schmidt, H.-W.; Altstädt, V. Influence of supramolecular additives on foam morphology of injection-molded i-PP. *J. Cell. Plast.* **2011**, *47*, 519–534. [[CrossRef](#)]
34. Urushihara, T.; Ueda, N.; Kawamoto, N. Polyolefin Resin Composition. U.S. Patent 2010/0240815A1, 23 September 2010.
35. Material Data Sheet, Polystyrene 168N, Ineos Styrolution. Available online: [https://www.ineos-styrolution.com/Product/GPPS\\_Styrolution-PS-168N-L\\_SKU200300060596.html](https://www.ineos-styrolution.com/Product/GPPS_Styrolution-PS-168N-L_SKU200300060596.html), (accessed on 3 March 2021).
36. Xu, X.; Park, C.B.; Xu, D.; Pop-Iliev, R. Effects of die geometry on cell nucleation of PS foams blown with CO<sub>2</sub>. *Polym. Eng. Sci.* **2003**, *43*, 1378–1390. [[CrossRef](#)]
37. Kumar, V.; Weller, J. Production of Microcellular Polycarbonate Using Carbon Dioxide for Bubble Nucleation. *J. Eng. Ind.* **1994**, *116*, 413–420. [[CrossRef](#)]
38. Steiner, T. The Hydrogen Bond in the Solid State. *Angew. Chem. Int. Ed.* **2002**, *41*, 48–76. [[CrossRef](#)]
39. Grüninger, H.; Schmutzler, A.; Siegel, R.; Armstrong, K.; Frost, D.J.; Senker, J. Quantitative description of 1H SQ and DQ coherences for the hydroxyl disorder within hydrous ringwoodite. *Phys. Chem. Chem. Phys.* **2018**, *20*, 15098–15105. [[CrossRef](#)]
40. Lee, K.-M.; Lee, E.K.; Kim, S.G.; Park, C.B.; Naguib, H.E. Bi-cellular Foam Structure of Polystyrene from Extrusion Foaming Process. *J. Cell. Plast.* **2009**, *45*, 539–553. [[CrossRef](#)]

## Kinked Bisamides as Efficient Supramolecular Foam Cell Nucleating Agents for Low-Density Polystyrene Foams With Homogeneous Microcellular Morphology

Bastian Klose <sup>1</sup>, Daniel Kremer <sup>1</sup>, Merve Aksit <sup>2</sup>, Kasper P. van der Zwan <sup>3</sup>, Klaus Kreger <sup>1</sup>, Jürgen Senker <sup>3,4,\*</sup>, Volker Altstädt <sup>2,4,\*</sup> and Hans-Werner Schmidt <sup>1,4,\*</sup>

<sup>1</sup> Macromolecular Chemistry I, University of Bayreuth, Universitaetsstrasse 30, 95447 Bayreuth, Germany; bastian.klose@uni-bayreuth.de (B.K.); daniel.kremer@uni-bayreuth.de (D.K.); klaus.kreger@uni-bayreuth.de (K.K.); hans-werner.schmidt@uni-bayreuth.de (H.-W.S.)

<sup>2</sup> Department of Polymer Engineering, University of Bayreuth, Universitaetsstrasse 30, 95447 Bayreuth, Germany; merve.aksit@uni-bayreuth.de (M.A.); altstaedt@uni-bayreuth.de (V.A.)

<sup>3</sup> Inorganic Chemistry III, University of Bayreuth, Universitaetsstrasse 30, 95447 Bayreuth, Germany; kasper.van-der-Zwan@uni-bayreuth.de (K.P.Z.); juergen.senker@uni-bayreuth.de (J.S.)

<sup>4</sup> Bavarian Polymer Institute and Bayreuth Institute of Macromolecular Research, University of Bayreuth, Universitaetsstrasse 30, 95447 Bayreuth, Germany

\* Correspondence: hans-werner.schmidt@uni-bayreuth.de; altstaedt@uni-bayreuth.de; juergen.senker@uni-bayreuth.de; Tel.: +49 921553200 (H.-W.S.); +49 921557471 (V.A.); +49 921552532 (J.S.)

### Table of content

- S1. Schematic representation of foam cell nucleation with supramolecular nanoobjects
- S2. Synthesis and characterization of kinked bisamides
- S3. Thermal properties of kinked bisamides
- S4. PXRD investigation of kinked bisamide 3a
- S5. Solid-state NMR spectroscopy of kinked bisamide 3a
- S6. FTIR spectroscopy of kinked bisamide 3a
- S7. Cell morphologies of polystyrene foams by batch foaming with kinked bisamides
- S8. Summary of polystyrene batch foam properties with kinked bisamides
- S9. Photograph of an extruded neat polystyrene foam and a polystyrene foam with 0.5 wt.% 3a
- S10. Photograph and light microscopy image of neat polystyrene foams by extrusion foaming

### References

### S1. Schematic representation of foam cell nucleation with supramolecular nanoobjects

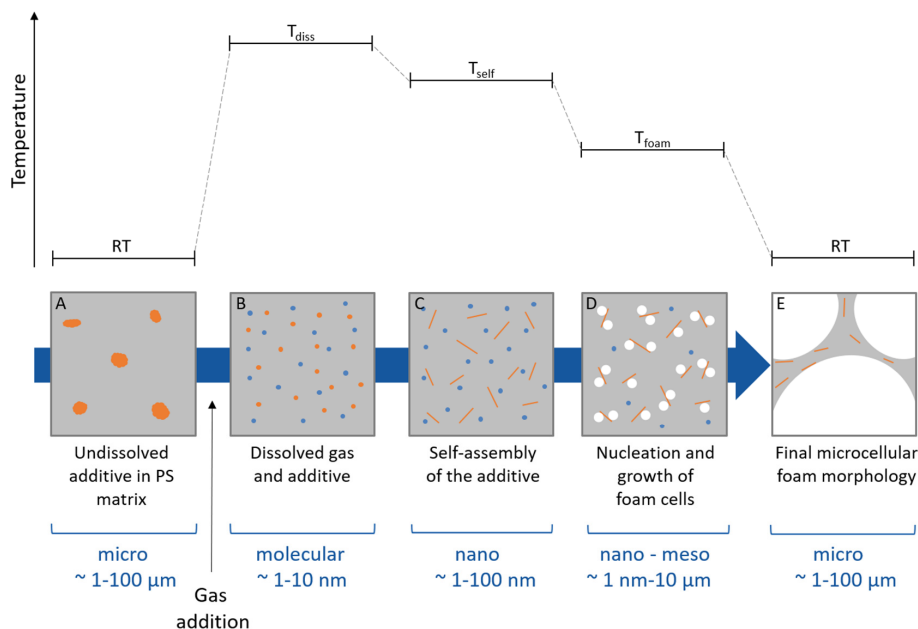


**Figure S1.** Schematic representation of the generalized process using supramolecular nanoobjects as heterogeneous cell nucleation agents for polymer foaming. The temperature and the relevant length scale, at which each individual step occurs, is indicated. The conceptual approach comprises: A) The preparation of a powder-powder mixture with the finely micro-sized supramolecular additive. B) Upon heating, the supramolecular additive is molecularly dissolved and both the additive as well as the added physical blowing agent is homogeneously dispersed in the polymer melt. C) Upon cooling, self-assembly of the supramolecular additive results into finely dispersed in-situ formed nanoobjects. D) Upon further cooling, these nanoobjects acts as heterogeneous nucleation sites for the foam cells, which subsequently grows during the foaming step on the nano and mesoscale. E) At room temperature, a solid foam with a microcellular foam morphology is obtained.

### S2. Synthesis and characterization of kinked bisamides

#### General synthetic procedure

1 eq. of 4,4'-Diaminodiphenylmethane, 4,4'-Methylenebis(2,6-dimethylaniline) or 4,4'-Methylenebis(2,6-diethylaniline) was added under nitrogen to a mixture consisting of N-methylpyrrolidone (NMP) or tetrahydrofuran (THF) and pyridine or triethylamine (Figure S2). A small amount of LiCl was added and the solution was cooled to 0 – 5 °C. 2.2 eq. of the respective acid chloride was added dropwise and the reaction mixture was heated to 20 – 80 °C. The reaction mixture maintained at this temperature for several hours. After cooling, the reaction mixture was precipitated in ice water under vigorous stirring. The precipitate was filtered off and dried under vacuum for 12h. All compounds were further purified by recrystallization.

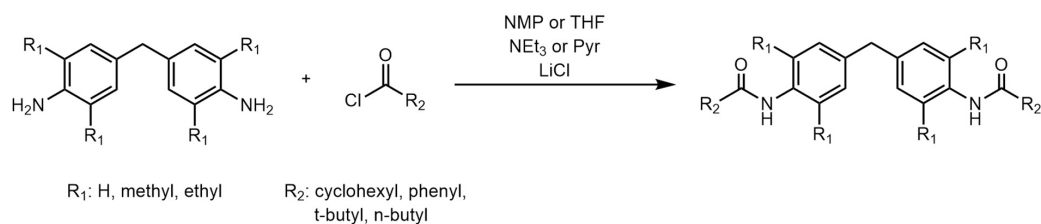


**Figure S2.** Schematic of the synthetic procedure of *N,N'*-[Methylenebis(4,1-phenylene)]bisamides.

#### Molecular characterization

$^1\text{H-NMR}$  spectra in solution were recorded on a Bruker Avance Ultrashield 300 (300 MHz) at room temperature. For the preparation of the NMR samples, approx. 5 mg of the compounds were dissolved in 1.2 mL of the respective deuterated solvent.

Mass spectra (MS) were carried out on a FINNIGAN MAT 8500 spectrometer from Thermo-Fisher Scientific using electron spray ionization.

HPLC analyses were performed using an Agilent 1100 equipped with a C18 column Agilent Eclipse Plus ( $d = 3.5 \mu\text{m}$ ,  $4.6 \times 150 \text{ mm}$ ). 0.1 mg – 1.0 mg of the compounds were dissolved in 10 mL acetonitrile or NMP at  $60^\circ\text{C}$ . 25  $\mu\text{L}$  of the solutions were injected. As mobile phase an acetonitrile:water mixture (90:10 v/v %) was used with a flowrate of 0.3 mL/min. Detections were performed using a UV-detector at 250 nm and the peak values of the elution volume were reported.

*Synthesis of N,N'*-[Methylenebis(4,1-phenylene)]bis[cyclohexanecarboxamide] **1a**: 3.0 g (15.0 mmol) 4,4'-diaminodiphenylmethane, 4.9 g (33.0 mmol) cyclohexanecarbonyl chloride, 100 mL NMP, 20.0 mL pyridine, 0.1 g LiCl. Reaction conditions: 12 h,  $80^\circ\text{C}$ . Recrystallization from 500 mL MeOH yielded 5.5 g (13.1 mmol, 88 %) of a white solid powder.

$^1\text{H-NMR}$  (DMSO- $d_6$ , 300 MHz,  $\delta$  in ppm): 9.73 (2H, s, NH), 7.49 (4H, d,  $\text{H}_{\text{Ar}}$ ), 7.08 (4H, d,  $\text{H}_{\text{Ar}}$ ), 3.79 (2H, s, Ar-CH<sub>2</sub>-Ar), 2.32-2.25 (2H, m, CH<sub>Cyc</sub>), 1.75-1.20 (20H, m, CH<sub>2Cyc</sub>). MS-EI ( $m/z$ , %): 418 (M<sup>+</sup>, 100), 309 (46), 308 (100), 199 (14), 198 (95), 197 (20), 106 (17), 83 (42), 55 (32). HPLC (El.-Vol., area in %): 2.68 mL (96).

*Synthesis of N,N'*-[Methylenebis(4,1-phenylene)]bis[benzamide] **1b**: 5.0 g (25.2 mmol) 4,4'-diaminodiphenylmethane, 7.8 g (55.4 mmol) benzoyl chloride, 100 mL NMP, 4.5 mL pyridine. Reaction conditions: 1 h,  $20^\circ\text{C}$ . Boiling in 500 mL MeOH yielded 9.6 g (23.7 mmol, 95%) of a white solid powder.

$^1\text{H-NMR}$  (DMSO- $d_6$ , 300 MHz,  $\delta$  in ppm): 10.21 (2H, s, NH), 7.95-7.92 (4H, m,  $\text{H}_{\text{Ar}}$ ), 7.70 (4H, d,  $\text{H}_{\text{Ar}}$ ), 7.60-7.49 (6H, m,  $\text{H}_{\text{Ar}}$ ), 7.20 (4H, d,  $\text{H}_{\text{Ar}}$ ), 3.89 (2H, s, Ar-CH<sub>2</sub>-Ar). MS-EI ( $m/z$ , %): 406 (M<sup>+</sup>, 100), 301 (36), 210 (11), 106 (58), 105 (98), 78 (23), 77 (98), 51 (55). HPLC (El.-Vol., area in %): 2.07 mL (100).

*Synthesis of N,N'*-[Methylenebis(4,1-phenylene)]bis[tertbutylcarboxamide] **1c**: 3.0 g (15.0 mmol) 4,4'-diaminodiphenylmethane, 4.0 g (33.0 mmol) pivaloyl chloride, 100 mL NMP, 20.0 mL pyridine, 0.1 g LiCl. Reaction conditions: 24 h,  $80^\circ\text{C}$ . Recrystallization from 500 mL ethyl acetate yielded 4.1 g (11.1 mmol, 75 %) of a white solid powder.

$^1\text{H-NMR}$  (CDCl<sub>3</sub>, 300 MHz,  $\delta$  in ppm): 7.45 (2H, d,  $\text{H}_{\text{Ar}}$ ), 7.28 (2H, m, NH), 7.13 (2H, d,  $\text{H}_{\text{Ar}}$ ), 3.92 (2H, s, Ar-CH<sub>2</sub>-Ar), 1.32 (18H, s, CH<sub>3</sub>). MS-EI ( $m/z$ , %): 366 (M<sup>+</sup>, 100), 309 (15), 283 (15), 282 (64), 198 (11), 197 (16), 132 (10), 58 (91), 42 (12). HPLC (El.-Vol., area in %): 2.17 mL (100).

*Synthesis of N,N'-[Methylenebis(4,1-phenylene)]bis[pentanamide] 1d:* 5.0 g (25.2 mmol) 4,4'-diaminodiphenylmethane, 6.0 g (55.5 mmol) valeroyl chloride, 100 mL NMP, 4.5 mL pyridine. Reaction conditions: 1 h, 20 °C. Recrystallization from 300 mL MeOH yielded 8.8 g (24.0 mmol, 95 %) of a white solid powder.

<sup>1</sup>H-NMR (DMSO-d<sub>6</sub>, 300 MHz, δ in ppm): 9.80 (2H, s, NH), 7.48 (4H, d, H<sub>Ar</sub>), 7.10 (4H, d, H<sub>Ar</sub>), 3.80 (2H, s, Ar-CH<sub>2</sub>-Ar), 2.29-2.24 (4H, t, CO-CH<sub>2</sub>), 1.58-1.53 (4H, quint, CH<sub>2</sub>-CH<sub>2</sub>), 1.34-1.29 (4H, sext, CH<sub>2</sub>-CH<sub>3</sub>), 0.91-0.86 (6H, t, CH<sub>2</sub>-CH<sub>3</sub>). MS-EI (m/z, %): 366 (M<sup>+</sup>, 99), 324 (22), 323 (20), 283 (48), 282 (100), 240 (18), 199 (24), 198 (100), 197 (53), 182 (19), 180 (12), 132 (15), 106 (44), 57 (31), 41 (16). HPLC (El.-Vol., area in %): 2.14 mL (100).

*Synthesis of N,N'-[Methylenebis(2,6-dimethyl-4,1-phenylene)]bis[cyclohexanecarboxamide] 2a:* 3.6 g (14.0 mmol) 4,4'-methylenebis(2,6-dimethylaniline), 4.5 g (30.8 mmol) cyclohexanecarbonyl chloride, 100 mL THF (dried), 4.3 mL triethylamine. Reaction conditions: 48 h, 60 °C. Recrystallization from 250 mL DMF yielded 5.6 g (11.8 mmol, 84 %) of a white solid powder.

<sup>1</sup>H-NMR (DMSO-d<sub>6</sub>, 300 MHz, δ in ppm): 8.99 (2H, s, NH), 6.88 (4H, s, H<sub>Ar</sub>), 3.73 (2H, s, Ar-CH<sub>2</sub>-Ar), 2.38-2.26 (2H, m, CHCyc), 2.05 (12H, s, CH<sub>3</sub>), 1.84-1.15 (20H, m, CH<sub>2</sub>Cyc). MS-EI (m/z, %): 474 (M<sup>+</sup>, 99), 391 (12), 366 (10), 365 (67), 364 (100), 255 (11), 254 (45), 253 (10), 239 (15), 132 (18), 83 (40), 55 (29). HPLC (El.-Vol., area in %): 2.75 mL (94).

*Synthesis of N,N'-[Methylenebis(2,6-dimethyl-4,1-phenylene)]bis[benzamide] 2b:* 5.0 g (19.7 mmol) 4,4'-methylenebis(2,6-dimethylaniline), 6.1 g (43.2 mmol) benzoyl chloride, 100 mL NMP, 3.5 mL pyridine. Reaction conditions: 1 h, 20 °C. Boiling in 500 mL MeOH yielded 7.5 g (16.2 mmol, 82 %) of a white solid powder/crystals.

<sup>1</sup>H-NMR (DMSO-d<sub>6</sub>, 300 MHz, δ in ppm): 9.70 (2H, s, NH), 7.99-7.97 (4H, m, H<sub>Ar</sub>), 7.55-7.52 (6H, m, H<sub>Ar</sub>), 6.99 (4H, s, H<sub>Ar</sub>), 3.84 (2H, s, Ar-CH<sub>2</sub>-Ar), 2.15 (12H, s, CH<sub>3</sub>). MS-EI (m/z, %): 463 (M<sup>+</sup>, 61), 462 (98), 434 (20), 359 (17), 358 (27), 357 (90), 106 (27), 105 (100), 77 (80). HPLC (El.-Vol., area in %): 2.08 mL (99).

*Synthesis of N,N'-[Methylenebis(2,6-dimethyl-4,1-phenylene)]bis[tertbutylcarboxamide] 2c:* 4.0 g (15.7 mmol) 4,4'-methylenebis(2,6-dimethylaniline), 4.2 g (34.6 mmol) pivaloyl chloride, 100 mL THF (dried), 2.8 mL pyridine. Reaction conditions: 1 h, 20 °C. The crude product was recrystallized from 100 mL MeOH, filtration of the solid product and drying. Filtration of the dissolved product in DMF over silica gel, subsequent precipitation in water and drying yielded 4.9 g (11.6 mmol, 74 %) of a white solid powder.

<sup>1</sup>H-NMR (DMSO-d<sub>6</sub>, 300 MHz, δ in ppm): 8.74 (2H, s, NH), 6.89 (4H, s, H<sub>Ar</sub>), 3.77 (2H, s, Ar-CH<sub>2</sub>-Ar), 2.05 (12H, s, Ar-CH<sub>3</sub>), 1.22 (18H, s, CH<sub>3</sub>). MS-EI (m/z, %): 423 (M<sup>+</sup>, 63), 422 (98), 366 (22), 365 (80), 339 (87), 338 (100), 337 (29), 323 (22), 254 (11), 253 (13), 239 (17), 238 (15), 237 (12), 222 (11), 160 (47), 134 (15), 57 (100), 41 (19.5). HPLC (El.-Vol., area in %): 2.24 mL (96).

*Synthesis of N,N'-[Methylenebis(2,6-dimethyl-4,1-phenylene)]bis[pentanamide] 2d:* 3.0 g (11.8 mmol) 4,4'-methylenebis(2,6-dimethylaniline), 2.8 g (25.9 mmol) valeroyl chloride, 200 mL THF (dried), 2.4 mL pyridine. Reaction conditions: 1 h, 20 °C. Recrystallization from 300 mL MeOH yielded 3.6 g (8.5 mmol, 72 %) of a white solid powder.

<sup>1</sup>H-NMR (DMSO-d<sub>6</sub>, 300 MHz, δ in ppm): 9.09 (2H, s, NH), 6.89 (4H, s, H<sub>Ar</sub>), 3.74 (2H, s, Ar-CH<sub>2</sub>-Ar), 2.31-2.26 (4H, t, CO-CH<sub>2</sub>), 2.07 (12H, s, Ar-CH<sub>3</sub>), 1.63-1.54 (4H, quint, CH<sub>2</sub>-CH<sub>2</sub>), 1.41-1.28 (4H, sext, CH<sub>2</sub>-CH<sub>3</sub>), 0.93-0.89 (6H, t, CH<sub>2</sub>-CH<sub>3</sub>). MS-EI (m/z, %): 423 (M<sup>+</sup>, 54), 422 (100), 380 (23), 365 (12), 339 (98), 338 (100), 337 (29), 323 (15), 296 (31), 255 (26), 254 (94), 253 (37), 240 (14), 239 (59), 237 (13), 223 (12), 222 (14), 160 (20), 134 (52), 57 (14), 41 (16). HPLC (El.-Vol., area in %): 2.17 mL (99).

*Synthesis of N,N'-[Methylenebis(2,6-diethyl-4,1-phenylene)]bis[cyclohexanecarboxamide] 3a:* 9.0 g (28.0 mmol) 4,4'-methylenebis(2,6-diethylaniline), 9.4 g (63.0 mmol) cyclohexanecarbonyl chloride, 120 mL NMP, 5.1 mL pyridine. Reaction conditions: 2 h, 20 °C. Boiling in 200 mL acetone yielded 14.2 g (26.7 mmol, 92 %) of a white solid powder.

<sup>1</sup>H-NMR (CDCl<sub>3</sub>/CF<sub>3</sub>COOD, 300 MHz, δ in ppm): 6.95 (4H, m, H<sub>Ar</sub>), 3.90 (2H, m, Ar-CH<sub>2</sub>-Ar), 2.61-2.53 (2H, m, CH<sub>Cyc</sub>), 2.51-2.43 (8H, m, CH<sub>2</sub>-CH<sub>3</sub>), 2.15-1.26 (20H, m, CH<sub>2</sub><sub>Cyc</sub>), 1.15-1.10 (12H, m, CH<sub>2</sub>-CH<sub>3</sub>). MS-EI (m/z, %): 531 (M<sup>+</sup>, 42), 530 (97), 448 (40), 447 (100), 421 (24), 420 (85), 419 (41), 310 (11), 309 (10), 293 (12), 281 (13), 188 (26), 162 (37), 160 (43), 83 (41), 55 (29). HPLC (El.-Vol., area in %): 2.49 mL (95).

*Synthesis of N,N'-[Methylenebis(2,6-diethyl-4,1-phenylene)]bis[benzamide] 3b:* 5.0 g (16.1 mmol) 4,4'-methylenebis(2,6-diethylaniline), 5.0 g (35.5 mmol) benzoyl chloride, 100 mL NMP, 2.8 mL pyridine. Reaction conditions: 1 h, 20 °C. Boiling in 500 mL MeOH yielded 7.0 g (13.5 mmol, 83 %) of a white solid powder.

<sup>1</sup>H-NMR (DMSO-d<sub>6</sub>, 300 MHz, δ in ppm): 9.69 (2H, s, NH), 7.99-7.96 (4H, m, H<sub>Ar</sub>), 7.59-7.50 (6H, m, H<sub>Ar</sub>), 7.04 (4H, s, H<sub>Ar</sub>), 3.94 (2H, s, Ar-CH<sub>2</sub>-Ar), 2.52-2.49 (8H, s, CH<sub>2</sub>-CH<sub>3</sub>), 1.09 (12H, t, CH<sub>3</sub>). MS-EI (m/z, %): 519 (M<sup>+</sup>, 34), 518 (86), 414 (24), 413 (70), 161 (11), 160 (77), 106 (15), 105 (100), 77 (34). HPLC (El.-Vol., area in %): 3.75 mL (99).

*Synthesis of N,N'-[Methylenebis(2,6-diethyl-4,1-phenylene)]bis[tertbutylcarboxamide] - 3c:* 4.3 g (14.0 mmol) 4,4'-methylenebis(2,6-diethylaniline), 3.7 g (30.7 mmol) pivaloyl chloride, 50 mL THF (dried), 4.3 mL triethylamine. Reaction conditions: 48 h, 60 °C. Recrystallization from 500 mL MeOH and subsequent recrystallization from 250 mL DMF yielded 4.8 g (10.1 mmol, 71 %) of a white solid powder.

<sup>1</sup>H-NMR (DMSO-d<sub>6</sub>, 300 MHz, δ in ppm): 8.74 (2H, s, NH), 6.93 (4H, s, H<sub>Ar</sub>), 3.86 (2H, s, Ar-CH<sub>2</sub>-Ar), 2.41 (8H, q, CH<sub>2</sub>-CH<sub>3</sub>), 1.22 (18H, s, CH<sub>3</sub>), 1.04 (12H, t, CH<sub>2</sub>-CH<sub>3</sub>). MS-EI (m/z, %): 479 (M<sup>+</sup>, 24.8), 478 (71), 449 (13), 422 (54), 421 (100), 394 (29), 393 (24), 188 (64), 162 (16), 160 (36), 57 (66). HPLC (El.-Vol., area in %): 2.89 mL (99).

*Synthesis of N,N'-[Methylenebis(2,6-diethyl-4,1-phenylene)]bis[pentanamide] - 3d:* 4.3 g (14.0 mmol) 4,4'-methylenebis(2,6-diethylaniline), 3.7 g (30.8 mmol) valeroyl chloride, 50 mL THF (dried), 4.3 mL triethylamine. Reaction conditions: 3 h, 50 °C. Recrystallization from 200 mL MeOH yielded 3.7 g (7.7 mmol, 56 %) of a white solid powder.

<sup>1</sup>H-NMR (DMSO-d<sub>6</sub>, 300 MHz, δ in ppm): 9.08 (2H, s, NH), 6.93 (4H, s, H<sub>Ar</sub>), 3.83 (2H, s, Ar-CH<sub>2</sub>-Ar), 2.42 (8H, q, CH<sub>2</sub>-CH<sub>3</sub>), 2.29 (4H, t, CO-CH<sub>2</sub>), 1.58 (4H, quint, CH<sub>2</sub>-CH<sub>2</sub>-CH<sub>2</sub>), 1.35 (4H, sext, CH<sub>2</sub>-CH<sub>3</sub>), 1.04 (12H, t, CH<sub>2</sub>-CH<sub>3</sub>), 0.91 (6H, t, CH<sub>2</sub>-CH<sub>2</sub>-CH<sub>3</sub>). MS-EI (m/z, %): 479 (M<sup>+</sup>, 43), 478 (100), 460 (10), 422 (15), 421 (49), 395 (26), 394 (96), 393 (64), 310 (11), 309 (18), 293 (15), 281 (20), 188 (22), 162 (49), 161 (10), 160 (58), 57 (26), 41 (11). HPLC (El.-Vol., area in %): 2.67 mL (88).

### S3. Thermal properties of kinked bisamides

To reveal their thermal behavior at elevated temperatures and the phase transitions, the kinked bisamides were investigated by means of thermogravimetric analysis (TGA) and differential scanning calorimeter (DSC) under nitrogen atmosphere.

#### *Thermal characterization methods*

For TGA, an automated Mettler Toledo TGA/DSC 3+ operated under nitrogen atmosphere was used to determine the thermal behavior and the weight loss of the kinked bisamides. About 5 to 10 mg of the kinked bisamides were weighed in Al<sub>2</sub>O<sub>3</sub> pans and heated from 50 °C to 700 °C at a rate of 10 K/min under nitrogen (60 mL/min). T<sub>-5wt.%</sub> value corresponds to the temperature at which 5 wt.% of the sample is lost.

Thermal phase behavior (melting points and crystallization behavior of the kinked bisamides) were determined by means of DSC. Here, an automated Mettler Toledo DSC 2/3 operated under nitrogen atmosphere was used. About 6 to 12 mg of the compounds were weighed into 30 µL high pressure crucible pans. The phase transitions for compounds **1a** – **1d**, **2b**, **2d**, **3b** and **3d** were determined in a temperature range of 25 to 300 °C and for the compounds **2a**, **2c**, **3a** and **3c** in a temperature range of 25 to 350 °C, respectively. All measurements were performed with a heating and cooling rate of 10 K/min. Every heating and cooling scan was repeated three times.

#### *Discussion of the thermal behavior*

TGA experiments determine the temperature at which mass loss occurs. Mass loss can be either attributed to decomposition of the compounds or sublimation and evaporation, which should be avoided during polymer processing to ensure functioning of the self-assembly process and to keep the concentration constant. TGA reveals that all kinked bisamides show no significant mass loss at temperatures below 290 °C with T<sub>-5wt.%</sub> values being between 293 °C (**3d**) and 408 °C (**1b**). This finding renders all kinked bisamides in general suitable to be used as additives during processing of the polystyrene melt. Equally important are the temperatures at which phase transitions of the compounds in bulk occur, because the melting points as well as the crystallization temperatures can be regarded as a first approximation at which temperature the kinked bisamides dissolve in the polystyrene melt and at which temperature the supramolecular building blocks may self-assemble into nano-objects. In particular, the latter has to take place at a temperature before the foaming of the polymer melt is performed demanding reasonable high crystallization temperatures. It was found that all kinked bisamides show high melting transitions in the range of 192 °C (**1d**) to 328 °C (**3c**). Considering the kinked bisamides with aliphatic peripheral side groups, cyclohexyl (**a**), tert-butyl (**c**) and n-butyl (**d**), a clear trend can be observed with respect to the melting and crystallization behavior: Derivatives of the series with unsubstituted aromatic central units (**1**) show lower melting transitions than their derivatives with methyl- (**2**) and ethyl (**3**) substituents at the ortho-position of the amide groups. This is attributed to a torsion of amide groups, which leads to a stronger H bonding between the different amides causing a higher melting temperature. Within this series, the bisamides of category **2** and **3** with cyclohexyl (**a**) and t-butyl (**c**) substituents exhibit the highest melting transitions with temperatures of 307 °C (**2a**), 311 °C (**2c**), 297 °C (**3a**) and 328 °C (**3c**). This difference is attributed to the comparable stiff and rigid peripheral side groups in contrast to the series with the rather flexible n-butyl side groups. For kinked bisamide **3c** it should be noted that the melting temperature is very close to the T<sub>-5wt.%</sub> value

of 320 °C indicating also an evaporation or decomposition at this temperature. All kinked bisamides with phenyl substituents (**b**) exhibit reasonable high melting temperatures in the range of 225 °C to 258 °C without featuring a clear trend, which may be attributed to the partial conjugation over the amide group rendering a comparison complicated. The  $T_{-5wt\%}$  values from TGA and the peak values of the endothermic transitions from the second heating and cooling run (DSC) are summarized in Table S1.

*Summary of thermal properties*

**Table S1.** Thermal properties of the kinked bisamides including melting points and crystallization temperatures (peak values) and  $T_{-5wt\%}$  values.

Compound	R <sub>1</sub>	R <sub>2</sub>	Melting Point [°C] <sup>a, b)</sup>	Crystallization [°C] <sup>d)</sup>	T <sub>-5wt.%</sub> [°C] <sup>a)</sup>
<b>1a</b>	H	cyclohexyl	222	173	380
<b>2a</b>	methyl	cyclohexyl	307	285	369
<b>3a</b>	ethyl	cyclohexyl	297	266	347
<b>1b</b>	H	phenyl	249	216	408
<b>2b</b>	methyl	phenyl	225	206 <sup>e</sup>	401
<b>3b</b>	ethyl	phenyl	258	234	389
<b>1c</b>	H	tert-butyl	239	176	320
<b>2c</b>	methyl	tert-butyl	311	251	323
<b>3c</b>	ethyl	tert-butyl	328	307	320
<b>1d</b>	H	n-butyl	192	183	351
<b>2d</b>	methyl	n-butyl	190, 257 <sup>c</sup>	252	339
<b>3d</b>	ethyl	n-butyl	121, 220 <sup>c</sup>	86, 199, 210 <sup>f</sup>	293

<sup>a</sup> Upon heating, heating rate 10 K/min, under N<sub>2</sub>

<sup>b</sup> Second heating scan

<sup>c</sup> Polymorphic melting behavior

<sup>d</sup> First cooling run, cooling rate 10 K/min, under N<sub>2</sub>

<sup>e</sup> Value refers to recrystallization upon heating of the second heating scan

<sup>f</sup> Polymorphic crystallization behavior

#### S4. PXRD investigation of kinked bisamide **3a**

Recrystallization of kinked bisamide **3a** from acetone (see section S1) yielded a crystalline white powder with sufficiently high order and was therefore subjected to powder X-ray diffraction (PXRD). A sample of **3a** was filled in a capillary tube with a diameter of 0.5 mm and a tube wall thickness of 0.1 mm. PXRD measurements were carried out in Debye–Scherrer geometry on a STOE StadiP diffractometer using a Cu K $\alpha_1$  radiation ( $\lambda = 1.5406 \text{ \AA}$ ) and a curved germanium monochromator (oriented according to the 111 plane). The measurements were performed in the  $2\Theta$  range of  $3 - 50^\circ$  with a step size of  $0.015^\circ$ .

Prior to the refinement of the crystal structure, the molecular structure of **3a** was optimised using DFT methods with the CASTEP code [1]. Powder indexing and Pawley refinement was done with the programme TOPAS [2]. Simulated annealing with a rotational freedom of the ethyl substituents in ortho-position to the amide units and the cyclohexyl side-groups was performed with the Endeavour programme [3]. Moreover, additional rotational freedoms were allowed for the C<sub>Ar</sub>-CH<sub>2</sub>-C<sub>Ar</sub> bonds. The obtained solution was again geometry-refined with DFT methods. A final Rietveld refinement was done with TOPAS. An  $R_{wp}$  of 3.56 has been obtained, a preferred orientation of the 4<sup>th</sup> order using spherical harmonics has been applied [4]. The x-ray diffractogram together with the Rietveld profile plot and the difference of the two for **3a** recrystallized from acetone is shown in Figure S3. The structural elucidation reveals that the kinked bisamide **3a** crystallizes in the triclinic space group  $P\bar{1}$  with the parameters  $a = 4.6882(8) \text{ \AA}$ ,  $b = 15.4521(19) \text{ \AA}$ ,  $c = 22.5115(66) \text{ \AA}$ ,  $\alpha = 105.23(2)^\circ$ ,  $\beta = 93.88(4)^\circ$ ,  $\gamma = 93.07(3)^\circ$ . All relevant crystallographic data are summarized in Table S2. A CIF (crystallographic information file) is provided as additional supporting information.

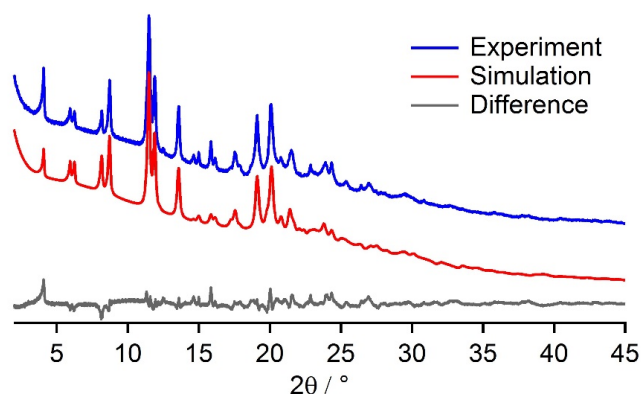


**Figure S3.** X-ray diffraction pattern (blue) together with the Rietveld profile plot (red) and the difference plot (grey) of **3a** recrystallized from acetone.

**Table S2.** Crystallographic data of kinked bisamide **3a**.

Crystal System/ Space group	a/Å	b/Å	c/Å	$\alpha/^\circ$	$\beta/^\circ$	$\gamma/^\circ$	V/Å <sup>3</sup>	Z'/Z	$\rho/g \text{ cm}^{-3}$	T/K	$R_{wp}$
Triclinic / $P\bar{1}$	4.6882 (8)	15.4521 (19)	22.5115 (66)	105.23 (2)	93.88 (4)	93.07 (3)	1565.57 (1)	1/2	1.125 91	293	3.56 (3)

### S5. Solid-state NMR spectroscopy of kinked bisamide **3a**

Solid-state NMR spectroscopy measurements have been performed on recrystallized samples from acetone (see section S1) and self-assembled samples from xylene of kinked bisamide **3a**. To prepare the latter, 500 ppm of **3a** was molecularly dissolved in xylene by refluxing the mixture for 30 minutes. Subsequent cooling to room temperature yielded a turbid dispersion. Evaporation of the solvent under high vacuum yielded a white powder, which was used for the measurement.

Solid-state NMR spectroscopy has been performed on a Bruker Avance III spectrometer operating at a proton resonance frequency of 400 MHz. The two differently prepared samples were packed in 3.2 mm zirconia rotors and analysed in 3.2 mm triple resonance probe. High resolution proton NMR spectra have been recorded under Magic-Angle-Spinning (MAS) with a spinning frequency of 11.5 kHz using the DUMBO decoupling sequence [5]. The  $^{13}\text{C}$  NMR spectra were acquired with a cross polarisation pulse programme at 12.5 kHz MAS frequency. The  $^{13}\text{C}\{^1\text{H}\}$  CP NMR experiments were done with a ramped CP sequence where the nutation frequency on the  $^1\text{H}$  channel was varied linearly from 50 – 100% [6]. The maximum nutation frequency during the contact time was set to 59 kHz. During acquisition on the  $^{13}\text{C}$  channel,  $^1\text{H}$  were decoupled using the Spinal64 decoupling sequence with a nutation frequency of 68 kHz [7]. The CP contact time was set to 3 ms.

The number and chemical shifts of the resonances match the molecular structure and the fact that just one molecule is present in the asymmetric unit. The sample that is recrystallized from xylene shows the same amount and position of the resonances as the one recrystallized from acetone (Figure S4). This strongly hints that the crystal structure and packing are the same. However, all resonances are broader, indicating less ordering in the sample.

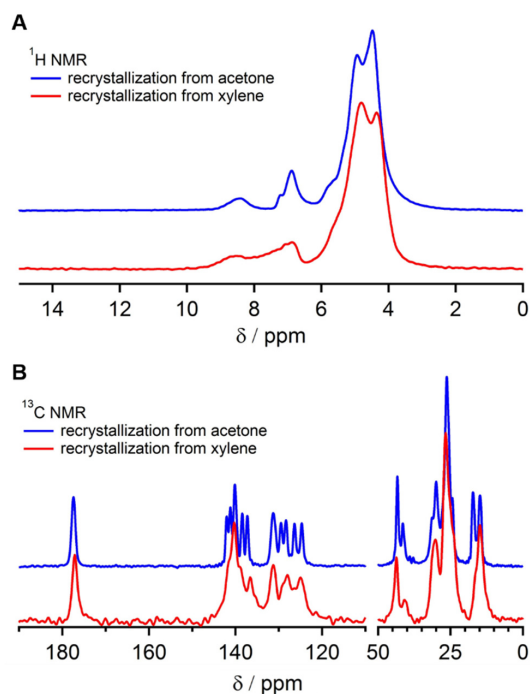


**Figure S4.** Solid-state NMR spectroscopy of powder samples of **3a**.  $^1\text{H}$  solid state NMRs (A) of **3a** prepared from acetone (blue) and xylene (red), respectively.  $^{13}\text{C}$  solid state NMRs (B) of **3a** prepared from acetone (blue) and xylene (red), respectively.

### S6. FTIR spectroscopy of kinked bisamide 3a

Solid powder samples of kinked bisamide **3a** for FTIR spectroscopy were prepared from acetone and xylene as described in section S1 and S4. FTIR spectra were measured with a PerkinElmer 100 FTIR spectrometer equipped with an ATR sampling accessory. Measurements were performed in a wave number range of 650  $\text{cm}^{-1}$  to 4000  $\text{cm}^{-1}$  with a resolution of 4  $\text{cm}^{-1}$ .

The FTIR spectra of **3a** from acetone (blue) and xylene (red) are shown in Figure S5 demonstrating that they are almost identical. Significant vibrations attributed to the amide groups are indicated by grey boxes. This includes the Amide A (N-H stretch vibrations) with a maximum of 3258  $\text{cm}^{-1}$  (blue) and 3255  $\text{cm}^{-1}$  (red), the Amide I (C=O stretch vibrations) both with a maximum of 1644  $\text{cm}^{-1}$  and the Amide II (typically a superposition of C-N-H bend and C-N stretch vibrations) with a maximum at around 1515  $\text{cm}^{-1}$  (blue) and 1514  $\text{cm}^{-1}$  (red), respectively. We note that the N-H stretch vibrations is typically in the range of 3400  $\text{cm}^{-1}$  for non-hydrogen bonded N-H groups. [8]

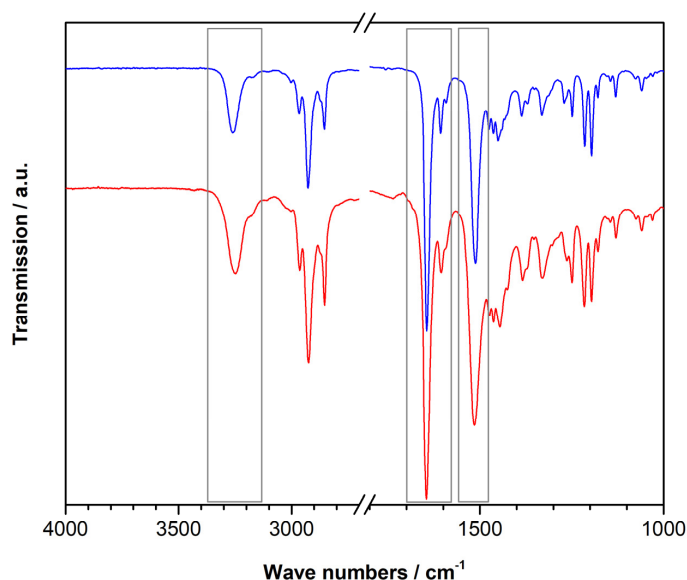


**Figure S5.** FT-IR spectra of **3a** prepared from acetone (blue) and xylene (red), respectively. The grey boxes indicate the Amide A (N-H stretch vibrations) with a maximum at around 3255  $\text{cm}^{-1}$ , the Amide I (C=O stretch vibrations) with a maximum at around 1645  $\text{cm}^{-1}$  and Amide II (superposition of N-H bend and C-N stretch vibrations) with a maximum at around 1515  $\text{cm}^{-1}$ .

### S7. Cell morphologies of polystyrene foams by batch foaming with kinked bisamides

Polystyrene foams with different supramolecular additive concentrations were prepared in a standard thermally-induced batch foam process as described in the experimental section comprising a master batch preparation, compounding and injection molding to polystyrene specimens, CO<sub>2</sub>-saturation of the specimens at room temperature and foaming at elevated temperatures. Each foam was characterized and evaluated in view of morphology, cell size, cell density and foam density.

#### *Foam morphology and cell size histograms of PS batch foams with 1.0 wt.% of kinked bisamides 1a, 2a and 3a*

SEM micrographs of the cell morphologies and the respective histograms with the kinked bisamides **1a**, **2a** and **3a** are shown in Figure S6 revealing their influence at a concentration of 1.0 wt.%. While the PS foam containing 1.0 wt.% of **1a** exhibits an inhomogeneous foam morphology with two types of cells and a mean cell size of  $6.4 \pm 3.5 \mu\text{m}$ , the PS foams with 1.0 wt.% of **2a** and **3a** show homogeneous cell morphologies with mean cell sizes of  $3.5 \pm 1.1 \mu\text{m}$  and  $3.9 \pm 1.3 \mu\text{m}$ , respectively. Moreover, the foam densities of the latter two are slightly lower with  $52.1 \pm 3.4 \text{ kg/m}^3$  and  $56.0 \pm 3.5 \text{ kg/m}^3$  compared to the foam with **1a** with  $69.8 \pm 3.3 \text{ kg/m}^3$ .

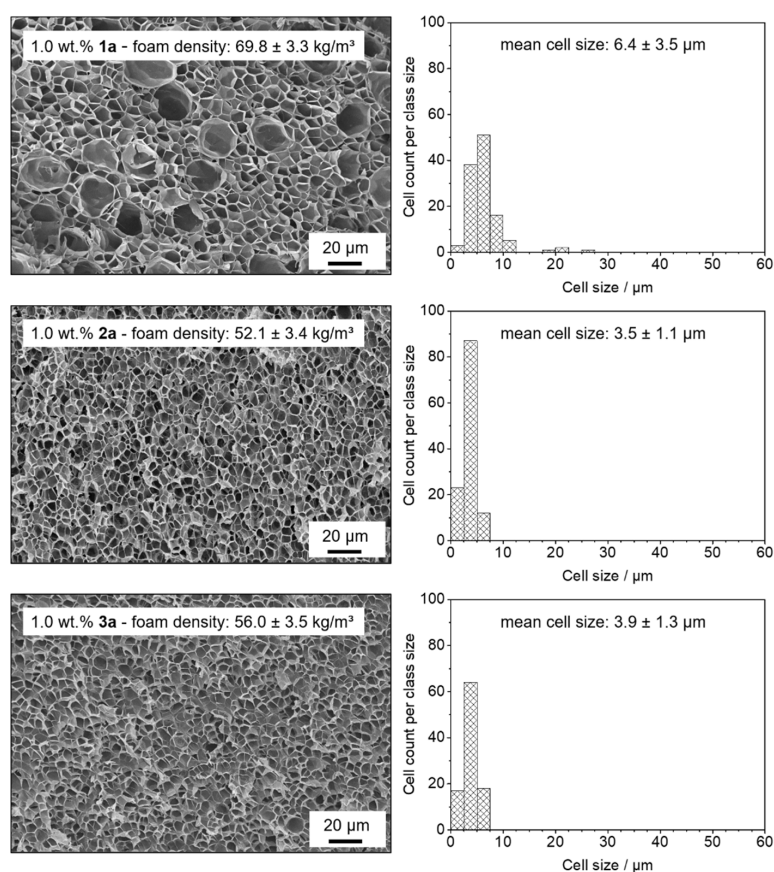


**Figure S6.** Left: SEM micrographs (500×) depicting the cell morphologies of batch foamed polystyrene specimens with 1.0 wt.% of kinked bisamides **1a**, **2a** and **3a**. The mean foam density is given for each concentration. Right: Corresponding histograms of the cell sizes including the mean cell sizes.

---

*Concentration-dependent evolution of the mean cell sizes of PS batch foams with kinked bisamides **1b**, **2b** and **3b***

Figure S7 shows the mean cell size of polystyrene batch foams with kinked bisamides with phenyl substituents **1b**, **2b** and **3b** at the concentrations of 1.0, 0.75, 0.5, 0.25, 0.1, 0.05, 0.025 and 0.01 wt.%. Exemplarily, the SEM micrographs for the concentration of 0.5 wt.% for each kinked bisamide are also shown. All kinked bisamides are capable of reducing the mean cell size in the investigated additive concentration range from 0.01 wt.% to 1.0 wt.% compared to the reference neat polystyrene foam. A significant reduction of the mean cell size by more than 40% was found at concentrations larger than 0.5 wt.%. Moreover, a significant reduction of the standard deviations of the mean cell sizes was achieved at these concentrations for the additives **1b**, **2b** and **3b**. Polystyrene foams with an additive concentration of 1.0 wt.% of **3b** was found to feature a microcellular morphology with the smallest foam cells (mean cell size of  $5.8 \pm 2.6 \mu\text{m}$ ). The SEM micrographs at an additive concentration of 0.5 wt.% for all three batch foam samples (Figure S7) reveal foam morphologies with a pronounced homogeneity. All mean foam densities of the samples nucleated with **1b**, **2b** and **3b** are in the range between 53.7 – 82.9 kg/m<sup>3</sup>. The mean foam density of the reference neat polystyrene was found to be 67.1 kg/m<sup>3</sup>. Therefore, all foamed samples show low foam densities with volume expansion ratios between 10 – 20.

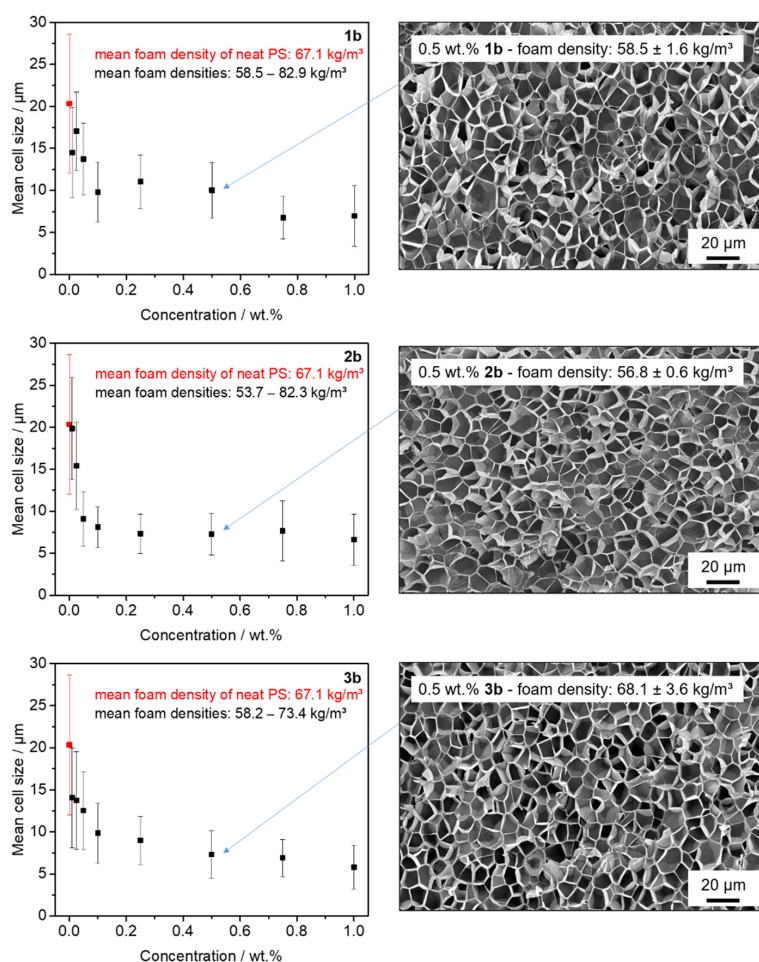


**Figure S7.** Left: Evolution of the mean cell size with increasing concentration of the kinked bisamides **1b**, **2b** and **3b** of batch foamed polystyrene specimens. Data for the neat PS reference foam are shown in red. Right: SEM micrographs (500×) depicting the homogeneous microcellular morphology of batch foamed polystyrenes at a concentration of 0.5 wt.% of **1b**, **2b** and **3b**, including the mean foam densities.

*Concentration-dependent evolution of the mean cell sizes of PS batch foams with kinked bisamides 1c, 2c and 3c*

In Figure S8, the mean cell size of polystyrene batch foams with kinked bisamides with tert-butyl substituents **1c**, **2c** and **3c** at the concentrations of 1.0, 0.75, 0.5, 0.25, 0.1, 0.05, 0.025 and 0.01 wt.% are depicted. Moreover, the SEM micrographs for the concentration of 0.5 wt.% for each kinked bisamide are shown. In a similar manner as described before, all kinked bisamides are capable of reducing the mean cell size in the investigated additive concentration range compared to the reference neat polystyrene sample. A significant but slightly smaller reduction of the mean cell size by more than 30% featuring also a reduction of the standard deviation was achieved at concentrations larger than 0.5 wt.%. PS foams with **2c** at an additive concentration of 1.0 wt.% yielded the smallest microcellular morphology with a mean cell size of  $6.4 \pm 1.9 \mu\text{m}$ . The SEM micrographs at an additive concentration of 0.5 wt.%

reveal homogeneous foam morphologies for all three batch foam samples. The mean foam densities of the samples nucleated with **1c** to **3c** are in the range between 51.6 – 124.4 kg/m<sup>3</sup>. Thus, most of the samples can be regarded as low-density polymer foams with volume expansion ratios between 9 – 20.

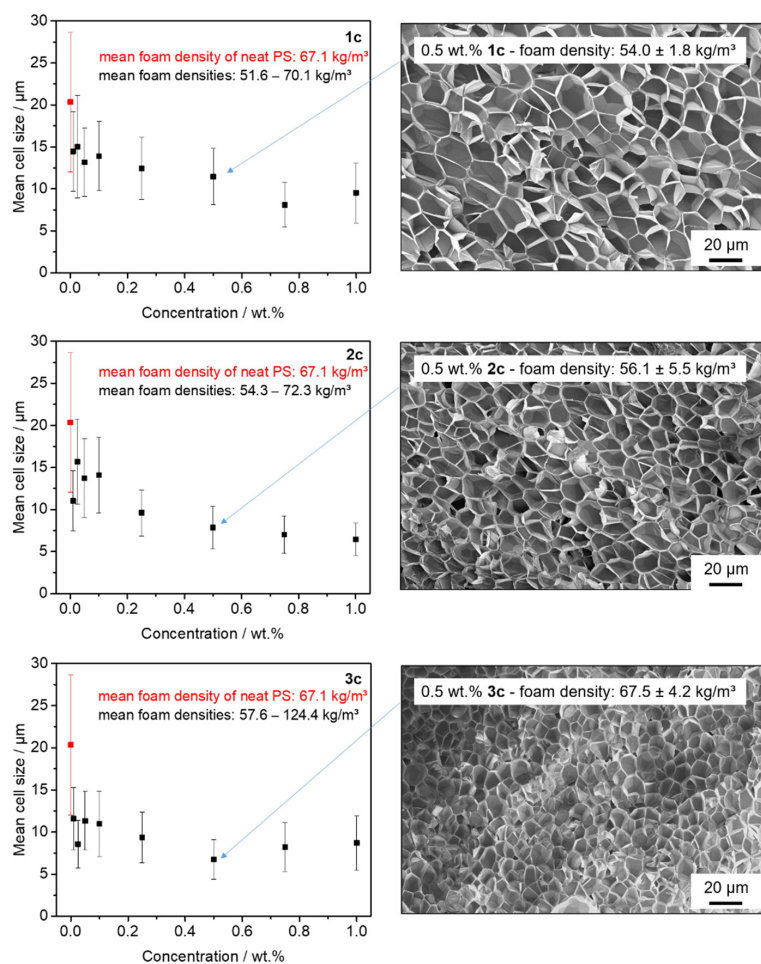


**Figure S8.** Left: Evolution of the mean cell size with increasing concentration of the kinked bisamides **1c**, **2c** and **3c** of batch foamed polystyrene specimens. Data for the neat PS reference foam are shown in red. Right: SEM micrographs (500 $\times$ ) depicting the homogeneous microcellular morphology of batch foamed polystyrenes at a concentration of 0.5 wt.% of **1c**, **2c** and **3c**, including the mean foam densities.

#### *Concentration-dependent evolution of the mean cell sizes of PS batch foams with kinked bisamides **1d**, **2d** and **3d***

Figure S9 shows the mean cell size of polystyrene batch foams with kinked bisamides with *n*-butyl substituents **1d**, **2d** and **3d** at the concentrations of 1.0, 0.75, 0.5, 0.25, 0.1, 0.05, 0.025 and 0.01 wt.%. Exemplarily the SEM micrographs for the concentration of 0.5 wt.% for each bisamide is shown. All kinked bisamides are capable of reducing the mean cell size in the investigated additive concentration compared to the reference neat polystyrene sample. A significant reduction of the mean cell size by

more than 40% was found at concentrations larger than 0.5 wt.%. Moreover, a significant reduction of the standard deviations of the mean cell sizes was achieved at these concentrations. **2d** features the smallest microcellular morphology with a mean cell size of  $5.2 \pm 2.7 \mu\text{m}$  at an additive concentration of 0.75 wt.%. The SEM micrographs at an additive concentration of 0.5 wt.% reveal an inhomogeneous foam morphology for samples nucleated with **1d** and homogeneous foam morphologies for samples nucleated with **2d** and **3d**. The mean foam densities of the samples nucleated with **1d**, **2d** and **3d** are in the range between  $49.2 - 76.0 \text{ kg/m}^3$ , while the mean foam density of the reference neat polystyrene is  $67.1 \text{ kg/m}^3$ . Therefore, all foamed samples show low foam densities with volume expansion ratios between 15 – 20.

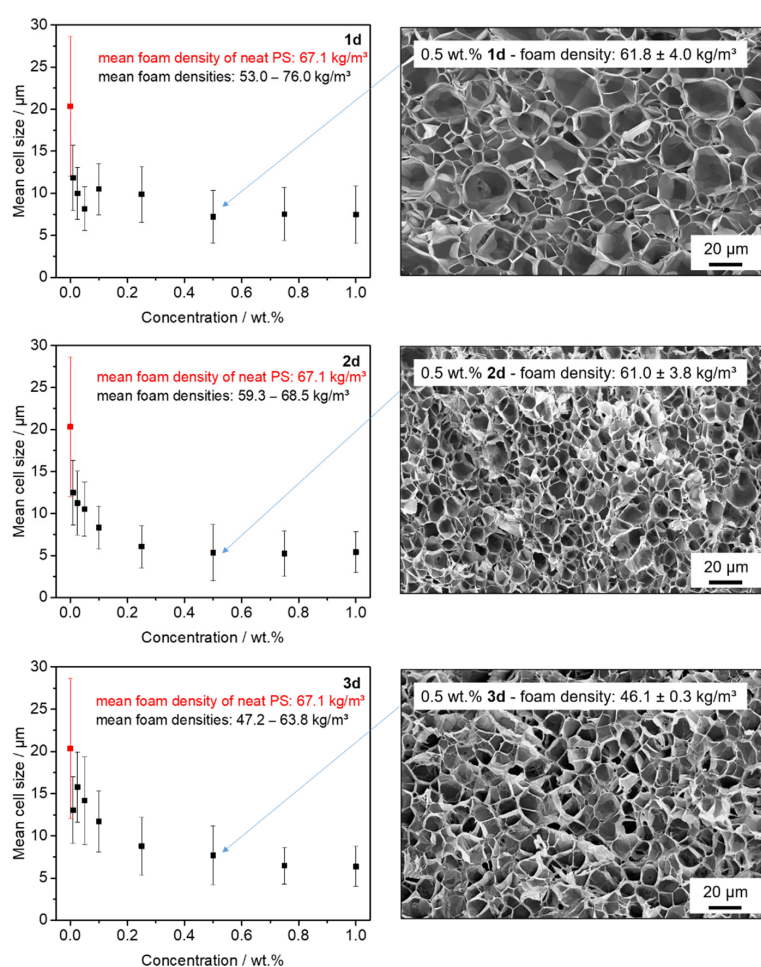


**Figure S9.** Left: Evolution of the mean cell size with increasing concentration of the kinked bisamides **1d**, **2d** and **3d** of batch foamed polystyrene specimens. Data for the neat PS reference foam are shown in red. Right: SEM micrographs (500 $\times$ ) depicting the homogeneous microcellular morphology of batch foamed polystyrenes at a concentration of 0.5 wt.% of **1d**, **2d** and **3d**, including the mean foam densities.

### S8. Summary of polystyrene batch foam properties with kinked bisamides

*Foam densities and volume expansion ratio of polystyrene batch foams with kinked bisamides*

Foam densities were calculated by the water-displacement method in agreement with ISO 1183 based on the Archimedes principle using a Mettler Toledo XP 205 with density kit. For this, a small rectangle was cut out of the specimen and weighed in air ( $m_{\text{air}}$ ). Afterwards, the specimen was submerged in water and its apparent mass ( $m_{\text{water}}$ ), which is reduced by the buoyant force, was measured. The resulting density ( $\rho_{\text{foam}}$ ) was calculated with equation 1.

$$\rho_{\text{foam}} = \frac{m_{\text{air}}}{m_{\text{air}} - m_{\text{water}}} \cdot \rho_{\text{water}} \quad \text{with } \rho_{\text{water}} (296.3 \text{ K}) = 0.997541 \text{ g/cm}^3 \quad (1)$$

Foam densities were measured on at least three cut samples from different locations of the respective foam and the mean values of the foam densities are given. All average foam densities are summarized in Table S3.

**Table S3.** Average foam densities of batch foamed polystyrene specimens with and without kinked bisamides.

Foam density [kg/m <sup>3</sup> ]								
neat PS	67.1 ± 16.3							
Concentration of kinked bisamide [wt.%]								
	0.01	0.025	0.05	0.1	0.25	0.5	0.75	1.0
<b>1a</b>	70.4 ± 2.9	65.4 ± 1.4	55.9 ± 1.6	72.8 ± 2.7	59.0 ± 2.3	50.0 ± 2.8	57.4 ± 5.7	69.8 ± 3.3
<b>2a</b>	58.2 ± 4.0	50.6 ± 0.6	59.9 ± 5.0	58.5 ± 2.7	49.2 ± 1.6	53.8 ± 3.0	50.3 ± 0.7	52.1 ± 3.4
<b>3a</b>	61.2 ± 2.9	47.8 ± 0.5	51.5 ± 5.3	54.5 ± 4.0	56.4 ± 5.4	46.8 ± 0.5	49.1 ± 3.7	56.0 ± 3.5
<b>1b</b>	82.9 ± 9.3	64.6 ± 1.4	71.4 ± 7.7	73.1 ± 1.6	61.4 ± 1.9	58.5 ± 1.6	63.2 ± 4.3	62.3 ± 3.7
<b>2b</b>	61.5 ± 1.0	56.8 ± 1.1	58.9 ± 5.7	76.7 ± 1.8	74.8 ± 2.2	56.8 ± 0.6	82.3 ± 0.5	53.7 ± 1.2
<b>3b</b>	71.6 ± 3.6	63.6 ± 1.6	58.2 ± 4.5	71.2 ± 8.9	73.4 ± 2.7	68.1 ± 3.6	65.7 ± 10.3	62.5 ± 0.8
<b>1c</b>	53.7 ± 2.5	63.6 ± 6.4	70.1 ± 5.8	58.2 ± 1.4	55.7 ± 6.2	54.0 ± 1.8	62.5 ± 3.5	51.6 ± 3.5
<b>2c</b>	72.3 ± 2.1	56.8 ± 3.6	67.9 ± 3.6	61.2 ± 2.9	63.8 ± 9.5	56.1 ± 5.5	54.3 ± 2.3	66.2 ± 5.4
<b>3c</b>	124.4 ± 9.4	77.9 ± 2.7	59.4 ± 1.6	61.5 ± 4.1	64.3 ± 5.7	67.5 ± 4.2	57.6 ± 4.6	57.6 ± 2.6
<b>1d</b>	66.9 ± 2.6	62.3 ± 4.5	74.9 ± 10.0	76.0 ± 3.4	62.7 ± 1.6	61.8 ± 4.0	53.0 ± 1.9	61.8 ± 4.3
<b>2d</b>	68.5 ± 2.6	59.3 ± 5.1	64.7 ± 5.7	59.5 ± 2.4	59.6 ± 1.4	61.0 ± 3.8	65.5 ± 5.8	65.6 ± 5.1
<b>3d</b>	63.8 ± 3.9	47.2 ± 0.3	60.4 ± 7.1	53.0 ± 0.9	50.1 ± 0.8	46.1 ± 0.3	47.4 ± 1.6	51.2 ± 3.0

The volume expansion ratios (VER) were calculated by dividing the average foam densities by the polystyrene density, according to equation 2.

$$VER = \frac{\rho_{PS,bulk}}{\rho_{foam}} \quad \text{with } \rho_{PS,bulk} = 1040 \text{ kg/m}^3 \quad (2)$$

All VER are summarized in Table S4.

**Table S4.** Volume expansion ratio of batch foamed polystyrene specimens with and without kinked bisamides.

VER		Concentration of kinked bisamide [wt.%]							
		0.01	0.025	0.05	0.1	0.25	0.5	0.75	1.0
<b>neat PS</b>	15.5								
<b>1a</b>		14.8	15.9	18.6	14.3	17.6	20.8	18.1	14.9
<b>2a</b>		17.9	20.6	17.4	17.8	21.1	19.3	20.7	20.0
<b>3a</b>		17.0	21.8	20.2	19.1	18.4	22.2	21.2	18.6
<b>1b</b>		12.5	16.1	14.6	14.2	16.9	17.8	16.5	16.7
<b>2b</b>		16.9	18.3	17.7	13.6	13.9	18.3	12.6	19.4
<b>3b</b>		14.5	16.4	17.9	14.6	14.2	15.3	15.8	16.6
<b>1c</b>		19.4	16.4	14.8	17.9	18.7	19.3	16.6	20.2
<b>2c</b>		14.4	18.3	15.3	17.0	16.3	18.5	19.2	15.7
<b>3c</b>		8.4	13.4	17.5	16.9	16.2	15.4	18.1	18.1
<b>1d</b>		15.5	16.7	13.9	13.7	16.6	16.8	19.6	16.8
<b>2d</b>		15.2	17.5	16.1	17.5	17.4	17.0	15.9	15.9
<b>3d</b>		16.3	22.0	17.2	19.6	20.8	22.6	21.9	20.3

---

*Cell densities of polystyrene batch foams with kinked bisamides*

Cell densities  $\rho_{cell}$  with respect to the unfoamed solid polymer were calculated according to equation 3, with  $N_c$  the number of cells in the selected area,  $A_s$  the area of the selected section and the volume expansion ratio. The results of the cell densities are summarized in Table S5.

$$\rho_{cell} = \left(\frac{N_c}{A_s}\right)^{\frac{3}{2}} \cdot VER \quad (3)$$

**Table S5.** Cell densities of batch foamed polystyrene specimens with and without kinked bisamides.

Cell density [cm <sup>-3</sup> ]		Concentration of kinked bisamide [wt.%]							
		0.01	0.025	0.05	0.1	0.25	0.5	0.75	1.0
<b>neat</b>	2.14E9								
<b>PS</b>									
<b>1a</b>		1.25E10	9.80E09	1.58E10	3.13E10	3.88E10	4.16E10	5.85E10	5.02E10
<b>2a</b>		8.45E09	7.44E09	8.99E09	9.71E09	7.17E10	4.64E11	2.79E11	5.67E11
<b>3a</b>		8.79E09	8.88E09	6.44E09	2.08E10	7.49E10	1.89E11	3.05E11	3.49E11
<b>1b</b>		6.25E09	5.72E09	7.94E09	2.22E10	2.08E10	2.83E10	7.59E10	5.79E10
<b>2b</b>		3.15E09	6.74E09	2.90E10	3.09E10	4.52E10	5.40E10	3.12E10	3.47E10
<b>3b</b>		9.79E09	8.91E09	1.25E10	2.19E10	3.19E10	5.24E10	2.53E10	9.37E10
<b>1c</b>		9.78E09	7.34E09	8.47E09	1.06E10	1.61E10	1.91E10	4.69E10	3.16E10
<b>2c</b>		1.48E10	6.74E09	7.28E09	7.49E09	2.58E10	4.34E10	5.32E10	7.02E10
<b>3c</b>		7.06E09	3.15E10	1.67E10	1.68E10	2.83E10	5.89E10	4.57E10	3.65E10
<b>1d</b>		1.29E10	2.27E10	3.60E10	1.98E10	2.17E10	4.31E10	5.46E10	4.70E10
<b>2d</b>		1.11E10	1.65E10	2.09E10	4.04E10	8.79E10	1.10E11	1.13E11	1.10E11
<b>3d</b>		9.00E09	7.69E09	8.01E09	2.20E10	3.90E10	6.38E10	9.04E10	8.59E10

**S9. Photograph of an extruded neat polystyrene foam and a polystyrene foam with 0.5 wt.% 3a**

Foam extrusion experiments were carried out using a tandem extrusion line (Dr. Collin GmbH) comprising a twin-screw extruder with a 25 mm screw and a L/D ratio of 42 (A-Extruder) and a single-screw extruder with a 45 mm screw and L/D ratio of 30 (B-Extruder) equipped with a slit die with a gap of 0.6 mm and a width of 30 mm. For the extrusion foaming with kinked bisamide **3a**, a 5.0 wt.% masterbatch powder-powder mixture was used and foams were prepared by diluting the masterbatch with neat PS granulates. 4 wt.% CO<sub>2</sub> and 3 wt.% EtOH was used as physical blowing agent. As processing parameters, a screw speed of 8 rpm at the B-Extruder with an overall throughput of 4.5 kg h<sup>-1</sup> was selected. The melt temperature in the A-Extruder was adjusted to 220 °C. The melt temperature near to the outlet of the B-extruder and the die temperature were selected between 110 – 120 °C and 126 °C, respectively. The PS reference foam was prepared using neat PS granulates in the same manner. Figure S10 shows exemplarily photographs of non-calibrated extruded foams of a neat polystyrene reference foam and polystyrene foam with 0.5 wt.% **3a** featuring almost the same foam density but very different cell sizes.



**Figure S10.** Photograph of a neat extruded polystyrene foam (left) with a mean foam density of  $61.6 \pm 4.1 \text{ kg/m}^3$  and a mean cell size of  $1094 \pm 377 \text{ }\mu\text{m}$  and an extruded polystyrene foam with 0.5 wt.% **3a** (right) with a mean foam density of  $63.9 \pm 1.9 \text{ kg/m}^3$  and a mean cell size of  $18.8 \pm 8.5 \text{ }\mu\text{m}$ , produced at very similar processing conditions.

### S10. Photograph and light microscopy image of neat polystyrene foams by extrusion foaming

Extruded foams of neat polystyrene foam possess very large cell sizes, which cannot reliably be determined by means of scanning electron microscopy. Thus, photographs and light microscopy images were taken (Figure S11) and evaluated. For this, a small rectangle was cut out of the neat polystyrene foam. The interface was colored black to make the cell morphology visible. Figure S11 A shows a photograph of an inhomogeneous cell morphology with cell sizes in the range between 0.1 mm and 2.0 mm. Figure S11 B shows a micrograph of a foam cell demonstrating that neat polystyrene foams feature comparable thick cell walls in the range between 50  $\mu\text{m}$  and 150  $\mu\text{m}$ .

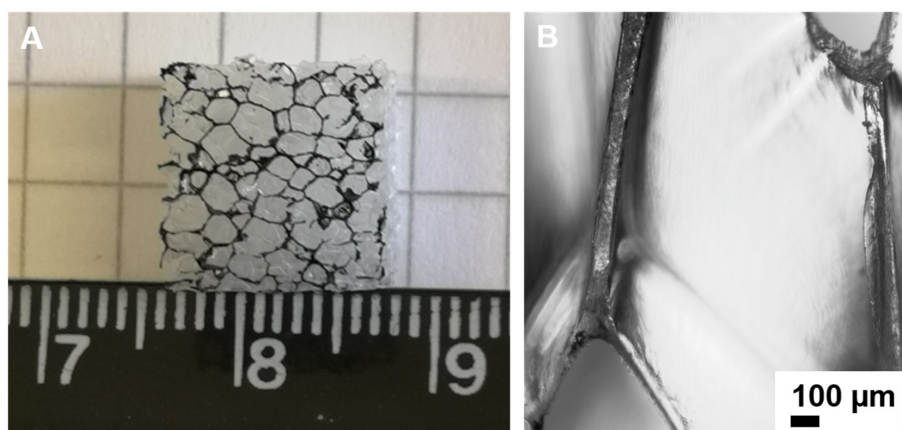


**Figure S11.** Photograph (A) and light microscopy image (B,10 $\times$ ) of extruded foams of neat polystyrene.

### References

1. Clark, S.J.; Segall, M.D.; Pickard, C.J.; Hasnip, P.J.; Probert, M.I.J.; Refson, K.; Payne, M.C. First principles methods using CASTEP. *Z. Kristallogr.* **2005**, *220*, 567–570.
2. Coelho, A.A. TOPAS and TOPAS-Academic : an optimization program integrating computer algebra and crystallographic objects written in C++. *J Appl Crystallogr* **2018**, *51*, 210–218.
3. Putz, H.; Schön, J.C.; Jansen, M. Combined method for ab initio structure solution from powder diffraction data. *J Appl Crystallogr* **1999**, *32*, 864–870.
4. Järvinen, M. Application of symmetrized harmonics expansion to correction of the preferred orientation effect. *J Appl Crystallogr* **1993**, *26*, 525–531.
5. Sakellariou, D.; Lesage, A.; Hodgkinson, P.; Emsley, L. Homonuclear dipolar decoupling in solid-state NMR using continuous phase modulation. *Chem. Phys. Lett.* **2000**, *319*, 253–260.
6. Metz, G.; Wu, X.L.; Smith, S.O. Ramped-Amplitude Cross Polarization in Magic-Angle-Spinning NMR. *J Magn Reson. Series A* **1994**, *110*, 219–227.
7. Fung, B.M.; Khitrin, A.K.; Ermolaev, K. An improved broadband decoupling sequence for liquid crystals and solids. *J Magn Reson.* **2000**, *142*, 97–101.
8. Günzler, H.; Gremlich, H.-U. *IR-Spektroskopie*; Wiley-VCH Verlag GmbH & Co. KGaA: Weinheim, Germany, 2003, ISBN 9783527662852.

## 4.6 $^{19}\text{F}$ MAS DNP for Probing Molecules in Nanomolar Concentrations: Direct Polarization as Key for Solid-State NMR Spectra without Solvent and Matrix Signals

This work is a cooperation between the Inorganic Chemistry III and the Macromolecular Chemistry I of the University of Bayreuth, the Physical and Theoretical Chemistry of the FU Berlin, the Eduard-Zintl-Institute of the TU Darmstadt and Bruker BioSpin and will be reprinted with permission from K.P. van der Zwan, W. Riedel, F. Aussenac, C. Reiter, K. Kreger, H.-W. Schmidt, T. Risse, T. Gutmann, J. Senker, *Journal of Physical Chemistry C* **2021**, *125*, 7287-7296. Copyright 2021 American Chemical Society.

My contributions are:

- conception and main authorship
- performing all conventional and DNP enhanced NMR experiments
- performing the extraction experiments
- sample preparation for the EPR experiments

The contributions of the other authors are:

- conception and authorship of the article
- assistance with the DNP enhanced NMR experiments
- synthesis of the materials and preparation of the compounds
- recording the SEM images
- performing EPR measurements

# <sup>19</sup>F MAS DNP for Probing Molecules in Nanomolar Concentrations: Direct Polarization as Key for Solid-State NMR Spectra without Solvent and Matrix Signals

Published as part of *The Journal of Physical Chemistry virtual special issue "Hellmut Eckert Festschrift"*.

Kasper P. van der Zwan, Wiebke Riedel, Fabien Aussenac, Christian Reiter, Klaus Kreger, Hans-Werner Schmidt, Thomas Risse, Torsten Gutmann,\* and Jürgen Senker\*

 Cite This: *J. Phys. Chem. C* 2021, 125, 7287–7296

 Read Online

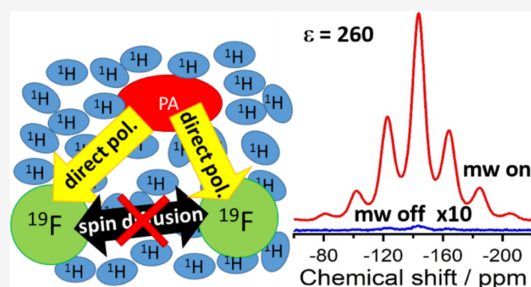
ACCESS |

 Metrics & More

 Article Recommendations

 Supporting Information

**ABSTRACT:** The efficiency of dynamic nuclear polarization (DNP) enhanced <sup>19</sup>F MAS NMR spectroscopy without <sup>19</sup>F-containing solvents and matrices, which transport polarization via <sup>19</sup>F–<sup>19</sup>F spin diffusion, is demonstrated. By preventing solvent and matrix signals respectively masking the corresponding resonances, this enables the detection of fluorinated target molecules in nanomolar amounts. As model compound, 1,3,5-tris(2-fluoro-2-methylpropionylamino)benzene (F-BTA) is investigated in a frozen 1,1,2,2-tetrachloroethane (TCE) solution and incorporated into a matrix of isotactic polypropylene (*i*-PP). While the polarizing agent is homogeneously dissolved within the frozen solution, for the *i*-PP/F-BTA blend, it is distributed via the incipient wetness impregnation (IWI) technique. For the frozen solutions with an F-BTA concentration of 187.5 mM an  $\epsilon_{\text{on/off}}$  of 260 was obtained. For F-BTA concentrations of 10 and 2.5 mM the sensitivity trend suggests even higher DNP gains. The substantial enhancements could be achieved by direct polarization transfer over distances up to at least 20 Å, derived from a simple geometric model assuming a homogeneous solution, engaging a large part of the sample volume. Cross-polarization (CP) to <sup>13</sup>C nuclei allowed selection of the NMR spectroscopic resonances of the minority species in the *i*-PP/F-BTA blend suppressing the otherwise dominating resonances of the IWI solvent and the polymer matrix. The possibility of exciting <sup>19</sup>F via DNP directly and of transferring the polarization to other heteronuclei within close proximity enables spatial spectral editing to clear up spectra otherwise crowded by matrix and solvent signals. We thus expect direct polarization transfer techniques for DNP enhanced NMR spectroscopy to become more important in the future.



## INTRODUCTION

The introduction of solid-state dynamic nuclear polarization (DNP) at high magnetic fields and high spectral resolution (magic-angle-spinning; MAS) by the pioneering works of Griffin and co-workers<sup>1–4</sup> led to an increasing interest to use this technique in structural biology<sup>5</sup> and materials science.<sup>6,7</sup> DNP uses electronic polarization of stable radicals to enhance nuclear polarization.<sup>8</sup> For this, the radicals and the target molecules need to be in close contact, which, in the early days, was mainly realized by frozen solutions.<sup>9</sup> Still, frozen solutions are the systems for which the highest enhancement factors were observed.<sup>10</sup> To investigate materials that cannot be dissolved or if the crystal structure needs to be kept unaltered, the incipient wetness impregnation (IWI) technique is the most common protocol to study samples with DNP NMR spectroscopy in materials science.<sup>11–13</sup> In recent works, IWI has been successfully employed to enhance a variety of spin 1/2 and quadrupolar nuclei including <sup>13</sup>C,<sup>14–16</sup> <sup>15</sup>N,<sup>17,18</sup> <sup>27</sup>Al<sup>19,20</sup>

and <sup>17</sup>O<sup>21–23</sup> by either polarization transfer via the proton spin bath<sup>19</sup> or direct excitation.<sup>22</sup> Many works on DNP solid-state NMR spectroscopy are summarized in comprehensive reviews that have been published recently.<sup>5,7,24–33</sup>

<sup>19</sup>F solid-state NMR spectroscopy is an important technique in both materials science<sup>34,35</sup> and pharmaceutical research.<sup>36</sup> Especially in the fast-growing field of organic solar cells, fluorine-containing small molecules are increasingly used<sup>34,35</sup> and analyzed by <sup>19</sup>F solid-state NMR spectroscopy.<sup>37</sup> Many active pharmaceutical ingredients contain at least one fluorine

Received: February 8, 2021

Revised: March 18, 2021

Published: March 31, 2021



atom.<sup>38</sup> Furthermore, introducing  $^{19}\text{F}$  to a sample can be used as a spin label to selectively examine a certain part of a sample.<sup>39,40</sup> While standard  $^{19}\text{F}$  MAS NMR spectroscopy is well established, DNP enhanced solid-state NMR spectroscopic studies on  $^{19}\text{F}$  are limited up to now,<sup>41–43</sup> since they are technically more demanding for conventional DNP NMR spectroscopic probes and the underlying transfer mechanisms are not yet thoroughly investigated.

Important polarization mechanisms for DNP are the solid<sup>44</sup> and the cross<sup>45</sup> effects. At high magnetic fields and MAS the cross effect (CE) is more efficient.<sup>45</sup> For CE, two coupled electrons, mostly from biradicals<sup>46–48</sup> like TEKPol<sup>49</sup> or AMUPol,<sup>50</sup> need to have a difference of their Larmor frequencies in the order of the Larmor frequency of the nucleus that is polarized.<sup>51</sup> Nuclei in close proximity ( $<10$  Å) to the electrons are polarized quickly, and they usually transfer the polarization to bulk nuclei via spin diffusion.<sup>52</sup> In the absence of spin diffusion, it was recognized that even distant nuclei can be polarized directly by both solid<sup>53</sup> and cross<sup>54,55</sup> effects. While Schäfer et al.<sup>53</sup> observed polarization transfer to  $^{13}\text{C}$  nuclei up to distances of 30–60 Å under static conditions, Amoureux<sup>54</sup> and Oschkinat<sup>55</sup> and co-workers reported direct polarization transfer to  $^{29}\text{Si}$  up to distances of 35 and 57 Å for MAS experiments in high fields. Typically, spin diffusion is quenched for spins either with a low natural abundance for the probed isotope or by a reduced concentration for a high abundant isotope. In contrast, spin diffusion is switched on if a dense, homonuclear spin bath sufficiently coupled by the dipolar interaction is present. These are typically introduced to the sample with the solvent matrix in which the radical is dissolved. In this context, a drawback of proton mediated DNP solid-state NMR spectroscopy is the introduction of unwanted peaks in the respective spectra, caused by the solvent matrix used for the frozen solution or the impregnation of the materials.

This issue might become critical when measuring  $^{19}\text{F}$  DNP solid-state NMR spectroscopy. Here, the solvent signal overlaps with the signals of  $^{19}\text{F}$  spin labels of the sample that are then harder to identify. For example, Viger-Gravel et al.<sup>42</sup> used trifluoroethanol as a  $^{19}\text{F}$  containing solvent to transport the polarization to their target molecules. This, however, introduces a solvent peak with spinning side bands and makes it, therefore, more challenging to probe  $^{19}\text{F}$  spins in very low concentrations. In principle, the solvent peaks can be removed by solvent suppression techniques like FEDex<sup>56</sup> or TRAP-DORED<sup>56</sup> and  $T_2$  filters.<sup>57</sup> In the case of CP to  $^{13}\text{C}$  nuclei, also the depletion of  $^{13}\text{C}$  from the DNP matrix is an alternative, as shown by Griffin et al.<sup>58</sup> However, solvent suppression is either expensive (i.e.  $^{13}\text{C}$  depletion) or reduces the intensity of the target signals as well and is thus feasible only at higher contents of the target molecules.

In this work, our aim is to establish a protocol for  $^{19}\text{F}$  DNP on materials that works without a  $^{19}\text{F}$  containing solvent. Pioneering work on this topic has been done by Lu et al.<sup>41</sup> for  $^{19}\text{F}$ -labeled proteins using a regular AMUPol DNP matrix to polarize specific parts of the protein. We show that samples with fluorine contents, too low to allow for spin diffusion, are easily polarized with DNP in frozen solutions as well as in polymer blends. We chose 1,3,5-tris(2-fluoro-2-methylpropionylamino)benzene (F-BTA)<sup>59</sup> as a model compound (a sketch of the molecular structure is shown in Figure 1). On the one hand, the molecular structure of F-BTA is very similar to pharmaceuticals as it is a low molecular weight

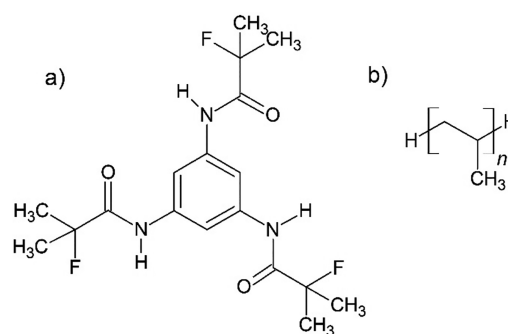


Figure 1. Molecular structures of F-BTA (a) and *i*-PP (b).

compound with amide groups. On the other hand, it resembles commercially used supramolecular polymer additives, i.e., IRGACLEAR XT386.<sup>60</sup> Therefore, F-BTA is a well-suited model for compounds occurring in pharmaceutical and materials science.<sup>61</sup> In the first section, we study frozen solutions for different F-BTA concentrations to see how far we can push the sensitivity limit. In the second section, we extend our investigation to blends of F-BTA in isotactic polypropylene (*i*-PP) excited by the IWI technique (the structure of *i*-PP is shown in Figure 1). In the last section, we explore the potential of  $^{19}\text{F} \rightarrow ^{13}\text{C}$  cross-polarization (CP) for selecting  $^{13}\text{C}$  NMR resonances of the fluorinated target molecules from the otherwise crowded  $^1\text{H} \rightarrow ^{13}\text{C}$  CP spectra of the polymer blends.

## METHODS

**Materials.** The *i*-PP homopolymer grade Profax PH 350 was purchased from LyondellBasell. The *i*-PP was ground with the ultracentrifugal mill Retsch ZM200 yielding a fine powder with a grain size of approximately 100  $\mu\text{m}$ . The synthesis of F-BTA was performed according to literature procedures and obtained as a fine white powder.<sup>59</sup> Two dry-blended powder–powder mixtures of *i*-PP and F-BTA were prepared with a F-BTA content of 2 and 0.06 wt %, respectively. The *i*-PP/F-BTA blends were homogenized using a corotating twin-screw compounder (DSM Xplore) at a rotational speed of 50 rpm at 220 °C under nitrogen atmosphere for 5 min. The extrudate was then milled to a fine powder with a grain size of approximately 100  $\mu\text{m}$  or smaller using a mesh size of 100  $\mu\text{m}$ .

**Sample Preparation for DNP Experiments.** TEKPol<sup>49</sup> and AMUPol<sup>50</sup> were purchased from CortecNet (France) and used as received. A TEKPol stock solution in TCE with a concentration of 15 mM was prepared. This solution was used to dissolve F-BTA at three different concentrations, i.e., 187.5, 10, and 2.5 mM, which were subsequently utilized for the “frozen solution experiments”. Samples of the *i*-PP/F-BTA blend were prepared using the IWI technique. For this, typically 25 mg of a milled *i*-PP/F-BTA blend was impregnated with 20  $\mu\text{L}$  of the 15 mM TEKPol stock solution in TCE. For the solid-state DNP NMR spectra of neat F-BTA, the powder was impregnated with a 15 mM AMUPol solution in a DMSO- $d_6$ /D $_2$ O/H $_2$ O mixture with volume ratios of 6/3/1.

**DNP Experiments.** DNP and conventional NMR spectroscopic measurements at 120 K were performed on a Bruker Avance III 400 DNP spectrometer working at  $B_0 = 9.7$  T equipped with a Bruker gyrotron (9.7 T, 263.4 GHz, 115 mA beam current) and a low-temperature  $^1\text{H}/X/Y$  triple resonance

probe. NMR spectra were recorded at frequencies of 376.35 MHz for  $^{19}\text{F}$ , 400.02 MHz for  $^1\text{H}$ , and 100.59 MHz for  $^{13}\text{C}$  and 8 or 12 kHz MAS spinning speed. The DNP experiments at 100 K for the frozen solutions were performed at a Bruker Avance NEO spectrometer equipped with an Ascend 400 DNP magnet, a 4.8 T Bruker gyrotron generating microwaves at a frequency of 263 GHz using the second harmonics. A similar 3.2 mm MAS triple resonance probe was used. The  $^{19}\text{F}$  frequency for these experiments was 376.52 MHz and the MAS spinning speed 8 kHz. The samples were packed in sapphire rotors covered with silicone plugs and sealed with zirconia caps. Recycle delays between 1.9 and 5 s were chosen to ensure a sufficiently long DNP build-up. The observed magnetization  $M$  was refined using eq 1, modeling a stretched exponential build-up with  $T_b$  and  $b$  being the build-up time and the stretching parameter, respectively.  $c$  and  $a$  are related to the initial ( $t = 0$ ) and final ( $t \rightarrow \infty$ ) magnetization, respectively.

$$M = c + a e^{-((t/T_b)^b)} \quad (1)$$

For the  $^{19}\text{F}$  NMR spectroscopic rotor synchronized Hahn echo experiments, 4–4096 and 1024–19 600 transients were recorded for the frozen solutions and the blends, respectively. The corresponding nutation frequency matched 78.1 kHz (frozen solution) and 45 kHz (blends). The  $^1\text{H}/^{19}\text{F} \rightarrow ^{13}\text{C}$  CP experiments were done with a ramped CP sequence<sup>62</sup> where the nutation frequency on the  $^1\text{H}$  or  $^{19}\text{F}$  channel was varied linearly from 50% to 100%. The maximum nutation frequencies during the contact time were set to 83 kHz ( $^1\text{H}$ ) and 45 kHz ( $^{19}\text{F}$ ), respectively. During acquisition on the  $^{13}\text{C}$  channel,  $^1\text{H}$  or  $^{19}\text{F}$  was decoupled using the Spinal64<sup>63</sup> decoupling sequence with nutation frequencies of 83 and 45 kHz, respectively. The CP contact time was set to 2.5 and 4 ms for the  $^{19}\text{F} \rightarrow ^{13}\text{C}$  and  $^1\text{H} \rightarrow ^{13}\text{C}$  CP experiments, respectively. For the  $^{19}\text{F} \rightarrow ^{13}\text{C}$  CP experiments of the neat sample 64 and of the blend 17408 transients were recorded. The  $^1\text{H} \rightarrow ^{13}\text{C}$  CP measurements used 2048 transients.

For the CP build-up curves a square pulse was used for the spin-lock, and the build-up times were varied between 0.5 and 15 ms. The  $^{19}\text{F} \rightarrow ^{13}\text{C}$  CP NMR spectra for the build-up curves were deconvoluted to extract the integral intensities. The latter were plotted against the applied CP build-up time. The data were fitted with eq 2 taken from ref 64.  $T_{\text{IS}}$  denotes the CP build-up time and  $T_{1\rho}$  reflects the time constant for the spin-lattice relaxation time of the  $^{19}\text{F}$  spin bath in the rotating frame.

$$I(t) = I_0 \left( 1 - \frac{T_{\text{IS}}}{T_{1\rho}} \right)^{-1} \left( e^{-t/T_{1\rho}} - e^{-t/T_{\text{IS}}} \right) \quad (2)$$

**EPR Experiments.** Continuous wave (cw) electron paramagnetic resonance (EPR) measurements at X-band frequencies (9.52 GHz) were conducted at 150 K with a Bruker B-ER420 spectrometer upgraded with a Bruker ECS 041XG microwave bridge and a lock-in amplifier (Bruker ER023M) using a Bruker TE<sub>102</sub> resonator applying a modulation amplitude of 1 G and a modulation frequency of 100 kHz. The samples were measured in quartz tubes of 2.9 mm outer diameter containing typically 20  $\mu\text{L}$  of the solutions. For comparison, the spectra were normalized to the peak-to-peak amplitude.

**Extraction Experiments.** Three extraction experiments on an *i*-PP/F-BTA blend with 1.5 wt % of F-BTA were performed.

For the first experiment 25 mg of dry powder was added to a syringe equipped with a syringe filter and directly flushed with 1.8 mL of TCE. For the other two experiments an amount of 25 mg of the blend was impregnated with 20  $\mu\text{L}$  of TCE. The wet powder was again transferred into the syringe and flushed with 1.8 mL of TCE after 5 and 10 min impregnation time. The extracts were analyzed by gas chromatography (GC) and gas chromatography coupled with a mass spectrometer (GC-MS). GC analyses were carried out using an Agilent Technologies 6890N system equipped with an Agilent HP-5 column (30 m, 320  $\mu\text{m}$ , 0.25  $\mu\text{m}$ ). GC-MS analyses were conducted on an Agilent 7890A GC system equipped with a HP SMS column (30 m, 320  $\mu\text{m}$ , 0.25  $\mu\text{m}$ ) and a 5975C inert MSD detector (EI, 70 eV).

**Electron Microscopy.** Scanning electron microscopy (SEM) images were obtained using a Leo Gemini FESEM Zeiss 1530 (Carl Zeiss AG) equipped with a field emission cathode using an acceleration voltage of 3.0 kV. The ground blend particles were sprinkled on a double-sided adhesive conductive carbon tape attached to SEM aluminum pin stubs. The blend particles were sputtered with a 2.0 nm thick platinum layer under argon atmosphere using a Cressington sputter coater 208HR.

## RESULTS AND DISCUSSION

**$^{19}\text{F}$  DNP MAS NMR Experiments on Frozen Solutions of F-BTA.** We start exploring the potential of  $^{19}\text{F}$  DNP enhanced MAS NMR spectroscopy with frozen solutions. As they are homogeneous, frozen solutions allow for avoiding phase boundary issues and usually yield the highest enhancement factors  $\epsilon$ , which may even approach the theoretical limit of DNP.<sup>10</sup> Starting from the previously established protocol<sup>49</sup> of 15 mM TEKPol 1,1,2,2-tetrachloroethane (TCE) solutions, three mixtures with F-BTA concentrations of 187.5, 10, and 2.5 mM were prepared. The build-up of  $^{19}\text{F}$  polarization for the  $^{19}\text{F}$  DNP enhanced Hahn echo spectra (Figure 2) differed depending on the concentration. In all cases, a stretched exponential function (eq 1) was used to model the data with build-up times of 3.3, 5.6, and 5.7 s and  $b$  values between 0.88 and 0.78 for the solutions with 187.5, 10, and 2.5 mM, respectively (Figure S1 and Table S1).

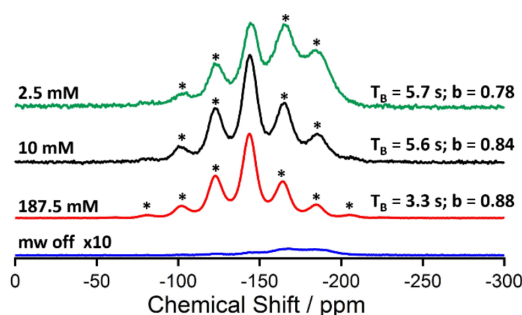


**Figure 2.**  $^{19}\text{F}$  DNP MAS NMR spectra of F-BTA/TCE frozen solutions with TEKPol. Displayed are, from bottom to top, mw off spectrum for 187.5 mM BTA with an intensity multiplied by 10 (blue), mw on spectrum for 187.5 mM F-BTA (red), mw on spectrum for 10 mM F-BTA (black), and mw on spectrum for 2.5 mM F-BTA (green). All spectra were recorded with a spinning speed of 8 kHz at a temperature of 100 K. Resonances marked with an asterisk represent spinning side bands.

For the following discussion we use the conventional  $\epsilon_{\text{on/off}}$  factor as a measure for the DNP enhancement, being aware that the real polarization gain is lower due to depolarization effects within the microwave (mw) off spectrum.<sup>65</sup> The highest F-BTA concentration yields an  $\epsilon$  of 260, calculated directly from the corresponding mw on and off spectra. For the less concentrated mixtures no microwave off spectra with sufficient S/N ratios (SNR) could be obtained. Thus, no  $\epsilon_{\text{on/off}}$  values could be calculated for these two samples. To still be able to provide an estimate for the DNP gain, we calculated the sensitivity  $S$  (defined as signal-to-noise-ratio per square root of time and unit mass:  $S = \text{SNR}/(m\sqrt{t})$ )<sup>66</sup> for the three concentrations. For the highest F-BTA concentration an  $S$  of  $753 \pm 16 \text{ mg}^{-1} \text{ h}^{-1/2}$  was obtained. The  $S$  values for 10 and 2.5 mM are with  $1005 \pm 11$  and  $973 \pm 39 \text{ mg}^{-1} \text{ h}^{-1/2}$  larger by a factor of 1.3 and quite similar. The increase in sensitivity shows that the DNP gain is more effective for the lower two concentrations.

The theoretical maximal enhancement factor for  $^{19}\text{F}$  is 698; however several experimental parameters influence the observable  $\epsilon$ . Typically, the highest enhancement factors were obtained for temperatures significantly lower than the 100 K used for the  $^{19}\text{F}$  DNP NMR spectra acquired within this work. For example, Bouleau et al.<sup>10</sup> showed that the enhancement increases by 100% when reducing the temperature from 110 to 55 K. Furthermore, Mentink-Vigier et al.<sup>67</sup> showed in simulations that the polarization enhancement of the nuclei strongly depends on the distance of the nucleus to the hyperfine coupled electron<sup>52</sup> and the number of nuclei that need to be polarized. As such, an  $\epsilon$  of 260 is regarded as high, since it almost triples the highest  $\epsilon$  reported for  $^{19}\text{F}$  DNP MAS so far,<sup>42</sup> indicating that the polarization transfer of TEKPol to the  $22 \mu\text{mol}$   $^{19}\text{F}$  nuclei within the 187.5 mM sample is quite efficient. Nevertheless, the DNP gain larger by a factor of 1.3 for the diluted samples even allowed for probing 300 nmol of  $^{19}\text{F}$  nuclei straightforwardly. In agreement with Mentink-Vigier,<sup>67</sup> the higher DNP gains were obtained for the systems where the amount of  $^{19}\text{F}$  nuclei and TEKPol molecules are on the order of magnitude.

To evaluate if direct polarization is the main polarization mechanism or if  $^{19}\text{F}$ – $^{19}\text{F}$  spin diffusion plays an essential role, we estimated average distances between the  $^{19}\text{F}$  nuclei within the F-BTA molecules and the TEKPol radicals as well as other F-BTA molecules based on a simple geometric model. It assumes random, homogeneous distributions of both molecules, which is consistent with no or only weak interactions present between them. For the TEKPol–TEKPol environments this assumption is substantiated by the concentration independence of the line shapes and line widths of the EPR spectra obtained for frozen solutions (Figure S2) with concentrations lower than 30 mM. This concentration is twice as high as the maximal one used for the DNP experiments in this work. Furthermore,  $^{19}\text{F}$ – $^{19}\text{F}$  DQ-filtered NMR spectra (Figure S4) show that no close contacts between the F-BTA molecules are present even for the frozen solution with the highest F-BTA concentration (187.5 mM). This demonstrates that the conventional cluster growth typical for this class of molecules is efficiently avoided by vitrifying the TCE solutions.

Assuming a spherical appearance of both species within the frozen solutions, the TEKPol radicals are separated from each other by roughly 30–50 Å (for more detail on the derivation of the model see Supporting Information section 4). Depending

on the F-BTA concentrations, average F-BTA–F-BTA distances of 16, 55, and 91 Å are estimated. As the largest TEKPol–TEKPol distances are smaller than 50 Å, their distance toward F-BTA molecules should be smaller than 25 Å for the three frozen solutions. This leads to two limiting cases: In the first case the majority of components are the F-BTA molecules (187.5 mM). The mean TEKPol–F-BTA distance will then be shorter than the mean F-BTA–F-BTA distance of 16 Å. In the second case, the majority of components are the TEKPol radicals (10 and 2.5 mM) for which the mean F-BTA–F-BTA distance (55 and 91 Å) exceeds the TEKPol–TEKPol ones (30–50 Å) leading to mean TEKPol–F-BTA distances on the order of 20 Å (Figure S5).

The, on average, shorter TEKPol–F-BTA distances for the first scenario are in accordance with the shorter  $T_B$  value of 3.3 s measured for the frozen solution with 187.5 mM F-BTA, while the two solutions (10 and 2.5 mM) matching the second scenario showed significantly longer and similar  $T_B$  values of 5.7 s. The build-up time for the first scenario is on the order regularly expected for TEKPol.<sup>68</sup> The longer build-up times for the second scenario are in line with the direct polarization of  $^{29}\text{Si}$  over long distances measured by Amoureux<sup>54</sup> and Oschkinat.<sup>55</sup> The similar polarization build-up behavior for the lower two F-BTA concentrations indicates similar F-BTA–TEKPol environments for both cases. The distribution of  $T_B$  times expressed by a stretching parameter smaller than 1 ( $b \approx 0.8$ ) furthermore supports a homogeneous model with a continuous distance distribution. Strong attractive interactions between both species are thus unlikely.

As the average F-BTA–F-BTA distances in our samples are  $\geq 16$  Å, the intermolecular  $^{19}\text{F}$ – $^{19}\text{F}$  distances are expected to be larger than the intramolecular ones, which are around 9.2 Å. The largest  $^{19}\text{F}$ – $^{19}\text{F}$  dipolar couplings are thus around 136 Hz, which is too weak to provide a dipolarly coupled  $^{19}\text{F}$  spin bath under the applied MAS conditions ( $\nu_{\text{rot}} = 8 \text{ kHz}$ ). Consequently,  $^{19}\text{F}$ – $^{19}\text{F}$  spin diffusion is quenched, rendering fast polarization transfer between the individual  $^{19}\text{F}$  nuclei unlikely as visualized in Figure 3.

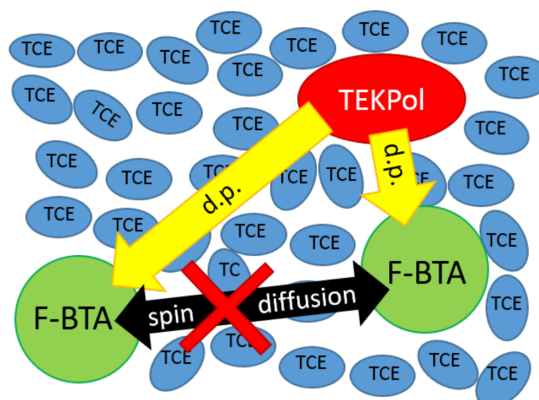


**Figure 3.** Schematic representation of the situation in the frozen solution. The blue ovals represent the TCE molecules. The F-BTA molecules (green circles) are well separated from each other, and spin diffusion is efficiently quenched under MAS. Nonetheless, the polarizing agent, TEKPol (red oval), is still able to directly polarize (yellow arrow) the  $^{19}\text{F}$  spins of the F-BTA molecules due to the much stronger  $e^-$ – $^{19}\text{F}$  dipolar couplings.

As the gyromagnetic ratio of the electron is 698 times larger than that of fluorine, the dipolar coupling between a radical and  $^{19}\text{F}$  nuclei amounts to almost 5 kHz, even for the longest estimated distance of 25 Å. As the dipolar coupling scales with the inverse cube of the distance, the coupling is much higher for shorter distances (e.g., 43 kHz for 12 Å) and therefore not sufficiently averaged by MAS, thus enabling a polarization transfer.

From these results, we conclude that the  $^{19}\text{F}$  polarization build-up mainly arises by direct transfer from the biradicals. The increase of the DNP enhancement, by a factor of 1.3, upon reducing the F-BTA concentration from 187.5 to 2.5 mM suggests a more efficient polarization transfer when the total number of  $^{19}\text{F}$  nuclei that need to be polarized is reduced. Although sensitivity  $S$  depends on both the DNP gain and the number of excited  $^{19}\text{F}$  spins, its order of magnitude and the stretched exponential build-up for the frozen solutions for the lower two concentrations make it likely that we polarize the majority of  $^{19}\text{F}$  spins in the frozen solutions.

**$^{19}\text{F}$  DNP MAS NMR Experiments on *i*-PP/F-BTA Blends.** We showed above that it is possible to transfer the polarization over distances of at least 20 Å without the need of a  $^{19}\text{F}$  spin bath. With regular concentrations of polarization agents, a major part of the sample volume is covered, and thus probing even minority species without parasitic solvent signals should be feasible. Now, we transfer these results to a particular system of a finely ground *i*-PP/F-BTA blend. For this system, the IWI technique is used to apply the polarizing agent. We probe two blends, one with a F-BTA content of 2 wt % and one with a content of 0.06 wt %.

Figure 4 shows the spectra for two *i*-PP/F-BTA blends with F-BTA contents of 2 and 0.06 wt % (green and blue) and a

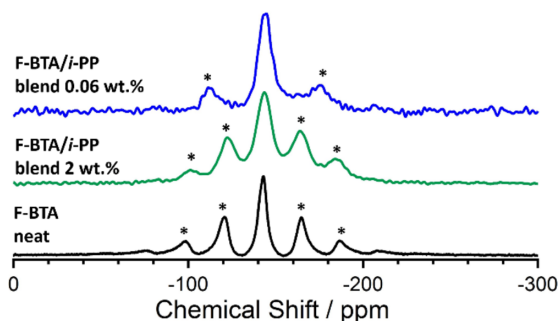


**Figure 4.** DNP enhanced  $^{19}\text{F}$  MAS spectra, from top to bottom: *i*-PP with 0.06 wt % of F-BTA in 15 mM TEKPol in TCE,  $\nu_{\text{rot}} = 12$  kHz (blue); *i*-PP with 2 wt % of F-BTA in 15 mM TEKPol in TCE,  $\nu_{\text{rot}} = 8$  kHz (green). For comparison a conventional  $^{19}\text{F}$  MAS spectrum of neat F-BTA without IWI treatment,  $\nu_{\text{rot}} = 8$  kHz (black), is depicted. Resonances marked with an asterisk represent spinning side bands.

spectrum of neat F-BTA (black). Due to  $^{19}\text{F}$  chemical shift dispersions and  $^{19}\text{F}$ - $^1\text{H}$  dipolar couplings that could not be decoupled with the accessible probe, all resonances are relatively broad. The DNP build-up for the sample with 2 wt % F-BTA is monoexponential with a build-up time of 2.8 s (Figure S6 and Table S2). For none of the samples could  $\varepsilon_{\text{DNP}}$  be determined, since the sensitivities in the mw off spectra are too low. The absolute sensitivities were determined to  $497 \pm 8$  and  $425 \pm 12 \text{ mg}^{-1} \text{ h}^{-1/2}$  for the blends containing 2 and 0.06 wt % F-BTA, respectively. The  $S$  values for the blends are by a

factor 2 lower compared to the ones obtained for the frozen solutions. This shows that the IWI technique does polarize the  $^{19}\text{F}$  nuclei for a significant part of the sample volume and is quite efficient in this case.

This is unexpected, as samples treated with IWI are usually less polarized, since the polarization agent is confined to the surfaces of the particles and will not excite those F-BTA species deeper within the *i*-PP matrix as efficiently as the ones close to the surfaces. This is even more important as the  $^{19}\text{F}$  spin density within the *i*-PP matrix is zero, preventing  $^{19}\text{F}$ - $^{19}\text{F}$  spin diffusion in the polymer matrix and the IWI solvent. Thus, polarization transfer toward the F-BTA nanoobjects inside the blend particles will be based on a direct mechanism. Once reaching a nanoobject's surface,  $^{19}\text{F}$ - $^{19}\text{F}$  spin diffusion will, however, be able to polarize most of the fluorine spins inside this object, as typical  $^{19}\text{F}$ - $^{19}\text{F}$  distances are around 3 Å<sup>61</sup> within the self-assembled objects.

Nevertheless, for particles with an average size of around 100  $\mu\text{m}$  (Figure 5a) only a small part of the F-BTA nanoobjects

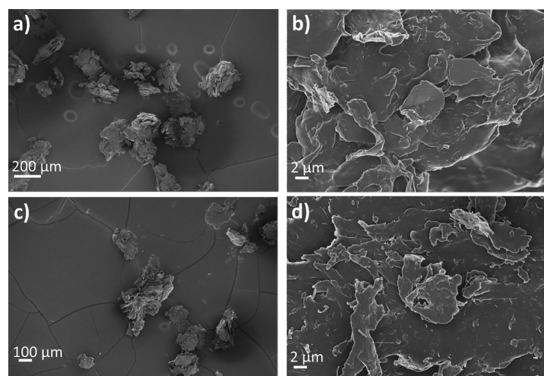


**Figure 5.** SEM images of the *i*-PP/F-BTA blend with an F-BTA content of 0.06 wt % after (a, b) and prior to (c, d) IWI.

close to the surfaces of the blend particles (<2 nm) should be excited. This seems to be contradictory compared to the high  $S$  values around 500 obtained from the DNP experiments. An image of the particles with larger magnification (Figure 5b) reveals that the surfaces are rough, with cracks and smaller particles agglomerated. This suggests that the DNP juice covers significantly larger surface areas than expected for homogeneous particles with an average size of 100  $\mu\text{m}$ . In consequence, a larger part of the F-BTA nanoobjects will be excited. Notably, the surfaces of the blend particles do not change in morphology before (Figure 5c and Figure 5d) and after (Figures 5a and Figure 5b) IWI treatment, rendering a large dissolution effect of the DNP juice unlikely.

To confirm, that leaching of F-BTA molecules from the blend particles into the DNP juice is a minor effect, we reconstructed the IWI experiment and analyzed the extracted solvent by gas chromatographic (GC) and mass spectrometric (MS) experiments (compare Supporting Information section 6 and Figures S7–S9). These experiments show that the extraction of F-BTA already saturates in less than 5 min. The maximum F-BTA loss of the blend particles amounts to 3.7%. This shows that dissolution of the F-BTA molecules occurs only very close to the surfaces. Assuming that only these 3.7% of the F-BTA molecules are polarized within the DNP

experiment, a sensitivity  $S$  larger than 13 200 would result. Considering that the highest  $S$  for the frozen solutions is around 1000, this is a physically unreasonably high value. For these reasons, we are convinced that the possibility of IWI altering the solid sample<sup>29</sup> is a negligible effect in our case and the majority of the excited F-BTA aggregates are located well within the blend particles.<sup>69</sup>

Additionally, little is known about the distribution of the F-BTA nanoobjects within the *i*-PP particles. The higher  $S$  value for the blend with the larger F-BTA content indicates that for this sample the proportion of F-BTA objects close to the surfaces of the *i*-PP particles is higher.

Although the resonances are relatively broad, we still observe differences in the spectra. The line widths obtained for the mw on spectra for the two blends samples are similar (full width at half-maximum fwhm  $\approx$  3800 Hz). For the neat reference of crystalline F-BTA a line width of 2100 Hz is observed without radical containing solution measured on the same NMR spectrometer with the same conditions (120 K,  $\nu_{\text{rot}} = 8$  kHz, no proton decoupling). Since the heteronuclear  $^1\text{H}$ - $^{19}\text{F}$  dipolar couplings will be similar for the neat, crystalline F-BTA and the F-BTA nanoobjects within the polymer blends as the arrangement of the side chains of the F-BTA molecules does not change, a broader resonance for the blend originates from changes of chemical shift dispersions. Both interactions commute and thus contribute additively to the total line width.<sup>70</sup> The increased line width compared to the neat F-BTA thus suggests that significantly smaller supramolecular objects with more disorder are formed upon crystallization from the *i*-PP melt.

Summarizing, in the 0.06 and 2 wt % *i*-PP/F-BTA blend, total amounts of 94 nmol and 3  $\mu\text{mol}$  of  $^{19}\text{F}$  spins are present. Many, if not all, of these spins appear to be polarized regardless of the absence of a  $^{19}\text{F}$  spin bath through which the polarization can be transferred via spin diffusion.

#### $^{19}\text{F} \rightarrow ^{13}\text{C}$ DNP CP Experiments on *i*-PP/F-BTA Blends.

Being able to enhance such small amounts of  $^{19}\text{F}$  nuclei opens up the opportunity to selectively enhance carbon nuclei close to fluorine via  $^{19}\text{F} \rightarrow ^{13}\text{C}$  CP transfer. For the 2 wt % *i*-PP/F-BTA blend, we were able to observe resonances for the four F-BTA carbons closest to the fluorine atom (Figure 6, green line), namely, the quaternary carbon 1 (100 ppm), the methyl groups 2 (30 ppm), the amide 3 (175 ppm), and the quaternary aromatic 4 (145 ppm). While the resonances for the carbon atoms 1–3, close to the fluorine atoms, are quite intense, the signal for carbon atom 4 is very weak. The corresponding chemical shifts match the resonances obtained in the DNP enhanced  $^{19}\text{F} \rightarrow ^{13}\text{C}$  CP MAS spectrum of the neat F-BTA (Figure 6, black line) prepared with the IWI method using AMUPol in  $\text{DMSO-}d_6/\text{D}_2\text{O}/\text{H}_2\text{O}$  6/3/1 to prevent dissolution of the F-BTA powder (Figure S10). The similarity of the chemical shifts of the F-BTA molecules in the blend compared to the neat crystal confirms the self-assembly of the F-BTA within the blend. The 1.4 ppm upfield shift of the carbonyl resonance in the blend indicates a slightly weaker hydrogen bond,<sup>71</sup> which is in line with the line shape analysis that the nanoobjects are less ordered compared to the neat crystal.

In contrast, the DNP enhanced  $^1\text{H} \rightarrow ^{13}\text{C}$  CP MAS spectrum of the 2 wt % *i*-PP/F-BTA blend (Figure 6, blue line) is very crowded. It is dominated by the resonances originating from the solvent (TCE), *i*-PP, and other additives such as antioxidants present in the used *i*-PP grade (Profax PH 350,

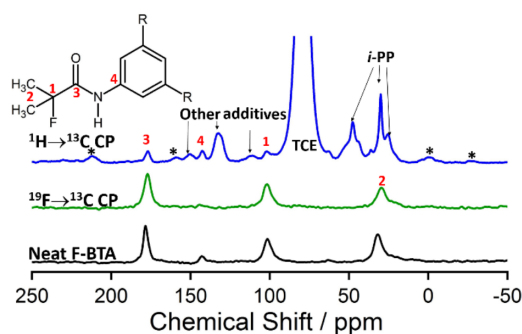


**Figure 6.**  $^{19}\text{F} \rightarrow ^{13}\text{C}$  CP DNP NMR spectra of neat F-BTA in 15 mM AMUPol in  $\text{DMSO-}d_6/\text{D}_2\text{O}/\text{H}_2\text{O}$  6/3/1 v/v/v (black) and 2 wt % *i*-PP/F-BTA blend with 15 mM TEKPol in TCE (green).  $^1\text{H} \rightarrow ^{13}\text{C}$  CP DNP NMR spectrum of the same sample (blue). All spectra were measured with a MAS frequency of  $\nu_{\text{rot}} = 8$  kHz. In the top left, the molecular structure of F-BTA is depicted with an assignment of the NMR signals. For the sake of clarity, the side branches at positions 3 and 5 of the benzene core are abbreviated as R. Resonances marked with an asterisk represent spinning side bands.

LyondellBasell). Therefore, it is challenging to identify the signals of F-BTA exclusively from the DNP enhanced  $^1\text{H} \rightarrow ^{13}\text{C}$  CP MAS spectrum. The signals for 3 and 4 are relatively easy to assign, whereas the resonances for 1 and 2 are partly or completely hidden by the shoulder of the solvent peak and the *i*-PP resonances. This convincingly demonstrates the advantage of DNP enhanced  $^{19}\text{F} \rightarrow ^{13}\text{C}$  CP MAS NMR spectroscopy over DNP enhanced  $^1\text{H} \rightarrow ^{13}\text{C}$  CP MAS for identifying the spectral signature of  $^{19}\text{F}$  spin-labeled molecules in nanomolar amounts, such as F-BTA in blended materials. With  $^{19}\text{F} \rightarrow ^{13}\text{C}$  CP MAS NMR we are therefore able to selectively probe and enhance very specific parts of the sample, and by use of DNP, the amount of  $^{19}\text{F}$  spin labels can be lower compared to regular solid-state NMR spectroscopy.

To probe the spatial range for this spectral filter, we determined the CP build-up kinetics (Figure 7 and Table 1).

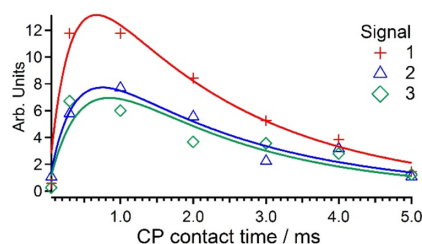


**Figure 7.**  $^{19}\text{F} \rightarrow ^{13}\text{C}$  CP DNP NMR build-up curves of 2 wt % *i*-PP/F-BTA blend with 15 mM TEKPol in TCE  $\nu_{\text{rot}} = 8$  kHz.

The contact time dependent intensities for carbon atoms 1–3 were modeled according to eq 2. Due to limitations of the measurement time frame and the very low (2 wt %) F-BTA content, only a limited amount of 1D spectra could be acquired. Therefore, the  $T_{\text{IS}}$  values were adopted from the DNP CP build-up kinetics (Figure S11 and Table S3) on the neat F-BTA with only refining  $T_{1\rho}$ . The good quality of the fit (Figure 7) demonstrates that the  $T_{\text{IS}}$  values do not change between the blend and the neat F-BTA material. In contrast, the  $T_{1\rho}$  values for the carbon atoms 1–3 are identical within

**Table 1. Fitting Results of the  $^{19}\text{F} \rightarrow ^{13}\text{C}$  CP DNP NMR Build-Up Curves of 2 wt % *i*-PP/F-BTA Blend with 15 mM TEKPol in TCE,  $\nu_{\text{rot}} = 8 \text{ kHz}^a$**

signal	$T_{\text{IS}}$ , ms	$T_{1\rho}$ , ms	$r_{\text{F-C}}$ , Å
1	<0.05	2.2(5)	1.4
2	0.34	2.3(3)	2.3
3	0.43	2.0(6)	2.4
4	2.36	not observed	3.9

<sup>a</sup>The last column lists the distance from the fluorine to the respective carbon.

the error margins (2.15 ms) and are roughly 2–3 times smaller compared to the neat system (4.15–7.19 ms). These values are up to 1 order of magnitude smaller compared to  $T_{1\rho}$  values found for non-DNP  $^{19}\text{F} \rightarrow ^{13}\text{C}$  CP transfer.<sup>72</sup> This originates from the hyperfine interactions of the TEKPol radicals with the F-BTA molecules. Although the CP build-up kinetics for the blend and the neat F-BTA powder were acquired with different DNP juices (TEKPol in TCE and AMUPol in DMSO-*d*<sub>6</sub>/D<sub>2</sub>O/H<sub>2</sub>O), we expect the hyperfine interactions between the F-BTA molecules and the nitroxide radicals to be similar, as the same radical concentrations were used. Additionally, we found the wetting of *i*-PP with TCE and F-BTA powder with DMSO/water mixtures to be comparable. As a consequence, similar  $T_{1\rho}$  values should arise for both samples, and thus we attribute the shorter  $T_{1\rho}$  of the blends to smaller and structurally less ordered F-BTA objects. This is in line with the increasing line width of the  $^{19}\text{F}$  DNP enhanced Hahn echo spectra (Figure 4) of neat F-BTA (fwhm = 2100 Hz) compared to the blends (fwhm = 3800 Hz) and the difference of 1.4 ppm observed for  $^{13}\text{C}$  chemical shifts of the carbonyl resonances.

$T_{1\rho}$  sets the detection limit, and only resonances with  $T_{\text{IS}}$  values significantly smaller than  $T_{1\rho}$  can be observed. Since  $T_{\text{IS}}$  is proportional to  $r^{-6}$  (with  $r$  being the distance between nucleus I and S), the relation  $T_{\text{IS}} \leq T_{1\rho}$  allows us to estimate how far polarization can be transferred by CP under IWI conditions. The carbon atoms corresponding to the signals of 1–3 that are 1.4, 2.3, and 2.4 Å away from the fluorine nucleus and have  $T_{\text{IS}}$  values of <0.05, 0.34, and 0.43 ms, respectively, are easily detectable. Carbon 4 is 3.9 Å away from the fluorine. With its longer  $T_{\text{IS}}$  of 2.36 ms it is barely detectable. We can thus conclude that it is possible to visualize carbons closer than 4 Å to the fluorine atoms.

## CONCLUSION

Using F-BTA as a fluorine containing model compound, we prepared both F-BTA/TCE frozen solutions and *i*-PP/F-BTA blends to evaluate further the potential of  $^{19}\text{F}$  DNP enhanced NMR spectroscopy for probing minority components in materials. While the polarizing agent TEKPol is distributed homogeneously in the F-BTA/TCE solution, the *i*-PP/F-BTA particles treated with the IWI technique exhibit an inherently, inhomogeneous distribution of the polarizing agent. Both  $^{19}\text{F}$  Hahn echo and  $^{19}\text{F} \rightarrow ^{13}\text{C}$  CP MAS NMR spectra could be acquired down to only  $\approx 100 \text{ nmol}$   $^{19}\text{F}$  spins within the rotor. The key to the high sensitivities around 1000 is the excellent DNP gain reflected in an  $\varepsilon_{\text{on/off}}$  enhancement of 260 for the frozen solution with the highest concentration. This is surprising, in particular, since no fluorinated solvent was used to allow for polarization transfer over larger distances via spin diffusion. We show that direct  $^{19}\text{F}$  DNP enhancement is

efficient over distances to at least 20 Å and is able to polarize large parts of the sample volume.

Compared to the conventional  $^1\text{H} \rightarrow ^{13}\text{C}$  CP MAS NMR spectra of the *i*-PP/F-BTA blend, the ones acquired with  $^{19}\text{F} \rightarrow ^{13}\text{C}$  CP are free of solvent and polymer matrix signals. This allows for an undisturbed view of the minority target molecules and their internal structure, neither possible with  $^{19}\text{F} \rightarrow ^{13}\text{C}$  CP NMR spectroscopy in thermal polarization nor with conventional  $^1\text{H} \rightarrow ^{13}\text{C}$  CP DNP NMR spectroscopy. The observed CP build-up kinetics suggests that this technique works as a spatial filter with an excitation radius of smaller than 4 Å around a fluorine atom. This relatively small sphere arises due to the hyperfine interaction with the biradicals shortening  $T_{1\rho}$  by roughly 1 order of magnitude compared to conventional NMR spectroscopy. For the future, we expect that the proposed concept can be transferred to other heteronuclei like  $^{15}\text{N}$  and  $^{29}\text{Si}$  and the investigation of minority species for a broad range of complex materials will benefit.

## ASSOCIATED CONTENT

### Supporting Information

The Supporting Information is available free of charge at <https://pubs.acs.org/doi/10.1021/acs.jpcc.1c01167>.

$^{19}\text{F}$  DNP build-up of F-BTA frozen solutions, EPR measurements of frozen solutions,  $^{19}\text{F}$ – $^{19}\text{F}$  double quantum experiments on a F-BTA frozen solution and F-BTA powder, geometric model of the frozen solutions,  $^{19}\text{F}$  DNP build-up of the *i*-PP/F-BTA blend, extraction experiments on the *i*-PP/F-BTA blend,  $^{19}\text{F}$  DNP enhanced NMR spectra of F-BTA powder prepared with IWI, and  $^{19}\text{F} \rightarrow ^{13}\text{C}$  CP build-up of the F-BTA powder with DNP (PDF)

## AUTHOR INFORMATION

### Corresponding Authors

**Torsten Gutmann** – *Eduard-Zintl Institute for Inorganic and Physical Chemistry, Technical University Darmstadt, D-64287 Darmstadt, Germany; Institute of Chemistry and Center for Interdisciplinary Nanostructure Science and Technology, University of Kassel, D-34132 Kassel, Germany; [orcid.org/0000-0001-6214-2272](https://orcid.org/0000-0001-6214-2272); Email: [gutmann@chemie.tu-darmstadt.de](mailto:gutmann@chemie.tu-darmstadt.de)*

**Jürgen Senker** – *Inorganic Chemistry III and North Bavarian NMR Center, University of Bayreuth, D-95447 Bayreuth, Germany; [orcid.org/0000-0002-7278-7952](https://orcid.org/0000-0002-7278-7952); Email: [juergen.senker@uni-bayreuth.de](mailto:juergen.senker@uni-bayreuth.de)*

### Authors

**Kasper P. van der Zwan** – *Inorganic Chemistry III and North Bavarian NMR Center, University of Bayreuth, D-95447 Bayreuth, Germany*

**Wiebke Riedel** – *Physical and Theoretical Chemistry, Institute of Chemistry and Biochemistry, Freie Universität Berlin, 14195 Berlin, Germany; [orcid.org/0000-0001-6561-2305](https://orcid.org/0000-0001-6561-2305)*

**Fabien Aussenac** – *Bruker BioSpin, 67166 Wissembourg, France*

**Christian Reiter** – *Bruker BioSpin GmbH, 76287 Rheinstetten, Germany*

**Klaus Kreger** – *Macromolecular Chemistry I, University of Bayreuth, D-95447 Bayreuth, Germany; [orcid.org/0000-0003-3021-1311](https://orcid.org/0000-0003-3021-1311)*

Hans-Werner Schmidt – *Macromolecular Chemistry I, University of Bayreuth, D-95447 Bayreuth, Germany;*  
 orcid.org/0000-0002-1761-1153

Thomas Risse – *Physical and Theoretical Chemistry, Institute of Chemistry and Biochemistry, Freie Universität Berlin, 14195 Berlin, Germany;* orcid.org/0000-0003-0228-9189

Complete contact information is available at:  
<https://pubs.acs.org/10.1021/acs.jpcc.1c01167>

## Notes

The authors declare no competing financial interest.

## ACKNOWLEDGMENTS

We gratefully acknowledge financial support that was granted by the Deutsche Forschungsgemeinschaft DFG within the SFB 840 Subproject B4 and Contract GU 1650/3-1. We thank Prof. Gerd Buntkowsky (TU Darmstadt) for generous allocation of measurement time at his Bruker Avance III 400 DNP spectrometer. We thank the Elite Network of Bavaria for support by the study program "Macromolecular Science". Sandra Ganzleben (Macromolecular Chemistry I, University of Bayreuth) is gratefully acknowledged for the synthesis of F-BTA and her technical assistance. Martin Schlagbauer (Inorganic Chemistry II, University of Bayreuth) is acknowledged for performing the GC and GC-MS measurements and assistance with the data evaluation. Marco Schwarzmann (Inorganic Chemistry I, University of Bayreuth) is acknowledged for performing the SEM measurements. We thank Gaël de Paëpe (CEA Grenoble) for fruitful discussions on the subject.

## REFERENCES

- Hall, D. A.; Maus, D. C.; Gerfen, G. J.; Inati, S. J.; Becerra, L. R.; Dahlquist, F. W.; Griffin, R. G. Polarization-Enhanced NMR Spectroscopy of Biomolecules in Frozen Solution. *Science* **1997**, *276*, 930–932.
- Maly, T.; Debelouchina, G. T.; Bajaj, V. S.; Hu, K.-N.; Joo, C.-G.; Mak-Jurkauskas, M. L.; Sirigiri, J. R.; van der Wel, P. C. A.; Herzfeld, J.; Temkin, R. J.; Griffin, R. G. Dynamic Nuclear Polarization at High Magnetic Fields. *J. Chem. Phys.* **2008**, *128*, 052211.
- Bajaj, V. S.; Farrar, C. T.; Hornstein, M. K.; Mastovsky, I.; Vieregg, J.; Bryant, J.; Eléna, B.; Kreischer, K. E.; Temkin, R. J.; Griffin, R. G. Dynamic Nuclear Polarization at 9 T Using a Novel 250 GHz Gyrotron Microwave Source. *J. Magn. Reson.* **2003**, *160*, 85–90.
- Gerfen, G. J.; Becerra, L. R.; Hall, D. A.; Griffin, R. G.; Temkin, R. J.; Singel, D. J. High Frequency (140 GHz) Dynamic Nuclear Polarization: Polarization Transfer to a Solute in Frozen Aqueous Solution. *J. Chem. Phys.* **1995**, *102*, 9494–9497.
- Cheng, C.-Y.; Han, S. Dynamic Nuclear Polarization Methods in Solids and Solutions to Explore Membrane Proteins and Membrane Systems. *Annu. Rev. Phys. Chem.* **2013**, *64*, 507–532.
- Le, D.; Casano, G.; Phan, T. N. T.; Ziarelli, F.; Ouari, O.; Aussenac, F.; Thureau, P.; Mollica, G.; Gimes, D.; Tordo, P.; et al. Optimizing Sample Preparation Methods for Dynamic Nuclear Polarization Solid-State NMR of Synthetic Polymers. *Macromolecules* **2014**, *47*, 3909–3916.
- Rankin, A. G.M.; Trébosch, J.; Pourpoint, F.; Amoureux, J.-P.; Lafon, O. Recent Developments in MAS DNP-NMR of Materials. *Solid State Nucl. Magn. Reson.* **2019**, *101*, 116–143.
- Overhauser, A. W. Polarization of Nuclei in Metals. *Phys. Rev.* **1953**, *92*, 411–415.
- Rosay, M.; Tometich, L.; Pawsey, S.; Bader, R.; Schauwecker, R.; Blank, M.; Borchard, P. M.; Cauffman, S. R.; Felch, K. L.; Weber, R. T.; et al. Solid-State Dynamic Nuclear Polarization at 263 GHz: Spectrometer Design and Experimental Results. *Phys. Chem. Chem. Phys.* **2010**, *12*, 5850–5860.
- Bouleau, E.; Saint-Bonnet, P.; Mentink-Vigier, F.; Takahashi, H.; Jacquot, J.-F.; Bardet, M.; Aussenac, F.; Purea, A.; Engelke, F.; Hediger, S.; et al. Pushing NMR Sensitivity Limits Using Dynamic Nuclear Polarization with Closed-Loop Cryogenic Helium Sample Spinning. *Chem. Sci.* **2015**, *6*, 6806–6812.
- Lesage, A.; Lelli, M.; Gajan, D.; Caporini, M. A.; Vitzthum, V.; Mieville, P.; Alauzun, J.; Roussey, A.; Thieuleux, C.; Mehdi, A.; et al. Surface Enhanced NMR Spectroscopy by Dynamic Nuclear Polarization. *J. Am. Chem. Soc.* **2010**, *132*, 15459–15461.
- Lelli, M.; Gajan, D.; Lesage, A.; Caporini, M. A.; Vitzthum, V.; Miéville, P.; Héroguel, F.; Rascón, F.; Roussey, A.; Thieuleux, C.; et al. Fast Characterization of Functionalized Silica Materials by Silicon-29 Surface-Enhanced NMR Spectroscopy Using Dynamic Nuclear Polarization. *J. Am. Chem. Soc.* **2011**, *133*, 2104–2107.
- Grätz, S.; de Olivera Junior, M.; Gutmann, T.; Borchardt, L. A Comprehensive Approach for the Characterization of Porous Polymers Using <sup>13</sup>C and <sup>15</sup>N Dynamic Nuclear Polarization NMR Spectroscopy. *Phys. Chem. Chem. Phys.* **2020**, *22*, 23307–23314.
- Ni, Q. Z.; Daviso, E.; Can, T. V.; Markhasin, E.; Jawla, S. K.; Swager, T. M.; Temkin, R. J.; Herzfeld, J.; Griffin, R. G. High Frequency Dynamic Nuclear Polarization. *Acc. Chem. Res.* **2013**, *46*, 1933–1941.
- Rossini, A. J.; Zagdoun, A.; Lelli, M.; Lesage, A.; Coperet, C.; Emsley, L. Dynamic Nuclear Polarization Surface Enhanced NMR Spectroscopy. *Acc. Chem. Res.* **2013**, *46*, 1942–1951.
- Mollica, G.; Dekhil, M.; Ziarelli, F.; Thureau, P.; Viel, S. Quantitative Structural Constraints for Organic Powders at Natural Isotopic Abundance Using Dynamic Nuclear Polarization Solid-State NMR Spectroscopy. *Angew. Chem., Int. Ed.* **2015**, *54*, 6028–6031.
- Thankamony, A. S. L.; Lion, C.; Pourpoint, F.; Singh, B.; Perez Linde, A. J.; Carnevale, D.; Bodenhausen, G.; Vezin, H.; Lafon, O.; Polshettiwar, V. Insights into the Catalytic Activity of Nitridated Fibrous Silica (KCC-1) Nanocatalysts from <sup>15</sup>N and <sup>29</sup>Si NMR Spectroscopy Enhanced by Dynamic Nuclear Polarization. *Angew. Chem., Int. Ed.* **2015**, *54*, 2190–2193.
- Gutmann, T.; Liu, J. Q.; Rothermel, N.; Xu, Y. P.; Jaumann, E.; Werner, M.; Breitzke, H.; Sigurdsson, S. T.; Buntkowsky, G. Natural Abundance <sup>15</sup>N NMR by Dynamic Nuclear Polarization: Fast Analysis of Binding Sites of a Novel Amine-Carboxyl-Linked Immobilized Dirhodium Catalyst. *Chem. - Eur. J.* **2015**, *21*, 3798–3805.
- Vitzthum, V.; Miéville, P.; Carnevale, D.; Caporini, M. A.; Gajan, D.; Copéret, C.; Lelli, M.; Zagdoun, A.; Rossini, A. J.; Lesage, A.; et al. Dynamic Nuclear Polarization of Quadrupolar Nuclei Using Cross Polarization from Protons: Surface-enhanced Aluminium-27 NMR. *Chem. Commun.* **2012**, *48*, 1988–1990.
- Lee, D.; Takahashi, H.; Thankamony, A. S. L.; Dacquin, J.-P.; Bardet, M.; Lafon, O.; De Paëpe, G. Enhanced Solid-State NMR Correlation Spectroscopy of Quadrupolar Nuclei Using Dynamic Nuclear Polarization. *J. Am. Chem. Soc.* **2012**, *134*, 18491–18494.
- Blanc, F.; Sperrin, L.; Jefferson, D. A.; Pawsey, S.; Rosay, M.; Grey, C. P. Dynamic Nuclear Polarization Enhanced Natural Abundance <sup>17</sup>O Spectroscopy. *J. Am. Chem. Soc.* **2013**, *135*, 2975–2978.
- Michaelis, V. K.; Corzilius, B.; Smith, A. A.; Griffin, R. G. Dynamic Nuclear Polarization of <sup>17</sup>O: Direct Polarization. *J. Phys. Chem. B* **2013**, *117*, 14894–14906.
- Perras, F. A.; Kobayashi, T.; Pruski, M. Natural Abundance <sup>17</sup>O DNP Two-Dimensional and Surface-Enhanced NMR Spectroscopy. *J. Am. Chem. Soc.* **2015**, *137*, 8336–8339.
- Gutmann, T.; Buntkowsky, G. Solid-State NMR Studies of Supported Transition Metal Catalysts and Nanoparticles. In *Modern Magnetic Resonance*; Webb, G. A., Ed.; Springer International Publishing: Cham, Switzerland, 2017; pp 1–21.
- Thankamony, A. S. L.; Wittmann, J. J.; Kaushik, M.; Corzilius, B. Dynamic Nuclear Polarization for Sensitivity Enhancement in

Modern Solid-State NMR. *Prog. Nucl. Magn. Reson. Spectrosc.* **2017**, *102–103*, 120–195.

(26) Perras, F. A.; Wang, L. L.; Manzano, J. S.; Chaudhary, U.; Opembe, N. N.; Johnson, D. D.; Slowing, I. L.; Pruski, M. Optimal Sample Formulations for DNP SENS: The Importance of Radical-Surface Interactions. *Curr. Opin. Colloid Interface Sci.* **2018**, *33*, 9–18.

(27) Liao, W.-C.; Ghaffari, B.; Gordon, C. P.; Xu, J.; Copéret, C. Dynamic Nuclear Polarization Surface Enhanced NMR Spectroscopy (DNP SENS): Principles, protocols, and practice. *Curr. Opin. Colloid Interface Sci.* **2018**, *33*, 63–71.

(28) Rossini, A. J. Materials Characterization by Dynamic Nuclear Polarization-Enhanced Solid-State NMR Spectroscopy. *J. Phys. Chem. Lett.* **2018**, *9*, 5150–5159.

(29) Zhao, L.; Pinon, A. C.; Emsley, L.; Rossini, A. J. DNP-Enhanced Solid-State NMR Spectroscopy of Active Pharmaceutical Ingredients. *Magn. Reson. Chem.* **2018**, *56*, 583–609.

(30) Akbey, U.; Franks, W. T.; Linden, A.; Orwick-Rydmark, M.; Lange, S.; Oschkinat, H. Dynamic Nuclear Polarization Enhanced NMR in the Solid-State. In *Hyperpolarization Methods in NMR Spectroscopy*; Kuhn, L. T., Ed.; Topics in Current Chemistry Series; Springer, 2013; pp 181–228.

(31) Rossini, A. J.; Zagdoun, A.; Hegner, F.; Schwarzwälder, M.; Gajan, D.; Copéret, C.; Lesage, A.; Emsley, L. Dynamic Nuclear Polarization NMR Spectroscopy of Microcrystalline Solids. *J. Am. Chem. Soc.* **2012**, *134*, 16899–16908.

(32) Gutmann, T.; Groszewicz, P. B.; Buntkowsky, G. Solid-State NMR of Nanocrystals. *Annual Reports on NMR Spectroscopy*; Academic Press, 2019; pp 1–82.

(33) De Paëpe, G. Dipolar Recoupling in Magic Angle Spinning Solid-State Nuclear Magnetic Resonance. *Annu. Rev. Phys. Chem.* **2012**, *63*, 661–684.

(34) Wang, J.-L.; Yin, Q.-R.; Miao, J.-S.; Wu, Z.; Chang, Z.-F.; Cao, Y.; Zhang, R.-B.; Wang, J.-Y.; Wu, H.-B.; Cao, Y. Rational Design of Small Molecular Donor for Solution-Processed Organic Photovoltaics with 8.1% Efficiency and High Fill Factor via Multiple Fluorine Substituents and Thiophene Bridge. *Adv. Funct. Mater.* **2015**, *25*, 3514–3523.

(35) Zhang, F.; Kim, D. H.; Lu, H.; Park, J.-S.; Larson, B. W.; Hu, J.; Gao, L.; Xiao, C.; Reid, O. G.; Chen, X.; et al. Enhanced Charge Transport in 2D Perovskites via Fluorination of Organic Cation. *J. Am. Chem. Soc.* **2019**, *141*, 5972–5979.

(36) Brus, J.; Urbanova, M.; Sedenkova, I.; Brusova, H. New Perspectives of  $^{19}\text{F}$  MAS NMR in the Characterization of Amorphous Forms of Atorvastatin in Dosage Formulations. *Int. J. Pharm.* **2011**, *409*, 62–74.

(37) Goossens, P.; Martineau-Corcus, C.; Saïdi, F.; Martens, J. A.; Taulelle, F. Unlocking the Observation of Different Proton Populations in Fluorinated Polymers by Solid-State  $^1\text{H}$  and  $^{19}\text{F}$  Double Resonance NMR Spectroscopy. *Phys. Chem. Chem. Phys.* **2016**, *18*, 28726–28731.

(38) Zhou, Y.; Wang, J.; Gu, Z.; Wang, S.; Zhu, W.; Aceña, J. L.; Soloshonok, V. A.; Izawa, K.; Liu, H. Next Generation of Fluorine-Containing Pharmaceuticals, Compounds Currently in Phase II-III Clinical Trials of Major Pharmaceutical Companies: New Structural Trends and Therapeutic Areas. *Chem. Rev.* **2016**, *116*, 422–518.

(39) Shi, P.; Li, D.; Chen, H.; Xiong, Y.; Wang, Y.; Tian, C. In Situ  $^{19}\text{F}$  NMR Studies of an E. Coli Membrane Protein. *Protein Sci.* **2012**, *21*, 596–600.

(40) Ahrens, E. T.; Zhong, J. In Vivo MRI Cell Tracking Using Perfluorocarbon Probes and Fluorine-19 Detection. *NMR Biomed.* **2013**, *26*, 860–871.

(41) Lu, M.; Wang, M.; Sergeyev, I. V.; Quinn, C. M.; Struppe, J.; Rosay, M.; Maas, W.; Gronenborn, A. M.; Polenova, T.  $^{19}\text{F}$  Dynamic Nuclear Polarization at Fast Magic Angle Spinning for NMR of HIV-1 Capsid Protein Assemblies. *J. Am. Chem. Soc.* **2019**, *141*, 5681–5691.

(42) Viger-Gravel, J.; Avalos, C. E.; Kubicki, D. J.; Gajan, D.; Lelli, M.; Ouari, O.; Lesage, A.; Emsley, L.  $^{19}\text{F}$  Magic Angle Spinning Dynamic Nuclear Polarization Enhanced NMR Spectroscopy. *Angew. Chem., Int. Ed.* **2019**, *58*, 7249–7253.

(43) Hope, M. A.; Rinkel, B. L. D.; Gunnarsdóttir, A. B.; Märker, K.; Menkin, S.; Paul, S.; Sergeyev, I. V.; Grey, C. P. Selective NMR Observation of the SEI-metal Interface by Dynamic Nuclear Polarisation from Lithium Metal. *Nat. Commun.* **2020**, *11*, 2224.

(44) Abragam, A.; Proctor, W. G. Dynamic Polarization of Atomic Nuclei in Solids. *C. R. Hebd. Seances Acad. Sci.* **1958**, *246*, 2253–2256.

(45) Corzilius, B. Theory of Solid Effect and Cross Effect Dynamic Nuclear Polarization with Half-Integer High-Spin Metal Polarizing Agents in Rotating Solids. *Phys. Chem. Chem. Phys.* **2016**, *18*, 27190–27204.

(46) Shimon, D.; Feintuch, A.; Goldfarb, D.; Vega, S. Static  $^1\text{H}$  Dynamic Nuclear Polarization with the Biradical TOTAPOL: A Transition Between the Solid Effect and the Cross Effect. *Phys. Chem. Chem. Phys.* **2014**, *16*, 6687–6699.

(47) Zagdoun, A.; Casano, G.; Ouari, O.; Lapadula, G.; Rossini, A. J.; Lelli, M.; Baffert, M.; Gajan, D.; Veyre, L.; Maas, W. E.; et al. A Slowly Relaxing Rigid Biradical for Efficient Dynamic Nuclear Polarization Surface-Enhanced NMR Spectroscopy: Expedient Characterization of Functional Group Manipulation in Hybrid Materials. *J. Am. Chem. Soc.* **2012**, *134*, 2284–2291.

(48) Mentink-Vigier, F.; Marin-Montesinos, I.; Jagtap, A. P.; Halbritter, T.; van Tol, J.; Hediger, S.; Lee, D.; Sigurdsson, S. T.; De Paëpe, G. Computationally Assisted Design of Polarizing Agents for Dynamic Nuclear Polarization Enhanced NMR: The AsymPol Family. *J. Am. Chem. Soc.* **2018**, *140*, 11013–11019.

(49) Zagdoun, A.; Casano, G.; Ouari, O.; Schwarzwälder, M.; Rossini, A. J.; Aussenac, F.; Yulikov, M.; Jeschke, G.; Copéret, C.; Lesage, A.; et al. Large Molecular Weight Nitroxide Biradicals Providing Efficient Dynamic Nuclear Polarization at Temperatures up to 200 K. *J. Am. Chem. Soc.* **2013**, *135*, 12790–12797.

(50) Sauvée, C.; Rosay, M.; Casano, G.; Aussenac, F.; Weber, R. T.; Ouari, O.; Tordo, P. Highly Efficient, Water-Soluble Polarizing Agents for Dynamic Nuclear Polarization at High Frequency. *Angew. Chem., Int. Ed.* **2013**, *52*, 10858–10861.

(51) Hediger, S.; Lee, D.; Mentink-Vigier, F.; De Paëpe, G. MAS-DNP Enhancements: Hyperpolarization, Depolarization, and Absolute Sensitivity. *eMagRes* **2018**, *7*, 105–117.

(52) Mentink-Vigier, F.; Akbey, Ü.; Oschkinat, H.; Vega, S.; Feintuch, A. Theoretical Aspects of Magic Angle Spinning - Dynamic Nuclear Polarization. *J. Magn. Reson.* **2015**, *258*, 102–120.

(53) Afeworki, M.; Vega, S.; Schaefer, J. Direct Electron-to-Carbon Polarization Transfer in Homogeneously Doped Polycarbonates. *Macromolecules* **1992**, *25*, 4100–4105.

(54) Lafon, O.; Rosay, M.; Aussenac, F.; Lu, X.; Trébosc, J.; Cristini, O.; Kinowski, C.; Touati, N.; Vezin, H.; Amoureux, J.-P. Beyond the Silica Surface by Direct Silicon-29 Dynamic Nuclear Polarization. *Angew. Chem., Int. Ed.* **2011**, *50*, 8367–8370.

(55) Akbey, Ü.; Altin, B.; Linden, A.; Özcelik, S.; Gradzielski, M.; Oschkinat, H. Dynamic Nuclear Polarization of Spherical Nanoparticles. *Phys. Chem. Chem. Phys.* **2013**, *15*, 20706–20716.

(56) Lee, D.; Chaudhari, S. R.; De Paëpe, G. Solvent Signal Suppression for High-Resolution MAS-DNP. *J. Magn. Reson.* **2017**, *278*, 60–66.

(57) Yarava, J. R.; Chaudhari, S. R.; Rossini, A. J.; Lesage, A.; Emsley, L. Solvent Suppression in DNP Enhanced Solid State NMR. *J. Magn. Reson.* **2017**, *277*, 149–153.

(58) Frederick, K. K.; Michaelis, V. K.; Corzilius, B.; Ong, T.-C.; Jacovone, A. C.; Griffin, R. G.; Lindquist, S. Sensitivity-Enhanced NMR Reveals Alterations in Protein Structure by Cellular Milieus. *Cell* **2015**, *163*, 620–628.

(59) Zehe, C.; Schmidt, M.; Siegel, R.; Kreger, K.; Daebel, V.; Ganzleben, S.; Schmidt, H.-W.; Senker, J. Influence of Fluorine Side-Group Substitution on the Crystal Structure Formation of Benzene-1,3,5-Trisamides. *CrystEngComm* **2014**, *16*, 9273–9283.

(60) Schmidt, M.; Wittmann, J. J.; Kress, R.; Schneider, D.; Steuernagel, S.; Schmidt, H.-W.; Senker, J. Crystal Structure of a Highly Efficient Clarifying Agent for Isotactic Polypropylene. *Cryst. Growth Des.* **2012**, *12*, 2543–2551.

(61) Zehe, C. S.; Hill, J. A.; Funnell, N. P.; Kreger, K.; van der Zwan, K. P.; Goodwin, A. L.; Schmidt, H.-W.; Senker, J. Mesoscale Polarization by Geometric Frustration in Columnar Supramolecular Crystals. *Angew. Chem., Int. Ed.* **2017**, *56*, 4432–4437.

(62) Metz, G.; Wu, X. L.; Smith, S. O. Ramped-Amplitude Cross Polarization in Magic-Angle-Spinning NMR. *J. Magn. Reson., Ser. A* **1994**, *110*, 219–227.

(63) Fung, B. M.; Khitrin, A. K.; Ermolaev, K. An Improved Broadband Decoupling Sequence for Liquid Crystals and Solids. *J. Magn. Reson.* **2000**, *142*, 97–101.

(64) Kolodziejski, W.; Klinowski, J. Kinetics of Cross-Polarization in Solid-State NMR: A Guide for Chemists. *Chem. Rev.* **2002**, *102*, 613–628.

(65) Mentink-Vigier, F.; Paul, S.; Lee, D.; Feintuch, A.; Hediger, S.; Vega, S.; De Paëpe, G. Nuclear Depolarization and Absolute Sensitivity in Magic-Angle Spinning Cross Effect Dynamic Nuclear Polarization. *Phys. Chem. Chem. Phys.* **2015**, *17*, 21824–21836.

(66) Ernst, R. R.; Bodenhausen, G.; Wokaun, A. *Principles of Nuclear Magnetic Resonance in One and Two Dimensions*; The International Series of Monographs on Chemistry 14; Clarendon Press: Oxford, U.K., 1988; Reprint with corrections.

(67) Mentink-Vigier, F.; Vega, S.; De Paëpe, G. Fast and Accurate MAS-DNP Simulations of Large Spin Ensembles. *Phys. Chem. Chem. Phys.* **2017**, *19*, 3506–3522.

(68) Mentink-Vigier, F.; Barra, A.-L.; van Tol, J.; Hediger, S.; Lee, D.; De Paëpe, G. De Novo Prediction of Cross-Effect Efficiency for Magic Angle Spinning Dynamic Nuclear Polarization. *Phys. Chem. Chem. Phys.* **2019**, *21*, 2166–2176.

(69) Schmidt, M.; Wittmann, J. J.; Kress, R.; Schmidt, H.-W.; Senker, J. Probing Self-Assembled 1,3,5-Benzenetrisamides in Isotactic Polypropylene by  $^{13}\text{C}$  DQ Solid-State NMR Spectroscopy. *Chem. Commun.* **2013**, *49*, 267–269.

(70) Slichter, C. P. *Principles of Magnetic Resonance*, 3rd enlarged and updated ed.; Springer Series in Solid-State Sciences 1; Springer: Berlin, 1990.

(71) Tsuchiya, K.; Takahashi, A.; Takeda, N.; Asakawa, N.; Kuroki, S.; Ando, I.; Shoji, A.; Ozaki, T. Hydrogen-Bonding Effect on  $^{13}\text{C}$  NMR Chemical Shifts of Amino Acid Residue Carbonyl Carbons of Some Peptides in the Crystalline State. *J. Mol. Struct.* **1995**, *350*, 233–240.

(72) Ando, S.; Harris, R. K.; Hirschinger, J.; Reinsberg, S. A.; Scheler, U. Solid-State  $^{19}\text{F}$  MAS,  $^{19}\text{F}$  CRAMPS, and  $^{19}\text{F} \rightarrow ^{13}\text{C}$  CP/MAS NMR Study of an Amorphous Perfluoropolymer. *Macromolecules* **2001**, *34*, 66–75.

**Supporting Information for****<sup>19</sup>F MAS DNP for Probing Molecules in Nanomolar Concentrations: Direct Polarization as Key for Solid-State NMR Spectra without Solvent and Matrix Signals**

Kasper P. van der Zwan,<sup>a</sup> Wiebke Riedel,<sup>b</sup> Fabien Aussenac,<sup>c</sup> Christian Reiter<sup>d</sup>,  
Klaus Kreger,<sup>e</sup> Hans-Werner Schmidt,<sup>e</sup> Thomas Risse,<sup>b</sup>  
Torsten Gutmann,<sup>f,g\*</sup> Jürgen Senker<sup>a\*</sup>

<sup>a</sup> Inorganic Chemistry III and North Bavarian NMR Center, University of Bayreuth,  
Universitätsstraße 30, D-95447 Bayreuth, Germany

<sup>b</sup> Physical and Theoretical Chemistry, Institute of Chemistry and Biochemistry  
Freie Universität Berlin, Arnimallee 22, 14195 Berlin, Germany

<sup>c</sup> Bruker BioSpin, 34 rue de l'Industrie BP 10002  
67166 Wissembourg Cedex, France

<sup>d</sup> Bruker BioSpin GmbH  
Silberstreifen 4, 76287 Rheinstetten, Germany

<sup>e</sup> Macromolecular Chemistry I, University of Bayreuth,  
Universitätsstraße 30, D-95447 Bayreuth, Germany

<sup>f</sup> Eduard-Zintl Institute for Inorganic and Physical Chemistry, Technical University Darmstadt,  
Alarich-Weiss-Str. 8, D-64287 Darmstadt, Germany

<sup>g</sup> Institute of Chemistry and Center for Interdisciplinary Nanostructure Science and Technology,  
University of Kassel, Heinrich-Plett Straße 40, D-34132 Kassel, Germany

\* [juergen.senker@uni-bayreuth.de](mailto:juergen.senker@uni-bayreuth.de)  
[gutmann@chemie.tu-darmstadt.de](mailto:gutmann@chemie.tu-darmstadt.de)

**Table of Content**

1. $^{19}\text{F}$ DNP Build-Up of F-BTA Frozen Solutions .....	S3
2. EPR Measurements of Frozen Solutions .....	S4
3. $^{19}\text{F}$ - $^{19}\text{F}$ Double Quantum Experiments on a F-BTA Frozen Solution and F-BTA Powder .....	S5
4. Geometric Model of the Frozen Solutions .....	S7
5. $^{19}\text{F}$ DNP Build-Up of the <i>i</i> -PP/F-BTA Blend .....	S9
6. Extraction Experiments on the <i>i</i> -PP/F-BTA Blend .....	S10
7. $^{19}\text{F}$ DNP Enhanced NMR Spectra of F-BTA Powder with IWI .....	S13
8. $^{19}\text{F} \rightarrow ^{13}\text{C}$ CP Build-Up of the F-BTA Powder with DNP .....	S14
References .....	S15

### 1. $^{19}\text{F}$ DNP Build-Up of F-BTA Frozen Solutions

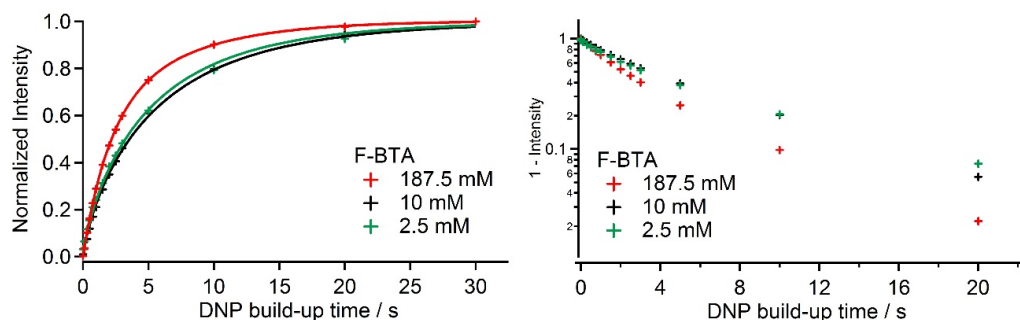


**Figure S1.** DNP build-up curves in regular (left) and power plot representation (right) for the frozen solutions of 187.5 mM F-BTA (red), 10 mM F-BTA (black) and 2.5 mM F-BTA (green) in 15 mM TEKPol in TCE. All spectra were recorded with a spinning speed of 8 kHz at a temperature of 100 K.

The polarization build-up times ( $T_B$ ) were determined by saturation recovery experiments. For each time increment, the area under the peak was integrated. The highest intensity was normalized to 1. The data was fitted with a stretched exponential (eq 1, main text) and the resulting fitting parameters are listed in Table S1.

**Table S1.** Fitting Parameters of the Saturation Recovery Experiment to Estimate  $T_B$ .

Concentration	$T_B$ / s	a	b	c
187.5 mM	$3.3 \pm 0.1$	$-0.99 \pm 0.01$	$0.88 \pm 0.02$	$0.99 \pm 0.01$
10 mM	$5.6 \pm 0.2$	$-1.00 \pm 0.01$	$0.84 \pm 0.02$	$1.01 \pm 0.01$
2.5 mM	$5.7 \pm 0.3$	$-0.99 \pm 0.02$	$0.78 \pm 0.02$	$1.01 \pm 0.01$

## 2. EPR Measurements of Frozen Solutions

To confirm that TEKPol is homogeneously dissolved in TCE during the DNP experiments, we performed cw EPR measurements at 9.52 GHz on a concentration series of TEKPol in TCE at 150 K (Figure S2).

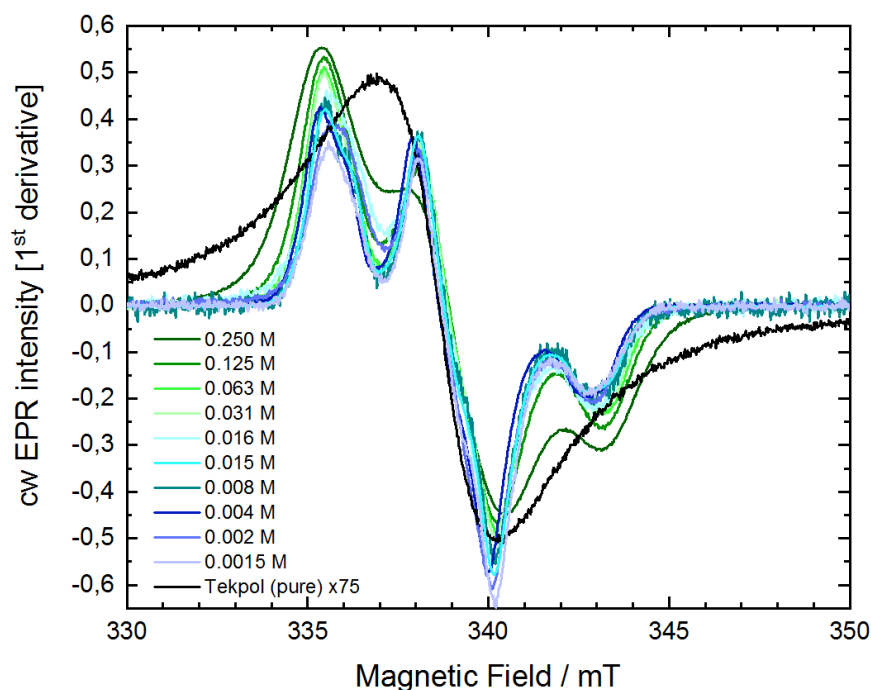


**Figure S2.** cw EPR spectra of a concentration series of TEKPol in TCE frozen solutions measured at 150 K. For comparison, the spectra are normalized to peak-to-peak amplitude.

In the spectrum of the solid powder, the hyperfine interactions add to one broad line. In the frozen solutions distinct shoulders are present and the overall linewidth is smaller. Upon dilution, the linewidth decreases further. Below a TEKPol concentration of 31 mM no significant decrease in linewidth is observed. From this, we concluded that the dominant effect determining the linewidth arises from the intramolecular hyperfine and dipolar interactions. This indicates that in this concentration regime isolated biradical molecules are present in the sample.

### 3. $^{19}\text{F}$ - $^{19}\text{F}$ Double Quantum Experiments on a F-BTA Frozen Solution and F-BTA Powder

To confirm that F-BTA molecules are isolated in the used frozen solutions, we performed  $^{19}\text{F}$ - $^{19}\text{F}$  double quantum (DQ) NMR spectroscopic experiments on the frozen solution with the highest concentration and compared the results to a crystalline powder sample. To recouple the DQ intensity the symmetry based pulse sequence  $\text{R}12_2^5$  was used.<sup>1</sup> A sketch of the pulse programme and the construction of the R sequence is depicted in Figure S3. A DQ-filtered spectrum was recorded after every  $\text{RR}'$  block. This results in recoupling increments of 41.67  $\mu\text{s}$ . In total, 40 experiments with DQ-recoupling times ranging from 0 to 1.624 ms were performed. The experiment is set up in a way that two experiments with the same recoupling time follow each other. For the first experiment the phase cycle is chosen to filter only DQ-intensity. For the following experiment all coherences will pass. This gives an easy way to normalise the intensity of the DQ-filtered spectrum.

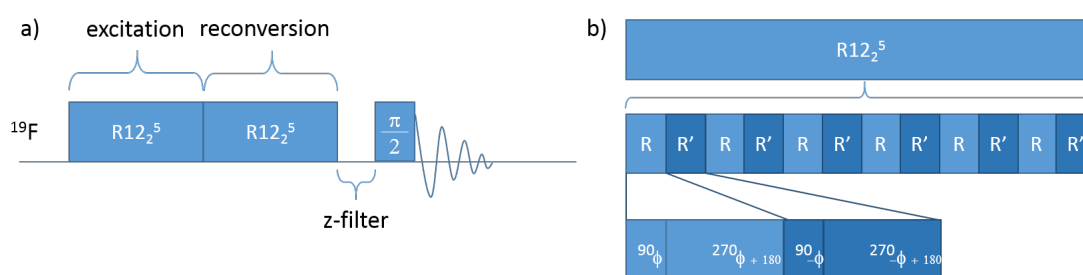


**Figure S3.** Schemes of the used pulse programme (a) and the used DQ-recoupling sequence (b). A full R block consists of 12  $180^\circ$  pulses within 2 rotor periods. Each block R with a phase  $\phi$  is followed by a block R' with a phase  $-\phi$ . The  $180^\circ$  pulses of the R blocks are performed with a  $90_\phi$ - $270_{\phi+180}$ -composite pulse to compensate for rf-field imperfections.

The number of scans for the experiments on the frozen solution and the powder were adjusted on non-DQ-filtered spectra to reach sufficient and similar signal to noise ratios. This ensures that the intensity of the DQ-filtered experiment is comparable as well. The DQ-filtered spectrum shows a maximum peak intensity at a DQ-recoupling time of 290  $\mu\text{s}$ . For the frozen solution, no spectrum with significant DQ-intensity could be recorded (Figure S4 right). This demonstrates, that the F-BTA molecules do not show any close contacts to other F-BTA molecules.

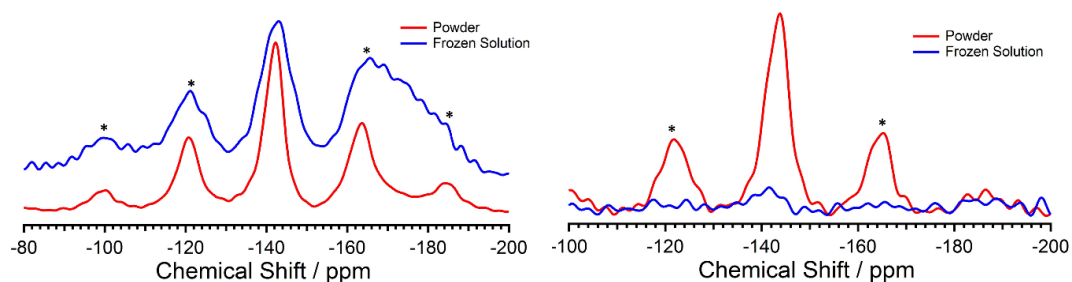


**Figure S4.**  $^{19}\text{F}$  non-DQ-filtered (left) and DQ-filtered (right) ss-NMR spectroscopic experiments of F-BTA powder (red) and frozen solution (blue). The non-DQ-filtered  $^{19}\text{F}$  MAS NMR spectra were corrected for the probe background by removing a  $^{19}\text{F}$  NMR spectrum of an empty rotor. For the DQ-filtered  $^{19}\text{F}$  MAS NMR spectra exemplarily the maximum of the DQ build-up curve with a recoupling time of 290  $\mu\text{s}$  is shown. All experiments were done at 120 K and with  $\nu_{\text{rot}} = 8$  kHz. Spinning side bands are marked with an asterisk.

#### 4. Geometric Model of the Frozen Solutions

For the distance estimation, we describe the arrangement of the majority component within the frozen solutions according to closed packings. The majority component is TEKPol for the 2.5 and 10 mM F-BTA frozen solutions and F-BTA for the 187.5 mM one. We calculated the radius for the spheres for the concentrations of 15 mM TEKPol and 187.5 mM F-BTA respectively and placed the respective molecule in the center of the sphere. Now, we can measure the distance between two adjacent molecules. Since both TEKPol and F-BTA, in first approximation, can be described as disks (Figure S5a), we do not get one distinct distance, but depending on the orientation of the molecules shorter and longer distances. This results in closest TEKPol-TEKPol distances of 30-55 Å (Figure S5b). For the 187.5 mM F-BTA frozen solution, this results in F-BTA-F-BTA distances between 10 and 23 Å (Figure S5c).

For the diluted F-BTA solutions, a homogenous placement of the F-BTA molecules according to the same strategy leads to F-BTA-F-BTA distances of 55 and 91 Å, respectively. For the DNP polarization transfer it is important to probe the distance from the  $^{19}\text{F}$  nuclei to the radical centers. In all cases, the longest possible distance is 25 Å. This happens, if the F-BTA molecule is in the middle between two TEKPol molecules (Figure S5b). For the diluted systems, the average F-BTA-F-BTA distance exceeds the TEKPol-TEKPol one and thus the average F-BTA-TEKPol distance can be estimated by randomly placing a F-BTA molecule in a sphere with a radius of roughly 27 Å around a TEKPol molecule. A Monte Carlo analysis with 10000 repetitions<sup>2</sup> shows that the mean distance then is around 20 Å. For the concentrated case, however, we assume both species to be homogeneously distributed. Therefore, there will be more than one F-BTA molecule between two TEKPol molecules, leading to a pronounced appearance of shorter distances than the evaluated statistical mean distance. Thus, TEKPol-F-BTA distances will be shorter than the mean F-BTA-F-BTA distance of 16 Å.

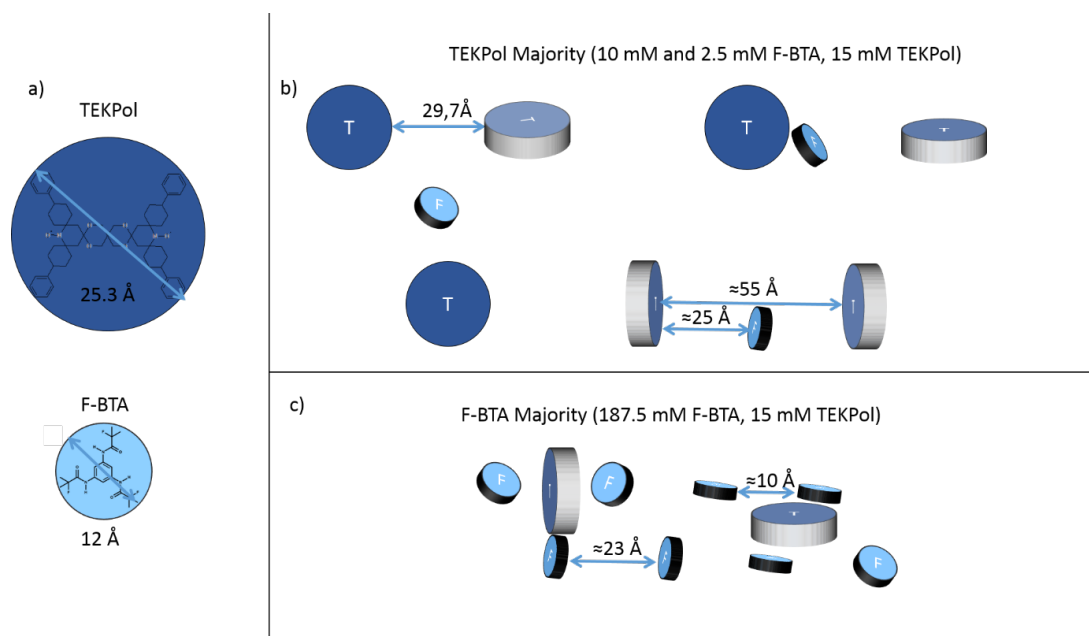


**Figure S5.** a) Sketch of the TEKPol (dark blue) and F-BTA (light blue) disks used for the model. b) Model where TEKPol is the majority component. The disks marked with “T” and “F” represent the TEKPol and F-BTA molecules, respectively. c) Model where F-BTA is the majority species.

### 5. $^{19}\text{F}$ DNP Build-Up of the *i*-PP/F-BTA Blend

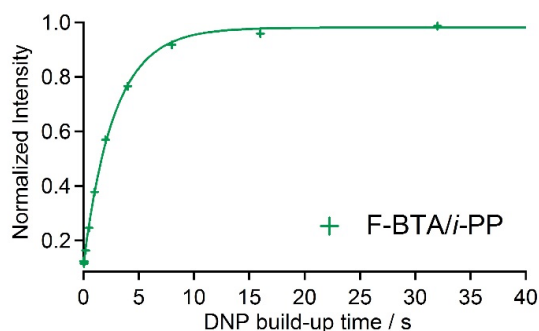


**Figure S6.** Saturation recovery experiment of 2 wt % *i*-PP/F-BTA blend recorded with mw on at 120 K.

The polarization build-up time ( $T_B$ ) was determined by saturation recovery experiment, just as to determine  $T_1$ . For each time increment, the area under the peak was integrated. The highest intensity was normalized to 1. The data was fitted with eq 1 with  $b$  fixed to 1. The fitting parameters are given in Table S2 and the plot of the saturation recovery experiment together with the fit function are presented in Figure S6. The DNP build-up time is 2.77 s. When  $b$  is refined as well a build-up time 2.79 s is obtained for the blend, showing that the data is indeed monoexponential.

**Table S2.** Fitting Parameters of the Saturation Recovery Experiment to Estimate  $T_B$ .

	$T_B / \text{s}$	$a$	$b$	$c$
<i>i</i> -PP/F-BTA	$2.77 \pm 0.09$	$-0.87 \pm 0.01$	1	$0.98 \pm 0.01$
<i>i</i> -PP/F-BTA	$2.79 \pm 0.10$	$-0.87 \pm 0.01$	$0.98 \pm 0.04$	$0.98 \pm 0.01$

## 6. Extraction Experiments on the *i*-PP/F-BTA Blend

Three extraction experiments were performed. For two experiments 25 mg of a blend containing 1.5 wt % of F-BTA were impregnated with 20  $\mu$ L of TCE. The powder was then transferred into a syringe that was equipped with a syringe filter. The wet powder was compressed with the syringe plunger. This also minimizes the evaporation of TCE. After 5 and 10 minutes, respectively, 1.8 mL of TCE was added to the syringe to transfer the extract into a glass vial. For the third experiment dry powder was added to the syringe and directly 1.8 mL of TCE were added. The extracts were analysed by gas chromatography coupled with a mass spectrometer (GC-MS).

To evaluate the retention time of F-BTA in the GC column a 10 mM solution of F-BTA in TCE was prepared.

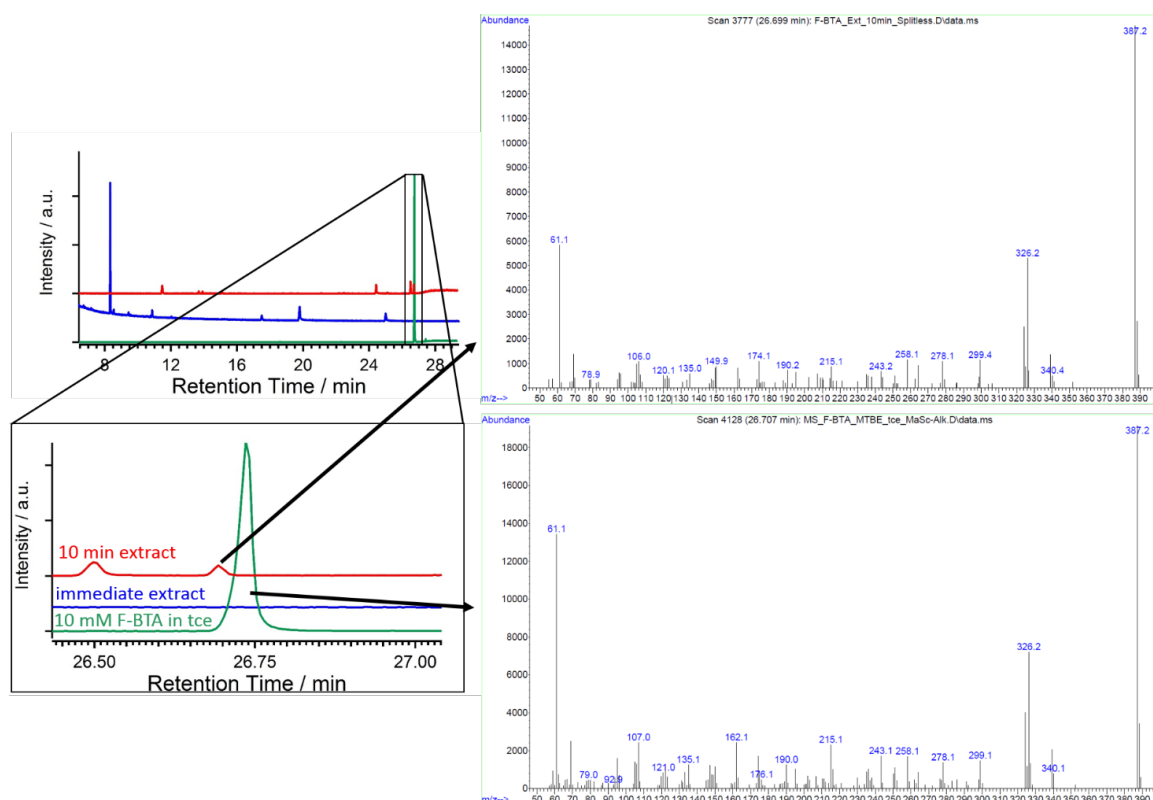


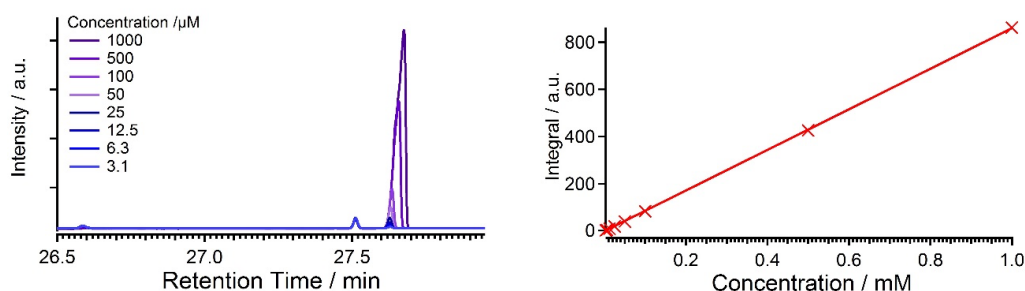
**Figure S7.** Left: GC-MS of long extraction (red), immediate extraction (blue) and F-BTA reference (green). Right: MS of the extracted (top) and the F-BTA reference (bottom).

From Figure S7 (blue chromatogram) can be seen that an immediate extraction is not sufficient to dissolve a detectable amount of F-BTA. When the wet powder soaks for ten minutes, F-BTA is however visible (red chromatogram) and the MS analysis confirms the presence of the substance. This soaking time matches reasonably the time needed for impregnating the sample, packing the rotor and inserting it into the magnet.

To quantify the amount of F-BTA that is extracted a concentration series of F-BTA is analysed with GC. First, we checked whether the integral of the peak scales linearly with concentration of the solution. Figure S8 shows that this is the case and therefore, a linear fit can be applied to the data that is shown in Figure S8 as well, yielding the following fitting function:

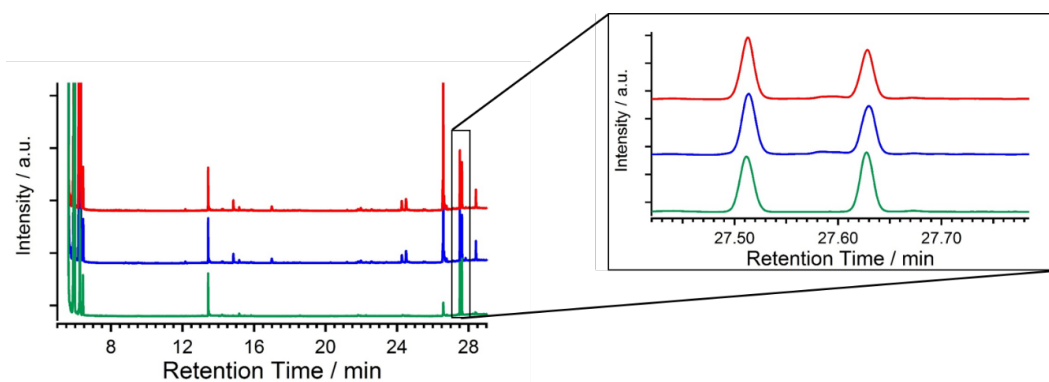
$$I = 859.6 \pm 1.82 \frac{l}{mol} \cdot c \quad (S1)$$

Since the fit must go through the origin, the intercept is fixed to zero.



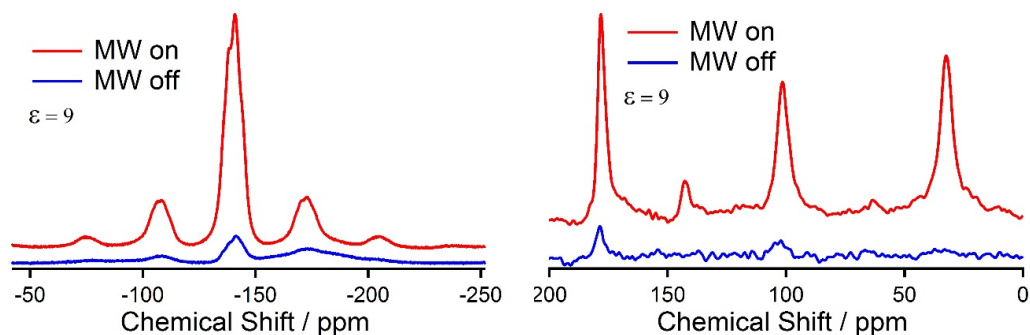
**Figure S8.** Concentration series of F-BTA measured with GC (left). Fitting curve of the integrals at the different concentrations (right).

In 25 mg of the blend with 1.5 wt % of F-BTA a total of 0.375 mg of F-BTA is present. This corresponds to 0.97 μmol. When all of the molecules out of the blend would be extracted, the 1.8 mL TCE solution would have a concentration of 538 μM. Figure S9 shows that extraction with five or ten minutes gives within the error of the method the same result. In fact, the extract that soaked for 5 minutes has a slightly higher integral (17.641) compared to the extract that had 10 minutes time to extract the F-BTA molecules (16.269). According to eq S1 these integrals correspond to concentrations of  $20.5 \pm 2.1$  μM and  $18.9 \pm 2.1$  μM. When averaging these values 3.65 % of the F-BTA molecules are dissolved from the polymer. Thus, we can confidently say that we only dissolve F-BTA from the particle surfaces and that leaching from inside the *i*-PP particles is a negligible effect.



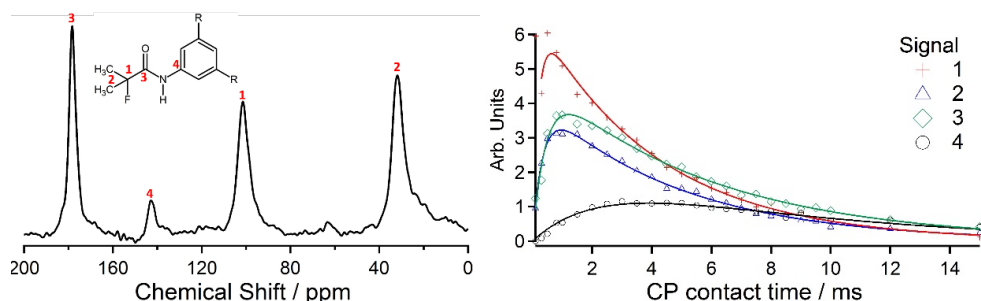
**Figure S9.** GC-chromatograms of the extract that soaked for 10 minutes (red) and 5 minutes (blue) as well as the standard measurement of the concentration series with a concentration of 25  $\mu\text{M}$  (green).

### 7. $^{19}\text{F}$ DNP Enhanced NMR Spectra of F-BTA Powder with IWI



**Figure S10.**  $^{19}\text{F}$ -onepulse (left) and  $^{19}\text{F} \rightarrow ^{13}\text{C}$  CP (right) MAS NMR spectra of F-BTA impregnated with AMUPol in  $\text{DMSO-}d_6/\text{D}_2\text{O}/\text{H}_2\text{O}$  6/3/1 measured with mw on (red) and mw off (blue). Spectra were recorded at spinning speeds of 12 kHz (onepulse) and 8 kHz (CP), respectively at 120 K.

Figure S10 shows the DNP enhanced  $^{19}\text{F}$  and  $^{19}\text{F} \rightarrow ^{13}\text{C}$  CP DNP NMR spectrum of the microcrystalline F-BTA powder prepared by IWI with a matrix of 15mM AMUPol in  $\text{DMSO-}d_6/\text{D}_2\text{O}/\text{H}_2\text{O}$  6/3/1. The  $\epsilon_{\text{on/off}}$  is in both cases 9. This is in accordance with other  $\epsilon$  values obtained for microcrystalline powders<sup>3</sup>. The sensitivity  $S$  is  $180 \pm 4 \text{ mg}^{-1} \text{ h}^{-1/2}$ . The DNP build-up time for the neat F-BTA prepared with IWI was 1.6 s when fitted with eq 1 (main text).

8.  $^{19}\text{F} \rightarrow ^{13}\text{C}$  CP Build-Up of the F-BTA Powder with DNP

**Figure S11.** DNP enhanced  $^{19}\text{F} \rightarrow ^{13}\text{C}$  CP NMR spectrum (left) and CP build-up curve (right) of F-BTA in 15 mM AMUPol in DMSO- $d_6$ /D $_2$ O/H $_2$ O 6/3/1 v/v/v.

To determine the CP build-up time ( $T_{1S}$ ) and  $T_{1\rho}$  of neat F-BTA multiple CP experiments with increasing contact times were recorded on F-BTA impregnated with a 15 mM solution of AMUPol in DMSO- $d_6$ /D $_2$ O/H $_2$ O 6/3/1. For resonances **1 - 4** (Figure S10, left) the area under the peak was integrated for each experiment. The intensities were plotted against the respective CP contact times (Figure S11, right). The data was fitted with eq 2 (main text). The obtained values are given in Table S3. The values of  $T_{1S}$  were used for the fit of the data of the composite.

**Table S3.** Refinement Parameter of the  $^{19}\text{F} \rightarrow ^{13}\text{C}$  CP DNP NMR Build-Up Curve of F-BTA in 15 mM AMUPol in DMSO- $d_6$ /D $_2$ O/H $_2$ O 6/3/1 v/v/v  $\nu_{\text{rot}} = 8$  kHz Fitted with eq 2 (Main Text).

Signal	Chemical shift	$I_0$	$T_{1S} / \text{ms}$	$T_{1\rho} / \text{ms}$
1	100 ppm	6.53(0)	0.02(0)	4.15(7)
2	30 ppm	3.94(6)	0.34(1)	4.76(11)
3	170 ppm	4.54(12)	0.43(3)	5.74(25)
4	145 ppm	1.90(25)	2.36(43)	7.19(139)

## References

- (1) Carravetta, M.; Edén, M.; Johannessen, O. G.; Luthman, H.; Verdegem, P. J. E.; Lugtenburg, J.; Sebald, A.; Levitt, M. H. Estimation of Carbon–Carbon Bond Lengths and Medium-Range Internuclear Distances by Solid-State Nuclear Magnetic Resonance. *J. Am. Chem. Soc.* **2001**, *123*, 10628–10638.
- (2) Stafford, R *Random points in an n-Dimensional Hypersphere (Matlab Code)*, version 1.0.0.0, Mathworks, [www.mathworks.com/matlabcentral/fileexchange](http://www.mathworks.com/matlabcentral/fileexchange), **2005**
- (3) Mollica, G.; Dekhil, M.; Ziarelli, F.; Thureau, P.; Viel, S. Quantitative structural constraints for organic powders at natural isotopic abundance using dynamic nuclear polarization solid-state NMR spectroscopy. *Angew. Chem. Int. Ed. Engl.* **2015**, *54*, 6028–6031.

## 4.7 DNP Enhanced $^{19}\text{F}$ - $^{19}\text{F}$ DQ Build-Up Curve Confirms Crystal Structure of Supramolecular Additive in PS at Technical Concentration for Batch Foaming

This work is a cooperation between the Inorganic Chemistry III and the Macromolecular Chemistry I of the University of Bayreuth, the Physical and Theoretical Chemistry of the FU Berlin, the CEA Grenoble and Bruker BioSpin with the following authors: K.P. van der Zwan, W. Riedel, B. Klose, T. Fischer, R. Siegel, F. Aussenac, C. Reiter, A. Mael, K. Kreger, G. de Paëppe, H.-W. Schmidt, T. Risse, J. Senker.

My contributions are:

- conception and main authorship
- performing all conventional and DNP enhanced NMR experiments
- preparing all polymer/radical compounds
- sample preparation for the EPR experiments
- parts of the NMR simulations

The contributions of the other authors are:

- conception and authorship of the article
- synthesis of the materials
- recording the SEM images
- performing EPR measurements
- additional NMR simulations
- foaming experiment and evaluation of the foam properties

## DNP Enhanced $^{19}\text{F}$ - $^{19}\text{F}$ DQ Build-Up Curve Confirms Crystal Structure of Supramolecular Additive in PS at Technical Concentration for Batch Foaming

Kasper P. van der Zwan,<sup>a</sup> Wiebke Riedel,<sup>b</sup> Bastian Klose,<sup>c</sup> Tamara Fischer,<sup>a</sup> Renée Siegel,<sup>a</sup> Fabien Aussenac,<sup>d</sup> Christian Reiter,<sup>e</sup> Anika Mauel,<sup>a</sup> Klaus Kreger,<sup>c</sup> Hans-Werner Schmidt,<sup>c</sup> Thomas Risse,<sup>b</sup> Gaël de Paëpe,<sup>f</sup> Jürgen Senker<sup>a\*</sup>

<sup>a</sup> Inorganic Chemistry III, University of Bayreuth,  
Universitätsstraße 30, D-95447 Bayreuth, Germany

<sup>b</sup> Physical and Theoretical Chemistry, Institute of Chemistry and Biochemistry  
Freie Universität Berlin, Arnimallee 22, 14195 Berlin, Germany

<sup>c</sup> Macromolecular Chemistry I, University of Bayreuth,  
Universitätsstraße 30, D-95447 Bayreuth, Germany

<sup>d</sup> Bruker BioSpin, 34 rue de l'Industrie BP 10002  
67166 Wissembourg Cedex, France

<sup>e</sup> Bruker BioSpin GmbH  
Silberstreifen 4, 76287 Rheinstetten, Germany

<sup>f</sup> Univ. Grenoble Alpes, CEA, CNRS, IRIG MEM,  
38000 Grenoble, France

\* [juergen.senker@uni-bayreuth.de](mailto:juergen.senker@uni-bayreuth.de) 0049-(0)921-552532;

### Abstract

Conventional preparation techniques for DNP enhanced NMR spectroscopy of materials focus on an enhancement of the surface species over the bulk. This is desired for porous materials but is inconvenient when studying the bulk properties of polymer/additive composites. A way to overcome this is to extrude the radical with the polymer. We report an optimisation of the sample preparation for (poly)styrene extruded with AsymPol and found that a concentration of 0.5 wt.% of AsymPol extruded at a temperature of 180 °C gives the highest sensitivity. With this parameter set, a sample including 0.5 wt.% of the supramolecular polymer additive F-BTA was prepared, as at this concentration F-BTA is an excellent foam cell nucleation agent for PS. DNP enhanced  $^{19}\text{F}$ - $^{19}\text{F}$  DQ experiments confirmed the existence of the columnar polymorph of F-BTA within PS leading to fibrous nanostructures in the polymer. We believe that extruding the polarizing agent into the polymer is a promising technique to study the minority components of amorphous polymers by DNP enhanced NMR spectroscopy.

### Introduction

Polystyrene (PS) foams are frequently used for applications ranging from packaging over construction to the automotive sector due to their low cost and their excellent mechanical and insulation properties.<sup>1-3</sup> Especially the insulation properties arise from the number of phase boundaries between foam cell and cell wall through the material that is directly linked to the foam density, the foam cell size and the homogeneity of the latter.<sup>4,5</sup> Therefore, foam cells with an average size smaller than 10  $\mu\text{m}$  are preferred.<sup>4</sup> For this purpose, a heterogeneous foam cell nucleation is necessary<sup>6</sup> that can be achieved by adding fillers to the PS to act as a foam cell nucleation agent.<sup>7-13</sup> A class of filler materials that is widely used because of its good dispersion within the PS are supramolecular additives.<sup>14-27</sup> They are dissolved in the polymer melt and form nanostructures that act as nucleating agents when cooled down.<sup>15</sup>

The crystal structures of the neat supramolecular polymer additives can often be solved by single X-ray or NMR crystallography.<sup>16,24,28-31</sup> However, the structure elucidation of the additive within the polymer, especially in industrial relevant concentrations between 100-5000 ppm is very challenging, since the signals of interest are weak and covered by the polymer matrix.<sup>23</sup> To still be able to obtain information the additive signals need to be highlighted. A common way to do this in NMR spectroscopy is to introduce a spin label.<sup>32,33</sup> For example a  $^{13}\text{C}$  enriched benzene trisamide can be used to measure a double quantum build-up curve of said trisamide within isotactic polypropylene and compare it to the build-up curve of the need material.<sup>23</sup> Since double quantum (DQ) resonances are strongly distance dependent, distances can be probed with this technique and herewith crystal structures confirmed.<sup>34-36</sup> However, for DQ experiments two NMR active nuclei need to be in close proximity, which is especially for nuclei with a low natural abundance like  $^{13}\text{C}$  and  $^{15}\text{N}$  a limiting factor. Furthermore, to probe distances the experiment needs to be repeated several times to obtain a DQ build-up curve.<sup>34</sup> This means, in the concentrations used for polymer additives together with the intrinsically low sensitivity of NMR spectroscopy, this is still a time consuming experiment.

Sensitivity of NMR spectroscopic experiments was highly boosted with the introduction of solid state dynamic nuclear polarisation at high magnetic fields and with magic-angle spinning (MAS).<sup>37-40</sup> This enabled NMR spectroscopic experiments in structural biology and materials science with lower amounts of NMR active nuclei, enabling, for example, experiments on  $^{13}\text{C}$ <sup>41-43</sup>,  $^{15}\text{N}$ <sup>44,45</sup>,  $^{27}\text{Al}$ <sup>46,47</sup> and  $^{17}\text{O}$ <sup>48-50</sup> in natural abundance and on  $^{19}\text{F}$ <sup>51-54</sup> in very low molecular concentrations. Furthermore, single quantum (SQ)-DQ correlation spectra<sup>55,56</sup> and DQ build-up curves on  $^{13}\text{C}$  in natural abundance were shown.<sup>43</sup> A drawback of DNP enhanced NMR spectroscopy is the need to apply persistent radicals like TEKPol<sup>57</sup>, AMUPol<sup>58</sup> or AsymPol<sup>59</sup> to the investigated material. The most common ways of doing this are either by dispersing the sample in a radical containing solution that is capable of forming a glass, when rapidly cooled

to the measurement temperature of 100K<sup>60</sup> or by impregnating a porous or powdered sample with the said solution.<sup>61,62</sup> Both techniques are well established and show high enhancements of the NMR signal.<sup>63</sup> However, these techniques are limited to the surfaces of the impregnated materials.<sup>61</sup> So, studying the bulk properties of a solid polymer are with neither technique ideal.<sup>64,65</sup> Incipient wetness impregnation can lead to a swelling of the polymer and therefore the bulk structure might be altered<sup>66</sup> or only the surface of the polymer particle is enhanced<sup>51</sup> and a frozen solution is by definition not a bulk technique and therefore only useful to probe the molecular structure of the polymer.<sup>67</sup> Several techniques have been tried to measure the bulk properties of polymer samples, for example, film casting, glass forming and co-polymerisation.<sup>65,68–70</sup> The group of Griffin showed that it is possible to compound a radical in a pharmaceutical formulation.<sup>71</sup> This new preparation technique is well suited to explore the structure of low concentrated additives within a bulk polymer phase.

In this work we apply this technique to a compound of 0.5 wt.% of a fluorinated benzene trisamide (1,3,5-tris(2-fluoro-2-methylpropionylamino)benzene, F-BTA, Figure 1a) in PS (Figure 1b) and investigate its capability as a foam nucleating agent. Additionally, AsymPol (Figure 1c) is added to the compound as a DNP polarization agent. We investigate the homogeneity of the radical distribution within the polymer, with EPR spectroscopy. Furthermore, the enhancement of the matrix signals is demonstrated and finally we show a <sup>19</sup>F-<sup>19</sup>F double quantum build-up curve of the F-BTA within PS to probe whether or not nanostructures of F-BTA are formed in PS and which of the two known F-BTA polymorphs forms the nanoobjects inside the polymer. This expands the use of <sup>19</sup>F DNP enhanced NMR spectroscopy from a surface method<sup>51</sup> to a bulk method that can directly probe additive structures.

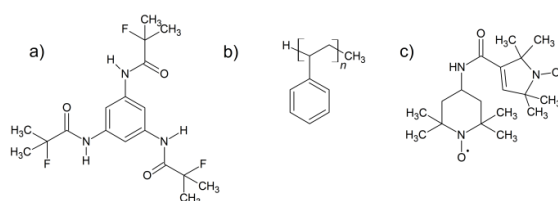


**Figure 1.** Molecular structures of a) F-BTA b) PS and c) AsymPol.

## Experimental Section

### Materials

The used Polystyrene grade was PS 168N (INEOS Styrolution, Frankfurt am Main, Germany). The pellets were grinded in a ZM200 freezer mill (Retsch, Haan, Germany) using a mesh size of 1000  $\mu\text{m}$ . 1,3,5-tris(2-fluoro-2-methylpropionylamino)benzene (F-BTA) was synthesised according to literature procedures and obtained as fine white powder.<sup>72</sup> The synthesis of AsymPol was inspired by literature procedures but slightly altered.<sup>59,73</sup> The complete synthesis is given in the supporting information section 1.

For the batch foaming experiments the powdered PS was mixed with 0.5 wt.% F-BTA powder. The powder mixture was shaken over night in an overhead shaker before it was compounded in a twin-screw micro-compounder, Xplore 15 mL (DSM, Heerlen, The Netherlands) under nitrogen atmosphere at 260 °C with a residence time of 5 minutes. Injection molding was performed using a micro-injection-molding machine, Xplore 12 mL (DSM, Heerlen, The Netherlands). The barrel temperature of the injection molding unit was set to 250 °C, and an injection pressure of 6 bar was used. The molten, compounded mixture was transferred from the compounder to the micro-injection-molding machine and subsequently injected into a polished mold for the duration of 20s, yielding round platelets with a diameter of 27 mm and a thickness of 1.1 mm. To eliminate the internal stress of the specimens resulting from the injection molding process, the samples were annealed in a closed iron mold at 135 °C for 4 h.

For the screening of the DNP parameters in total 14 PS samples were prepared with different AsymPol concentrations and extruded at temperatures between 140 and 180 °C according to Table 1. A twin-screw mini extruder ZE 5 HMI (Three-Tec, Seon, Switzerland) and a 1 mm nozzle plate were used. Parts of the obtained polymer strand were freeze crushed to obtain a powder.

**Table 1.** Sample preparation for AsymPol/PS compounds.

		extrusion temperature /°C		
		140	160	180
concentration/ wt. %	0.25	x	x	1 mg AsymPol + 399 mg PS
	0.5	2 mg AsymPol + 398 mg PS	2 mg AsymPol + 398 mg PS	2 mg AsymPol + 398 mg PS
	1	4 mg AsymPol + 396 mg PS	4 mg AsymPol + 396 mg PS	4 mg AsymPol + 396 mg PS
	1.5	x	x	6 mg AsymPol + 394 mg PS
	2	8 mg AsymPol + 392 mg PS	8 mg AsymPol + 392 mg PS	8 mg AsymPol + 392 mg PS
	5	20 mg AsymPol + 380 mg PS	20 mg AsymPol + 380 mg PS	20 mg AsymPol + 380 mg PS

For the  $^{19}\text{F}$  DNP experiments two samples were prepared. The first sample contained 396 mg of PS 168N, 2 mg of F-BTA (0.5 wt.%) and 2 mg of AsymPol (0.5 wt.%). The second contained 390 mg of PS 168N, 2 mg of F-BTA (0.5 wt.%) and 8 mg of AsymPol (2 wt.%). The powders were mixed and shaken. The mixtures were compounded with a twin-screw mini extruder ZE 5 HMI (Three-Tec, Seon, Switzerland) at 180 °C and a 1 mm nozzle plate. The polymer strand was directly collected from the nozzle. The polymers were freeze crushed to obtain a powder.

#### Batch Foaming

To saturate the injection-molded specimens with a physical blowing agent, a HR 500 high-pressure autoclave (Berghof, Eningen, Germany) was used. Saturation was performed at room temperature using  $\text{CO}_2$  at a pressure of 50 bar for 24 h. A  $\text{CO}_2$  uptake of approximately 6.5 wt.% was determined by weighing the specimens prior foaming. Batch foaming experiments were performed by immersing the  $\text{CO}_2$ -loaded injection-molded specimens in a silicon oil bath at 130 °C for 15 s. The foamed samples were allowed to cool in an oil bath at ambient conditions for 20 s and then in a water bath for further 20 s. Oil residues were removed by washing the foams with soap water, and the foamed specimens were dried at ambient conditions for 24 h prior analysis.

#### Electron Microscopy

Scanning electron microscopy (SEM) images were obtained using a Leo Gemini FESEM Zeiss 1530 (Carl Zeiss AG) equipped with a field emission cathode using an acceleration voltage of 3.0 kV. The foamed sample was cryo-fractured and glued on a silicon wafer. For better conductivity it was additionally wrapped with a copper foil. The sample was sputtered with a 2.0 nm thick platinum layer under argon atmosphere using a Cressington Sputter Coater 208HR.

#### Foam analysis

The foam cell sizes were determined on the SEM images with the help of the software ImageJ. The areas of 94 cells were measured and the diameter was calculated assuming a circular foam cell.

The densities were calculated with the water-displacement method (ISO 1183) with a XP 205 balance equipped with a density kit. Three cubes were cut out of the foam and the calculated densities were averaged.

#### EPR Experiments

Between 10 and 20 mg of the PS/AsymPol compounds were put in a quartz tube of 2.9 mm outer diameter to measure the EPR spectra at ambient conditions.

For the EPR experiments of the frozen solutions a stock solution of 500 mM Asympol in 1,1,2,2-tetrachloro ethane (TCE) was prepared. The TCE was used as received. The stock solution was subsequently diluted to obtain solutions with concentrations of 250, 125, 63, 31, 16, 8 and 4 mM. The samples were measured in quartz tubes of 2.9 mm outer diameter containing 20  $\mu$ L. Continuous wave (cw) Electron Paramagnetic Resonance (EPR) measurements at X-band frequencies (9.52 GHz or 9.86 GHz) were conducted at room temperature and 150 K with a Bruker B-ER420 spectrometer upgraded with a Bruker ECS 041XG microwave bridge and a lock-in amplifier (Bruker ER023M) using a Bruker TE<sub>102</sub> resonator applying a modulation amplitude of 1 G and a modulation frequency of 100 kHz.

#### DNP Experiments

DNP enhanced NMR spectroscopic measurements to determine the ideal AsymPol concentration were performed on a Bruker Avance III 400 DNP spectrometer working at  $B_0 = 9.7$  T equipped with a Bruker gyrotron (9.7 T, 263.4 GHz, 115 mA beam current) using a low-temperature <sup>1</sup>H/<sup>X</sup>/<sup>Y</sup> triple resonance probe. The resonance frequencies were 401.63 MHz for <sup>1</sup>H and 100.99 MHz for <sup>13</sup>C at 110 K and a MAS frequency of 8 kHz was chosen. Recycle delays were set to match 1.3 times the beforehand estimated build-up time and were typically 0.5 – 1 s.

<sup>13</sup>C{<sup>1</sup>H} CP MAS spectra were performed with 128 scans and a ramped CP<sup>74</sup> sequence with a linear variation of the power (94 kHz) on the proton channel from 50-100 % . The CP contact time was 2 ms and the protons were decoupled at 87 kHz using the spinal 64 decoupling sequence.<sup>75</sup>

For the <sup>19</sup>F DNP experiments the PS compounds 11.05 mg of the powders were put in a 3.2 mm sapphire rotor and sealed with a rubber plug and a ZrO<sub>2</sub> cap.

All DNP NMR spectroscopic measurements of the F-BTA containing compounds were performed on a Bruker Avance Neo 400 spectrometer system equipped with an Ascend 400 DNP magnet, a 9.7 T (263.4 GHz, 130 mA beam current) Bruker gyrotron and a low-temperature <sup>1</sup>H/<sup>19</sup>F/<sup>X</sup> triple resonance probe. NMR spectra were recorded at frequencies of 376.52 MHz for <sup>19</sup>F, and 100.64 MHz for <sup>13</sup>C at 100 K and 12 kHz MAS spinning speed. A recycle delay of 10 s was chosen.

For the <sup>19</sup>F NMR spectroscopic rotor synchronised Hahn echo experiments, 16-128 transients were recorded at a nutation frequency of 66.6 kHz. During the acquisition protons were decoupled at 51 kHz using the spinal64<sup>75</sup> sequence.

<sup>19</sup>F-<sup>19</sup>F DQ build-up curves were recorded with the R12<sub>2</sub><sup>5</sup> sequence<sup>34</sup>. 19 experiments with increasing DQ excitation time were conducted. The first point was taken with two RR' blocks, corresponding to a DQ excitation time of 55.56  $\mu$ s. The increment for the other points was set

to the same value. The reconversion block was kept constant at two full R cycles corresponding to a reconversion time of 361  $\mu\text{s}$ . One R block was made of a composite pulse consisting of a  $90^\circ$  and a  $270^\circ$  pulse with a  $180^\circ$  phase shift.<sup>35</sup> Theoretical DQ build-up curves were simulated with the software simpson.<sup>76</sup>

#### Conventional NMR Experiments

Conventional NMR experiments were performed on a Bruker Avance III HD spectrometer at a field of 14.1 T on a Bruker 3.2 mm H/X/Y triple resonance probe operating in double resonance mode. The proton channel has a double resonance minimum with the possibility to pulse simultaneously on  $^{19}\text{F}$  and  $^1\text{H}$ . The resonance frequencies are 564.64 MHz for  $^{19}\text{F}$ , 600.15 MHz for  $^1\text{H}$ . The DQ build-up curves on the neat F-BTA were done in a 3.2 mm  $\text{ZrO}_2$  rotor with a point taken every RR' block corresponding to excitation increments of 27.78  $\mu\text{s}$ . In total 50 increments were measured.

NMR experiments to determine the blind sphere radius of AsymPol were performed on a Bruker Avance III 400 DNP spectrometer working at  $B_0 = 9.7$  T using a low-temperature  $^1\text{H}/\text{X}/\text{Y}$  triple resonance probe at proton resonance frequency of 400.02 MHz. For the excitation a  $90^\circ$  pulse with a nutation field of 109 kHz was used. A stock solution of 125 mM AsymPol in TCE was prepared. This solution was diluted in 5 steps until a concentration of 3.97 mM was achieved. At each step 25  $\mu\text{l}$  were transferred to a 3.2 mm sapphire rotor. The sample was sealed with a rubber plug and a  $\text{ZrO}_2$  cap.

### **Results and Discussion**

#### Foam Performance

We started by investigating the foam nucleation properties of F-BTA for PS. Therefore, a thermally induced batch foaming process with 0.5 wt.% of F-BTA was used. The foam density and the mean foam cell size were analysed. A SEM image (Figure 2) shows a very homogeneous foam cell distribution with a mean cell size of  $3.9 \pm 1.4$   $\mu\text{m}$ . The foam density is  $50.6 \pm 2.6$   $\text{kg m}^{-3}$ . Comparing these results to previously obtained results on a kinked bisamides additive and neat PS<sup>18</sup> shows that F-BTA is an efficient foam cell nucleating agent. According to the concept of supramolecular polymer nucleation, the F-BTA forms nanostructures inside PS on which the foam bubbles nucleate. However, these structures have only been shown indirectly by plasma etching<sup>77</sup> and nothing is known about the crystal structure or morphology of F-BTA within PS.

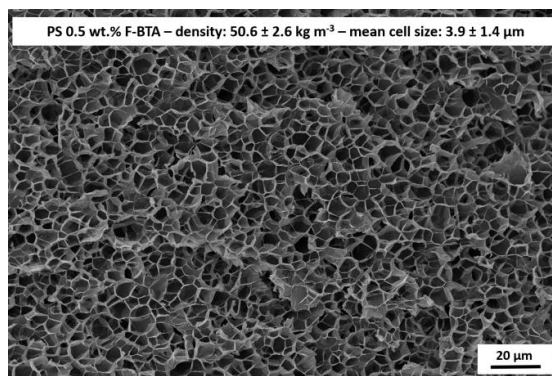


**Figure 2.** SEM image of a batch foamed PS foam with 0.5 wt.% F-BTA.

#### Optimising the sample preparation for DNP enhanced NMR spectroscopy

As stated previously, NMR spectroscopy suffers from an intrinsic lack of sensitivity. Therefore, NMR spectroscopic experiments of 0.5 wt.% F-BTA in PS are almost impossible. To increase the sensitivity we used DNP enhanced NMR spectroscopy in this work. Since we want to study bulk properties, we extrude the polarizing agent with PS. Since this has not been done for PS before, the preferred sample preparation needs to be developed. Therefore, AsymPol is extruded into PS at different concentrations with different extrusion temperatures. According to the TGA measurement (SI, Fig. S2) 180 °C is the highest temperature that AsymPol can be exposed to for a short time. We found that 140 °C is the lowest temperature for which PS can be extruded. At lower temperatures, the viscosity of the polymer is too high to emerge from the nozzle. Therefore, we choose these 2 temperatures and 160 °C as extrusion temperatures for the screening of the parameters. For the AsymPol concentrations we choose 0.5, 1, 2 and 5 wt.% for all extrusion temperatures and additionally 0.25 and 1.5 wt.% for 180 °C. These concentrations correspond to 7.3, 14.6, 28.6, 42.9, 57.2 and 143 μmol AsymPol per gram PS, respectively. Because the density of PS is roughly 1 these values can also be 1:1 expressed as mmol/l and in this way compared to the concentrations of frozen solutions of AsymPol in TCE. After extrusion, the samples were freeze crushed to obtain a powder.

The first questions are, whether the harsh conditions of the extrusion process – high temperature and shear forces – effect the radicals and if the process functions to homogeneously distribute the radical in the polymer. Both questions can be answered by EPR spectroscopy. As a comparison we prepared solutions of AsymPol in concentrations from 4 to 500 mM in TCE, when rapidly cooled to 150 K these solutions form a glass, similar as for the 100 K present in the probes for DNP enhanced NMR spectroscopy. Since AsymPol is a biradical its EPR spectrum (SI, Fig S3) is dominated by the intramolecular electron-electron interaction resulting in a distinct shape of the EPR spectrum that has been modelled and

measured by Mentink-Vigier et al.<sup>59</sup> When the concentration becomes higher, the intermolecular electron-electron interactions start to dominate. Because they do not have one distinct distance and orientation this results in a broadening and a smearing out of the EPR line as can be seen in Figure S3 (SI). Interestingly, we observe the same effect for the extruded samples (180 °C), albeit less pronounced (Figure 3). The spectra of the samples with concentrations between 0.5 and 2 wt.% show a very strong resemblance towards each other. Only the sample with 5 wt. % of AsymPol and the one with 0.25 wt.% show distinct changes, where the former shows less and the latter more features in the line shape. The presence of these line shapes, confirms that extrusion is capable of homogeneously distributing the radical. Because a complete clustering would result in a complete features line as can be seen for the 500 mM frozen solution (SI, Fig S3).

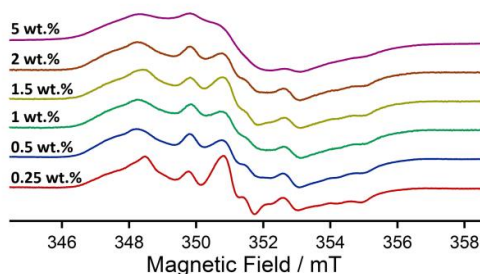


**Figure 3.** EPR spectra of AsymPol extruded in PS at concentrations between 0.25 and 5 wt.% from bottom to top as indicated on the respective spectra.

When comparing the EPR spectra within one concentration series (SI Figs. S4-S7), the spectrum of the sample that was extruded at the highest temperature always shows the most features, this effect is strongest for the 5 wt.% sample. When scaling the EPR spectra to the sample weight (SI Figs. S4-S7), it is remarkable that the spectrum of the sample with the lowest extrusion temperature shows the highest amplitude, indicating the most radical present. This means that although TGA measurements confirm the stability of the radical, the extrusion conditions at 160 and 180 °C are too harsh to leave the entire radical unharmed. However, the discussion of the line shapes shows that most of the radical remains intact.

The DNP performance is firstly investigated by comparing the DNP enhancement factor ( $\epsilon_{on/off}$ ) for all samples (SI, Fig. S8). Here we found that within one concentration the sample extruded at the highest temperature always exhibits the highest enhancement. Furthermore, within the temperature series the enhancement became better when reducing the concentration. The maximum being 7.6 for the 0.25 and the 0.5 wt.% sample. This again shows that for higher extrusion temperatures the radical can be better distributed within the sample.

The  $\epsilon_{\text{on/off}}$ , however, can be a misleading parameter. Therefore, we compared the absolute sensitivity – the signal to noise ratio per square root of time and sample mass – for the samples extruded at 180 °C. From Figure 4 can be see that the maximum sensitivity is obtained for the sample with an AsymPol content of 0.5 wt.%. It is with a value of 203.35  $\text{h}^{-1/2}\text{mg}^{-1}$  a factor of 2-10 higher compared to the samples with a higher concentration, although the  $\epsilon_{\text{on/off}}$  does not change markedly. This can be attributed to the bleaching – or blind sphere – radius that every radical has.<sup>78,79</sup> Because of the paramagnetic relaxation enhancement,<sup>80–82</sup> directly around the radical the corresponding spectrum is broadened in a way that no resonances are visible. For AsymPol we found this bleaching radius to be 10.42 Å (For details refer to the SI section 5). This means that for the sample with 5 wt.% - assuming a homogeneous distribution – 41 % of the sample would lie within this bleaching radius whereas for the 0.5. wt.% sample only 4.1 % would be bleached out. Note, that the calculation of the bleaching radius includes an error of  $\pm 1.23$  Å and that we assume non-overlapping bleaching radii, which will probably not be the case for the 5 wt. % sample. However, this calculation explains why the samples containing that much radical do not yield a good sensitivity.

The very short DNP build-up times (40-450 ms, see Table S1) of all samples, typical for AsymPol,<sup>59</sup> achieves the overall good sensitivity. However, the enhancements are slightly lower compared to the enhancements obtained for glass forming and film casting that used TEKPol as polarizing agent.<sup>65</sup> An even better sensitivity might be achievable by a partly deuteration of PS or an efficient removal of oxygen from the sample.<sup>69</sup>

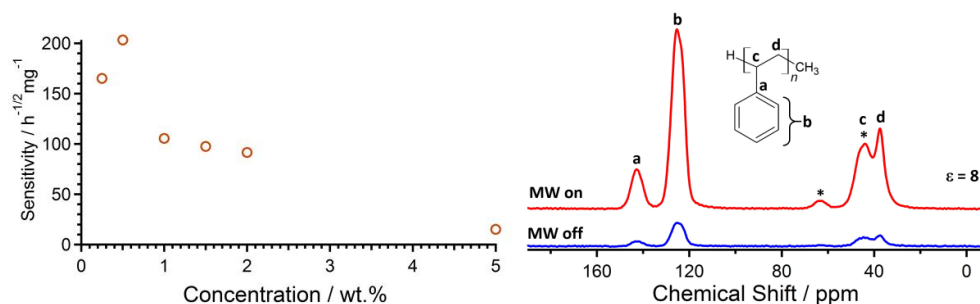


**Figure 4.** Left: Absolute Sensitivity Ratio for the aromatic C-H resonance of PS at different AsymPol concentrations. Right:  $^{13}\text{C}\{^1\text{H}\}$  CP (right) NMR spectra of PS with 0.5 wt.% AsymPol with an assignment of the resonances. The spectrum with microwave irradiation (red) shows an 8-fold enhancement compared to the blue spectrum without microwave irradiation. For the ASR determination on the left resonance b is used. Note that at 8 kHz MAS frequency the spinning side band of b overlaps with resonance c.

### DNP Performance of F-BTA within PS

Since our aim is to investigate the structure of F-BTA in PS, we prepared two samples with 0.5 wt.% F-BTA at 180 °C extrusion temperature. One with the optimal AsymPol content of 0.5 wt.% for the  $^1\text{H}$  enhancement according to the previous section and another with 2 wt.% of AsymPol to see, if the minority species needs more radical for optimal sensitivity.

The  $^{19}\text{F}$  DNP build-up time around 8 s for both samples is significantly longer compared to the one for  $^1\text{H}$ . This is in line with the direct polarization transfer to  $^{19}\text{F}$  that we already observed in a frozen solution.<sup>51</sup> The  $\epsilon_{\text{on/off}}$  is 17 and 11 with absolute sensitivities of 2646 and 1212  $\text{h}^{-1/2}\text{mg}^{-1}$  for the samples with 0.5 and 2 wt.% of AsymPol, respectively. This shows that the 0.5 wt.% of AsymPol is the optimal concentration for the DNP enhancement of all components in the sample. Furthermore, this also shows that the F-BTA molecules or nanoobjects are homogeneously distributed in the sample as we already confirmed the homogeneous distribution of the radicals that lead to their polarization.

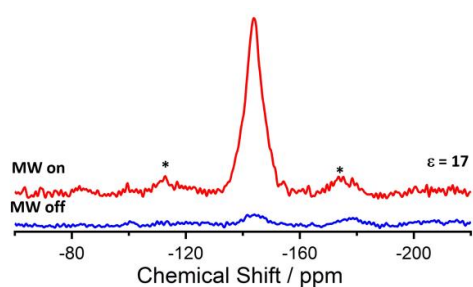


**Figure 4.** DNP enhanced  $^{19}\text{F}$  NMR spectra of PS with 0.5 wt.% F-BTA and 0.5 wt.% AsymPol with (red) and without (blue) microwave irradiation. The resonances marked with an asterisk are spinning side bands. The  $^{19}\text{F}$  spectrum without microwave irradiation was measured with 8 times more scans to ensure sufficient sensitivity. The intensities are scaled to the same amount of scans.

### DQ build-up curves

This high enhancement of F-BTA enables the measurement of a DQ build-up curve, although there are only  $\approx 600$  nmol  $^{19}\text{F}$  spins in the rotor. For F-BTA it is known that depending on the crystallisation conditions two polymorphs exist.<sup>72,83</sup> One polymorph crystallises in a layered crystal structure where the closest F-F distance is 3.90 Å.<sup>72</sup> The other polymorph crystallises in a hexagonal, columnar structure where the closest F-F distance is 2.91 Å.<sup>83</sup> These different crystal structures will have an impact on the morphology of the supramolecular nanoobject formed within the polymer.<sup>84</sup> The layered structure will guide the self-assembly to platelets because of its two directions of favoured crystal growth, whereas the columnar polymorph is more likely to self-assemble to ribbons or fibres because of only one direction of favoured

crystal growth. Due to the distinct difference in the distance of the  $^{19}\text{F}$ - $^{19}\text{F}$  spin pair a double quantum build-up curve can reliably probe the existence of a crystalline phase, even confirm the realised polymorph, and therefore hint towards the nanoobject morphology inside the polymer.

We tested a variety of DQ-recoupling pulse sequences on the neat polymorph from reference <sup>83</sup> at room temperature and without DNP enhancement. For all sequences we simulated the build-up for a spin pair and the robustness towards unpaired electrons in the close proximity. We found that the symmetry based pulse programme  $\text{R}12_2^5$  with a constant reconversion time and a 90-270 composite pulse for  $\text{R}^{34,35}$  performed best. The whole optimisation process is shown in the supporting info section 6.

From the build-up curves in Figure 5 can be seen that the neat F-BTA (red) is well resembled by a simulated build-up curve (salmon) where the F-F distance is set to 2.91 Å that corresponds to the closest F-F distance in that polymorph. The maximum of the DQ efficiency is at a recoupling time of 277 μs. The layered polymorph of reference <sup>72</sup> has its maximum at 667 μs (Figure 5, green). Therefore, their DQ build-up curves can easily distinguish the two polymorphs. The blue curve in Figure 5 shows the experimental DQ build-up curve of 0.5 wt.% F-BTA in PS. The existence of this build-up curve already confirms the formation of crystalline nanoobjects within the polymer. Furthermore, the curve follows the curve of the neat additive until the zero crossing before the slope gets gentler but still reaches the minimum at the same recoupling time.

The good resemblance of the two measured build-up curves confirms the formation of the columnar polymorph within PS that, because of its one direction of favoured growth, tends to form one dimensional nanostructures. These nanostructures, therefore, act as nucleation sites for the foam cell nucleation to yield the homogeneous foam with small foam cells of Figure 2.

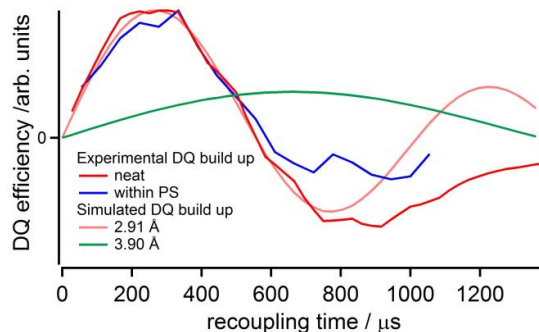


**Figure 5.** Experimental  $^{19}\text{F}$ - $^{19}\text{F}$  DQ build-up curves of neat F-BTA (red) at room temperature and of PS with 0.5 wt.% of F-BTA (blue) with DNP enhancement. Simulated DQ build-up curves of  $^{19}\text{F}$ - $^{19}\text{F}$  spin pairs with distances of 2.91 Å (salmon) and 3.90 Å (green).

### Conclusion

We reported an optimised sample preparation to investigate minority species within the bulk phase of PS with DNP enhanced NMR spectroscopy. The easy to synthesize polarizing agent AsymPol can be extruded at 180 °C with 0.5 wt.% in PS to maximise the sensitivity of both the bulk phase PS and the minority species as confirmed by  $^{13}\text{C}$  CP and  $^{19}\text{F}$  hahnecho experiments. The  $^{19}\text{F}$  DNP build-up time of the F-BTA molecules that were only present at 0.5 wt.% was with 8 s much longer than the one measured for the protons of PS (0.3 s), due to the direct polarization mechanism for  $^{19}\text{F}$  minority species as previously reported. The high sensitivity allowed us to measure the first reported DNP enhanced  $^{19}\text{F}$ - $^{19}\text{F}$  DQ build-up curve of the highly efficient foam cell nucleation agent F-BTA. This measurement not only confirms the presence of nanoobjects within PS but also shows the obtained polymorph that is very likely to form one dimensional structures.

We believe that extruding cheap but efficient radicals, like AsymPol (2 step synthesis), as DNP polarizing agents within polymers bears a high potential for the examination of minority species like additives and defects inside the bulk phase of amorphous polymers that is complementary to the surface enhancement obtained with other preparation techniques.

### Acknowledgment

We gratefully acknowledge financial support that was granted by the Deutsche Forschungsgemeinschaft DFG within the project number 391977956 - SFB 1357 Microplastics, subproject C01. We thank the Elite Network of Bavaria for support by the study program “Macromolecular Science”. Sandra Ganzleben (Macromolecular Chemistry I,

University of Bayreuth) was gratefully acknowledged for the synthesis of F-BTA and her technical assistance. We thank Prof. Gerd Buntkowsky (TU Darmstadt) for generous allocation of measurement time at his Bruker Avance III 400 DNP spectrometer.

## References

- (1) Kumar, A.; Patham, B.; Mohanty, S.; Nayak, S. K. Polyolefinic nanocomposite foams: Review of microstructure-property relationships, applications, and processing considerations. *J. Cell. Plast* **2020**, *117*, 0021955X2097975.
- (2) Dugad, R.; Radhakrishna, G.; Gandhi, A. Recent advancements in manufacturing technologies of microcellular polymers: A review. *J Polym Res* **2020**, *27*, 500.
- (3) Zhao, C.; Mark, L. H.; Kim, S.; Chang, E.; Park, C. B.; Lee, P. C. Recent progress in micro - /nano - fibrillar reinforced polymeric composite foams. *Polym Eng Sci* **2021**, *61*, 926–941.
- (4) Guo, A.; Li, H.; Xu, J.; Li, J.; Li, F. Effect of microstructure on the properties of polystyrene microporous foaming material. *e-Polymers* **2020**, *20*, 103–110.
- (5) Okolieocha, C.; Raps, D.; Subramaniam, K.; Altstädt, V. Microcellular to nanocellular polymer foams: Progress (2004–2015) and future directions – A review. *European Polymer Journal* **2015**, *73*, 500–519.
- (6) Colton, J. S.; Suh, N. P. The nucleation of microcellular thermoplastic foam with additives: Part I: Theoretical considerations. *Polym. Eng. Sci.* **1987**, *27*, 485–492.
- (7) Yang, J.; Huang, L.; Zhang, Y.; Chen, F.; Zhong, M. Mesoporous silica particles grafted with polystyrene brushes as a nucleation agent for polystyrene supercritical carbon dioxide foaming. *J. Appl. Polym. Sci.* **2013**, *65*, 4308–4317.
- (8) Wong, A.; Park, C. B. The effects of extensional stresses on the foamability of polystyrene–talc composites blown with carbon dioxide. *Chemical Engineering Science* **2012**, *75*, 49–62.
- (9) Wang, M. Y.; Zhu, R. M.; Zhou, N. Q.; Park, C. B. Effects of Nanoclay and CO<sub>2</sub> Content on Foaming Behaviors of PP/PS Alloys. *AMR* **2014**, *898*, 107–110.
- (10) Okolieocha, C.; Köppl, T.; Kerling, S.; Tölle, F. J.; Fathi, A.; Mülhaupt, R.; Altstädt, V. Influence of graphene on the cell morphology and mechanical properties of extruded polystyrene foam. *J. Cell. Plast* **2015**, *51*, 413–426.
- (11) Gong, P.; Buahom, P.; Tran, M.-P.; Saniei, M.; Park, C. B.; Pötschke, P. Heat transfer in microcellular polystyrene/multi-walled carbon nanotube nanocomposite foams. *Carbon* **2015**, *93*, 819–829.
- (12) Kausar, A. Synthesis and properties of novel polystyrene/polyurea and functional graphene-based nanocomposite foams. *J. Cell. Plast* **2017**, *53*, 305–318.
- (13) Fu, D.; Kuang, T.; Yen, Y.-C.; Li, D.; Benatar, A.; Peng, X. F.; Lee, L. J. Polystyrene/multi-wall carbon nanotube composite and its foam assisted by ultrasound vibration. *J. Cell. Plast* **2017**, *53*, 273–285.
- (14) Lehn, J.-M. Perspectives in Supramolecular Chemistry—From Molecular Recognition towards Molecular Information Processing and Self-Organization. *Angew. Chem. Int. Ed.* **1990**, *29*, 1304–1319.
- (15) Mörl, M.; Steinlein, C.; Kreger, K.; Schmidt, H.-W.; Altstädt, V. Improved compression properties of polypropylene extrusion foams by supramolecular additives. *J. Cell. Plast* **2018**, *54*, 483–498.
- (16) Hu, D.; Wang, G.; Feng, J.; Lu, X. Exploring supramolecular self-assembly of a bisamide nucleating agent in polypropylene melt: The roles of hydrogen bond and molecular conformation. *Polymer* **2016**, *93*, 123–131.
- (17) Wang, Z.; Yang, W.; Liu, G.; Müller, A. J.; Zhao, Y.; Dong, X.; Wang, K.; Wang, D. Probing into the epitaxial crystallization of  $\beta$  form isotactic polypropylene: From experimental observations to molecular mechanics computation. *J. Polym. Sci. Part B: Polym. Phys.* **2017**, *55*, 418–424.
- (18) Klose, B.; Kremer, D.; Aksit, M.; van der Zwan, K. P.; Kreger, K.; Senker, J.; Altstädt, V.; Schmidt, H.-W. Kinked Bisamides as Efficient Supramolecular Foam Cell Nucleating Agents for Low-Density Polystyrene Foams with Homogeneous Microcellular Morphology. *Polymers* **2021**, *13*, 1094.
- (19) Abraham, F.; Schmidt, H.-W. 1,3,5-Benzenetrisamide based nucleating agents for poly(vinylidene fluoride). *Polymer* **2010**, *51*, 913–921.
- (20) Blomenhofer, M.; Ganzleben, S.; Hanft, D.; Schmidt, H.-W.; Kristiansen, M.; Smith, P.; Stoll, K.; Mäder, D.; Hoffmann, K. "Designer" Nucleating Agents for Polypropylene. *Macromolecules* **2005**, *38*, 3688–3695.
- (21) Cantekin, S.; Greef, T. F. A. de; Palmans, A. R. A. Benzene-1,3,5-tricarboxamide: a versatile ordering moiety for supramolecular chemistry. *Chem. Soc. Rev.* **2012**, *41*, 6125–6137.
- (22) Wang, T.; Yang, Y.; Zhang, C.; Tang, Z.; Na, H.; Zhu, J. Effect of 1,3,5-trialkyl-benzenetricarboxylamide on the crystallization of poly(lactic acid). *J. Appl. Polym. Sci.* **2013**, *130*, 1328–1336.
- (23) Schmidt, M.; Wittmann, J. J.; Kress, R.; Schmidt, H.-W.; Senker, J. Probing self-assembled 1,3,5-benzenetrisamides in isotactic polypropylene by <sup>13</sup>C DQ solid-state NMR spectroscopy. *Chem. Commun.* **2013**, *49*, 267–269.
- (24) Schmidt, M.; Wittmann, J. J.; Kress, R.; Schneider, D.; Steuernagel, S.; Schmidt, H.-W.; Senker, J. Crystal Structure of a Highly Efficient Clarifying Agent for Isotactic Polypropylene. *Cryst. Growth Des.* **2012**, *12*, 2543–2551.
- (25) Gahleitner, M.; Grein, C.; Kheirandish, S.; Wolfschwenger, J. Nucleation of Polypropylene Homo- and Copolymers. *Int. Polym. Process.* **2011**, *26*, 2–20.
- (26) Libster, D.; Aserin, A.; Garti, N. Advanced nucleating agents for polypropylene. *Polym. Adv. Technol.* **2007**, *18*, 685–695.
- (27) Kristiansen, M.; Werner, M.; Tervoort, T.; Smith, P.; Blomenhofer, M.; Schmidt, H.-W. The Binary System Isotactic Polypropylene/Bis(3,4-dimethylbenzylidene)sorbitol: Phase Behavior, Nucleation, and Optical Properties. *Macromolecules* **2003**, *36*, 5150–5156.
- (28) Harris, R. K.; Wasylishen, R. L. *eMagRes*; John Wiley & Sons, Ltd: Chichester, UK, 2007.
- (29) Martineau, C.; Senker, J.; Taulelle, F. NMR Crystallography. *Annu. Rep. NMR Spectrosc.* **2014**, *82*, 1–57.
- (30) Ashbrook, S. E.; Hodgkinson, P. Perspective: Current advances in solid-state NMR spectroscopy. *J. Chem. Phys.* **2018**, *149*, 40901.
- (31) Hofstetter, A.; Emsley, L. Positional Variance in NMR Crystallography. *J. Am. Chem. Soc.* **2017**, *139*, 2573–2576.
- (32) Shi, P.; Li, D.; Chen, H.; Xiong, Y.; Wang, Y.; Tian, C. In situ <sup>19</sup>F NMR studies of an E. coli membrane protein. *Protein. Sci.* **2012**, *21*, 596–600.

- (33) Ahrens, E. T.; Zhong, J. In vivo MRI cell tracking using perfluorocarbon probes and fluorine-19 detection. *NMR Biomed.* **2013**, *26*, 860–871.
- (34) Carravetta, M.; Edén, M.; Johannessen, O. G.; Luthman, H.; Verdegem, P. J. E.; Lugtenburg, J.; Sebald, A.; Levitt, M. H. Estimation of Carbon–Carbon Bond Lengths and Medium-Range Internuclear Distances by Solid-State Nuclear Magnetic Resonance. *J. Am. Chem. Soc.* **2001**, *123*, 10628–10638.
- (35) Kristiansen, P. E.; Carravetta, M.; van Beek, J. D.; Lai, W. C.; Levitt, M. H. Theory and applications of supercycled symmetry-based recoupling sequences in solid-state nuclear magnetic resonance. *J. Chem. Phys.* **2006**, *124*, 234510.
- (36) Kristiansen, P. E.; Mitchell, D. J.; Evans, J. N. S. Double-quantum dipolar recoupling at high magic-angle spinning rates. *J. Magn. Reson.* **2002**, *157*, 253–266.
- (37) Hall, D. A.; Maus, D. C.; Gerfen, G. J.; Inati, S. J.; Becerra, L. R.; Dahlquist, F. W.; Griffin, R. G. Polarization-Enhanced NMR Spectroscopy of Biomolecules in Frozen Solution. *Science* **1997**, *276*, 930–932.
- (38) Gerfen, G. J.; Becerra, L. R.; Hall, D. A.; Griffin, R. G.; Temkin, R. J.; Singel, D. J. High frequency (140 GHz) dynamic nuclear polarization: Polarization transfer to a solute in frozen aqueous solution. *J. Chem. Phys.* **1995**, *102*, 9494–9497.
- (39) Maly, T.; Debelouchina, G. T.; Bajaj, V. S.; Hu, K.-N.; Joo, C.-G.; Mak-Jurkauskas, M. L.; Sirigiri, J. R.; van der Wel, P. C. A.; Herzfeld, J.; Temkin, R. J. *et al.* Dynamic nuclear polarization at high magnetic fields. *J. Chem. Phys.* **2008**, *128*, 52211.
- (40) Bajaj, V. S.; Farrar, C. T.; Hornstein, M. K.; Mastovsky, I.; Vieregg, J.; Bryant, J.; Eléna, B.; Kreisler, K. E.; Temkin, R. J.; Griffin, R. G. Dynamic nuclear polarization at 9 T using a novel 250 GHz gyrotron microwave source. *J. Magn. Reson.* **2003**, *160*, 85–90.
- (41) Ni, Q. Z.; Daviso, E.; Can, T. V.; Markhasin, E.; Jawla, S. K.; Swager, T. M.; Temkin, R. J.; Herzfeld, J.; Griffin, R. G. High frequency dynamic nuclear polarization. *Acc. Chem. Res.* **2013**, *46*, 1933–1941.
- (42) Rossini, A. J.; Zagdoun, A.; Lelli, M.; Lesage, A.; Coperet, C.; Emsley, L. Dynamic Nuclear Polarization Surface Enhanced NMR Spectroscopy. *Acc. Chem. Res.* **2013**, *46*, 1942–1951.
- (43) Mollica, G.; Dekhil, M.; Ziarelli, F.; Thureau, P.; Viel, S. Quantitative structural constraints for organic powders at natural isotopic abundance using dynamic nuclear polarization solid-state NMR spectroscopy. *Angew. Chem. Int. Ed.* **2015**, *54*, 6028–6031.
- (44) Thankamony, A. S. L.; Lion, C.; Pourpoint, F.; Singh, B.; Perez Linde, A. J.; Carnevale, D.; Bodenhausen, G.; Vezin, H.; Lafon, O.; Polshettiwar, V. Insights into the Catalytic Activity of Nitridated Fibrous Silica (KCC-1) Nanocatalysts from  $^{15}\text{N}$  and  $^{29}\text{Si}$  NMR Spectroscopy Enhanced by Dynamic Nuclear Polarization. *Angew. Chem. Int. Ed.* **2015**, *54*, 2190–2193.
- (45) Gutmann, T.; Liu, J. Q.; Rothermel, N.; Xu, Y. P.; Jaumann, E.; Werner, M.; Breitzke, H.; Sigurdsson, S. T.; Buntkowsky, G. Natural Abundance  $^{15}\text{N}$  NMR by Dynamic Nuclear Polarization: Fast Analysis of Binding Sites of a Novel Amine-Carboxyl-Linked Immobilized Dirhodium Catalyst. *Chem. Eur. J.* **2015**, *21*, 3798–3805.
- (46) Vitzthum, V.; Miéville, P.; Carnevale, D.; Caporini, M. A.; Gajan, D.; Copéret, C.; Lelli, M.; Zagdoun, A.; Rossini, A. J.; Lesage, A. *et al.* Dynamic nuclear polarization of quadrupolar nuclei using cross polarization from protons: Surface-enhanced Aluminium-27 NMR. *Chem. Commun.* **2012**, *48*, 1988–1990.
- (47) Lee, D.; Takahashi, H.; Thankamony, A. S. L.; Dacquin, J.-P.; Bardet, M.; Lafon, O.; De Paëpe, G. Enhanced Solid-State NMR Correlation Spectroscopy of Quadrupolar Nuclei Using Dynamic Nuclear Polarization. *J. Am. Chem. Soc.* **2012**, *134*, 18491–18494.
- (48) Blanc, F.; Sperrin, L.; Jefferson, D. A.; Pawsey, S.; Rosay, M.; Grey, C. P. Dynamic Nuclear Polarization Enhanced Natural Abundance  $^{17}\text{O}$  Spectroscopy. *J. Am. Chem. Soc.* **2013**, *135*, 2975–2978.
- (49) Michaelis, V. K.; Corzilius, B.; Smith, A. A.; Griffin, R. G. Dynamic Nuclear Polarization of  $^{17}\text{O}$ : Direct Polarization. *J. Phys. Chem. B* **2013**, *117*, 14894–14906.
- (50) Perras, F. A.; Kobayashi, T.; Pruski, M. Natural Abundance  $^{17}\text{O}$  DNP Two-Dimensional and Surface-Enhanced NMR Spectroscopy. *J. Am. Chem. Soc.* **2015**, *137*, 8336–8339.
- (51) van der Zwan, K. P.; Riedel, W.; Aussenac, F.; Reiter, C.; Kreger, K.; Schmidt, H.-W.; Risse, T.; Gutmann, T.; Senker, J.  $^{19}\text{F}$  MAS DNP for Probing Molecules in Nanomolar Concentrations: Direct Polarization as Key for Solid-State NMR Spectra without Solvent and Matrix Signals. *J. Phys. Chem. C* **2021**, *125*, 7287–7296.
- (52) Lu, M.; Wang, M.; Sergeev, I. V.; Quinn, C. M.; Struppe, J.; Rosay, M.; Maas, W.; Gronenborn, A. M.; Polenova, T.  $^{19}\text{F}$  Dynamic Nuclear Polarization at Fast Magic Angle Spinning for NMR of HIV-1 Capsid Protein Assemblies. *J. Am. Chem. Soc.* **2019**, *141*, 5681–5691.
- (53) Viger - Gravel, J.; Avalos, C. E.; Kubicki, D. J.; Gajan, D.; Lelli, M.; Ouari, O.; Lesage, A.; Emsley, L.  $^{19}\text{F}$  Magic Angle Spinning Dynamic Nuclear Polarization Enhanced NMR Spectroscopy. *Angew. Chem. Int. Ed.* **2019**, *58*, 7249–7253.
- (54) Hope, M. A.; Rinkel, B. L. D.; Gunnarsdóttir, A. B.; Märker, K.; Menkin, S.; Paul, S.; Sergeev, I. V.; Grey, C. P. Selective NMR observation of the SEI–metal interface by dynamic nuclear polarisation from lithium metal. *Nat. Commun.* **2020**, *11*, 1–8.
- (55) Takahashi, H.; Lee, D.; Dubois, L.; Bardet, M.; Hediger, S.; De Paëpe, G. Rapid Natural-Abundance 2D  $^{13}\text{C}$ - $^{13}\text{C}$  Correlation Spectroscopy Using Dynamic Nuclear Polarization Enhanced Solid-State NMR and Matrix-Free Sample Preparation. *Angew. Chem. Int. Ed.* **2012**, *51*, 11766–11769.
- (56) Märker, K.; Hediger, S.; Paëpe, G. de. Efficient 2D double-quantum solid-state NMR spectroscopy with large spectral widths. *Chemical communications (Cambridge, England)* **2017**, *53*, 9155–9158.
- (57) Zagdoun, A.; Casano, G.; Ouari, O.; Schwarzwälder, M.; Rossini, A. J.; Aussenac, F.; Yulikov, M.; Jeschke, G.; Copéret, C.; Lesage, A. *et al.* Large molecular weight nitroxide biradicals providing efficient dynamic nuclear polarization at temperatures up to 200 K. *J. Am. Chem. Soc.* **2013**, *135*, 12790–12797.

- (58) Sauvée, C.; Rosay, M.; Casano, G.; Aussenac, F.; Weber, R. T.; Ouari, O.; Tordo, P. Highly efficient, water-soluble polarizing agents for dynamic nuclear polarization at high frequency. *Angew. Chem. Int. Ed.* **2013**, *52*, 10858–10861.
- (59) Mentink-Vigier, F.; Marin-Montesinos, I.; Jagtap, A. P.; Halbritter, T.; van Tol, J.; Hediger, S.; Lee, D.; Sigurdsson, S. T.; De Paëpe, G. Computationally Assisted Design of Polarizing Agents for Dynamic Nuclear Polarization Enhanced NMR: The AsymPol Family. *J. Am. Chem. Soc.* **2018**, *140*, 11013–11019.
- (60) Rosay, M.; Tometich, L.; Pawsey, S.; Bader, R.; Schauwecker, R.; Blank, M.; Borcard, P. M.; Cauffman, S. R.; Felch, K. L.; Weber, R. T. *et al.* Solid-state dynamic nuclear polarization at 263 GHz: Spectrometer design and experimental results. *Phys. Chem. Chem. Phys.* **2010**, *12*, 5850–5860.
- (61) Lesage, A.; Lelli, M.; Gajan, D.; Caporini, M. A.; Vitzthum, V.; Miéville, P.; Alauzun, J.; Roussey, A.; Thieuleux, C.; Mehdi, A. *et al.* Surface Enhanced NMR Spectroscopy by Dynamic Nuclear Polarization. *J. Am. Chem. Soc.* **2010**, *132*, 15459–15461.
- (62) Lelli, M.; Gajan, D.; Lesage, A.; Caporini, M. A.; Vitzthum, V.; Miéville, P.; Héroguel, F.; Rascón, F.; Roussey, A.; Thieuleux, C. *et al.* Fast characterization of functionalized silica materials by silicon-29 surface-enhanced NMR spectroscopy using dynamic nuclear polarization. *J. Am. Chem. Soc.* **2011**, *133*, 2104–2107.
- (63) Bouleau, E.; Saint-Bonnet, P.; Mentink-Vigier, F.; Takahashi, H.; Jacquot, J.-F.; Bardet, M.; Aussenac, F.; Pureau, A.; Engelke, F.; Hediger, S. *et al.* Pushing NMR sensitivity limits using dynamic nuclear polarization with closed-loop cryogenic helium sample spinning. *Chem. Sci.* **2015**, *6*, 6806–6812.
- (64) Brownbill, N. J.; Sprick, R. S.; Bonillo, B.; Pawsey, S.; Aussenac, F.; Fielding, A. J.; Cooper, A. I.; Blanc, F. Structural Elucidation of Amorphous Photocatalytic Polymers from Dynamic Nuclear Polarization Enhanced Solid State NMR. *Macromolecules* **2018**, *51*, 3088–3096.
- (65) Le, D.; Casano, G.; Phan, T. N. T.; Ziarelli, F.; Ouari, O.; Aussenac, F.; Thureau, P.; Mollica, G.; Gignes, D.; Tordo, P. *et al.* Optimizing Sample Preparation Methods for Dynamic Nuclear Polarization Solid-state NMR of Synthetic Polymers. *Macromolecules* **2014**, *47*, 3909–3916.
- (66) Tanaka, S.; Liao, W.-C.; Ogawa, A.; Sato, K.; Copéret, C. DNP NMR spectroscopy of cross-linked organic polymers: Rational guidelines towards optimal sample preparation. *Phys. Chem. Chem. Phys.* **2020**, *22*, 3184–3190.
- (67) Kanda, T.; Kitawaki, M.; Arata, T.; Matsuki, Y.; Fujiwara, T. Structural analysis of cross-linked poly(vinyl alcohol) using high-field DNP-NMR. *RSC Adv.* **2020**, *10*, 8039–8043.
- (68) Verde-Sesto, E.; Goujon, N.; Sardon, H.; Ruiz, P.; Huynh, T. V.; Elizalde, F.; Mecerreyes, D.; Forsyth, M.; O'Dell, L. A. DNP NMR Studies of Crystalline Polymer Domains by Copolymerization with Nitroxide Radical Monomers. *Macromolecules* **2018**, *51*, 8046–8053.
- (69) Le, D.; Ziarelli, F.; Phan, T. N. T.; Mollica, G.; Thureau, P.; Aussenac, F.; Ouari, O.; Gignes, D.; Tordo, P.; Viel, S. Up to 100% Improvement in Dynamic Nuclear Polarization Solid-State NMR Sensitivity Enhancement of Polymers by Removing Oxygen. *Macromol. Rapid Commun.* **2015**, *36*, 1416–1421.
- (70) Neudert, O.; Reh, M.; Spiess, H. W.; Münnemann, K. X-Band DNP Hyperpolarization of Viscous Liquids and Polymer Melts. *Macromol. Rapid Commun.* **2015**, *36*, 885–889.
- (71) Ni, Q. Z.; Yang, F.; Can, T. V.; Sergeyev, I. V.; D'Addio, S. M.; Jawla, S. K.; Li, Y.; Lipert, M. P.; Xu, W.; Williamson, R. T. *et al.* In Situ Characterization of Pharmaceutical Formulations by Dynamic Nuclear Polarization Enhanced MAS NMR. *The Journal of physical chemistry. B* **2017**, *121*, 8132–8141.
- (72) Zehe, C.; Schmidt, M.; Siegel, R.; Kreger, K.; Daebel, V.; Ganzleben, S.; Schmidt, H.-W.; Senker, J. Influence of fluorine side-group substitution on the crystal structure formation of benzene-1,3,5-trisamides. *CrystEngComm* **2014**, *16*, 9273–9283.
- (73) Zhang, K.; Noble, B. B.; Mater, A. C.; Monteiro, M. J.; Coote, M. L.; Jia, Z. Effect of heteroatom and functionality substitution on the oxidation potential of cyclic nitroxide radicals: Role of electrostatics in electrochemistry. *Phys. Chem. Chem. Phys.* **2018**, *20*, 2606–2614.
- (74) Metz, G.; Wu, X. L.; Smith, S. O. Ramped-Amplitude Cross Polarization in Magic-Angle-Spinning NMR. *J. Magn. Reson.* **1994**, *110*, 219–227.
- (75) Fung, B. M.; Khitrin, A. K.; Ermolaev, K. An improved broadband decoupling sequence for liquid crystals and solids. *J. Magn. Reson.* **2000**, *142*, 97–101.
- (76) Bak, M.; Rasmussen, J. T.; Nielsen, N. C. SIMPSON: A general simulation program for solid-state NMR spectroscopy. *J. Magn. Reson.* **2000**, *147*, 296–330.
- (77) Aksit, M.; Klose, B.; Zhao, C.; Kreger, K.; Schmidt, H.-W.; Altstädt, V. Morphology control of extruded polystyrene foams with benzene-trisamide-based nucleating agents. *J. Cell. Plast* **2019**, *55*, 249–261.
- (78) Li, W.; Zhang, Q.; Joos, J. J.; Smet, P. F.; Schmedt Auf der Günne, J. Blind spheres of paramagnetic dopants in solid state NMR. *Phys. Chem. Chem. Phys.* **2019**, *21*, 10185–10194.
- (79) Li, W.; Smet, P. F.; Martin, L. I. D. J.; Pritzl, C.; Schmedt Auf der Günne, J. Doping homogeneity in co-doped materials investigated at different length scales. *Phys. Chem. Chem. Phys.* **2020**, *22*, 818–825.
- (80) Solomon, I. Relaxation Processes in a System of Two Spins. *Phys. Rev.* **1955**, *99*, 559–565.
- (81) Maliakal, A. J.; Turro, N. J.; Bosman, A. W.; Cornel, J.; Meijer, E. W. Relaxivity Studies on Dinitroxide and Polynitroxyl Functionalized Dendrimers: Effect of Electron Exchange and Structure on Paramagnetic Relaxation Enhancement. *J. Phys. Chem. A* **2003**, *107*, 8467–8475.
- (82) Clore, G. M.; Iwahara, J. Theory, practice, and applications of paramagnetic relaxation enhancement for the characterization of transient low-population states of biological macromolecules and their complexes. *Chem. Rev.* **2009**, *109*, 4108–4139.
- (83) Zehe, C. S.; Hill, J. A.; Funnell, N. P.; Kreger, K.; van der Zwan, K. P.; Goodwin, A. L.; Schmidt, H.-W.; Senker, J. Mesoscale Polarization by Geometric Frustration in Columnar Supramolecular Crystals. *Angew. Chem. Int. Ed.* **2017**, *56*, 4432–4437.

**Supporting Information for****DNP Enhanced <sup>19</sup>F-<sup>19</sup>F DQ Build-Up Curve Confirms Crystal Structure of  
Supramolecular Additive in PS at Technical Concentration for Batch Foaming**

Kasper P. van der Zwan,<sup>a</sup> Wiebke Riedel,<sup>b</sup> Bastian Klose,<sup>c</sup> Tamara Fischer,<sup>a</sup> Renée Siegel,<sup>a</sup>  
Fabien Aussenac,<sup>d</sup> Christian Reiter,<sup>e</sup> Anika Mauel,<sup>a</sup> Klaus Kreger,<sup>c</sup> Hans-Werner Schmidt,<sup>c</sup>  
Thomas Risse,<sup>b</sup> Gaël de Paëpe,<sup>f</sup> Jürgen Senker<sup>a\*</sup>

<sup>a</sup> Inorganic Chemistry III, University of Bayreuth,  
Universitätsstraße 30, D-95447 Bayreuth, Germany

<sup>b</sup> Physical and Theoretical Chemistry, Institute of Chemistry and Biochemistry  
Freie Universität Berlin, Arnimallee 22, 14195 Berlin, Germany

<sup>c</sup> Macromolecular Chemistry I, University of Bayreuth,  
Universitätsstraße 30, D-95447 Bayreuth, Germany

<sup>d</sup> Bruker BioSpin, 34 rue de l'Industrie BP 10002  
67166 Wissembourg Cedex, France

<sup>e</sup> Bruker BioSpin GmbH  
Silberstreifen 4, 76287 Rheinstetten, Germany

<sup>f</sup> Univ. Grenoble Alpes, CEA, CNRS, IRIG MEM,  
38000 Grenoble, France

\* [juergen.senker@uni-bayreuth.de](mailto:juergen.senker@uni-bayreuth.de) 0049-(0)921-552532;

**Table of Content**

1. Synthesis of AsymPol.....	3
2. TGA of AsymPol .....	4
3. EPR Measurements .....	4
4. DNP Enhancement.....	7
5. Determining the blind sphere radius of AsymPol .....	8
6. Choosing the R-Sequence.....	9
References.....	16

### 1. Synthesis of AsymPol

Synthesis of AsymPol was performed in a 2 step synthesis:

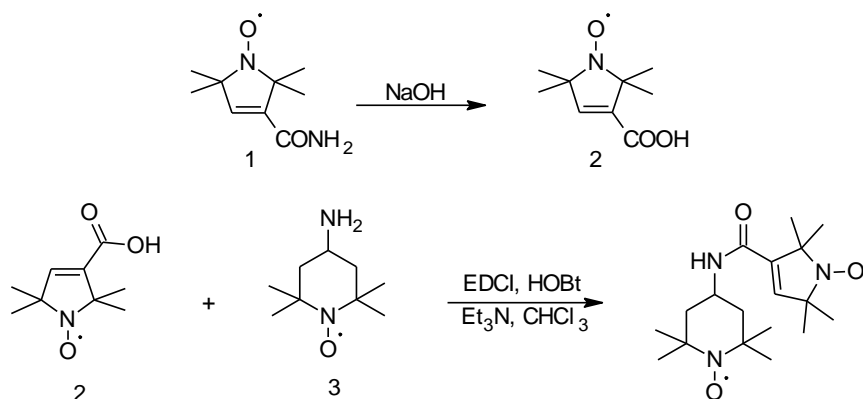


**Figure S1.** Sketch of the AsymPol synthesis.

449.13 mg (2.4 mmol) 3-carbamoyl-2,2,5,5-tetramethyl-3-pyrrolin-1-oxyl (**1**) were added to 15 ml of a 15 wt.% aqueous NaOH solution. The mixture was stirred at 95 °C for three hours to yield a transparent, yellow solution. Concentrated HCl has been added until a pH of 4 was reached. Subsequently the solution was washed twice with EtOAc (25 and 50 ml) The organic phase was collected and dried with MgSO<sub>4</sub>. The filtered solution was dried under vacuum to yield a yellow solid (**2**).

To 150.86 mg (0.8 mmol) of **2** 245.97 mg (1.8 mmol) of 1*H*-1,2,3-Benzotriazol-1-ol (HOBt), 173.34 mg (1.1 mmol) 1-Ethyl-3-(3-dimethylaminopropyl)carbodiimide (EDCI), 0.35 ml Et<sub>3</sub>N and 18.75 ml chloroform were added under a nitrogen blanket and stirred for 15 minutes at room temperature. 140.01 mg (0.8 mmol) of 4-aminotempo (**3**) were added and stirred over night at room temperature. Afterwards 50 ml chloroform were added and the solution was washed with a 50 ml of saturated NaHCO<sub>3</sub> solution and afterwards with 50 ml of a saturated NaCl solution. The organic phase was dried under vacuum to yield an orange powder. The powder was purified by flash column chromatography (silica) using a gradient elution (EtOAc:pet ether; 0:100 to 30:70); TLC (silica) 2.5 % MeOH in DCM: R<sub>f</sub> ≈ 0.15. The product fractions were dried under vacuum and yielded 222 mg (79%) of the orange product. Successful syntheses and purification was monitored by mass spectrometry.

## 2. TGA of AsymPol

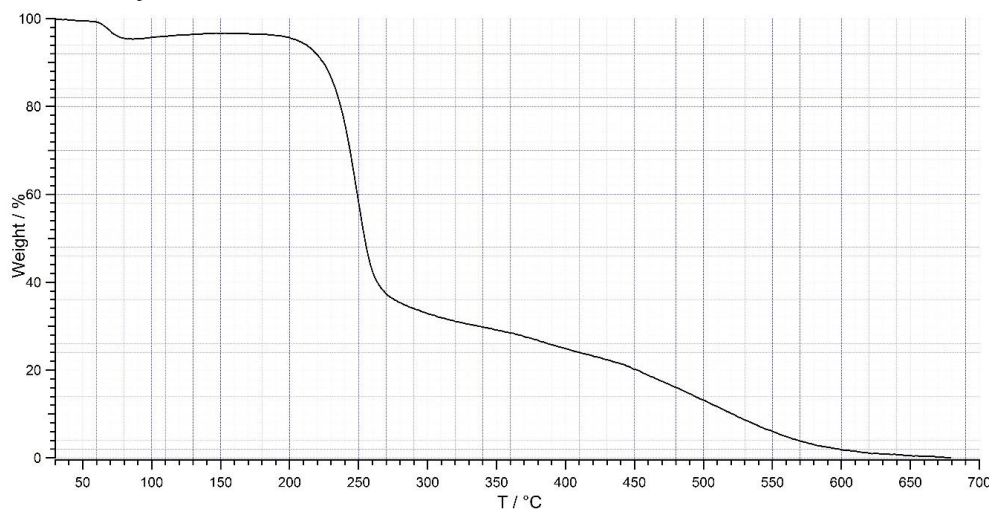


**Figure S2.** Thermogravimetric analysis of AsymPol with a heat rate of 10 Kmin<sup>-1</sup> and regular atmosphere.

## 3. EPR Measurements

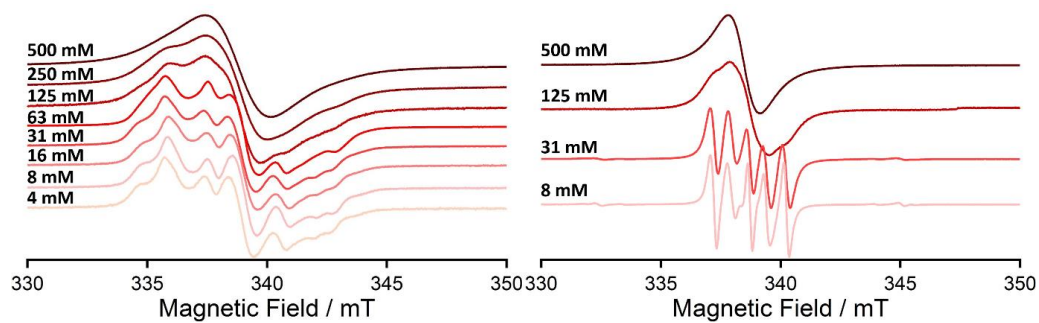


**Figure S3.** Left: EPR measurements of frozen solutions of AsymPol in tce measured at 150 K. right: EPR measurements of solutions of AsymPol in tce at room temperature. Please note that these measurements were performed at a resonance frequency of 9.51 GHz, whereas the measurements in the main text were performed at 9.86 GHz resulting in a baseline shift of 12.3 mT.

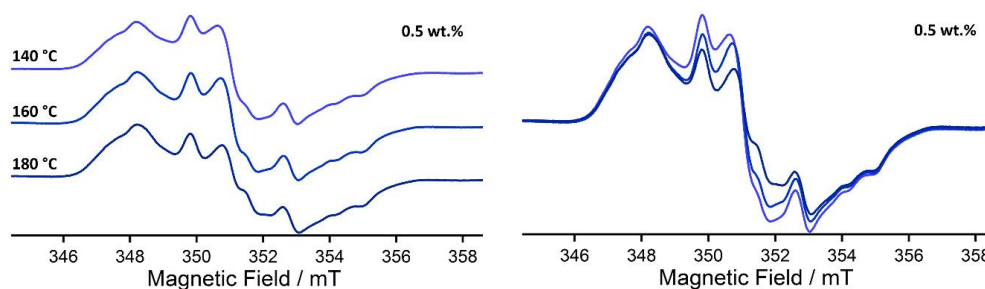


**Figure S4.** EPR measurements of AsymPol extruded in PS at 0.5 wt.% with extrusion temperatures as listed on the respective spectra. Left: The spectra are scaled to their amplitude to compare the shapes. Right: The spectra are scaled to their nominal AsymPol content to compare the AsymPol loss during the extrusion process. The colours represent the same temperatures as in the left part of the Figure.

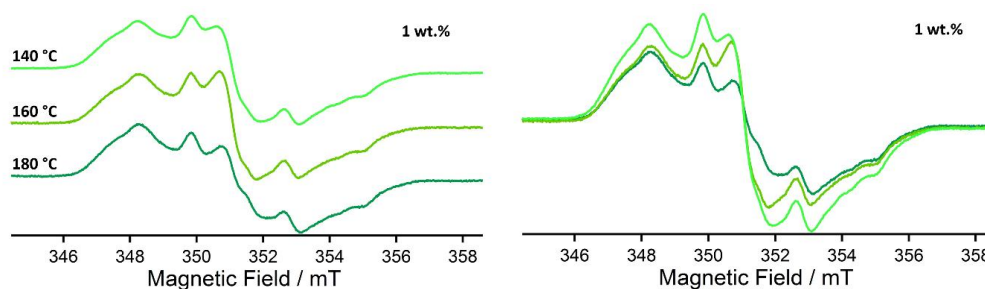


**Figure S5.** EPR measurements of AsymPol extruded in PS at 1 wt.% with extrusion temperatures as listed on the respective spectra. Left: The spectra are scaled to their amplitude to compare the shapes. Right: The spectra are scaled to their nominal AsymPol content to compare the AsymPol loss during the extrusion process. The colours represent the same temperatures as in the left part of the Figure.

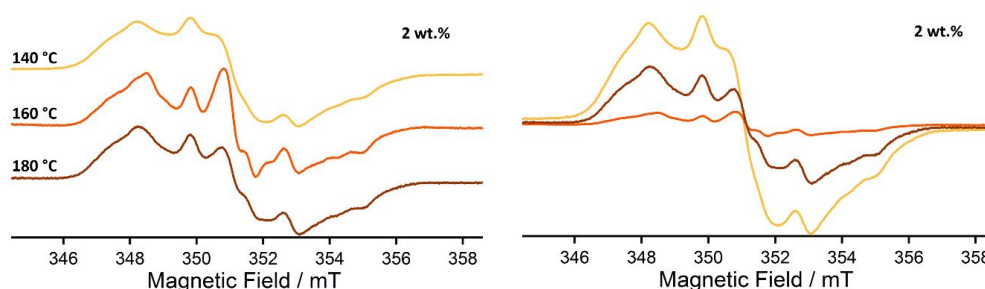


**Figure S6.** EPR measurements of AsymPol extruded in PS at 2 wt.% with extrusion temperatures as listed on the respective spectra. Left: The spectra are scaled to their amplitude to compare the shapes. Right: The spectra are scaled to their nominal AsymPol content to compare the AsymPol loss during the extrusion process. The colours represent the same temperatures as in the left part of the Figure. Note that the 2 wt.% sample extruded at 160 °C

falls out of the line, probably due to mixing errors. Intensity and line shape suggests a much lower concentration than the nominal concentration of 2 wt.%.

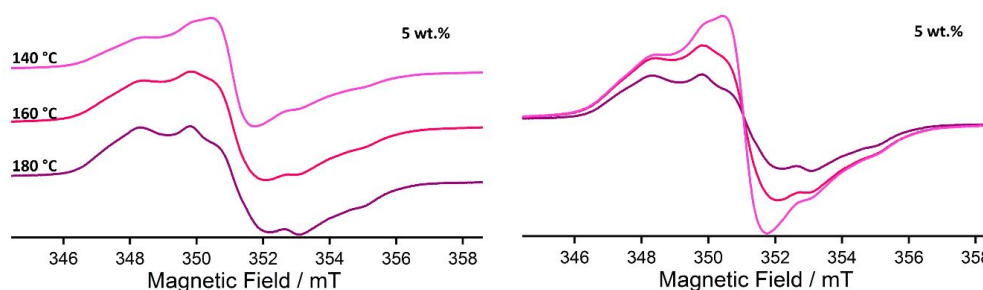


**Figure S7.** EPR measurements of AsymPol extruded in PS at 5 wt.% with extrusion temperatures as listed on the respective spectra. Left: The spectra are scaled to their amplitude to compare the shapes. Right: The spectra are scaled to their nominal AsymPol content to compare the AsymPol loss during the extrusion process. The colours represent the same temperatures as in the left part of the Figure.

#### 4. DNP Enhancement and build up

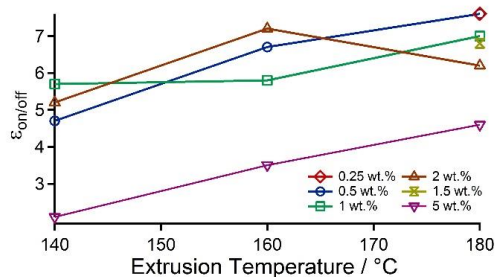


**Figure S8.** DNP enhancements ( $\epsilon_{\text{on/off}}$ ) for all concentrations and extrusion temperatures. The factor is calculated by comparing the integrals of the spectra measured with and without microwave irradiation and the same amount of scans. Note that as for the EPR measurements the sample with 2 wt.% AsymPol extruded at 160 °C is not following the general trend.

**Table S1.** DNP build up times for AsymPol/PS compounds. As for all other results the sample with 2 wt.% AsymPol at 160 °C behaves inconsistently.

		extrusion temperature /°C		
		140	160	180
concentration/ wt. %	0.25	x	x	451 ms
	0.5	227 ms	273 ms	291 ms
	1	137 ms	170 ms	190 ms
	1.5	x	x	142 ms
	2	91 ms	645 ms	163 ms
	5	40 ms	39 ms	57 ms

### 5. Determining the blind sphere radius of AsymPol

The blind sphere radius of AsymPol was estimated by a series of 1D proton experiments on frozen solutions of TCE with varying AsymPol concentrations from 0 to 125 mol/l. We assume a homogeneous distribution of the radical within the solution, which is justified by the previous EPR discussion. The integral of the whole spectrum was normalised to the integral of the neat TCE sample. This value is subtracted from 1 to give the percentage of the bleached out volume. Dividing this value by the twice the concentration of the solution – taking into account that AsymPol is a biradical – and Avogadro's number gives the bleached volume per single N-O radical moiety. This can be transformed into a bleaching radius by assuming a spherical bleaching volume. In principle, one concentration would already give an estimate for this calculation. However, for a more profound value we choose to measure the concentration series. For an even better sampling, we performed the measurement at 4 different MAS spinning speeds (6, 8, 10 and 12 kHz), since MAS averages out spin-spin interactions and therefore should effect the bleaching radius as well. However, we could not see a clear trend in these measurements. Therefore, we averaged the 4 bleached volumes at one spinning speed to reduce the error. Averaging the bleaching radius for all concentrations (Table S1) gives a bleaching radius of  $10.42 \pm 1.23 \text{ \AA}$ .

**Table S2.** Calculation of the blind sphere radii for the different AsymPol concentrations in TCE.

Concentration / mmol l <sup>-1</sup>	Integral	lost signal	bleached Volume per radical / $\text{\AA}^3$	bleaching radius / $\text{\AA}$
125	0.569	0.431	2860	8.81
62.5	0.707	0.293	3898	9.76
31.75	0.802	0.198	5185	10.74
15.875	0.922	0.078	4105	9.93
7.9375	0.954	0.046	4817	10.48
3.969	0.958	0.042	8807	12.81
0	1	0	n.a	n.a.

### 6. Choosing the R-Sequence

In general, the R-sequences used for recoupling DQ resonances are constructed in the following way: A sequence  $RN_n^v$  consists of  $N$   $180^\circ$  pulses during  $n$  rotor periods. The phase of the  $180^\circ$  pulses is alternated between  $\phi = \pi v/N$  and  $\phi = -\pi v/N$ . The  $180^\circ$  pulse can be replaced by a composite pulse consisting of a back-to-back  $90^\circ$  pulse with a phase  $\phi$  followed by a  $270^\circ$  pulse with a phase  $\phi + \pi$ . The pulse sequence consists of a DQ-excitation block where a certain number of  $RN$  cycles is performed and a DQ-reconversion block where the  $RN$  cycles are repeated with a  $\pi/2$  phase shift. After a z-filter a  $90^\circ$  detection pulse is performed to collect the signal. To collect DQ build up curves there are symmetric and asymmetric pulse schemes. In a symmetric pulse programme the excitation and reconversion block are incremented together in the same way after each experiment. In the asymmetric pulse programme the reconversion block is kept constant roughly at the maximum of the DQ excitation time and only the excitation time is incremented.

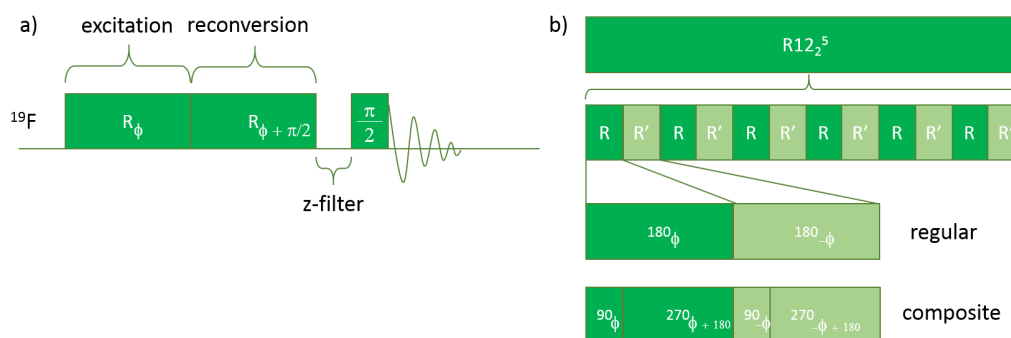


**Figure S9.** a) General scheme of an R-sequence with one excitation and one reconversion block. For a symmetric pulse scheme the two blocks are both incremented. In the asymmetric scheme the reconversion block is kept constant and only the excitation block is incremented. b) Construction of the R block with the example  $R12_2^5$ . On R block consists of 6  $RR'$  pulses of the phase  $\phi$  and  $-\phi$  that are performed within 2 rotor periods. The pulse can be either a  $180^\circ$  pulse or a composite of a back-to-back  $90^\circ$  and  $270^\circ$  pulse.

Before being able to perform DQ experiments we had to look for the R-sequence that suits best our needs. First, we were limited with the MAS spinning speed to 12 kHz, as this is the maximum MAS frequency of the used 3.2 mm  $^1\text{H}/^{19}\text{F}/\text{X}$  triple resonance probe head. There were at the moment of writing this manuscript 1.9 and 1.3 mm DNP probes present or under development, however their tuneability to  $^{19}\text{F}$  was not guaranteed. Furthermore, with the low concentrations of F-BTA in the PS the bigger capacity of the 3.2 mm rotor is also favourable.

Because of the strong  $^{19}\text{F}$ - $^{19}\text{F}$  spin coupling (2.91 Å, 4326 Hz) of the investigated F-BTA polymorph (ref 83, main text), an R sequence that does not need to perform the full R cycle to collect a point, but for which a point can be taken after every RR' block of the full R cycle is needed to be able to see the starting slope. Lastly, the R sequence needs to have a strong CSA compensation to be robust against unpaired electrons in the proximity, since those are needed to enhance the NMR signal by DNP.

Before testing different R sequences it was required to identify the spin system needed for the simulations. The  $^{19}\text{F}$ - $^{19}\text{F}$  spin pair in F-BTA is surrounded by the protons of the methyl and amide groups that exhibit heteronuclear  $^1\text{H}$ - $^{19}\text{F}$  couplings of up to 12 kHz. These couplings can interfere with the DQ build up curve. Therefore, we included the 14 closest protons of fluorine atoms of F-BTA into the simulation with a R12<sub>2</sub><sup>5</sup> sequence and compared the resulting build up curve with the one of a neat spin pair and the experimentally obtained one. The four methyl groups were treated as one proton, each and the position of this proton was set in the middle of the crystallographic positions of the three methyl protons. So, in total 6 dipolar couplings were included for each fluorine atom.

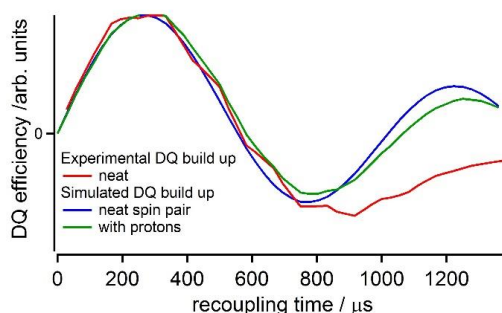


**Figure S10.** Measured (red) and simulated build up curves for the neat F-BTA system. In the blue curve the simulation just includes the isolated spin pair. The green curve includes the 14 protons closest to the spin pair.

The build up curve in Figure S10 that includes the protons is different from the one without the added protons, but it is not deviating significantly from it. The measured build up curve is mostly in between the two curves. This shows that the effect of the coupled protons on the R12<sub>2</sub><sup>5</sup> is already negligible at a spinning speed of 12 kHz and the simulation of a spin pair suffices for testing the different R sequences.

We performed a vast testing routine where we simulated the DQ build up curves for the  $^{19}\text{F}$ - $^{19}\text{F}$  spin pair from reference 83 (main text) for 6 pulse programs. For each pulse program, we tested the influence of an electron with a distance of 9.5 to 20 Å to the fluorine atoms in simulations. Additionally, we tested the effect of the composite pulse and the difference between the asymmetric and symmetric pulse sequence. The pulse sequences were chosen to have the least 2<sup>nd</sup> order terms, high rf stabilities, high nutation frequencies and a good DQ

efficiency.<sup>1</sup> Relevant information of the pulse sequences is given in Table S2. We measured the DQ build up on the neat F-BTA sample at room temperature and compared the resulting curve with the simulations.

**Table S3.** Nutation frequency at 12 kHz MAS frequency and the number of 2<sup>nd</sup> order dipolar and CSA terms for the tested pulse sequences. For all but the R12<sub>2</sub><sup>5</sup> only the nutation frequency of a composite pulse is given.

Sequence	$\nu_{\text{nut}}/\text{kHz}$	#2 <sup>nd</sup> order dipolar	#2 <sup>nd</sup> order CSA
R12 <sub>2</sub> <sup>5</sup> R=180°	36.0	24	36
R12 <sub>2</sub> <sup>5</sup> R=90°-270°	72.0	24	36
R14 <sub>2</sub> <sup>6</sup>	84.0	48	16
R18 <sub>2</sub> <sup>8</sup>	108.0	32	16
R18 <sub>4</sub> <sup>7</sup>	54.0	24	22
R20 <sub>2</sub> <sup>9</sup>	120.0	24	20
R20 <sub>6</sub> <sup>7</sup>	40.0	24	20

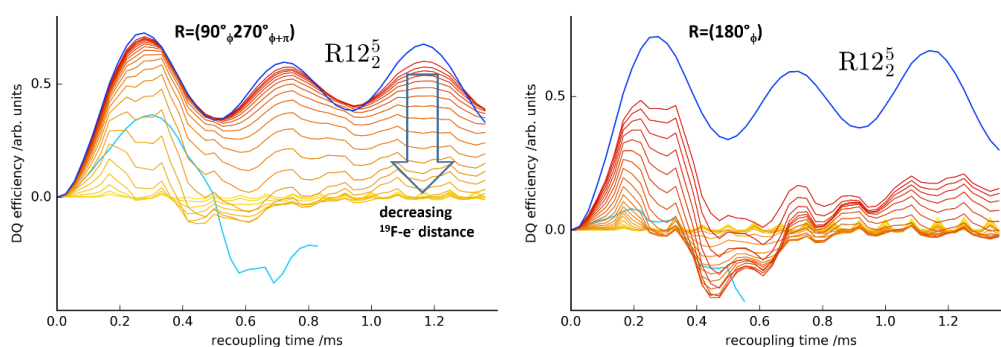


**Figure S11.** Experimental (F-BTA, light blue) and simulated DQ build up curves with a symmetric R12<sub>2</sub><sup>5</sup>-sequence. The dark blue curve is a build up curve for an isolated <sup>19</sup>F-<sup>19</sup>F spin pair. For the other curves a radical is added to the spin pair with a distances from 9.5 to 20 Å in 0.5 Å increments. The brightest yellow corresponds to the shortest distance the darkest orange to the longest distance. On the left a 90°-270°-composite pulse is used and on the right a plain 180° pulse is used for the R-block.

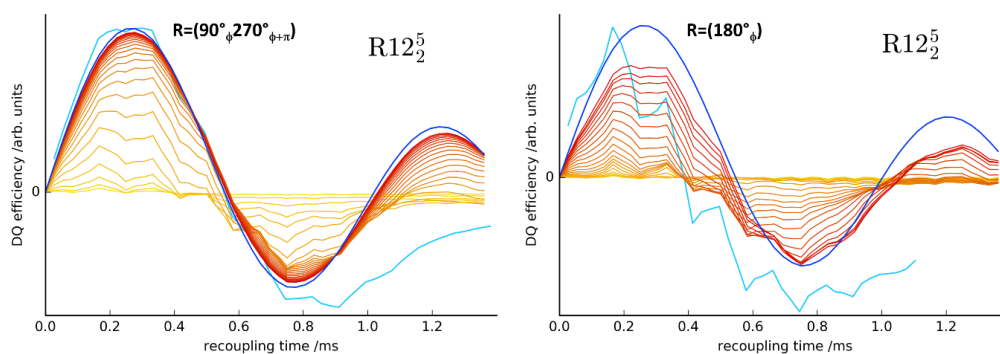


**Figure S12.** Experimental (F-BTA, light blue) and simulated DQ build up curves with an asymmetric  $R12_2^5$ -sequence. The dark blue curve is a build up curve for an isolated  $^{19}\text{F}$ - $^{19}\text{F}$  spin pair. For the other curves a radical is added to the spin pair with a distances from 9.5 to 20 Å in 0.5 Å increments. The brightest yellow corresponds to the shortest distance the darkest orange to the longest distance. On the left a  $90^\circ$ - $270^\circ$ -composite pulse is used and on the right a plain  $180^\circ$  pulse is used for the R-block.

Figures S11 and S12 show that the composite pulse is enhancing the performance of the R-sequence significantly. In the simulations for both the symmetric and the asymmetric sequence the composite ensured stability towards the influence of the radical. In the measurement on the neat F-BTA sample the asymmetric sequence (Figure S12) can be simulated nicely until a recoupling time of 0.8 ms. Whereas for the symmetric sequence not sufficient DQ intensity is reached and the measured build up curve goes negative after 0.5 ms which is not supposed to happen, as can be seen by the simulations. We checked if this effect also holds for other pulse sequences. For those, however, we only evaluated composite pulses, since their effect was so striking.

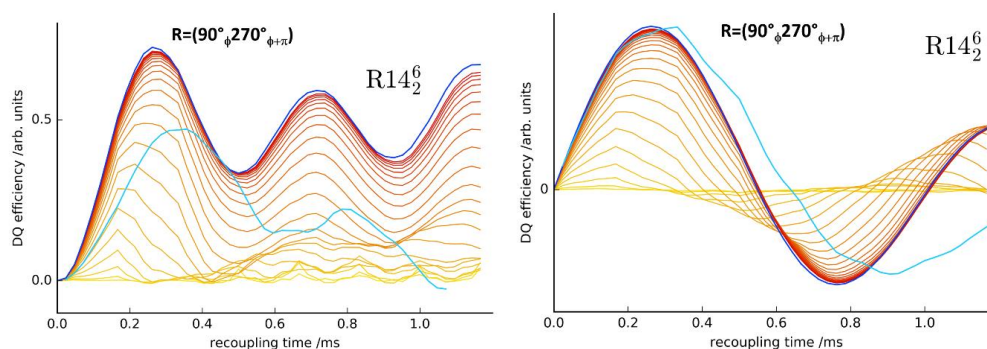


**Figure S13.** Experimental (F-BTA, light blue) and simulated DQ build up curves with a symmetric (left) and asymmetric (right)  $R14_2^6$ -sequence with a composite pulse. The dark blue curve is a build up curve for an isolated  $^{19}\text{F}$ - $^{19}\text{F}$  spin pair. For the other curves a radical is added to the spin pair with a distances from 9.5 to 20 Å in 0.5 Å increments. The brightest yellow corresponds to the shortest distance the darkest orange to the longest distance.

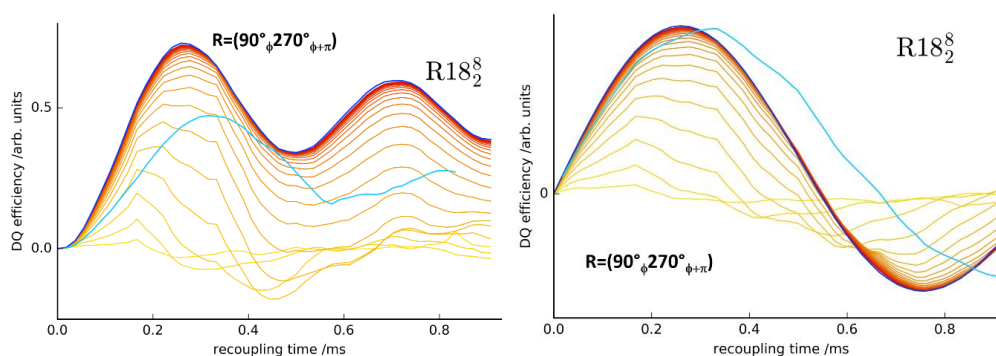


**Figure S14.** Experimental (F-BTA, light blue) and simulated DQ build up curves with a symmetric (left) and asymmetric (right)  $R18_2^8$ -sequence with a composite pulse. The dark blue curve is a build up curve for an isolated  $^{19}\text{F}$ - $^{19}\text{F}$  spin pair. For the other curves a radical is added to the spin pair with a distances from 9.5 to 20 Å in 0.5 Å increments. The brightest yellow corresponds to the shortest distance the darkest orange to the longest distance.

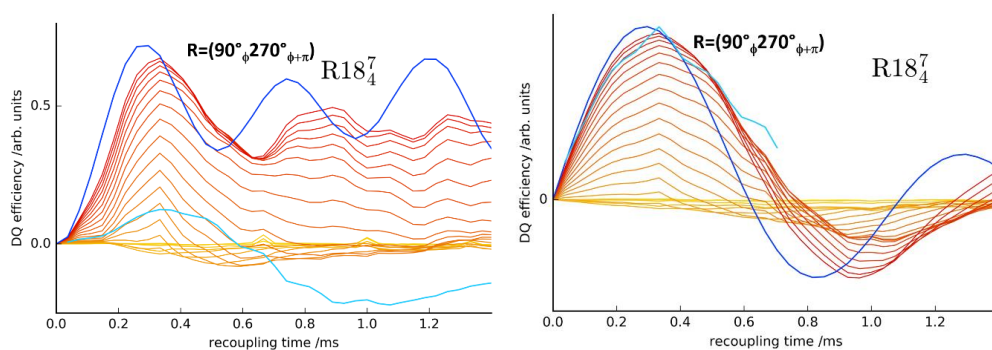


**Figure S15.** Experimental (F-BTA, light blue) and simulated DQ build up curves with a symmetric (left) and asymmetric (right)  $R18_4^7$ -sequence with a composite pulse. The dark blue curve is a build up curve for an isolated  $^{19}\text{F}$ - $^{19}\text{F}$  spin pair. For the other curves a radical is added to the spin pair with a distances from 9.5 to 20 Å in 0.5 Å increments. The brightest yellow corresponds to the shortest distance the darkest orange to the longest distance.

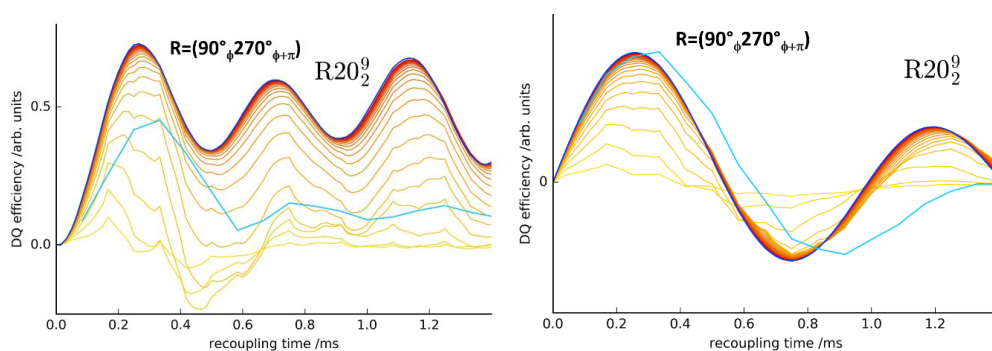


**Figure S16.** Experimental (F-BTA, light blue) and simulated DQ build up curves with a symmetric (left) and asymmetric (right)  $R20_2^9$ -sequence with a composite pulse. The dark blue curve is a build up curve for an isolated  $^{19}\text{F}$ - $^{19}\text{F}$  spin pair. For the other curves a radical is added to the spin pair with a distances from 9.5 to 20 Å in 0.5 Å increments. The brightest yellow corresponds to the shortest distance the darkest orange to the longest distance.

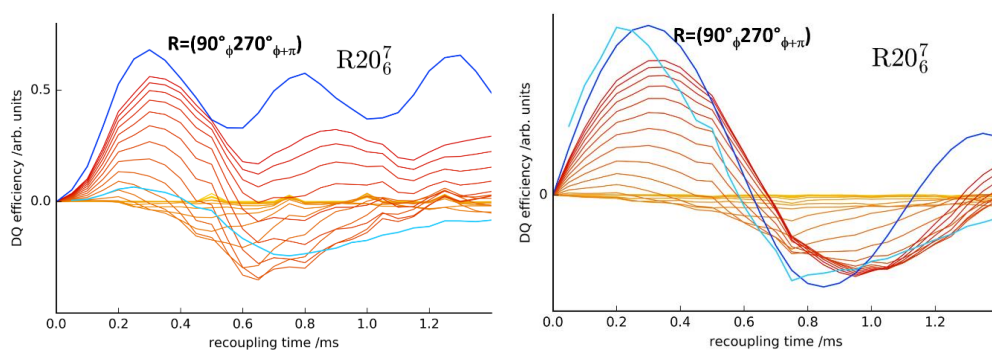


**Figure S17.** Experimental (F-BTA, light blue) and simulated DQ build up curves with a symmetric (left) and asymmetric (right)  $R20_6^7$ -sequence with a composite pulse. The dark blue curve is a build up curve for an isolated  $^{19}\text{F}$ - $^{19}\text{F}$  spin pair. For the other curves a radical is added to the spin pair with a distances from 9.5 to 20 Å in 0.5 Å increments. The brightest yellow corresponds to the shortest distance the darkest orange to the longest distance.

For all sequences it is evident that the asymmetric sequence is performing better than the symmetric one as the agreement between the measured build up curve and the simulated build up curve for the isolated spin pair is always higher than for the corresponding symmetric build up curve. Therefore, we focus the forthcoming discussion on the asymmetric sequences. The different sequences are reacting differently to the presence of the electron. For short distances of the radical to the spin pair, the build up curve is significantly attenuated and the frequency of the build up curve is reduced, meaning the maximum and the minimum are shifted to shorter recoupling times. Although this effect is less pronounced for  $R12_2^5$  and  $R20_2^9$ . For  $R18_4^7$  and  $R20_6^7$  this frequency is reversed for longer distances. At longer distances the build up curves for  $R18_2^8$ ,  $R14_2^6$ ,  $R12_2^5$  and  $R20_2^9$  almost perfectly follow the curve of the isolated spin pair. However, the agreement between the measurement and the simulation is only very good for  $R12_2^5$ . This is why we took this pulse sequence for our measurement of the F-BTA within PS.

**References**

- (1) Kristiansen, P. E.; Mitchell, D. J.; Evans, J. N. S. Double-quantum dipolar recoupling at high magic-angle spinning rates. *J. Magn. Reson.* **2002**, *157*, 253–266.

## 4.8 DNP Enhanced Solid-State NMR Spectroscopy Meets Microplastic - Sample Preparation for Optimal Sensitivity Enhancement

This work is a cooperation between the Inorganic Chemistry III and the Macromolecular Chemistry I of the University of Bayreuth and the Physical and Theoretical Chemistry of the FU Berlin, with the following authors: K.P. van der Zwan, A. Mauel, W. Riedel, N. Meides, T. Fischer, M. Meinhart, P. Strohriegel, T. Risse, J. Senker.

My contributions are:

- conception and shared main authorship
- performing all DNP enhanced NMR experiments
- shared preparation of all polymer/radical compounds
- sample preparation for the EPR experiments

The contributions of the other authors are:

- conception and authorship of the article
- synthesis of the materials
- controlled weathering of PS
- performing EPR measurements
- conventional ss-NMR and liquid state NMR experiments

## DNP Enhanced Solid-State NMR Spectroscopy Meets Microplastic – Sample Preparation for Optimal Sensitivity Enhancement

Kasper P. van der Zwan,<sup>a‡</sup> Anika Mauel,<sup>a‡</sup> Wiebke Riedel,<sup>b</sup> Nora Meides,<sup>c</sup> Tamara Fischer,<sup>a</sup> Marcel Meinhart,<sup>a</sup> Peter Strohriegel,<sup>c</sup> Thomas Risse,<sup>b</sup> Jürgen Senker<sup>a\*</sup>

<sup>a</sup> Inorganic Chemistry III and Northern Bavarian NMR Center, University of Bayreuth, Universitätsstraße 30, D-95447 Bayreuth, Germany

<sup>b</sup> Physical and Theoretical Chemistry, Institute of Chemistry and Biochemistry Freie Universität Berlin, Arnimallee 22, 14195 Berlin, Germany

<sup>c</sup> Macromolecular Chemistry I, University of Bayreuth, Universitätsstraße 30, D-95447 Bayreuth, Germany

\* [juergen.senker@uni-bayreuth.de](mailto:juergen.senker@uni-bayreuth.de) 0049-(0)921-552532;

<sup>‡</sup>These authors contributed equally to the manuscript

### Abstract

Pollution with microplastic particles is a major environmental problem of our time. However, little is known about the ecological hazards degraded polymer particles pose. To answer this, a qualification and quantification of the functional groups created by photooxidation of the polymer is necessary. A versatile tool to study this is the bulk method NMR spectroscopy. However, the low sensitivity of this technique makes it difficult to identify and correctly quantify defects in small concentrations. The sensitivity of NMR spectroscopy can be boosted by dynamic nuclear polarisation. For this technique persistent radicals are applied to the sample. In this work, we investigate four methods to apply these radicals to weathered microplastic samples and discuss the benefits and drawbacks of each method. Our findings show that dissolving the microplastic particles in a solution of AsymPol in trichloroethylene and evaporating the solvent, to create a film yields the best sample for DNP enhanced NMR spectroscopy, as no disturbing solvent peaks remain in the spectrum and the measurement time can be decreased by a factor 35 compared to conventional solid state NMR spectroscopy. With this enhanced sensitivity we were able to measure and identify all defects of a microplastic sample weathered for 3200 h in less than a minute. Furthermore, in a microplastic sample weathered for 400 h, defects are observed for the first time. This application of DNP enhanced NMR spectroscopy will allow for rapid screening of weathered microplastic particles enabling defect quantification at low concentrations.

## Introduction

Plastics became indispensable in our everyday life since their beginning mass production in the 1950s.<sup>1</sup> Despite their advantageous material properties leading to a wide range of applications, accumulation of mismanaged plastic waste in the environment poses an emerging ecological risk.<sup>2</sup> Until 2015, 6300 million metric tons of plastic waste were generated worldwide. Thereof, 79 % accumulate in landfills or the natural environment.<sup>1</sup> Particularly polyethylene (PE), polypropylene (PP) and polystyrene (PS) are found in marine and terrestrial debris.<sup>2-4</sup> This is not surprising since they are commonly used in disposable single-use items such as packaging.<sup>1</sup> After entering the environment polymers undergo biotic and abiotic degradation processes causing fragmentation and consequently the formation of secondary microplastic (MP) particles.<sup>3,5,6</sup> The definition of MP particles covers plastic fragments of all polymer types with their largest dimension ranging from 1 – 1000  $\mu\text{m}$ .<sup>7</sup> Degradation of commodity plastics with carbon backbones such as PE, PP and PS is mainly driven by photooxidation and mechanical stress.<sup>6,8-10</sup> During photooxidation crosslinking and chain scissions occur.<sup>6</sup> The latter results in the formation of polar defects such as ketones, carboxylic acids, vinylidenes, peroxides and alcohols.<sup>11-15</sup>

While the ecological risks of microplastic regarding additive leaching,<sup>16-18</sup> biofilm formation<sup>19-23</sup> and persistent organic pollutant (POP) delivery are vastly discussed,<sup>24-28</sup> little is known about the hazards which the polymers and degradation products pose itself. To evaluate these potential environmental hazards, knowledge about the quantities of polymer defects is essential. To analyse polymer defects typically Fourier-Transform Infrared (FTIR) spectroscopy is applied.<sup>9,29-33</sup> However, the surface dependence of attenuated total reflection (ATR)-FTIR spectroscopy hinders quantification.<sup>34</sup> As alternative Nuclear Magnetic Resonance (NMR) spectroscopy can be used. This bulk method is a versatile tool to analyse and quantify molecular groups that form during photooxidative degradation of the microplastic particles.<sup>6</sup> However, NMR spectroscopy suffers from intrinsic low sensitivity leading to very long measurement times, especially when investigating defects that occur at low concentrations.

A powerful technique to overcome this lack of sensitivity is enhancing the NMR signal by dynamic nuclear polarisation.<sup>35,36</sup> With this technique the spin polarisation of the electron is transferred to the nuclear spin polarisation.<sup>35,36</sup> Since the electron spin is by a factor of 658 higher polarised than the proton nuclear spin, this number sets the theoretical limit for the signal enhancement of proton spectra.<sup>37</sup> As the sensitivity – the signal to noise ratio per square root of time – and with it the measurement time scales with the square of the intensity enhancement, DNP is theoretically capable to reduce the measurement time by a factor of 433248.<sup>38,39</sup>

At the end of the last century this polarisation technique was introduced to solid state NMR spectroscopy at high magnetic fields and with magic-angle-spinning (MAS).<sup>40–43</sup> This drastically reduced the detection limit of solid state NMR spectroscopy by enhancing the signal intensity by a factor greater than 600 for idealised samples.<sup>44</sup> Regularly and easily enhancements of 5-100 are achieved for materials samples.<sup>45–53</sup> To use DNP enhanced NMR spectroscopy persistent radicals<sup>54–59</sup> must be introduced to the sample.

The first way the radicals were applied in solid state chemistry was by dispersing the sample in a radical containing solution that forms a glass when rapidly cooled to 100 K.<sup>60</sup> This technique is mainly used in structural biology and referred to as a frozen solution.<sup>47</sup> For materials the powdered – often porous – sample is impregnated by a radical containing solution and transferred to the rotor as a wet powder. This technique is known as incipient wetness impregnation (IWI).<sup>45,52,61</sup>

For polymer samples other preparation methods were tested like co-polymerisation with a monomer containing nitroxide radicals.<sup>62</sup> If the radical containing solution is a solvent for the polymer, a 1:1 mixture of the two leads to a gel that forms a glass, when cooled to the measurement temperature of 100 K.<sup>63</sup> The solvent can also be evaporated so that the polymer forms a film and incorporates the radical.<sup>64</sup> An approach to completely work solvent free has been shown for a pharmaceutical formulation for which the radical was co-extruded with a polymer and an active pharmaceutical ingredient.<sup>65</sup>

In this work, we compare the four preparation techniques IWI, glass forming (GF), film casting (FC) and extrusion (EX) towards their applicability for micropalstic samples. We discuss the benefits and drawbacks of each technique and what an idealised sample preparation for microplastic should look like.

## **Experimental Section**

### Materials

The used Polystyrene grade was PS 158N (INEOS Styrolution, Frankfurt am Main, Germany) containing only 600 ppm of zinc stearate as additive. The pellets were grinded in a ZM200 freezer mill (Retsch, Haan, Germany) and sieved to 125 – 200  $\mu\text{m}$  sized particles with an Alpine Air Jet Sieve E200 LS (Hosokawa Alpine AG, Augsburg, Germany). The synthesis of AsymPol was inspired by literature procedures but slightly altered.<sup>55,66</sup> The complete synthesis is given in the supporting information section 1. AMUPol was obtained from Cortecnet (France) and used as received. Amidine functionalised PS was synthesised according to the supporting information section 1.

#### Controlled aging

For controlled accelerated weathering the industrial test chamber Q-SUN XE-3 (Q-LAB Corporation, Westlake, OH) equipped with three xenon arc lamps with Daylight-Q filter systems was used. The relative humidity was set to 50% and the total irradiance amounted to  $594 \text{ W/m}^2$  which corresponds to a 5-fold enhancement compared to average mid-European irradiation. The PS particles were constantly stirred in deionised water ( $55^\circ\text{C}$ ) in the test chamber. For more details see reference <sup>6</sup>.

#### Sample preparation for DNP Experiments

*IWI.* For the samples prepared by IWI 25 mg of powder was impregnated by 25  $\mu\text{l}$  of a 15 mM AMUPol solution in a solvent mixture of Glycerol-d8,  $\text{D}_2\text{O}$ ,  $\text{H}_2\text{O}$  in a ratio 6:3:1. The solvent/powder mixture was stirred on a watch glass until the powder looked homogeneously wetted. Then it was transferred to the 3.2 mm sapphire rotor and sealed with a Teflon plug and a  $\text{ZrO}_2$  cap.

*Glass forming.* For the GF procedure 25 mg of powder were mixed with 25  $\mu\text{l}$  of a 15 mM solution of AsymPol in 1,1,2,2-tetrachloroethane (TCE). The mixture was stirred on a watch glass. The resulting gel was transferred to the 3.2 mm sapphire rotor and sealed with a Teflon plug and a  $\text{ZrO}_2$  cap. Note, that not the whole gel could be transferred and a challenge exist in reducing the air bubbles in the rotor.

*Film casting.* To prepare the films 50 or 100 mg of PS were spread out on a glass plate. 250 or 500  $\mu\text{l}$  of a 3 mM AsymPol solution in either TCE, tetrahydrofuran (THF) or trichloroethylene (TriCE) were pipetted onto the powder and thorough fully stirred. The resulting viscous solution was equally distributed on the glass plate. The films were either dried for 60 h in a vacuum oven at  $50^\circ\text{C}$  or in the fume hood at ambient conditions. The films were scratched of the glass plate and transferred into the 3.2 mm sapphire rotor. The sample mass was between 9 and 19 mg. The exact masses and an analysis of the solvent remaining in the films is found in the supporting information sections 2-4.

*Extrusion.* For the DNP experiments 392 mg of weathered or non-weathered PS 158N, and 8 mg of AsymPol powders were mixed and shaken. The mixture was preheated on a glass plate to increase the particle size. Afterwards it was compounded with a twin-screw mini extruder ZE 5 HMI (Three-Tec, Seon, Switzerland) at  $180^\circ\text{C}$  and a 1 mm nozzle plate. The polymer strand was directly collected from the nozzle and cut into pieces of roughly 1 cm length. Typically 3-6 of this small pieces of strand were put into a rotor and sealed with a  $\text{ZrO}_2$  cap. This resulted in sample masses between 15.64 mg.

### EPR Experiments

Continuous wave (cw) Electron Paramagnetic Resonance (EPR) measurements at X-band frequencies were conducted with a Bruker B-ER420 spectrometer upgraded with a Bruker ECS 041XG microwave bridge and a lock-in amplifier (Bruker ER023M). For the measurements, a Bruker SHQ resonator or a Bruker TE<sub>102</sub> resonator was used applying a modulation amplitude of 1 G and a modulation frequency of 100 kHz. For direct comparison of the spectra obtained with different resonators, the magnetic field axis were shifted to account for differences in the microwave resonance frequency. The EPR measurements were conducted either at room temperature or at 150 K. The samples were measured in quartz tubes of 2.9 mm outer diameter containing typically 10 mg of powder or a few pieces of the polymer strand. For the frozen solutions typically 20  $\mu$ l of the solution was added to the quartz tube. All spectra are normalized to their peak-to-peak amplitude.

### DNP Experiments

All DNP enhanced NMR spectroscopic measurements were performed on a Bruker Avance III 400 DNP spectrometer working at  $B_0 = 9.7$  T equipped with a Bruker gyrotron (9.7 T, 263.4 GHz, 115 mA beam current). The low-temperature <sup>1</sup>H/X/Y triple resonance probe was installed. The resonance frequencies were 401.63 MHz for <sup>1</sup>H and 100.99 MHz for <sup>13</sup>C at 110 K and if not stated differently, a MAS frequency of 11.5 kHz was chosen. Recycle delays were set to match 1.3 times the beforehand estimated build-up time and were typically 0.5 – 3 s.

<sup>13</sup>C{<sup>1</sup>H} CP MAS spectra with 32-51200 scans were recorded with a ramped CP<sup>67</sup> where the power on the proton channel was varied linearly during the contact of 1.1 ms from 50-100% with a maximum of 94 kHz. During acquisition protons were decoupled at 87 kHz using the spinal 64<sup>68</sup> decoupling sequence.

### Conventional solid-state NMR Experiments

Conventional NMR experiments were performed on a Bruker Avance III HD spectrometer at a field of 9.7 T on a Bruker 3.2 mm H/X/Y triple resonance probe. The Larmor frequencies are 400.13 MHz for <sup>1</sup>H and 100.63 MHz for <sup>13</sup>C. The same experiments as under DNP conditions were performed. The maximum proton power during the CP contact was 63 kHz and the decoupling was 70 kHz on the proton channel. DNP enhanced and conventional NMR spectra were referenced to tetramethylsilane (TMS) using adamantane as a secondary reference.

### Liquid state NMR Experiments

Liquid state <sup>1</sup>H NMR spectroscopic experiments were recorded on a Bruker Avance-III HD spectrometer with 5 mm CryoProbe™ Prodigy BBO 500 S2 head operating at a  $B_0$  field of 11.7 T (<sup>1</sup>H:  $\nu_0 = 500.1$  MHz). Single pulse (SP) excitation with a recycle delay of 1 s and a pulse length of 3.8  $\mu$ s corresponding to a 30° tip angle was used. Samples were dissolved in

deuterated chloroform ( $\text{CDCl}_3$ ). Via the residual solvent resonance all spectra were referenced to TMS.

### Results and Discussion

Forthcoming, we investigate four different preparation techniques for DNP enhanced NMR spectroscopy, namely glass forming (GF), incipient wetness impregnation (IWI), extrusion and film casting (FC) towards their applicability for weathered microplastic samples. The reason to use DNP enhanced NMR spectroscopy is to reduce the measurement time and the detection limit of NMR spectroscopy, while still being quantitative. The enhancement originates from the phenomenon that upon microwave irradiation the high electron magnetic polarisation of persistent radicals that are applied to the sample is transferred to the nuclear magnetic polarisation.<sup>36,69</sup> This promises a significant gain in sensitivity and thus grants an opportunity for a faster investigation of MP samples or an earlier detection of minority species in natural samples. A successful DNP enhanced NMR spectrum of weathered MP that is still quantitative fulfils the following conditions:

- Enhancement of the spectrum with microwave irradiation
- Homogeneous radical distribution and thus homogeneous enhancement
- No decrease in resolution
- No disturbance by additional resonances
- Preferably reduction in measurement time
- Minimum sample usage

Not all preparation techniques fulfil these requirements. With the example of the GF technique the challenges of the different preparation techniques are introduced and discussed.

For GF, roughly 20 mg of the 3200 h weathered MP sample is dissolved in a solution of 15 mM AsymPol (Figure 1b) in TCE. The resulting gel is transferred to the MAS rotor, before it is inserted into the pre-cooled NMR magnet where the gel vitrifies and forms a glass. First, we check for an enhancement of the signal. This is done by performing the same (short) measurement once with microwave irradiation and once without (Figure 1a).<sup>40</sup> From the intensity difference of those two spectra, the enhancement is calculated. In the case of the DNP enhanced NMR spectrum of the 3200 h weathered microplastic particles prepared with the GF technique in Figure 1 the enhancement ( $\epsilon_{\text{on/off}}$ ) is 12. Since the signal to noise ratio increases with the square of the enhancement, this enhancement corresponds to a reduction of measurement time by a factor of 144.

Additionally, the waiting time between consecutive scans is crucial for the measurement time. In conventional NMR spectroscopic experiments, the required waiting time depends on the spin-lattice relaxation time  $T_1$  ( $T_1$  ( $^1\text{H}$ ) of PS = 5 s at RT) and should typically amount to 3-5 times  $T_1$ . In contrast, in DNP enhanced NMR spectroscopic experiments the waiting time relies on the DNP build-up time  $T_b$ . This value is determined with the same type of experiment as  $T_1$  and is for the GF technique 1.1 s (Figure 1b). Since  $T_b$  is in this case almost by a factor 5 smaller than  $T_1$ , the measurement time is further reduced by the same factor.

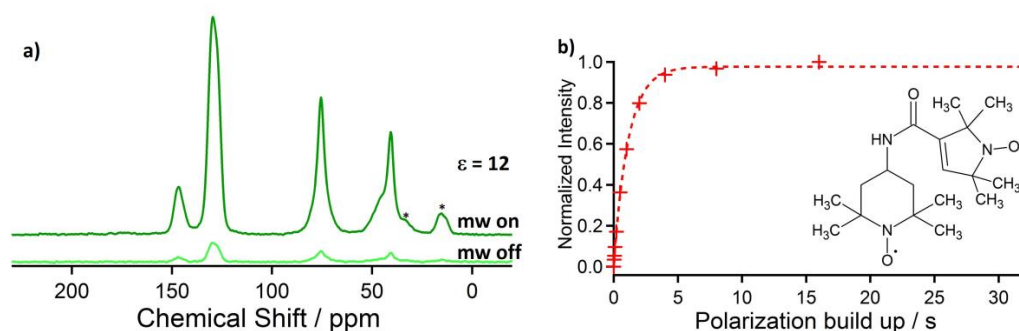


**Figure 1.** a) DNP enhanced  $^{13}\text{C}\{^1\text{H}\}$ CP NMR spectra of 3200 h weathered PS microplastic particles with a 1:1 mixture with a 15 mM AsymPol solution in TCE. The bright green spectrum shows the non-enhanced spectrum without microwave irradiation and 32 scans. The dark green spectrum shows the same measurement with microwave irradiation. Spinning side bands are marked with an asterisk. b) Measurement of the DNP build-up time with a saturation recovery experiment. The inset shows the molecular formula of AsymPol.

The presence of the radicals reduces the nuclear relaxation times ( $T_1$ ,  $T_2$ ).<sup>70,71</sup> The reduction of  $T_2$  leads to an increased linewidth of the spectrum. The low temperatures used for DNP further decrease  $T_2$ . Therefore, the resolution of the spectra needs to be compared to a spectrum without any DNP treatment at room temperature. The conventional NMR spectrum of PS microplastic (Figure 2a other) already shows broad resonances (550 – 561 Hz) due to its polymeric nature. The peak widths of the NMR resonances of the DNP enhanced spectrum (Figure 2a green) are slightly enhanced (592 – 650 Hz). This shows that the  $T_2$  relaxation enhancement is not significant. Consequently, reduction of resolution is not a limiting factor for DNP analysis of microplastic.

For quantitative measurements, a homogeneous enhancement of the sample is essential. To ensure this, the radicals must be homogeneously distributed. This might be probed by EPR spectroscopy. When the radicals are homogeneously distributed and sufficiently diluted the EPR spectrum is dominated by the intramolecular interactions, whereas radical clusters with pronounced interactions between different AsymPol molecules would be indicated by a broad

featureless EPR signal.<sup>72</sup> To investigate the radical distribution for the GF method, in total eight solutions with AsymPol concentrations between 4 and 500 mM in TCE were prepared. To create a frozen solution the EPR tube was inserted in the pre-cooled EPR set up at 150 K to ensure fast freezing. The line shapes of the EPR spectra do not significantly change for AsymPol concentrations below 31 mM (Figure 1b) indicating that for these concentrations, intermolecular interactions between different AsymPol molecules are overall small. Since the shape at 150 K also does not change when adding PS (SI Figure S6), we can safely assume a homogeneous radical distribution for the concentration used to enhance the signal in Figure 1a (15 mM).

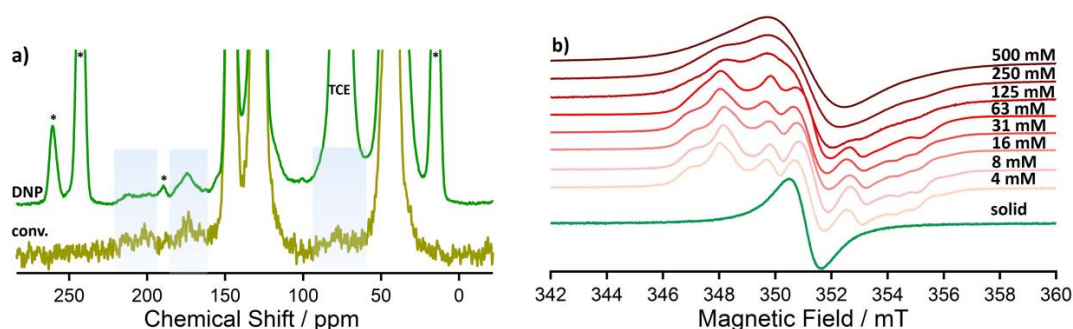


**Figure 2. a)** DNP enhanced  $^{13}\text{C}\{^1\text{H}\}$ CP NMR spectrum of 3200 h weathered PS microplastic particles (green) and a conventional  $^{13}\text{C}\{^1\text{H}\}$ CP NMR spectrum (ochre). With the light blue boxes the spectral regions for ketones, carboxylic acids and peroxides (from left to right) are marked. Spinning side bands are marked with an asterisk. For the spectra, 2976 and 23052 scans were recorded for the DNP enhanced and the conventional spectrum, respectively. The MAS frequencies were 11.5 (DNP) and 20 kHz (conv.). **b)** EPR measurements of frozen solutions of AsymPol in TCE with concentrations from 4 to 500 mM as indicated in the Figure. The green curve shows a spectrum of AsymPol crystals.

For instance, the resonances of the ketone (210-190 ppm) and carboxylic acid (180-160 ppm) defects are very well resolved, although the spectrum was recorded with just 2976 scans, whereas for the conventional NMR spectroscopy a similar sensitivity could not be obtained with 23052 scans. The spectral region of the peroxide resonances (85-60 ppm) shows a drawback of DNP enhanced NMR spectroscopy. To apply the persistent radical with the GF method a solvent is needed. The signal of the solvent is enhanced as well and overlaps completely with the peroxide resonances. The spinning side band of the solvent signal is also interfering with the quantification of the spectrum since it shows up between the other two defect resonances.

Another standard preparation method for DNP enhanced NMR spectroscopy is the incipient wetness impregnation (IWI). Here, the sample is impregnated with a radical containing solution that deposits the radical on the surface of the sample. Therefore, the surface of the

impregnated particle is stronger enhanced than the bulk of the material. This can be an interesting feature, since it is proposed that the defects for MP degradation primarily form at the surface of the particles. A prerequisite is therefore, that the radical solution is not dissolving the sample but still wetting the surface and that it still forms a glass upon rapid cooling. Especially for the weathered MP samples that have short chain lengths, not many solvents fulfilled this requirements. Therefore, 25 mg of the weathered MP sample were impregnated by a 15 mM AmuPol solution in Glycerol-d6/D<sub>2</sub>O/H<sub>2</sub>O with a solvent ratio of 6/3/1. However, we see that the NMR spectrum is not enhanced at all (Figure 3a). The only resonances that are enhanced are the ones of the glycerol that is used in the impregnation matrix. This is because PS is not easily wetted without being dissolved. Only when there are a lot of polar groups at the surface, like amidine groups, a weak enhancement of 2 is obtained (Figure 3b). Another small disadvantage is the compared to AsymPol longer T<sub>b</sub> of 3.1 s that is common for AMUPol.<sup>55,57</sup> Furthermore, isotropic resonances and the spinning side bands of the glycerol that is part of the impregnation solution dominate the spectral regions where the defects are expected, regardless of the spinning speed. Since for both, GF and IWI, the solvent signal is overlapping with interesting spectral regions, sample preparation without solvents or with solvent removal would be desirable.

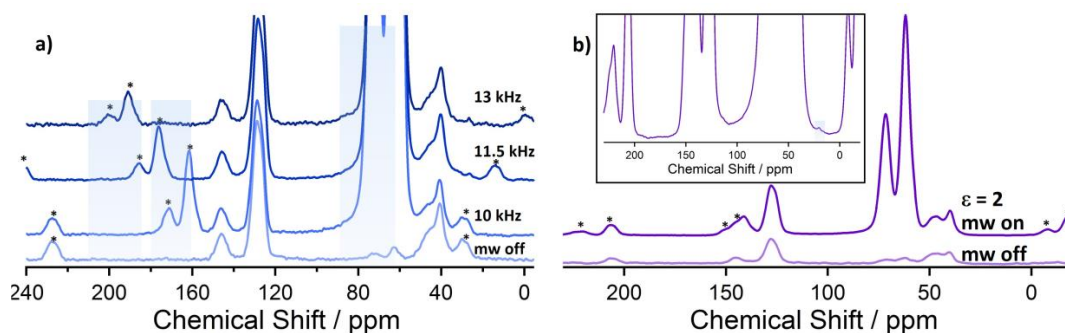


**Figure 3. a)** DNP enhanced  $^{13}\text{C}\{^1\text{H}\}$ CP NMR spectra of 3200 h weathered PS microplastic particles. The bottom most spectrum shows the non-enhanced spectrum without microwave irradiation at 10 kHz MAS frequency. The above spectrum shows the same measurement with microwave irradiation. The other two spectra are measured at MAS frequencies of 11.5 and 13 kHz, respectively. With the light blue boxes the spectral regions for the ketone, carboxylic acids and peroxides (from left to right) are highlighted. **b)** DNP enhanced  $^{13}\text{C}\{^1\text{H}\}$ CP NMR spectra of amidine functionalised microplastic particles. The dark violet spectrum is recorded with microwave irradiation, the lighter one without. The inset is a zoomed in spectrum recorded with 8192 scans. The light blue box highlights the amidine resonance. Spinning side bands are marked with an asterisk.

For sample preparation without solvents, the radical can be compounded by extrusion.<sup>65</sup> The microplastic particles are mixed with AsymPol and then extruded in a twin-screw extruder at

180 °C to get an AsymPol concentration of 60  $\mu\text{mol/g}$ . According to the TGA measurement this does not affect the radical (SI Figure S7). While this technique works well for the virgin PS particles, it is not applicable for the weathered samples. This might be due to the distorted mechanical properties, the degraded polymer chains consisting of highly polar poly- and oligomers or the high cross-linking degree of the weathered MP.<sup>6</sup> When the PS particles weathered for 3200 h were extruded, they were not properly transported by the extrusion screws and needed to be flushed out by virgin PS. Weathered and virgin PS mixed in the process making quantitative analysis impossible. Additionally, the method has the disadvantage of requiring considerable sample amounts ( $\sim 300$  mg). Still, it shows a decent enhancement of 8 (Figure 4) and the radical is homogeneously distributed within the sample as confirmed by an EPR measurement (SI Figure S8).

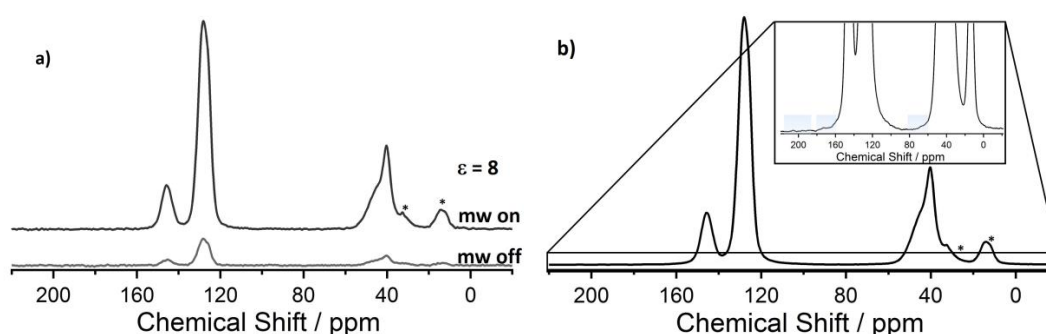


**Figure 4.** a) DNP enhanced  $^{13}\text{C}\{^1\text{H}\}$ CP NMR spectra of 3200 h aged PS microplastic particles extruded with AsymPol. The light grey spectrum shows the non-enhanced spectrum without microwave irradiation and 32 scans. The dark grey spectrum shows the same measurement with microwave irradiation. b) The same measurement as in a) with 3072 scans. With the light blue boxes the spectral regions for the ketone, carboxylic acids and peroxides (from left to right) are highlighted. Spinning side bands are marked with an asterisk.

Another option to reduce the intensity of the solvent signal is the use of the FC technique.<sup>30,31</sup> 50 mg of the microplastic particles are dissolved in a solvent with a 3 mM AsymPol content. Afterwards the films are cast on glass plates. The glass plates were dried either in a fume hood or in a vacuum oven at 50 °C. We investigated the potential of TCE, THF and TriCE as solvents. The AsymPol concentration of the solutions is chosen to obtain films with a radical concentration of 25  $\mu\text{mol/g}$  PS, which corresponds to 25 mmol/l. Since it is known that treating samples with DNP juices bears a potential to alter the sample<sup>73</sup> and heat might do so as well, reference films with virgin PS were prepared for each solvent.

For all films, an  $\varepsilon_{\text{on/off}}$  of 7 or 8 is obtained in the spectra (SI Figure S9) with a  $T_b$  between 0.31 and 0.67 s. The line width is similar as for the spectrum obtained with the GF method.

Reference measurements at room temperature show that the same line width is obtained for a film with and without radical. These are smaller than the one obtained in the DNP enhanced spectra (SI Figure S10). This shows that the  $T_2$  reduction due to the decrease in temperature is the main factor that determines the resolution and that sample preparation and even the introduction of the radical plays a minor role. Therefore, the ketone and carboxylic acid defects are again well resolved in the respective NMR spectra, especially when comparing them to the unweathered PS film (Fig 5a). The residual solvent in the film obtained from TCE covers the area with the expected peroxide defects. Also in the film obtained from THF, parts of the solvent remain in the polymer. However, the corresponding resonances at 64.7 and 22.7 ppm are much smaller and sharper, so that the broad peroxide resonance is visible. The films obtained from TriCE show a very weak shoulder at 114 ppm corresponding to that solvent. This signal, however, is not interfering with any photooxidative aging defects and is only slightly broadening the backbone signal. A detailed analysis and quantification of the residual solvents was done by liquid state NMR and is found in the supporting information (SI sections 3 and 4). It confirmed that the TriCE films have the smallest residual solvent content (0.6 – 1.5 %), whereas the films from TCE and THF both have 5-10 % residual solvent.

In the final films, the main component is PS. The distribution of AsymPol in these films was investigated by EPR measurements (Fig. 5b). The EPR spectra of the film samples measured at room temperature show a similar – albeit not the same - line shape as a frozen solution of AsymPol in TCE at 150 K. The differences to the frozen solution spectrum are most pronounced for samples with higher amounts of residual solvent, i.e. for TCE and THF. Please note that the spectra cannot be described by a simple convolution of the frozen AsymPol in TCE solution spectra with either the spectra of a liquid AsymPol in TCE solution or of pure AsymPol. The characteristic feature that the peak at 351 mT is higher than the one at 348 mT is also present in the RT measurement of the GF sample (Figure S6), indicating that the high amount of residual solvent in the films cast from TCE and THF leads to residual viscosity of these films, allowing for faster AsymPol dynamics than in the film cast from TriCE.

It is interesting to note that the differences in line shape are less pronounced for the unweathered samples (Fig. S7) suggesting a different solubility and thus interaction of AsymPol and PS in the different solvents leading also to different drying behaviours of the films. Since the virgin PS films are less affected the different polarity, chain length and crosslinking density of the weathered film<sup>6</sup> apparently effects the AsymPol distribution in the polymer. Yet, the low amount of residual solvent in the film cast from TriCE giving an EPR spectrum very similar to the frozen solution suggests a rather homogeneous distribution of AsymPol also in the weathered PS and thus, TriCE to be best suited as solvent for the weathered samples.

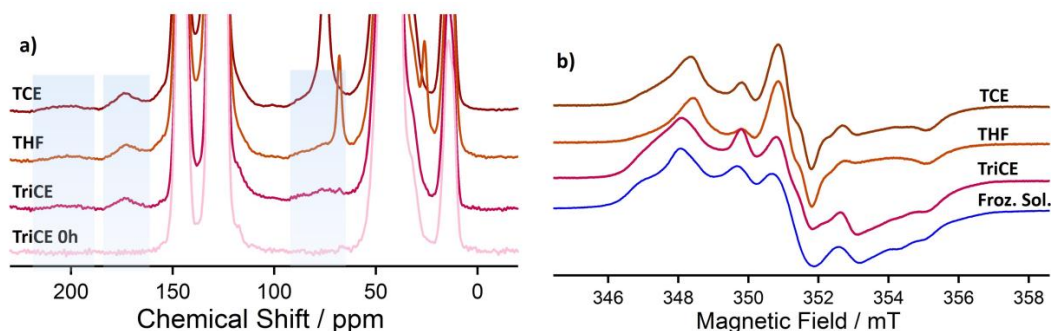


**Figure 5 a)** DNP enhanced  $^{13}\text{C}\{^1\text{H}\}$ CP NMR spectra of 3200 h weathered PS microplastic films obtained from TCE, THF and TriCE (top to bottom) as well as a reference film of unweathered PS obtained from TriCE, the respective spectra of the 0h TCE and THF films are in the SI (Figure S12). The spectrum of the film obtained from TCE was measured with 2048 scans. The other spectra were recorded with 1024 scans. The spectra are scaled to sample weight and amount of scans. With the light blue boxes the spectral regions for the ketone, carboxylic acids and peroxides (from left to right) are marked. **b)** EPR spectra of the weathered PS films with AsymPol obtained from TCE, THF and TriCE measured at room temperature, as well as a 31 mM frozen solution of AsymPol in TCE measured at 150 K.

The only drawback of the FC method compared to the GF method is that twice as much sample is used, which especially for samples from a natural sources might be a limiting factor.

All preparation methods for DNP enhanced NMR spectroscopy have in common that they are – compared to regular NMR – destructive methods. This means the sample needs to be altered to obtain a result and can therefore not be retained in its original shape as microparticles. For the IWI technique thoroughly cleaning might preserve the particle shape but residues of the radical or the solvent might still remain. The other techniques obviously change the material morphology. Qualitatively, the film casting method outperforms the other techniques because here only a small solvent signal is visible in the spectrum and the microplastic defects remain intact throughout the process. Whereas, for the IWI and GF techniques the solvent signals are dominating the respective spectra.

For a quantitative comparison of the sensitivity gain, the obvious value to compare would be the  $\varepsilon_{\text{on/off}}$  values of each sample. However, this value might be misleading as depolarisation of the spectrum without microwave might occur.<sup>74,75</sup> A better value, especially when comparing different techniques is the absolute sensitivity ratio ASR.<sup>76</sup> To calculate the ASR the signal to noise ratio is divided by the square root of the measurement time.<sup>38</sup> For an even better comparison, it can also be weighed by the sample mass, if this is heavily deviating between samples. Since the ASR takes the measurement time into account, it accounts for the reduced recycle delay of the DNP enhanced NMR spectra, compared to conventional NMR

measurements. Furthermore, it also features different polarisation speeds ( $T_b$ ) of different DNP samples. So, the ASR reports for which sample the highest signal to noise in the shortest time is obtained.

We measured  $T_b$  and calculated the ASR for all samples. Table 1 only lists the 3200 h weathered PS sample of each technique. The signal to noise ratio was always determined for the aromatic CH resonance. The effective PS mass of the IWI and GF sample had to be estimated from the solvent to PS ratio in the weighed rotor as not the whole powder (IWI) or gel (GF) could be transferred into the rotor. For all samples  $T_b$  lies within the range of what has been reported for Amupol (IWI)<sup>77</sup> and AsymPol (GF, FC)<sup>55</sup>. Table 1 shows that for all techniques that exhibited an enhancement the sensitivity is increased by a factor 11 to 35 compared to regular NMR measurements. This directly translates into the same reduction of measurement time. Within the sample preparation techniques the film obtained from TriCE stands out, whereas the other samples show quite similar sensitivities. The main reason for the high sensitivity of the FC technique with TriCE is the very short DNP build-up time that allows for a faster measurement.

**Table 1.** DNP build-up times and ASR values of the different preparation techniques.

	DNP build-up / s	ASR / h <sup>-1/2</sup> mg <sup>-1</sup>
Regular NMR	5 s ( $T_1$ )	15.91
IWI	2.45	12.96
GF	1.1	348.34
FC TCE	0.67	255.52
FC THF	0.49	181.63
FC TriCE	0.37	572.39

### Quantification

The main advantage of NMR spectroscopy is the quantification of the bulk functional groups. The most common NMR measurement technique for <sup>13</sup>C (CP) is not quantitative.<sup>78</sup> With this measurement technique, the proton polarisation is transferred to the carbon nuclei. Therefore, the intensity of the carbon resonances are – apart from their quantity – also governed by their proton surrounding. A main parameter of the CP experiment is the CP contact time that is the time in which the polarisation transfer between the two nuclear species takes place. For short contact times, the carbons with many protons in close proximity are over represented. Whereas, for very long contact times, the relaxation in the rotating frame ( $T_{1\rho}$ ) that might be different for the different carbons leads to a decay of the intensities.<sup>79</sup> However, as discussed in previous papers,<sup>6,80</sup> it is possible to modify the pulse sequence<sup>6,80</sup> to quantify the measurement even with DNP.<sup>81</sup> A way to do this is to use the so-called multiCP pulse sequence.<sup>81,82</sup> This pulse sequence consists of a series of CP contact blocks. Between the individual blocks the

carbon magnetisation is stored along the main magnetic field to overcome  $T_{1\rho}$  and the protons relax to “refresh” their polarisation or in the case of DNP to get hyperpolarised again. In this way, a quantitative CP spectrum is obtained. Due to the fact that between each block a waiting time of three times  $T_1$  (conventional NMR spectroscopy) or  $T_b$  (DNP enhanced NMR spectroscopy) is needed, the measurement of multiCP spectra takes correspondingly longer.<sup>82</sup> However, by carefully choosing the CP contact time the spectra might already be almost quantitative. For this to happen a contact time must be chosen for which the relative (quantity corrected) intensity for all resonances is similar. For example, for a certain contact time this means that the intensity of quaternary carbon is still increasing, whereas the intensity of a primary carbon might already decay due to  $T_{1\rho}$ .<sup>80</sup> Therefore, we compared the integrals of all resonances for the FC sample once measured with a multiCP sequence and once with a regular CP sequence. Since the peaks in all spectra are highly overlapping, a simple integration of the resonances is not feasible. Instead, the spectra need to be deconvoluted to obtain the integrals, as shown exemplarily for the multiCP spectrum of the 3200h weathered FC sample cast from TCE in Figure 6a. This sample is chosen to keep the same solvent as for GF and to show the ability to deconvolute the solvent and defect resonance with the same chemical shift.

From Table 2 we see that the integrals of the multiCP and CP spectra do not change markedly and are even comparable to values obtained with a quantitative CP at room temperature for both backbone and defect resonances. Even the integrals of the peroxide defects are reasonable, although they completely overlap with the TCE resonance and might therefore be erroneous (Figure 6b). This shows that the regular DNP enhanced CP spectrum is to a first approximation quantitative and gives a very fast tool to obtain quantitative information on the microplastic defects.

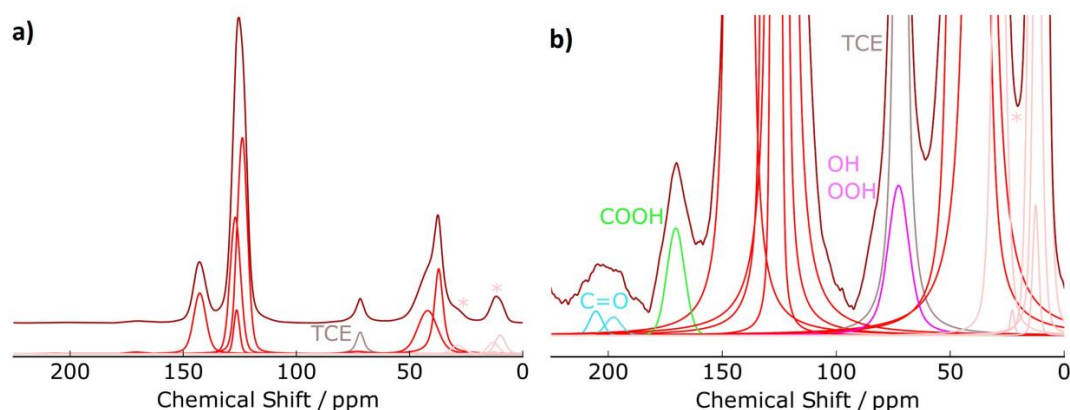


**Figure 6.** **a)** DNP enhanced  $^{13}\text{C}\{^1\text{H}\}$  multi-CP spectrum (brown) of the 3200 h weathered FC sample that used TCE as a solvent with a deconvolution of all resonances. The isotropic backbone resonances are plotted in red, the solvent in grey and the spinning side bands in salmon. The latter are additionally marked with an asterisk. **b)** The same spectrum zoomed in to see the defects. The resonances for ketones are shown in turquoise, the carboxylic acid in green and the alcohol and peroxides in purple. The CP spectrum of the same sample is shown in Figure 5a.

**Table 2.** Integration of the deconvoluted spectra of the FC method. The values for conventional NMR are obtained from reference <sup>6</sup>.

	IpsO	CH <sub>arom</sub>	CH <sub>2</sub> +CH	Acid	Ketone	OOH
Regular NMR	1.05	5	1.92	0.08	0.04	0.06
FC Mul CP	1.11	5	1.97	0.03	0.01	0.06
FC CP	1.04	5	2.05	0.03	0.02	0.02

### Reduction of the detection limit

Having found the optimal preparation technique, we tried to reduce the detection limit and prepared a sample of 400 h weathered MP with the FC technique and TriCE as solvent (Figure 7a). For this sample, the ketone and peroxide resonances are already visible. Unfortunately, the peroxide resonances are superimposed by a small sharp resonance that arises from an impurity of this batch. The ketone resonance is split into two signals that can be assigned to the end-chain (201 ppm) and in-chain (187 ppm) ketones. A deconvolution of the spectrum gives integrals of  $4 \cdot 10^{-4}$  (end-chain) and  $8 \cdot 10^{-4}$  (in-chain) when setting the aromatic C-H resonances to 5 as before. The OOH resonance has an integral of  $3 \cdot 10^{-3}$ . A conventional NMR spectrum with 1.4 times the measurement time clearly does not show enough sensitivity to identify these defects. In our previous paper no defects with a smaller integral than  $8 \cdot 10^{-3}$  were determined,<sup>6</sup> these, however, with an error of the same magnitude. We thus decreased

the detection limit for defects by at least one order of magnitude by DNP enhanced NMR spectroscopy.

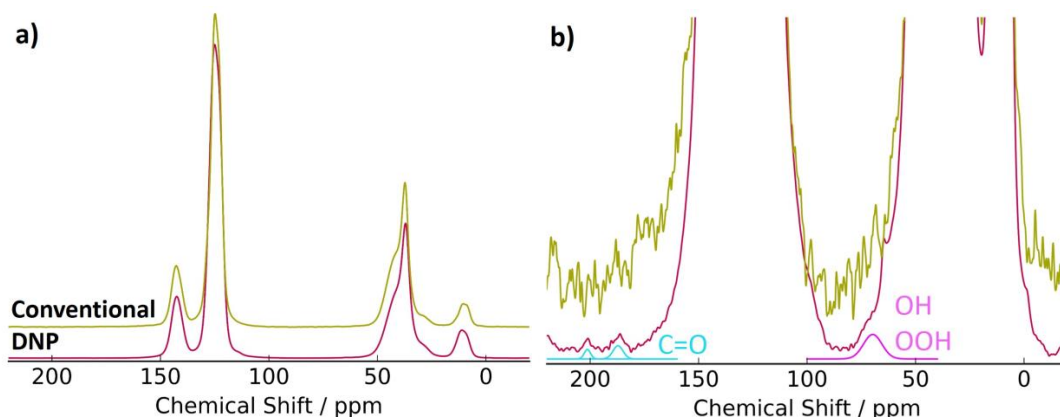


**Figure 7. a)** FC DNP enhanced (violet) and powdered conventional (ochre)  $^{13}\text{C}\{^1\text{H}\}$ CP NMR spectra of film casted 400 h weathered PS microplastic particles. The DNP enhanced CP NMR spectrum is measured with 51200 (10 h) and the conventional with 17152 (14 h) scans. For a better comparison the spectra are scaled to the same intensity. **b)** Same spectra as in a) zoomed in to see the ketone (turquoise) and peroxide (purple) defects. For the sake of clarity, only the deconvolution of the defects is plotted.

Because the mechanic properties of the PS sample weathered for 400 h should be much better than the one of the 3200 h weathered sample, we tried extruding this sample as well. Interestingly, the resulting spectrum looks different compared to the FC one (Figure 8). The sharp impurity at 65 ppm has vanished, indicating the low molecular nature of the corresponding material. The end-chain ketone resonance also vanished. Therefore the carboxylic resonance appears. This shows that the heat and shear forces in the extruder lead to an oxidation of the end-chain ketone to carboxylic acid, finally disqualifying this preparation technique for the introduction of radicals into the sample. Therefore, we recommend using the FC technique with TriCE to apply persistent radicals like AsymPol to the MP samples to obtain the best results for DNP enhanced NMR spectra.

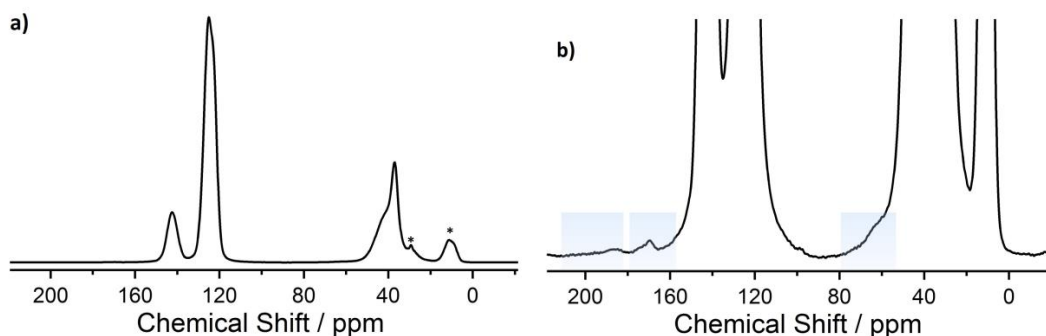


**Figure 8.** a) DNP enhanced  $^{13}\text{C}\{^1\text{H}\}$ CP NMR spectra of extruded 400 h weathered PS microplastic particles. The DNP enhanced CP NMR spectrum is measured with 61440 (8.5 h) b) Same spectrum as in a) zoomed in. With the light blue boxes the spectral regions for the ketone, carboxylic acids and peroxides (from left to right) are marked. Spinning side bands are marked with an asterisk.

## Conclusion

We compared four polarisation techniques to obtain DNP enhanced NMR spectra towards their applicability for weathered microplastic PS particles. The challenge is to find a way to nicely distribute the radical used as polarising agent on or in the PS. The standard IWI method is not suitable for microplastic as no enhancement is obtained. For GF a high enhancement and sensitivity is achieved. However, the remaining solvent resonances overlap with spectral regions where the microplastic defects are expected, resulting in a difficult detection of the aging defects. To get rid of solvent signals the sample was co-extruded with a radical. This technique, however, altered the microplastic markedly, so that the aging defects were not visible anymore. The best compromise is FC, especially with TriCE as a solvent, as it results in films with high sensitivity enabling an up to a factor of 35 reduced measurement time compared to regular NMR spectroscopy making DNP enhanced NMR spectroscopy a versatile tool to quickly and easily determine defects in microplastic particles. This reduces the detection limit of MP defects by one order of magnitude.

## Acknowledgment

We gratefully acknowledge financial support that was granted by the Deutsche Forschungsgemeinschaft DFG within the project number 391977956 - SFB 1357 Microplastics, subproject C01. We thank the Elite Network of Bavaria for support by the study program "Macromolecular Science". We thank Prof. Gerd Buntkowsky (TU Darmstadt) for generous allocation of measurement time at his Bruker Avance III 400 DNP spectrometer.

Additionally we acknowledge Lisa Weber and Martina Fried (Macromolecular Chemistry I, University of Bayreuth) for particle preparation and Sandra Ganzleben (Macromolecular Chemistry I, University of Bayreuth) for the TGA measurement of AsymPol.

## References

- (1) Geyer, R.; Jambeck, J. R.; Law, K. L. Production, use, and fate of all plastics ever made. *Science advances* **2017**, *3*, e1700782.
- (2) Lebreton, L.; Andrady, A. Future scenarios of global plastic waste generation and disposal. *Palgrave Commun* **2019**, *5*, 2922.
- (3) Andrady, A. L. Microplastics in the marine environment. *Marine pollution bulletin* **2011**, *62*, 1596–1605.
- (4) Erni-Cassola, G.; Zadjelovic, V.; Gibson, M. I.; Christie-Oleza, J. A. Distribution of plastic polymer types in the marine environment; A meta-analysis. *Journal of hazardous materials* **2019**, *369*, 691–698.
- (5) Johannessen, C.; Shetranjiwalla, S. Role of Structural Morphology of Commodity Polymers in Microplastics and Nanoplastics Formation: Fragmentation, Effects and Associated Toxicity in the Aquatic Environment. *Reviews of environmental contamination and toxicology* **2021**, *259*, 123–169.
- (6) Meides, N.; Menzel, T.; Poetzschner, B.; Löder, M. G. J.; Mansfeld, U.; Strohriegl, P.; Altstaedt, V.; Senker, J. Reconstructing the Environmental Degradation of Polystyrene by Accelerated Weathering. *Environmental science & technology* **2021**, *55*, 7930–7938.
- (7) Hartmann, N. B.; Hüffer, T.; Thompson, R. C.; Hassellöv, M.; Verschoor, A.; Daugaard, A. E.; Rist, S.; Karlsson, T.; Brennholt, N.; Cole, M. *et al.* Are We Speaking the Same Language? Recommendations for a Definition and Categorization Framework for Plastic Debris. *Environmental science & technology* **2019**, *53*, 1039–1047.
- (8) Gewert, B.; Plassmann, M. M.; MacLeod, M. Pathways for degradation of plastic polymers floating in the marine environment. *Environmental science. Processes & impacts* **2015**, *17*, 1513–1521.
- (9) Fairbrother, A.; Hsueh, H.-C.; Kim, J. H.; Jacobs, D.; Perry, L.; Goodwin, D.; White, C.; Watson, S.; Sung, L.-P. Temperature and light intensity effects on photodegradation of high-density polyethylene. *Polymer Degradation and Stability* **2019**, *165*, 153–160.
- (10) Song, D.; Gao, J.; Lu, L.; Li, X. Evaluation of Service Life of Polystyrene in Tropical Marine Environment by Principal Component Analysis. *Advances in Materials Science and Engineering* **2015**, *2015*, 1–7.
- (11) Vaillant, D.; Lacoste, J.; Dauphin, G. The oxidation mechanism of polypropylene: Contribution of <sup>13</sup>C-NMR spectroscopy. *Polymer Degradation and Stability* **1994**, *45*, 355–360.
- (12) Mowery, D. M.; Assink, R. A.; Derzon, D. K.; Klamo, S. B.; Clough, R. L.; Bernstein, R. Solid-State <sup>13</sup>C NMR Investigation of the Oxidative Degradation of Selectively Labeled Polypropylene by Thermal Aging and  $\gamma$ -Irradiation. *Macromolecules* **2005**, *38*, 5035–5046.
- (13) Chabira, S. F.; Sebaa, M.; G'sell, C. Oxidation and crosslinking processes during thermal aging of low-density polyethylene films. *J. Appl. Polym. Sci.* **2011**, *79*, n/a-n/a.
- (14) Shi, Y.; Qin, J.; Tao, Y.; Jie, G.; Wang, J. Natural weathering severity of typical coastal environment on polystyrene: Experiment and modeling. *Polymer Testing* **2019**, *76*, 138–145.
- (15) Grause, G.; Chien, M.-F.; Inoue, C. Changes during the weathering of polyolefins. *Polymer Degradation and Stability* **2020**, *181*, 109364.
- (16) Schrank, I.; Trotter, B.; Dummert, J.; Scholz-Böttcher, B. M.; Löder, M. G. J.; Laforsch, C. Effects of microplastic particles and leaching additive on the life history and morphology of *Daphnia magna*. *Environmental pollution (Barking, Essex : 1987)* **2019**, *255*, 113233.
- (17) Kühn, S.; Booth, A. M.; Sørensen, L.; van Oyen, A.; van Franeker, J. A. Transfer of Additive Chemicals From Marine Plastic Debris to the Stomach Oil of Northern Fulmars. *Front. Environ. Sci.* **2020**, *8*, 1977.
- (18) Fauvelle, V.; Garel, M.; Tamburini, C.; Nerini, D.; Castro-Jiménez, J.; Schmidt, N.; Paluselli, A.; Fahs, A.; Papillon, L.; Booth, A. M. *et al.* Organic additive release from plastic to seawater is lower under deep-sea conditions. *Nat. Commun.* **2021**, *12*, 4426.
- (19) Zettler, E. R.; Mincer, T. J.; Amaral-Zettler, L. A. Life in the "plastisphere": Microbial communities on plastic marine debris. *Environmental science & technology* **2013**, *47*, 7137–7146.
- (20) Imhof, H. K.; Ivleva, N. P.; Schmid, J.; Niessner, R.; Laforsch, C. Contamination of beach sediments of a subalpine lake with microplastic particles. *Current biology : CB* **2013**, *23*, R867-8.
- (21) Harrison, J. P.; Schratzberger, M.; Sapp, M.; Osborn, A. M. Rapid bacterial colonization of low-density polyethylene microplastics in coastal sediment microcosms. *BMC microbiology* **2014**, *14*, 232.
- (22) McGivney, E.; Cederholm, L.; Barth, A.; Hakkarainen, M.; Hamacher-Barth, E.; Ogonowski, M.; Gorokhova, E. Rapid Physicochemical Changes in Microplastic Induced by Biofilm Formation. *Frontiers in bioengineering and biotechnology* **2020**, *8*, 205.
- (23) Kirstein, I. V.; Kirmizi, S.; Wichels, A.; Garin-Fernandez, A.; Erler, R.; Löder, M.; Gerdts, G. Dangerous hitchhikers? Evidence for potentially pathogenic *Vibrio* spp. on microplastic particles. *Marine environmental research* **2016**, *120*, 1–8.
- (24) Heskett, M.; Takada, H.; Yamashita, R.; Yuyama, M.; Ito, M.; Geok, Y. B.; Ogata, Y.; Kwan, C.; Heckhausen, A.; Taylor, H. *et al.* Measurement of persistent organic pollutants (POPs) in plastic resin pellets from remote islands: Toward establishment of background concentrations for International Pellet Watch. *Marine pollution bulletin* **2012**, *64*, 445–448.
- (25) Engler, R. E. The complex interaction between marine debris and toxic chemicals in the ocean. *Environmental science & technology* **2012**, *46*, 12302–12315.
- (26) Law, K. L.; Thompson, R. C. Oceans. Microplastics in the seas. *Science (New York, N.Y.)* **2014**, *345*, 144–145.
- (27) Li, W. C.; Tse, H. F.; Fok, L. Plastic waste in the marine environment: A review of sources, occurrence and effects. *The Science of the total environment* **2016**, *566-567*, 333–349.
- (28) Hong, S. H.; Shim, W. J.; Hong, L. Methods of analysing chemicals associated with microplastics: A review. *Anal. Methods* **2017**, *9*, 1361–1368.
- (29) Ojeda, T.; Freitas, A.; Birck, K.; Dalmolin, E.; Jacques, R.; Bento, F.; Camargo, F. Degradability of linear polyolefins under natural weathering. *Polymer Degradation and Stability* **2011**, *96*, 703–707.

- (30) Martínez-Romo, A.; González-Mota, R.; Soto-Bernal, J. J.; Rosales-Candelas, I. Investigating the Degradability of HDPE, LDPE, PE-BIO, and PE-OXO Films under UV-B Radiation. *Journal of Spectroscopy* **2015**, *2015*, 1–6.
- (31) Da Costa, J. P.; Nunes, A. R.; Santos, P. S. M.; Girão, A. V.; Duarte, A. C.; Rocha-Santos, T. Degradation of polyethylene microplastics in seawater: Insights into the environmental degradation of polymers. *Journal of environmental science and health. Part A, Toxic/hazardous substances & environmental engineering* **2018**, *53*, 866–875.
- (32) Canopoli, L.; Coulon, F.; Wagland, S. T. Degradation of excavated polyethylene and polypropylene waste from landfill. *The Science of the total environment* **2020**, *698*, 134125.
- (33) Fernández-González, V.; Andrade-Garda, J. M.; López-Mahía, P.; Muniategui-Lorenzo, S. Impact of weathering on the chemical identification of microplastics from usual packaging polymers in the marine environment. *Analytica chimica acta* **2021**, *1142*, 179–188.
- (34) Shim, W. J.; Hong, S. H.; Eo, S. E. Identification methods in microplastic analysis: A review. *Anal. Methods* **2017**, *9*, 1384–1391.
- (35) Müller-Warmuth, W.; van Steenwinkel, R.; Noack, F. Dynamic Nuclear Polarization Experiments on  $^{19}\text{F}$  in Solutions and their Interpretation by the “Pulse Model” of Molecular Collisions. *Zeitschrift für Naturforschung A* **1968**, *23*, DOI: 10.1515/zna-1968-0408.
- (36) Abragam, A.; Proctor, W. G. Dynamic polarization of atomic nuclei in solids. *C. R. Hebd. Seances Acad. Sci* **1958**, *246*, 2253–2256.
- (37) Kundu, K.; Mentink-Vigier, F.; Feintuch, A.; Vega, S. DNP Mechanisms. *e.Mag.Res.* **2019**, *8*, 295–337.
- (38) Ernst, R. R.; Bodenhausen, G.; Wokaun, A. *Principles of nuclear magnetic resonance in one and two dimensions*, Reprint. with corr; The international series of monographs on chemistry 14; Clarendon Press: Oxford, 1988.
- (39) Corzilius, B. Theory of solid effect and cross effect dynamic nuclear polarization with half-integer high-spin metal polarizing agents in rotating solids. *Phys. Chem. Chem. Phys.* **2016**, *18*, 27190–27204.
- (40) Hall, D. A.; Maus, D. C.; Gerfen, G. J.; Inati, S. J.; Becerra, L. R.; Dahlquist, F. W.; Griffin, R. G. Polarization-Enhanced NMR Spectroscopy of Biomolecules in Frozen Solution. *Science* **1997**, *276*, 930–932.
- (41) Gerfen, G. J.; Becerra, L. R.; Hall, D. A.; Griffin, R. G.; Temkin, R. J.; Singel, D. J. High frequency (140 GHz) dynamic nuclear polarization: Polarization transfer to a solute in frozen aqueous solution. *J. Chem. Phys.* **1995**, *102*, 9494–9497.
- (42) Bajaj, V. S.; Farrar, C. T.; Hornstein, M. K.; Mastovsky, I.; Vieregg, J.; Bryant, J.; Eléna, B.; Kreischer, K. E.; Temkin, R. J.; Griffin, R. G. Dynamic nuclear polarization at 9 T using a novel 250 GHz gyrotron microwave source. *J. Magn. Reson.* **2003**, *160*, 85–90.
- (43) Maly, T.; Debelouchina, G. T.; Bajaj, V. S.; Hu, K.-N.; Joo, C.-G.; Mak-Jurkauskas, M. L.; Sirigiri, J. R.; van der Wel, P. C. A.; Herzfeld, J.; Temkin, R. J. *et al.* Dynamic nuclear polarization at high magnetic fields. *J. Chem. Phys.* **2008**, *128*, 52211.
- (44) Bouleau, E.; Saint-Bonnet, P.; Mentink-Vigier, F.; Takahashi, H.; Jacquot, J.-F.; Bardet, M.; Aussenac, F.; Pureau, A.; Engelke, F.; Hediger, S. *et al.* Pushing NMR sensitivity limits using dynamic nuclear polarization with closed-loop cryogenic helium sample spinning. *Chem. Sci.* **2015**, *6*, 6806–6812.
- (45) Lesage, A.; Lelli, M.; Gajan, D.; Caporini, M. A.; Vitzthum, V.; Mieville, P.; Alauzun, J.; Roussey, A.; Thieuleux, C.; Mehdi, A. *et al.* Surface Enhanced NMR Spectroscopy by Dynamic Nuclear Polarization. *J. Am. Chem. Soc.* **2010**, *132*, 15459–15461.
- (46) Takahashi, H.; Lee, D.; Dubois, L.; Bardet, M.; Hediger, S.; De Paëpe, G. Rapid Natural-Abundance 2D  $^{13}\text{C}$ - $^{13}\text{C}$  Correlation Spectroscopy Using Dynamic Nuclear Polarization Enhanced Solid-State NMR and Matrix-Free Sample Preparation. *Angew. Chem. Int. Ed.* **2012**, *51*, 11766–11769.
- (47) Frederick, K. K.; Michaelis, V. K.; Corzilius, B.; Ong, T.-C.; Jacavone, A. C.; Griffin, R. G.; Lindquist, S. Sensitivity-enhanced NMR reveals alterations in protein structure by cellular milieu. *Cell* **2015**, *163*, 620–628.
- (48) Berruyer, P.; Lelli, M.; Conley, M. P.; Silverio, D. L.; Widdifield, C. M.; Siddiqi, G.; Gajan, D.; Lesage, A.; Coperet, C.; Emsley, L. Three-Dimensional Structure Determination of Surface Sites. *J. Am. Chem. Soc.* **2017**, *139*, 849–855.
- (49) Perras, F. A.; Wang, L. L.; Manzano, J. S.; Chaudhary, U.; Opembe, N. N.; Johnson, D. D.; Slowing, II; Pruski, M. Optimal sample formulations for DNP SENS: The importance of radical-surface interactions. *Curr. Opin. Colloid Interface Sci.* **2018**, *33*, 9–18.
- (50) Rossini, A. J. Materials Characterization by Dynamic Nuclear Polarization-Enhanced Solid-State NMR Spectroscopy. *J. Phys. Chem. Lett.* **2018**, *9*, 5150–5159.
- (51) Thankamony, A. S. L.; Wittmann, J. J.; Kaushik, M.; Corzilius, B. Dynamic nuclear polarization for sensitivity enhancement in modern solid-state NMR. *Prog. Nucl. Magn. Reson. Spectrosc.* **2017**, *120*–195.
- (52) Grätz, S.; Olivera Junior, M. de; Gutmann, T.; Borchardt, L. A comprehensive approach for the characterization of porous polymers using  $^{13}\text{C}$  and  $^{15}\text{N}$  dynamic nuclear polarization NMR spectroscopy. *Phys. Chem. Chem. Phys.* **2020**, *22*, 23307–23314.
- (53) Mollica, G.; Dekhil, M.; Ziarelli, F.; Thureau, P.; Viel, S. Quantitative structural constraints for organic powders at natural isotopic abundance using dynamic nuclear polarization solid-state NMR spectroscopy. *Angew. Chem. Int. Ed.* **2015**, *54*, 6028–6031.
- (54) Lund, A.; Casano, G.; Menzildjian, G.; Kaushik, M.; Stevanato, G.; Yulikov, M.; Jabbour, R.; Wisser, D.; Renom-Carrasco, M.; Thieuleux, C. *et al.* TinyPols: A family of water-soluble binitroxides tailored for dynamic nuclear polarization enhanced NMR spectroscopy at 18.8 and 21.1 T. *Chem. Sci.* **2020**, *46*, 1933.
- (55) Mentink-Vigier, F.; Marin-Montesinos, I.; Jagtap, A. P.; Halbritter, T.; van Tol, J.; Hediger, S.; Lee, D.; Sigurdsson, S. T.; De Paëpe, G. Computationally Assisted Design of Polarizing Agents for Dynamic Nuclear Polarization Enhanced NMR: The AsymPol Family. *J. Am. Chem. Soc.* **2018**, *140*, 11013–11019.

- (56) Jagtap, A. P.; Geiger, M.-A.; Stöppler, D.; Orwick-Rydmark, M.; Oschkinat, H.; Sigurdsson, S. T. bcTol: A highly water-soluble biradical for efficient dynamic nuclear polarization of biomolecules. *Chemical communications (Cambridge, England)* **2016**, *52*, 7020–7023.
- (57) Sauvée, C.; Rosay, M.; Casano, G.; Aussenac, F.; Weber, R. T.; Ouari, O.; Tordo, P. Highly efficient, water-soluble polarizing agents for dynamic nuclear polarization at high frequency. *Angew. Chem. Int. Ed.* **2013**, *52*, 10858–10861.
- (58) Zagdoun, A.; Casano, G.; Ouari, O.; Schwarzwälder, M.; Rossini, A. J.; Aussenac, F.; Yulikov, M.; Jeschke, G.; Copéret, C.; Lesage, A. *et al.* Large molecular weight nitroxide biradicals providing efficient dynamic nuclear polarization at temperatures up to 200 K. *J. Am. Chem. Soc.* **2013**, *135*, 12790–12797.
- (59) Zagdoun, A.; Casano, G.; Ouari, O.; Lapadula, G.; Rossini, A. J.; Lelli, M.; Baffert, M.; Gajan, D.; Veyre, L.; Maas, W. E. *et al.* A Slowly Relaxing Rigid Biradical for Efficient Dynamic Nuclear Polarization Surface-Enhanced NMR Spectroscopy: Expeditious Characterization of Functional Group Manipulation in Hybrid Materials. *J. Am. Chem. Soc.* **2012**, *134*, 2284–2291.
- (60) Rosay, M.; Tometich, L.; Pawsey, S.; Bader, R.; Schauwecker, R.; Blank, M.; Borchard, P. M.; Cauffman, S. R.; Felch, K. L.; Weber, R. T. *et al.* Solid-state dynamic nuclear polarization at 263 GHz: Spectrometer design and experimental results. *Phys. Chem. Chem. Phys.* **2010**, *12*, 5850–5860.
- (61) Lelli, M.; Gajan, D.; Lesage, A.; Caporini, M. A.; Vitzthum, V.; Miéville, P.; Héroguel, F.; Rascón, F.; Roussey, A.; Thieuleux, C. *et al.* Fast characterization of functionalized silica materials by silicon-29 surface-enhanced NMR spectroscopy using dynamic nuclear polarization. *J. Am. Chem. Soc.* **2011**, *133*, 2104–2107.
- (62) Verde-Sesto, E.; Goujon, N.; Sardon, H.; Ruiz, P.; Huynh, T. V.; Elizalde, F.; Mecerreyes, D.; Forsyth, M.; O'Dell, L. A. DNP NMR Studies of Crystalline Polymer Domains by Copolymerization with Nitroxide Radical Monomers. *Macromolecules* **2018**, *51*, 8046–8053.
- (63) Le, D.; Casano, G.; Phan, T. N. T.; Ziarelli, F.; Ouari, O.; Aussenac, F.; Thureau, P.; Mollica, G.; Gignes, D.; Tordo, P. *et al.* Optimizing Sample Preparation Methods for Dynamic Nuclear Polarization Solid-state NMR of Synthetic Polymers. *Macromolecules* **2014**, *47*, 3909–3916.
- (64) Le, D.; Ziarelli, F.; Phan, T. N. T.; Mollica, G.; Thureau, P.; Aussenac, F.; Ouari, O.; Gignes, D.; Tordo, P.; Viel, S. Up to 100% Improvement in Dynamic Nuclear Polarization Solid-State NMR Sensitivity Enhancement of Polymers by Removing Oxygen. *Macromol. Rapid Commun.* **2015**, *36*, 1416–1421.
- (65) Ni, Q. Z.; Yang, F.; Can, T. V.; Sergeev, I. V.; D'Addio, S. M.; Jawla, S. K.; Li, Y.; Lipert, M. P.; Xu, W.; Williamson, R. T. *et al.* In Situ Characterization of Pharmaceutical Formulations by Dynamic Nuclear Polarization Enhanced MAS NMR. *The journal of physical chemistry. B* **2017**, *121*, 8132–8141.
- (66) Zhang, K.; Noble, B. B.; Mater, A. C.; Monteiro, M. J.; Coote, M. L.; Jia, Z. Effect of heteroatom and functionality substitution on the oxidation potential of cyclic nitroxide radicals: Role of electrostatics in electrochemistry. *Phys. Chem. Chem. Phys.* **2018**, *20*, 2606–2614.
- (67) Metz, G.; Wu, X. L.; Smith, S. O. Ramped-Amplitude Cross Polarization in Magic-Angle-Spinning NMR. *J. Magn. Reson.* **1994**, *110*, 219–227.
- (68) Fung, B. M.; Khitrin, A. K.; Ermolaev, K. An improved broadband decoupling sequence for liquid crystals and solids. *J. Magn. Reson.* **2000**, *142*, 97–101.
- (69) Overhauser, A. W. Polarization of Nuclei in Metals. *Phys. Rev.* **1953**, *92*, 411–415.
- (70) Solomon, I. Relaxation Processes in a System of Two Spins. *Phys. Rev.* **1955**, *99*, 559–565.
- (71) Chapter 3 Relaxation. *Coordination Chemistry Reviews* **1996**, *150*, 77–110.
- (72) van der Zwan, K. P.; Riedel, W.; Aussenac, F.; Reiter, C.; Kreger, K.; Schmidt, H.-W.; Risse, T.; Gutmann, T.; Senker, J. <sup>19</sup>F MAS DNP for Probing Molecules in Nanomolar Concentrations: Direct Polarization as Key for Solid-State NMR Spectra without Solvent and Matrix Signals. *J. Phys. Chem. C* **2021**, *125*, 7287–7296.
- (73) Zhao, L.; Pinon, A. C.; Emsley, L.; Rossini, A. J. DNP-enhanced solid-state NMR spectroscopy of active pharmaceutical ingredients. *Magn. Reson. Chem.* **2018**, *56*, 583–609.
- (74) Hediger, S.; Lee, D.; Mentink-Vigier, F.; De Paëpe, G. MAS - DNP Enhancements: Hyperpolarization, Depolarization, and Absolute Sensitivity. *e.Mag.Res.* **2018**, *7*, 105–117.
- (75) Mentink-Vigier, F.; Vega, S.; De Paëpe, G. Fast and accurate MAS-DNP simulations of large spin ensembles. *Phys. Chem. Chem. Phys.* **2017**, *19*, 3506–3522.
- (76) Mentink-Vigier, F.; Paul, S.; Lee, D.; Feintuch, A.; Hediger, S.; Vega, S.; De Paëpe, G. Nuclear depolarization and absolute sensitivity in magic-angle spinning cross effect dynamic nuclear polarization. *Phys. Chem. Chem. Phys.* **2015**, *17*, 21824–21836.
- (77) Mentink-Vigier, F.; Barra, A.-L.; van Tol, J.; Hediger, S.; Lee, D.; De Paëpe, G. De novo prediction of cross-effect efficiency for magic angle spinning dynamic nuclear polarization. *Phys. Chem. Chem. Phys.* **2019**, *21*, 2166–2176.
- (78) Pines, A.; Gibby, M. G.; Waugh, J. S. Proton - enhanced NMR of dilute spins in solids. *J. Chem. Phys.* **1973**, *59*, 569–590.
- (79) Kolodziejski, W.; Klinowski, J. Kinetics of Cross-Polarization in Solid-State NMR: A Guide for Chemists. *Chem. Rev.* **2002**, *102*, 613–628.
- (80) Mauel, A.; Pötzschner, B.; Meides, N.; Siegel, R.; Strohriegl, P.; Senker, J. Quantification of photooxidative defects in weathered microplastics using <sup>13</sup>C multiCP NMR spectroscopy. *RSC Adv.* **2022**, *12*, 10875–10885.
- (81) Bertarello, A.; Berruyer, P.; Skantze, U.; Sardana, S.; Sardana, M.; Elmore, C. S.; Schade, M.; Chiarparin, E.; Schantz, S.; Emsley, L. Quantification of magic angle spinning dynamic nuclear polarization NMR spectra. *J. Magn. Reson.* **2021**, *329*, 107030.
- (82) Johnson, R. L.; Schmidt-Rohr, K. Quantitative solid-state <sup>13</sup>C NMR with signal enhancement by multiple cross polarization. *J. Magn. Reson.* **2014**, *239*, 44–49.

## Supporting Information

### **DNP Enhanced Solid-State NMR Spectroscopy Meets Microplastic – Sample Preparation for Optimal Sensitivity Enhancement**

Kasper P. van der Zwan,<sup>a‡</sup> Anika Mauel,<sup>a‡</sup> Wiebke Riedel,<sup>b</sup> Nora Meides,<sup>c</sup> Tamara Fischer,<sup>a</sup>  
Marcel Meinhart,<sup>a</sup> Peter Strohrigel,<sup>c</sup> Thomas Risse,<sup>b</sup> Jürgen Senker<sup>a\*</sup>

<sup>a</sup> Inorganic Chemistry III and Northern Bavarian NMR Center, University of Bayreuth,  
Universitätsstraße 30, D-95447 Bayreuth, Germany

<sup>b</sup> Physical and Theoretical Chemistry, Institute of Chemistry and Biochemistry  
Freie Universität Berlin, Arnimallee 22, 14195 Berlin, Germany

<sup>c</sup> Macromolecular Chemistry I, University of Bayreuth,  
Universitätsstraße 30, D-95447 Bayreuth, Germany

\* [juergen.senker@uni-bayreuth.de](mailto:juergen.senker@uni-bayreuth.de) 0049-(0)921-552532;

<sup>‡</sup>These authors contributed equally to the manuscript

## Table of content

1. Synthesis.....	3
2. Rotor contents.....	5
3. Residual solvent after FC determined via $^1\text{H}$ liquid-state NMR spectroscopy .....	6
4. $^1\text{H}$ liquid-state NMR spectra .....	7
5. Additional EPR Spectra .....	8
6. TGA of AsymPol .....	9
7. EPR spectrum of the extruded sample.....	9
8. Additional spectra for FC.....	10

## 1. Synthesis

Synthesis of AsymPol was performed in a 2 step synthesis:

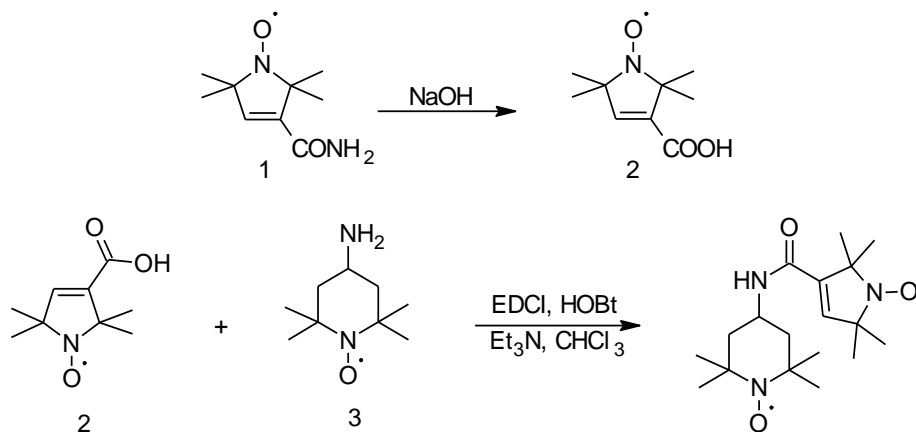


**Figure S1.** Sketch of the AsymPol synthesis.

449.13 mg (2.4 mmol) 3-carbamoyl-2,2,5,5-tetramethyl-3-pyrrolin-1-oxyl (**1**) were added to 15 ml of a 15 wt.% aqueous NaOH solution. The mixture was stirred at 95 °C for three hours to yield a transparent, yellow solution. Concentrated HCl has been added until a pH of 4 was reached. Subsequently the solution was washed twice with EtOAc (25 and 50 ml) The organic phase was collected and dried with MgSO<sub>4</sub>. The filtered solution was dried under vacuum to yield a yellow solid (**2**).

To 150.86 mg (0.8 mmol) of **2** 245.97 mg (1.8 mmol) of 1*H*-1,2,3-Benzotriazol-1-ol (HOBt), 173.34 mg (1.1 mmol) 1-Ethyl-3-(3-dimethylaminopropyl)carbodiimide (EDCI), 0.35 ml Et<sub>3</sub>N and 18.75 ml chloroform were added under a nitrogen blanket and stirred for 15 minutes at room temperature. 140.01 mg (0.8 mmol) of 4-aminotempo (**3**) were added and stirred over night at room temperature. Afterwards 50 ml chloroform were added and the solution was washed with a 50 ml of saturated NaHCO<sub>3</sub> solution and afterwards with 50 ml of a saturated NaCl solution. The organic phase was dried under vacuum to yield an orange powder. The powder was purified by flash column chromatography (silica) using a gradient elution (EtOAc:pet ether; 0:100 to 30:70); TLC (silica) 2.5 % MeOH in DCM: R<sub>f</sub> ≈ 0.15. The product fractions were dried under vacuum and yielded 222 mg (79%) of the orange product. Succesfull syntheses and purification was monitored by mass spectrometry.

Amidine functionalised PS was synthesised by heating 90 ml MilliQ H<sub>2</sub>O to 90 °C and adding 1.306 g of 2,2'-azobis(2-amidinopropane) (4.82 mmol, 1 eq) dissolved in 11 ml MilliQ H<sub>2</sub>O. Afterwards 9.99 g (92.92 mmol, 19.9 eq) styrene were added. The solution was stirred for 20 h at 90 °C. The polymer was obtained from the solution as a white powder by centrifugation.

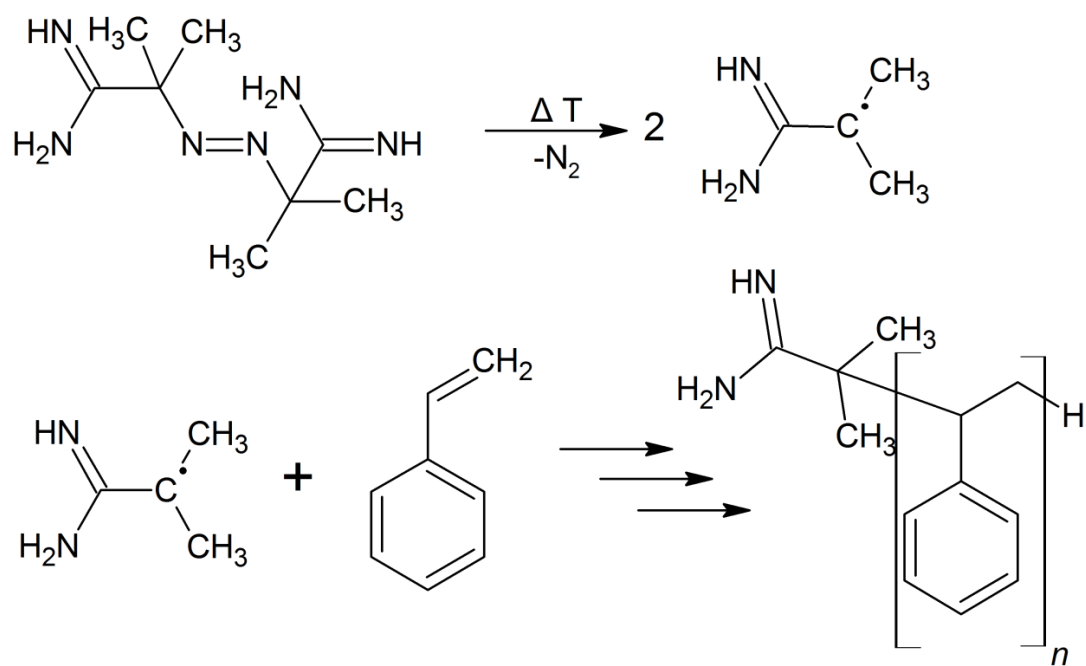


**Figure S2.** Sketch of the amidine functionalised PS synthesis.

## 2. Rotor contents

**Table S1.** Amount of sample in the rotors.

<b>Incipient Wettnes Impregnation</b>		
<i>Solvent</i>	<i>Sample</i>	<i>Amount / mg</i>
Glycerol-d8/D2O/H2O	3200 h	21.96
<b>Glass Forming</b>		
<i>Solvent</i>	<i>Sample</i>	<i>Amount / mg</i>
TCE	3200 h	10
<b>Casted Films</b>		
<i>Solvent</i>	<i>Sample</i>	<i>Amount / mg</i>
TriCE	PS_0 h	9.16
	PS_400 h	8.99
	PS_3200 h	14.43
		13.53
	PS + Amidin	10.08
TCE	PS_0 h	14.16
	PS_3200 h	17.67
THF	PS_0 h	10.89
	PS_3200 h	13.46
<b>Extrusion</b>		
<i>Solvent</i>	<i>Sample</i>	<i>Amount / mg</i>
	3200 h	15.64

### 3. Residual solvent after FC determined via $^1\text{H}$ liquid-state NMR spectroscopy

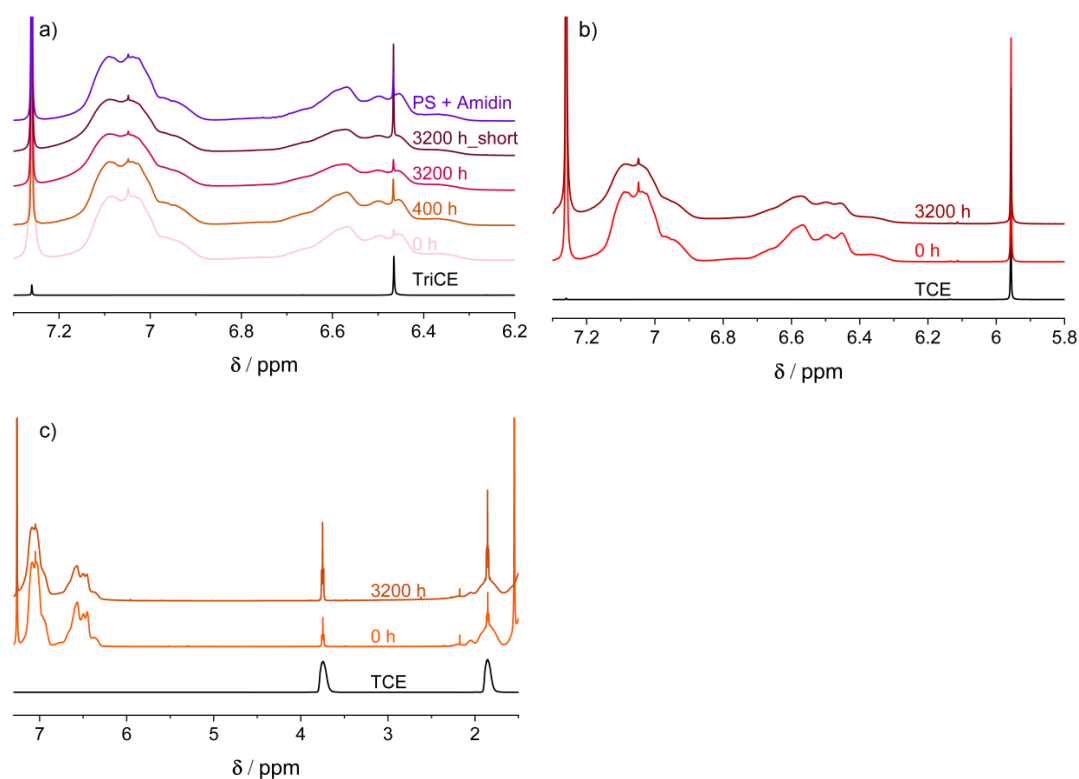
**Table S2.** Residual solvent proportions present in casted films after drying process. Proportions determined via  $^1\text{H}$  liquid-state NMR. The drying procedures were as follows: (1) 5 days (3 days at 50°C in fume hood, 1 day in vacuum oven at 30°C and 1 day under high vacuum); (2) 16 h at room temperature in fume hood and (3) 3 h at 50°C.

Casted Films			Integral of resonances			Solvent proportion
Solvent	Sample	Drying Procedure	Aromatic PS Resonances	Solvent resonance of film	$\text{CDCl}_3$ resonance	[%]
TriCE	PS_0 h	(1)	5	0.006	1.884	0.62
	PS_400 h	(1)	5	0.015	0.473	1.45
	PS_3200 h	(1)	5	0.007	0.465	0.69
		(2)	5	0.055	0.559	5.49
	PS + Amidin	(1)	5	0.016	0.489	1.58
TCE	PS_0 h	(1)	5	0.177	1.438	8.86
	PS_3200 h	(3)	5	0.159	1.251	7.94
THF	PS_0 h	(1)	5	0.165	1.251	4.13
	PS_3200 h	(1)	5	0.392	0.305	9.81

All  $^1\text{H}$  spectra were calibrated to the residual  $\text{CDCl}_3$  signal at 7.26 ppm. For the aromatic PS resonances the area between 7.35 – 6.00 ppm (7.35 – 6.15 ppm for TCE) was integrated and the integral of the  $\text{CDCl}_3$  resonance (7.26 ppm) subtracted. In case of TriCE (6.4 ppm) additionally its integral was subtracted. For the residual solvents typical shifts of 6.4 ppm (TriCE, corresponding to 1 proton), 6.0 ppm (TCE, corresponding to 2 proton) and 3.7 ppm as well as 1.9 ppm (THF, corresponding to 4 protons) were observed.

Calculation of proportion: 
$$\text{Solvent proportion} = \frac{I_S / n}{I_{PS} / 5}$$

With:  $I_S$  Integral of solvent resonance  
 $I_{PS}$  Integral of aromatic PS resonances  
 $n$  Number of protons corresponding to solvent signal

4.  $^1\text{H}$  liquid-state NMR spectra

**Figure S3.**  $^1\text{H}$  liquid-state NMR spectra of the unaged and aged PS films and amidine functionalised PS with AsymPol obtained from TriCE (a), TCE (b) and THF (c). The spectra were normalised to the aromatic PS resonances between 6.150 and 7.125 ppm and are compared to the respective solvent spectra. All films were dried for 5 days. Exceptions are the TriCE film 3200 h\_short which was dried 16 h at room temperature in a fume hood and the TCE film 3200 h which was dried 3 h at 50°C.

## 5. Additional EPR Spectra

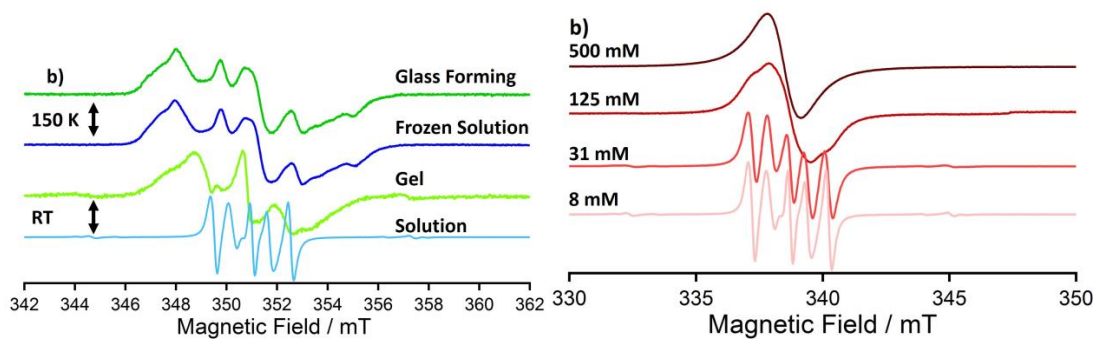


**Figure S6. a)** EPR measurements of a frozen solutions of AsymPol in TCE (blue) and of a GF sample (green) measured at 150 K with the same AsymPol concentration in the TCE phase. In brighter colours the same measurements are shown at room temperature. **b)** EPR measurements of solutions of AsymPol in tce at room temperature. Please note that these experiments were conducted with a resonance frequency of 9.51 GHz.

## 6. TGA of AsymPol

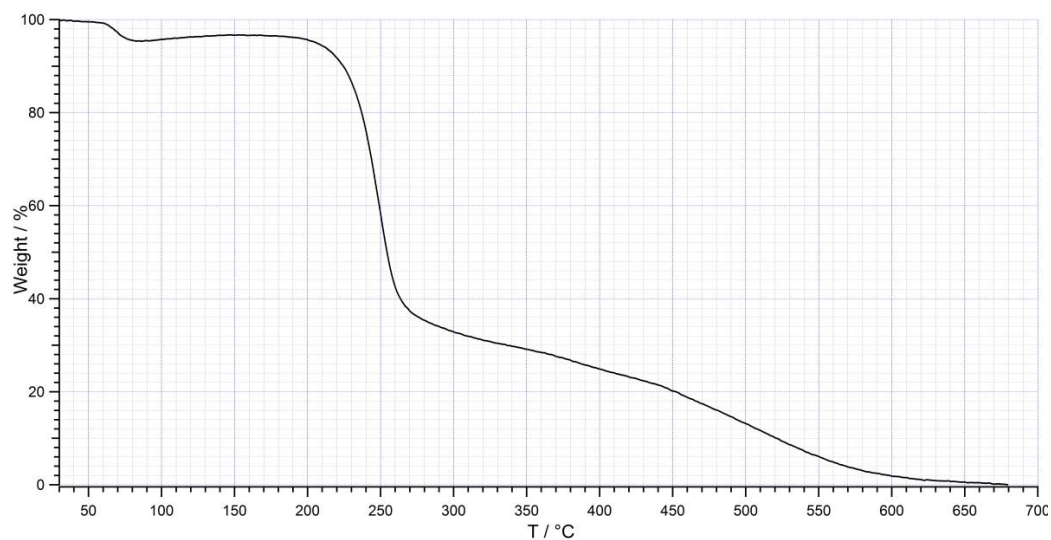


**Figure S7.** Thermogravimetric analysis of AsymPol with a heat rate of  $10 \text{ Kmin}^{-1}$  and regular atmosphere.

## 7. EPR spectrum of the extruded sample

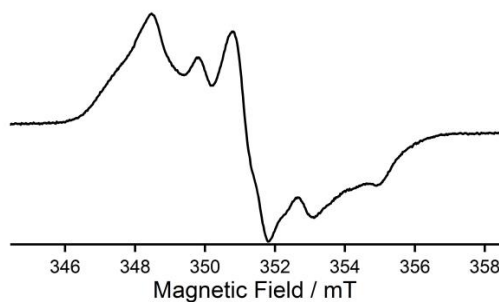


**Figure S8.** EPR spectrum of the extruded microplastic particle aged for 3200h.

## 8. Additional spectra for FC

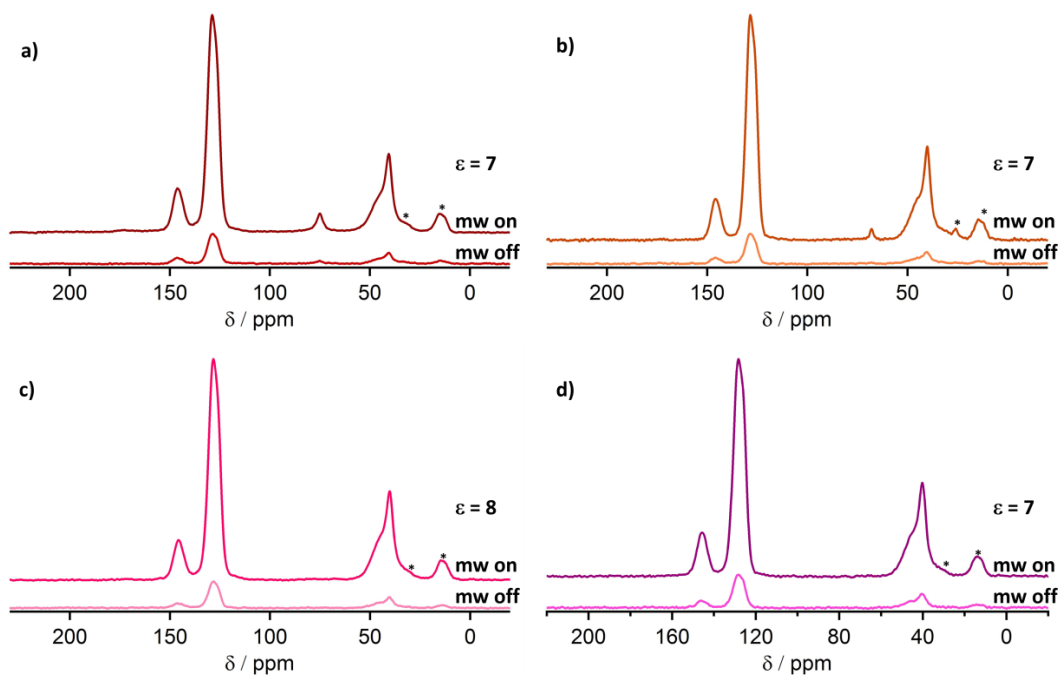


**Figure S9.** DNP enhanced  $^{13}\text{C}\{^1\text{H}\}$ CP NMR spectra of 3200 h aged PS microplastic films obtained from **a)** TCE, **b)** THF and **c)** TriCE. **d)** DNP enhanced  $^{13}\text{C}\{^1\text{H}\}$ CP NMR spectra of unaged PS microplastic films obtained from TriCE. In all Figures, the brighter spectrum shows the non-enhanced spectrum without microwave irradiation and 32 scans and the darker spectrum shows the same measurement with microwave irradiation. Spinning side bands are marked with an asterisk.

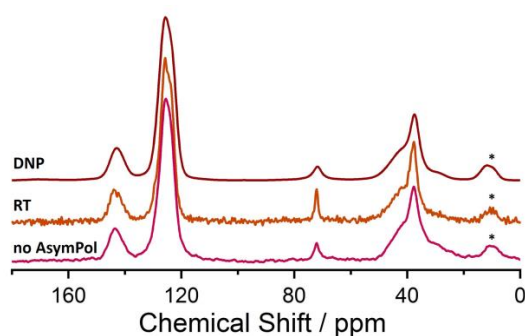


**Figure S10.** DNP enhanced  $^{13}\text{C}\{^1\text{H}\}$ CP NMR spectra of 3200 h aged PS microplastic films obtained from TCE (top). Same Sample measured at RT without microwave irradiation (middle). 3200h microplastic film from TCE without AsymPol (bottom).

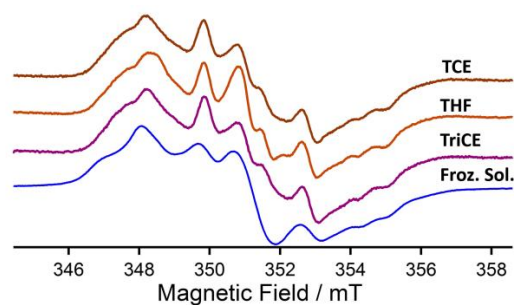


**Figure S11.** EPR spectra of the unaged PS films with AsymPol obtained from TCE, THF and TriCE, as well as a 31 mM frozen solution of AsymPol in TCE.

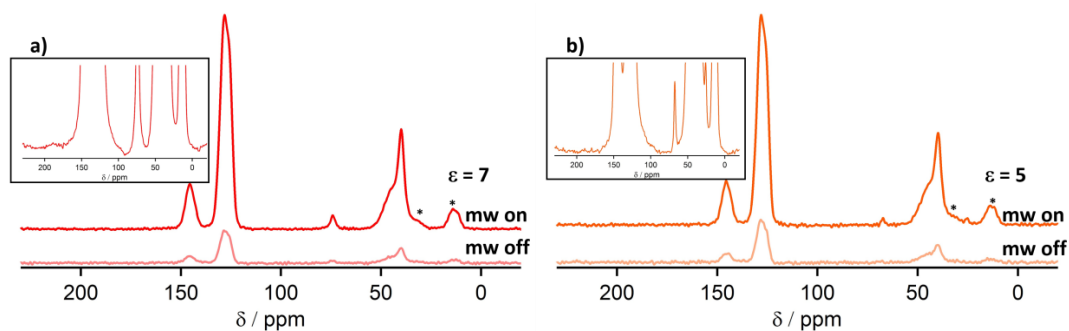


**Figure S12.** DNP enhanced  $^{13}\text{C}\{^1\text{H}\}$ CP NMR spectra of unaged PS microplastic films obtained from **a)** TCE, **b)** THF. In all figures the brighter spectrum shows the non-enhanced spectrum without microwave irradiation and 32 scans and the darker spectrum shows the same measurement with microwave irradiation. The inset shows a spectrum with more scans zoomed in to prove that not defects are present in the unaged samples. Spinning side bands are marked with an asterisk.



## Erklärung

Hiermit versichere ich eidesstattlich, dass ich die Arbeit selbstständig verfasst und keine anderen als die von mir angegebenen Quellen und Hilfsmittel benutzt habe. Hiermit erkläre ich, dass ich die Dissertation nicht bereits zur Erlangung eines akademischen Grades eingereicht habe und dass ich nicht bereits diese oder eine gleichartige Doktorprüfung endgültig nicht bestanden habe.

Hiermit erkläre ich, dass ich Hilfe gewerblichen Promotionsberatern bzw. –vermittlern oder ähnlichen Dienstleistern weder bisher in Anspruch genommen habe noch künftig in Anspruch nehmen werde.

Hiermit erkläre ich mein Einverständnis, dass die elektronische Fassung meiner Dissertation unter Wahrung meiner Urheberrechte und des Datenschutzes einer gesonderten Überprüfung unterzogen werden kann.

Hiermit erkläre ich mein Einverständnis, dass bei Verdacht wissenschaftlichen Fehlverhaltens Ermittlungen durch universitätsinterne Organe der wissenschaftlichen Selbstkontrolle stattfinden können.

Bayreuth, den 09. Mai 2023

---

KASPER VAN DER ZWAN